Effect of o-MMT Content on Properties of Poly (vinyl chloride)/Poly (acrylonitrile styrene acrylate) Blends

Yunus Emre Kökçan[1] ✉ iD **, Yasemin Tamer[1]*** ✉ iD

[1]Department of Polymer Materials Engineering, Faculty of Engineering, Yalova University, 77100, Yalova, Turkey

Abstract: In this study, poly(vinyl chloride) (PVC)/poly(acrylonitrile styrene acrylate) (ASA)/ organophilic montmorillonite (o-MMT) nanocomposites were prepared and the effects of o-MMT content on the properties of PVC/ASA blends were investigated. The thermal stability, mechanical properties and water absorption percentages of the nanocomposites were studied. Surface morphology studies of the o-MMT containing blends were also performed using scanning electron microscopy (SEM). Thermogravimetric analysis (TGA) test results showed that o-MMT inclusion enhanced the thermal stability of PVC/ASA/o-MMT nanocomposites and the decomposition temperature at 50% weight loss (T_{d50}) increased by 7.5 $^\circ$C when the o-MMT content was 10 wt%. The tensile strength value of the neat blend was obtained as 32.51 MPa and found to increase as 36.01 MPa when the o-MMT content was 6 wt% in the system. The water absorption test results demonstrated that the water-resistance of the samples enhanced as the o-MMT content increased. Moreover, PVC/ASA blends exhibited a significant increase in the contact angle by the presence of hydrophobic o-MMT. The weathering test results demonstrated that the PVC/ASA/o-MMT nanocomposite films could be used for outdoor applications without apparently losing their properties.

INTRODUCTION

Poly(vinyl chloride), PVC) is currently the third most commercially produced plastic after polyethylene and polypropylene, which is used extensively for window profiles, transportation, construction, and packaging due to its versatility, excellent mechanical strength, high chemical resistance and low cost (1-3). PVC is produced in two types, first rigid PVC and second soft or plasticized PVC (4). Flexible, plasticized PVC is softer and capable of bending due to the addition of plasticizers and is commonly used in construction. Rigid PVC is one of the most economically and technically important thermoplastic polymers; however, the major weakness of PVC such as brittleness and poor thermal stability limits its application (5, 6).

Therefore, to give more flexibility, to enhance impact strength and to expand the application range of PVC, impact modifiers can be used as additives, or processes such as chemical modification, compounding or blending with conventional polymers can be applied. Improving desired material properties or giving new properties to PVC with these methods, have become of great academic and industrial interest and various studies have been reported in recent years (7, 8).

Among these methods, polymer blending is a versatile, handy, and low-cost method to obtain a new material with desired features by combining two or more different polymers. The low impact strength of rigid PVC can be enhanced by adding a low glass transition temperature (T_g) impact

modifiers (9). It has been shown that the impact strength of rigid PVC enhances by blending with traditional rubber/elastomers such as ethylene-vinyl acetate (EVA), chlorinated polyethylene (CPE) and acrylonitrile-butadiene rubber (NBR). But, they form semi-compatible polymers and therefore become insufficient to meet the desired material properties (10-12). Recently, styrene-based copolymers with core-shell structure such as acrylonitrile butadiene styrene (ABS), methacrylate butadiene styrene (MBS) and methacrylate acrylonitrile butadiene styrene (MABS) have been widely studied to improve the impact strength and lower thermal dimensional stability of the PVC matrix by increasing the interfacial interaction between the PVC matrix and the rubber particles (13-16).

However, for outdoor applications, blending PVC using ABS, MBS or MABS can cause lower weathering durability of the PVC and the blends tend to yellow over time due to the unsaturated polybutadiene rubber moiety that is unstable to heat and UV light (17, 18). To overcome this problem, a new thermal stable polymer, poly (acrylonitrile styrene acrylate) (ASA) having saturated main polymer chains, might be used as an impact modifier for PVC. ASA has a core-shell structure, comprising a polyacrylate rubber core which is surrounded by styrene-acrylonitrile (SAN) copolymer shell (19). PVC easily interacts with the rigid shell phase due to their respective polarities rather than the rubber core phase. The interfacial adhesion between SAN and PVC is a significant factor to ensure optimum compatibility between the softcore and PVC matrix and is influenced by the acrylonitrile content in the SAN. The polyacrylate core is usually responsible for the toughening of the rigid PVC (14, 20, 21). When exposed to UV, heat, or moisture, ASA copolymer exhibits a low level of discoloration and anti-aging performance due to the acrylic ester moiety in the matrix compared to ABS terpolymer. Furthermore, the thermal stability of the rubber core of ASA is much higher than the polybutadiene in ABS, and this is very important for the blend systems that need high processing temperatures (2, 22).

Polymer nanocomposites have remarkable potential and industrial interest in the development of advanced materials for countless applications. Nanoparticles in the form of fiber, tube, sphere or platelet are used to enhance mechanical, electrical, and thermal properties of the polymers even at low concentrations (23, 24). Montmorillonite (MMT) clay is one of the common nanofillers used for the development of new polymeric nanocomposites due to its high surface area, high aspect ratio, wide availability and relatively low cost (25). Pristine MMT clay has a hydrophilic structure and the silicate layers are held tightly together by electrostatic forces. It can form a homogeneous mixture with hydrophilic polymers such as poly(vinyl alcohol) and poly(ethylene oxide); however, it forms poor nanoclay dispersion in hydrophobic organic matrices. For instance, the dispersion of multilayer MMT clay into the PVC matrix is inhibited by incompatibility between hydrophilic layered silicate and the low polarity of PVC (26). To facilitate the compatibility, and create a homogenous mixture, surface modification is generally required. This can be easily achieved by replacing inorganic cations with organic cations that make hydrophilic MMT more organophilic. Therefore, MMT clay is often treated with alkylammonium salts to alter the surface polarity of the clay and to improve the wettability of the polymer by widening the interlayer spacing of MMT (27). So the polymer chains can easily reach the gap between the organophilic MMT (o-MMT) layers.

Several studies have reported regarding the PVC/ASA blends and its nanocomposites. Wang et al. (28) studied the influence of multi-walled carbon nanotubes (MWCNTs) on plasticizing behavior, mechanical properties and thermal stability of PVC/ASA blends, and the impact strength was found to be 83.7 % higher than pure PVC/ASA blend for MWCNT content of 0.054 wt%. Rimdusit et al. (2) discussed the effect of coconut fiber contents on mechanical, thermal, and physical properties of PVC/ASA blends, and they found a tensile strength value of 45 MPa with the addition of 50 wt% coconut fibers to the blend structure. In another study conducted by Rimdusit et al. (8), the effect of ASA content on water absorption, mechanical properties, and outdoor weathering durability of PVC/ASA blends was investigated. By increasing ASA content, a drastic increase in the impact strength of the PVC/ASA blends was observed and the highest value was obtained as 77.6 kJ/m^2 when ASA content is 50 wt%.

Although there have been various studies revealing the properties of PVC/ASA blends, authors believe that this is the first work that shows the effects of organophilic montmorillonite content on the mechanical and thermal properties, and the weatherability of PVC/ASA blends. In this research, PVC/ASA blends at a fixed ratio of 70/30 wt%, and its o-MMT nanocomposites were prepared through solution casting. The effects of the o-MMT content on physical, mechanical, thermal, and weather resistance properties of the obtained composites were determined.

MATERIALS AND METHODS

Materials
PVC powder (Suspension PVC K-70, density 0.44-0.53 g/cm^3) and ASA granules were kindly supplied by Bayegan Plastics Co. (Istanbul, Turkey) and Chemieuro (Istanbul, Turkey), respectively.

Organophilic montmorillonite (Nanomer I.31PS) was obtained from Sigma-Aldrich, which is clay modified by 15-35 wt% octadecylamine and 0.5-5 wt% aminopropyltriethoxysilane. The solvent tetrahydrofuran (THF, 99.5 %) was purchased from Sigma–Aldrich. Before solving, PVC powder and ASA granules, and o-MMT nanoparticles were dried at 80 °C for 5 h.

Preparation of PVC/ASA/o-MMT Nanocomposites Başlık 2 yana yaslanmadan yazılabilir mi?
The PVC/ASA/o-MMT nanocomposite films with different of o-MMT ratios were prepared by solution blending of PVC and ASA. In a typical preparation procedure, PVC and ASA were individually dissolved in THF; and afterward, the solutions were brought together and stirred overnight at room temperature. o-MMT dispersions were prepared in THF by using an ultrasonic homogenizer (Bandelin HD2200) for 60 min and then magnetically stirred for 24 h until the solutions became homogeneous. Subsequently, the prepared o-MMT dispersions were added to the solutions of PVC/ASA, and the resulting dispersions were placed in an ultrasonic bath for 3 h to obtain a homogeneous mixture. The dispersions were poured in Petri dishes and were allowed to dry at room temperature for 72 h, under vacuum for 24 h, and finally at 70 °C for 6 h. The obtained films were hot-pressed at 170 °C for 2 min followed by cooling to room temperature for further tests. The o-MMT content of the PVC/ASA/o-MMT nanocomposites was given in Table 1.

Characterization Methods
The Fourier transform infrared spectrophotometer (FTIR, Perkin Elmer, Spectrum 100) was used in ATR (Attenuated Total Reflection) mode in the wavenumber range 650–4000 cm^{-1} to confirm the structure of the PVC/ASA/o-MMT nanocomposites.

The thermal stability of PVC/ASA blends with various o-MMT amounts was determined using a thermogravimetric analyzer (Seiko, TG/DTA 6300) in the temperature ranges between room temperature to 800 °C at a heating rate of 10 °C min^{-1} under N_2 atmosphere.

The surface morphology of the PVC/ASA/o-MMT nanocomposite films was assessed by using a scanning electron microscope (SEM, FEI Inc., Inspect S50) operating at the 15 kV accelerating voltage in secondary electron imaging mode. The tensile fracture surface of the samples was coated with thin gold film before measurement.

Tensile properties of the neat PVC, neat ASA, PVC/ASA blend, and its nanocomposites were determined using a universal tensile test machine (Zwick/Roell) equipped with a 1 kN load cell at 25 °C according to ASTM D882. The crosshead speed was 10.0 mm min^{-1}. The test specimens with a rectangular shape (1 cm x 10 cm) and 0.8 mm thickness were cut from pressed thin plastic sheets. Mean values were obtained from five measurements of each sample.

Water absorption measurement was conducted according to gravimetric methods. Before testing, initial weights (m_i) of specimens were recorded after drying them in an oven at 80 °C for 24 h and cooled down to room temperature. These dry specimens were immediately soaked in distilled water and waited for the samples to reach constant weight by weighing periodically. These final weights (m_f) of the samples were recorded and the water absorption percentage of the samples (WA) was calculated by using the following equation:

$$WA\,(\%) = \left(\frac{m_f - m_i}{m_i} \right) \times 100 \quad \text{(Eq.1)}$$

Contact angle measurement was carried out using a contact angle meter (KSV Instruments Cam 200) by measuring the contact angle of 5 µL volume of distilled water drop on the film surface. The mean contact angle value of each sample was calculated from 5 measurements.

The density of samples was measured by water displacement method with a density kit attached to a balance (AND brand AHR-AZ model) using ethanol as a reference liquid. The mean of 5 measurements was given as the density value of each sample.

The heating-cooling cycling tests were performed. In a typical test, the sample was immersed in distilled water for 24 h at room temperature followed by freezing in a freezer at -40 °C for 24 h. Then, the sample was removed from the freezer and allowed to thaw at room temperature, and afterward, it was placed in an oven at 40 °C for another 24 h. The same procedure was repeated four times; and at the end of the test, the SEM image of the sample was taken, and the tensile test was performed to assess the property changes.

RESULTS AND DISCUSSION

The hydrophilic nature of MMT prevents the formation of homogeneous nanocomposites. Therefore, the silicate layers of MMT must be organically modified with a proper modification agent to enhance dispersion in polymer matrix before polymer/MMT composites are prepared. In this work, a commercial o-MMT modified with 15-35 wt% octadecylamine (ODA) and 0.5-5 wt% aminopropyltriethoxysilane (APTES) was used to prepare the PVC/ASA/o-MMT nanocomposites with a fixed PVC/ASA weight ratio of 70/30. Octadecylamine is a primary alkyl amine mainly used as a hydrophobic surface modifier for different

carbon nanomaterials; while APTES, an amino silane, is generally used in the chemical modification of surfaces; and acts as an adhesion promoter between the polymer and the filler (29, 30). Since the carbon chain length of organically modified MMT is decisive on the size of the interlayer space, the chemical structure of the surface modifier group is of primary importance (31). Also, there have been several research papers addressing the usage of ODA modified clay in the preparation of PVC nanocomposites (26, 32, 33).

FTIR Analysis

To identify the possible intermolecular interaction between PVC, ASA, and o-MMT nanoparticles, FTIR spectra of neat PVC, neat ASA, PVC/ASA blends, and its o-MMT nanocomposites was depicted in Figure 1a,b. For neat PVC, the characteristic peak belong to C-Cl stretching vibration was seen at 694 cm^{-1}, and the peak at 1428 cm^{-1} attributed to the C-H deformation vibration of CH$_2$ groups. The peaks at 2916 and 2854 cm^{-1} matched with the stretching vibrations of C-H bonds (34). FTIR spectrum of ASA exhibited a characteristic broad peak at 1733 cm^{-1} assigned to the C=O stretching vibration of the carboxyl group in PBA and a tiny peak at 2236 cm^{-1} belonging to C≡N stretching vibration of the nitrile group in SAN. The peaks at 1452, 1495, 1604 cm$^{-1,}$ and 701-762 cm^{-1} were attributed to the stretching and bending vibrations of the benzene ring (17, 35). Moreover, the stretching vibrations of C-H groups in benzene ring and polymer backbone were observed at 3027 cm^{-1} and 2928 cm^{-1}, respectively.

Figure 1. FTIR spectra of (a) PVC, ASA, and o-MMT, (b) PVC/ASA blend, and PVC/ASA/o-MMT nanocomposites.

FTIR spectrum of o-MMT nanoparticles exhibited a characteristic complex band at the position of about 1002 cm^{-1} attributed to the stretching vibrations of Si–O groups (Figure 1a). The peak corresponding to stretching vibrations of structural OH groups of the montmorillonite appeared at 3626 cm^{-1}. The octadecylamine intercalated into the gallery of the MMT was verified with the bands at around 2923, 2851, and 3243 cm^{-1}, for C–H asymmetric and symmetric stretching of CH$_2$ or CH$_3$, and N–H stretching of alkylammonium, respectively (36). In the FTIR spectra of PVC/ASA/o-MMT nanocomposite films, the distinctive peaks of both PVC and ASA, and the nanofiller were observed, proving the intermolecular interactions between them (Figure 1b). Moreover, the increment of o-MMT content in the nanocomposite enhanced the intensities of the characteristic o-MMT peaks (for PVC/ASA-6, PVC/ASA-8, and PVC/ASA-10).

Thermal Analysis

Thermogravimetric analysis (TGA) is an analytical technique used to characterize the decomposition and thermal stability of materials and to determine the fraction of moisture and volatile compounds present in the structure by monitoring the mass change (37). The thermal decomposition of neat PVC, neat ASA, PVC/ASA blend, and its o-MMT composites investigated thermogravimetrically. The thermal weight loss curves of samples were shown in Figure 2 a,b. On the TGA thermogram of neat PVC, the observed first step degradation from room temperature to about 160 °C was related to the removal of trapped THF and volatile compounds. As seen from the curve, two main weight loss regions occurred; the first weight loss region up to 350 °C corresponding to dehydrochlorination of polymer, and the second main weight loss in the temperature range between 410–530 °C due to the formation of volatile aromatic compounds and pyrolysis to low hydrocarbons (38,39). It is clear from Figure 2a that ASA had the highest initial decomposition temperature due to the presence of the SAN shell of ASA. The degradation profile of PVC/ASA between 260 and 400°C exhibited both the dehydrochloration of PVC and the degradation of ASA.
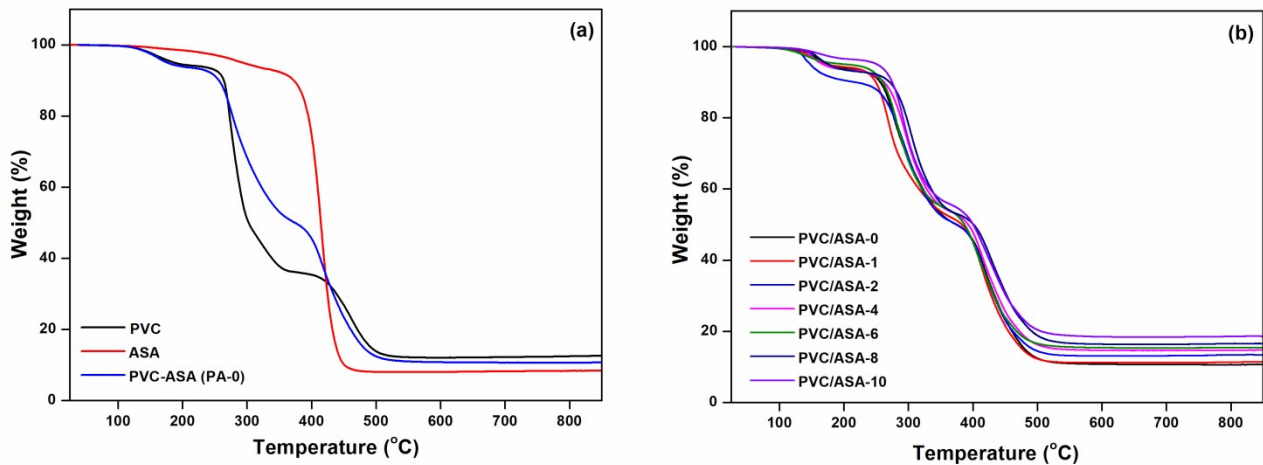
Figure 2. TGA thermograms of (a) neat PVC, neat ASA, and PVC/ASA blend, (b) PVC/ASA/o-MMT nanocomposites.

Figure 2b displayed the TGA thermograms of PVC/ASA/o-MMT nanocomposite films which were shifted to higher temperatures with the addition of o-MMT nanoparticles and their increased amounts in the PVC/ASA blend matrix. This result indicated the strong interaction between the components of the blend, thus led to restricted mobility of the polymer molecules which took part in the degradation process. Therefore, increased o-MMT amounts contributed to the increase in thermal stability (40).

Burada 1 satır fazladan boşluk var sanırım.

The thermal stability of a material can be characterized as the temperature at which 50 % mass is retained or lost (T_{d50}) (41). The T_{d50} and residue values of nanocomposites were given in Table 1. The T_{d50} of PVC/ASA/o-MMT nanocomposites increased by about 26 °C as a function of o-MMT content. Moreover, the residual mass amounts were found to be increased with increasing o-MMT amounts, as expected.

Table 1. Thermal analysis and tensile properties of neat PVC, neat ASA, PVC/ASA blend and its nanocomposites at various o-MMT contents.

Samples	o-MMT content (wt%)	T_{d50}[a] (°C)	Char yield[b] (wt%)	Tensile Strength (MPa)	Tensile Modulus (GPa)
PVC	0	302.30	12.76	37.63 ± 0.97	1.86 ± 0.18
ASA	0	414.45	8.48	27.88 ±1.42	1.27 ± 0.92
PVC/ASA-0	0	374.09	10.00	32.51 ± 2.24	1.48 ± 0.73
PVC/ASA-1	1	375.10	11.50	32.55 ± 1.72	1.48 ± 0.55
PVC/ASA-2	2	382.73	13.50	34.79 ± 2.43	1.46 ± 0.82
PVC/ASA 4	4	386.80	14.90	35.60 ± 0.97	1.70 ± 0.47
PVC/ASA-6	6	392.50	15.50	36.01 ± 1.75	1.76 ±0. 19
PVC/ASA-8	8	400.10	16.80	31.42 ± 1.34	1.45 ±0. 81
PVC/ASA-10	10	402.10	18.70	27.82 ± 1.18	0.54 ± 1.12

[a] Temperature at which 50% weight loss was verified by TGA.
[b] The weight percentage of undecomposed material after TGA analysis at 800 °C.

Tensile Properties

The tensile properties of neat PVC, neat ASA, and PVC/ASA blends with different o-MMT content were given in Figure 3 and Table 1. The tensile strength and tensile modulus of neat PVC were 37.630 MPa and 1.862 GPa whereas those of ASA were 27.880 MPa and 1.269 GPa, respectively. PVC/ASA blend displayed tensile strength and tensile modulus values as 32.510 MPa and 1.478 GPa, respectively; that is between neat PVC and neat ASA, as also being predicted by a rule of mixture. Previous studies in the literature such as PVC/ABS blends (42, 43), PC/ASA/SAN blends (44), and the PC/ABS blend (45) have also reported similar behavior.
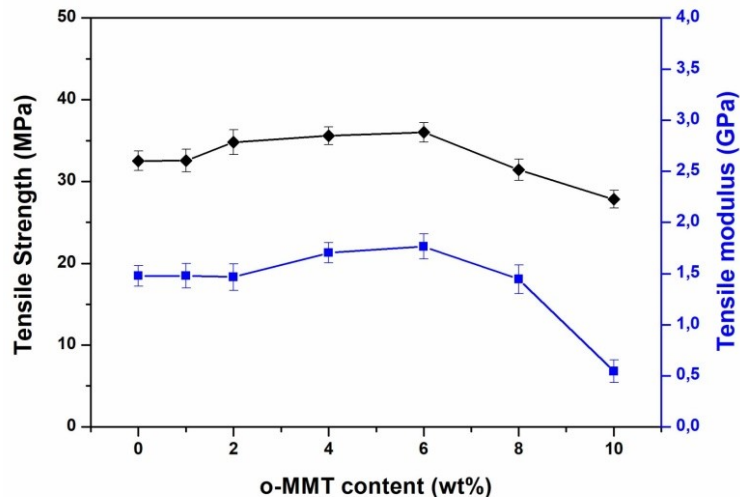
Figure 3. Tensile strength and tensile modulus of PVC/ASA/o-MMT nanocomposites. The data are represented as mean ± standard deviation (n = 5).

For PVC/ASA/o-MMT nanocomposites, the tensile strength initially remained unchanged, and then an increment was observed with further increasing o-MMT content. Although low concentrations of filler materials seemed ineffective, they contributed to load distribution as the concentration of filler materials increased (46). For instance, the tensile strength of the nanocomposites increased from 32.510 to 36.010 MPa when the o-MMT amount increased from 2 to 6 wt%. As can be seen from Figure 4, the tensile properties of PVC/ASA blends were negatively influenced by the high amount of o-MMT (10 wt%) used. This could be attributed to the poor dispersity of o-MMT and thus the formation of agglomerates. Homogeneous dispersion of nanofillers in the matrix is crucial to obtain nanocomposites with good mechanical properties (47).

In the case of increasing o-MMT amounts, tensile modulus showed similar behavior with tensile strength. As the o-MMT content increased up to a certain amount, the tensile modulus of PVC/ASA nanocomposites was found to increase, suggesting that o-MMT contributed to an improved stiffness of the nanocomposite (Figure 3). For example, by the increase in the o-MMT amount from 2 to 6 wt%, the tensile modulus value increased from 1.478 to 1.764 GPa.

SEM Analysis
SEM micrographs of the tensile fracture surface of the samples were illustrated in Figure 4. Neat PVC exhibited typical rigid and brittle fracture morphology with a relatively smooth surface (17, 48). The fracture surface of the PVC/ASA blend (Figure 4) appeared rougher than pure PVC and

exhibited microlayer structure due to the core-shell morphology of ASA with internal PBA core layer and outer SAN shell layer (28, 49). The structure gained some ductile characteristics with the incorporation of ASA and a corrugated and irregular fracture surface was observed.

As seen in Figure 4, the fracture surface of PVC/ASA/o-MMT nanocomposites was also rough as the neat blend, and there was no obvious change in SEM micrographs with the increase in the o-MMT content. SEM images of nanocomposites clearly showed that the good dispersion of o-MMT was achieved without the formation of any particle clusters, and most of the o-MMT was embedded in the PVC/ASA matrix. For the nanocomposites containing 1-6 wt% of o-MMT, observation of no gaps, cavity, or agglomerates in the fracture surface indicated the good interfacial adhesion between filler and matrix. This finding was also consistent with the improved tensile properties of the PVC/ASA/o-MMT nanocomposites. Increasing o-MMT content from 6 wt% to 8-10 wt% resulted in the formation of a rough surface with some holes throughout the fractured sample surface (Figure 4). Although not detectable from SEM images, it was believed that o-MMT aggregates were formed in the case of PVC/ASA-8 and PVC/ASA-10 nanocomposites. As can be seen in the higher magnification SEM image of PVC/ASA-10 (Figure 4), the regions marked by red circles were thought to be related to the agglomeration of o-MMT nanoparticles in the polymer matrix. Besides, the weak mechanical properties obtained in this high o-MMT content could be attributed to the formation of these agglomerates.
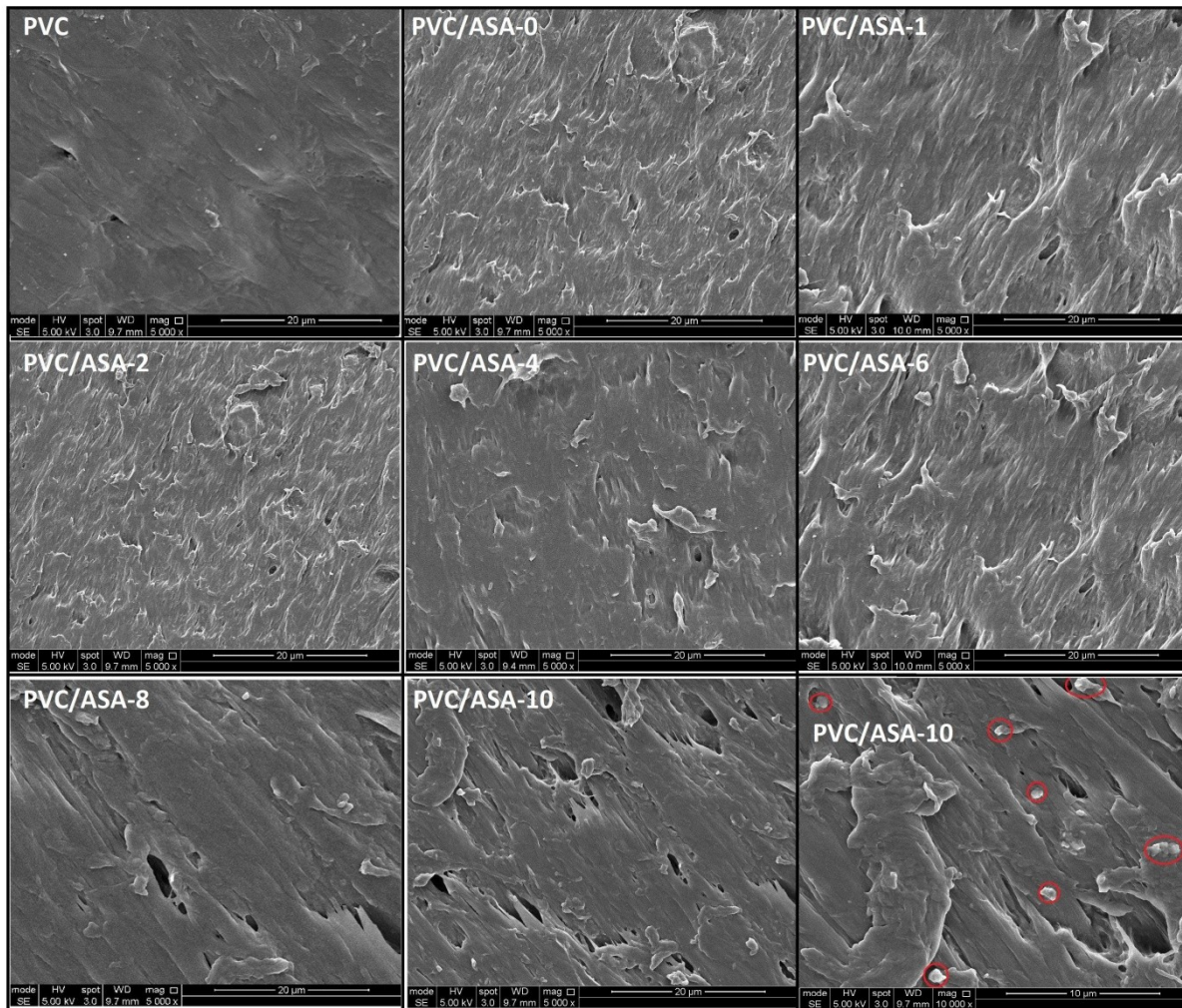
Figure 4. SEM micrographs of PVC and PVC/ASA/o-MMT nanocomposites

Water Absorption, Contact Angle and Density Analysis

The capability of plastics to absorb moisture is a significant durability parameter to understand the performance of the materials. The moisture/water absorption can result in defects in the polymeric material such as swelling or dissolution of polymeric material, extraction of water-soluble components, or changes in mechanical (tensile strength, impact strength, elasticity) and electrical performance (2, 50).

The results of water absorption percentages as a function of time were shown in Figure 5. After soaking for around 24 hours, the water absorption percentage of pure PVC was 0.08 wt% while PVC/ASA blend showed a higher value of 0.29 wt%. The reason was the high water absorption value of pure ASA of about 0.42 wt% due to its highly polar acrylonitrile moiety. As depicted in Figure 5, no significant changes were observed in the water absorption percentages of the nanocomposites with small amounts of o-MMT incorporation. (PVC/ASA-1 and PVC/ASA-2) Then, the water uptakes of nanocomposites were found to decrease from 0.29 wt% to 0.10 wt% as the amount of 0-MMT reaches 4 wt% to 8 wt%. Furthermore, the absorption increased to about 0.20 wt% with the addition of 10 wt% o-MMT to the structure due to the formation of agglomerates. This phenomenon was also proved by contact angle measurement.
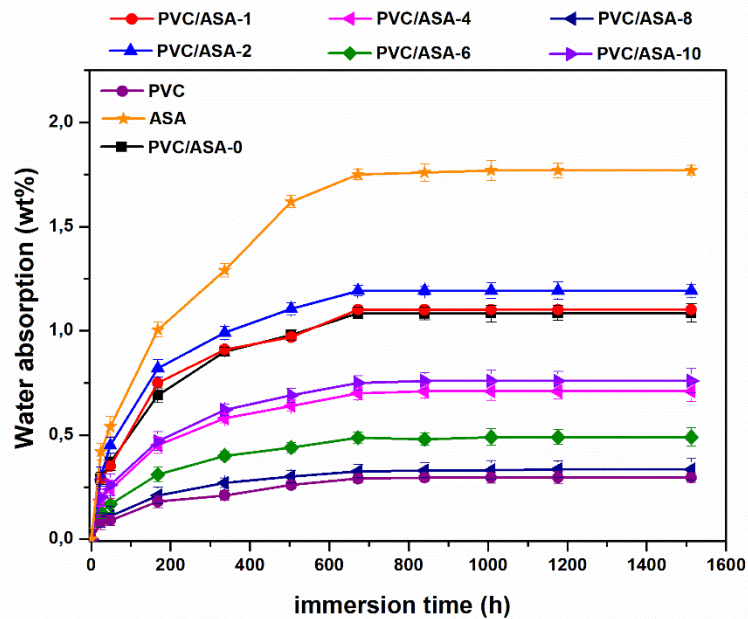
Figure 5. Water absorption of PVC, ASA, PVC/ASA, and PVC/ASA/o-MMT nanocomposites. The data are represented as mean ± standard deviation (n = 3).

The measured water contact angle values of the nanocomposites as a function of o-MMT content were given in Figure 6. The contact angle value was found to be 97° and 87° for the pure PVC and ASA, respectively. The PVC/ASA blend prepared by adding 30 wt% ASA showed a contact angle of about 94° between these values, similar to water absorption results. The contact angle measurement gives information about the affinity of the surface for water. Higher contact angle values show the hydrophobic surfaces that are more resistant against water while lower values represent hydrophilic surfaces that have an affinity for water. The contact angle value is directly related to the chemical composition of the surface (51).
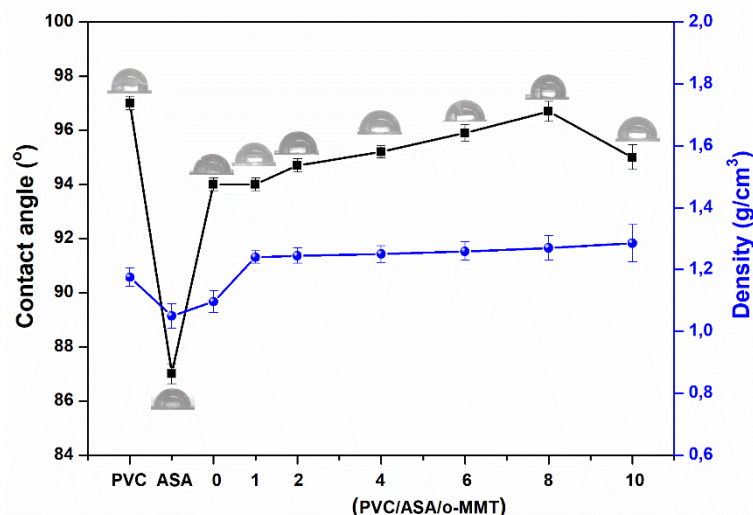

Figure 6. Contact angle and density values of PVC, ASA, PVC/ASA, and PVC/ASA/o-MMT nanocomposites. The data are represented as mean ± standard deviation (n = 5).

The incorporation of hydrophobic o-MMT into the PVC/ASA blend matrix caused no significant differences in the physicochemical surface characteristics of nanocomposites for PVC/ASA-1 and PVC/ASA-2, while its increasing amounts considerably increased the surface contact angle of PVC/ASA nanocomposites (Figure 6). As expected, the increment in o-MMT content enhanced the hydrophobic character of the nanocomposite surface. However, a sudden decrease in contact angle value of about 95° was observed for the blends with high o-MMT content (PVC/ASA-10) due to agglomeration of o-MMT particles. As the nanoparticles aggregate, the nanoparticle and

642

polymer interface became narrower and non-homogeneous surfaces were formed, and this led to a decrease in the hydrophobicity effect of the o-MMT. The contact angle measurements were consistent with SEM analysis and tensile test results.

Density measurement of a nanocomposite is an important physical parameter and can be effectively used to ensure product quality and homogeneity and to monitor manufacturing processes. For instance, the presence of voids or defects has several negative effects on the material properties particularly mechanical properties of the composite (8). The experimental densities determined by weighing the sample in air and then in ethanol of known density were given in Figure 6. It can be seen that PVC/ASA structure gave an experimental density value of about 1.096 g cm^{-3} between the density of the neat PVC of 1.175 g cm^{-3} and the density of the neat ASA of 1.050 g cm^{-3}. The theoretical density of PVC/ASA (70/30 wt%) blend was also estimated according to the rule of a mixture by using the measured density values of PVC and ASA, and it is found to be 1.137 g cm^{-3}. The obtained theoretical density value is in good agreement with the measured experimental density value, suggesting the negligible amount of void in

the blend sample. Thus, the homogeneity of the obtained structure proved again. The density of PVC/ASA/o-MMT composites as increasing o-MMT content to 1, 2, 4,6,8, and 10 wt% was measured to be 1.240, 1.245, 1.250, 1.259, 1.270 and 1.285 g cm^{-3}, respectively (Figure 6). Based on the measured density values, o-MMT reinforced composites showed higher density values compared to neat PVC/ASA blend, and the obtained density values tended to increase slightly with increasing o-MMT amounts.

Weathering Test

Plastic materials are exposed to the effects of climate changes (cool, heat, rain, UV, etc.) during their life cycle. Fluctuations in ambient temperature directly affect the mobility of the long polymer chains, and thus the final properties of plastics such as color, brilliance, hardness, flexural, or impact strength. Accordingly, it is important to know how polymers perform when subjected to external heat changes. High temperatures can cause the mobility of the polymer chains and crystalline structure changes occur, or temperatures lower than Tg of material immobilize polymer chains and the material becomes fragile (52).

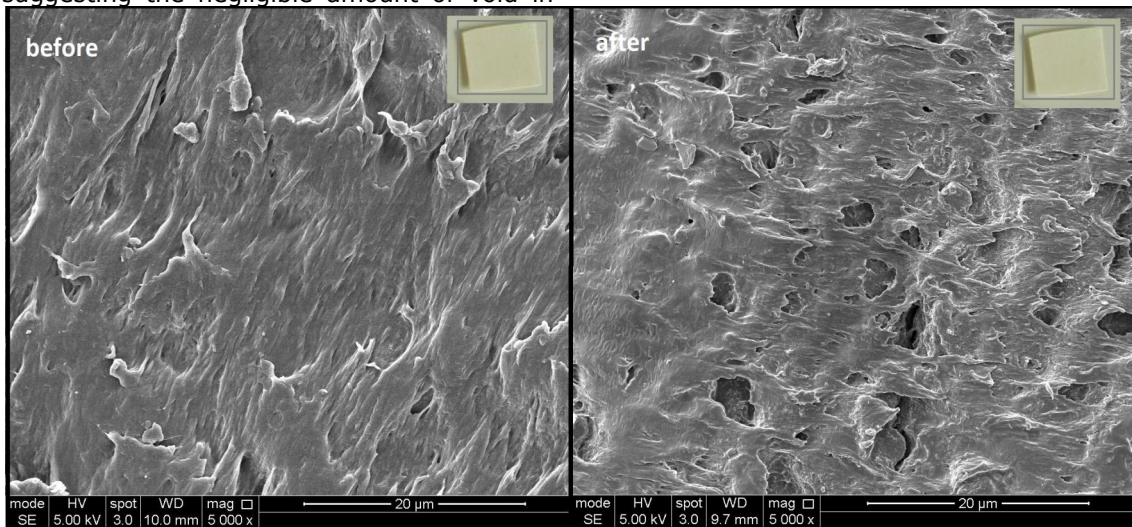Figure 7 paragrafa çok yakın. 1 satır boşluk bırakılabilir mi?

Figure 7. SEM micrographs of PVC/ASA-6 before and after four heating-cooling cycles.

A modified freeze-thaw cycling test was applied to determine the effect of ambient temperature changes on the durability of PVC/ASA-6 nanocomposite having the best material properties. After four heating-cooling cycles, comparisons were performed on the mechanical properties and morphology of the exposed and unexposed samples. SEM images of the two samples were taken of the fracture surface after tensile testing to assess if temperature changes affected the interfacial adhesion between o-MMT and PVC-ASA matrix. As seen from the embedded images in Figure 8, no changes in the visual appearance of PVC/ASA-6

samples were detected such as crack formation, color change, or surface roughness. However, there were some gaps or crevices in the SEM image (Figure 7) of the exposed PVC/ASA-6 sample; these were probably due to the decreased interfacial adhesion between PVC and ASA polymers.

The tensile strength and tensile modulus of unexposed PVC/ASA-6 samples were 36.010 MPa and 1.764 GPa; whereas the values decreased to 34.920 MPa and 1.645 GPa, respectively, after exposure to four heating-cooling cycles. This decline could be attributed to the degradation of interfacial

adhesion between PVC and ASA and hence low-stress transfer at the interface as a result of exposure to moisture. Besides, the sample was immersed in water to ensure enough moisture before freeze-thaw cycles and then, the volume expansion of water occurred while the sample freezes down. Then, removal of the water during the thawing process might result in voids which could lead to mechanical failure (Figure 7) (53).

CONCLUSIONS

In this research, the fabrication of PVC/ASA/o-MMT nanocomposites with a fixed PVC/ASA weight ratio of 70/30 was demonstrated. The resultant nanocomposites were characterized using FTIR, TGA, SEM, and tensile test units. The effects of o-MMT content on the mechanical properties, thermal properties, and water absorption of the PVC/ASA blends examined in detail. With the addition of 6 wt % o-MMT, the highest tensile strength value, i.e. 36.01 MPa was obtained for PVC/ASA-6 nanocomposite. Also, the thermal stability of PVC/ASA/o-MMT nanocomposites improved with o-MMT incorporation to the blend; the temperature referring 50% mass loss, T_{d50} increases as a function of o-MMT content. Furthermore, water absorption of these nanocomposites slightly decreased with the o-MMT content due to increased hydrophobicity of the structure. Weathering test results demonstrated that the loss in tensile properties due to the exposure to heating-cooling cycles was not critical, although some voids were observed on the PVC/ASA nanocomposite fracture surface.

ACKNOWLEDGMENT

REFERENCES

1. Sree KB, Kumar YM, Gopal NO, Ramu C. Preparation and characterization of pure and copper-doped PVC films. J Polym Eng. 2017;37(1):83–92. DOI:10.1515/polyeng-2015-0446.

2. Sarawut R, Siriporn D, Patima W, Duangporn S, Sunan T. Characterization of coconut fiber-filled polyvinyl chloride/acrylonitrile styrene acrylate blends. J Reinf Plast Comp. 2011;30(20):1691–1702 DOI:10.1177/0731684411427484.

3. Bijhanmanesh MJ, Etesami N, Darvishi R. Continuous dosing of fast initiator during vinyl chloride suspension polymerization: thermal stability of PVC resin. J Appl Polym Sci. 2017;134(1):44480-87. DOI:10.1002/APP.44480.

4. Zhang X, Zhang J. Effect of temperature on the impact behavior of PVC/ASA binary blends with various ASA terpolymer contents. J Polym Eng. 2019;39(5):407–414. DOI:10.1515/polyeng-2018-0349.

5. Yu J, Feng P, Zhang H. Effects of core-shell acrylate particles on impact properties of chlorinated polyethylene/polyvinyl chloride blends. Polym Eng Sci. 2010;50(2):295-301. DOI:10.1002/pen.21539.

6. Zhang Z, Wang S, Zhang J, Zhu W, Tian T. Remarkably improved toughness and thermal stability of poly (vinyl chloride) (PVC)/poly (α-methylstyrene-acrylonitrile) (α-MSAN) blend with the assistance of two impact modifiers. Polym Test. 2016;51:1-5. DOI:10.1016/j.polymertesting.2016.02.003.

7. Zhang Z, Chen S, Zhang J. Improvement in the heat resistance of poly(vinyl chloride) profile with styrenic polymers. J Vinyl Addit Techn. 2011;17(2):85-91. DOI:10.1002/vnl.20251.

8. Rimdusit S, Wongmanit P, Damrongsakkul S, Saramas D, Jubsilp C, Dueramae I. Characterizations of poly(vinyl chloride)/acrylonitrile styrene acrylate blends for outdoor applications. Eng J. 2013;18(1):105-118. DOI:10.4186/ej.2014.18.1.105.

9. Mao Z, Zhang J. Largely improved the low temperature toughness of acrylonitrile-styrene-acrylate (ASA) resin: Fabricated a core-shell structure of two elastomers through the differences of interfacial tensions. Appl Surf Sci. 2018;444,345–354. DOI:10.1016/j.apsusc.2018.03.066.

10. You F, Chen G, Zou J, Yang Z, Guo S. The experimental results and simulation of temperature dependence of brittle-ductile transition in PVC/CPE blends and PVC/CPE/nano-CaCO3 composites. J. Appl. Polym. Sci. 2012,123(3), 1833-1842. DOI:10.1002/app.34662.

11. Chen M, Wang S, Zhou C, Liu Z, Zhang H. Toughening Poly (Vinyl Chloride) by PS/PB/PMMA Three-Layer Particles. Polym Plast Dent Eng. 2013;52(8):814-819. DOI:10.1080/03602559.2013.763359.

12. Markarian J. Impact modifiers: how to make your compound tougher. Plast Addit Compd 2004;6(3):46-49. DOI:10.1016/S1464-391X(04)00203-X.

13. Wang HL, Tan HS, Li YJ, Yu YZ. Phase morphology and dynamic mechanical behavior for

MIS toughened polyvinyl chloride. J Appl Polym Sci. 2013;129(6):3466-3472. DOI:10.1002/app.39095.

14. Wu S, Chen M, Wu G, Zhou C. Variation of core-shell structural particles and their toughening behavior in poly (vinyl chloride) (PVC) matrix. J Polym Res (2015);22:82. DOI:10.1007/s10965-015-0730-6.

15. Scott G, Tahan M. The photo-oxidation of PVC and impact modified PVC. Chemical changes. Eur Polym J. 1977;13(12):989-996. DOI:10.1016/0014-3057(77)90171-9.

16. Zhang LX, Zhou C, Sun SL, Ren L, Ma XL, Zhang MY, Zhang HX. Study of compatibility, morphology structure and mechanical properties of CPVC/ABS blends. J Appl Polym Sci. 2010;116(6):3448-3454. DOI:10.1002/app.31855.

17. Zhang Y, Xu Y, Song Y, Zheng Q. Study of poly(vinyl chloride)/acrylonitrile–styrene–acrylate blends for compatibility, toughness, thermal stability and UV irradiation resistance. J Appl Polym Sci. 2013;130(3):2143-2151. DOI:10.1002/APP.39405.

18. Pickett JE, Gibson DA, Gardner MM. Effects of irradiation conditions on the weathering of engineering thermoplastics. Polym Degrad Stab. 2008;93(8):1597-1606. DOI:10.1016/j.polymdegradstab.2008.02.009.

19. Du YG, Gao JG, Yang JB, Liu XQ. Dynamic rheological behavior and mechanical properties and of PVC/ASA blends. J Polym Res. 2012;19(11):9993. DOI:10.1007/s10965-012-9993-3.

20. Gawade AR, Lodha AV, Joshi PS. PVC/ABS blends: Thermal and morphological studies. J Macr Sci. Part B: Physics. 2008;47(1):201–210. DOI:10.1080/00222340701748701.

21. Yin B, Hakkarainen M. Core–shell nanoparticle–plasticizers for design of high-performance polymeric materials with improved stiffness and toughness. J. Mater. Chem. 2010;21(24):8670-8677. DOI:10.1039/C1JM10624D.

22. Szamborski G. Superior balance of weatherability and impact performance with acrylic-capped vinyl siding. J Vinyl Addit Tech. 2007;13(1):26-30. DOI:10.1002/vnl.20094.

23. Crosby AJ, Lee JY. Polymer nanocomposites: The "nano" effect on mechanical properties. Polym. Rev. 2007;47(2):217-229. DOI:10.1080/15583720701271278.

24. Pagacz J, Pielichowski K. PVC/MMT nanocomposites. J Therm Anal Calorim 2013;111(2):1571-1575. DOI:10.1007/s10973-012-2484-2.

25. Guo F, Aryana S, Han Y, Jiao Y. A review of the synthesis and applications of polymer–nanoclay composites. Appl Sci. 2018;8(9):1696. DOI:10.3390/app8091696.

26. Ismail H, Munusamy Y. Polyvinyl Chloride/Organoclay Nanocomposites: Effects of Filler Loading and Maleic Anhydride. J Reinf Plastc Comp. 2007;26(16):1681-1694. DOI: 10.1177/0731684407081446.

27. Mondragon M, Valdes SS, Sanchez-Espindola ME, Rivera-Lopez JE. Morphology, mechanical properties, and thermal stability of rigid PVC/Clay nanocomposites. Polym Eng Sci. 2011;51(4):641-646. DOI:10.1002/pen.21867.

28. Wang C, Li N, Huo L, Gao J. Effect of carbon nanotube on the mechanical, plasticizing behavior and thermal stability of PVC/poly(acrylonitrile–styrene–acrylate) nanocomposites. Polym Bul. 2015;72(8):1849–1861. DOI:10.1007/s00289-015-1376-6.

29. Li W, Tang XZ, Zhang HB, Jiang ZG, Yu ZZ, Du XS, Mai YW. Simultaneous surface functionalization and reduction of graphene oxide with octadecylamine for electrically conductive polystyrene composites. Carbon. 2011;49(14)4724-4730. DOI:10.1016/j.carbon.2011.06.077.

30. Pasternack RM, Amy SR, Chabal YJ. Attachment of 3-(aminopropyl) triethoxysilane on silicon oxide surfaces: Dependence on solution temperature. Langmuir. 2008;24(22):12963-12971. DOI:10.1021/la8024827.

31. Liang ZM, Wan CY, Zhang Y, Wei P, Yin J. PVC/Montmorillonite Nanocomposites Based on a Thermally Stable, Rigid-Rod Aromatic Amine Modifier. J Appl Polym Sci. 2004;92:567-575. DOI:10.1002/app.20041.

32. Shimpi NG, Mishra S. Influence of surface modification of montomorillonite on properties of PVC nanocomposites. J Comp Mat. 2011;45(23):2447–2453. DOI: 10.1177/0021998311401095.

33. Wan C, Qiao X, Zhang Y, Zhang Y. Effect of different clay treatment on morphology and mechanical properties of PVC-clay nanocomposites. Polym Test. 2003;22(4):453-461. DOI: 10.1016/S0142-9418(02)00126-5

34. Ramesh S, Leen KH, Kumutha K, Arof AK. FTIR studies of PVC/PMMA blend based polymer electrolytes. Spectrochim Acta Part A Mol Biomol

Spectrosc. 2007;66(4-5):1237-1242. DOI:10.1016/j.saa.2006.06.012.

35. Orlov AS, Kiselev SA, Kiseleva EA, Budeeva AV, Mashukov VI. Determination of styrene-butadiene rubber composition by attenuated total internal reflection infrared spectroscopy. J Appl Spectrosc. 2013;80(1):47-53. DOI:10.1007/s10812-013-9719-2.

36. Chuayjuljit S, Thongraar R, Saravari O. Preparation and properties of PVC/EVA/Organomodified montmorillonite nanocomposites. J Reinf Plast Comp. 2008;27(4):431-442. DOI:10.1177/0731684407084124.

37. Datta P, Guha C, Sarkhel G. Effect of Zn^{+2} poly(ethylene-co-methacrylic acid) ionomer on mechanical properties, thermal properties, morphology and process rheology of acrylonitrile styrene acrylate (ASA) terpolymer. Polym Plast Tech Eng. 2014;53(1):80-89. DOI:10.1080/03602559.2013.843692.

38. Hasan M, Kumar R, Barakat MA, Lee M. Synthesis of PVC/CNT nanocomposite fibers using a simple deposition technique for the application of Alizarin Red S (ARS) removal. RSC Adv. 2015;5:14393-14399. DOI:10.1039/C4RA16043F.

39. Joseph J, Deshmukh K, Chidambaram K, Faisal M, Selvarajan E, Sadasivuni KK, Ahamed MB, Khadheer Pasha SK. Dielectric and electromagnetic interference shielding properties of germanium dioxide nanoparticle reinforced poly(vinyl chloride) and poly(methylmethacrylate) blend nanocomposites. J Mat Sci: Mat Elect. 2018;29(23):20172–20188. DOI:10.1007/s10854-018-0150-6.

40. Sathyanarayana S, Olowojoba G, Weiss P, Caglar B, Pataki B, Mikonsaari I, Hübner C, Henning F. Compounding of MWCNTs with PS in a twin-screw extruder with varying process parameters: Morphology, interfacial behavior, thermal stability, rheology, and volume resistivity. Macromol. Mater. Eng. 2013;298(1):89-105. DOI:10.1002/mame.201200018.

41. Datta P, Guha C, Sarkhel G. Thermal, dynamic mechanical, and creep behavior of carbon nanotube reinforced ASA/Na-ionomer blend. Polym Adv Technol. 2015;26(10):1294–1301. DOI:10.1002/pat.3567.

42. Rimdusit S, Atthakorn D, Damrongsakkul S, Saramas D, Tiptipakorn S. Mechanical, thermal, and water uptake characteristics of woodflour-filled polyvinyl chloride/acrylonitrile butadiene styrene

blends. J Appl Polym Sci. 2012;124(2):943-950. DOI:10.1002/app.35130.

43. Belhaneche-Bensemra N, Bedda A. Study of the properties of PVC /ABS blends. Polymer Reactive Processing, Stabilisation and Functionalisation. Italy: Wiley-VCH Verlag GmbH;2001.

44. Han Y, Tai ZX, Zhou C, Zhang MY, Zhang HX, Liu FQ. Influence of blend composition on the mechanical properties and morphology of PC/ASA/SAN ternary blends. Polym Bull. 2009;62(6):855-866. DOI:10.1007/s00289-009-0057-8.

45. Greco R, Astarita MF, Dong L, Sorrentino A. Polycarbonate/ABS blends: Processability, thermal properties, and mechanical and impact behavior. Adv Polym Technol. 1994;13(4):259-274. DOI:10.1002/adv.1994.060130402.

46. Ghazinezami A, Khan WS, Jabbarnia A, Asmatulu R. Impacts of nanoscale inclusions on fire retardancy, thermal stability, and mechanical properties of polymeric PVC nanocomposites. J Therm Eng. 2017;3(4-5):1308-1318. DOI:10.18186/journal-of-thermal-engineering.330150.

47. Abu-Abdeen M. Static and dynamic mechanical properties of Poly(vinyl chloride) loaded with aluminum oxide nanopowder. Mat. Des. 2012;33:523–528. DOI:10.1016/j.matdes.2011.04.059.

48. Saengiet B, Unob F, Srikulkit K. Effect of Styrene-Methyl Methacrylate/Styrene-Butadiene Rubber on Properties of Poly(vinyl chloride). J. Met. Mater. Miner. 2014;24(2):9-13. DOI:10.14456/jmmm.

49. Zhang X, Zhang J. Effect of core–shell structures of acrylonitrile–styrene–acrylate (ASA) terpolymer on the properties of poly(vinyl chloride) (PVC)/ASA blends: Miscibility, toughness, and heat resistance. J. Appl. Polym. Sci. 2018;135(43):46839(1-8). DOI:10.1002/app.46839.

50. Miri V, Persyn O, Lefebvre JM, Seguela R. Effect of water absorption on the plastic deformation behavior of nylon 6. Europ Polym J. 2009;45(3):757-762. DOI:10.1016/j.eurpolymj.2008.12.008.

51. Pedroso AG, Rosa DS. Effects of the compatibilizer PE-g-GMA on the mechanical, thermal and morphological properties of virgin and reprocessed LDPE/corn starch blends. Polym Adv Technol. 2005;16:310-317. DOI:10.1002/pat.581.

52. Pilarski JM, Matuana LM. Durability of wood flour-plastic composites exposed to accelerated freeze–thaw cycling. Part I. Rigid PVC matrix. J Vinyl Addtv. Techn. 2005;11(1):1-8. DOI:10.1002/vnl.20029.

53. Tajvidi M, Haghdan S. Effects of accelerated freeze–thaw cycling on physical and mechanical properties of wood flour/PVC Composites. J Reinf Plastc Comp. 2009;28(15):1841-1846. DOI:10.1177/0731684408090367.

648. sayfa boş ve gereksiz gözüküyor.

RESEARCH ARTICLE

The Effects of Blending Ratio of Poly(lactic acid)/POSS Cored Star Poly(ε-caprolactone) Biopolymers

M. DANDAN DOĞANCI ✉ iD

Department of Chemistry and Chemical Processing Tech., Kocaeli University, Kocaeli, Turkey

Abstract: A$_8$-type eight-arm star-shaped poly(ε-caprolactone) (PCL) polymers with polyhedral oligomeric silsesquioxane (POSS) (SP) core having different molecular weight with different chain lengths (n=10, 20, 30, and 50 repeating units) were synthesized via arm-first approach by a combination of ring-opening polymerization (ROP) and "click" chemistry reactions. The obtained polymers were then melt-blended with neat poly(lactic acid) (PLA) to improve some of the properties like the toughness of PLA. These blends were prepared depending on the blend ratio (95/5 and 80/20 wt%) via utilizing laboratory-scale twin-screw mini extruder to examine morphological, thermal, and mechanical properties of PLA/SP composite as a function of SP and blending ratio. Also, the PLA/SP composites containing a blend ratio of 90/10 wt%, which were prepared in the previous study, was used to compare with other composite having different blend ratio. The incorporation of SP polymers improved some of the mechanical properties of PLA. It was verified that SP20 (n=20) is the most proper SP-type for enhancing the mechanical behavior of PLA at a blending ratio of 90/10. Also, 1,4-phenylene diisocyanate (PDI), which was used as a commercial compatibilizer, was incorporated to blends at a fixed amount (%1). It is concluded that the incorporation of SP polymers into PLA matrix decreased the tensile modulus with increasing blending ratio and increased the elongation at break values in the presence of PDI.

INTRODUCTION

Poly(lactic acid) (PLA) and poly(ε-caprolactone) (PCL) are two crucial biodegradable aliphatic polyesters that are commonly used together, although the two polymers are incompatible. These polymers have quite different features, such as the fact that PLA is fragile, and PCL is ductile. The mechanical properties of PLA generally enhanced by adding PCL polymers to PLA matrix with different methods such as blending, synthesizing copolymers, etc. (1-3). The miscibility, viscoelastic, thermodynamic, and mechanical behaviors of the PLA/PCL blend system have been extensively studied. Broz and coworkers produced a series of PLA/PCL blends via different mass fractions to examine the mechanical and structural characteristics of the blends. They concluded that these two biodegradable polymers, PLA and PCL, are immiscible, and there occurs some adhesion between two polymers when the PCL phase is dominant (4). Simoes et al. also reported some degree of adhesion between PLA and PCL biodegradable polymers and determined that PCL acted like a plasticizer for PLA by improving the ductility, flexibility, and mechanical properties of PLA (5). Rao and coworkers studied with these two polymers and examined 80/20% PLA/PCL blend exhibited the highest impact strength and elongation at break among the various blend proportions (6, 7). Vainio et al. synthesized ε-caprolactone and L-lactide (ε-CL/L-LA) copolymers with different compositions (40/60, 60/40, and

80/20) and found that tensile properties were much higher than pure polymers (8) .

Recently, multiarmed star-shaped polymers have attracted increasing attention due to their excellent properties and three-dimensional structures. The star-shaped polymers are generally characterized by lower glass transition temperature (T_g) and melt viscosity. They are more compact and less crystalline in comparison to linear counterparts of the same molecular weights (3, 9). The star-branched block and random copolymers of LA and ε-CL are a candidate for enhancing the toughness of PLA. Several studies in the literature prepared blends of PLA with synthesized star-shaped polymers (3, 9, 10). Deokar et al. prepared three, four, and six-armed random and block star polymers of PCL-PLA and blended with PLA. They concluded that maximum enhancement in elongation and toughness was observed with six-armed block copolymers (3). Li et al. produced a series of star-shaped PCLs with different molecular weights and mixed with PLA to obtain blended fiber membranes via electrospinning technique. They examined the influence of multiple-armed structure on the mechanics and thermodynamics feature of the electrospun fiber membranes (9). Qin et al. prepared blends of PLA and star-shaped poly(ε-caprolactone-*co*-L-lactide) (s-PCLA) at varying compositions and concluded that PLA/s-PCLA blends showed limited miscibility and better elongation at break (10).

Polyhedral oligomeric silsesquioxane (POSS) are new generation nanofillers with a general formula of $(RSiO_{1.5})_n$. It is generally used to improve the mechanical and thermal properties of PCL, PLA, and its blends by physical blending or chemical reactions (11-19). It can also be utilized as a polymerizable monomer or initiator to synthesize star-shaped polymers. Sun and He synthesized (octaPOSS)-initiated poly(ε-caprolactone-*co*-lactide) (PCLLA) as rubbery core and mixed it with commercial poly(L-lactide) (PLLA) by solution blending for toughening. The obtained biodegradable nanocomposites showed higher elongation at break to that of pure PLA (20). Pan et al. synthesized star POSS-$(PLLA)_x$ (x=6, 9, 11, and 12) polymers and blended with PLA. The effects of molecular geometry and arm length of star polymers on crystallinity and properties of PLA were investigated. They concluded that the highest crystallinity was observed with 12-armed POSS-$(PLLA)_{12}$ blends (12). Liu et al. synthesized POSS-$(PLLA)_8$ and blended this polymer with PLA via the solvent casting method. The interfacial interactions were considerably developed, and a good increase was observed in toughness and mechanical properties (11). In the previous study, star-shaped PCLs (SPs) with POSS core were synthesized and prepared melt-blend with commercial PLA by utilizing mini twin-screw extruder to increase the toughness properties of PLA. The mechanical,

thermal, and morphological behaviors of these blends were examined as a function of star-shaped polymer type possessing different molecular weight depending on different chain lengths at constant PLA/SP ratio. It was found that increasing the toughness of commercial PLA thanks to ductile PCL having relatively low T_g. Besides, the addition of SP polymers into commercial PLA improved morphological and some mechanical properties (like elongation at break and izod impact strength) (19).

In this work, eight-armed POSS cored star-shaped PCL (POSS-$(PCL)_8$, SP) polymers having various chain lengths (n= 10, 20, 30, and 50) were produced and compounded with commercial PLA with different blending ratios (PLA/SP, 95/5 and 80/20). In a previous study, the effects of 90/10 blended PLA/SP polymers were discussed (19). Here, these blends having different blending ratios were compared with neat PLA. Also, the PDI, a commercial compatibilizer, was added to blends at a constant amount of 1 wt%, and their effects on PLA's properties and phase morphology were investigated.

EXPERIMENTAL SECTION

Materials and Method
All materials and polymers used in this work, and the preparation of PLA/SP blends, have been described in the previously published paper (19). The commercial PLA (PLI005) was procured from NaturePlast, having a molecular weight 71,900 g/mol (determined by GPC) and used after drying at 65 °C under vacuum overnight. A commercial compatibilizer, 1,4-phenylene diisocyanate (PDI) was purchased from Sigma Aldrich. The chlorine functionalized POSS (POSS-$(Cl)_8$), azide functionalized POSS (POSS-$(N_3)_8$) and POSS cored star-shaped PCL (SP) polymers having various chain lengths (n= 10, 20, 30 and 50) were synthesized according to a method in the previous work, too. Subsequently, synthesized polymers were melt-blended with PLA with a blending ratio of 95/5 and 80/20 wt%. Some of the results belong to blends of 90/10 wt% ratio were extracted from the previous study (19) to make comparisons of blend ratios.

The morphology of blends was searched via scanning electron microscopy (FEI- QUANTA FEG 250- Field Emission Scanning Electron Microscope (FE-SEM)). Instron universal testing machine (Model 3345) and Zwick/Roell impact testing machine were used for tensile tests and impact strength analysis respectively to determine mechanical characters of the blends. Melting temperature and crystallization behaviors of blends were analyzed via DSC by Mettler Toledo DSC-1 Star Model calorimeter with a 10 °C/min scan rate, from room temperature to 250 °C with N_2 atmosphere. Thermal decomposition properties were determined via Mettler Toledo TGA 1 Star System TGA between 25 and 650 °C at a

heating rate of 15 °C min^{-1} under an argon atmosphere.

Synthesis of Alkyne Functional Linear PCL Polymers (Alkyne PCL)

Alkyne-PCL polymers with different repeating units (n=10, 20, 30, and 50) to prepare different chain lengths were again synthesized according to the previous procedure described elsewhere (19). ROP successfully helped prepare these polymers by utilizing an initiator (propargyl alcohol) and a catalyst (tin octanoate, Sn(Oct)$_2$).

Synthesis of A$_8$-type homo-arm POSS cored star-shaped PCLs (POSS-(PCL)$_8$)

POSS-N$_3$, as a multifunctional core, was prepared according to the previously published literature procedures (19). A$_8$-type homo-arm POSS cored star-shaped PCLs were successfully synthesized via copper(I)-catalyzed click reaction using POSS(N$_3$)$_8$

as clickable azide and alkyne-PCL having three different chain lengths under ambient conditions with high yield.

Blend preparation with micro- extruder and injection

A laboratory-scale twin-screw mini extruder (max. feeding volume 15 mL) was utilized to prepare PLA/ SP blends (Xplore Instruments MC 15, The Netherlands). The blend ratios and contents wt% of PLA/SP and PLA/PDI/SP blends are given in Table 1. The mixing of two polymers was performed at 190 °C and 2 min mixing time, the screw speed of the extruder was 100 rpm, following injection molding machine (Xplore 12 mL) was used to produce mechanical test specimens. The temperatures for mold and melt were 25 °C and 190 °C. The PDI was used as a commercial compatibilizer and added a constant amount as 1.0 wt%.

Table 1: The blend ratios and contents wt% of PLA/SP and PLA/PDI/SP blends.

Blend ratio		PLA (wt%)	SP (wt%)	PDI (wt%)
Pure PLA		100.0	-	-
PLA/PDI		99.0	-	1.0
95/5	PLA/SP	95.0	5.0	-
	PLA/PDI/SP	94.05	4.95	1.0
80/20	PLA/SP	80.0	20.0	-
	PLA/PDI/SP	79.2	19.8	1.0

RESULTS AND DISCUSSION

Vertical Force (VF) Measurements

The vertical force is generally used to get information about melt viscosity of the polymers or blends. It is measured while the molten polymer was pumped through the recirculation channel or die during the extrusion process. In this study, PLA and SP polymers were compounded in the lab-scale extruder machine at the rates of 100/0, 95/5, 90/10

and 80/20% w/w and the vertical force (N) values, which were recorded during the blending process, were used to compare melt viscosities of blends. The studies were carried out at 190 ºC at 100 rpm mixing speed for 2 minutes of retention time. The changes in vertical force (N) values recorded against time for pure PLA, and PLA/SP and PLA/PDI/SP blends with 95/5 and 80/20 (w/w) are given in Figure 1.
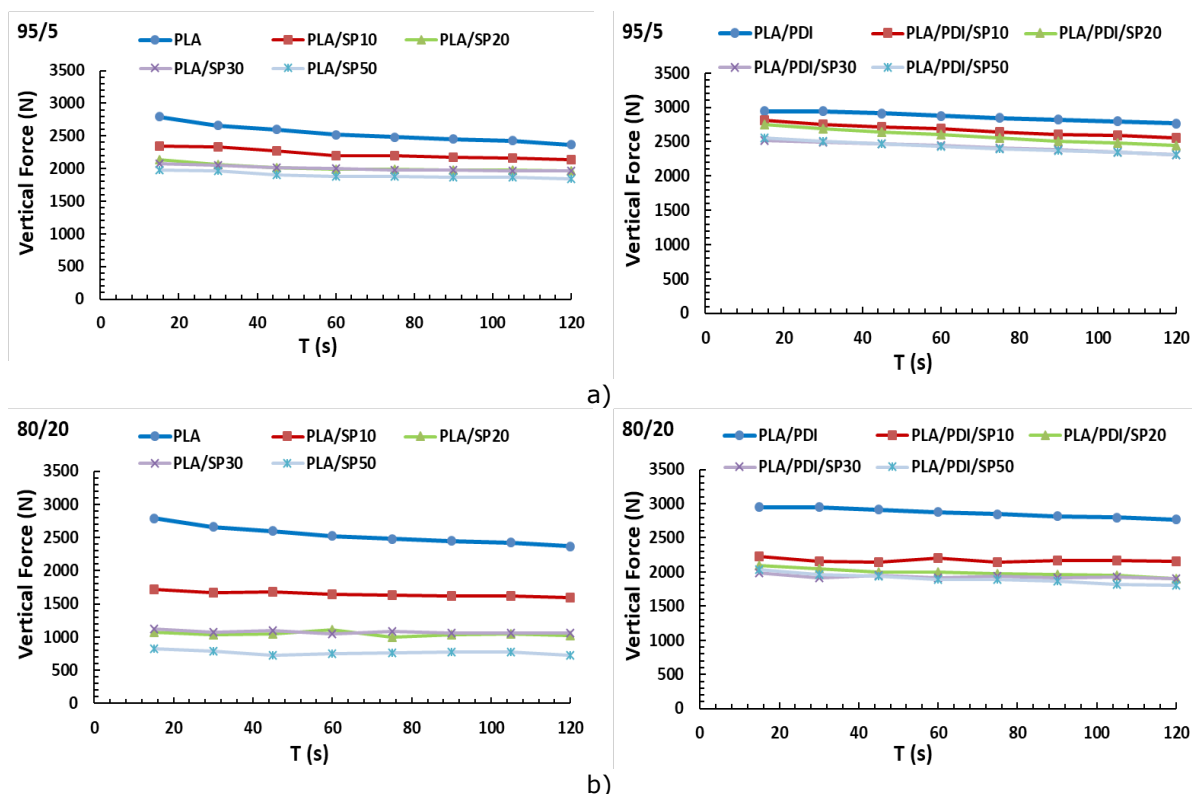
Figure 1: The variation of vertical force of PLA/SP and PLA/PDI/SP blends at a rate of a) 95/5 and b) 80/20 (w/w).

As well as being a fragile polymer, PLA is a problematic polymer to process due to its high melting point and high viscosity at processing temperatures. The melt viscosity value of pure PLA is higher than PLA/SP blends for any time, as seen in Figure 1. When SPs were added to the PLA, it caused a decrease in melt viscosity due to the plasticizing effect of PCL. Also, the star polymers generally have a smaller solution and melt viscosity in comparison to linear ones and cause more natural blending with a reduction in vertical force values (3, 10, 21). However, POSS molecules in the star polymer act as an internal slip agent, helping to reduce the melt viscosity of the mixtures (13, 19, 22, 23). As can be seen from Figure 1, the melt viscosity is higher in the mixtures of 95/5 compared to the mixtures of 90/10 and 80/20, and a good decrease was detected proportional to the blending ratio as the amount of SPs was more significant in 80/20 blends (19). The melt viscosity decreased with the increase of arm length of the SPs, and this is more noticeable in 80/20 blends, as seen in Figure 1b. In PLA/PDI/SP blends, PDI behaves as a compatibilizer between two polymers and causes chain extension reactions between end groups of SPs and PLA. The chain extension mechanism has been described in detail in a previous study (19). The occurrence of PLA-*co*-SP structures in the blends results in in-situ compatibilization and causes a slight increment in the melt viscosity of the triplet blends when compared to binary blends (24-26). In

any case, the melt viscosity is higher in the mixtures of 95/5, 90/10 and 80/20, respectively.

Mechanical Properties of PLA/SP and PLA/PDI/SP Blends
The mechanical properties of polymer blends are generally among the properties of each component. Besides, the blending ratio, the miscibility and compatibility levels of the mixtures play an essential role in defining the final properties of the mixture. PLA is inherently fragile with very low elongation at break (EAB) and relatively low impact strength (5, 7, 19, 27, 28). Since it is a very fragile material, it is generally used by adding plasticizers to improve its mechanical properties and obtain a stricter structure. In this study, SP polymers act as a plasticizer, providing improvements in the mechanical behaviors of PLA. The change in the tensile modulus of PLA/SP and PLA/PDI/SP blends at different blending ratios 95/5, 90/10, and 80/20 are given in Figure 2a. It can be seen that there is a significant decrease in the tensile modulus values of star polymer blends with and without PDI compared to neat PLA. The decrease in the tensile modulus of PLA/SP blends was supposed since PCL polymers generally have lower tensile strength and modulus compared to neat PLA. The lower values were generally obtained in 90/10 and 80/20 blend ratios according to 95/5 blends. The inclusion of SP polymers caused a decrement in the tensile modulus of pure PLA rather than linear ones (29). The lowest

tensile modulus value was found in the PLA/PDI/SP20 blend. It was observed that there was an increase in tensile modulus values in 80/20 blends due to both increasing arm number (hence increasing molecular weight) and increasing SP blend ratio. The significant enhancement in mechanical properties was observed in EAB values of PLA/SP, and PLA/PDI/SP blends in Figure 2b. The 90/10 blends have the highest EAB showing that the most proper ratio for interaction between PLA and star PCL polymers. In the case of PDI, it is more evident that SP20 polymer has a significant increase in 90/10 blends proving SP20 is the reasonable saturation level of molecular arm length and shows maximum interaction with PLA due to chain extension (19). The blend ratio effect also can be seen in yield strength. The values of 95/5 blends were found to be higher compared to that of pure PLA, however, the lowest value was determined in 90/10 blends in Figure 2c.

The Izod impact strength values of PLA/SP and PLA/PDI/SP blends at different blending ratios 95/5, 90/10, and 80/20 were given in Figure 3a. The impact strength of the blends showed an increasing trend in both cases with and without PDI compared to pure PLA. It is concluded that the SPs behaved as an impact modifier, and maximum effect was observed at 90/10 blends in concordance with EAB results. Here again, PLA/PDI/SP20 blends had maximum value proving that SP20 has the most available arm length (or molecular weight) at interaction with PLA in the presence of PDI with the help of chain extension reactions (19). The Shore D Hardness values of blends are given in Figure 3b. There is a slight decrease in hardness when compared to pure PLA. 90/10 blends have lower values when compared to that of 95/5 and 80/20 blends.

a)

b)

c)
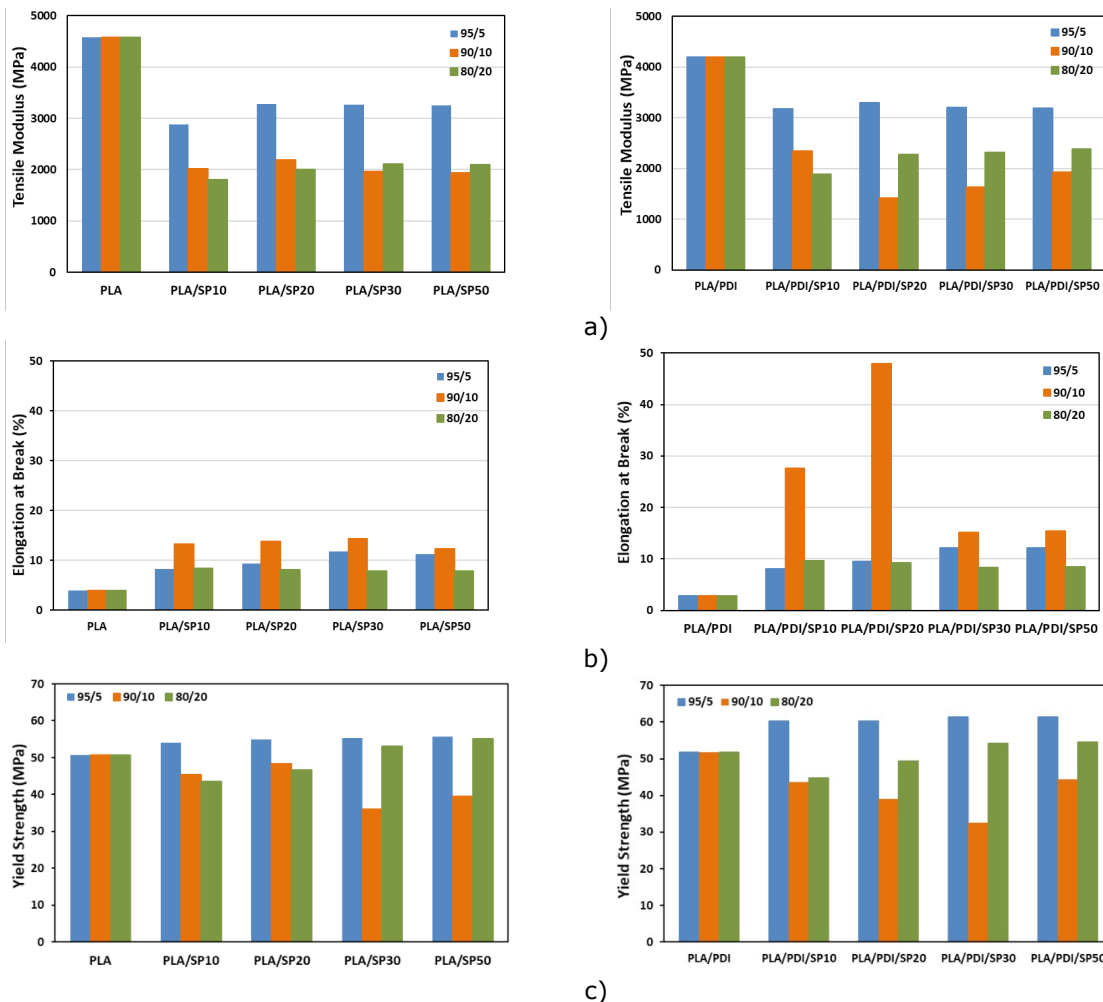
Figure 2: Mechanical properties of PLA/SP and PLA/PDI/SP blends a) tensile modulus, b) elongation at break (%), c) yield strength at different blending ratios 95/5, 90/10 and 80/20.
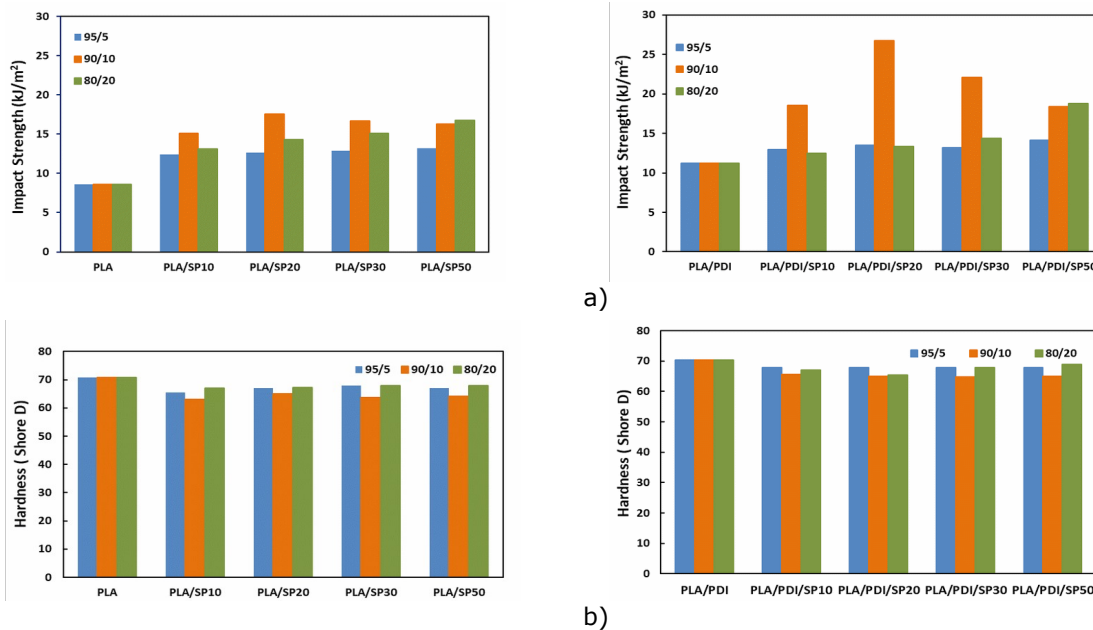
Figure 3: a) The Izod impact strength and b) hardness of PLA/SP and PLA/PDI/SP blend at different blending ratios 95/5, 90/10, and 80/20.

Thermal Properties of PLA/SP and PLA/PDI/SP Blends

The thermal properties of PLA/SP and PLA/PDI/SP blends at 95/5, and 80/20 blend ratios are given in Table 2, and DSC thermograms are depicted in Figure 4. A good decrease was observed in glass transition temperature (T_g) with the change of blend ratio from 95/5 to 80/20, and the lowest T_g value was found as 47 °C for the 80/20 blends. The decrease in T_g is an expected phenomenon due to the plasticizing effect of star PCL arms having very low T_g (10, 30). The incorporation of PDI to PLA/SP blends did not significantly affect the T_g values of 80/20 blend, but it caused an increase of 2-3 °C in 95/5 blends due to the formation of PLA-*co*-SPs structures (19, 25). The pure PLA has a high melting temperature (T_m) around 149.8 °C (31). There is an increment in the T_m values of neat PLA with increasing PCL content.

It is observed that the crystallization temperature (T_c) of PLA is also influenced by the incorporation of SPs, and there an increase with an increase of PCL ratio consistent with the literature (30). The addition of PDI caused an increase in T_c when compared to the blends only PLA/SP in any of the blend ratios.

The degree of crystallinity (X_c) for all the blends was calculated from the equation in the following form:

$$\%X_c = \frac{\Delta H_m - \Delta H_c}{\Delta H^*_m \phi}$$

(Eq. 1)

where ΔH_m value shows the melting enthalpy of samples (J/g), ΔH_c value shows crystallization enthalpy (J/g) and ΔH^*_m value is the standard melting enthalpy of pure PLA (93.1 J/g) . φ is the weight fraction of PLA in the blends. In general, the crystallinity values of the blends are below 13%. Pure PLA has a crystalline value of 0.2%, indicating that the crystals formed during cold crystallization. The addition of SP polymers results in a significant increase in the crystallinity of PLA. Similarly, PLA crystallinity causes an increase with the addition of PDI, but this increase is lower than pure blends. Also, there is a reduction in the crystallinity values with the increment of PCL concentration in the blend (7).

Table 2: The results of DSC analysis PLA/SP and PLA/PDI/SP blends at 95/5 and 80/20.

Blends		T_g (°C)	T_c (°C)	T_m (°C)	X_c (%)
PLA		55.4	117.4	149.8	0.2
PLA/PDI		54.8	113.7	152.1	1.6
95/5	PLA/SP10	52.9	99.01	153.9	12.6
	PLA/SP20	52.9	98.05	154.6	12.6
	PLA/SP30	52.8	98.4	154.8	12.3
	PLA/SP50	52.4	98.7	154.8	12.1
	PLA/PDI/SP10	55.3	110.4	155.9	6.9
	PLA/PDI/SP20	54.5	103.4	155.5	6.4
	PLA/PDI/SP30	54.5	102.1	155.6	6.4
	PLA/PDI/SP50	54.1	101.1	156.6	6.1
80/20	PLA/SP10	47.3	108.5	154.5	5.1
	PLA/SP20	47.8	106.7	154.9	4.8
	PLA/SP30	48.8	106.8	154.1	4.7
	PLA/SP50	48.8	106.8	154.5	4.2
	PLA/PDI/SP10	48.1	110.7	155.1	5.5
	PLA/PDI/SP20	48.4	110.5	154.2	4.9
	PLA/PDI/SP30	49.1	110.3	154.7	3.7
	PLA/PDI/SP50	49.03	110.1	155.1	2.4
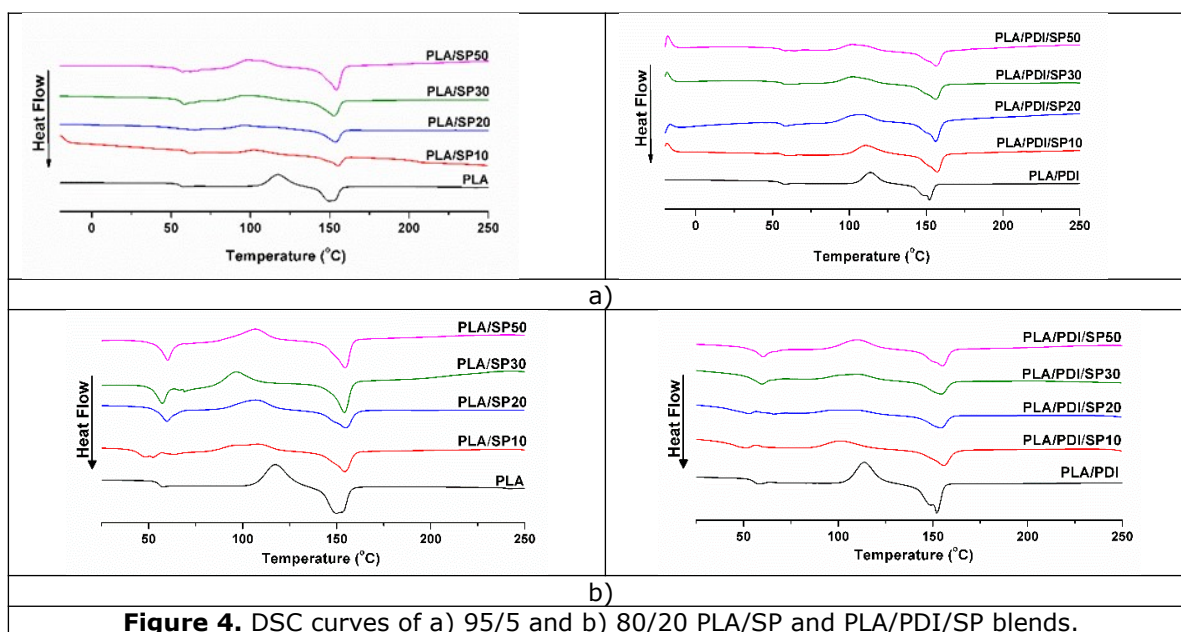
Figure 4. DSC curves of a) 95/5 and b) 80/20 PLA/SP and PLA/PDI/SP blends.

TGA helped investigate the thermal stability of PLA/SP, and PLA/PDI/SP blends in Figure 5 and the values of T_5, T_{10}, and T_{50} (the temperatures at which a weight loss of 5, 10, and 50% occurred), T_{onset} (the onset decomposition temperature), T_{max} (the maximum decomposition temperature), and the char yield of these blends were given in Table 3. PLA has the highest thermal stability, while a decrease is seen with the addition of SP polymers to PLA matrix due to the structural differences of the PLA and PCL polymers and the low thermal stability of PCL. PDI also has a decreasing effect on thermal properties, as seen in Table 3. The char yield values increased with the increment in the PCL amount in the blends.

Table 3: The results of the TGA analysis of PLA/SP and PLA/PDI/SP blends at 95/5 and 80/20.

	Blends	T_{onset} (°C)[a]	T_5 (°C)[b]	T_{10} (°C)[b]	T_{90} (°C)[b]	T_{max} (°C)[c]	Char yield (%)[d]
	PLA	351.0	350.8	345.8	379.7	381.1	0.9
	PLA/PDI	350.1	348.6	342.3	386.0	382.5	0.1
95/5	PLA/SP10	342.6	315.9	328.3	385.1	383.1	1.2
	PLA/SP20	342.2	313.6	325.7	385.5	382.3	1.1
	PLA/SP30	341.3	310.7	322.5	385.7	382.8	0.9
	PLA/SP50	340.8	308.9	322.1	384.1	381.3	0.9
	PLA/PDI/SP10	340.6	309.0	322.5	379.4	379.5	0.6
	PLA/PDI/SP20	338.9	308.8	321.9	380.1	378.6	0.6
	PLA/PDI/SP30	337.2	308.7	320.0	380.4	377.2	0.5
	PLA/PDI/SP50	337.1	308.2	319.5	380.1	376.2	0.5
80/20	PLA/SP10	289.5	283.8	281.9	345.9	314.8	2.9
	PLA/SP20	288.7	283.6	281.5	346.3	314.3	2.8
	PLA/SP30	284.2	275.8	281.6	348.3	316.2	2.8
	PLA/SP50	283.3	275.8	281.6	343.6	319.3	2.8
	PLA/PDI/SP10	288.3	281.1	281.0	345.1	313.2	3.0
	PLA/PDI/SP20	285.2	280.6	282.1	345.8	312.8	2.9
	PLA/PDI/SP30	283.3	277.1	279.5	345.8	312.4	2.9
	PLA/PDI/SP50	280.9	272.6	278.1	340.1	313.7	2.9

[a]T_{onset} is the onset decomposition temperature of the blends in TGA experiments.
[b]T_5, T_{10}, and T_{50} are the temperatures of weight losses at 5%, 10%, and 50%, respectively.
[c]T_{max} is the temperature corresponding to the maximum rate of weight loss.
[d]The percent of char yield at 600 ºC.
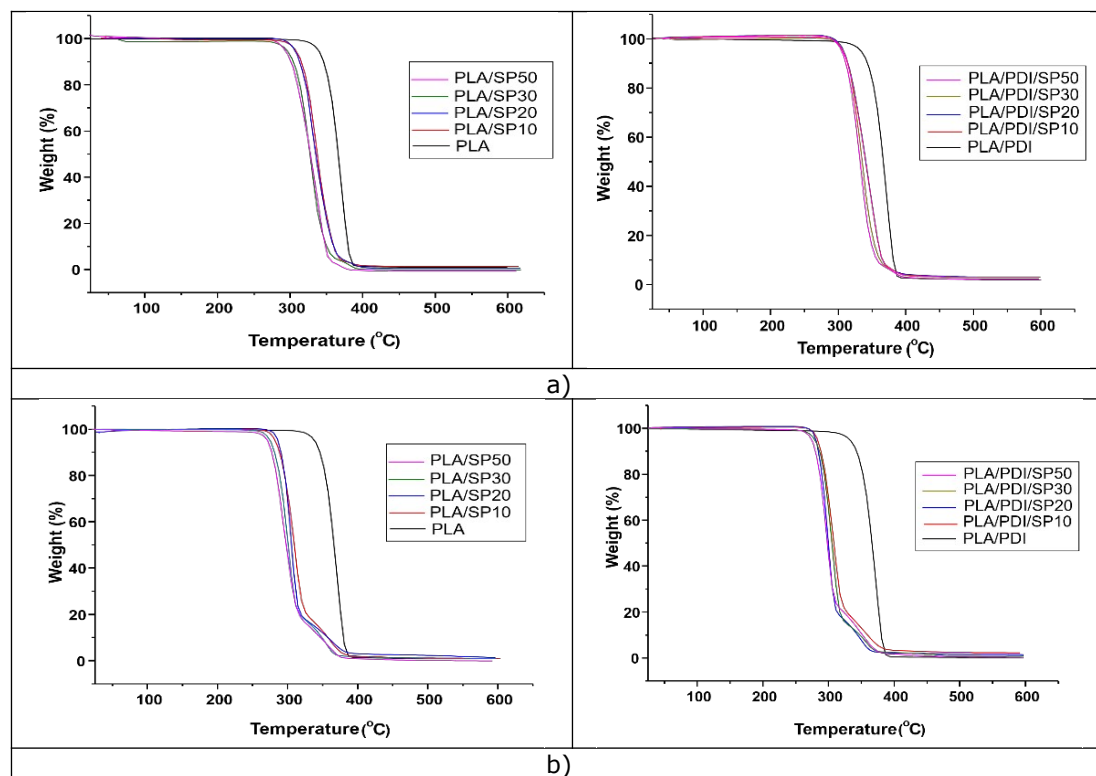
Figure 5. TGA thermograms of a) 95/5 and b)80/20 PLA/SP and PLA/PDI/SP blends.

Morphology
The compatibility and the blending ratios of the blends are two critical parameters that affect the interfacial adhesion and the phase dispersions, as well as the size, uniformity, and distributions of the dispersed phase in the continual phase. Correlatively, the toughness and mechanical properties of the blends are precisely influenced. Figure 6 shows the SEM photos of fracture surfaces of PLA/SP and PLA/PDI/SP blends at 95/5 and 80/20 ratios at 5000x magnification.

Neat PLA is a brittle polymer showing large cracks on the fracture surface (10, 19). PLA matrix is a continuous phase, and PDI and the added SP polymers are dispersed phase in this multi-component blend system. In 95/5 blends, in which PLA is a rich component, the surfaces prepared with SPs having 10, 20 and 30 arm length have large cracks as seen Figure 6, however, these larger cracks disappear with SP50, and globular PCL structures appear in the PLA matrix this is due to longer PCL arms penetrate PLA matrix easily with its star shape structure. Besides, the globular PCL structure appears with SP10 at 80/20 blends. The SP polymers act as stress concentrators and cause a decrement of tensile modulus (Figure 2a) (7). The distribution of SP in PLA is homogeneous, and this shows that SP is better miscible than linear PCL polymers (4, 19). Two distinct phases cannot be seen with the addition of PDI, so it enhances the immiscibility, and the SEM results are coherent with the formation of a PLA-*co*-SP due to the reactive compatibilization.

CONCLUSION

A_8-type eight-armed POSS cored star-shaped PCL polymers (SP) with different arm lengths (SP10, SP20, SP30, and SP50) were synthesized and melt-blended with commercial PLA at different ratios as 95/5 and 80/20 to examine the effects on the mechanical, morphological behavior and toughness of PLA. The results are compared with the results of a previous study that was at a 90/10 ratio (19). It was reported that using a star-shaped polymer rather than linear ones enhanced morphological and mechanical properties. The incorporation of SP polymers into the PLA matrix decreased the tensile modulus and increased the EAB values. The impact properties of the blends were also considerably improved. PLA/PDI/SP20 blends with a blending ratio of 90/10 have the maximum EAB and the impact strength values thanks to chain extension reactions between PDI and SP20. Here, it is also showed that when the blending ratio was increased, it improves the morphology, and there are no large cracks that are seen on pure PLA surface. Also, there are no two distinct phases with the addition of PDI due to the chain extension reactions. It can be concluded that the fragile nature of pure PLA turned to ductile by blending via SP polymers, and using SP polymers rather than linear ones is more successful in enhancing mechanical properties of neat PLA. Hence, the application field of PLA was broadened by blending with SP biopolymers, and these blends can be utilized for various daily and industrial applications such as food packaging, disposable products, biomedical, etc.
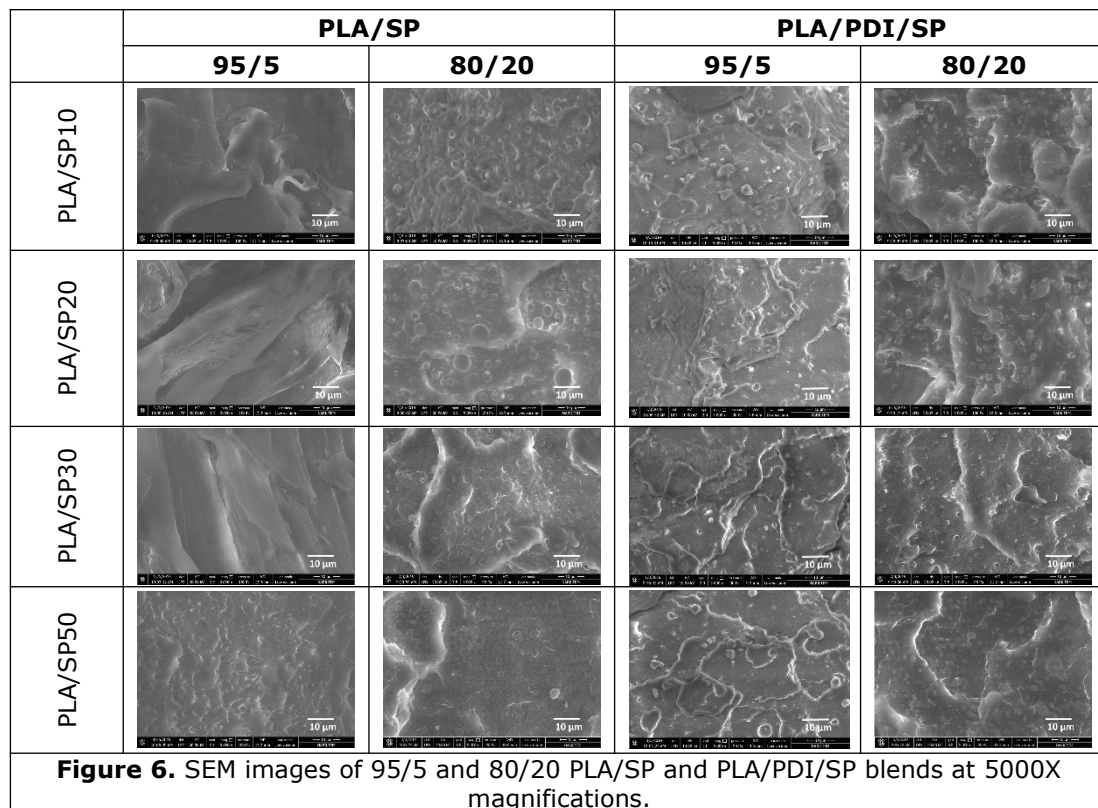
	PLA/SP		PLA/PDI/SP	
	95/5	**80/20**	**95/5**	**80/20**
PLA/SP10				
PLA/SP20				
PLA/SP30				
PLA/SP50				

Figure 6. SEM images of 95/5 and 80/20 PLA/SP and PLA/PDI/SP blends at 5000X magnifications.

REFERENCES

1.   Urquijo J, Guerrica-Echevarría G, Eguiazábal JI. Melt processed PLA/PCL blends: Effect of processing method on phase structure, morphology, and mechanical properties. Journal of Applied Polymer Science. 2015;132(41).

2.   López-Rodríguez N, López-Arraiza A, Meaurio E, Sarasua JR. Crystallization, morphology, and mechanical behavior of polylactide/poly(ε-caprolactone) blends. Polymer Engineering & Science. 2006;46(9):1299-308.

3.   Deokar MD, Idage SB, Idage BB, Sivaram S. Synthesis and characterization of well-defined random and block copolymers of ε-caprolactone with l-lactide as an additive for toughening polylactide: Influence of the molecular architecture. Journal of Applied Polymer Science. 2016;133(14).

4.   Broz ME, VanderHart DL, Washburn NR. Structure and mechanical properties of poly(d,l-lactic acid)/poly(ε-caprolactone) blends. Biomaterials. 2003 2003/10/01/;24(23):4181-90.

5.   Simões CL, Viana JC, Cunha AM. Mechanical properties of poly(ε-caprolactone) and poly(lactic acid) blends. Journal of Applied Polymer Science. 2009;112(1):345-52.

6.   Rao RU, Suman KNS, Rao VVSK, Bhanukıran K. Study of rheological and mechanical properties of biodegradable polylactide and polycaprolactone blends. International Journal of Engineering Science and Technology. 2011:6259-65.

7.   Matta AK, Rao RU, Suman KNS, Rambabu V. Preparation and Characterization of Biodegradable PLA/PCL Polymeric Blends. Procedia Materials Science. 2014 2014/01/01/;6:1266-70.

8.   Hiljanen-Vainio M, Karjalainen T, Seppälä J. Biodegradable lactone copolymers. I. Characterization and mechanical behavior of ε-caprolactone and lactide copolymers. Journal of Applied Polymer Science. 1996;59(8):1281-8.

9.   Li H, Qiao T, Song P, Guo H, Song X, Zhang B, et al. Star-shaped PCL/PLLA blended fiber membrane via electrospinning. Journal of Biomaterials Science, Polymer Edition. 2015 2015/05/03;26(7):420-32.

10.   Qin Y, Liu S, Zhang Y, Yuan M, Li H, Yuan M. Effect of poly(ε-caprolactone-co-l-lactide) on thermal and functional properties of poly(l-lactide). International Journal of Biological Macromolecules. 2014 2014/09/01/;70:327-33.

11.   Liu Z, Hu D, Huang L, Li W, Tian J, Lu L, et al. Simultaneous improvement in toughness,

strength and biocompatibility of poly(lactic acid) with polyhedral oligomeric silsesquioxane. Chemical Engineering Journal. 2018 2018/08/15/;346:649-61.

12.   Pan R, Shanks R, He Y, Su Y. Molecular shape conversion of POSS-(PLLA)x with various arm lengths and its effect on the compatibility of PLLA/POSS-(PLLA)x as a nanofiller blended into PLLA matrix: From spiky ball to panel-like. Computational Materials Science. 2019 2019/06/15/;164:1-7.

13.   Kodal M, Sirin H, Ozkoc G. Effects of reactive and nonreactive POSS types on the mechanical, thermal, and morphological properties of plasticized poly(lactic acid). Polymer Engineering & Science. 2014;54(2):264-75.

14.   Dilek T, Humeyra S, Guralp O. Effects of POSS particles on the mechanical, thermal, and morphological properties of PLA and Plasticised PLA. Journal of Applied Polymer Science. 2011;121(2):1067-75.

15.   Pan H, Yu J, Qiu Z. Crystallization and morphology studies of biodegradable poly(ε-caprolactone)/polyhedral oligomeric silsesquioxanes nanocomposites. Polymer Engineering & Science. 2011;51(11):2159-65.

16.   Monticelli O, Calabrese M, Gardella L, Fina A, Gioffredi E. Silsesquioxanes: Novel compatibilizing agents for tuning the microstructure and properties of PLA/PCL immiscible blends. European Polymer Journal. 2014 2014/09/01/;58:69-78.

17.   Wang W, Fei M, Jie X, Wang P, Cao H, Yu J. Synthesis and characterization of star-shaped block copolymers with polyhedral oligomeric silsesquioxane (POSS)core via ATRP. Polymer Bulletin. 2010 December 01;65(9):863-72.

18.   Lee KS, Chang YW. Thermal and mechanical properties of poly (ε-caprolactone)/polyhedral oligomeric silsesquioxane nanocomposites. Polymer International. 2013;62(1):64-70.

19.   Dandan Doganci M, Aynali F, Doganci E, Ozkoc G. Mechanical, thermal and morphological properties of poly(lactic acid) by using star-shaped poly(ε-caprolactone) with POSS core. European Polymer Journal. 2019 2019/12/01/;121:109316.

20.   Sun Y, He C. Biodegradable "Core–Shell" Rubber Nanoparticles and Their Toughening of Poly(lactides). Macromolecules. 2013 2013/12/23;46(24):9625-33.

21.   Aloorkar N, Kulkarni A, Patil R, Ingale D. Star polymers: an overview. Int J Pharm Sci Nanotech. 2012;5:1675-84.

22.   Turan D, Sirin H, Ozkoc G. Effects of POSS particles on the mechanical, thermal, and morphological properties of PLA and Plasticised PLA. Journal of Applied Polymer Science. 2011;121(2):1067-75.

23.   Romero-Guzmán ME, Romo-Uribe A, Zárate-Hernández BM, Cruz-Silva R. Viscoelastic properties of POSS–styrene nanocomposite blended with polystyrene. Rheologica Acta. 2009 July 01;48(6):641-52.

24.   Meredith JC, Amis EJ. LCST phase separation in biodegradable polymer blends: poly(D,L-lactide) and poly(ε-caprolactone). Macromolecular Chemistry and Physics. 2000;201(6):733-9.

25.   Dogan SK, Reyes EA, Rastogi S, Ozkoc G. Reactive compatibilization of PLA/TPU blends with a diisocyanate. Journal of Applied Polymer Science. 2014;131(10).

26.   Kilic NT, Can BN, Kodal M, Ozkoc G. Compatibilization of PLA/PBAT blends by using Epoxy-POSS. Journal of Applied Polymer Science. 2019;136(12):47217.

27.   Zhao X, Hu H, Wang X, Yu X, Zhou W, Peng S. Super tough poly (lactic acid) blends: a comprehensive review. RSC Advances. 2020;10(22):13316-68.

28.   Fortelny I, Ujčić A, Fambri L, Slouf M. Phase structure, compatibility and toughness of PLA/PCL blends: a review. Frontiers in Materials. 2019;6:206.

29.   Zhao H, Zhao G. Mechanical and thermal properties of conventional and microcellular injection molded poly (lactic acid)/poly (ε-caprolactone) blends. Journal of the Mechanical Behavior of Biomedical Materials. 2016 2016/01/01/;53:59-67.

30.   Yeh J-T, Wu C-J, Tsou C-H, Chai W-L, Chow J-D, Huang C-Y, et al. Study on the Crystallization, Miscibility, Morphology, Properties of Poly(lactic acid)/Poly(ε-caprolactone) Blends. Polymer-Plastics Technology and Engineering. 2009 2009/05/18;48(6):571-8.

31.   Garlotta D. A Literature Review of Poly(Lactic Acid). Journal of Polymers and the Environment. 2001 April 01;9(2):63-84.

32.   Migliaresi C, Cohn D, De Lollis A, Fambri L. Dynamic mechanical and calorimetric analysis of compression-molded PLLA of different molecular weights: Effect of thermal treatments. Journal of Applied Polymer Science. 1991;43(1):83-95.

33.   Lim LT, Auras R, Rubino M. Processing technologies for poly(lactic acid). Progress in Polymer Science. 2008 2008/08/01/;33(8):820-52.

SIMULTANEOUS DETERMINATION OF FLUORIDE, ACETATE, FORMATE, CHLORIDE, NITRATE, AND SULFATE IN DISTILLED ALCOHOLIC BEVERAGES WITH ION CHROMATOGRAPHY/CONDUCTIVITY DETECTOR

Melike Güler Şimşek[1] ✉ iD **, Orhan Destanoğlu[2*]** ✉ iD **, Gülçin Gümüş[1]** ✉ iD

[1] *Istanbul Technical University, Faculty of Science and Letters, Department of Chemistry, 34469, Maslak, Istanbul, Turkey*
[2] *The Council of Forensic Medicine (ATK), Department of Chemistry, 34196, Bahçelievler, Istanbul, Turkey*

Abstract: A novel method of ion chromatography with suppressed conductivity detection was developed for simultaneous determination of fluoride, acetate, formate, chloride, nitrate, and sulfate in distilled alcoholic beverages. In this study, bromide was used as an internal standard. The separation of the anions was accomplished by utilizing an anion exchange column with a gradient eluent program. The chromatographic conditions were as follows: the suppressor current was 31 mA; the flow rate of the mobile phase was 0.25 mL min^{-1}; the column and detector compartment temperatures were 35 °C and 40 °C, respectively; and the sample loop volume was 10 µL. All the calibration curves showed excellent linearity ($r^2 \geq 0.999$). The limits of detection (LOD) values were between 0.56 and 13.2 µg L^{-1}, while the limits of quantification (LOQ) values were between 1.80 and 43.9 µg L^{-1}. A raki sample was spiked with standard solutions at three different concentration levels to evaluate the accuracy, and the average recoveries were found in the range of 94.90% - 101.71%. Intra-day and inter-day precision studies were also investigated, and the relative standard deviations (RSDs %) were less than 5.99%. The validated method was applied to the three kinds of commercial samples: Turkish raki, vodka, and gin.

INTRODUCTION

The chemical composition of the beverages is an essential issue in terms of nutritional, toxicologic, and monitoring of the product quality. Distilled beverages are a mixture of all compounds produced from raw materials such as fruits, cereals, and spices. The process of distillation defines its sensory identity and quality of the drink. Every spirit has its unique aroma and flavoring components which reflect raw materials, distillation, and maturation

process. The analysis of lower and higher alcohols is essential in terms of the quality of the product (1). Added to the lower and higher alcohols, the anions in the beverages should be controlled as well for quality purposes.

Determination of organic acids in food and beverages is a critical topic because these compounds define organoleptic quality and may also influence the stability of the product. Moreover, the dose of some organic acids, especially formic acid in food and beverages, is toxicologically significant. Additionally, the measurement of formate may identify methanol contamination (2-4).

Formic acid is an inhibitor leading hypoxia by disrupting cytochrome oxidase activity in the body. Cellular death arising from inhibition of cytochrome oxidase is thought to be based on the discharge of ATP, decreasing level of energy fundamental cell functions cannot be kept on (5). The retinal and optical nerves are vulnerable tissues and easily affected by formate toxicity (6). According to U.S. Environmental Protection Agency (US EPA), the threshold oral dose for formic acid-induced acute mortality ranged from nearly 30 to 45 g (429 to 643 mg/kg, assuming a bodyweight of 70 kg)(7).

Ethyl acetate has an essential effect on the organoleptic characteristics of alcoholic beverages. It is found mainly in the heading fraction. Passing to its following fraction influence the sensory quality of the spirit in an adverse manner (8). Under unsuitable storage conditions, acetate concentration can be increased in the product utilizing bacterial degradation. Besides, some operations such as fermentation process and distillation techniques affect the level of acetate (9). Acetate is a significant source of acetyl-CoA in hypoxia. Prevention of acetate metabolism may weaken tumoral growth (10). According to US EPA 900 mg/ kg/ day considered as No Observed Adverse Effect Level (NOAEL) for ethyl acetate and 3600 mg/ kg/ day was shown a significant toxic effect, and 23 % of rats have died (11).

Fluoride is the smallest anion. It reduces bacterial enzymic activity. Although fluoride is an essential nutrient for the skeletal bone and dental health, high levels of fluoride give rise to skeletal and dental fluorosis (12, 13). According to US EPA, the current maximum contaminant level goal for fluoride in water is set at 4.0 mg/L. The minimum dose that could lead to toxic signs and symptoms, including death for fluoride intoxication, has been set at 5 mg/kg body weight (14).

Chloride is one of the most common anions found in foods. It plays a vital role in the metabolic acid-base equilibrium and responsible for muscular irritability. Excess chloride content leads to severe adverse effects not only on human health but also production and storage process (15, 16). As a result of an extraordinary degree of chloride concentration in biological fluids, cystic fibrosis, myotonia, Bartter syndrome, and startle disease emerge (17). According to the World Health Organization (WHO), a dietary intake for adults of 9 mg of chloride per kg of body weight has been recommended (18).

Because of the widespread use of nitrogenous fertilizers, nitrite and nitrate level increase in foods, nitrites, and nitrates cause methemoglobinemia. Nitrites react with the secondary and tertiary amines in foods, so forming highly carcinogenic nitrosamines (19). The current acceptable daily intakes (ADIs) for nitrite and nitrate, set by the Joint Food and Agriculture Organization /WHO (FAO/WHO) Expert Committee on Food Additives (JECFA) in 2002, is 0.07 mg/kg bw/day and 3.7 mg/kg bw/day, respectively (20).

Sulfate, a basic anion for the human body, plays an essential role in the detoxification and catabolism of various endogenous and exogenous compounds. Sulfate exerts a laxative effect following exposures to high concentrations (21). Even though there is no health-based guideline value for sulfate in drinking water, above 500 mg/liter, a noticeable taste will arise (22).

In the literature, several analytical methods have been utilized for the analysis of small organic acids. The Gas Chromatography (GC) method for direct determination of 13 short-chain volatile organic acids including acetic acid in liquid foods was established, and a method based on continuous solid-phase extraction and GC method was reported for the direct determination of 29 organic acids including acetic acid in food and beverages (23, 24). Similarly, High-Performance Liquid Chromatography (HPLC) methods (25, 26) been reported for the analysis of carboxylic acids. Moreover, short-chain carboxylic acids, including formic and acetic acid in vegetable oils and fats, have been determined using Ion exclusion chromatography (IEC) electrospray ionization mass spectrometry (27). The

systems, coupled with mass spectrometry (MS), eliminate the resolution problem and provides a good separation for the small organic acids. Even though MS coupled instruments are advanced technology products, they have some handicaps such as being expensive and time-consuming, requiring clean-up and derivatization procedures, coupled instrumentation, and use/waste of toxic organic solvents. Additionally, in the literature, there are capillary electrophoretic (CE) (28) and ion chromatographic (IC) (29, 30) methods allowing simultaneous quantification of common inorganic anions and small organic acids. However, less sensitivity (31) and precision problems of CE methods make suppressed IC the most potent method for the simultaneous determination of anions in various beverages.

Today, ion chromatography is a well-established method for the analysis of routine inorganic anions for many samples, especially for water analyses. Reagent-free ion chromatography (RFIC) has been utilized for about two decades. The ability to produce high purity eluents from the eluent generator system gives extra accuracy and reproducibility. Besides, suppressor systems decrease the baseline noise. There are few studies in which ion chromatography is employed for the analysis of distilled spirits.

Lachenmeier et al. (32) analyzed 107 different vodka samples with a conductivity meter. They found out that the conductivity of vodka purely derived from inorganic ions. The total ion content had an excellent linear relation with the conductivity. Arbuzov and Savchuk (33) analyzed the vodka samples by IC in combination with GC for the identification of ions. The ionic composition depends on water used for the production of vodka. They indicated that the conductivity of vodka could be affected by additives that were used for water treatment and adjustment of alkalinity. Also, Lachenmeier et al. (34) found that there were no significant differences in anion concentrations between the same samples, which were bottled at different dates. Balcerzak and Kapica (29) analyzed formate by using the IC system. In their study, they eliminated the volatile compounds from the matrices by utilizing an infrared (IR) source. They found LOD and LOQ values to be 0.014 mg L^{-1} and 0.042 mg L^{-1} for formate ion, respectively.

As being distinct from the previous study, to evaporate the volatile compounds from the raki samples, we used a water bath for more effective insulation. So, the time of vaporization was shortened under the nitrogen stream. It was observed that the broad peak disappeared on the IC chromatograms after the water bath vaporization process. Moreover, in our study, LOD and LOQ values were as smaller as 13 times than the previously published results.

This paper presents a simple, sensitive, reliable, and greener IC-CD method for the simultaneous determination of formate, acetate, fluoride, chloride, nitrate, and sulfate in alcoholic beverages. To the best of our knowledge, the proposed method is the first study to describe an IC-CD analysis of the anions in distilled alcoholic beverages utilizing bromide as an internal standard (IS), which minimizes the margin error arising from the loss of analyte in sample preparation procedure and during storage. Moreover, no study on anion analysis in Turkish raki samples has been published in the literature so far. This paper presents and discusses the anion concentration results of the Turkish raki samples. Besides, neither organic solvents nor reagents were used thanks to the RFIC system, which also provides repeatable results and sensitive measurements. In conclusion, it can be claimed that the proposed method is suitable for the determination of the anions in distilled alcoholic beverages at the routine laboratories where an IC system is used.

EXPERIMENTAL

Chemicals and Materials
All reagents were of analytical reagent grade. Sodium acetate (≥ 99.5%) was obtained from Sigma-Aldrich (St. Louis, MO, USA) and ammonium formate (≥ 99.5%) were taken from Honeywell-Fluka (Morris Plains, NJ, USA). Stock solutions (1000 mg L^{-1}) of sodium acetate and ammonium formate were prepared by weighing and dissolving accurate amounts in ultrapure water.

Ultrapure water (min. 18.2 MΩ/cm), which was used for the preparation of standard solutions and dilutions, was supplied by the water purification system of New Human Power I Scholar UV (Human Corporation, Seoul, Korea).

1000 mg L^{-1} of pure standard solutions of fluoride, chloride, nitrate, sulfate, and bromide was purchased from Merck (Darmstadt, Germany). All these stock solutions were stored at 4 °C in tightly closed polypropylene (PP) bottles.

Polyether Sulfone (PES) filter (pore size 0.2 μm, 17 mm) was purchased from Analytical Columns (New Addington, Croydon, CR0 9UG, England).

Instrumentation

Chromatographic separations and analyses were conducted by using Dionex ICS-3000 (Sunnyvale, CA, USA) IC system. A suppressed conductivity detector (ASRS 300 suppressor and conductivity cell) was employed to collect signals after separation in the system. The separation of fluoride, acetate, formate, chloride, nitrate, and sulfate in the samples was accomplished by utilizing Dionex IonPac®AS20 analytical column (2 × 250 mm) with a Dionex IonPac® AG20 guard column (2 × 50 mm) as stationary phases. NaOH was used as a mobile phase automatically generated by the Dionex Eluent Generating Cartridge (EGC)-NaOH EluGen II cartridge using solely ultrapure water. The sample loop volume was 10 μL. Possible contaminants in the IC system were eliminated using Continuously Regenerating Trap Columns (CR-ATC). It is well known that the RFIC systems are superior compared to systems with manually prepared eluents in terms of stability, reproducibility, and minimum contamination risk.

Analysis of volatile compounds present in a raki sample was carried out by performing a Perkin Elmer Clarus 500 Headspace Gas Chromatography/Mass Spectrometry (HS-GC/MS) system.

Calibration and Calculations

0.0354 g of ammonium formate salt was dissolved with some UP water, and then an appropriate volume of UP water was added to bring the volume to the mark on the 25 mL PP of the volumetric flask to prepare the formate stock solution at 1000 mg L^{-1} concentration.

Acetate stock solutions at 100 mg L^{-1} concentration were prepared by dissolving 0.014 g of sodium acetate with 100 mL of UP water in a PP volumetric flask.

A range of working standard solutions containing 2 mg L^{-1} bromide (IS) was prepared by diluting the stock solutions with ultrapure water.

Peaks from the sample were identified by comparing the retention time with those obtained from the individual standard samples. The concentrations of fluoride, acetate, formate, chloride, nitrate, and sulfate were separately calculated by utilizing the IS method. The ratio of the analyte peak area to the IS peak area was measured, and standard calibration curves constructed by plotting concentration versus peak area ratios. All the data acquisition and instrument control were performed via the Dionex Chromeleon® Client (Ver. 6.80) software.

Sample Collection

Three brands of Turkish raki samples, three brands of vodka samples, and three brands of gin samples were purchased from local supermarkets (Istanbul, Turkey). An ouzo sample was also bought from a local supermarket in Greece.

Sample Preparation

Firstly, 5 mL of sample solutions were prepared by mixing 4,990 μL of sample and 10 μL of 1000 mg L^{-1} bromide (IS) solution. Samples containing 2.0 mg L^{-1} bromide (IS) were evaporated approximately until 0.5 mL remains in a water bath at 40 – 50 °C under a nitrogen stream. When the temperature of the sample solutions has reached to room temperature after the evaporation process, samples were diluted to 2.0 mL with ultrapure water. Consequently, final solutions were filtered through a PES filter before IC analysis.

RESULTS AND DISCUSSION

Optimal Chromatography Conditions

The optimized chromatographic conditions were as follows: the suppressor current was 31 mA; the flow rate of the mobile phase was 0.25 mL min^{-1}; the column and detector compartment temperatures were 35 °C and 40 °C, respectively; sample loop volume was 10 μL.

The gradient elution of the mobile phase program provided by EGC was as follows: 0-7 min 5 mM NaOH isocratic, 7-17 min gradient from 5 mM to 23 mM NaOH, 17-22.5 min 23 mM NaOH isocratic, 22.5-23 min gradient from 23 mM to 50 mM NaOH, 23-28 min gradient from 50 mM to 5 mM NaOH, and 28-33 min 5mM NaOH isocratic.

Matrix Elimination

The significant compounds of raki, vodka, and gin samples are alcohols, higher alcohols, and white sugar. When compared to vodka and gin samples, raki has a more complex nature by including trans-anethol and extra white sugar, and it was chosen as a representative sample

for validation studies and optimization of pretreatment processes.

Primarily, to eliminate the volatile compounds from the sample solution, a raki sample was exposed to an IR source obeying the method mentioned in the literature (29). However, even though all apparatus were covered with aluminum foil, only max half of the sample could be evaporated within 3 hours. This solution was filtered and directly injected into the IC system. IC chromatogram of the brand, raki sample "a" exposed to IR radiation was shown in **Figure 1**. A broad peak interfered with the other anions in the IC chromatogram. Therefore, we decided to carry out an alternative vaporization method. Then, a pretreatment method employing a water bath (40 – 50 °C) and nitrogen stream was applied. By utilizing this process, sample volume was reached to 0.5 mL within only 1 hour. This solution was diluted to 2 mL, and it was loaded to IC for analysis. As it seen in **Figure 2**, no broad peak on IC chromatogram was observed after applying the water bath accompanied nitrogen stream vaporization process.
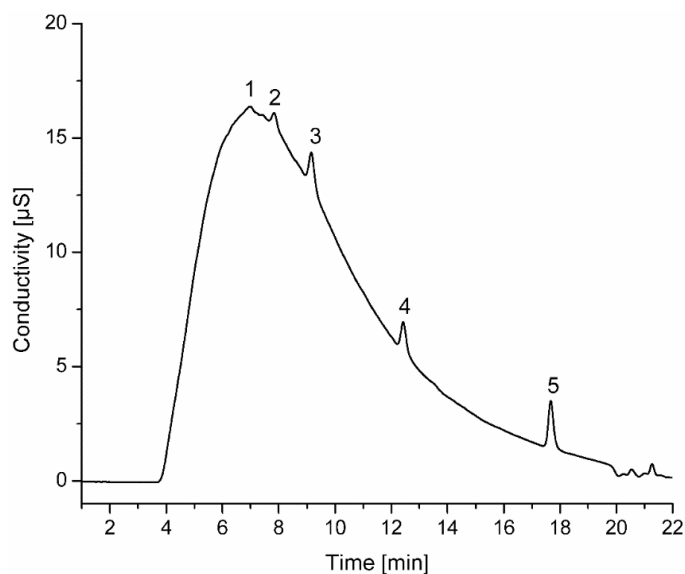
Figure 1. An IC chromatogram of the brand "*a*" raki sample after IR vaporization pretreatment.
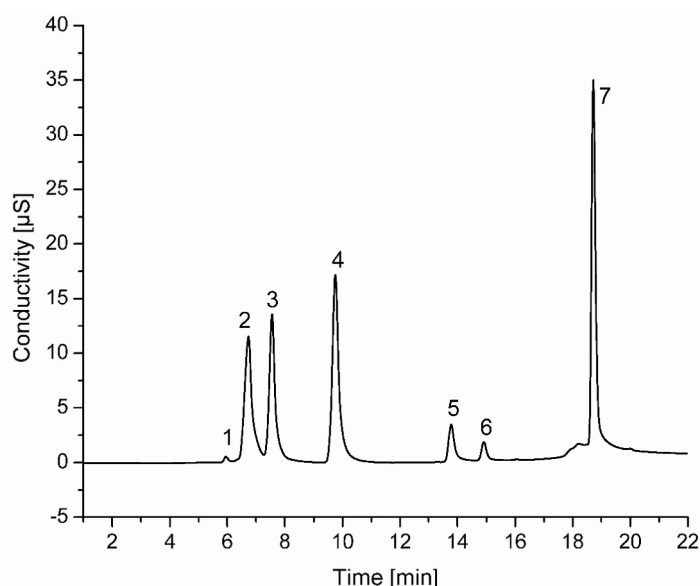
Figure 2. An IC chromatogram of the brand *"a"* raki sample after water bath vaporization. *1*: Fluoride; *2*: Acetate; *3*: Formate; *4*: Chloride; *5*: Nitrate; *6*: Bromide; *7*: Sulfate.

An aliquot 200 µL of the raki sample solutions were transferred into the HS vials and analyzed qualitatively by HS-GC/MS before and after the vaporization process to evaluate whether the pretreatment procedure was effective in terms of elimination of volatile compounds. HS-GC/MS total ion chromatograms were given in **Figure 3**. All volatile compounds of the brand "*a*" raki sample were eliminated by carrying out the latter process.

On the other hand, according to the Turkish Food Codex Distilled Alcoholic Beverage Regulation (35), the permitted maximum concentration of white sugar is 10 g L^{-1}, which is used for taste harmonization during the production of raki. The added sugar did not lead to any damage or interference problem to the IC-CD system since sugars eluted from the anion exchange column (AEC) (36), and they have no response to the conductivity detector.
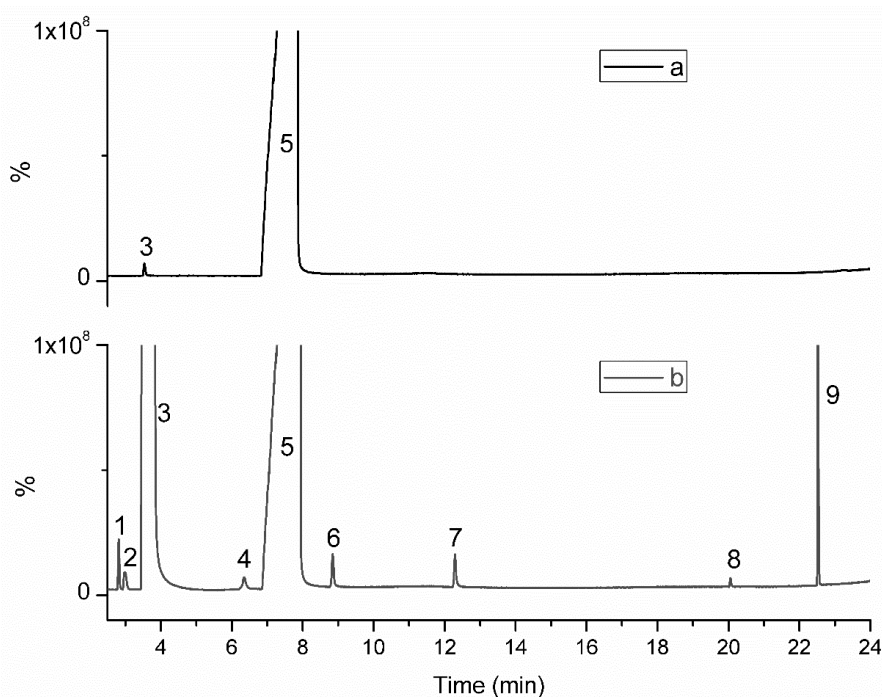
Figure 3. HS-GC/MS total ion chromatogram of the brand "a" raki sample. A) after water bath vaporization; B) before water bath vaporization. *1*: Ethyl acetate; *2*: Methanol; *3*: Ethanol; *4*: 1-Propanol; *5*: Water; *6*: 2-methyl-1-propanol; *7*: 3-methyl-1-butanol; *8*: Estragole; *9*: Anethole.

Method Validation
Some performance characteristics were investigated to evaluate linearity, selectivity, and repeatability.

Linearity
In this study, bromide was used as an IS at 2.0 mg L^{-1}. Thus, the stability and accuracy of the method could be improved. Bromide peak did

not interfere with the peaks of fluoride, acetate, formate, chloride, nitrate, and sulfate on the chromatogram of the brand *a* raki sample (See **Figure 2**). Similarly, all analyte peaks of brand "g" vodka sample and brand "h" gin samples could be sufficiently separated from each other on AEC under optimized chromatographic conditions (See **Figure 4** and **Figure 5**, respectively).
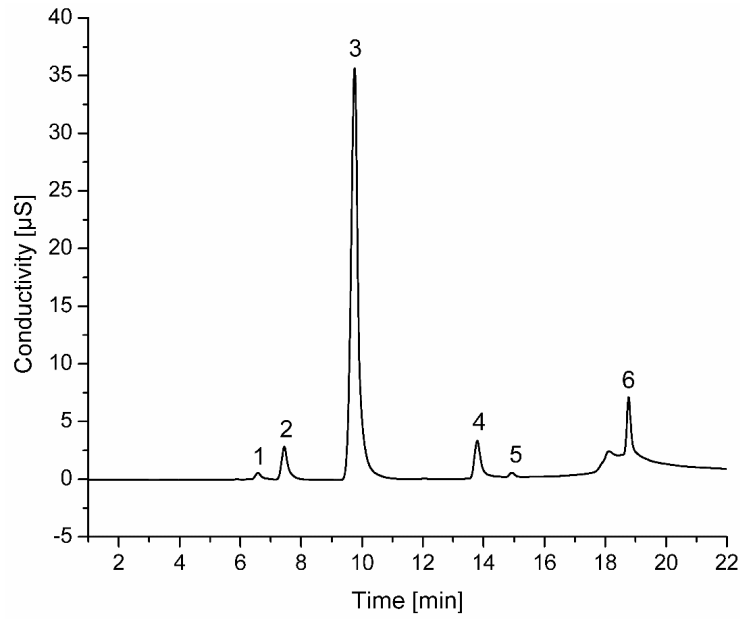
Figure 4. An IC chromatogram of the brand "g" vodka sample. *1*: Acetate; *2*: Formate; *3*: Chloride; *4*: Nitrate; *5*: Bromide; *6*: Sulfate.
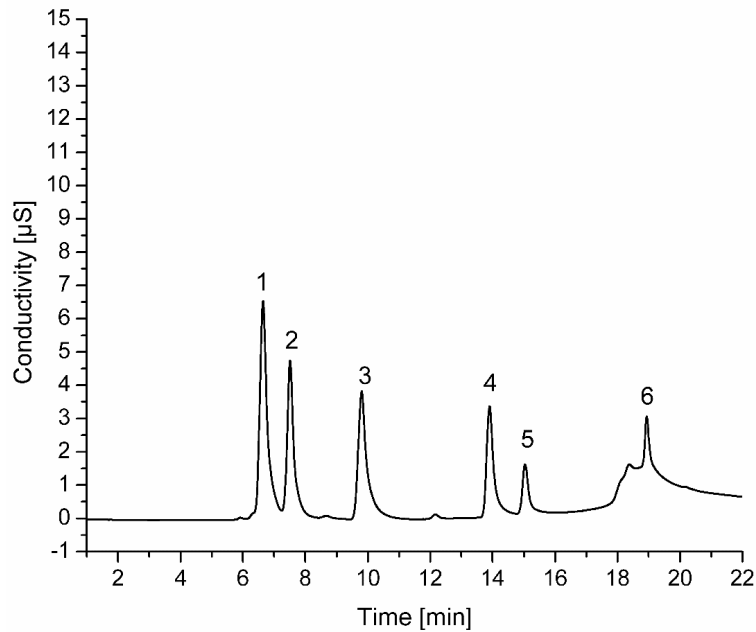
Figure 5. An IC chromatogram of the brand "h" gin sample. *1*: Acetate; *2*: Formate; *3*: Chloride; *4*: Nitrate; *5*: Bromide; *6*: Sulfate.

The linear calibration ranges and correlation coefficients of fluoride, acetate, formate, chloride, nitrate, and sulfate were summarized in **Table 1**. It was clear that a good linear relationship and correlation coefficients ($r^2 \geq$ 0.999) were achieved.

Table 1. Linear calibration curve parameters, t_R, LOD, and LOQ.

Analyte	Linear Range (mg L^{-1})	Regression equation	t_R (minute)	LOD (µg L^{-1})	LOQ (µg L^{-1})
Fluoride	0.004-10	y = 0.5912x − 0.0023	5.98	1.40	4.64
Acetate	0.010-20	y = 0.0510x − 0.0002	6.64	3.20	10.40
Formate	0.003-10	y = 0.2566x − 0.001	7.54	0.97	3.25
Chloride	0.002-30	y = 0.4927x − 0.0019	9.84	0.56	1.80
Nitrate	0.006-20	y = 0.4927x − 0.0019	15.05	1.70	5.85
Sulfate	0.044-20	y = 0.4927x − 0.0019	18.94	13.20	43.9

r^2 for all analytes were 0.999.

LOD and LOQ
According to the Eurachem Guide, LOD and LOQ were calculated by the standard deviation (s'_0) obtained from ten replicate measurements of low concentration of analytes in the samples, multiplied by k_Q factors, which were 3 and 10 (the IUPAC default values), respectively (37). Linear range, regression equation, the limit of detection (LOD), limit of quantification (LOQ), and retention time (t_R) values were given in **Table 1**.

The values given in **Table 1** confirm that the developed method was highly sensitive even at low ppb levels.

Selectivity
The proposed study offers enhanced selectivity. Quaternary ammonium functional group of the analytical AEC has (+) charge and anionic forms of small organic acids and inorganic anions separated on AEC. Then, each anion is converted into H-form in the suppressor part before arriving at CD. Therefore, the H-form of target analytes must be dissociated for responding to the CD. Sugar molecules, thus, can not be detected by CD since their H-forms can not be dissociated in CD.
In addition to separation on the column, some possibly interfering compounds in the samples were eliminated by suppressed CD. Thanks to the water bath vaporization process, the matrix effect was significantly decreased. Any shouldered or interfered peak was not observed in IC chromatograms.
By considering all these properties, the samples were successfully separated within 20 min without any interference, and it can be confidently asserted that a highly selective method was developed.

Trueness
Trueness is a criterion for the accuracy of a method. One of the statistical methods for

accepting accuracy is the significance test (t-test). To evaluate the trueness of the proposed method, brand "a" raki sample was spiked with three concentration levels, about half, equal, and two-fold of the first measured concentration values of the analytes. **Table 2** summarizes the average values of the recovery percentage results. Measured concentration values of the analytes in the solutions were given directly without calculating with a correction factor, which was 2.5. The recovery percentages for the analytes were found between 94.90 and 101.71 %, and they were acceptable according to the AOAC guideline (38). Besides, one of the statistical methods for accepting accuracy is the significance test (t-test). According to the results, the calculated t values were smaller than the theoretical, critical t value for 5 degrees of freedom equal to 2.57 at a level of significance α = 0.05 (see **Table 2**).

Precision
The precision of the proposed method was evaluated by carrying out inter-day and intra-day repeatability studies. Repeatability was expressed with RSD% values. Precision was evaluated by continuously performing six replicates each day within 3 days for the determination of the brand *a* raki sample. RSD % values of concentration, area, height, and t_R of the anions were given in **Table 3**, and the results were acceptable according to the AOAC guideline (38). The proposed method was successfully validated.

Analysis of the Samples
Three brands of Turkish raki, an ouzo sample, three brands of vodka, and three brands of gin samples were analyzed. **Table 4** shows the results of the analysis for different brands of distilled alcoholic beverages.

In raki samples, fluoride was the anion with the lowest concentration levels among all analytes, whereas acetate concentrations were the highest compared to the other anions except for sample "c". Although Ouzo is also an anise-flavored drink, acetate was not detected in this sample. Additionally, chloride, nitrate, and sulfate concentrations of the Ouzo sample were found about 75, 135, and 30 times higher than their average concentrations in Turkish raki samples, respectively. These differences between the anise-flavored beverages might arise from the water qualities and distillation procedures.

Nitrate and sulfate concentrations were found below 1.75 mg L^{-1} in all vodka and gin samples. Additionally, chloride concentrations were similarly found low, except brand "g" vodka had 7.03 mg L^{-1}. Formate concentrations were ≤ 2.61 mg L^{-1}, whereas acetate concentrations were measured at a wide range, which was between 0.41 – 15.02 mg L^{-1}.

For instance, according to the average results, when a person weighing 70 kg drinks three double shots (3 × 80 mL) of any legally produced raki sample, he/she approximately takes to his body about 0.42 mg of formate, 0.003 mg of fluoride, 1.39 mg of acetate, 0.46 mg of chloride, 0.03 mg of nitrate and 0.19 mg of sulfate. Similarly, drinking three glasses of vodka (3× 100 mL), he/she takes about 0.29 mg of formate, 0.003 mg of fluoride, 1.39 mg of acetate, 0.46 mg of chloride, 0.03 mg of nitrate and 0.19 mg of sulfate and when he/she drinks three glasses of gin (3× 100 mL) 0.44 mg of formate, 3.01 mg of acetate, 0.29 mg of chloride, 0.06 mg of nitrate and 0.20 mg of sulfate enter to his body. Besides, brand *c* sample has the maximum content of formate brand "a" sample has the maximum anion contents except for formate ion among the branded raki samples. On the one hand, brand *"g"* sample has the maximum contents of chloride and sulfate, brand *"e"* sample has the maximum anion contents except for chloride and sulfate ions among the branded vodka samples. On the other hand, sample "h" has the maximum content of nitrate, brand "i" sample has the maximum anion content except for nitrate ion among the gin samples. According to the results, a similar trend among the types of distilled beverages was not observed. When the legally produced beverage sample possessing maximum examined anion is consumed, taken amounts of all the anions are considerably lower than their toxic doses (7, 11, 14, 18, 20, 22). It was found in this study that no analyte found in the samples exceeded toxic levels.

In comparison, according to the previous studies and this study, one can say that the anionic composition of the distilled alcoholic beverage samples varies from brand to brand. It is well known that the anionic composition of the beverages depends on water used for production. However, among the analyzed brands, some of the anion content was relatively bigger than the other anions, these amounts are not out of the limit values set by the authorities based on average consumption habits (7, 11, 14, 18, 20, 22). Ionic composition of the water allows the differentiation of spirits, which are obtained from different manufacturers (34). If excellently demineralized soft water is used, the stability and sensory properties of drink will be improved.

On the other hand, the incremental amount of minerals may result in precipitation and instability problems (32). Moreover, the conductivity of the beverages is tightly related to the ionic composition. On the other hand, we put forward an argument that the proposed method can be used for authentication of illicit or inadequate quality alcoholic beverages by analyzing their anionic composition in addition to common higher alcohols analyses.

CONCLUSIONS

A reliable method of analysis for the determination of formate, acetate, and the other inorganic anions in alcoholic beverages is crucial for assessing product quality. In this paper, a new ion chromatographic method was developed for the simultaneous determination of fluoride, acetate, formate, chloride, nitrate, and sulfate in distilled alcoholic beverages using bromide as IS. The anion content analysis of the Turkish raki samples utilizing the developed method was performed for the first time in the literature. Experimental results indicated that the method has many advantages, which are smooth to operate, excellent repeatability, and sensitivity. It should be noted that the proposed method was environmentally friendly since no organic solvent or compound was not used throughout analyses. The total time for obtaining the results, including sample preparation, was about 1.5 h. In conclusion, the proposed method can be applied to various distilled alcoholic beverages to analyze the anions at food control laboratories and forensic laboratories.

Table 2. Recovery results of the brand a raki sample for evaluating the trueness of the method.

Analyte	Concentration (mg L^{-1})							Average Recovery (%)		
	Initial	SD	RSD % (n=6)	Added	Found	SD	RSD % (n=6)	Average	SD (n=6)	t_{cal}
Fluoride	2.20×10^{-2}	7.48×10^{-5}	0.34	0.01	3.17×10^{-2}	1.68×10^{-4}	0.53	97.00	3.83	1.92
				0.02	4.13×10^{-2}	2.56×10^{-4}	0.62	96.50	4.53	1.89
				0.04	6.14×10^{-2}	1.53×10^{-4}	0.25	98.50	3.36	1.09
Acetate	8.15	2.45×10^{-3}	0.03	4.21	12.23	8.56×10^{-3}	0.07	96.91	4.23	1.79
				8.42	16.31	2.60×10^{-2}	0.16	96.91	4.50	1.68
				16.84	24.50	1.47×10^{-2}	0.06	97.09	3.49	2.04
Formate	1.76	2.99×10^{-3}	0.17	0.88	2.62	6.03×10^{-3}	0.23	97.73	4.71	1.18
				1.76	3.55	6.03×10^{-3}	0.17	101.71	1.88	2.23
				3.52	5.33	3.73×10^{-3}	0.07	101.42	2.11	1.65
Chloride	1.32	3.43×10^{-3}	0.26	0.66	1.95	4.87×10^{-3}	0.25	95.45	5.83	1.91
				1.32	2.62	4.72×10^{-3}	0.18	98.48	3.52	1.06
				2.64	3.90	3.90×10^{-3}	0.10	97.72	3.19	1.75
Nitrate	1.94×10^{-1}	9.12×10^{-4}	0.47	9.65×10^{-2}	2.87×10^{-1}	1.00×10^{-3}	0.35	96.37	4.83	1.84
				1.93×10^{-1}	3.51×10^{-1}	2.00×10^{-3}	0.57	95.33	4.99	2.29
				3.86×10^{-1}	5.08×10^{-1}	1.88×10^{-3}	0.37	95.34	5.42	2.11
Sulfate	1.97	4.33×10^{-3}	0.22	0.98	2.91	2.91×10^{-3}	0.10	95.92	4.39	2.28
				1.96	3.89	5.45×10^{-3}	0.14	97.96	3.24	1.54
				3.92	5.69	1.71×10^{-3}	0.03	94.90	5.50	2.27

Table 3. Inter-day and intra-day RSD % (n=6) values of concentration, peak area, peak height, and t_R.

Analyte	Concentration		Area		Height		t_R	
	intra-day	inter-day	intra-day	inter-day	intra-day	inter-day	intra-day	inter-day
Fluoride	0.34	0.84	0.61	2.84	1.08	1.95	0.38	0.63
Acetate	0.04	0.20	0.31	2.43	0.78	1.41	0.44	0.70
Formate	0.17	0.99	0.43	3.28	2.10	5.99	0.46	0.75
Chloride	0.26	1.35	0.49	2.17	1.74	3.58	0.54	0.85
Nitrate	0.47	0.78	0.61	2.90	2.54	3.21	0.28	0.45
Sulfate	0.22	0.76	0.46	2.08	1.92	1.49	0.16	0.26

COMPLIANCE WITH ETHICS REQUIREMENTS

Conflict of Interest: No conflict of interest exists in the submission of this manuscript, and all authors approve the manuscript for publication. This work described was an original research that has not been published previously and not under consideration for publication elsewhere, in whole or in part. All the authors listed have approved the manuscript that is submitted. Melike Güler Şimşek, Orhan Destanoğlu, and Gülçin Gümüş have no conflict of interest.

Ethical Approval: This article does not contain any studies with human or animal subjects.

Table 4. IC results of anion concentrations of the raki, vodka and gin samples.

Analyte	Raki Brands						Ouzo Brand		Vodka Brands						Gin Brands					
	a		b		c		d		e		f		g		h		i		j	
	C (mgL^{-1})	RSD (%)	C (mgL^{-1})	RSD (%)	C (mgL^{-1})	RSD (%)	C (mgL^{-1})	RSD (%)	C (mgL^{-1})	RSD (%)	C (mgL^{-1})	RSD (%)	C (mgL^{-1})	RSD (%)	C (mgL^{-1})	RSD (%)	C (mgL^{-1})	RSD (%)	C (mgL^{-1})	RSD (%)
Fluoride	2.20×10^{-2}	0.34	ND	-	ND	-	ND	-	0.11×10^{-1}	0.23	ND	-	ND	-	ND	-	ND	-	ND	-
Acetate	8.15	0.03	7.54	0.04	1.70	0.05	ND	-	9.39	0.03	0.41	0.65	0.52	0.57	10.05	0.02	15.02	0.02	5.02	0.14
Formate	1.76	0.17	1.41	0.17	2.05	0.05	0.57	0.01	2.61	0.24	0.11	0.64	0.13	0.03	1.26	0.15	1.53	0.12	1.64	0.99
Chloride	1.32	0.26	0.39	0.13	0.56	0.47	60.43	0.24	2.10	0.31	0.73	0.12	7.03	0.01	0.75	0.85	1.06	0.13	1.03	0.14
Nitrate	0.19	0.47	0.03	0.96	0.10	0.95	13.50	0.02	0.50	0.76	0.12	0.42	0.06	0.39	0.34	0.65	0.15	0.69	0.12	0.89
Sulfate	1.97	0.22	0.29	0.21	0.13	0.78	22.32	0.02	0.22	0.64	0.25	0.15	0.63	0.40	0.18	0.78	1.75	0.07	0.09	0.85

*ND: Not Detected

REFERENCES

1. Destanoğlu O, Ateş İ. Determination and Evaluation of Methanol, Ethanol and Higher Alcohols in Legally and Illegally Produced Alcoholic Beverages. Journal of the Turkish Chemical Society, Section A: Chemistry. 2019;6(1):21-8.

2. Hovda KE, Urdal P, Jacobsen D. Increased serum formate in the diagnosis of methanol poisoning. Journal of analytical toxicology. 2005;29(6):586-8.

3. Zakharov S, Navrátil T, Pelclova D. Analysis of serum anion gap and osmolal gap in diagnosis and prognosis of acute methanol poisoning: clinical study in 86 patients. Monatshefte für Chemie-Chemical Monthly. 2015;146(5):787-94.

4. Destanoğlu O, İsmail A. Evaluation of Formic Acid Concentrations in Postmortem Blood Samples Using Hs-GcMs System. Türkiye Klinikleri Journal of Forensic Medicine and Forensic Sciences. 2019;16(3):155-63.

5. Treichel JL, Henry MM, Skumatz CM, Eells JT, Burke JM. Antioxidants and ocular cell type differences in cytoprotection from formic acid toxicity in vitro. Toxicological sciences. 2004;82(1):183-92.

6. Grzybowski A, Zülsdorff M, Wilhelm H, Tonagel F. Toxic optic neuropathies: an updated review. Acta ophthalmologica. 2015;93(5):402-10.

7. US.EPA. Provisional Peer-Reviewed Toxicity Values for Formic Acid. 2010. Contract No.: EPA/690/R-10/015F

8. Cortés S, Gil ML, Fernández E. Volatile composition of traditional and industrial Orujo spirits. Food Control. 2005;16(4):383-8.

9. Osobamiro T. Analysis of some contaminants commonly found in alcoholic beverages. Am-Eur J Sci Res. 2013;8(1):53-6.

10. Kamphorst JJ, Chung MK, Fan J, Rabinowitz JD. Quantitative analysis of acetyl-CoA production in hypoxic cancer cells reveals substantial contribution from acetate. Cancer & metabolism. 2014;2(1):23.

11. US.EPA. Reassessment of One Exemption from the Requirement of a Tolerance for Ethyl Acetate and One Exemption from the Requirement of a Tolerance for Amyl Acetate. 2006.

12. Browne D, Whelton H, O'Mullane D. Fluoride metabolism and fluorosis. Journal of Dentistry. 2005;33(3):177-86.

13. DenBesten P, Li W. Chronic fluoride toxicity: dental fluorosis. Fluoride and the oral environment. 22: Karger Publishers; 2011. p. 81-96.

14. Martínez-Mier EA. Fluoride: its metabolism, toxicity, and role in dental health. Journal of Evidence-Based Complementary & Alternative Medicine. 2012;17(1):28-32.

15. Buldini PL, Cavalli S, Trifirò A. State-of-the-art ion chromatographic determination of inorganic ions in food. Journal of Chromatography A. 1997;789(1-2):529-48.

16. Jagadish R, Shanmugaselvan VA. Quantification of Inorganic Anions in Tea (Camellia Sinensis (L) O. Kuntze) Tissues and Soil Using Ion Chromatography Coupled with Conductivity Detector. Communications in soil science and plant analysis. 2018;49(8):875-88.

17. Zhang F, Ma C, Wang Y, Liu W, Liu X, Zhang H. Fluorescent probes for chloride ions in biological samples. Spectrochimica Acta Part A: Molecular and Biomolecular Spectroscopy. 2018;205:428-34.

18. WHO. Chloride in Drinking-water. 2003. Contract No.: WHO/SDE/WSH/03.04/03

19. Chow C, Hong C. Dietary vitamin E and selenium and toxicity of nitrite and nitrate. Toxicology. 2002;180(2):195-207.

20. EFSA. Nitrites and nitrates added to food. 2017: [1-4 pp.].

21. US.EPA. Drinking Water Advisory: Consumer Acceptability Advice and Health Effects Analysis on Sulfate. 2003. Contract No.: EPA 822-R-03-007

22. WHO. Sulfate in Drinking-water 2004. Contract No.: WHO/SDE/WSH/03.04/114

23. Jurado-Sánchez B, Ballesteros E, Gallego M. Gas chromatographic determination of 29 organic acids in foodstuffs after continuous solid-phase extraction. Talanta. 2011;84(3):924-30.

24. Yang M-H, Choong Y-M. A rapid gas chromatographic method for direct determination of short-chain (C2–C12) volatile organic acids in foods. Food Chemistry. 2001;75(1):101-8.

25. Brondz I. Development of fatty acid analysis by high-performance liquid chromatography, gas chromatography, and related techniques. Analytica Chimica Acta. 2002;465(1-2):1-37.

26. Molnár-Perl I. Role of chromatography in the analysis of sugars, carboxylic acids and amino acids in food. Journal of Chromatography A. 2000;891(1):1-32.

27. Viidanoja J. Determination of short chain carboxylic acids in vegetable oils and fats using ion exclusion chromatography electrospray ionization mass spectrometry. Journal of Chromatography A. 2015;1383:96-103.

28. Kubáň P, Ďurč P, Bittová M, Foret F. Separation of oxalate, formate and glycolate in human body fluid samples by capillary electrophoresis with contactless conductometric detection. Journal of Chromatography A. 2014;1325:241-6.

29. Balcerzak M, Kapica D. Fast ion chromatographic method for the determination of formates in alcoholic drinks. Food Analytical Methods. 2017;10(7):2358-64.

30. Uzhel A, Zatirakha A, Smolenkov A, Shpigun O. Quantification of inorganic anions and organic acids in

apple and orange juices using novel covalently-bonded hyperbranched anion exchanger with improved selectivity. Journal of Chromatography A. 2018;1567:130-5.

31.   Souza SR, Tavares MF, de Carvalho LR. Systematic approach to the separation of mono-and hydroxycarboxylic acids in environmental samples by ion chromatography and capillary electrophoresis. Journal of Chromatography A. 1998;796(2):335-46.

32.   Lachenmeier DW, Schmidt B, Bretschneider T. Rapid and mobile brand authentication of vodka using conductivity measurement. Microchimica Acta. 2008;160(1-2):283.

33.   Arbuzov V, Savchuk S. Identification of vodkas by ion chromatography and gas chromatography. Journal of Analytical Chemistry. 2002;57(5):428-33.

34.   Lachenmeier DW, Attig R, Frank W, Athanasakis C. The use of ion chromatography to detect adulteration of

vodka and rum. European Food Research and Technology. 2003;218(1):105-10.

35.   Distilled Alcoholic Beverage Regulation, 2016/55 (2017).

36.   Suksom W, Wannachai W, Boonchiangma S, Chanthai S, Srijaranai S. Ion chromatographic analysis of monosaccharides and disaccharides in raw sugar. Chromatographia. 2015;78(13-14):873-9.

37.   Magnusson B, Örnemark U. Eurachem Guide: The Fitness for Purpose of Analytical Methods—A Laboratory Guide to Method Validation and Related Topics, ; Eurachem: Torino, Italy, 2014. Google Scholar.

38.   AOAC. AOAC Guidelines for Single Laboratory Validation of Chemical Methods for Dietary Supplements and Botanicals 2002.

RESEARCH ARTICLE

The Phytochemical, Proximate and Mineral Contents of Cassava Leaves and Nutritive Values of Associated Arthropod Pests

Sebiomo Adewole* ✉ iD, Banjo F. Mary ✉ iD

Department of Biological Sciences, Tai Solarin University of Education Ijagun, Ijebu-Ode, Nigeria

Abstract: Cassava (*Manihot esculenta*) is the most important staple food crops grown in Nigeria. This study investigated the following; (1) the nutritive values of insect pests associated with cassava leaves (2) phytochemical, mineral, and proximate content of cassava leaves (3) the antimicrobial activities of cassava leaves. Phytochemicals (Alkaloids, flavonoids, saponins, tannin, phytate, oxalate, phenol, and cyanogenic glycosides), proximate (ash, moisture, crude fiber, crude protein, crude fats), mineral (Zn, Fe, Cu, Mg, Ca, K, Fe, Mn, Na) and vitamin contents of samples were analyzed using the method of Association of Official Analytical Chemists. Results showed high amounts of crude protein, crude fat, moisture content, carbohydrate, and mineral content in all arthropod insects examined. The highest quantity of Ca (1152.84±0.67 mg/100g) was obtained in ABF4, followed by ABF5 (1148.72±1.09 mg/kg). The lowest phenol content of 0.10±0.00 ppm was obtained in the cassava branch. The leaf recorded the highest phenol value of 0.74±0.01 ppm. The highest alkaloid value was 3.51±2.45 ppm in *Manihot esculenta* branch. The highest crude protein and crude fat values of 3.41±0.13 % and 4.83±0.02 % were obtained in ABF5. Vitamin C was found in very high quantities compared to the other types of vitamins examined in this work. The highest Vitamin C content of 34.930±0.136 mg/100 g was obtained. Cassava leaves and the arthropod pests are good sources of nutrients. Cassava leaves could also be used as an antimicrobial agent.

INTRODUCTION

Cassava (*Manihot esculenta*) is an essential food crop grown and commonly consumed in the tropics (1). Cassava plays a significant role in making sure food security in a developing country; namely, Nigeria, is sustained. Approximately 750 million people, of which 45% of sub-Saharan Africans, depend entirely on cassava as a primary food source (1). All the parts of the crop in its entirety are useful for consumption by man and animals. Cassava is easily cultivated, and it adapts to soils with depleted fertility, low rainfall, high temperature, and resistance to drought (2). These essential qualities are vital in adapting to climate change. Cassava constitutes an important source of income for a lot of farmers, traders, and industries. It also contributes in no small measure to the economy of most developing and tropical countries like Nigeria through processing it into various products. The roots

are processed into flour, starch, and other end products like chips, flakes, biofuel, textiles, and glue (3).

Arthropods are found in the *Phylum euartbropoda* which includes insects, arachnids, myriapods, and crustaceans. Arthropods possess jointed limbs and cuticles containing chitin as well as calcium carbonate, while the body plan is made up of segments, and each of these is made up of a pair of appendages. The rigid cuticle slows down growth; hence, they are replaced periodically by molting. Arthropods aerate and mix the soil, which aids plants and microbial growth. They also control the population size of other soil organisms and help in breaking down organic materials. Arthropods recognizably affect plant performance, competition among plants thereby impacting the plant community composition due to series of mechanisms which include below ground herbivory as well as accelerates cycling of nutrient as a result of the action of arthropod detritivores (4).

The total count of arthropods attached to plants, which includes and not limited to cassava, is one of the crucial determinants of the diversity of species on land thus constituting the most critical ecological variable in relationships among living organisms which includes processes that are important for maintaining biodiversity in tropical forests (5;6). Species attached to plant species differ considerably. These variations are influenced by several factors such which include geography, abundance, and geological history, biochemical composition, phytochemical, mineral composition, diversity of habitat, as well as the structure of the host plant. Factors such as temperature and patterns of rainfall, interactions among living organisms can affect

them in their reproduction rate, adaptation, and longevity (7).

Arthropods possess many features, including high diversity and small body size, that make them essential for environmental monitoring. Arthropods are the most species-rich and morphologically diverse animal group of living organisms on earth (8). Arthropods sampling can be carried out using various survey methods. Thus, arthropods are often used as biological indicators of ecosystem integrity and could be used reliably to infer ecosystem function and habitat conditions (9).

Cassava (*Manihot esculenta*) leaves are a good source of dietary proteins and vitamin-K, which has a potential role in bone-strengthening by stimulating cell activity in the bones. Cassava carries some of the valuable B-complex group of vitamins such as folates, thiamin, pyridoxine (vitamin B-6), riboflavin, and pantothenic acid. It is one of the chief sources of some essential minerals like zinc, magnesium, copper, iron, and manganese. Also, it has adequate amounts of potassium, which is an essential component of cell and body fluids that help regulate heart rate and blood pressure. Hence this study investigated the following; (1) the nutritive values of insect pests associated with cassava leaves (2) phytochemical, mineral and proximate content of cassava leaves (3) the antimicrobial activities of cassava leaves.

MATERIALS AND METHODS

Study Area
The experiment was carried out in five cassava farmlands in Abapawa, Odogbolu Local Government Area of Ogun State (Fig. 1). The collection was done between the periods; April to August 2019. The region lies between

Figure 1. Map showing the location of sampling sites.

6°46'37" N latitude and 3°55'30" E longitude. The five cassava farmlands have a plot size of 18m x 36m (648 sqm) each.

Plant Material, Sample Preparation, and Extraction
Manihot esculenta leaves were collected from farmlands in Abapawa, Odogbolu Local Government area Ogun State, Nigeria. The leaves were sorted, de-stalked, and washed thoroughly in water several times until they became clean and free of debris, after which they were sun-dried. Dried leaf materials were pulverized into fine powdered form, filtered through a mesh, and an approximate amount of powdered material was subjected to Soxhlet extraction method with analytical grade solvents (ethanol and acetone). The crude leaf extracts obtained were evaporated completely and processed for further use.

Visual Sampling Method and Collection of Arthropods
A selected sample of cassava plants was used. Ten stands of cassava plants, which were observed for arthropod pests in each location of the leaves, stems, branch and the root, were tagged in each farmland. Arthropod pests affecting cassava plants were surveyed on the leaves, stems, and roots of the selected cassava stand. Arthropod pests were collected separately on different specimen bottles and labeled accordingly based on the part of the plant collection and the date of collection. The counts were made before 08:00h (GMT) each day to avoid excursive mobility of the adult pest after this time, but the migration of the fast-moving and mobile adults from one plot to the other could not be avoided.

Preservation of Arthropod Pests
Arthropods pests collected were sorted according to the species. These were later preserved separately in different specimen bottles containing 70% ethanol.

Identification of Arthropods
The cassava arthropods collected were then taken to the Department of Agriculture and Environmental Biology, University of Ibadan, Nigeria, for identification.

Phytochemical and Proximate Analysis of Samples
Phytochemicals (Alkaloids, flavonoids, saponins, tannin, phytate, oxalate, phenol, cyanogenic glycosides), proximate content (ash, moisture, crude fiber, crude protein, crude fats), mineral

contents (Zn, Fe, Cu, Mg, Ca, K, Fe, Mn, Na) were analyzed using the method of AOAC (10).

Determination of Alkaloid Content
0.5 g of the sample was dissolved in 96% ethanol: 20% H_2SO_4 (1:1). 1 mL of the filtrate was added to 5 mL of 60% sulfuric acid and left undisturbed for 5 minutes. Then, 5 mL of 0.5% formaldehyde was added and left to stand for 3 hours. The absorbance was read at 565 nm.

Determination of Flavonoid Content
The flavonoid content was determined using the aluminum chloride colorimetric assay method. An aliquot of 500 µL extract was mixed with the following: 1500 µL of 99.9% ethanol, 100 µL of 1 M potassium acetate, 100 µL of 10% aluminum chloride and 3000 µL of distilled water. The resulting mixture was incubated for 30 minutes at room temperature and corresponding absorbance measured at 415 nm.

Determination of Phenolic Content
50 µL of each of the samples was mixed with 3 mL of distilled water and 250 µL of a 1 in 10 diluted Folin-Ciocalteu phenol reagent. The mixtures were allowed to stand for 5 minutes, after which 750 µL of 20% Na_2CO_3 was added to each. They were thoroughly mixed and incubated for 30 minutes at room temperature in a dark place. Absorbance was measured at 760 nm using a UV-Vis Spectrophotometer.

Determination of Saponin Content
The samples were ground, and 20 g of each plant samples were dispersed in 200 mL of 20% ethanol. The suspension was heated over a hot water bath for 4 h with continuous stirring at about 55°C. The mixture was filtered, and the residue re-extracted with another 200 ml of 20% ethanol. The extracts were reduced to 40 mL over a water bath at about 90°C. The extract was then transferred into a 250 mL separator funnel, and 20 mL of diethyl ether was added and shaken vigorously. The aqueous layer was recovered while the ether layer was discarded. The process was repeated, after which 60 mL of n-butanol was added. The combined n-butanol extracts were washed twice with 10 mL of 5% aqueous sodium chloride. The remaining solution was heated in a water bath. After evaporation, the samples were dried in the oven to a constant weight. The saponin content was then calculated.

Determination of Tannins
0.2 g of the sample was measured into a 50 mL beaker. 20 mL of 50 % methanol was added

and covered with parafilm and placed in a water bath at 77-80 °C for 1 hour. It was then shaken thoroughly. The extract was filtered using a double-layered Whatman No. 1 filter paper. The filtrate was then dispensed into a 100 mL volumetric flask. 20 mL of water, 2.5 ml Folin-Denis reagent and 10 mL of 17% Na_2CO_3 were added and mixed thoroughly. The mixture was made up to the marked level with distilled water mixed well and left undisturbed for 20 minutes for the development of a bluish-green color. The absorbance was read after color development on a UV-Vis spectrophotometer model 752, at a wavelength of 760 nm.

Determination of Phytate Content
5 g of the sample was extracted with 20 mL of 3% trichloroacetic acid and filtered. 5 mL of 1 M NaOH was added to precipitate the phytate as ferric phytate and converted to ferric hydroxide and soluble sodium phytate. The precipitate was dissolved with hot 3.2 M HNO_3, and the absorbances were read immediately at 480 nm.

Determination of the Oxalate Content
150 mL of 15 N H_2SO_4 was added to 5 g of the pulverized sample, and the solution was carefully stirred intermittently with a magnetic stirrer for 30 minutes and filtered using Whatman No 1 filter paper, after which 25 mL of the filtrate was collected and titrated against 0.05 M standardized KMnO4 solution until a faint pink color appeared that persisted for 30 seconds.

Determination of Cyanogenic Glycoside
5 g of powdered sample was dissolved in 50 mL of distilled water in a conical flask, and the extraction was allowed to stand over-night, then filtered. 1 mL of sample filtered was mixed with 4 mL alkaline picrate in a corked test tube and incubated in a water bath for 5mins. After color development (reddish-brown color) the absorbance was read at 490nm.

Moisture Content Analysis
The moisture content was determined by heating 10.0 g of each sample to constant weight in a hot air-circulating thermostatic oven at 110 °C, cooling in desiccators, and obtaining a constant weight using Mettler P1210 Analytical Balance, Switzerland.

% MC = 10^2 [(wt. of crucible + sample before drying) – (dry wt. of crucible + sample)]/wt. of sample

Ash Content Analysis
Percentage ash was determined by charring 3.0 g of the sample on a hot plate in a fume cupboard and incinerating in a pre-heated muffle furnace (Bamford, Sheffield England) at 600oC for 4 h.

% Ash = 10^2 [(wt. of crucible + Ash) – (wt. of crucible)]/wt. of the sample before dry ashing

Fat Content Analysis
The fat content was determined by exhaustively extracting 2.0 g of each sample for 6 h in a Soxhlet extractor using petroleum ether.

% Fat = 10^2 Wt. of fat/Wt. of sample

Crude protein analysis
Crude protein was estimated by the Kjeldahl method. Total nitrogen, N, in the sample was first determined, and % N in the food protein was multiplied with a factor, 6.25 to obtain the % total protein in the sample. The sample was digested with conc. H_2SO_4 and the digest was distilled with Markham distiller in a fume cupboard to liberate NH_3 trapped into a 5 mL of 2 % H_3BO_3. The resulting ammonium borate was titrated against 0.01 M H_2SO_4.

% N = 10^2 [(Va – Vb) x 0.01 x 0.01401]/wt. of sample

Where Va = titer vol. of acid, Vb = titer vol. of blank

Mineral analysis
To 2.0 g of sample, 30ml of 1 N NH_4OAc (ammonium acetate solution) was added, and the flasks were shaken on a mechanical shaker for 2 h. The mixture was centrifuged at 2000 rpm for 10 min, and the clear supernatant was decanted into 100 ml volumetric flasks. About 30 ml of ammonium acetate solution (NH_4OAc) was added twice into the flasks, and shaken on a mechanical shaker for 30 min each, and centrifuged at 2000 rpm and the clear supernatant was then transferred into the same volumetric flasks respectively. The sample extract was made up to 100 mL volume with the NH_4OAc solution.

Ca, K, Na, Mn, Mg, Fe, Zn, and Cu in samples in the samples were determined using the atomic absorption spectrophotometer fitted with a hollow cathode lamp and a fuel-rich flame (air acetylene). Sample solutions (extract) and standard solutions for each mineral were injected into the atomic absorption spectrophotometer into sample fray, and the

mean signal response was recorded for each of the elements at their respective wavelength. The concentration of the minerals was calculated (10).

Determination of Vitamins Content
The vitamin contents (vitamins A, B1, B2, B6, C, D, E, and K) of the cassava leaves were determined by the methods of AOAC (10).

Test microorganisms for Antimicrobial Activities
Cultures of test microorganisms (*Salmonella typhi, Escherichia coli, Pseudomonas aeruginosa, Staphylococcus aureus, Aspergillus flavus, and Fusarium oxysporum*) were collected from University College Hospital Ibadan (UCH). The clinical isolates of bacteria were checked for purity and maintained on the nutrient agar plate at 4 °C in the refrigerator until required for use.

Preparation of Nutrient Agar (NA)
28 g of powdered nutrient agar was weighed on the analytical Mettler balance and dispensed into a 1-liter conical flask containing 1000 mL of distilled water. The suspension was then dissolved by heating in a water bath at 100 °C. Then 20 mL volume each of the molten agar was dispensed into McCartney bottles and sterilized inside the autoclave at 121 °C for 15 min. the sterile molten nutrient agar was allowed to cool to 40 °C before use.

Preparation of Potato Dextrose Agar (PDA)
39 g of powdered PDA was weighed into a 1-liter capacity conical flask containing 1000 mL of distilled water. The suspension was then dissolved by heating in a water bath at 100 °C. 20 mL volume each of the molten agars were dispensed into McCartney bottles and sterilized inside the autoclave at 121 °C for 15 min. The sterile molten nutrient agar was allowed to cool to 40 °C before use.

Test for Anti-bacterial Activity
15 mL of sterile nutrient agar was dispensed into each sterile petri dish of equal size and allowed to solidify. The surface of this sterile nutrient agar plate was streaked with a pure culture of standardized, *Escherichia coli, Pseudomonas aeruginosa*, and *Staphylococcus aureus* suspensions. A cork borer (8 mm in diameter) was sterilized by flaming and used to create ditch at the center of the plate. It was then filled with plant extracts. The plates were allowed to stand for one hour for pre-diffusion of the extracts, and incubation was done at 37 °C for 24 hrs. At the end of the incubation

period, the diameter of the zone of inhibition was measured in millimeters.

Test for Antifungal Activity
Potato Dextrose agar was melted and cooled to about 45 °C and was then poured into clean, sterile Petri-dishes and allowed to set. The overnight cultures of *A. flavus* and *F. oxysporum* were then inoculated into the sterile Petri-dishes. The plates were gently swirled round to enable the fungal suspensions to cover the whole surface of the plates. A standard cork borer was used to cut uniform equidistant wells on the surface of the agar into which known dilutions of the extracts were added. The plates were allowed to stand for one hour for pre-diffusion of the extracts and incubation was done at 25 °C for 48-72 h. The diameters of the zone of inhibition were measured and recorded.

Statistical Analysis
Data generated from this study were subjected to analysis of variance (ANOVA). Means were compared at 5% level of significance using Duncan's multiple range tests.

ANOVA was calculated as follows:

(1) The correction for mean (CM) was computed as shown below:

$$s^2 = \frac{1}{n-1} \sum (y_i - \bar{y})^2 \qquad (1)$$

(2) The total sum of squares (SS) were then determined as shown below;

$$SS_{\text{Total}} = SS_{\text{Error}} + SS_{\text{Treatments}} \qquad (2)$$

(3) The treatment sum of squares (SST) was then computed

$$SST = \sum_{i=1}^{3} \frac{T_i^2}{n_i} - CM = \qquad (3)$$

(4) The error sum of squares (SSE) was computed;

$$SSE = SS\ (TOTAL) - SST \qquad (4)$$

(5) The MST, MSE, and their ratio, F were computed;

$$MST = \frac{SST}{k-1}, \quad MSE = \frac{SSE}{N-k}, \quad F = \frac{MST}{MSE} \qquad (5)$$

RESULTS

Arthropod Pests

The following arthropod pests were obtained from the cassava plants; whitefly, *Convolvulus hawkmoth*, centipede, and grasshopper.

Proximate, Mineral and Microbial Contents of Arthropod Pests

Proximate analysis showed that the highest values for crude protein (7.64%), crude fiber (0.72%), fat (5.65%), ash (0.79%) and moisture content (16.05%) were obtained in whitefly, *Convolvulus hawkmoth*, centipede, and grasshopper respectively (Figure 2). Meanwhile, there were no significant differences (P≥0.05) in the crude fiber values of *Convolvulus hawkmoth* and Centipede.

Figure 3 shows the mineral contents of selected pests. Ca (4.53 mg/100 g), K (8.28 mg/100 g), Na (5.81 mg/100 g), P (6.86 mg/100 g), Fe (3.51 mg/100 g) and Mg (2.47 mg/100 g) were found to be highest in whitefly, grasshopper, Centipede and *Convolvulus hawkmoth* respectively. There were significant differences (P≤ 0.05) in the Ca, K, Na, P, Fe, and Mg values for the selected pests. The centipede had the lowest Mg, Fe, and K values of 1.18 mg/100 g, 1.48 mg/100 g, and 5.70 mg/100 g, respectively. There were no significant differences (p≥0.05) in the phosphorus values of *Convolvulus hawkmoth*, Centipede, and grasshopper. Grasshopper recorded the lowest Ca content of 3.03mg/100g while whitefly had the lowest Na content of 3.53 mg/100 g.

In Figure 4, microbial content analysis shows that the highest values for TBC (0.67×10^5 cfu g^{-1}), TFC (0.08×10^5 cfu g^{-1}), and TCC (0.23×10^5 cfu g^{-1}) were obtained in Whitefly and grasshopper. There were no significant differences (P≥0.05) in the total fungi counts of Whitefly, *Convolvulus hawkmoth*, and Centipede. *Convolvulus hawkmoth* (0.47×10^5 cfu g^{-1}) showed the lowest total bacterial count, while whitefly recorded the lowest total coliform count of 0.10×10^5 cfu g^{-1}.

In Figure 5, the highest values for crude protein (7.70%), crude fiber (0.74%), fat (5.71%), ash (0.81%) and moisture content (16.11%) were obtained in *Convolvulus hawkmoth* and grasshopper respectively. Meanwhile, the crude fiber content in *Convolvulus hawkmoth* and Centipede showed there were no significant differences (P≥0.05) in their values.

Figure 6 showed that Ca (4.60 mg/100 g), K (8.34 mg/100 g), Na (5.87 mg/100 g), P (6.92 mg/100 g), Fe (3.57 mg/100 g) and Mg (2.53 mg/100 g) were found to be highest in whitefly, grasshopper, Centipede and *Convolvulus hawkmoth* respectively. There were significant differences (P≤ 0.05) in the Ca, K, Na, P, Fe, and Mg values for the selected pests. Centipede had the lowest Mg, Fe, and K values of 1.24 mg/100 g, 1.54 mg/100 g, and 5.76 mg/100 g, respectively. Grasshopper recorded the lowest Ca content of 3.09 mg/100 g. There were no significant differences (P≥0.05) in the phosphorus values of Centipede and grasshopper (6.92 mg/100 g).
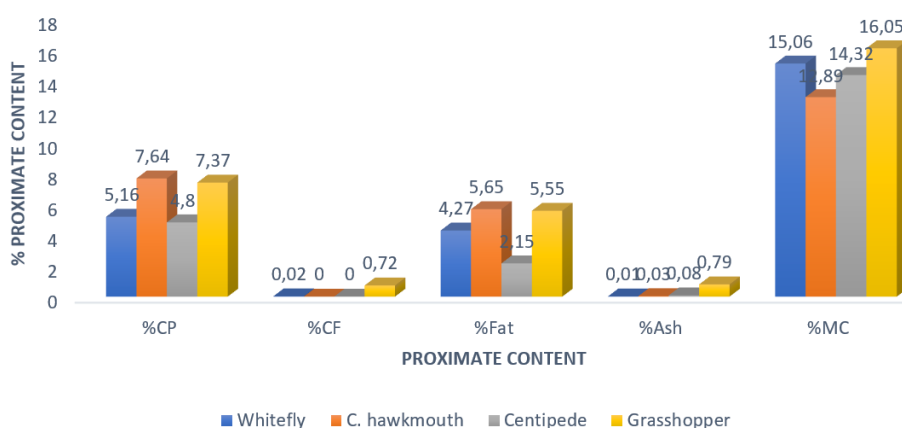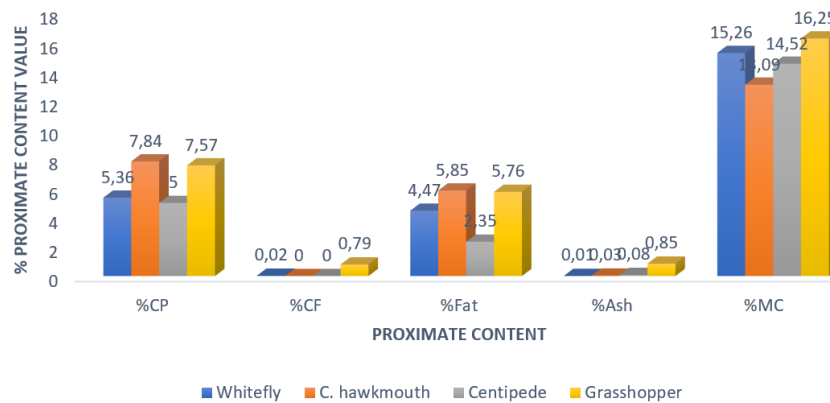

Figure 2. Proximate analysis of pests obtained from ABF1 (ABF1=Abapawa Farmland 1) (CP= Crude Protein, CF= Crude Fiber, MC= Moisture Content)
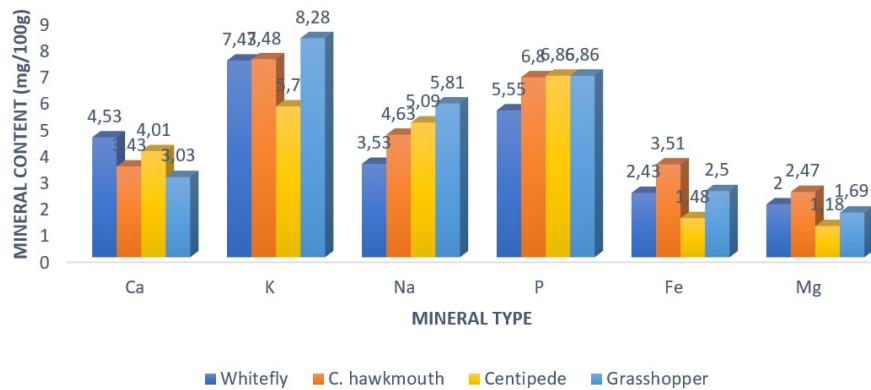
Figure 3. Mineral contents of selected pests obtained from ABF1 (ABF1=Abapawa Farmland 1)
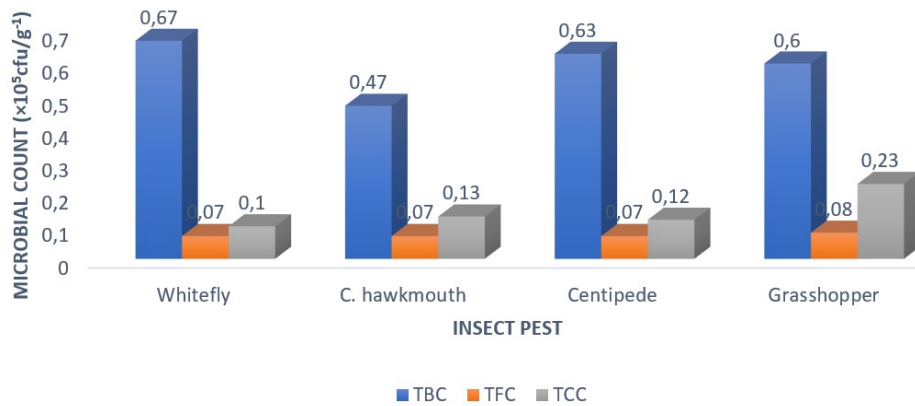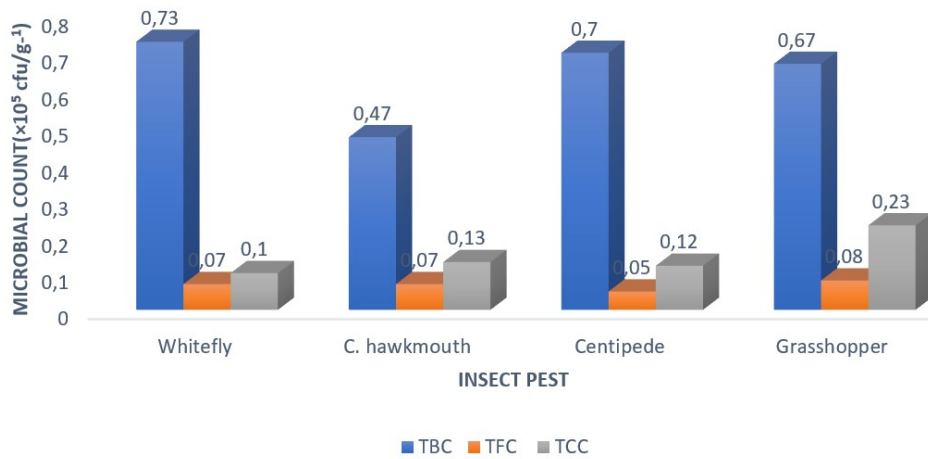

Figure 4. Microbial content analysis of pests obtained from ABF1 (ABF1=Abapawa Farmland 1)
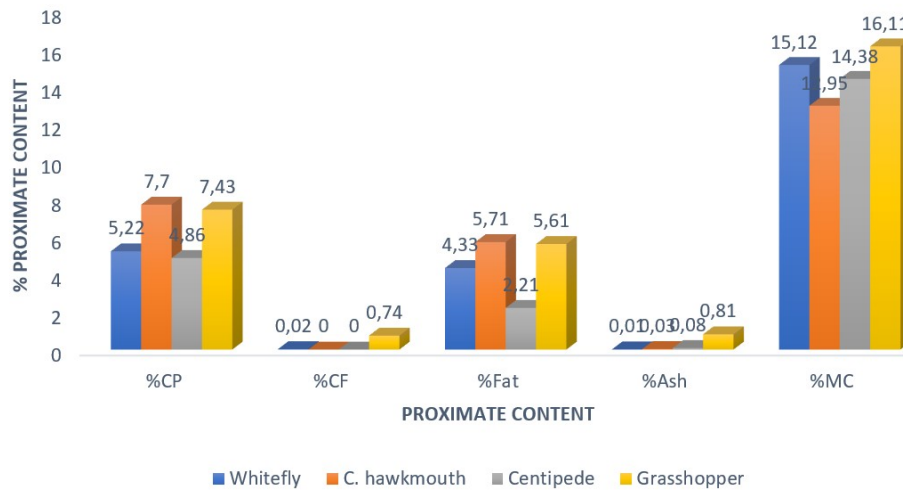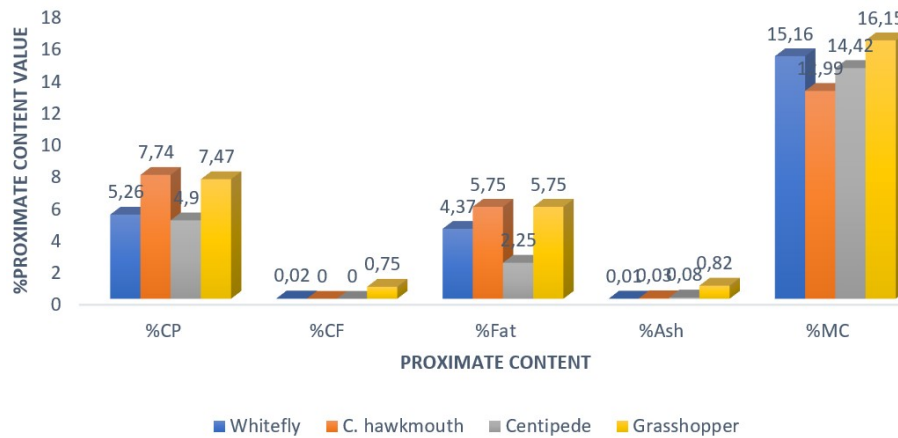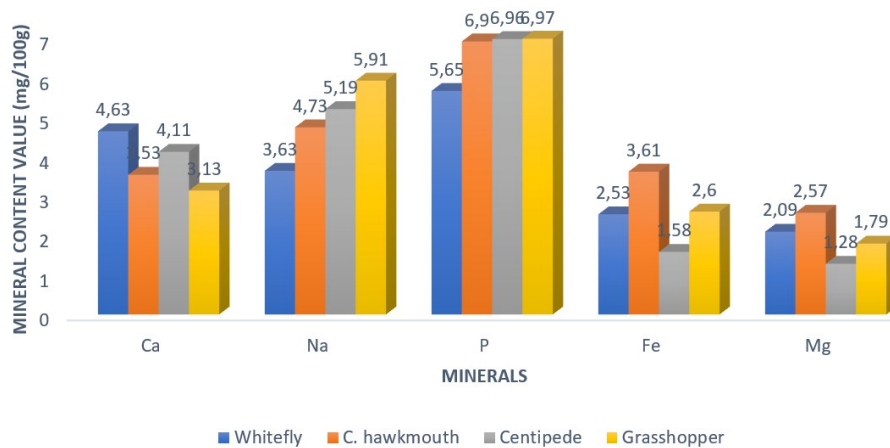

Figure 5. Proximate analysis of pests obtained from ABF2 (ABF 2=Abapawa Farmland 2)
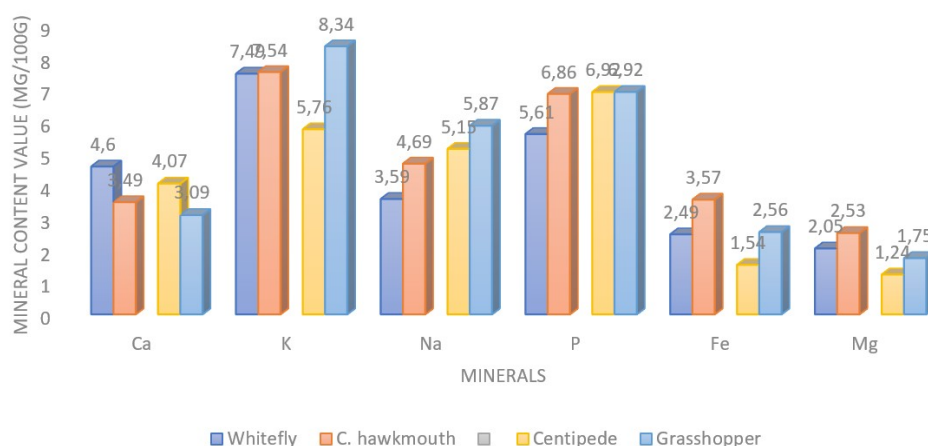
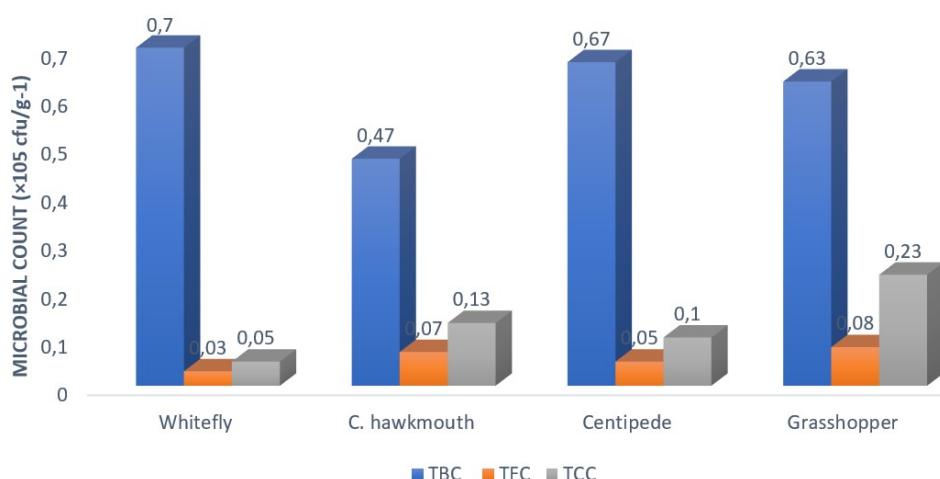**Figure 6.** Mineral content analysis of pests obtained from ABF2 (ABF 2=Abapawa Farmland

The highest values for TBC (0.69×10^5cfu g^{-1}) and TCC (0.23×105cfu g^{-1}) were obtained in whitefly and grasshopper, respectively (Figure 7). There were no significant differences (P≥0.05) in the total fungi counts of Whitefly, *Convolvulus hawkmoth*, grasshopper, and Centipede. *Convolvulus hawkmoth* (0.47×10^5cfu g^{-1}) showed the lowest total bacterial count, while whitefly recorded the lowest total coliform count of 0.10×10^5cfu g^{-1}.

In Figure 8, there were no significant differences in the (P≥0.05) crude fiber contents of *Convolvulus hawkmoth* and Centipede. The proximate analysis shows that the highest values for crude protein (7.84%), crude fiber (0.79%), fat (5.85%), ash (0.85%), and moisture content (16.25%) were obtained in *Convolvulus hawkmoth* and grasshopper respectively.

In Figure 9, the mineral content analysis showed that Ca (4.73 mg/100 g), K (8.48 mg/100 g), Na (6.01 mg/100 g), P (7.06 mg/100 g), Fe (3.71 mg/100 g) and Mg (2.67 mg/100 g) were found to be highest in whitefly, grasshopper, Centipede and *Convolvulus hawkmoth* respectively. There were significant differences (P≤ 0.05) in the Ca, K, Na, P, Fe, and Mg values for the selected pests. The centipede had the lowest Mg, Fe, Na, and K values of 1.38 mg/100g, 1.68 mg/100g, 5.29 mg/100g, and 5.90 mg/100g, respectively. There were no significant differences (P≥0.05) in the phosphorus values of Centipede and grasshopper. Grasshopper recorded the lowest Ca content of 3.23mg/100g while whitefly had the lowest Na content of 3.73mg/100g. There were significant differences (P≤0.05) in the values obtained for potassium in Centipede, Whitefly and *Convolvulus hawkmoth*.

In Figure 10, there were significant differences (P≤0.05) in the total bacterial count of the sampled pests. The highest values of TBC (0.73×10^5 cfu g^{-1}), TFC (0.08×10^5 cfu g^{-1}) and TCC (0.23×10^5 cfu g^-1) were obtained in Whitefly and grasshopper respectively. There were no significant differences (P≥0.05) in the total fungi counts of Whitefly and *Convolvulus hawkmoth*. *Convolvulus hawkmoth* had the lowest total bacterial count of 0.47×10^5 cfu g^{-1}, while whitefly recorded the lowest total coliform count of 0.10×10^5 cfu g^{-1}. There were significant differences in the TFC of Centipede and grasshopper.

In Figure 11, the highest crude protein (7.74%), crude fiber (0.75%), fat (5.75%), ash (0.82%), and moisture content (16.15%) values were obtained in *Convolvulus hawkmoth* and grasshopper respectively. Lowest ash content values were obtained in whitefly (0.01%), while *Convolvulus hawkmoth* had the lowest moisture content of 12.99%.

In Figure 12, Ca (4.63 mg/100 g), K (8.38 mg/100 g), Na (5.91 mg/100 g), P (6.97 mg/100 g), Fe (3.61 mg/100 g) and Mg (2.57 mg/100 g) were highest in whitefly, grasshopper, Centipede and *Convolvulus hawkmoth* respectively. There were significant differences (P≤ 0.05) in the Ca, K, Na, P, Fe, and Mg values for the selected pests. The centipede had the lowest Mg, Fe, Na, and K values of 1.28 mg/100g, 1.58 mg/100g, 5.19 mg/100g, and 5.80 mg/100 g, respectively. Grasshopper recorded the lowest Ca content of 3.13 mg/100 g while whitefly had the lowest Na content of 3.63 mg/100 g.

n Figure 13, there were significant differences (P≤0.05) in the total bacterial count of the sampled pests. The highest values of TBC (0.70 ×10^5 cfu g^{-1}), TFC (0.08 ×10^5 cfu g^{-1}) and TCC (0.23×10^5 cfu g^{-1}) which were obtained in Whitefly and grasshopper respectively. There were significant differences in the total fungi counts of Whitefly (0.03×10^5 cfu g^{-1}), *Convolvulus hawkmoth* (0.07×10^5 cfu g^{-1}), Centipede (0.05×10^5 cfu g^{-1}) and grasshopper (0.08×10^5 cfu g^{-1}). *Convolvulus hawkmoth* (0.47×10^5 cfu g^{-1}) had the lowest total bacterial count while whitefly recorded the lowest total coliform count of 0.05 ×10^5 cfu g^{-1}.
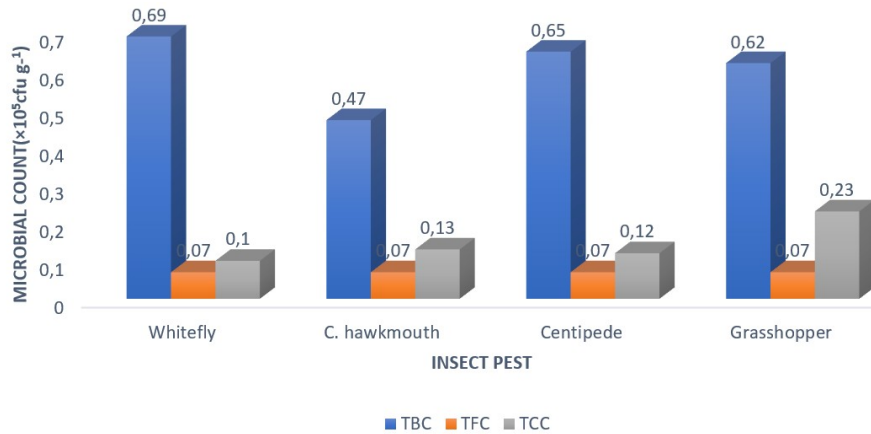
Figure 7. Microbial count analysis of pests obtained from ABF2 (ABF 2=Abapawa Farmland 2). TBC=Total Bacterial Count, TCC=Total Coliform Count, TFC= Total Fungal Count

Figure 8. Proximate analysis of pests obtained from ABF3 (ABF3=Abapawa Farmland 3) (CP= Crude Protein, CF= Crude Fiber, MC= Moisture Content)
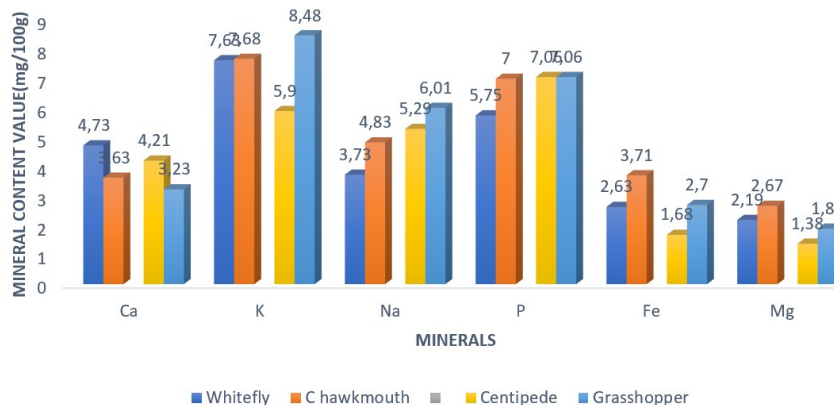
Figure 9. Mineral content analysis of pests obtained from ABF3 (ABF3=Abapawa Farmland 3)

Figure 10. Microbial count of pests obtained from ABF3 (ABF3=Abapawa Farmland 3). TBC=Total Bacterial Count, TCC=Total Coliform Count, TFC= Total Fungal Count

Figure 11. Proximate analysis of pests obtained from ABF4 (ABF4=Abapawa Farmland 4)

Figure 12. Mineral content analysis of pests obtained from ABF4 (ABF4=Abapawa Farmland 4)

Figure 13. Microbial content analysis of pests obtained from ABF4 (ABF4=Abapawa Farmland 4). TBC=Total Bacterial Count, TCC=Total Coliform Count, TFC= Total Fungal Count

Phytochemical Content in Various Parts of *Manihot Esculenta*

In Table 1, alkaloids were obtained in comparatively high concentrations in all parts of the plant (*Manihot esculenta)*. The lowest phenol and alkaloid content values of 0.10±0.00 ppm and 3.51±2.45 ppm respectively were obtained in the cassava branch. The leaf recorded the highest phenol value of 0.74±0.01 ppm. The highest flavonoid content of 2.06±0.05 ppm was obtained in the root of *Manihot esculenta*.

Table 1. Phytochemical content (ppm) in various parts of *Manihot esculenta*

Sample	Alkaloids	Flavonoids	Tannins	Phenols
Leaf	2.83±0.95	0.98±0.05	2.98±0.03	0.74±0.01
Stem	2.48±0.15	1.31±0.37	1.51±0.02	0.18±0.01
Root	2.83±0.15	2.06±0.05	0.85±0.01	0.25±0.01
Branch	3.51±2.45	1.42±0.06	1.89±0.35	0.10±0.00

Mineral, Phytochemicals, Proximate and Vitamin Contents of Cassava Leaves

The minerals analyzed in this study occurred in varying quantities (Table 2). Cassava leaves contained high quantities of Ca. The highest quantity (1152.84±0.67 mg/100 g) was obtained in ABF4 followed by ABF5 (1148.72±1.09 mg/kg), ABF3 (1141.23±2.12 mg/kg), ABF2 (1125.8±0.89 mg/kg), and ABF1 (791.96±0.16 mg/kg). K was also obtained in high quantities with ABF4 (764.13±1.14 mg/kg) containing the highest quantity followed by ABF5 (761.49±0.65 mg/kg), ABF3 (760.68±0.38 mg/kg), ABF1 (759.48±1.21 mg/kg) and ABF2 (692.82±0.92 mg/kg).

Table 2. The mineral content of cassava leaves (mg/kg)

	ABF1	ABF2	ABF3	ABF4	ABF5
Na	25.58±0.45[a]	27.09±0.30[c]	27.05±0.07[c]	28.25±0.34[d]	26.93±0.01[d]
K	759.48±1.21[c]	692.82±0.92[g]	760.68±0.38[g]	764.13±1.14[h]	761.49±0.65[h]
Ca	791.96±0.16[c]	1125.8±0.89[h]	1141.23±2.12[h]	1152.84±0.67[i]	1148.72±1.09[i]
P	66.68±3.82[ab]	76.22±0.83[d]	76.22±0.51[d]	76.60±0.34[e]	75.23±0.87[e]
Mg	313.12±0.50[ab]	320.75±1.14[e]	317.60±0.62[e]	330.40±0.78[f]	333.44±0.25[f]
Fe	412.70±0.58[d]	422.48±0.90[f]	418.15±0.31[f]	416.13±0.88[g]	416.79±1.10[g]
Zn	17.52±0.58[a]	17.54±0.31[b]	18.44±0.80[b]	22.46±0.17[c]	21.72±0.04[c]
Mn	16.90±0.03[a]	18.55±0.04[b]	17.15±0.66[b]	18.77±0.44[b]	18.43±0.14[b]
Cu	2.62±0.01[a]	4.65±0.02[a]	5.26±0.03[a]	4.73±0.02[a]	5.27±0.69[a]

Columns with values that have the same letter show that there is no significant differences (P≥0.05) between the values; columns with values that have different letters show that there is a significant difference (P≤0.05) between the values. ABF1=Abapawa Farm 1, ABF2= Abapawa Farm 2, ABF3= Abapawa Farm 3, ABF4= Abapawa Farm 4, ABF5= Abapawa Farm 5.

The cassava leaves were also found to contain high quantities of Fe. The highest quantity of Fe was obtained in ABF2 (422.48±0.90 mg/kg). However, Cu was obtained in low quantities. ABF1 recorded the lowest Cu content of 2.62±0.01 mg/kg, while the highest Cu content was obtained in ABF5 (5.27±0.69 mg/kg). Table 2 showed that there were significant differences (P≤0.05) in the mineral quantity values. However, there were no significant differences (P≥0.05) in the Zn and Mn values of ABF1 and ABF2.

This study revealed that cassava leaves contain the following phytochemical constituents; cyanogenic glycosides, flavonoids, saponin, alkaloids, phytate, oxalate, trypsin inhibitor, and phenol. The phytochemical contents analyzed in Table 3 revealed that cyanogenic glycosides were obtained in very high amounts. The highest cyanogenic glycoside value was obtained in ABF2 (32.82±0.16 mg/100 g), followed by ABF4 (32.70±0.29 mg/100 g), ABF3 (31.67±0.04 mg/100 g), ABF2 (30.96±0.24 mg/100 g) and ABF1 (30.89±0.57 mg/100 g). tannin was obtained in low amounts. ABF3 contained the lowest tannin value of 0.16±0.01 mg/100 g. Flavonoids were also obtained in appreciable amounts. ABF3 had the highest flavonoid content of 3.90±0.01 mg/100 g. There were significant differences (P≤0.05) in the phytochemical contents in Table 3. However, there were no significant differences (P≥0.05) in the tannin, phenol, trypsin inhibitor, phytate and oxalate values in ABF1.

Table 3. Phytochemical content of cassava leaves (mg/100 g)

	ABF1	ABF2	ABF3	ABF4	ABF5
ALKALOID	1.30 ± 0.01^b	1.22 ± 0.01^c	1.63 ± 0.01^e	2.31 ± 0.55^b	1.78 ± 0.01^d
SAPONIN	3.21 ± 0.03^c	3.63 ± 0.04^d	3.15 ± 0.01^f	3.14 ± 0.01^c	3.18 ± 0.02^f
FLAVONOID	3.71 ± 0.02^c	3.64 ± 0.02^d	3.90 ± 0.01^g	2.87 ± 0.05^{bc}	2.89 ± 0.04^h
TANIN	0.22 ± 0.01^a	0.25 ± 0.01^a	0.16 ± 0.01^a	0.22 ± 0.01^a	0.17 ± 0.01^a
PHENOL	0.17 ± 0.01^a	0.17 ± 0.01^a	0.14 ± 0.01^a	0.19 ± 0.01^a	0.15 ± 0.01^a
T INHIBITOR	0.42 ± 0.01^a	0.41 ± 0.02^{ab}	0.31 ± 0.01^b	0.25 ± 0.01^a	0.33 ± 0.01^b
PHYTATE	0.58 ± 0.01^a	0.61 ± 0.02^b	0.63 ± 0.01^d	0.66 ± 0.01^a	0.65 ± 0.01^c
OXALATE	0.63 ± 0.01^a	0.64 ± 0.02^b	0.55 ± 0.01^c	0.72 ± 0.01^a	0.59 ± 0.01^c
C GLYCO	30.89 ± 0.57^d	30.96 ± 0.24^e	31.67 ± 0.04^h	32.70 ± 0.29^d	32.82 ± 0.16^g

Columns with values that have the same letter show that there is no significant differences (P≥0.05) between the values; columns with values that have different letters show that there is a significant difference (P≤0.05) between the values. Note: T INHIBITOR= Trypsin Inhibitor, C GLYCO= Cyanogenic Glycosides ABF1=Abapawa Farm 1, ABF2= Abapawa Farm 2, ABF3= Abapawa Farm 3, ABF4= Abapawa Farm 4, ABF5= Abapawa Farm 5.

In Table 4, carbohydrates were obtained in appreciable quantities. The highest carbohydrate content of 66.68±0.08 % was obtained in ABF2. The moisture content values were also appreciable in quantity. The highest moisture content value of 24.1±0.27 % was obtained in ABF5. Crude proteins and fat were also found in cassava leaves. The highest crude protein and crude fat values of 3.41±0.13 % and 4.83±0.02 % were obtained in ABF5. There were significant differences (P≤0.05) in the proximate content values.

Table 4. Proximate content of cassava leaves (%)

	ABF1	ABF2	ABF3	ABF4	ABF5
CP	2.5 ± 0.02^{ab}	2.33 ± 0.02^b	3.13 ± 0.02^b	3.39 ± 0.01^b	3.41 ± 0.13^b
CF	3.43 ± 0.02^c	2.96 ± 0.01^c	3.19 ± 0.02^b	4.74 ± 0.03^c	4.83 ± 0.02^c
FAT	2.09 ± 0.03^a	2.12 ± 0.01^a	2.14 ± 0.02^a	2.15 ± 0.01^a	2.69 ± 0.03^a
ASH	2.86 ± 0.03^{bc}	2.91 ± 0.01^c	2.72 ± 0.06^{ab}	3.14 ± 0.02^b	3.59 ± 0.04^b
MOIST	23.15 ± 0.34^d	22.99 ± 0.09^d	23.25 ± 0.33^c	23.27 ± 0.24^d	24.1 ± 0.27^d
CHO	65.99 ± 0.34^e	66.68 ± 0.08^e	65.57 ± 0.32^d	63.31 ± 0.26^e	61.38 ± 0.23^e

Columns with values that have the same letter show that there are no significant differences (P≥0.05) between the values, columns with values that have different letters show that there is a significant difference (P≤0.05) between the values. Note: CP= Crude Protein, CF= Crude Fiber, MC= Moisture Content. ABF1=Abapawa Farm 1, ABF2= Abapawa Farm 2, ABF3= Abapawa Farm 3, ABF4= Abapawa Farm 4, ABF5= Abapawa Farm 5.

Vitamins A, B1, B2, B6, C, D, E, and K were obtained in the cassava leaves (Table 5). Vitamin C was found in very high quantities compared to the other types of vitamins examined in this work. The highest Vitamin C content of 34.930±0.136 mg/100 g was obtained. Vitamin K, however, occurred in meager quantities. The lowest vitamin K content of 0.002±0.000 mg/100g was obtained in ABF1, ABF2, ABF4, and ABF5. There were no significant differences in Vitamins A, B1, B2, B6, E, and K contents of ABF1 and ABF3.

Table 5. Analysis of vitamins present in cassava leaves (mg/100g)

	ABF1	ABF2	ABF3	ABF4	ABF5
VIT A	0.122±0.001[a]	0.126±0.000[ab]	0.307±0.231[a]	0.088±0.001[a]	0.085±0.001[b]
VIT B1	0.220±0.001[a]	0.222±0.002[bc]	0.221±0.001[a]	0.231±0.001[a]	0.234±0.002[d]
VIT B2	0.100±0.000[a]	0.110±0.000[ab]	0.105±0.001[a]	0.112±0.001[a]	0.113±0.001[c]
VIT B6	0.300±0.005[a]	0.280±0.001[c]	0.307±0.002[a]	0.323±0.002[a]	0.322±0.004[e]
VIT C	30.290±0.430[b]	34.930±0.136[d]	34.506±0.367[b]	33.163±0.512[b]	34.190±0.025[f]
VIT D	0.010±0.000[a]	0.003±0.000[a]	0.004±0.000[a]	0.005±0.001[a]	0.004±0.001[a]
VIT E	0.004±0.000[a]	0.002±0.000[a]	0.003±0.000[a]	0.004±0.000[a]	0.004±0.000[a]
VIT K	0.002±0.000[a]	0.002±0.000[a]	0.003±0.000[a]	0.002±0.000[a]	0.002±0.000[a]

Columns with values that have the same letter show that there are no significant differences (P≥0.05) between the values; columns with values that have different letters show that there is a significant difference (P≤0.05) between the values. ABF1=Abapawa Farm 1, ABF2= Abapawa Farm 2, ABF3= Abapawa Farm 3, ABF4= Abapawa Farm 4, ABF5= Abapawa Farm 5.

Antimicrobial Activities of Cassava Leaves
Table 6 shows the antimicrobial activities of the acetone extracts of cassava leaves. There were no significant differences in the zones of inhibitions of E. coli, S. aureus, P. aeruginosa, in ABF1, ABF2, and ABF3. The highest zone of inhibition of 13.50±0.43 mm was obtained in the culture plates of S. aureus in the cassava leaf extracts of ABF4. The lowest zone of inhibition of 2.67±0.42 mm was obtained in the culture plates of A. flavus in the cassava leaf extracts of ABF3.

Table 6. Antimicrobial activity of acetone extracts of cassava leaves (mm)

	ABF1	ABF2	ABF3	ABF4	ABF5
EC	10.5±0.85[b]	11.33±0.67[b]	12.17±0.75[b]	13.00±0.86[c]	11.33±0.62[b]
SA	12.17±0.75[b]	11.50±0.62[b]	12.83±0.83[b]	13.50±0.43[c]	13.17±0.48[c]
PA	10.83±0.75[b]	10.00±0.78[b]	13.33±0.88[b]	10.83±0.40[b]	11.67±0.42[b]
AF	3.83±0.31[a]	3.00±0.37[a]	2.67±0.42[a]	3.00±0.37[a]	2.83±0.31[a]
FO	3.67±0.42[a]	4.00±0.52[a]	3.17±0.31[a]	2.83±0.31[a]	3.83±0.31[a]

Columns with values that have the same letter show that there are no significant differences (P≥0.05) between the values; columns with values that have different letters show that there is a significant difference (P≤0.05) between the values. Note: EC= *Escherichia coli*, SA= *Staphylococcus aureus*, PA= *Pseudomonas aeruginosa*, AF= *Aspergillus flavus*, FO= *Fusarium oxysporium.* ABF1=Abapawa Farm 1, ABF2= Abapawa Farm 2, ABF3= Abapawa Farm 3, ABF4= Abapawa Farm 4, ABF5= Abapawa Farm 5.

In Table 7 there were significant differences (P≤0.05) in the zones of inhibition produced in all the culture plates. The highest zone of inhibition of 10.83±0.31 mm was obtained in S. aureus culture plates of the leaf extracts of ABF4 whereas the lowest zone of inhibition value of 2.00±0.26 mm was obtained in the A. flavus culture plates of the cassava leaf extracts of ABF2.

Table 7. Antimicrobial activity of ethanol extracts of cassava leaves (mm)

	ABF1	ABF2	ABF3	ABF4	ABF5
EC	8.33±0.56[b]	7.00±0.37[b]	9.00±0.52[b]	9.50±1.18[bc]	8.33±0.56[b]
SA	10.33±0.21[c]	9.67±0.67[c]	10.83±0.75[c]	10.83±0.31[c]	10.17±0.54[c]
PA	8.83±0.75[b]	8.17±0.98[bc]	10.17±0.54[bc]	8.33±0.67[b]	9.00±0.63[bc]
AF	2.50±0.22[a]	2.00±0.00[a]	2.33±0.21[a]	2.00±0.26[a]	2.17±0.17[a]
FO	2.67±0.21[a]	3.00±0.26[a]	2.33±0.21[a]	2.17±0.17[a]	2.83±0.31[a]

Columns with values that have the same letter show that there are no significant differences (P≥0.05) between the values, columns with values that have different letters show that there is a

significant difference (P≤0.05) between the values Note: EC= *Escherichia coli*, SA= *Staphylococcus aureus*, PA= *Pseudomonas aeruginosa*, AF= *Aspergillus flavus*, FO= *Fusarium oxysporium.* ABF1=Abapawa Farm 1, ABF2= Abapawa Farm 2, ABF3= Abapawa Farm 3, ABF4= Abapawa Farm 4, ABF5= Abapawa Farm 5.

DISCUSSION AND CONCLUSION

All the insects examined in this study contained high quantities of crude protein and crude fat. However, the highest crude protein and crude fat were obtained in *C. hawkmoth* and grasshopper. It is a good indicator that these insects are good sources of protein and fat, especially *C. hawkmoth*. The insects have also been shown to be rich in minerals, which include Ca, Na, K, P, Fe, and Mg. *C. hawkmoth*, whitefly, and grasshopper, contained the highest quantities of these minerals, especially potassium (K), sodium (Na) and phosphorus (P). Similar reports were recorded by Sani *et al.* (11). They stated that: the grasshoppers analyzed in their work had a high percentage of fat. Paiko *et al.* (12) stated that Sodium, potassium, and phosphorus concentration of 115 ± 0.07, 132.5 ± 0.08, and 126.30 ±0.50 mg/100g dry weight were obtained respectively in their study. However, lower potassium, sodium, and phosphorus contents were obtained in this study compared to what Paiko *et al.* (12) observed.

World Health Organization (W.H.O) standard for the fat content of edible insects, as reported in the development of the regional standard for edible crickets was 3.3 g (12). Fats are essential constituents of daily human diets because they increase the palatability of foods by absorbing and retaining their flavors. These are also important in the structure and biology of cells, and they also assist in the transport of nutritionally essential fat-soluble vitamins. Paiko *et al.* (12) reported that the crude protein, crude lipid, fiber and carbohydrate contents obtained in their study were 18.39 ± 0.4%, 10.5 ±1.0%, 32.20 ± 0.20% and 31.51 ± 0.11% respectively. Paiko *et al.* (12) reported that the ash quantity (2.30 ±0.30 %) obtained in their study was low. Similar to what Paiko *et al.* (12) observed in their study, the ash quantity obtained in this present study was also deficient.

The moisture contents of the insects examined in this study were found to be very high. High water content encourages deterioration of the insects hence making them dangerous for consumption. Similar observations were also made by Sani *et al.* (11). However, Paiko *et al.* (12) reported lower moisture content compared to the high moisture content obtained in this study. The high moisture content obtained in this study showed that these insects could not be stored for a long period without deterioration. Hence there is a need to employ proper drying and preservation techniques to avoid the quick deterioration of these insects.

The TBC (Total Bacterial Count) and TCC (Total Coliform Count) values of all the insects examined were found to be very high. Hence the need to rid the insects of these bacterial load before consumption. Drying can, however, help reduce the bacterial and total coliform load, hence making the insects suitable for food.

This study revealed that cassava leaves contain the following phytochemical constituents; cyanogenic glycosides, flavonoids, saponin, alkaloids, phytate, oxalate, trypsin inhibitor, and phenol. However, the cyanogenic glycosides obtained in the cassava leaves in this study were very high. The cyanogenic glycosides are plant toxins that can be produced in varieties of plants. Lawal *et al.* (13) reported that the antinutrients obtained in their study are; cyanide 1.08 mg/100 g, saponin 0.28 mg/100 g, oxalate 0.61 mg/100 g, and phytate 0.78 mg/100 g. Similar to what was obtained in this study, Lawal *et al.* (13) reported that cassava contained high cyanide value as well as a shallow saponin value. However, the content of the cyanogenic glycosides obtained in this study was extremely high compared to what Lawal *et al.* (13) reported. They also reported that the cyanide concentration of 1.08 mg/100 g could thus be classified as nontoxic because it fell below 10 mg/100 g powder. Lawal *et al.* (13) reported that the mineral concentration is in the order; Mg > Fe > Ca > N > P. however, in this study the mineral concentration is in the following order; Ca>K>Fe>Mg>P>Na>Mn>Cu. Ca was obtained in high quantities in this study. Lawal *et al.* (13), however, reported that Mg was highest in their study. It was also noted in this study that some farms recorded higher mineral content than others. It might be due to the level of minerals in the soils from where the plants take up their nutrients. The values of the mineral content in this study were also found to be higher than what was reported by Oresegun *et al.* (14). Similar to what was obtained in this

study Koubala *et al.* (15) reported that calcium (Ca) followed by potassium (K) and magnesium (Mg) are the main minerals found in cassava leaves.

The crude protein, crude fat, crude fiber, ash and carbohydrate values of cassava leaves, obtained from the different farmlands, reported in this study were lower than the values reported by Lawal *et al.* (13). However, the moisture content values reported in this study were higher than what was reported by Lawal *et al.* (13). In this study of all the vitamins examined, vitamin c was the most abundant in cassava leaves. Koubala *et al.* (15) also reported high quantities of vitamin c in cassava leaves.

CONCLUSION

Cassava leaves could be a good source of nutrients for man due to the avalanche of nutrients such as crude fiber, protein, carbohydrate, minerals (Ca, Na, K, Fe, Mg, P, Mn, and Cu) and vitamins. However, the high content of cyanide should be given adequate consideration because cyanide is poisonous to both man and animals. Cassava leaves could also serve as an excellent antimicrobial agent. This study has also shown that the arthropod parasites obtained from the cassava leaves contained high amounts of nutrients and under hygienic conditions could serve as a good nutrient source for man.

REFERENCES

1. Burns AE, Gleadow RM, Zacarias AM, Cuambe CE, Miller RE, Cavagnaro TR.Variations in the chemical composition of cassava (Manihotesculenta) leaves and roots as affected by genotypic and environmental variation. Journal of Agricultural and Food Chemistry. 2012; 60(19):4946–56.

2. Balamurugan T, Anbuselvi S. Physico-chemical characteristics of Manihotesculenta plant and its waste. Journal of Chemical and Pharmaceutical Research. 2013; 5(2): 258–60.

3. Agre AP, Kouchade S, Odjo T. Diversité et évaluation participative des cultivars du manioc (Manihot esculenta Crantz) au Centre Bénin, International Journal Biological and Chemical Sciences. 2015; 9(1): 388–408.

4. Endlweber K, Scheu S. Interaction between mycorrhizal fungi and collembolan: effects on

plant structure of competing plant species. Boil. Fert. Soils. 2007; 43: 741-9.

5. Basset Y, Novotny V, Millers S E, Kitching RL. Methodological advances and limitation in canopy entomology. Arthropods of tropical forests. Spatio-Temporal Dynamics and resource use in the canopy. Cambridge University Press. 2003; 3(2), 28-31.

6. Novotny V, Basset Y, Kitching RL. Herbivore assemblages and their food resources.Arthropods of tropical forest.Spatio-Temporal Dynamics and resource use in the canopy, Cambridge University Press, Cambridge. 2003; 40-53.

7. Boyer AG, Swearingen MA, Blaha CT, Fortson SK, Gremillion KA, Osborn H, Moran MD. Seasonal Variation in Top Down and Bottom- Up Processes in a Grassland Arthropod Community. Oecologia. 2003; 136:309-16.

8. Shelton J. Giant Sea Creature Hints at Early Arthropod Evolution Phytochemical. Biological Reviews. 2015; 203-361.

9. Weisser WW, Sieman E. (2004). Insects and Ecosytem Function, Ecological Studies. 2004; 415 (173).

10. Association of Official Analytical Chemists. Official Methods of Analysis of Association of Official Analytical Chemists. 18th Edition, Washington, DC. 2010.

11. Sani I, Haruna M, Abdulhamid A, Warra AA, Bello F, Fakai IM. Assessment of Nutritional Quality and Mineral Composition of Dried Edible Zonocerus variegatus (Grasshopper). Research and Reviews: Journal of Food and Dairy Technology.2014; 2(3): 1-6.

12. Paiko YB, Dagaci MZ, Yakubu A, Ibrahim IL, Umar MT. Proximate and Mineral Potential of Sun-Dried Short Horn Grasshopper (Zonocerus variegatus) Consumed in Paikoro Local Government, Niger State, Nigeria. Lapai Journal of Applied and Natural Sciences. 2016; 1(2): 1-6.

13. Lawal I A, Ajayi OA, Owonibi S K, Tajudeen A. Proximate, Minerals and Anti-Nutrient Evaluation of Cassava (Manihot Esculenta crantz) Leaves. International Conference of Science, Engineering & Environmental Technology. 2017; 2(27): 205-11.

14. Oresegun A, Fagbemiro OA, Ilona P, Edah B. Nutritional and anti-nutritional composition of cassava leaf protein concentrate from six cassava varieties for use in aqua feed. Journal of Cogent Food and Agriculture. 2016; 2(1): 269-76.

15. Koubala BB, Laya A, Massai H, Kouninki H, Nukenine EN. Physico-chemical Characterization Leaves from Five Genotypes of Cassava (Manihot esculenta Crantz) Consumed in the Far North Region (Cameroon). American Journal of Food Science and Technology. 2015; 3(2): 40-7.

In silico, 6LU7 protein inhibition using dihydroxy-3-phenyl coumarin derivatives for SARS-CoV-2

Mücahit Özdemir¹ ✉ iD **, Baybars Köksoy²,³*** ✉ iD **, Deniz Ceyhan⁴** ✉ iD **,**
Mustafa Bulut¹ ✉ iD **, and Bahattin Yalçın¹*** ✉ iD

¹Marmara University, Department of Chemistry, 34722 Istanbul, Turkey
²Gebze Technical University, Department of Chemistry, 41400 Kocaeli, Turkey
³Bursa Technical University, Department of Chemistry, 16310 Bursa, Turkey
⁴Tekirdağ Namık Kemal University, Department of Chemistry, 59030 Tekirdag, Turkey

Abstract: The new emerging coronavirus (SARS-CoV-2) has become a global health problem with very rapid transmission from person to person, causing severe acute respiratory problems. In the circumstance, the discovery of vaccines or drugs to eradicate or reduce the impact of the COVID-19 has made it imperative to develop new approaches. In the current situation, many drugs on the drug bank have been researched computationally, and there has not been an emphasis on synthetic effort. We tested 42 coumarin derivatives (**1a**-**14c**) containing 14 different substituents, which are secondary metabolites of plants, and the anticoagulant Coumadin (warfarin) drug as a reference by Molecular Docking calculation technique on 6LU7 main protease of the coronavirus. Optimized geometries, electron motions and energy values of all coumarins were also determined using the Density Functional Theory (DFT) method. The drug properties of coumarins were estimated using the ADME-Tox test method. Coumarins formed strong interactions with HIS41, CYS145, and other amino acids in the active site of the main protease. In general, 6,7-dihydroxy-3-phenylcoumarin derivatives gave relatively higher scores, and for all coumarins, biphenyl (for **10a**, -8.6 kcal/mol; **10b**, -8.3 kcal/mol; **10c**, -7.9 kcal/mol) and 4-trifluoromethylphenyl (for **13a**, -8.1 kcal/mol; **13b**, -8.1 kcal/mol; **13c** -8.3 kcal/mol) substituted coumarin had the highest score. The coumarins data reported in this study serves as a stepping stone for in vitro and in vivo experimental research for vaccine development purposes.

INTRODUCTION

The novel emerging coronavirus (SARS-CoV-2; Severe Acute Respiratory Syndrome Corona Virus 2) is a virus that is the source of serious infections that cause lung and respiratory disorders in both humans and animals (1, 2). This acute respiratory disease, which first appeared in Wuhan, Hubei province of China in December 2019, has spread worldwide in a short time, causing the COVID-19 (**Co**rona **Vi**rus **D**isease 2019) pandemic (3, 4). The coronavirus, like other respiratory viruses, is transmitted by airborne virus droplets of people carrying the virus during breathing, coughing, sneezing, laughing, or speaking (5). Common symptoms seen in the COVID-19 are fever,

cough, weakness, and shortness of breath (6, 7). Also, a considerable number of people pull through the coronavirus asymptomatically and are potential carriers (8). After exposure to the virus, the time until the symptoms begin to appear is called the incubation period, on average 5-6 days, but it reported to go up to 14 or more days (9).

According to the analysis of the cases, the course of the disease or death among patients with diabetes, high blood pressure, heart disease or respiratory problems is quite high compared to other standard groups of patients (10-12). Among the complications associated with COVID-19, abnormal clotting of the blood has also been reported (13, 14). It is believed that anticoagulant drugs may play an essential role in preventing severe damage or death due to blood clots caused by a coronavirus (15). In general, there is no evidence that dicoumarol, warfarin (coumadin), acenocoumarol, ethyl biscoumacetate (tromexan), and phenprocoumon (marcoumar) type blood thinners (vitamin K antagonist) should be taken

to prevent or remove blood clots caused by a coronavirus. Since blood thinners can cause bleeding, they should not be taken unless prescribed by a medical doctor. Coumarin can be considered as a useful target drug for coronavirus due to the natural presence of coumarins, secondary metabolites of plants, and high levels of pharmacophore properties such as antiviral, antimicrobial, anticoagulant and antibiotic (16-25).

In summary, our knowledge about COVID-19 and the effects of coronavirus on the body are increasing day by day. Researchers from around the world publish data almost every day, and some of the published research does not pass peer reviews. In all this information pollution, the findings of our study will contribute to drug development in the fight against COVID-19 by structure-activity analysis. In our study, the efficacy of 3-phenylcoumarin derivatives against the main protease (PBD: 6LU7) of the coronavirus was investigated using the Density Functional Theory and Molecular Docking calculation techniques.
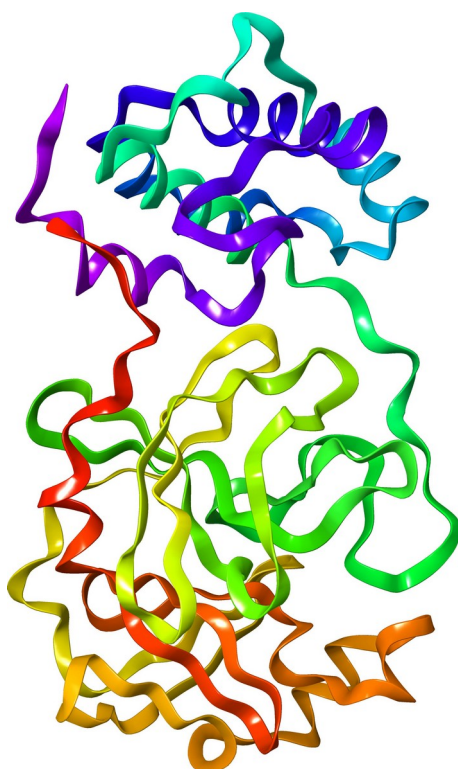
Figure 1. The structure of COVID-19 main protease (6LU7) with ribbon diagram.

MATERIAL AND METHODS

Coumarins
Natural organic 3-phenylcoumarin derivatives were selected for this study. 3-Phenylcoumarin derivatives are thought to have good scores, settlements to the active site of the receptor,

and interactions with residues. **2a**-**c**, **6a**-**8b**, **9a**-**c**, **13a**, **13b** and **14a** are synthesized compounds found in the literature. **1a**-**c**, **3a**-**c**, **10a**-**12c**, **13c**, **14b,** and **14c** are highly likely compounds to be synthesized.

DFT Studies

Gaussian 09 (26) was preferred for theoretical calculations, and GaussView 6.0 (27) was used for visualization. Geometry optimizations of the complex were conducted with Becke-3-Lee-Yang-Parr's functional correlation (B3LYP) (28-30) of the 6-311G(d,p) basis set for the density functional theory (31) method. The geometry optimization of the complex was chosen as a stable form with C1 symmetry. In addition to geometry optimization, frequency analysis was also performed. The total electron density surface was calculated according to electrostatic potential values. The total electron surface was visualized using SCF/ESP as the density matrix.

Molecular Docking Studies

Autodock Vina (32) was used to estimate binding energy for coumarins and was repeatedly supported with AutoDock 4.2 (33). The X-ray crystal structure of COVID-19 main protease (PDB code: 6LU7) was resolved using an X-ray diffraction method with a resolution factor of 2.16 Å was retrieved from the RCSB Protein Data Bank (https://www.rcsb.org). In the protein, the presence of water molecules from protein structure were removed and polar hydrogens and Kollman charges was added. Automatically the root of each ligand molecule is detected, and torsions were selected. All torsions of the ligand were allowed to rotate and checked for the selected residues. Blind docking was done to determine where the ligands would preferentially bind. The amino acids in the catalytic domain of 6LU7 M^{PRO} were determined using Discovery Studio Visualizer 2020 (34). Pre-calculated grid maps were required for running the program, which was calculated using the AutoGrid program. The energy scoring grid box was set to 32x32x32 dimension (x, y, and z) centered at X = -10.712; Y = 12.411; and Z = 68.831 with 0.325 Angstroms grid points spacing assigned with default atomic solvation parameters. Lamarckian Genetic Algorithm was selected as a docking engine, with all the docking parameters set to default. After the Lamarckian Genetic Algorithm run, AutoDock reports the best docking solution along with K_i values for the docked complex, and the results are reported based on the cluster analysis. The coumarin derivatives with the lowest energy placement score were selected from 10 conformations obtained from vina calculations. The Schrödinger Maestro for academics program (35) was used for visualization processes, and Discovery Studio Visualizer 2020 was also partially utilized.

ADMET Predictions

In drug design, the estimation of the pharmacophore properties of the target molecules saves time and investment and brings them closer to the targeted molecule. It is used to estimate the parameters of absorption, distribution, metabolism, excretion, and toxicity (ADMET). SwissADME online database (36) was used to estimate ADME parameters of the coumarin derivatives. Toxtree-v3.1.0.1851 software was used to estimate the toxicity parameters according to Cramer rules with extensions.

RESULTS AND DISCUSSION

DFT Studies

Designed dihyrdoxycoumarin derivatives for 6LU7 central protease inhibition were optimized with B3LYP-6-311G(d,p) basis set and HOMO-LUMO presentation, electron density configuration, bandgap, and total energy value were given in Table S3-5. Generally, the total energy and band gap value for all designed coumarin derivatives have increased for electron-withdrawing substituents as compared to the electron-donating substituents (total energy; 551,000-2,170,000 kcal/mol, bandgap; 3.346-4.025 eV).

The electron distributions of all dihydroxy-3-phenyl coumarin derivatives indicated that the π-electrons in the HOMO and LUMO are localized on the lactone ring and 3-phenyl part. Especially in electron-withdrawing substituents, this placement has been observed to shift towards the 3-phenyl group.

Molecular Docking

From a pharmacological perspective, 3-phenylcoumarin derivatives tested as inhibitors of main coronavirus protease are compounds with significant anti-HIV, antidepressant, and antiviral properties. The binding energies obtained from the docking of the active site of the SARS-CoV-2 main protease 6LU7 and the various interactions between coumarins and the active site residues of the receptor are presented in Tables 1, 2 and 3. The types of interactions are expressed with colorized amino acids and they are explained in the legend. Primary protease amino acids HIS41, CYS44, MET49, SER144, CYS145, and GLU166, are thought to play essential roles in drug-receptor interactions (37). To compare the docking results, AutoDock Vina scores supported by AutoDock 4.2. scores.

Table 1. Docking scores of 7,8-dihdyroxycoumarins on 6LU7 M^{PRO}.
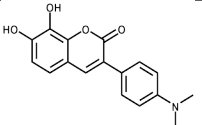
Ligands	No	Interactions	Docking Score (kcal/mol)	
			AutoDock	Vina
	1a	●ARG188, ●THR190, ●HIS41, ●MET49, ●●MET165, ●CYS145	-7.4	-7.3
	2a	●HIS41, ●●THR190, ●GLN189, ●MET49, ●●MET165, ●CYS145	-6.8	-7.6
	3a	●ARG188, ●HIS41, ●GLN189, ●●MET165, ●MET49, ●●CYS145	-7.0	-7.2
	4a	●HIS41, ●ASP187, ●PHE140, ●●HIS41, ●MET49, ●CYS145	-7.2	-7.4
	5a	●ARG188, ●●THR190, ●HIS41, ●MET165, ●●CYS145	-7.3	-7.3
	6a	●●●HIS41, ●LEU141, ●MET49, ●CYS145	-6.8	-7.4
	7a	●HIS41, ●PHE140, ●ARG188, ●MET49, ●ASP187, ●CYS145, ●MET49	-7.1	-7.8
	8a	●●THR190, ●GLN189, ●HIS41, ●MET165, ●MET49, ●●CYS145	-7.8	-7.4
	9a	●ARG188, ●GLN189, ●HIS41, ●●MET165, ●●CYS145	-7.9	-7.3
	10a	●THR190, ●●HIS41, ●LEU27, ●●MET165, ●●CYS145	-7.0	-8.6
	11a	●THR190, ●●HIS41, ●●MET165, ●LEU27, ●●CYS145	-7.8	-7.5
	12a	●GLU166, ●ARG188, ●LEU141, ●HIS41, ●●CYS145, ●MET165	-6.9	-7.6
	13a	●THR54, ●PHE140, ●ARG188, ●●●MET49, ●●ASP187, ●HIS41	-6.9	-8.1
	14a	●THR25, ●SER46, ●GLY143, ●●●CYS145, ●LEU141, ●●MET49	-7.1	-7.6
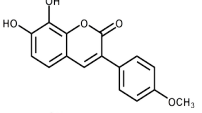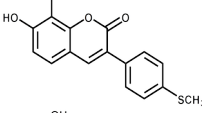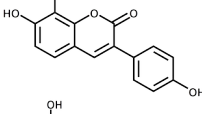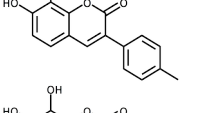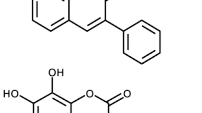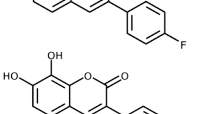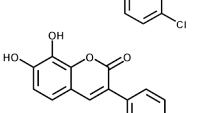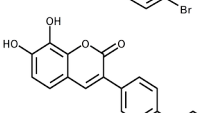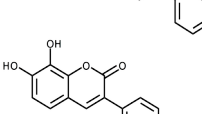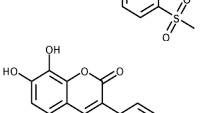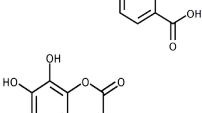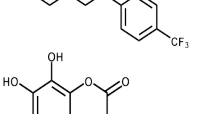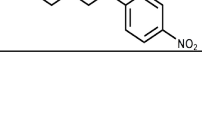
Table 2. Docking scores of 6,7-dihdyroxycoumarins on 6LU7 M^{PRO}.

Ligands	No	Interactions	Docking Score (kcal/mol)	
			AutoDock	Vina
	1b	●LEU141, ○GLN189, ○THR190, ○GLU166, ●○CYS145	-7.2	-7.5
	2b	●SER144, ●PHE140, ○GLU166, ○MET165, ●●HIS163, ●○CYS145	-7.4	-7.5
	3b	●HIS163, ○GLU166, ○MET165, ○PRO168, ●○CYS145,	-7.5	-7.4
	4b	●●●HIS41, ●ASN142, ○MET49, ○CYS145	-7.0	-7.7
	5b	●SER144, ●○GLU166, ●HIS41, ○MET165, ●○CYS145, ○○MET49	-7.7	-7.9
	6b	●SER144, ●●HIS163, ●○CYS145, ○GLU166, ○MET165	-7.4	-7.3
	7b	●PHE140, ○ASP187, ○GLU166, ○MET165, ●○CYS145, ●HIS41, ○MET49	-7.3	-7.7
	8b	●LEU141, ●○GLU166, ○MET165, ●HIS41, ●○CYS145, ○○MET49	-7.6	-7.8
	9b	●PHE140, ●LEU141, ●HIS163, ○GLU166, ●○CYS145, ○MET165	-7.7	-7.6
	10b	●LEU141, ●HIS163, ○GLU166, ○MET165, ●○CYS145, ●THR190, ●○ALA191	-6.6	-8.3
	11b	●SER144, ●○CYS145, ●THR190, ●ARG188, ○MET165	-8.2	-7.6
	12b	●SER144, ●GLN189, ●TYR54, ●ASP187, ●PHE140, ○GLU166, ○MET165, ●HIS41, ●○CYS145, ○MET49	-7.4	-8.1
	13b	●TYR54, ●HIS163, ●LEU141, ●○GLU166, ○ARG188, ○MET49, ●○ASP187, ●○CYS145, ○○MET49, ○HIS41	-6.9	-8.1
	14b	●GLY143, ●●SER144, ●○CYS145, ●THR190, ○MET165	-7.5	-7.8
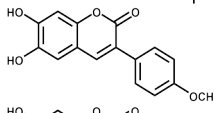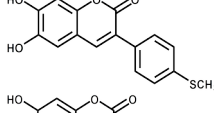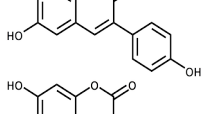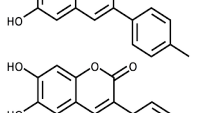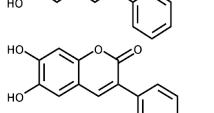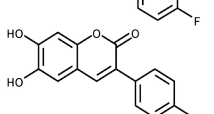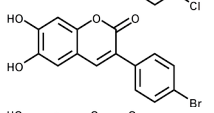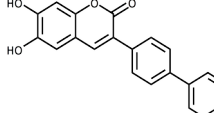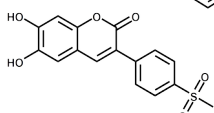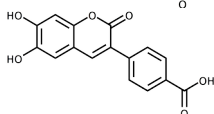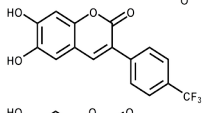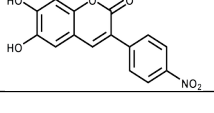
Table 3. Docking scores of 5,7-dihdyroxycoumarins on 6LU7 M^{PRO}.

Ligands	No	Interactions	Docking Score (kcal/mol)	
			AutoDock	Vina
	1c	PHE140, ASN142, GLU166, HIS41, CYS145, MET49	-6.8	-7.3
	2c	HIS41, ASN142, GLU166, MET49, CYS145	-6.6	-7.5
	3c	LEU141, HIS41, MET49, MET165	-6.9	-7.3
	4c	HIS41, ASP187, ASN142, MET49, CYS145	-6.5	-7.5
	5c	HIS163, PHE140, GLU166, HIS41, MET49, MET165	-6.7	-7.6
	6c	HIS41, GLU166, MET49, CYS145	-6.3	-7.7
	7c	HIS41, ASP187, MET165, CYS145, MET49	-6.5	-7.5
	8c	HIS41, GLU166, HIS163, PRO52, ARG188, CYS145, MET49	-6.8	-7.5
	9c	HIS163, GLU166, HIS41, MET49	-7.1	-7.4
	10c	HIS163, GLU166, CYS145, THR190, ALA191	-6.4	-7.9
	11c	HIS41, MET49	-7.7	-7.1
	12c	GLU166, MET165, LEU141, ASN142, MET49, CYS145	-6.7	-8.1
	13c	TYR54, HIS163, PHE140, ARG188, ASP187, MET49, HIS41, MET165	-6.3	-8.3
	14c	HIS163, ASP187, CYS145, MET49	-7.2	-8.0
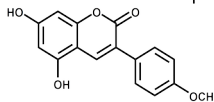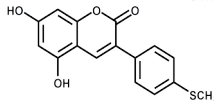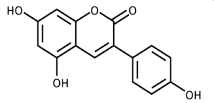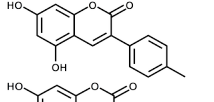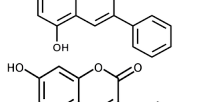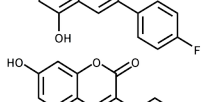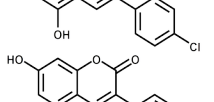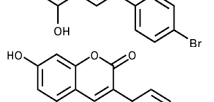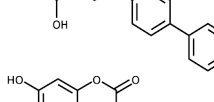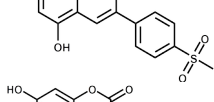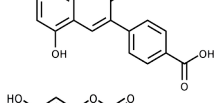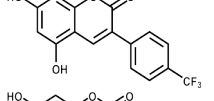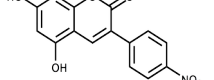
Legend for interactions of amino acids

Category	Types	Category	Types
● Electrostatic	π-Cation	● Hydrophobic	π-π Stacked or T-shaped
● Other	π-Sulfur	○ Hydrophobic	π-Alkyl
○ Hydrogen Bond	Carbon Hydrogen Bond	● Hydrophobic	π-Sigma
● Hydrogen Bond	Conventional Hydrogen Bond	● Halogen	Halogen

The first reference drug Coumadin (Warfarin) binding energies are -6.9 kcal/mol for Vina and -6.9 kcal/mol for AutoDock. Second reference drug Lopinavir binding energies are -7.5 kcal/mol for Vina and -6.9 kcal/mol for AutoDock. All 6,7-dihydroxy-3-phenylcoumarin, 7,8-dihydroxy-3-phenylcoumarin, and 5,7-dihydroxy-3-phenylcoumarin derivatives (**1a-14c**) have better binding energy than that of coumadin. The scores of all derivatives (**1a-14c**) containing the same functional groups as structure-activity are consistent with each other. In the drug Coumadin, the lactone group formed the π-alkyl bond with CYS145 and the π-π T-shaped bond with HIS41. The oxygen of the ketone group formed a hydrogen bond with SER144. The hydrogen bond distance is 2.520 Å, and the length of the hydrophobic bonds is in the range of 4.688 to 5.307 Å. In the drug Lopinavir, ligand-protein interactions are higher than all other compounds. The carbonyl oxygen of the amide group formed hydrogen bonds with ASN142 and GLU166. GLN189 formed a hydrogen bond with the opposite H–N– of the amide group. GLU166 formed a hydrogen bond again with the C-4 of tetrahyropyrimidin-2-one group. HIS41 formed two π-cationic bonds with 1,6-diphenylhexane aromatic rings. Hydrogen bond lengths are 2.596/2.809 Å for ASN142, 1.921/3.486 Å for GLU166, 2.516 Å for GLN189. Electrostatic π-cation bond lengths are 4.471 Å and 4.432 Å for HIS41, respectively.

For 7,8-dihydroxy-3-phenyl coumarin derivatives, the compounds with the highest scores are **7a** (-7.8 kcal/mol), **13a** (-8.1 kcal/mol) and **10a** (-8.6 kcal/mol), respectively. In 7,8-dihydroxy-3-(4-fluorophenyl) coumarin (**7a**), the hydroxy group at the C-7 position and lactone carbonyl group formed hydrogen bond with PHE140 and HIS41, respectively. The lactone group formed a π-alkyl bond with CYS145. Hydrogen bond lengths are 2.673 Å for HIS41 and 2.933 Å for PHE140. The carbon hydrogen bond length is 3.116 Å for ARG188. The length of hydrophobic bonds is between 4.384 and 5.068 Å.

In 7,8-dihydroxy-3-(4-trifluoromethylphenyl)-coumarin (**13a**), the hydroxy group at the C-7 position and one of the fluorines of trifluorophenyl functional group formed a hydrogen bond with PHE140 and TYR54, respectively. And also, one of the fluorines of the trifluorophenyl functional group formed a π-alkyl bond with HIS41. Hydrogen bond lengths are 2.725 Å for TYR54 and 2.201 Å for PHE140. The length of hydrophobic bonds is between 4.045 and 5.038 Å. In 7,8-dihydroxy-3-biphenyl-coumarin (**10a**), HIS41 formed a π-cation bond with each ring of the biphenyl

functional group attached to the C-3 position. CYS145 also formed a π-alkyl bond with each ring of the biphenyl functional group attached to the C-3 position. The hydrogen bond length is 2.573 Å. The length of hydrophobic bonds is between 4.286 and 5.470 Å. The compound with the lowest score of 7,8-dihydroxy-3-phenyl-coumarin derivatives is **3a** (-7.2 kcal/mol). In 7,8-dihydroxy-3-(4-methylthiophenyl)-coumarin (**3a**), the hydroxy group at the C-8 formed a hydrogen bond with ARG188. CYS145 formed π-alkyl with the methylthiophenyl group at the C-3 position and hydrophobic alkyl bond with the methylthio group. HIS41, on the other hand, formed an electrostatic π-cation bond with the methylthiophenyl group. The hydrogen bond length is 1.904 Å. The length of hydrophobic bonds is between 3.527 and 5.443 Å. In 7,8-dihydroxy-3-phenylcoumarin derivatives, CYS145 formed a π-alkyl bond for all compounds (**3a**, **7a**, **10a,** and **13a**).

For 6,7-dihydroxy-3-phenyl coumarin derivatives, the compounds with the highest scores are **12b** (-8.1 kcal/mol), **13b** (-8.1 kcal/mol) and **10b** (-8.3 kcal/mol), respectively. In 6,7-dihydroxy-3-(4-carboxyphenyl)-coumarin (**12b**), the hydroxy of the carboxyl group interacted with 3 different residues (ASP187, TYR54, and GLN189) by forming a hydrogen bond. The hydroxy group at the C-7 position formed a hydrogen bond with PHE140, and the hydroxy group at the C-6 position formed a hydrogen bond with SER144. HIS41 formed a hydrophobic π-π stacked bond with a 4-carboxyphenyl functional group attached to the C-3 position. CYS145 also formed two π-sulfur bonds with coumarin main benzene and lactone ring (α-pyrone). The lactone group interacted with GLU166 by the π-donor hydrogen bond. The length of hydrogen bonds is between 2.242 and 2.987 Å, and the hydrophobic bond lengths are 4.662 and 5.012 Å. In 6,7-dihydroxy-3-(4-trifluoromethylphenyl) coumarin (**13b**), GLU166 formed the conventional hydrogen bond with the hydroxy group at the C-7 position and the π-donor hydrogen bond with the lactone ring. HIS163 and LEU141 formed the conventional hydrogen bond with the hydroxy group at the C-6 position. CYS145 also formed two π-sulfur bonds with coumarin main benzene ring and α-pyrone, again. As at **13a**, one of the fluor of the trifluorophenyl functional group formed a hydrophobic π-alkyl bond with HIS41. The length of hydrogen bonds is between 2.056 and 3.006 Å, and the hydrophobic bond lengths are 3.994 and 4.846 Å. In 6,7-dihydroxy-3-biphenyl-coumarin (**10b**), the hydroxy group at the C-6 position formed a conventional hydrogen bond with LEU141, and GLU166

formed a π-donor hydrogen bond with GLU166. CYS145 formed two π-sulfur bonds with coumarin main benzene and lactone ring. The hydrogen bond lengths are 2.172 Å for LEU141 and 2.814 Å for GLU166. The electrostatic bond length is 4.277 Å, and the hydrophobic bond lengths are 3.771 Å for THR190:C,O;ALA191 and 5.435 Å for ALA191. The compound with the lowest score of 6,7-dihydroxy-3-phenyl-coumarin derivative is **6b** (-7.3 kcal/mol). In 6,7-dihydroxy-3-phenyl-coumarin (**6b**), the hydroxy group at the C-7 position formed a conventional hydrogen bond with SER144, and the lactone group interacted with GLU166 by a π-donor hydrogen bond.

CYS145 formed two π-sulfur bonds with coumarin main benzene and lactone ring. The hydrogen bond lengths are 2.083 Å for SER144 and 2.888 Å for GLU166. The electrostatic bond length is 4.503 Å, and the hydrophobic bond lengths are 5.451 Å for CYS145 and 5.474 Å for HIS163. In 6,7-dihydroxy-3-phenylcoumarin derivatives, CYS145 formed two π-sulfur bonds for all compounds' main benzene ring and lactone ring (**6b**, **10b**, **12b,** and **13b**).

For 5,7-dihydroxy-3-phenyl coumarin derivatives, the compounds with the highest scores are **14c** (-8.0 kcal/mol), **12c** (-8.1 kcal/mol) and **13c** (-8.3 kcal/mol), respectively. In 5,7-dihydroxy-3-(4-nitrophenyl)-coumarin (**14c**), HIS163 interacted with the uncoupled electron of the oxygen of the nitro group, forming a conventional hydrogen bond. The hydroxy group at the C-7 position formed a conventional hydrogen bond with ASP187. CYS145 formed one π-sulfur bond with a 4-nitrobenzene ring at the C-3 position. The hydrogen bond lengths are 2.456 Å for HIS163 and 2.951 Å for ASP187, and the hydrophobic bond lengths are 4.238 Å for MET49 and 5.164 Å for MET49, again. In 5,7-dihydroxy-3-(4-carboxyphenyl)-coumarin (**12c**), the hydroxy group at the C-5 position formed a conventional hydrogen bond with MET165. The hydroxy of the carboxyl group interacted with GLU166 by forming a conventional hydrogen bond. CYS145 formed a π-alkyl bond with a lactone ring. The hydrogen bond lengths are 2.200 Å for GLU166 and 2.743 Å for MET165, and the length of hydrophobic bonds is between 4.442 and 5.472 Å. In 5,7-dihydroxy-3-(4-trifluoromethylphenyl) coumarin (**13c**), the hydroxy group at the C-7 position and again the hydroxy group at the C-5 position and one of the fluor of trifluorophenyl functional group interacted with PHE140, HIS163, and TYR54 by conventional hydrogen bond, respectively. ARG188 formed a carbon-hydrogen bond (C-H) with another of the fluor of the trifluorophenyl functional group. The -CF$_3$ group interacted with HIS41 by a hydrophobic π-alkyl bond. The hydrogen bond lengths are 1.791 Å for PHE140, 2.340 Å for HIS163, 2.697 Å for TYR54, and 3.227 Å for ARG188. The length of hydrophobic bonds is between 4.111 and 5.498 Å. The compound with the lowest score of 5,7-dihydroxy-3-(4-methylsulfonylphenyl)-coumarin derivative is **11c** (-7.1 kcal/mol). In 5,7-dihydroxy-3-(4-methylsulfonylphenyl)-coumarin, HIS41 formed electrostatic π-cation bond with lactone ring. The electrostatic bond length is 4.275 Å for HIS41, and the length of hydrophobic bonds is between 4.147 and 4.803 Å.
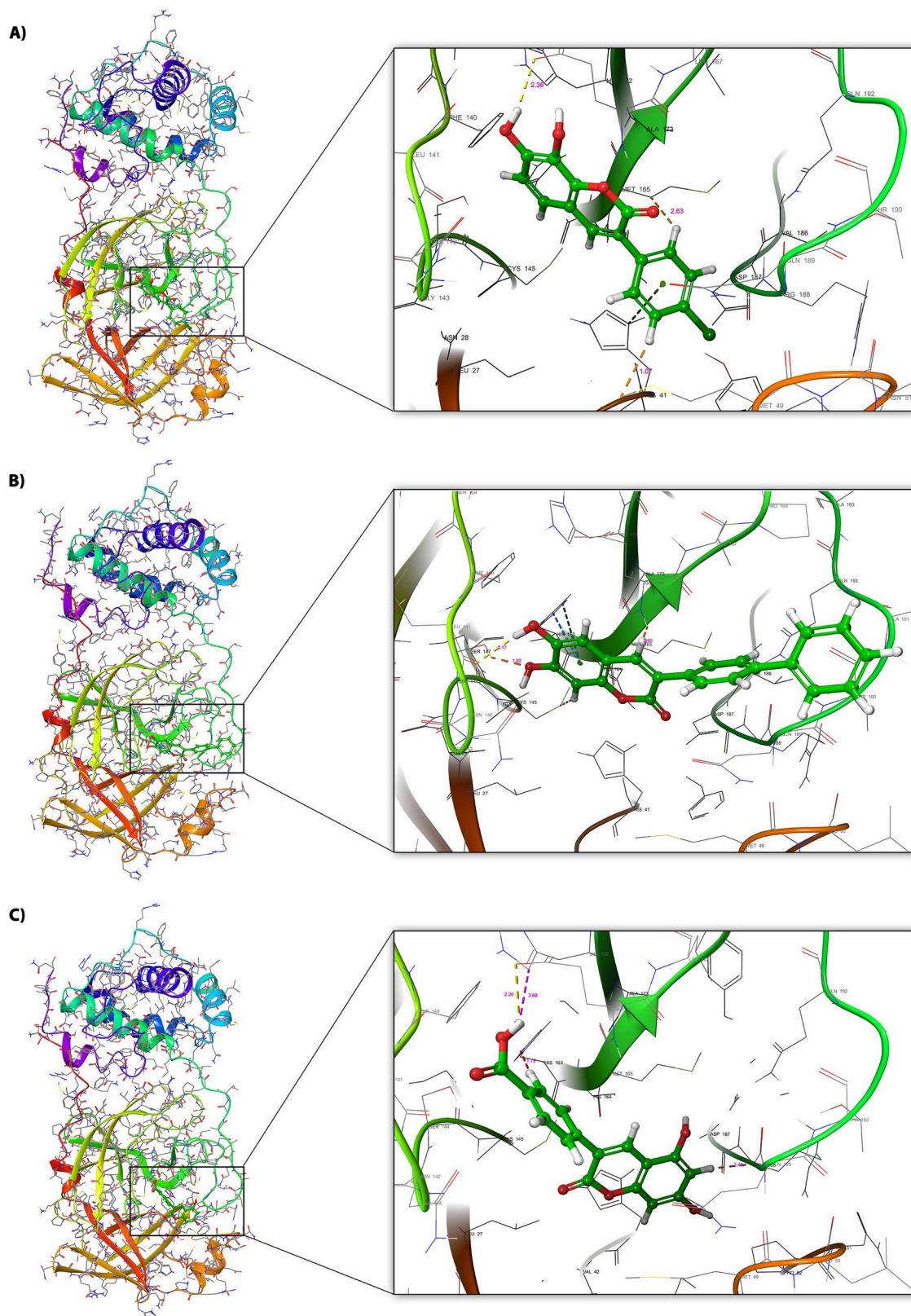
Figure 2. The interaction diagrams of 6LU7 main protease with coumarins in the catalytic domain (left, general, and right, focused on the active site). A for compound **8a**, B for compound **10b,** and C for compound **12c**.
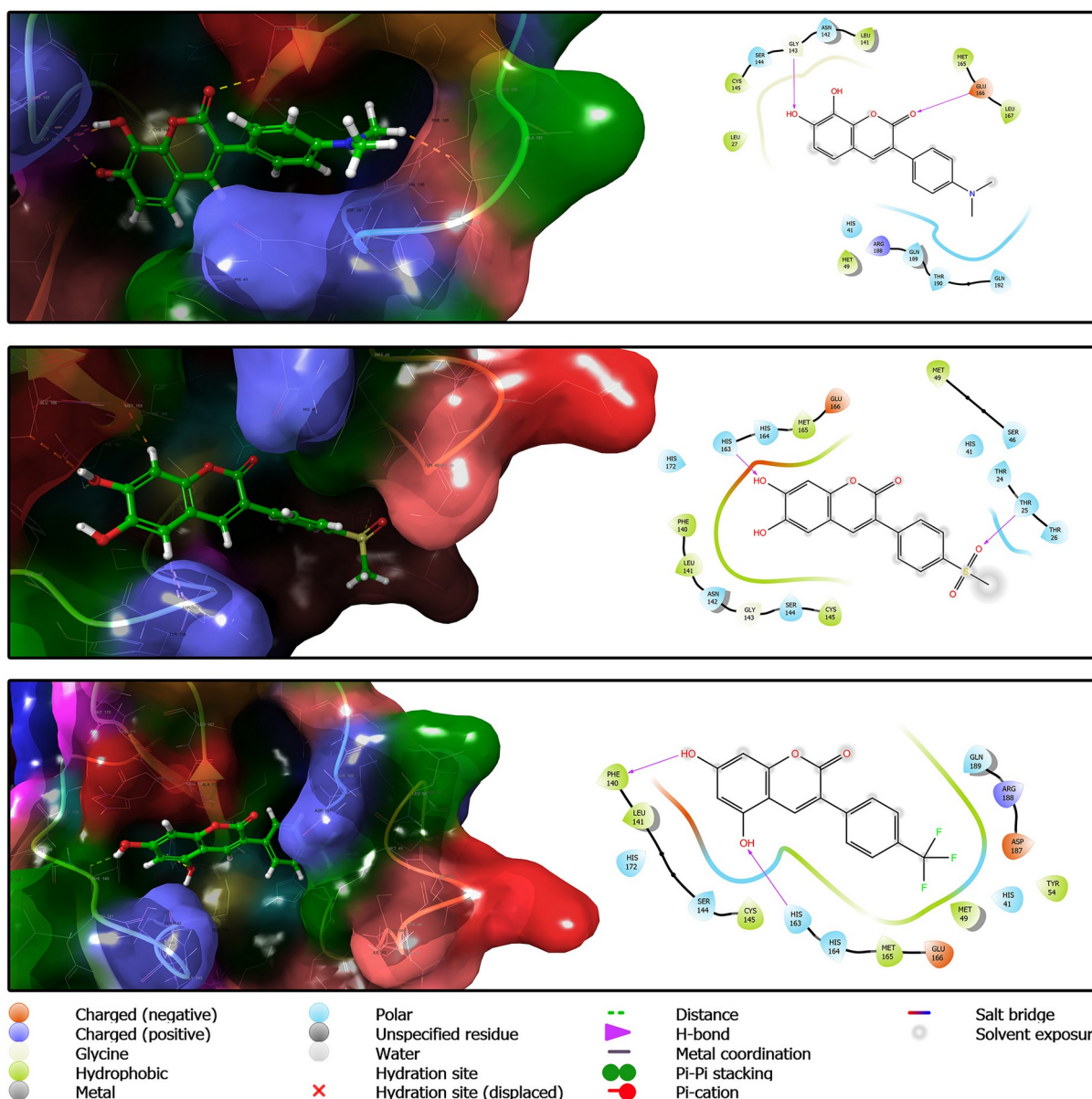
Figure 3. The interaction diagrams of 6LU7 main protease with docked coumarins in the catalytic domain (left, 3D with residue type surface, and right, 2D). A for compound **1a**, B for compound **11b** and C for compound **13c**.
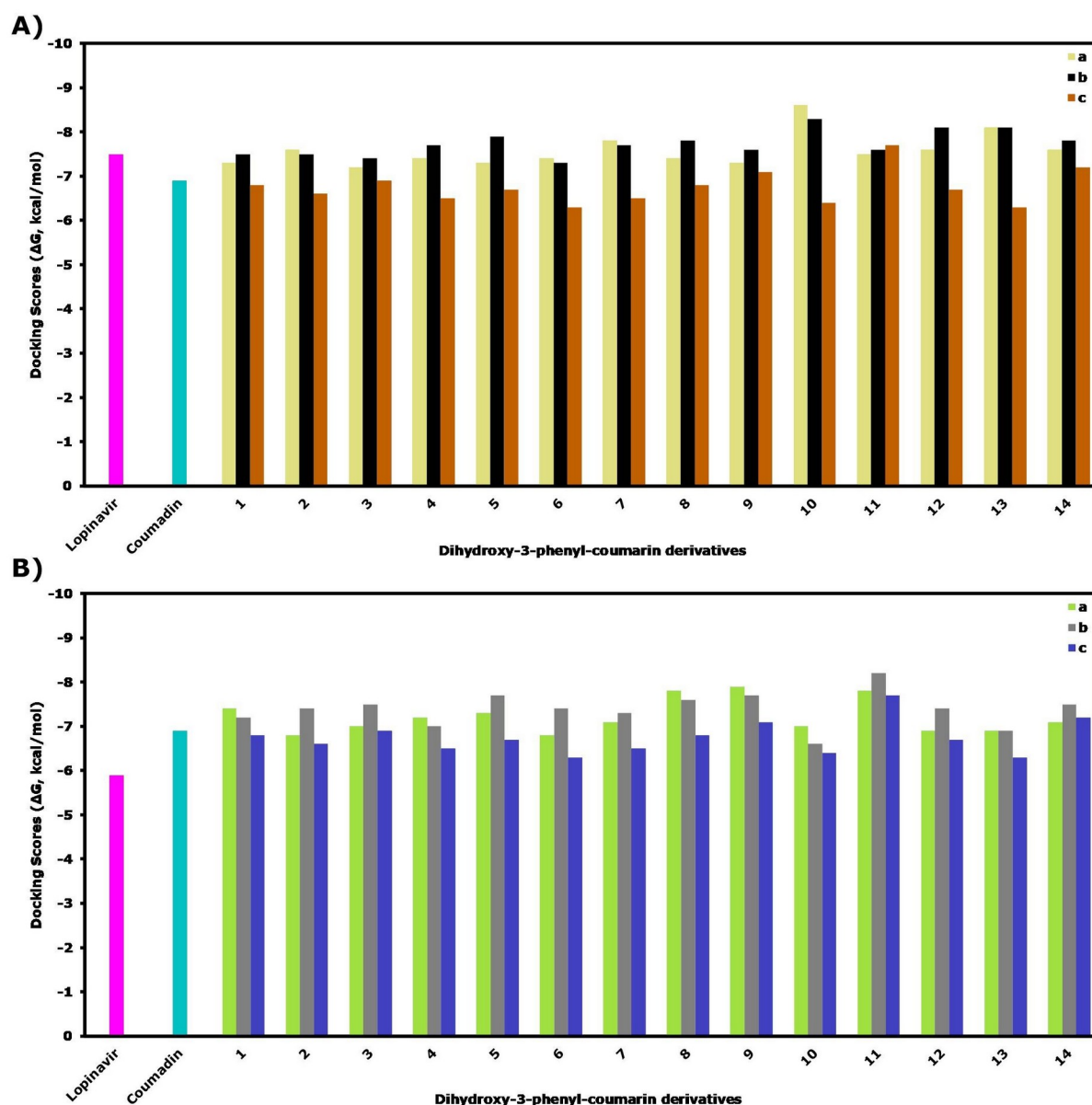
Figure 4. Docking score comparison of all coumarin derivatives (**1a**-**14c**) according to reference Coumadin and Lopinavir drug docking scores in Vina (A) and AutoDock (B) Software.

In general, it is observed that the most interaction and hydrogen bond are coumarins containing 4-trifluoromethylphenyl and biphenyl functional groups. The coumarins, which were determined as low scores, scored well compared to the reference drug Coumadin but interacted less with HIS41 and CYS145. Hydrogen bonds are also relatively less than other coumarin derivatives.

Carcinogenicity, Mutagenicity and Pharmacokinetic Properties Prediction
High results have been obtained from the results of tests in gastrointestinal absorption parameters, indicating that all coumarin derivatives are suitable for oral use. The meaning of yes in the cytochrome inhibitor parameter indicates that coumarin compounds have potential as an inhibitor that can lead to the toxic form in the process of cytochrome metabolism. The meaning of no in the cytochrome inhibitor parameter indicates that coumarin compounds have no potential as an inhibitor in the process of cytochrome metabolism.

Bioavailability is one of the basic pharmacokinetic properties of drugs and is used to indicate the rate of drug administration applied to the systemic circulation. The higher

the bioavailability value of a drug, the more efficiently the drug can be used orally. When the estimation results are examined, all the

compounds except **12a**-**c** coumarin are equal to 0.55. The bioavailability value of the **12a**-**c** coumarin compound is 0.56 (Table 4).

Table 4. The ADME parameters of all coumarin (**1a**-**14c**) and two references (Coumadin and Lopinavir) compounds via SwissADME software.

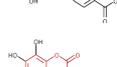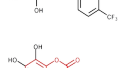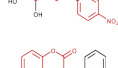| Ligand	TPSA ($Å^2$)	GI. Absorption	Cytochrome Inhibitor					Bioavailability Score
			CYP1A2	CYP2C19	CYP2C9	CYP2D6	CYP3A4	
1a-c	73.91	High	Yes	No	No	Yes	Yes	0.55
2a-c	79.90	High	Yes	No	No	Yes	Yes	0.55
3a-c	95.97	High	Yes	No	Yes	No	Yes	0.55
4a-c	90.90	High	Yes	No	No	Yes	No	0.55
5a-c	70.67	High	Yes	No	No	No	No	0.55
6a-c	70.67	High	Yes	No	No	No	No	0.55
7a-c	70.67	High	Yes	No	No	No	No	0.55
8a-c	70.67	High	Yes	No	No	No	No	0.55
9a-c	70.67	High	Yes	No	No	No	No	0.55
10a-c	70.67	High	Yes	Yes	No	Yes	No	0.55
11a-c	113.19	High	No	No	No	No	No	0.55
12a-c	107.97	High	No	No	No	No	No	0.56
13a-c	70.67	High	Yes	No	No	No	No	0.55
14a-c	116.49	High	Yes	No	Yes	No	No	0.55
Ref1	67.51	High	No	Yes	Yes	No	No	0.55
Ref2	120.00	High	No	Yes	No	No	Yes	0.55

ADMET properties of coumarin derivatives (**a**, **b,** and **c**) bearing the same substituent were the same. The change of the position to which the hydroxy functional group is attached did not cause any change in ADMET parameters.

The mutagenicity and carcinogenicity prediction of coumarin derivatives and two reference compounds (Coumadin and Lopinavir) were calculated using Toxtree-v3.1.0.1851 software based on Benigni/Bossa rule base (38) used to estimate carcinogenicity and mutagenicity of ligands according to their skeleton and substituents. The working potential of this process is to identify structure-dependent functional groups known to be associated with the carcinogenic activity of the compounds because if one or more carcinogenic functional groups are identified, the software will mark the carcinogenicity potential of the chemical.

The coumarin skeleton was positive for genotoxic carcinogenicity, but it was reported that warfarin (coumadin) was not carcinogenic and even gave good results in the human body

(39). Of course, unusual effects have also been reported in some cases (40-42). Based on this, carcinogenicity can only be neglected for coumarins, where the coumarin skeleton gives structural alerts. But to say the same thing for coumarins warning other functional groups may pose a risk. For compounds **1a**-**c**, the p-dimethylaminophenyl substituent attached to the C-3 position gave warning for genotoxic carcinogenicity. For compounds **14a**-**c**, the p-nitrophenyl substituent, linked to the C-3 position, also gave warning of genotoxic carcinogenicity. In the non-genotoxic carcinogenicity analysis, the p-halogenophenyl (F, Cl, and Br) substituents linked to the C-3 position are positive. Other substituted coumarins are negative except for coumarins that carry these substituents (**1a**-**c** and **14a**-**c**). The reference drug component Lopinavir is harmful for both genotoxic carcinogenicity and non-genotoxic carcinogenicity (Table 5). To be able to compare and be sure, all the coumarin derivatives must be validated for toxicity by experimental analysis.

Table 5. The Carcinogenicity and mutagenicity prediction test of all coumarin derivatives (**1a**-**14c**) and two reference compounds (Coumadin and Lopinavir) via Toxtree software.

Ligand	Genotoxic Carcinogenicity	Structural Alert for Genotoxic Carcinogenicity	Non-genotoxic Carcinogenicity	Structural Alert for Non-genotoxic Carcinogenicity
1a-c	Positive	*(structure)*	Negative	-
2a-c	Positive	*(structure)*	Negative	-
3a-c	Positive	*(structure)*	Negative	-
4a-c	Positive	*(structure)*	Negative	-
5a-c	Positive	*(structure)*	Negative	-
6a-c	Positive	*(structure)*	Negative	-
7a-c	Positive	*(structure)*	Positive	*(structure)*
8a-c	Positive	*(structure)*	Positive	*(structure)*
9a-c	Positive	*(structure)*	Positive	*(structure)*
10a-c	Positive	*(structure)*	Negative	-
11a-c	Positive	*(structure)*	Negative	-
12a-c	Positive	*(structure)*	Negative	-
13a-c	Positive	*(structure)*	Negative	-
14a-c	Positive	*(structure)*	Negative	-
Ref1[*]	Positive	*(structure)*	Negative	-
Ref2[*]	Negative	-	Negative	-
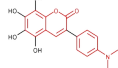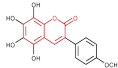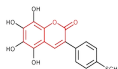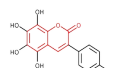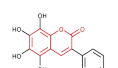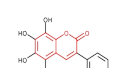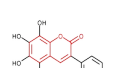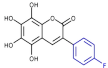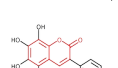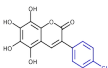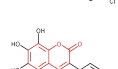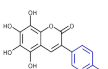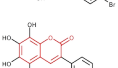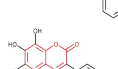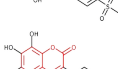
[*]Ref1: Reference drug Coumadin. It has been determined as a reference drug molecule because of its similarity to the subject compounds.

[*]Ref2: Reference drug Lopinavir. It has been determined as the reference drug molecule because it has an activity for the target protein.

The red-colored structural alert shows that the group has genotoxic carcinogenicity.

The blue-colored structural alert shows that the group has non-genotoxic carcinogenicity.

CONCLUSION

In this study, coumarin and its derivatives, which are natural pharmacophore compounds for the development of antiviral agents effective against the SARS-CoV-2 virus, were optimized by density functional theory method to estimate the ideal geometries and properties of molecules and screened using molecular placement studies against 6LU7 main protease. 42 coumarin derivatives also had better scores than the reference drug coumadin, interacting with residues in the catalytic domain of the main protease. These potential coumarin protease inhibitors have shown an energy score in the range of -7.1 kcal/mol to -8.6 kcal/mol. In general, 6,7-dihydroxy-3-phenylcoumarin derivatives gave relatively higher scores, and for all coumarins, biphenyl (for **10a**, -8.6 kcal / mol; **10b**, -8.3 kcal / mol; **10c** -7.9 kcal / mol) and 4-trifluoromethylphenyl (for **13a**, -8.1 kcal / mol; **13b**, -8.1 kcal / mol; **13c** -8.3 kcal / mol) substituted coumarin had the highest score. As potential protease inhibitors, in vitro, and in vivo research studies can be conducted to confirm the findings of these coumarin compounds or provide useful ideas and information to scientists working for coumarins.

ACKNOWLEDGEMENTS

Conflict of Interest: Authors have no conflict of interest.

REFERENCES

1.   Lai C-C, Shih T-P, Ko W-C, Tang H-J, Hsueh P-R. Severe acute respiratory syndrome coronavirus 2 (SARS-CoV-2) and corona virus disease-2019 (COVID-19): the epidemic and the challenges. International Journal of Antimicrobial Agents. 2020:105924.

2.   Guo Y-R, Cao Q-D, Hong Z-S, Tan Y-Y, Chen S-D, Jin H-J, et al. The origin, transmission and clinical therapies on coronavirus disease 2019 (COVID-19) outbreak–an update on the status. Military Medical Research. 2020;7(1):1-10.

3.   Lu H, Stratton CW, Tang YW. Outbreak of Pneumonia of Unknown Etiology in Wuhan China: the Mystery and the Miracle. Journal of Medical Virology.

4.   Zu ZY, Jiang MD, Xu PP, Chen W, Ni QQ, Lu GM, et al. Coronavirus disease 2019 (COVID-19): a perspective from China. Radiology. 2020:200490.

5.   Singhal T. A review of coronavirus disease-2019 (COVID-19). The Indian Journal of Pediatrics. 2020:1-6.

6.   Cascella M, Rajnik M, Cuomo A, Dulebohn SC, Di Napoli R. Features, evaluation and treatment coronavirus (COVID-19). Statpearls: StatPearls Publishing; 2020.

7.   Rothan HA, Byrareddy SN. The epidemiology and pathogenesis of coronavirus disease (COVID-19) outbreak. Journal of Autoimmunity. 2020:102433.

8.   Al-Tawfiq JA. Asymptomatic coronavirus infection: MERS-CoV and SARS-CoV-2 (COVID-19). Travel Medicine and Infectious Disease. 2020.

9.   Lauer SA, Grantz KH, Bi Q, Jones FK, Zheng Q, Meredith HR, et al. The incubation period of coronavirus disease 2019 (COVID-19) from publicly reported confirmed cases: estimation and application. Annals of Internal Medicine. 2020;172(9):577-82.

10.   Hill MA, Mantzoros C, Sowers JR. Commentary: COVID-19 in patients with diabetes. Metabolism. 2020.

11.   Fang L, Karakiulakis G, Roth M. Are patients with hypertension and diabetes mellitus at increased risk for COVID-19 infection? The Lancet Respiratory Medicine. 2020;8(4):e21.

12.   Zheng Y-Y, Ma Y-T, Zhang J-Y, Xie X. COVID-19 and the cardiovascular system. Nature Reviews Cardiology. 2020;17(5):259-60.

13.   Terpos E, Ntanasis-Stathopoulos I, Elalamy I, Kastritis E, Sergentanis TN, Politou M, et al. Hematological findings and complications of COVID-19. American Journal of Hematology. 2020.

14.   Ranucci M, Ballotta A, Di Dedda U, Bayshnikova E, Dei Poli M, Resta M, et al. The procoagulant pattern of patients with COVID-19 acute respiratory distress syndrome. Journal of Thrombosis and Haemostasis. 2020.

15.   Connors JM, Levy JH. COVID-19 and its implications for thrombosis and anticoagulation.

Blood, The Journal of the American Society of Hematology. 2020;135(23):2033-40.

16.   Hassan MZ, Osman H, Ali MA, Ahsan MJ. Therapeutic potential of coumarins as antiviral agents. European Journal of Medicinal Chemistry. 2016;123:236-55.

17.   Curini M, Epifano F, Maltese F, Marcotullio MC, Gonzales SP, Rodriguez JC. Synthesis of collinin, an antiviral coumarin. Australian Journal of Chemistry. 2003;56(1):59-60.

18.   Yang G, Chen D. Biflavanones, flavonoids, and coumarins from the roots of Stellera chamaejasme and their antiviral effect on hepatitis B virus. Chemistry & Biodiversity. 2008;5(7):1419-24.

19.   Ojala T, Remes S, Haansuu P, Vuorela H, Hiltunen R, Haahtela K, et al. Antimicrobial activity of some coumarin containing herbal plants growing in Finland. Journal of Ethnopharmacology. 2000;73(1-2):299-305.

20.   Smyth T, Ramachandran V, Smyth W. A study of the antimicrobial activity of selected naturally occurring and synthetic coumarins. International Journal of Antimicrobial Agents. 2009;33(5):421-6.

21.   O'reilly RA, Aggeler PM. Studies on coumarin anticoagulant drugs: initiation of warfarin therapy without a loading dose. Circulation. 1968;38(1):169-77.

22.   O'Reilly RA, Aggeler PM, Leong LS. Studies on the coumarin anticoagulant drugs: the pharmacodynamics of warfarin in man. The Journal of Clinical Investigation. 1963;42(10):1542-51.

23.   O'Reilly RA, Aggeler PM, Hoag MS, Leong L. Studies on the coumarin anticoagulant drugs: the assay of warfarin and its biologic application. Thrombosis and Haemostasis. 1962;8(02):082-95.

24.   Gormley NA, Orphanides G, Meyer A, Cullis PM, Maxwell A. The interaction of coumarin antibiotics with fragments of the DNA gyrase B protein. Biochemistry. 1996;35(15):5083-92.

25.   Maxwell A. The interaction between coumarin drugs and DNA gyrase. Molecular Microbiology. 1993;9(4):681-6.

26.   Frisch MJ, Trucks GW, Schlegel HB, Scuseria GE, Robb MA, Cheeseman JR, et al.

Gaussian 09 Revision C. 01. Wallingford CT: Gaussian, Inc.; 2009.

27.   Dennington R, Keith T, Millam J. GaussView, version 6. 2009.

28.   Becke AD. Density-functional exchange-energy approximation with correct asymptotic behavior. Physical Review A. 1988;38(6):3098.

29.   Becke AD. Becke's three parameter hybrid method using the LYP correlation functional. The Journal of Chemical Physics. 1993;98:5648-52.

30.   Lee C, Yang W, Parr RG. Development of the Colle-Salvetti correlation-energy formula into a functional of the electron density. Physical Review B. 1988;37(2):785.

31.   Kohn W, Sham LJ. Self-consistent equations including exchange and correlation effects. Physical Review. 1965;140(4A):A1133.

32.   Trott O, Olson AJ. AutoDock Vina: improving the speed and accuracy of docking with a new scoring function, efficient optimization, and multithreading. Journal of Computational Chemistry. 2010;31(2):455-61.

33.   Morris GM, Huey R, Lindstrom W, Sanner MF, Belew RK, Goodsell DS, et al. AutoDock4 and AutoDockTools4: Automated docking with selective receptor flexibility. Journal of Computational Chemistry. 2009;30(16):2785-91.

34.   BIOVIA DS. Discovery Studio Visualizer. San Diego, CA, USA. 2017.

35.   Schrödinger. Schrödinger Release 2020-2: Maestro. LLC, New York, NY; 2020.

36.   Daina A, Michielin O, Zoete V. SwissADME: a free web tool to evaluate pharmacokinetics, drug-likeness and medicinal chemistry friendliness of small molecules. Scientific reports. 2017;7:42717.

37.   Liu X, Wang X-J. Potential inhibitors against 2019-nCoV coronavirus M protease from clinically approved medicines. Journal of Genetics and Genomics. 2020;47(2):119.

38.   Benigni R, Bossa C, Tcheremenskaia O. Nongenotoxic carcinogenicity of chemicals: mechanisms of action and early recognition through a new set of structural alerts. Chemical reviews. 2013;113(5):2940-57.

39. Pollock BE. Clinical experience with warfarin (coumadin) sodium, a new anticoagulant. Journal of the American Medical Association. 1955;159(11):1094-7.

40. Nath SK, Sandhu AP, Rose BS, Simpson DR, Nobiensky PD, Wang J-Z, et al. Toxicity analysis of postoperative image-guided intensity-modulated radiotherapy for prostate cancer. International Journal of Radiation Oncology* Biology* Physics. 2010;78(2):435-41.

41. Keskin S, Gökmen İE, Koç O, Özbek O. Unusual complication of coumadin toxicity mimicking Crohn's disease. Case Reports. 2014;2014:bcr2013202755.

42. Baer S, Yarrow MW, Kravitz C, Markson V. Clinical experiences with warfarin (coumadin) sodium as an anticoagulant. Journal of the American Medical Association. 1958;167(6):704-8.

In silico, 6LU7 protein inhibition using dihydroxy-3-phenyl coumarin derivatives for SARS-CoV-2

Mücahit Özdemir, Baybars Köksoy, Deniz Ceyhan, Mustafa Bulut, Bahattin Yalçın

Supporting Information

CONTEXT

Figure S1. Present of 6LU7 Main Protease with wire (left) and residue type surface (right).

Figure S2. The active site of 6LU7 Main Protease.

Figure S3. Optimized geometry, HOMO-LUMO orbitals, electron density surface and energy values of 7,8-dihdyroxycoumarins (**1a**-**14a**).

Figure S4. Optimized geometry, HOMO-LUMO orbitals, electron density surface and energy values of 6,7-dihdyroxycoumarins (**1b**-**14b**).

Figure S5. Optimized geometry, HOMO-LUMO orbitals, electron density surface and energy values of 5,7-dihdyroxycoumarins (**1c**-**14c**).
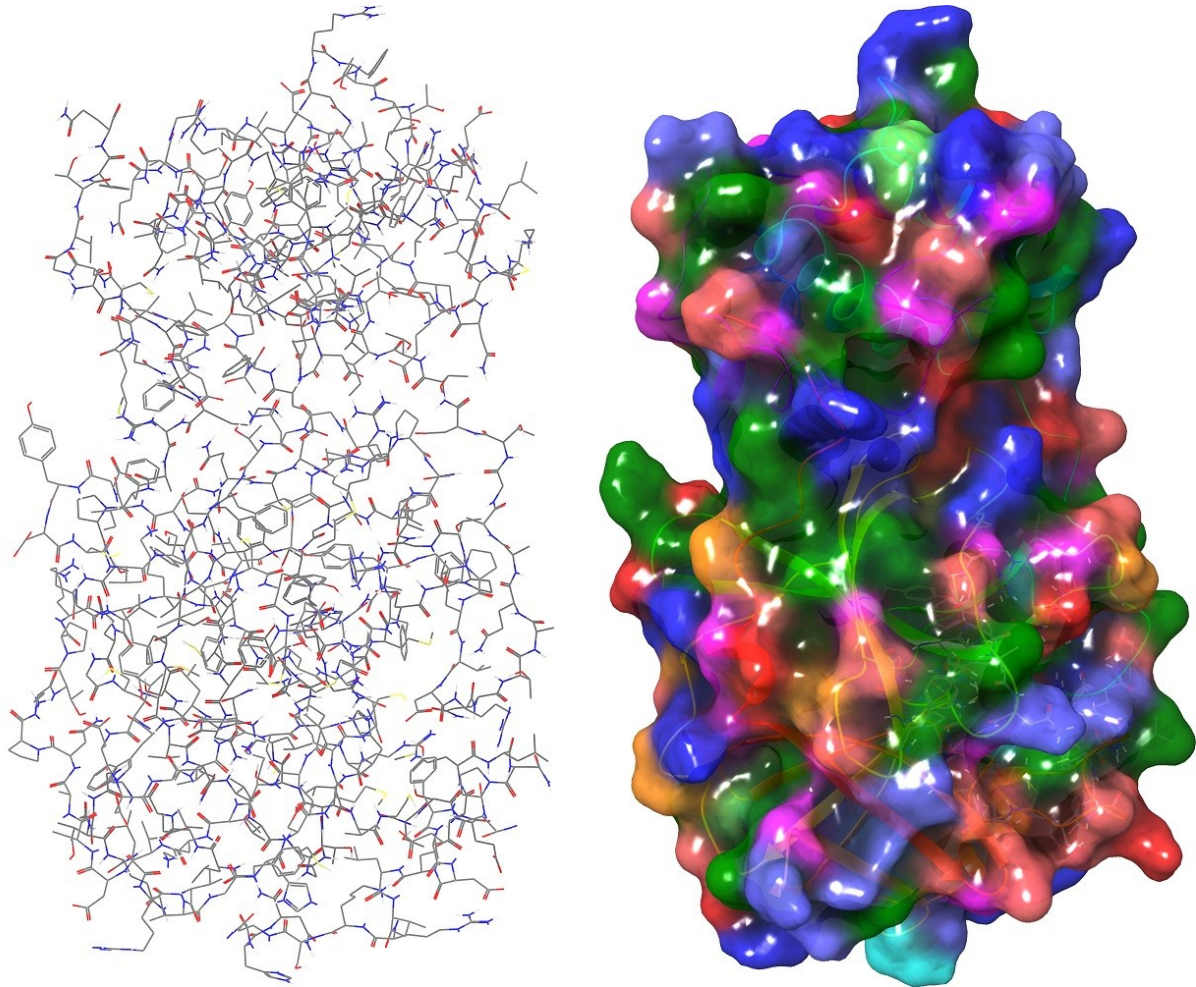
Figure S1. Present of 6LU7 Main Protease with wire (left) and residue type surface (right).
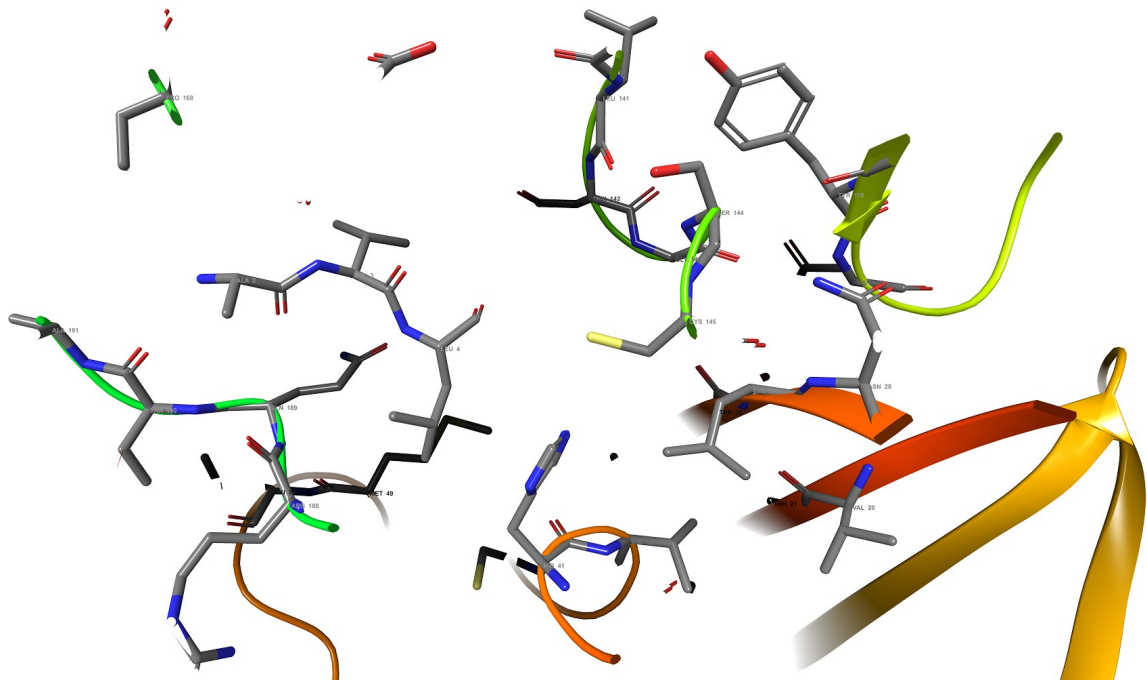
Figure S2. The active site of 6LU7 Main Protease.

No	Optimized Geometry	HOMO Orbitals	Band Gap (eV)	LUMO Orbitals	Electron Density	Isosurface Value	Total Energy (kcal/mol)
1a			3.346			-5.386e^{-2} 5.386e^{-2}	-635501.0
2a			3.718			-5.024e^{-2} 5.024e^{-2}	-623297.0
3a			3.835			-5.290e^{-2} 5.290e^{-2}	-825967.6
4a			3.746			-6.506e^{-2} 6.506e^{-2}	-598629.8
5a			3.862			-5.061e^{-2} 5.061e^{-2}	-576092.3
6a			3.907			-5.062e^{-2} 5.062e^{-2}	-551414.1
7a			3.871			-5.296e^{-2} 5.296e^{-2}	-613702.5
8a			3.842			-5.411e^{-2} 5.411e^{-2}	-839826.8
9a			3.830			-5.408e^{-2} 5.408e^{-2}	-2166311.9
10a			3.745			-5.097e^{-2} 5.097e^{-2}	-696435.6
11a			3.842			-5.866e^{-2} 5.866e^{-2}	-920361.6
12a			3.787			-5.478e^{-2} 5.478e^{-2}	-669780.1
13a			3.755			-5.596e^{-2} 5.596e^{-2}	-762968.8
14a			3.570			-5.938e^{-2} 5.938e^{-2}	-679773.1
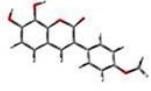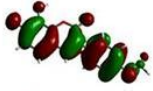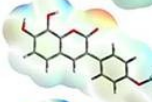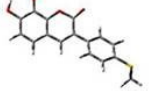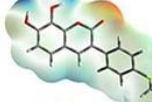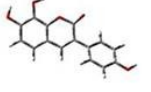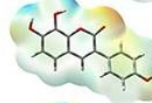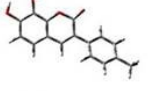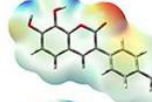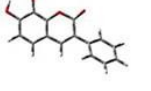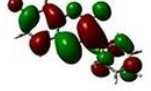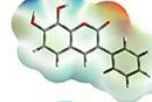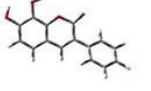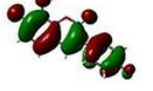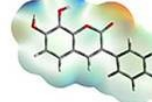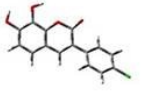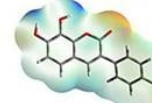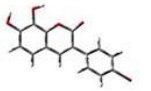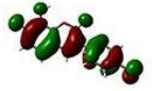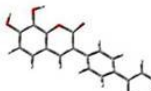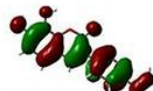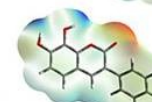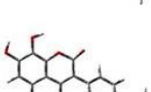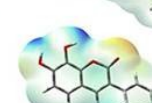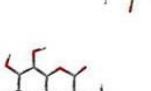
Figure S3. Optimized geometry, HOMO-LUMO orbitals, electron density surface and energy values of 7,8-dihdyroxycoumarins (**1a**-**14a**).

No	Optimized Geometry	HOMO Orbitals	Band Gap (eV)	LUMO Orbitals	Electron Density	Isosurface Value	Total Energy (kcal/mol)
1b			3.365			■ -7.700e⁻² ■ 7.700e⁻²	-635498.8
2b			3.725			■ -8.004e⁻² ■ 8.004e⁻²	-623294.8
3b			3.820			■ -8.327e⁻² ■ 8.327e⁻²	-825965.8
4b			3.715			■ -7.129e⁻² ■ 7.129e⁻²	-598623.7
5b			3.846			■ -8.085e⁻² ■ 8.085e⁻²	-576090.3
6b			3.828			■ -7.279e⁻² ■ 7.279e⁻²	-551408.0
7b			3.803			■ -7.451e⁻² ■ 7.451e⁻²	-613696.4
8b			3.821			■ -8.426e⁻² ■ 8.426e⁻²	-839824.9
9b			3.811			■ -8.418e⁻² ■ 8.418e⁻²	-2166310.0
10b			3.740			■ -8.177e⁻² ■ 8.177e⁻²	-696433.5
11b			3.792			■ -8.827e⁻² ■ 8.827e⁻²	-920359.8
12b			3.743			■ -8.558e⁻² ■ 8.558e⁻²	-669778.1
13b			3.818			■ -8.625e⁻² ■ 8.625e⁻²	-762966.9
14b			3.503			■ -8.974e⁻² ■ 8.974e⁻²	-679771.2
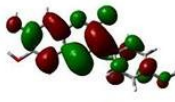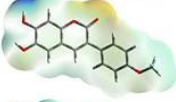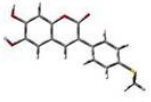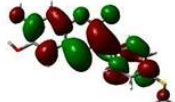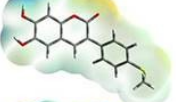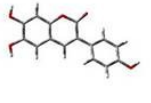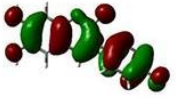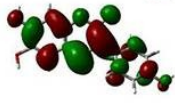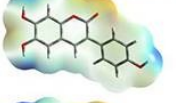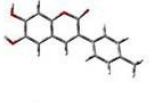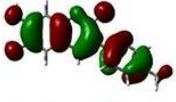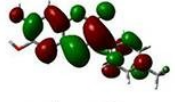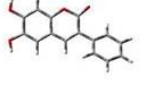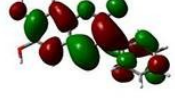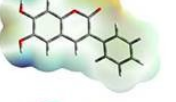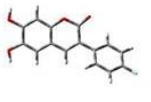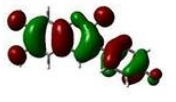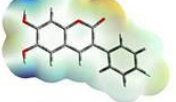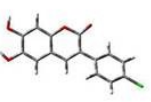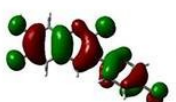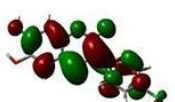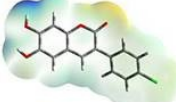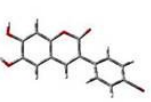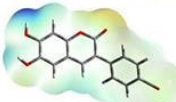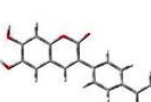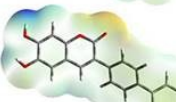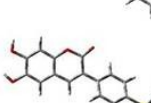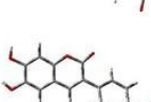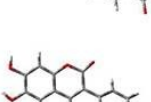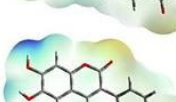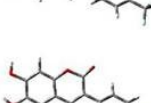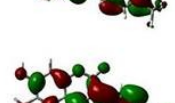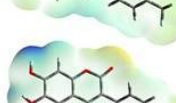
Figure S4. Optimized geometry, HOMO-LUMO orbitals, electron density surface and energy values of 6,7-dihdyroxycoumarins (**1b**-**14b**).
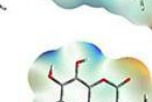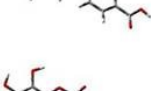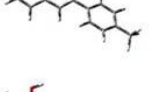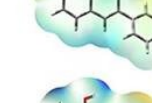
No	Optimized Geometry	HOMO Orbitals	Band Gap (eV)	LUMO Orbitals	Electron Density	Isosurface Value	Total Energy (kcal/mol)
1c			3.409			$-7.093e^{-2}$ $7.093e^{-2}$	-635500.3
2c			3.792			$-7.363e^{-2}$ $7.363e^{-2}$	-623296.4
3c			3.962			$-7.781e^{-2}$ $7.781e^{-2}$	-825967.6
4c			3.826			$-7.468e^{-2}$ $7.468e^{-2}$	-598629.4
5c			3.965			$-7.473e^{-2}$ $7.473e^{-2}$	-576091.9
6c			4.025			$-7.595e^{-2}$ $7.595e^{-2}$	-551413.7
7c			3.986			$-7.754e^{-2}$ $7.754e^{-2}$	-613702.2
8c			3.959			$-7.864e^{-2}$ $7.864e^{-2}$	-839826.7
9c			3.943			$-7.862e^{-2}$ $7.862e^{-2}$	-2166311.8
10c			3.830			$-7.597e^{-2}$ $7.597e^{-2}$	-696435.2
11c			3.993			$-8.160e^{-2}$ $8.160e^{-2}$	-920361.7
12c			3.910			$-7.907e^{-2}$ $7.907e^{-2}$	-669779.9
13c			4.006			$-8.040e^{-2}$ $8.040e^{-2}$	-762968.8
14c			3.685			$-8.364e^{-2}$ $8.364e^{-2}$	-679773.2
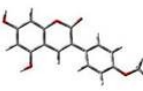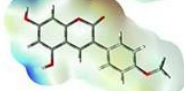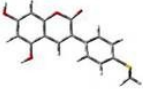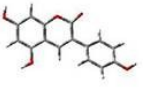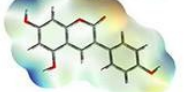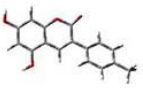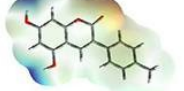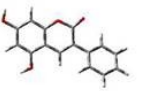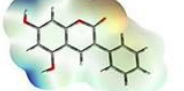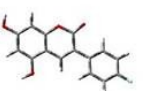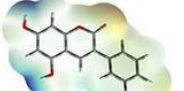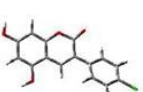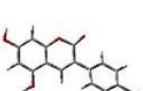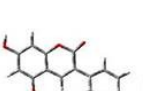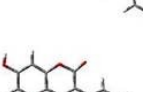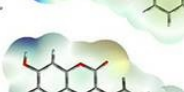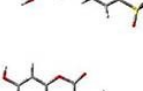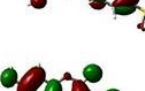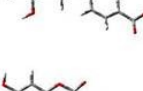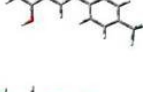
Figure S5. Optimized geometry, HOMO-LUMO orbitals, electron density surface, and energy values of 5,7-dihdyroxycoumarins (**1c**-**14c**).
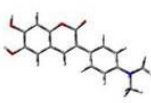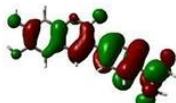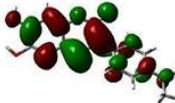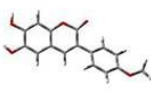
Equilibrium and Kinetic Studies of a Cationic Dye Adsorption onto Raw Clay

Eda GÖKIRMAK SÖĞÜT[1*] ✉ 🆔 **, Necla ÇALIŞKAN KILIÇ**[2] ✉ 🆔

[1] Van Security Vocational School
[2] Department of Physical Chemistry Faculty of Science, Van Yüzüncü Yıl University, 65080 Van, Turkey

Abstract: In this study, methylene blue (MB) dye adsorption from the aqueous solution on raw clay samples collected from the Tilkitepe in the east of Lake Van was presented. Batch adsorption studies were conducted to evaluate the effect of various experimental parameters such as pH, contact time and initial concentrations on the removal of MB. The five nonlinear adsorption equations were applied to describe the equilibrium isotherms. Considering the correlation coefficients, the order of the most suitable isotherm models was Sips> Freundlich> Temkin> Dubinin- Radushkevich>Langmuir. From the data applied to the pseudo-first-second order, Elovich and intra-particle diffusion kinetic models, it can be said that the best model describing the kinetics of MB dye adsorption is the pseudo-second order (PSO) kinetic model. The results are shown that Tilkitepe / Van raw clay material could be used as an economical and effective adsorbent for dye removal.

INTRODUCTION

The rapid development of technology caused many industries to release their wastes into the environment without subjecting them to a pre-cleaning process. Dyes and pigment industries often produce waste containing organic matter and high color (1). Nowadays, synthetic dyes are used more in the industry because of their low-cost production, stability, and color diversity compared to natural dyes. When these pigments are released into the environment, they damage the ecology in the soil and water they contact with sunlight. Therefore, the removal of industrial wastes containing dye

emerges as one of the most critical aims in environmental studies. There are more than 100.000 kinds of dye, which are classified as anionic and cationic. The cationic dyes contain protonated amine or sulfur-containing groups and have a net positive charge (2).

MB dye is not accepted among toxic dyes but has harmful effects on living organisms and is used in the coloring of many materials. It is also used as the determination of surface properties, oxidation-reduction indicator, pesticide industries, antiseptic, and for other medical purposes (3-5). Therefore, an effective method is required to remove the dye from the

wastewater. Some methods, such as chemical precipitation (6), ion-exchange (7), adsorption (8), membrane technologies (9), and photocatalysis (10), are used in the removal process. Adsorption is the most widely known and used; it is quite remarkable because it provides ease of design and use (11).

Generally, porous materials such as clay, chitin, peat, silica, and activated carbon have been used for the adsorption of heavy metals and dyes from aqueous solution (12). Some adsorbents are not economical due to regeneration problems. Also, the cost of production and other parameters such as regeneration, usability, environmental compatibility, and the energy consumption is essential in the selection of adsorbents (13). For this reason, the related studies aim to find a more economical and effective sorbent when compared to activated carbon (12). Due to their advantageous physicochemical characteristics such as high surface area, high cation exchange capacity, and layer structure, clays are known to be highly capable of removing waste from aqueous solution (14, 15). Balancing the negatively charged layers with the hydrated cations placed in the intermediate layers is an important feature of the clays (14).

In recent years, many scientific studies have centered on the investigation of locally available clay as low-cost adsorbents**.** Van lake basin is rich in some industrial raw materials. The people of the region use clayey soils in the region for personal cleaning practices and the production of pottery since ancient ages. There are no studies other than the structural characterization of the clayey soil in the region and the determination of its adsorption capacity of heavy metals (16). It is imperative to determine the chemical, physicochemical and adsorptive properties of the materials that can be used as an industrial raw material in the region and to use the raw material without pretreatment without energy expenditure and

secondary chemical waste. The adsorption of organic molecules onto clay is affected by its surface characteristics and the chemical properties of the molecules (15). Due to the high affinity of cationic dye molecules for clay surfaces, they are readily adsorbed by treated with clay suspensions (14).

This study aimed to evaluate the potential of Tilkitepe natural clay as a low-cost adsorbent to remove methylene blue from the aqueous solution as an ideal alternative to the expensive methods available for removing dyes from wastewater. The natural adsorbent was characterized by XRF, XRD, and FT-IR techniques. The batch experiments were applied to understand the nature of the adsorption of MB dye from the aqueous solution onto natural clay. The effects of initial dye concentration, contact time, temperature, and pH on adsorption were investigated to emphasize the importance of optimum conditions in determining the nature of adsorption. The obtained data were enforced to several isotherm models, kinetic models, and the advantages of natural material in waste dye removal were presented.

MATERIALS AND METHODS

Adsorbent
The natural clay samples were collected from the Tilkitepe/Van region was powdered in a mortar. No pretreatment has been applied to the material. After passing through a 230 mesh sieve (62.0 μm), it was stored in the polymer bags and denoted as TM.

Adsorbate
Methylene blue (MB, MF:$C_{16}H_{18}N_3SCl$ and MW: 319.852 g) was obtained from Merck. The dye's chemical structure is showed in Figure 1 and a stock solution (1000 mg L^{-1}) was prepared and then diluted with distilled water at different concentrations.
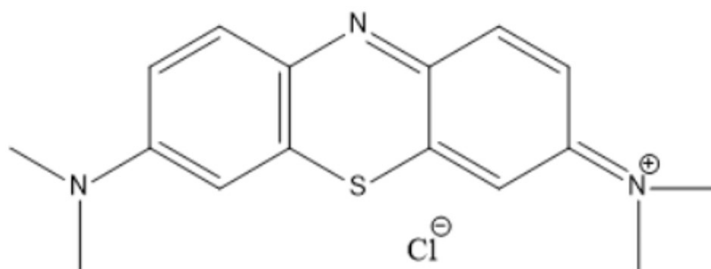
Figure 1. The chemical structure of methylene blue.

Characterization of the Sample
Chemical analysis of the Tilkitepe raw clay was made using the Philips 2400 XRF instrument. XRD analysis was obtained using an X-ray diffractometer (Philips PW 1830-40) with Ni-filtered Cu X-ray tube devices at 2-40 degrees. FT-IR analysis was performed before and after the adsorption process, using a Thermo Scientific Nicolet S10 FT-IR spectrometer with wavenumber range from 400 to 4000 cm^{-1} (16).

Methods
The adsorption experiments were applied at ambient temperature with a solution of 0.1 g of adsorbent in 10 mL of an aqueous solution of several concentrations of the dye (10, 20, 30, 45, and 60 mg L^{-1}). The effect of pH was investigated using HCl and NaOH solutions (pHs 2, 3, 4, 5, 6, 7, 8, 9). These measurements were made using a WTW pH meter (Series 720, Germany). The batch adsorption process was carried out using a heat-controlled shaker with a constant agitation speed of 125 rpm at 298 K. The samples were filtered, and the residual concentrations of MB in the filtrate were measured to learn about the final concentration of MB dye by using a UV / Vis Spectrophotometer (PG Instruments T80) at 664 nm. The amounts of dye adsorbed by the adsorbent and the adsorption efficiency (%) were calculated from using the following equation (17).

$$q_e = \frac{(C_0 - C_e)V}{m} \tag{1}$$

$$\%Adsorption = \frac{C_0 - C_e}{C_0} \times 100 \tag{2}$$

Where, C_0 (mg L^{-1}) is the initial liquid phase concentration, and C_e (mg L^{-1}) is equilibrium liquid-phase concentrations of the dye, q_e (mg g^{-1}) represents the amount of dye adsorbed, V (L) is the volume of the solution, and m (g) is the mass of the adsorbent used.

Adsorption Isotherms
Langmuir, Freundlich, Dubinin-Radushkevich, Temkin, and Sips and non-linear isotherms were used to explain the nature of the Methylene blue adsorption on the natural adsorbent (surface properties, mechanism of adsorption). The isotherm parameters were determined by non-linear regression analysis (with Originlab. 17). The C_e-q_e values obtained for dye adsorption on the natural adsorbent

were applied to each non-linear isotherm equation. For each isotherm model, standard errors (S.E) were also calculated to determine the isotherm that best fits the experimental data. Besides, a chi-square value (χ^2), which is a statistical data required for the suitability of the obtained adsorption system, was calculated using the same software (16, 18). The non-linear regression method, which was applied in the computerized process, that minimizes the error distribution between the experimental data and the estimated isotherms, was applied (19).

These parameters are determined in the following Eq.3 and 4 (20).

$$R^2 = \frac{\Sigma(q_{e,calc} - \overline{q_{e,exp}})^2}{\Sigma(q_{e,calc} - \overline{q_{e,exp}})^2 + \Sigma(q_{e,calc} - q_{e,exp})^2} \tag{3}$$

$$\chi^2 = \sum_{i=1}^{N} \frac{(q_{e,exp} - q_{e,calc})^2}{q_{e,calc}} \tag{4}$$

where $q_{e,calc}$ (mg g^{-1}) is calculated from the isotherm for corresponding $q_{e,exp}$(mg g^{-1}), which is obtained from the batch experiment and $q_{e,exp}$ is the average of q$_{e, exp}$. Also, N represents the number of observations in experimental data. The fact that R^2 is close to unity, χ2, and S.E close to zero is an indicator of the most suitable isotherm model (21)

Langmuir Isotherm
According to the Langmuir isotherm model, there are active adsorption centers on the surface of the sorbent, and they all have equivalent energy. Furthermore, according to this model, the adsorption equilibrium is a dynamic equilibrium and the molecules attached to the surface do not interact with each other (22).

$$q_e = \frac{q_M K_L C_e}{1 + K_L C_e} \tag{5}$$

Where q$_m$ is the maximum adsorption capacity (mg g^{-1}), and K$_L$ is the Langmuir isotherm constant (L g^{-1}).

Freundlich Isotherm
The Freundlich equation is used to describe heterogeneous systems and is expressed in the following equation.

$$q_e = K_F C_e^{1/n} \tag{6}$$

Where K_F is Freundlich isotherm constant (L g^{-1}), and n is the heterogeneity factor in the Freundlich model. If 1 / n value is below unity, it shows normal adsorption, but if 1 / n is above unity, it indicates cooperative adsorption (23).

Dubinin–Radushkevich Isotherm
This isotherm is usually applied by Gaussian energy distribution to express the adsorption mechanism on heterogeneous surfaces.

$$q_e = q_M \exp\left(-K_{DR}\varepsilon^2\right)$$

$$\varepsilon = RT ln(1 + \frac{1}{C_e})$$

(7), (8)

Where K_{DR} is D-R isotherm constant, R is the ideal gas constant (8.314 (J mol^{-1} K^{-1}), and ε is the Polanyi potential.

If the energy value is less 8 kJ mol^{-1}, the physical interactions are in the adsorption. Conversely, if the energy is more than 8 kJ mol^{-1}, the adsorption mechanism can be defined by chemical interactions (24).

Temkin Isotherm
Temkin isotherm model assumes that the adsorption heat (a function of temperature) of all molecules in the layer will decrease linearly (23).

$$q_e = \frac{RT}{b_T}\ln\left(K_T C_e\right)$$

(9)

where K_T is Temkin isotherm equilibrium binding constant (L g^{-1}),b_T is Temkin isotherm constant (kJ mol^{-1}), R is the ideal gas constant (8.314 (J mol^{-1} K^{-1}), T is the temperature (K).

Sips Isotherm
Sips isotherm model is used to describe adsorption on heterogeneous surfaces. Sips isotherm model is a combination of Langmuir and Freundlich isotherm models. It shows the characteristics of Freundlich isotherm at low concentrations and gives the characteristics of Langmuir isotherm by estimating the monolayer adsorption capacity at high concentrations (21).

$$q_e = \frac{K_s(a_s C_e)^{n_s\hat{}}}{1+(a_s C_e)^{n_s}}$$

(10)

Where K_S is Sips isotherm constant (L g^{-1}), a_S is Sips isotherm constant, (L mg $^{-1}$), and n_S is Sips isotherm exponent.

Kinetics
The pseudo-first-order (PFO) kinetic model is expressed as follows (25).

$$q_t = q_e[1 - \exp\left(-k_1 t\right)]$$

(11)

where k_1 (min^{-1}) is PFO rate constant and t (min) is the contact time.

Y.S. Ho developed the pseudo second order (PSO) kinetic model and was expressed as follows:

$$q_t = \frac{k_2 q_e^2\, t}{1+k_2 q_e t}$$

(12)

where k_2 (g mg^{-1} min^{-1}) is PSO rate constant.

The intra-particle diffusion model is as follows:

$$q_t = k_i\, t^{1/2} + C$$

(13)

where k_i is the rate constant (mg g^{-1} $min^{-0.5}$)

The Elovich equation, which is representative of the active solid regions being energetically heterogeneous and therefore representing different activation energies for chemical adsorption, interprets the absorption kinetics and is graphed with the following equation.

$$q_t = \frac{1}{\beta}\ln\left(1 + \alpha\beta t\right)$$

(14)

where α (mg g^{-1} min^{-1}) is the initial adsorption rate, β (g mg^{-1}) is the desorption constant related to the extent of surface coverage and activation energy for chemisorption (26).

RESULTS

Surface Properties and Characterization of Adsorbent
Tilkitepe raw clay is composed of SiO_2 37.5%, and it has 20.5% CaO, 6.2% MgO, 5.6% Al_2O_3, 5.4% Fe_2O_3, 0.6% TiO_2, 2.0% Na_2O, 1.3% K_2O, 0.1% MnO and 0.1% P_2O_5. The XRD analysis indicates the predominance of quartz and calcite in the raw clayey material, with the most intense peaks, a low quantity of feldspar, smectite, and illite. The surface properties and characterization of adsorbent, which include

clay minerals and non-clay minerals, are presented in detail in the previous paper (16). The functional groups contributing to the adsorption process were measured, and the FT-

IR spectrum of clay adsorbent before and after the adsorption is in the wavenumber range 4,000–400 cm^{-1} and is presented in Figure 2.
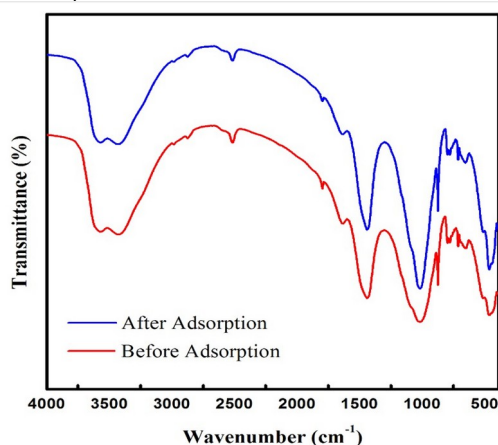
Figure 2. The FTIR spectra of before and after adsorption of methylene blue onto Tilkitepe-originated clayey material.

The two bands at 3568 and 3424 cm^{-1} were ascribed to hydroxyl groups involved in hydrogen bonds (Si–Si–OH or Al–Al–OH), respectively. 2985 and 1436 cm^{-1} peaks indicate the presence of (C – H) group vibrations. The band appearing at 1629 cm^{-1} is due to the H$_2$O bending vibration. Si-O-Al is bending vibration, 871.82 cm^{-1} attributed to Fe–Al–OH of montmorillonite, and Si-O-Si bending vibrations can be attributed to 509.21 cm^{-1} and 462.92 cm^{-1}, respectively (16). The FTIR spectra of the raw clay and MB adsorbed clay showed that is a noticeable change in intensity of the bands with no change locations. After the adsorption of MB, the density of Si-O-Si (siloxane peak) was increased in 1014 due to the electrostatic attraction between the positive dye cation and the negative clay surface (Figure 2). Furthermore, the band density of the hydroxyl

group observed in 3568, and 3424 cm^{-1} (Figure 2) appears to decrease after MB adsorption (27). The changes in the FTIR spectra confirmed that the process involved is type inclusion of methylene blue on the Tilkitepe raw clay (28).

Influence of pH on the Adsorption
The effect of pH on the ability of Tilkitepe raw clay to remove methylene blue (MB) from aqueous solution was investigated. The pH of the solution is one of the most effective parameters in the adsorption process, mainly due to the importance of adsorbents on the surface functional groups and adsorption properties (29). The effect of pH on the adsorption efficiency (%) was calculated using Eq. 2 and presented Figure 3.
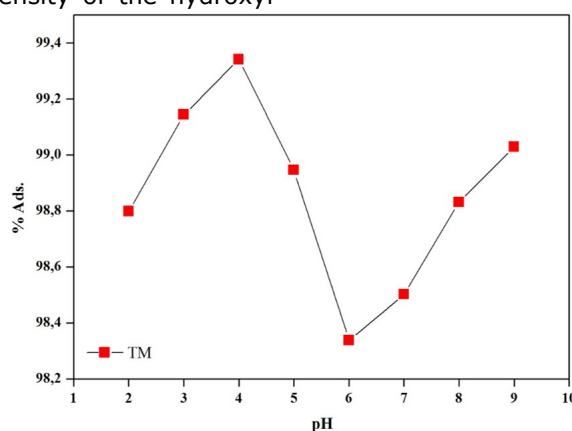
Figure 3. pH effect on the adsorption of methylene blue on raw clay at 30 mg L^{-1} initial solution concentration (298 K).

The pH control was adjusted by adding HCl and NaOH solutions, and the highest adsorption efficiency was achieved as 99.34% at pH = 4. It might be the result of increased protonation by neutralizing negative charges on the adsorbent surface because the cationic dye targets the electron-rich centers (30). It was observed that the amount of dye removal starts to increase again at higher than pH = 7. Alkaline solutions might cause the change in the polarity of the dye, and methylene blue might have demethylated to other conventional dyes. Similar results were presented in other publications (31-33). It indicated that the adsorption capacity of MB onto Tilkitepe in solution was pH-dependent. Therefore, it was decided to perform batch adsorption tests at pH = 4. In substance, Tilkitepe raw clay with a smectic clay density is composed of an octahedral alumina layer between the outer layers of tetrahedral silica. The silanol groups on the clay surface can be said to form a hydrogen bond to an amine group and to form an ionic bond with another amine group Si-O. Besides, in many studies, clay has also been interpreted to interact with dye molecules through hydrogen bonds and hydrophobic-hydrophobic mechanisms (34-36).

Effect of initial dye concentration with contact time

The determination of the effect of the initial ion concentration is critical because it provides the initial repulsive force necessary to get over the mass transfer opposition of the dye through the sol-sorbent interface (37). Fig.4a and b show the effect of the initial dye concentration (10-60 mg L^{-1}) as a function of contact time (1-120 min) at the removal of MB by Tilkitepe clay.

(a)

(b)
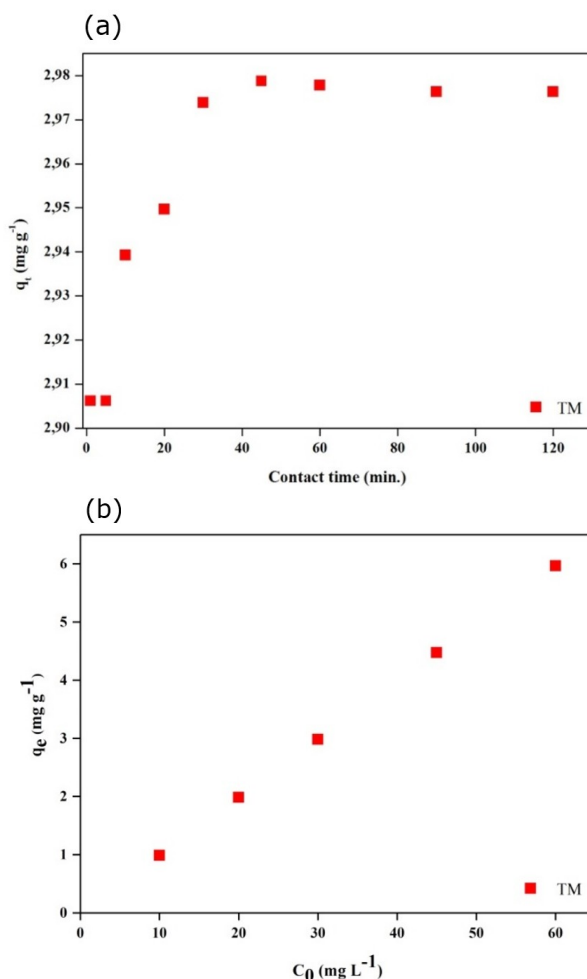
Figure 4. a) Effect of contact time for the adsorption of methylene blue onto Tilkitepe (C_0:30 mg L^{-1}, T: 298 K), b) The effects of the initial solution concentration on the adsorption at 298 K.

With increasing concentration for dye adsorption, as presented in Figures 4.a. and b., the adsorption initially increases. The experiments were decided to be performed for

90 minutes to ensure equilibrium saturation. The first rapid uptake may be for external diffusion of the dye to the adsorbent surface. As time progresses, slower uptake may be attributed to slower intracellular diffusion due to lower dye concentration and constant adsorbent amount in the adsorption system (38).

Adsorption isotherms

The analysis of isotherm results provides essential information, such as the nature of the adsorbent and its surface properties (39). Non-linear diagrams of isotherm models for dye (MB) adsorption on the Tilkitepe raw clay are given in Fig. 5. The values of isotherm models are listed in Table 1.
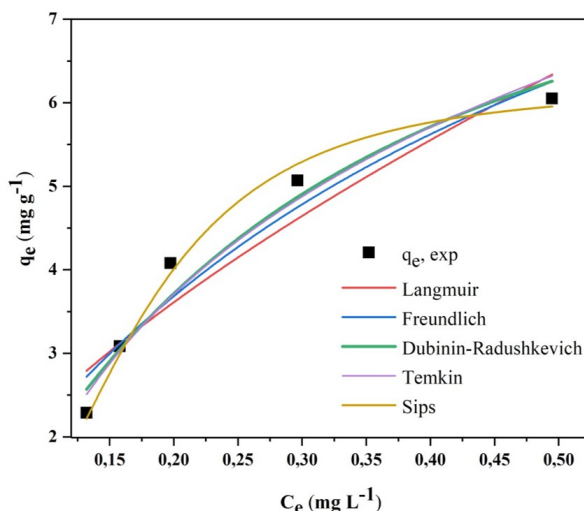
Figure 5. Comparison of adsorption isotherm models for the sorption of methylene blue on Tilkitepe at 298 K.

Table 1. The values of non-linear isotherm models for methylene blue adsorption onto Tilkitepe.

Isotherm/Model		Value	S.E
Langmuir	q_M (mg g^{-1})	11.870	1.2900
	K_L	2.2466	0.1042
	R_L	0.0426	
	R^2	0.9015	
	χ^2	0.2431	
Freundlich	K_F	9.8099	0.2598
	n	1.6098	0.3292
	R^2	0.9590	
	χ^2	0.8942	
Dubinin-Radushkevich	q_M (mg g^{-1})	9.9823	0.8061
	K_{D-R}	0.2623	0.0367
	E_{D-R}	1.3807	
	R^2	0.9350	
	χ^2	0.9512	
Temkin	b_T	0.8602	0.3757
	K_T	18.0560	1.5064
	R^2	0.9355	
	χ^2	0.8741	
Sips	q_M (mg g^{-1})	10.9787	0.3312
	a_S	6.1725	0.2137
	n_S	2.866	0.5234
	R^2	0.9819	
	χ^2	0.9096	

Langmuir isotherm, which accepts monolayer and homogeneous adsorption, can be caused not only by physical interactions but also by powerful electrostatic attractions. The R^2 value determined from the Langmuir equation is 0.9015; the χ^2 value is 0.2431 at 298 K. The q_m

value was determined to be 11.870, and S.E was found to be 1.2900. The R_L values were found to be 0.0426; it can be said that the Langmuir isotherm is favorable for the adsorption (40). However, the Freundlich isotherm model has a higher regression coefficient (0.9590) and lower S.E (0.2598) and χ^2 (0.8942) values. Also, the K_F and n values were calculated as 9.8099 and 1.6098, respectively. If n lies between one and ten, this indicates a favorable sorption process (23). 1/n (0,6211) value between 0 and 1 showed that the natural sorbent easily adsorbed MB. The D-R adsorption isotherm provided useful data for this study (R^2 = 0.9350). It has a lower S.E (0.8061) and χ^2 (0.9512) values. As the adsorption energy (E) values are below 8 kJ mol^{-1} at the studied temperature, thus, it can be said that the adsorption mechanism is a combination of physical adsorption and electrostatic interaction (41). In physical adsorption, adsorbates exhibit relatively low adsorption energies as they adhere to the adsorbent through weak Van der Waals interactions. The low value (0.8602) of the Temkin constant bT (kJ mol-1) obtained from the Temkin Isotherm model also supports a weak adsorbate-adsorbent interaction. The correlation coefficient obtained from Temkin

isotherm at 298 K is 0.9355, and lower S.E (0.3757) and χ^2 (0.8741) values (20, 42). If n_s = 1, a dimensionless heterogeneity factor in the Sips isotherm equation, this equation is reduced to the Langmuir isotherm equation and indicates that the adsorption process is homogenous (43). This isotherm model has a higher regression coefficient (0.9819) and lower S.E (0.3312) and χ^2 (0.9096) values. It has been verified that adsorption is heterogeneous from the Sips isotherm constant (6.1725) in Table 1.

Adsorption kinetics
Kinetic studies are critical in illuminating the adsorption mechanism. It is known that non-linear kinetic models are more accurate in assigning the correct models to the tested data (44). Different kinetic models such as pseudo-first-order, pseudo-second-order, Elovich non-linear kinetic models, and Weber and Morris intraparticle diffusion model were used in the evaluation of the experimental data in Figure 6. Higher R^2 and lower error function values are referred to as better model fitting. The results of the modeling data for the MB adsorption on the natural adsorbent are presented in Table 2 a-b.

Table 2 a. Pseudo-first and -second-order and Elovich kinetic parameters of Methylene Blue adsorption onto Tilkitepe clay at 30 mg L^{-1} initial dye concentrations (T = 298 K).

Kinetic Models		Value	SE.
	$q_{e\ (exp)}$ **(mg g^{-1})**	**2.9778**	-
Pseudo-first order	$q_{e.\ (cal)}$ (mg g^{-1})	0.0075	0.0059
	k_1 (min^{-1})	0.0075	0.0540
	χ^2	0.0024	
	R^2	0.5954	
Pseudo-second order	$q_{e.\ (cal)}$ (mg g^{-1})	2.9797	0.0030
	k_2 (g mg^{-1} min^{-1})	3.6686	0.2404
	χ^2	0.0043	
	R^2	0.9502	
Elovich	α (mg g^{-1} min^{-1})	1.2115	10.6052
	β (g mg^{-1})	35.8904	2.9699
	χ^2	0.0176	
	R^2	0.7451	

Table 2 b. Intraparticle diffusion parameters at (30 mg L^{-1} initial dye concentrations and T = 298 K).

Intraparticle Diffusion Model	Tilkitepe clay 298 (K)
k_{id} ((mg g^{-1}h$^{1/2}$)	**0.0011**
C_o	2.9326
R^2	0.7871

The pseudo-first-order kinetic model is usually among the applied kinetic models and has an expression based on the adsorption capacity of the adsorbent (Eq. (11)). It is seen that there is a significant difference between the calculated values (qe (calc)) and the experimental values (qe (exp)) from Table 2 a. Compared to other model parameters, lower correlation coefficient values that this model is not applicable for MB adsorption on the natural adsorbent (45).

The pseudo-second-order kinetic model helps predict the adsorption rate of a given adsorption system. The adsorption ratio is based on the assumption that the number of bonding areas on the adsorbent is proportional to the square (46). Equation (Eq.(12)) and corresponding constants are presented in Table 2 a. It is observed that the values of qe (calc) and qe (exp) are almost similar, and χ^2 is at a lower value, and R^2 value is 0.9502. Therefore, the MB adsorption on the natural adsorbent follows the pseudo second-order kinetic model sufficiently (47).
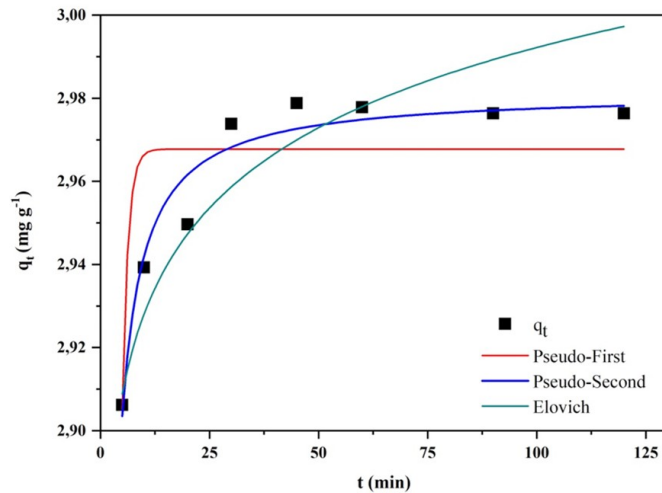
Figure 6. Non-linear kinetic model of pseudo-first-order, pseudo-second-order, and Elovich models for Methylene blue adsorption onto Tilkitepe at 298 K.

The Elovich model, a kinetic model, based on adsorption capacity, assumes that the adsorption mechanism is chemical or physical adsorption (48). The Elovich equation (Eq. (14)) and the characteristic parameter values are presented in Table 2 a, respectively. Table 2 shows the applicability of this model in that the value of χ^2 is significantly lower at 298 K. The low values of the correlation coefficients at the temperature discuss the suitability of this model for the experimental data (49).
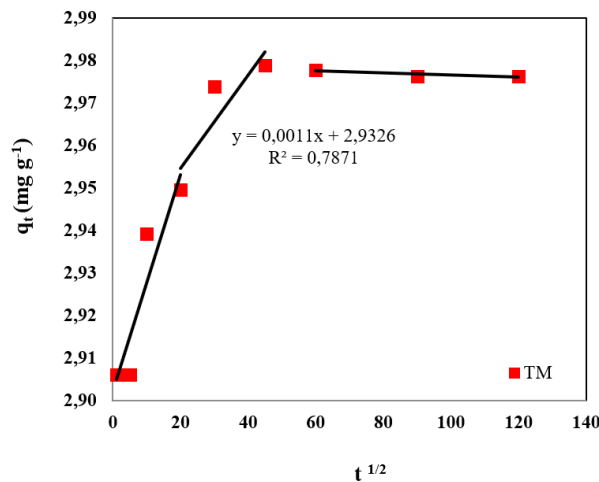
Figure 7. Intraparticle diffusion plots for adsorption (C_0= 30 mg L^{-1} and T = 298 K).

The intra-particle diffusion plot was calculated with Eq. 13 and presented in Figure 7. If the particle diffusion was involved in the adsorption process, the plot would appear a straight line,

and if the rate-limiting step were only particle diffusion, this line would pass through the origin (50). It is evident in Figure 7 that there are three separate stages in each case. i) The first stage with high slope represents the fastest process, mass or surface diffusion; ii) the second stage is slower than the first stage, which shows the effect of pore diffusion or intra-particle diffusion controlled region; iii) the last stage is almost linear and indicates the equilibrium state of the system (51). As can be seen, the plot did not pass through the origin; thus it can be said that intra-particle diffusion is not the only rate-limiting step in the adsorption process (52) The boundary layer thickness of the calculated diffusion coefficient is listed in Table 2 b.

CONCLUSION

The raw Tilkitepe clay is an excellent alternative adsorbent to remove the MB dye from the aqueous solutions. When this adsorbent is suspended in water, it interacts with the dye at the solid/liquid interface. The dye molecules in the structure of clay form active areas by hydrating in aqueous solution depending on pH. Thus, MB is attracted to negatively charged surfaces of clay or interlamellar can be replaced with cations in space; the charge density is pH-dependent (38). Equilibrium isotherm modeling of MB adsorption was performed, and the data best fit the Freundlich and Sips isotherm models. Among the most critical kinetic models evaluated in the adsorption mechanism, the pseudo-second kinetic (PSO) model is the most suitable model. Furthermore, the intra-particle diffusion model has linear regions, and it is proposed that multiple adsorption rates can follow adsorption. The maximum capacity (q_M) of this adsorbent, which is cheap and does not cause secondary pollution, was determined as 11.870 mg g^{-1} from the experimental data.

REFERENCES

1. Chakraborty S, Chowdhury S, Das P. Artificial neural network (ANN) modeling of dynamic adsorption of crystal violet from aqueous solution using citric-acid-modified rice (Oryza sativa) straw as adsorbent. Clean Technologies and Environmental Policy. 2012;15:doi: 10.1007/s10098-012.

2. Errais E, Duplay J, Darragi F, M'Rabet I, Aubert A, Huber F, et al. Efficient anionic dye adsorption on natural untreated clay: Kinetic study and thermodynamic parameters. Desalination. 2011;275(1):74-81.

3. Deng H, Lu J, Li G, Zhang G, Wang X. Adsorption of methylene blue on adsorbent materials produced from cotton stalk. Chemical Engineering Journal. 2011;172(1):326-34.

4. Chunjiaozhou, Zhenwu, Wenjiezhang, Mingxiaxia, Guozhangdai, Guangmingzeng, et al. FACILE SYNTHESIS OF HUMIC ACID-COATED IRON OXIDE NANOPARTICLES AND THEIR APPLICATIONS IN WASTEWATER TREATMENT. Functional Materials Letters. 2012;04.

5. Mouni L, Belkhiri L, Bollinger J-C, Bouzaza A, Assadi A, Tirri A, et al. Removal of Methylene Blue from aqueous solutions by adsorption on Kaolin: Kinetic and equilibrium studies. Applied Clay Science. 2018;153:38-45.

6. Alvarez MT, Crespo C, Mattiasson B. Precipitation of Zn(II), Cu(II) and Pb(II) at bench-scale using biogenic hydrogen sulfide from the utilization of volatile fatty acids. Chemosphere. 2007;66(9):1677-83.

7. Wong C-W, Barford JP, Chen G, McKay G. Kinetics and equilibrium studies for the removal of cadmium ions by ion exchange resin. Journal of Environmental Chemical Engineering. 2014;2(1):698-707.

8. Sadhukhan B, Mondal N, Chattoraj S. Biosorptive removal of cationic dye from aqueous system: A response surface methodological approach. Clean Technologies and Environmental Policy. 2013;16.

9. Qiu Y-R, Mao L-J. Removal of heavy metal ions from aqueous solution by ultrafiltration assisted with copolymer of maleic acid and acrylic acid. Desalination. 2013;329:78-85.

10. Gupta VK, Jain R, Nayak A, Agarwal S, Shrivastava M. Removal of the hazardous dye—Tartrazine by photodegradation on titanium dioxide surface. Materials Science and Engineering: C. 2011;31(5):1062-7.

11. Shen Z, Jin F, Wang F, McMillan O, Al-Tabbaa A. Sorption of lead by Salisbury biochar produced from British broadleaf hardwood. Bioresource technology. 2015;193:553-6.

12. Afroze S, Sen T, Ang H, Nishioka H. Adsorption of methylene blue dye from aqueous solution by novel biomass Eucalyptus sheathiana bark: equilibrium, kinetics,

thermodynamics and mechanism. Desalination and Water Treatment. 2015;57:1-21.

13. Mondal N, Das K, Das B, Sadhukhan B. Effective utilization of calcareous soil towards the removal of methylene blue from aqueous solution. Clean Technologies and Environmental Policy. 2015;18:1-17.

14. Gürses A, Doğar Ç, Yalçın M, Açıkyıldız M, Bayrak R, Karaca S. The adsorption kinetics of the cationic dye, methylene blue, onto clay. Journal of Hazardous Materials. 2006;131(1):217-28.

15. Fatiha M, Belkacem B. Adsorption of methylene blue from aqueous solutions using natural clay. Journal of Materials and Environmental Science. 2016;7(1):285-92.

16. Caliskana N, Sogutb EG, Savrana A, Kula AR, Kubilaya S. Removal of Cu (II) and Cd (II) ions from aqueous solutions using local raw material as adsorbent: a study in binary systems. DESALINATION AND WATER TREATMENT. 2017;75:132-47.

17. Ertaş M, Acemioğlu B, Alma MH, Usta M. Removal of methylene blue from aqueous solution using cotton stalk, cotton waste and cotton dust. Journal of Hazardous Materials. 2010;183(1):421-7.

18. Foo KY, Hameed BH. Insights into the modeling of adsorption isotherm systems. Chemical Engineering Journal. 2010;156(1):2-10.

19. Salarirad MM, Behnamfard A, editors. Modeling of equilibrium data for free cyanide adsorption onto activated carbon by linear and non-linear regression methods. International Conference on Environment and Industrial Innovation; 2011.

20. Rahman M, Sathasivam KV. Heavy metal adsorption onto Kappaphycus sp. from aqueous solutions: the use of error functions for validation of isotherm and kinetics models. BioMed research international. 2015;2015.

21. Samarghandi M, Hadi M, Moayedi S, BARJESTEH AF. Two-parameter isotherms of methyl orange sorption by pinecone derived activated carbon. 2009.

22. Wong YC, Szeto YS, Cheung WH, McKay G. Equilibrium Studies for Acid Dye Adsorption onto Chitosan. Langmuir. 2003;19(19):7888-94.

23. A.O D, Olalekan A, Olatunya A, Dada AO. Langmuir, Freundlich, Temkin and Dubinin–Radushkevich Isotherms Studies of Equilibrium Sorption of Zn 2+ Unto Phosphoric Acid Modified Rice Husk. J Appl Chem. 2012;3:38-45.

24. Ho Y. Adsorption of heavy metals from waste streams by peat, University of Birmingham, Birmingham, UK Ph. D: Thesis; 1995.

25. Al-Musawi TJ, Brouers F, Zarrabi M. Kinetic modeling of antibiotic adsorption onto different nanomaterials using the Brouers–Sotolongo fractal equation. Environmental Science and Pollution Research. 2017;24(4):4048-57.

26. Ahmad MA, Ahmad Puad NA, Bello OS. Kinetic, equilibrium and thermodynamic studies of synthetic dye removal using pomegranate peel activated carbon prepared by microwave-induced KOH activation. Water Resources and Industry. 2014;6:18-35.

27. Mohamed EA, Selim AQ, Zayed AM, Komarneni S, Mobarak M, Seliem MK. Enhancing adsorption capacity of Egyptian diatomaceous earth by thermo-chemical purification: Methylene blue uptake. Journal of Colloid and Interface Science. 2019;534:408-19.

28. Tarik A, Abdelmjid A, Kabbaj M, Elkouali M, Bennamara A, Charrouf M, et al. Valorization of natural clay from agadir (Morocco): Characterization and study of the isotherms adsorption of Methylene blue. Journal of Chemical and Pharmaceutical Research. 2014;6:599-606.

29. Feddal I, Ramdani A, Taleb S, Gaigneaux EM, Batis N, Ghaffour N. Adsorption capacity of methylene blue, an organic pollutant, by montmorillonite clay. Desalination and Water Treatment. 2014;52(13-15):2654-61.

30. Shahryari Z, Soltani Goharrizi A, Azadi M. Experimental study of methylene blue adsorption from aqueous solutions onto carbon nano tubes. Int J Water Resour Environ Eng. 2010;2.

31. Nsami N, Mbadcam J. The Adsorption Efficiency of Chemically Prepared Activated Carbon from Cola Nut Shells by ZnCl2 on

Methylene Blue. Journal of Chemistry. 2013;2013.

32. Goyal M, Singh S, Bansal R. Equilibrium and Dynamic Adsorption of Methylene Blue from Aqueous Solutions by Surface Modified Activated Carbons. Carbon letters. 2004;5.

33. Gottipati R, Susmita M. Aplication of Biowaste (Waste Generated in Biodiesel Plant) as an Adsorbent for the Removal of Hazardous Dye – Methylene Blue from Aqueous Phase. Brazilian Journal of Chemical Engineering. 2010;27:357-67.

34. Al-Degs YS, El-Barghouthi MI, El-Sheikh AH, Walker GM. Effect of solution pH, ionic strength, and temperature on adsorption behavior of reactive dyes on activated carbon. Dyes and Pigments. 2008;77(1):16-23.

35. Mukherjee K, Kedia A, Korukonda JR, Dhir S, Paria S. Adsorption Enhancement of Methylene Blue Dye at Kaolinite Clay – Water Interface Influenced by Electrolyte Solutions. RSC Advances. 2015;5.

36. Fang Y, Zhou A, Yang W, Araya T, Huang Y, Zhao P, et al. Complex Formation via Hydrogen bonding between Rhodamine B and Montmorillonite in Aqueous Solution. Scientific Reports. 2018;8.

37. Patil S, Renukdas S, Patel N. Removal of methylene blue, a basic dye from aqueous solutions by adsorption using teak tree (Tectona grandis) bark powder. International Journal of Environmental Sciences. 2011;1:711-26.

38. Tong Ks, Azraa A, Noordin M. Isotherms and Kinetics Studies on the Removal of Methylene Blue from Aqueous Solution by Gambir. International Journal of Environmental Science and Development. 2012:232-6.

39. Feddal I, Ramdani A, Taleb S, Gaigneaux E, Batis N, Ghaffour N. Adsorption capacity of methylene blue, an organic pollutant, by montmorillonite clay. Desalination and water treatment. 2013;52:1–8.

40. Tan IAW, Ahmad AL, Hameed BH. Adsorption of basic dye on high-surface-area activated carbon prepared from coconut husk: Equilibrium, kinetic and thermodynamic studies. Journal of Hazardous Materials. 2008;154(1):337-46.

41. Caliskan N, Kul AR, Alkan S, Sogut EG, Alacabey İ. Adsorption of Zinc(II) on diatomite and manganese-oxide-modified diatomite: A kinetic and equilibrium study. Journal of Hazardous Materials. 2011;193:27-36.

42. Araújo CST, Almeida ILS, Rezende HC, Marcionilio SMLO, Léon JJL, de Matos TN. Elucidation of mechanism involved in adsorption of Pb(II) onto lobeira fruit (Solanum lycocarpum) using Langmuir, Freundlich and Temkin isotherms. Microchemical Journal. 2018;137:348-54.

43. Nethaji S, Sivasamy A, Mandal A. Adsorption isotherms, kinetics and mechanism for the adsorption of cationic and anionic dyes onto carbonaceous particles prepared from Juglans regia shell biomass. International Journal of Environmental Science and Technology. 2013;10(2):231-42.

44. Bujdák J. Adsorption kinetics models in clay systems. The critical analysis of pseudo-second order mechanism. Applied Clay Science. 2020;191:105630.

45. Ponnusamy SK, K K. Equilibrium and Kinetic Study of Adsorption of Nickel from Aqueous Solution onto Bael Tree Leaf Powder. Journal of Engineering Science and Technology. 2009;4.

46. Plazinski W, Dziuba J, Rudzinski W. Modeling of sorption kinetics: The pseudo-second order equation and the sorbate intraparticle diffusivity. Adsorption. 2013;19.

47. Aljeboree AM, Alshirifi AN, Alkaim AF. Kinetics and equilibrium study for the adsorption of textile dyes on coconut shell activated carbon. Arabian Journal of Chemistry. 2017;10:S3381-S93.

48. Cestari AR, Vieira EF, Matos JD, dos Anjos DS. Determination of kinetic parameters of Cu (II) interaction with chemically modified thin chitosan membranes. Journal of Colloid and Interface Science. 2005;285(1):288-95.

49. Vilvanathan S, Shanthakumar S. Ni(2+) and Co(2+) adsorption using Tectona grandis biochar: kinetics, equilibrium and desorption studies. Environmental technology. 2018;39(4):464-78.

50. Zhang L, Loaiciga H, Xu M, Du C, Du Y. Kinetics and Mechanisms of Phosphorus Adsorption in Soils from Diverse Ecological Zones in the Source Area of a Drinking-Water

Reservoir. International Journal of Environmental Research and Public Health. 2015;12:14312-26.

51. Biswas S, Sen T, Yeneneh A, Meikap B. Synthesis and characterization of a novel Ca-alginate-biochar composite as efficient zinc (Zn 2+) adsorbent: Thermodynamics, process design, mass transfer and isotherm modeling. Separation Science and Technology. 2018:1-19.

52. Inyinbor AA, Adekola FA, Olatunji GA. Kinetics, isotherms and thermodynamic modeling of liquid phase adsorption of Rhodamine B dye onto Raphia hookerie fruit epicarp. Water Resources and Industry. 2016;15:14-27.

RESEARCH ARTICLE

Physicochemical Analysis and Heavy Metals Remediation of Pharmaceutical Industry Effluent Using Bentonite Clay Modified by H₂SO₄ and HCl

A. A. Abdullahi[1] ✉ iD **, Joshua O. Ighalo[2]** ✉ iD **, Oluwaseun Jacob. Ajala[3]*** ✉ iD **, Stephen Ayika[3]** ✉ iD

[1] Department of Chemistry, Faculty of Physical Sciences, University of Ilorin, P.M. B. 1515, Ilorin, Nigeria.
[2] Department of Chemical Engineering, Faculty of Engineering and Technology, University of Ilorin, P.M. B. 1515, Ilorin, Nigeria.
[3] Department of Industrial Chemistry, Faculty of Physical Sciences, University of Ilorin, P.M. B. 1515, Ilorin, Nigeria.

Abstract: Environmental pollution by industrial effluent has become a vital issue partly because of the detection of heavy metals in them, which need to be mitigated. Adsorbents were produced from Bentonite clay using 2 M H₂SO₄ and 2 M HCl as modifying agents in ratio 1:2 by wet impregnation method. Physicochemical properties of the pharmaceutical effluents such as pH, temperature, turbidity, conductivity, Chemical Oxygen Demand (COD), Biological Oxygen Demand (BOD), and heavy metals were determined. High concentrations of Fe(III) and Zn(II) were observed in the effluents when compared with standards. The optimal value of pH for Fe(III) and Zn(II) was 8, and a dose of 0.05 g was found to be the optimal value for all the adsorption system. The adsorption was best fit to Langmuir isotherm and the pseudo-second-order kinetic model. The results obtained in this study showed that the produced adsorbents could be used to supplement the commercial adsorbents in the specific application. Furthermore, the acid modification was helped to increase the sorption capacity of the clay to the heavy metals studied with H₂SO₄ being the better modification agent.

INTRODUCTION

The pollution of water by industrial effluents is a serious environmental challenge in recent times due to the increased activities of industries (such as pharmaceutical, mining, metallurgical, tannery, paint, nuclear, and batteries) (1, 2). Heavy metals can be considered as a group of trace elements with an atomic density greater than 4 ± 1 g/cm^3 (3). These include Al, Ni, As,

Abdullahi AA et al. JOTCSA. 2020; 7(3); 727-744.

RESEARCH ARTICLE

Co, Ag, Cr, Mn, Fe, Sn, Pb, Cd, Hg, Zn, and Cu, among others (4). Several characteristics of these heavy metals (i.e., high solubility, stability, and high migration activity in aqueous media) have led to their bio-magnification, causing varieties of human illness and other negative environmental impacts (5, 6).

A porous clay known as bentonite (with montmorillonite as its critical phase) is readily available (7, 8) and have been investigated by researchers as adsorbents to remove pesticides, herbicides (8, 9) various organic pollutants, heavy metals and a host of others (10, 11) from aqueous media. Bentonite is also very important and essential in many other fields such as iron ore pelletizing, drilling mud, foundry and binding, and civil engineering such as sealing and waterproofing (12).

Several recent modification techniques have been studied for bentonite clays in heavy metal adsorption (alongside the use of unmodified clays). Schütz *et. al* (13) modified bentonite with manganese to improve its affinity for Cd(II) uptake. Tohdee and Kaewsichan (14) utilized Bencylhexadecyldimethyl ammonium chloride for the modification of bentonite for Cu(II) and Zn(II) uptake via adsorption with positive results. Yan *et. al* (15) investigated the facile solvothermal synthesis of Fe_3O_4/bentonite for the adsorption of Pb(II), Cu(II), and Cd(II). Cantuaria *et. al* (16) studied the use of unmodified bentonite for the adsorption of silver from aqueous media. Alduaij *et. al* (17) studied the use of unmodified bentonite sourced from the Saudi area for the adsorption of Co(II).

Acid modification is a well-established preparation and modification technique for adsorbents (1). The use of inorganic acid-modified bentonite to study Zn(II) and Fe(III) sorption is unreported, leaving us a viable knowledge gap to explore. Furthermore, this study is geared towards a specific environmental problem in Nigeria, which it's Zn(II) and Fe(III) pollution from industrial effluents in Ilorin city. In this research work, the inherent adsorption strength of bentonite clays for the removal of heavy metals was investigated, and several factors (contact time, adsorbent dosage, pH, initial concentrations, and temperatures) were considered. Furthermore, isotherm, kinetics, and thermodynamics studies were conducted to gain more understanding of the adsorption process.

MATERIALS AND METHOD

Collection and Preparation of Adsorbents
The clay sample was collected from Afuze, Edo state, southern Nigeria. It was sun-dried, ground into fine powder by the use of a mortar and pestle and sieved using 2 μm geometrical sized screen. It was then transferred to a beaker and oven-dried at 110 °C for 24 h to remove water content and volatile impurities (18). The dried clay sample was removed and cooled in a desiccator containing $CaCl_2$ for 45-60 min. The dried clay was labeled as unmodified clay (UMBC) while the air-dried clay (size 2 μm) was equilibrated with 2.0 M sulfuric acid and stirred with a glass rod for 30 minutes and shaken for 1 h with a rotary shaker (19). The mixture was oven dried for 6 h at a temperature of 80 °C until a paste-like material is formed and allowed to cool. It was then washed several times using distilled water until the washed solution was of neutral pH. The same procedure was repeated for 2.0 M Hydrochloric acid. The two modified clays were then air-dried, sieved, and labeled as sulfuric acid modified clay (SMBC) and hydrochloric acid modified clay (HMBC), respectively (20).

Determination of Physicochemical Parameters of the Industrial Effluents
Effluent samples were analyzed to determine the pollutants/contaminants present through physicochemical analysis methods such as temperature, pH, turbidity, color and odor, and electrical conductivity.

Determination of Chemical Parameters of the Industrial Effluents
Chemical Oxygen Demand (COD)
A blank solution was prepared by pipetting a distilled water of 100 mL into a conical flask of 250 mL. A 10 mL portion of 25% H_2SO_4 and 20 mL of 0.01 M $KMnO_4$ was added to the solution. Then, 10 mL of the water sample was measured into another 250 mL conical flask and diluted with 90 mL of distilled water. A 10 mL portion of 25% H_2SO_4 and 20 mL of 0.01 M $KMnO_4$ was added to the solution. The solutions were heated on a boiling water bath for 30 minutes. Afterward, the solution in the flasks was allowed to cool, and 10 mL of 10% KI solution was added to each (21). The average values were taken by repeating the procedure three times. The chemical oxygen demand (COD) was calculated using **Eqn. 1**

$$COD = \frac{(A-B) \times M \times 40000}{Volume\,(mL)\,of\,sample} \qquad \textbf{Eqn. 1}$$

Where A is the titer value of the sample, B is the titer value of the blank solution; M is the molarity of $KMnO_4$ and V is the volume of sample.

Dissolved Oxygen (DO)

Dissolved oxygen is the determination of the amount of oxygen present in a sample of water or wastewater at the time of collection. Winkler's titration was used for measurement (22). The average values were taken by repeating the procedure three times. **Eqn. 2** was the expression used.

$$DO\ (mg/L) = \frac{1600 \times M \times V}{V2/V1\ (V1-V2)} \qquad \textbf{Eqn. 2}$$

Biochemical Oxygen Demand (BOD)

The effluent samples were divided into two. The DO level (ppm) of the first portion was measured immediately using the method described in the dissolved oxygen test and Recorded. The second portion of the effluent sample was placed in complete darkness by wrapping the effluent sample bottles with aluminum foil at room temperature for 3 days (ASTM, 1982). The average values were taken by repeating the procedure three times.

Acidity Level

Determination of acidity level was done usually by titration. An effluent's portion of the sample was pipetted into a conical flask. Phenolphthalein indicator was added in two drops, and the solution was titrated against a standardized 0.01 M sodium hydroxide solution to a pink end-point (23). The average values were taken by repeating the procedure three times. Acidity was calculated using **Eqn. 3**

$$Acidity(mg/L) = \frac{V \times M \times 100,000}{mL\,of\,sample\,used} \quad \textbf{Eqn. 3}$$

Alkalinity Level

A sample of the effluent's portion was pipetted into a conical flask. Methyl red indicator was added in two drops, and the solution was titrated against a standardized 0.01M HCl solution to a pink end-point (23). The average values were taken by repeating the procedure three times. Alkalinity was calculated using **Eqn. 4**

$$Alkalinity(mg/L) = \frac{V \times M \times 100,000}{mL\,of\,sample\,used} \quad \textbf{Eqn. 4}$$

Total Hardness

An effluent of 25 mL was pipetted into a different conical flask. To this, 3 mL of ammonium chloride in a concentrated ammoniacal buffer (NH_4Cl/conc.NH_3) and Eriochrome Black T indicator was added in two drops. It was titrated against 0.01 M EDTA solution until there is a color change from violet to blue. The average values were taken by repeating the procedure three times (21). Total Hardness was calculated using **Eqn. 5**

$$Hardness\ in\ mg/L\ CaCO_3 = \frac{V \times M \times 100,000}{mL\,of\,sample\,used} \quad \textbf{Eqn. 5}$$

Heavy Metals

Iron and zinc were determined using Atomic Absorption Spectrophotometer (model AA6800-SHIMADZU) according to APHA (24).

Batch Adsorption Experiment
Effect of Initial Metal Concentration

Effect of initial metal ion concentration on percentage removal of metal ions was investigated by varying the concentration of the metal ions in the range of 5 to 50 mg/L while keeping other factors constant (i.e., time – 180 minutes, dose – 0.05 g, pH - 6, temperature - 25° C). A 50 mL portion of separate concentrations of metal ions (i.e., 20, 40, 60, 80, and 100 mg/L) was introduced into 0.05 g of clay adsorbent. The mixture was shaken vigorously and continuously on a mechanical shaker for 150 minutes and then filtered. Atomic Absorption Spectrophotometer determined the final concentration of each filtrate solution. The amount of metal ions adsorbed q_e, and percentage removal of metal ions was determined.

Effect of pH

Effect of pH on percentage removal of metal ions was investigated by varying the pH from pH 2 to pH 10 with the use of 0.1 M NaOH or 0.1 M HNO_3 while keeping other factors constant (i.e., time – 180 minutes, dose – 0.05 g, temperature - 25°C, particle size - 2 μm). 0.05 g of the adsorbent was weighed into 5 beakers, and 20 mL of the industrial effluents were introduced into the beakers. The mixture was shaken vigorously and continuously on a mechanical shaker for 150 minutes and then filtered. Atomic Absorption Spectrophotometer will determine the final concentration of each filtrate solution. The amount of metal ions adsorbed q_e and percentage removal of metal ions was determined.

Effect of Contact Time

The effect of contact time on the removal of heavy metals from the industrial effluents was investigated by keeping other factors constant (i.e., dose – 0.05 g, pH - 6, temperature - 25°C, particle size - 2 µm). 1.0 g of the adsorbent was weighed into 6 beakers, and 20 mL of industrial effluents were introduced to each beaker. The mixture was shaken vigorously and continuously on a mechanical shaker for a varying period ranging from 30 – 150 minutes and then filtered. Atomic Absorption Spectrophotometer determined the final concentration of each filtrate solution. The amount of metal ions adsorbed q_e, and percentage removal of metal ions was determined.

Effect of Temperature

The effect of temperature on percentage removal of metal ions was investigated by varying the temperature of the mechanical shaker in the range of 15 to 40°C while keeping other factors constant (i.e., time – 180 minutes, pH - 6, dose – 0.05 g, particle size - 2 µm). 20 mL portions of the industrial effluent were introduced into each beaker containing 0.05 grams of the adsorbent. The mixture was shaken vigorously and continuously on a mechanical shaker for 150 minutes and then filtered at the specified temperature. Atomic Absorption Spectrophotometer determined the final concentration of each filtrate solution. The amount of the metal ions adsorbed q_e, and percentage removal of metal ions will be determined.

Effect of Adsorbent Dose

Effect of adsorbent dose on percentage removal of metal ions was investigated by varying adsorbent dose in the range of 0.05 to 2.5 g while keeping other factors constant (i.e., time – 180 minutes, pH - 6, temperature – 25 °C, particle size - 2 µm). A separate masses of the adsorbents (i.e. 0.05, 1.0, 1.5, 2.0, 2.5 g) were weighed into 5 beakers and 20 mL of the industrial effluent was introduced into each beaker. The mixture was shaken vigorously and continuously on mechanical shaker for 150 minutes and then filtered. The final concentration of filtrate solutions was then determined by atomic absorption spectrophotometer. The amount of metal ions adsorbed q_e and percentage removal of metal ions was determined.

RESULTS AND DISCUSSION

Physicochemical Parameters of Pharmaceutical Effluents

Pharmaceutical effluents were sourced from Ilorin, Nigeria. The results of the effluent obtained were compared with the standard values of the Federal Environmental Protection Agency (FEPA) for industrial effluents, United States - Environmental Protection Agency (USEPA). National recommended water quality criteria-correction; World Health Organization (WHO).Guidelines for drinking water recommendations. **Table 1** contains the physicochemical properties of various water samples. The concentrations of heavy metals in the effluents are in the following order Fe>Zn >Cu>Mn>Pb> Cr. Nickel (Ni) and cadmium (Cd) were not detected.

Table 1: Physicochemical properties of various water samples.

Properties	Effluent	WHO[a]	FEPA[b]	USEPA
pH	6.09	6-9.5	6.0-9.0	6.0 -8.5
Temperature	33.0		40^{0}C	
Color	Yellow	Colorless	NS	Colorless
Conductivity	451	NS	NS	NS
Turbidity	33.0	NS	NS	NS
COD	77.6	NS	NS	NS
BOD	43	NS	50	NS
TSS	71	NS	30	NS
TDS	248	<1200	2000	500
Cadmium	ND	0.003	<1	0.002
Chromium	0.001	0.05	0.015	0.05
Nickel	ND	0.02	<1	0.005
Iron	88.52	NS	20	0.3
Lead	0.002	0.01	<1	0.003
Zinc	3.276	0.01	<1	0.12
Copper	0.762	1.2	1.3	0.009
Manganese	0.701	NS	5	0.05

All values are in mg/L except conductivity ($^o/_\infty$), pH, and turbidity have no unit; NS: Not stated.

Thus, the highest genotoxic risk in this study will be primarily accounted for by the higher concentrations of Fe(III) and Zn(II) in which are above the permissible level of WHO, FEPA, and USEPA.

Adsorption Parameters
Effect of Initial Concentration
Initial concentrations were considered for the adsorption studies in other to determine the equilibrium concentration of adsorbate, which was used to study other parameters. The results obtained for this study are shown in **Figure 1a-**for Fe(III) and Zn(II), respectively, and varying the initial concentrations from 20 mg/L to 100 mg/L. The notifications for the

three adsorbents are as follows; unmodified bentonite clay (UMBC), H_2SO_4 modified bentonite clay (SMBC), and HCl Modified Bentonite clay (HMBC). In **Figures 1a-b**, it was observed that the Fe(III) and Zn(II) adsorption capacity increases with increasing initial concentration and their capacities were achieved at 15.01mg/g, 8.29mg/g and 8.29mg/g for UMBC, SMBC and HMBC with Fe(III) respectively while 14.87mg/g, 7.51mg/g, and 7.98mg/g are for UMBC, SMBC and HMBC with Zn(II) respectively. The increase in adsorption capacity with initial concentration is because the concentration provides a critical mass transfer driving force for the adsorption process (25).
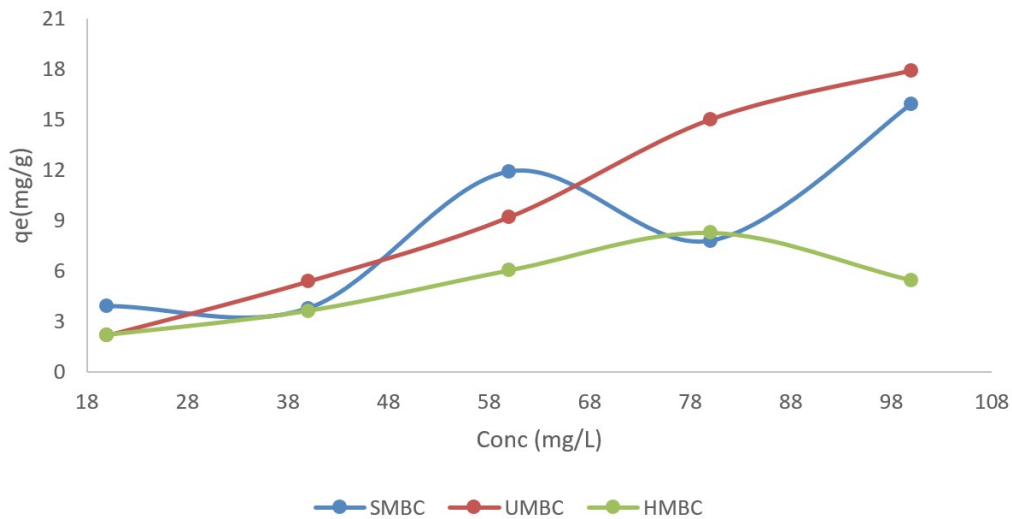
Figure 1a: Profile diagram of initial concentration on the amount of Fe(III) adsorbed using UMBC, SMBC, and HMBC.
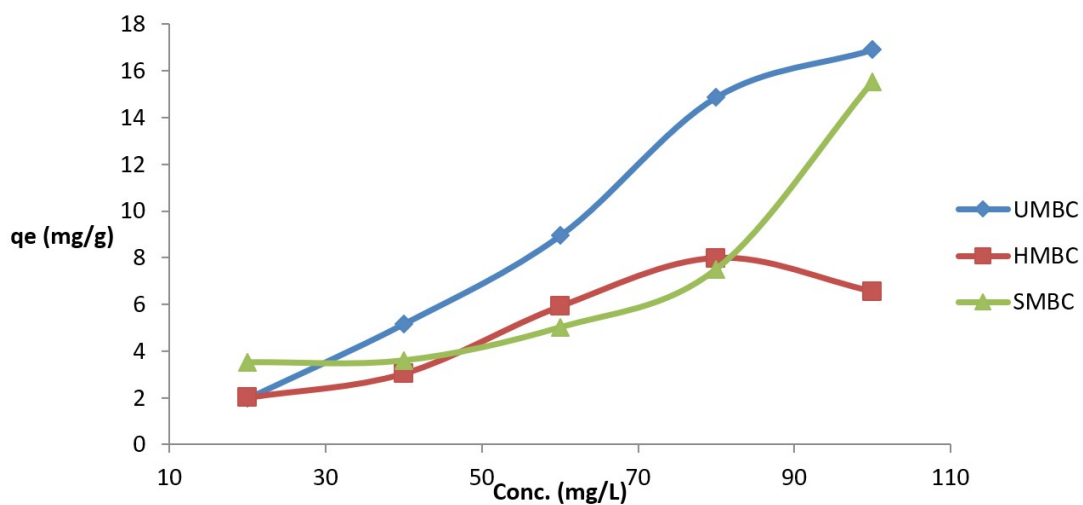
Figure 1b: Profile diagram of initial concentration on amount of Zn(II) adsorbed using UMBC, SMBC, and HMBC.

731

Effects of Contact Time
The pollutants' contact time with different clay adsorbents is valuable in the adsorption process due to its great deal of influence on the adsorption capacity (26).The results obtained as shown in Figures 1c-d investigate the adsorption capacity of Fe(III) and Zn(II) respectively with UMBC, SMBC, and HMBC using contact time varied from 30 min to 150 min at pH of 6, adsorbent dose of 0.05 g, the temperature of 303 K, volume of 25 mL and concentration of 88.52 mg/L and 3.26 mg/L for Fe(III) and Zn(II) respectively from the

effluent. It was noticed that as the contact time was increasing, the uptake capacity is also increased until equilibrium was achieved at 13.145 mg/g, 16.37 mg/g and 17.4624 mg/g for UMBC, SMBC and HMBC with Fe(III) respectively and 0.555 mg/g, 0.461mg/g and 0.460 mg/g for UMBC, SMBC and HMBC with Zn(II) respectively. The more significant contact times favors the adsorption process because it allows for more adsorbate molecules to overcome the mass transfer barrier (boundary layer effect) at the solid-liquid interphase.
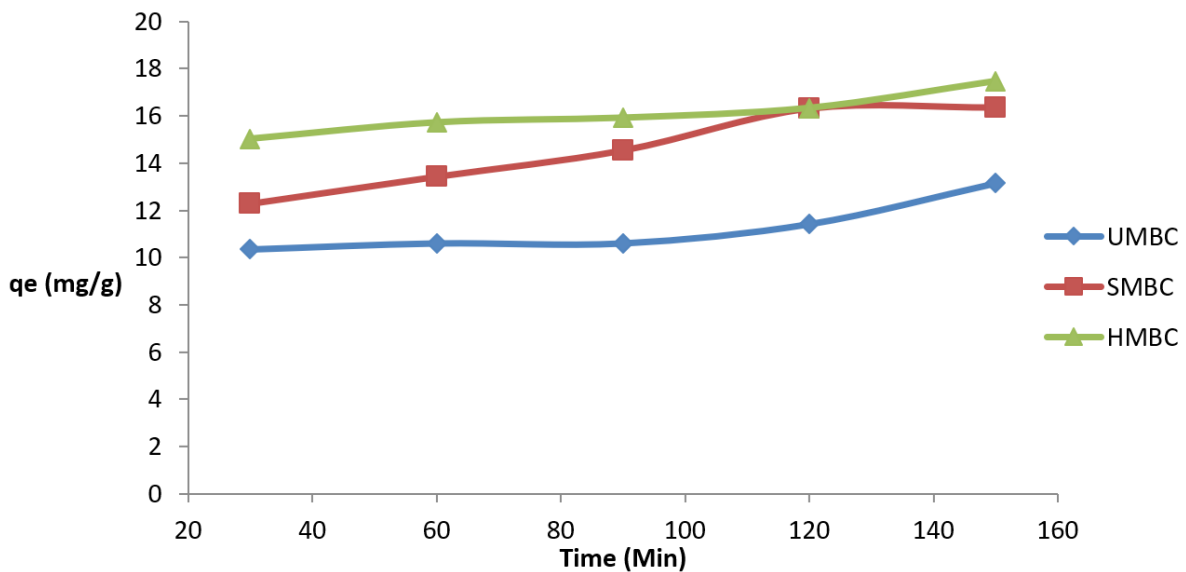
Figure 1c: Profile diagram of contact time on amount of Fe(III) adsorbed using UMBC, SMBC, and HMBC.
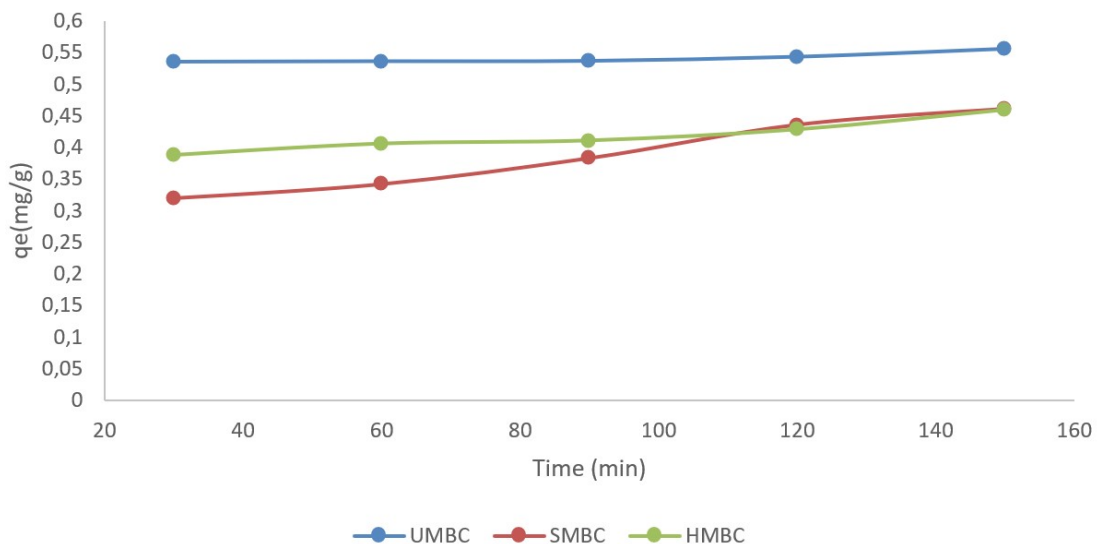
Figure 1d: Profile diagram of contact time on the amount of Zn(II) adsorbed using UMBC, SMBC, and HMBC.

Effects of Adsorbent Dose

The effect of adsorbent dose on the various adsorption systems was studied and was shown in the **Figures 1e-f** for UMBC, SMBC, and HMBC on Fe(III) and Zn(II) respectively. The parameters utilized for the adsorption process were contact time of 180 min, the volume of the adsorbate in 25 mL, pH at 6, the temperature at 303 K, and concentrations of 88.52 mg/L for Fe(III) and 3.276 mg/L for Zn(II). It was observed in **Figure 1e** that as the adsorbent dose was increased, the uptake capacity decreased and their maximum uptake was observed at 0.05 g mass of adsorbents in all the systems with the corresponding values of 24.145 mg/g, 19.78 mg/g, and 44.46 mg/g for

UMBC//Fe, SMBC//Fe, and HMBC//Fe systems respectively (27). Also in **Figure 1f**, it was observed that the adsorbent dose increase with a decrease in the uptake capacity. Maximum uptake was observed at 0.05 g mass of adsorbents in all the systems with the corresponding values of 0.933 mg/g, 0.9625 mg/g, 0.999 mg/g, 1.025 mg/g, 3.465 mg/g and 3.546 mg/g for UMBC//Fe, UMKC//Zn, SMBC//Fe, SMKC//Zn, HMBC//Fe, and HMKC//Zn system respectively. The higher uptake at a more massive adsorbent dose is due to greater availability of active sites in solution onto which the adsorbate can be adsorbed.
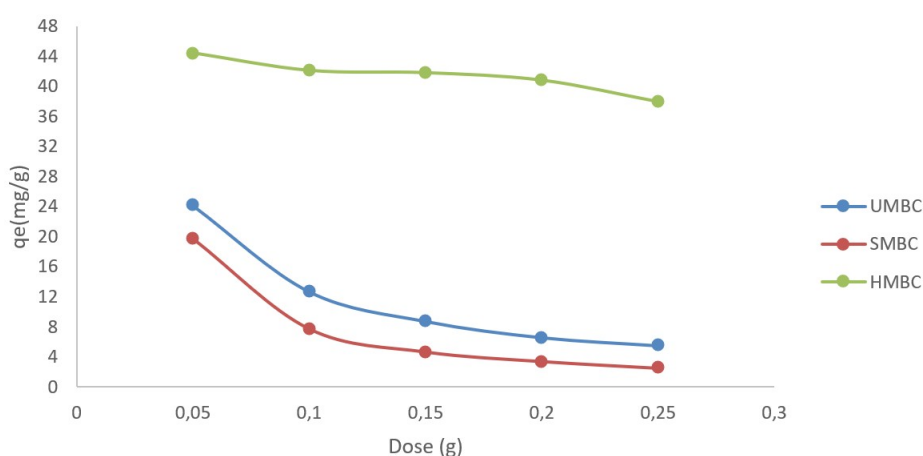
Figure 1e: Profile diagram of dose on amount of Fe(III) adsorbed using UMBC SMBC and HMBC.
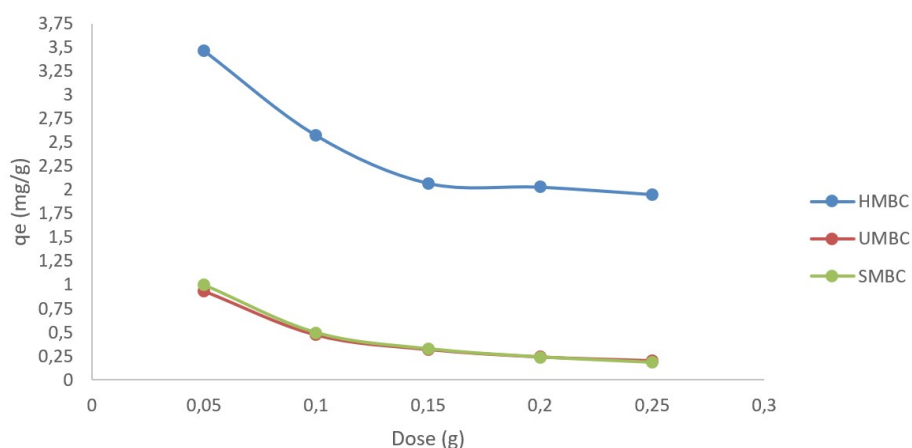
Figure 1f: Profile diagram of dose on amount of Zn(II) adsorbed using HMBC, UMBC, and SMBC

Effect of pH

The effect of the pH is an important parameter controlling the adsorption process. It determines the influence of the adsorption capacity on the surface properties of the adsorbents and ionic forms of the metal ions in solutions (28). The pH affects the solution

chemistry of the pollutant, the activity of the functional groups in the adsorbent, and the competition of ions for binding sites (1). pH affects the charges of the adsorbate and adsorbent in solution and hence the way they interact with each other. In this study, different

pH levels ranging between 3.0 to 10.0 were considered at adsorbents dosage of 0.05 g, Temperature: 303K, and concentration of 88.52 mg/L for Fe(III) and 3.276 mg/L for Zn(II). The pH profile diagrams for UMBC, SMBC, and HMBC of Fe(III) and Zn(II) are shown in **Figures 1g-h,** respectively. In the Fe(III) system, it was noticed that uptake capacity was lowest at pH value of 3.0 with 15.935 mg/g,

11.665 mg/g, and 13.0625 mg/g for UMBC, SMBC, and HMBC respectively (19). Uptake capacity, however, increased as pH was increased from pH 3– pH 8 (UMBC//Fe, SMBC//Fe, and HMBC//Fe), and after pH 8, it starts to decrease. While in the case of Zn(II), the maximum uptake capacity was obtained at pH 7 (UMBC//Zn, SMBC//Zn, and HMBC//Zn).
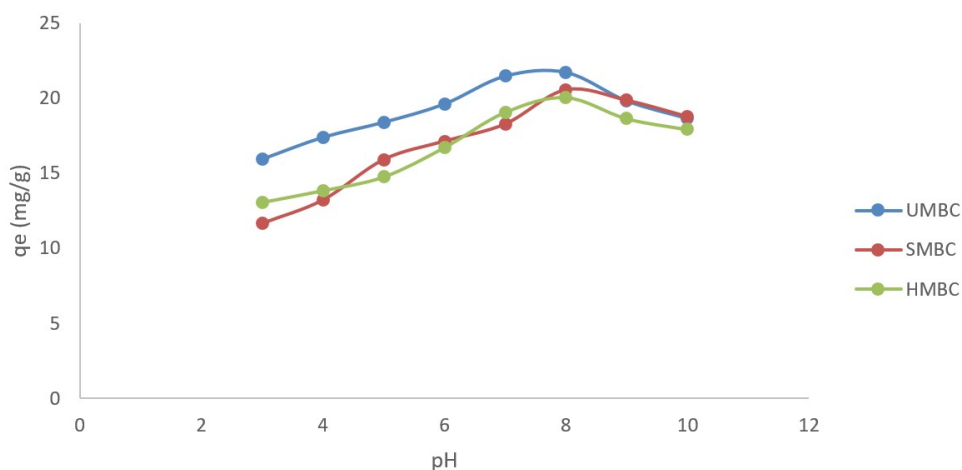
Figure 1g: Profile diagram of pH on the amount of Fe(III) adsorbed using UMBC SMBC and HMBC.
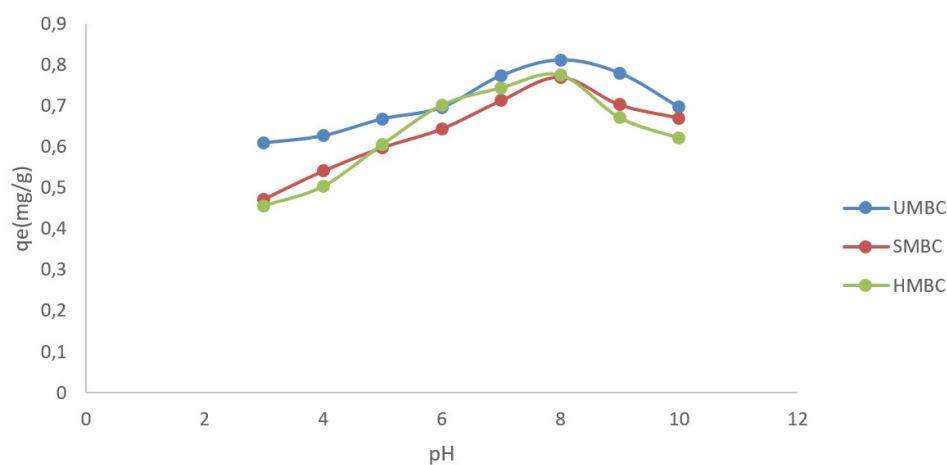
Figure 1h: Profile diagram pH on amount of Zn(II) adsorbed using UMBC, SMBC and SMBC.

Effect of Temperature

The effect of temperature on the adsorption of the Fe(III) and Zn(II) was studied using UMBC, SMBC, and HMBC. The temperature profile diagrams for the UMBC, SMBC, HMBC on Fe(III), and Zn(II) adsorption system are shown in **Figures 1i-j,** respectively. This work was studied at different temperatures ranging from 35°C to 45°C at adsorbents dosage of 0.05 g, time 180 min, 25 mL volume, the temperature is 303K, at pH 6 and concentration of 88.52 mg/L for Fe(III) and 3.276 mg/L for

Zn(II). All the sorption systems were observed to have a similar trend; as the temperature is increased, adsorbents' uptake capacity decreases. Generally, it is evidenced that the uptake capacity decreased with an increase in temperature. These observations suggest that process of adsorption in all the systems might be exothermic, and an increase in temperature could deteriorate the matrix structure of the adsorbents. The thermodynamics study confirmed this.
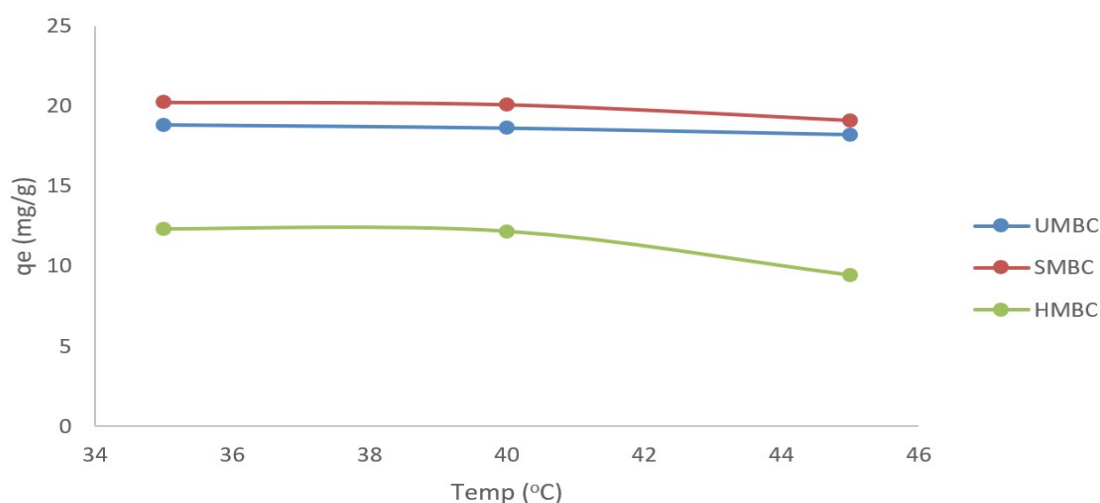
Figure 1i: Profile diagram of Temperature on the amount of Fe(III) adsorbed using HMBC, UMBC, and SMBC.
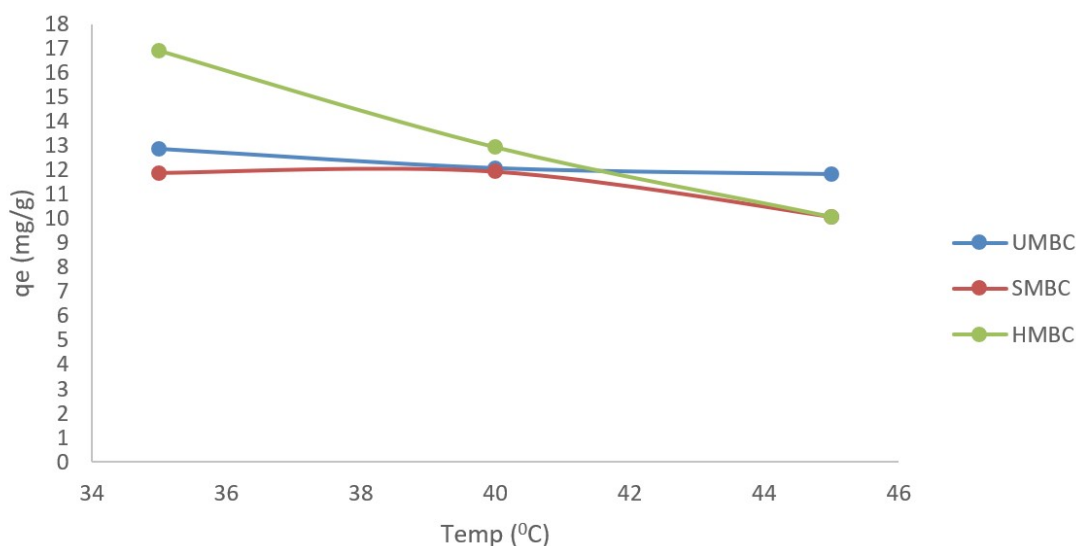
Figure 1j: Profile diagram of Temperature on amount of Zn(II) adsorbed using HMBC, UMBC, and SMBC.

Adsorption Isotherm Studies

The equilibrium adsorption data obtained in this study were fitted with two isotherms—namely, Langmuir isotherm and Freundlich isotherm, and which all explained the different degrees of success.

Langmuir Asorption Isotherm

The data obtained from Figures 2a-b was used on this isotherm, and the parameters obtained from these plots are summarized in **Tables 2-3**. The parameters are R^2 (Correlation coefficient), Q_{max} (maximum adsorption capacity), and R_L (dimensionless separation factor). It was noticed that the correlation coefficient for all the three systems is 0.933 for UMBC, 0.997 for SMBC, and 0.915 for HMBC. It was noted that HMBC has an adsorption capacity value of 13.00 mg/g, which is more than that of the UMBC (4.2 mg/g) and SMBC (2.8 mg/g). Also, R_L value (dimensionless separation factor) is explained as a valuable feature in this process, and it ranges from 0 to 1 (19). As shown in **Table 2,** it affirms that the removal of heavy metals molecules is appreciated onto all the adsorbents. Furthermore, it can be observed that acid modification helped to increase the sorption capacity of the clay to the heavy metals studied.

Table 2: Langmuir adsorption parameter for various sorption systems of Fe(III).

SYSTEM (Fe)	Q_{max} (mg/g)	K_L(l/mg)	R_L	R^2
SMBC	2.8	0.09	0.009	0.987
UMBC	4.2	0.03	0.009	0.933
HMBC	13.0	0.02	0.009	0.915

Q_{max}= Maximum Adsorption capacity, K_L = Rate of Adsorption, R_L = Separation factor

Table 3: Langmuir adsorption parameter for various sorption systems of Zn(II).

SYSTEM (Zn)	Q_{max} (mg/g)	K_L(l/mg)	R_L	R^2
UMBC	2.9	0.03	0.0097	0.937
SMBC	35.5	0.02	0.0098	0.922
HMBC	14.1	0.01	0.0099	0.921

Q_{max}= Maximum Adsorption capacity, K_L = Rate of Adsorption, R_L = Separation factor
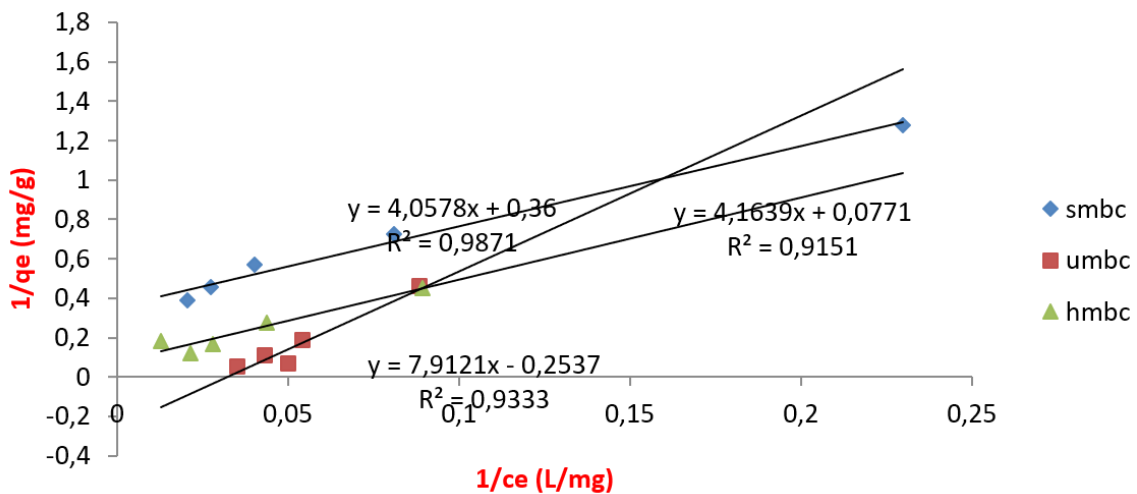
Figure 2a: Langmuir plot for UMBC//Fe, HMBC//Fe, and SMBC//Fe.
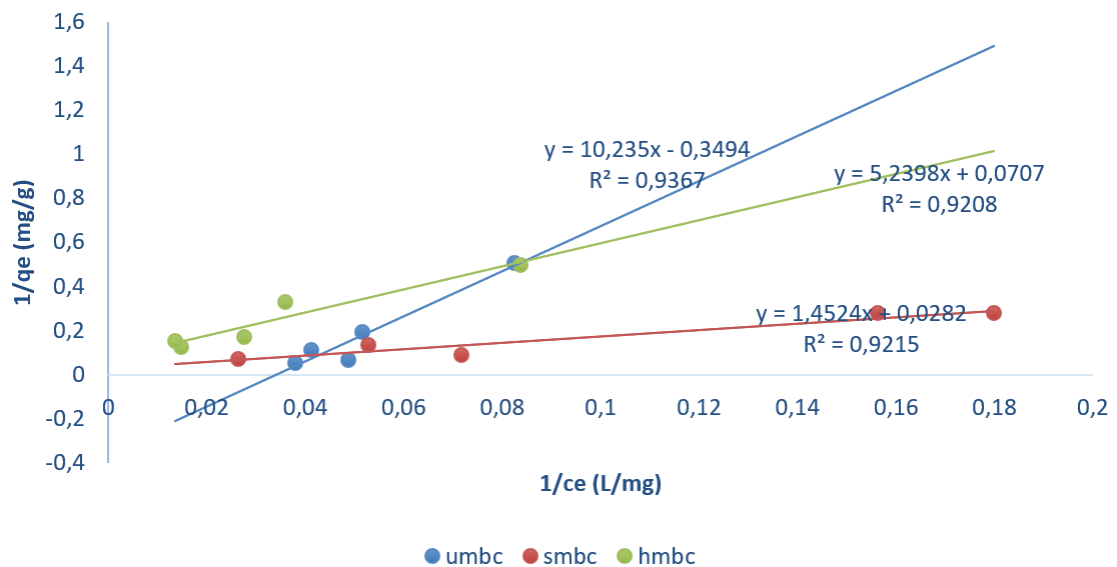
Figure 2b: Langmuir plot for UMBC//Zn, HMBC//Zn, and SMBC//Zn

Freundlich Adsorption Isotherm
The Freundlich plots for the various systems studied are given in **Figures 2c-d,** and the parameter obtained from these plots are summarized in **Tables 4-5**. The value of $1/n <$ 1 obtained in most of the adsorption system

studied indicated favorable adsorption while in the case of UMBC in which the value of 1/n is greater than 1 (1/n > 1), it indicates the unfavorable adsorption while the value of n within the range of 1 – 10 represent good adsorptions (29).

Table 4: Freundlich adsorption parameter for various adsorption systems of Fe(III)

SYSTEM (Fe)	n	1/n	K_f(mg/g)	R^2
SMBC	2.09	0.479	2.539	0.994
UMBC	0.58	1.729	13.131	0.873
HMBC	1.72	0.579	1.596	0.697

1/n is the adsorption intensity and K_f is the adsorption capacity.

Table 5: Freundlich adsorption parameter for various adsorption systems of Zn(II)

SYSTEM (Zn)	n	1/n	K_f(mg/g)	R^2
UMBC	0.37	2.682	399.578	0.816
SMBC	1.34	0.746	1.023	0.860
HMBC	1.36	0.737	3.107	0.891

1/n is the adsorption intensity and K_f is the adsorption capacity.
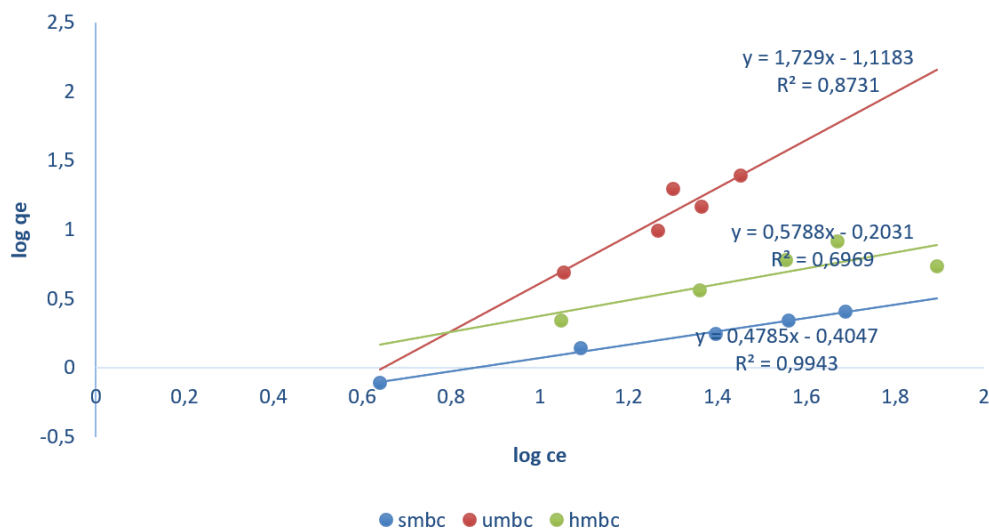
Figure 2c: Freundlich plot for UMBC//Fe, HMBC//Fe, and SMBC//Fe
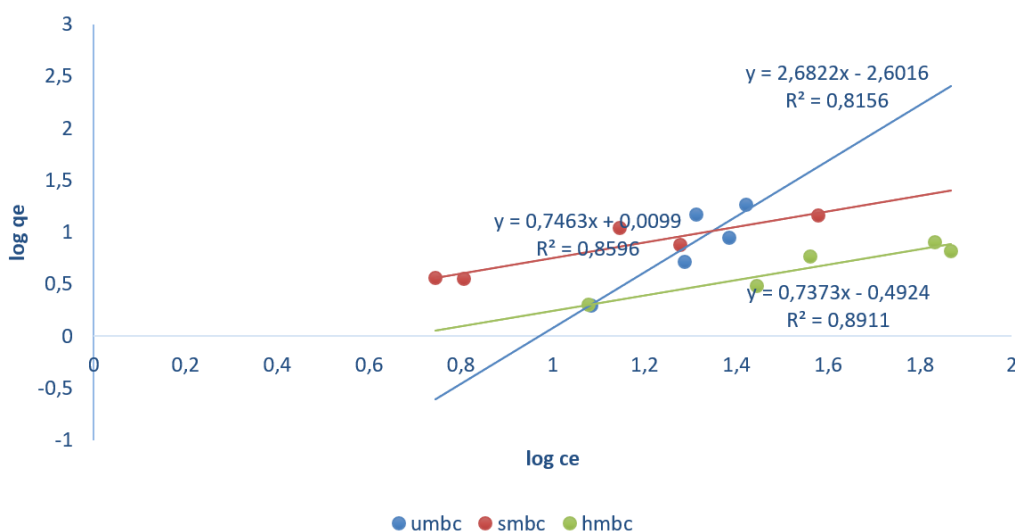
Figure 2d: Freundlich plot for UMBC//Zn, HMBC//Zn, and SMBC //Zn

Adsorption Kinetics and Mechanism

The kinetic study explains how fast the rate of adsorption occurs. Adsorption type depends on the characterization of the adsorbents and the system conditions such as contact time, concentration, and temperature. Calculation of the adsorption rate constant is fundamental to evaluate the necessary qualities of a suitable adsorbent, such as a time required for adsorbent to remove a particular compound and efficacy of the adsorbents (30). Pseudo first order and pseudo-second-order kinetic models were employed to study the adsorption process. The validity of the kinetic models was tested by employing the correlation coefficient value (R^2). The satisfactory model had excellent linearity of the plot (high R^2 values). The pseudo-first-order plot for various adsorbents is shown in **Figures 3a-b** while the plot for pseudo-second-order for the various adsorbents is also shown in **Figures 3c-d**.
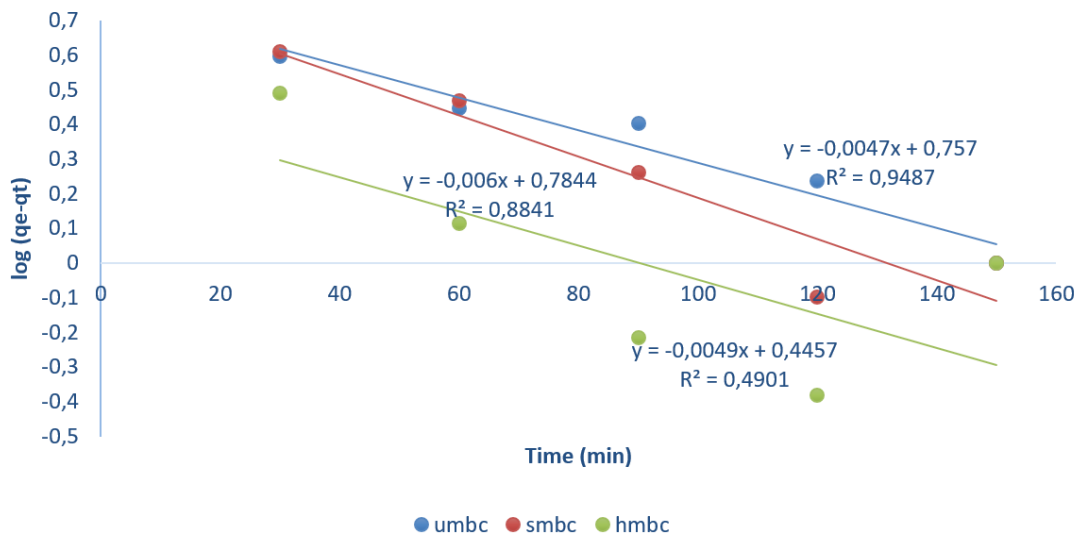
Figure 3a: Pseudo first order plot of UMBC//Fe, HMBC//Fe and SMBC//Fe.
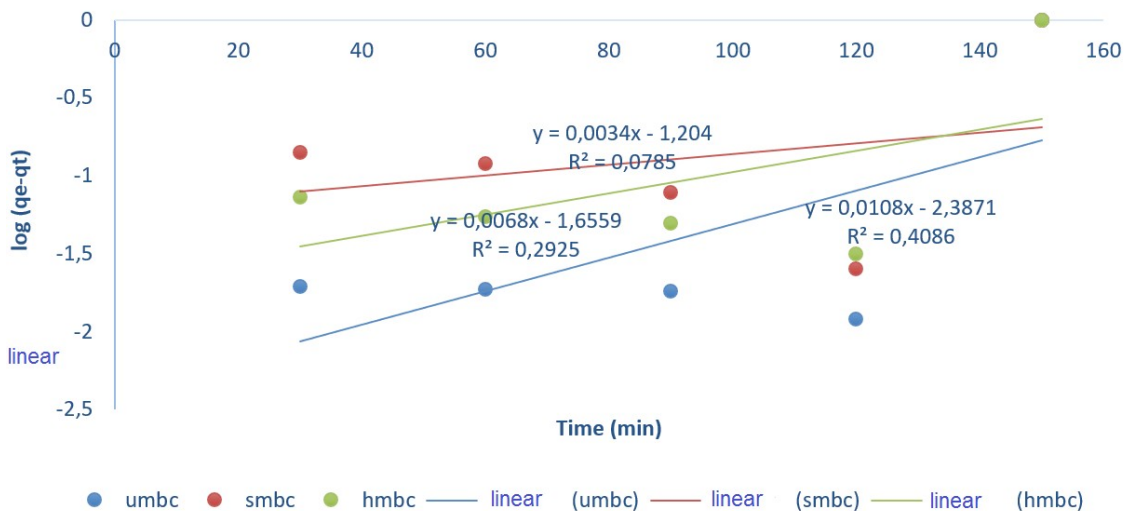
Figure 3b: Pseudo first-order plot of UMBC//Zn, HMBC//Zn, and SMBC//Zn.

The pseudo-first-order rate constant k_1 amount of Fe(III) and Zn(II) adsorbed at equilibrium q_e and correlation coefficient R^2 are shown in **Table 6-7**. Proper fitting with high R^2 was only observed for UMBC (0.948) for Fe(III), while the others showed poor agreement with kinetic

models based on their R^2 value. The parameters obtained from this model are summarised in **Table 6-7**. Therefore, the adsorption of Fe(III) and Zn(II) on different adsorbents of Bentonite clay revealed that pseudo-first-order kinetic model failed to explain the kinetic adsorption process.

Table 6: Pseudo first order parameter for various adsorption systems of Fe(III)

SYSTEM (Fe)	k_1	q_e(mg/g)	R^2
UMBC	0.010	5.71	0.948
SMBC	0.013	6.08	0.8841
HMBC	0.011	2.79	0.4901

K_1 is the pseudo-first-order rate constant; qe is the calculated equilibrium uptake capacities.

Table 7: Pseudo first order parameter for various adsorption systems of Zn(II)

SYSTEM (Zn)	k_1	q_e(mg/g)	R^2
UMBC	0.024	243.83	0.408
SMBC	0.007	15.99	0.078
HMBC	0.015	45.27	0.292

K_1 is pseudo-first-order rate constant; qe is the calculated equilibrium uptake capacities.

The pseudo-second-order model showed favorable linearly with experimental data obtained for all the adsorbents. The plots are shown in **Figures 3c-d,** respectively. **Tables 8-9** tell that R^2 values of 0.972, 0.995, and 0.999 were obtained for UMBC//Fe, SMBC//Fe, and HMBC//Fe, while the R^2 values of 0.999, 0.981 and 0.993 were obtained for UMBC, SMBC and HMBC//Zn adsorbent respectively. These are higher than corresponding R^2 values obtained in the pseudo-first-order model and described the kinetic data better. It informs that both the concentration of metal ions in solution and the number of available adsorption sites are critical in determining the rate/kinetics of the adsorption process.

Table 8: Pseudo second order parameter for various adsorption systems of Fe(III)

SYSTEM (Fe)	k_2	q_e(mg/g)	R^2
UMBC	128.53	14.29	0.972
SMBC	327.55	17.99	0.995
HMBC	563.61	17.24	0.999

K_2 is the pseudo-second-order rate constant; qe is the calculated equilibrium uptake capacities.

Table 9: Pseudo second order parameter for various adsorption systems of Zn(II)

SYSTEM (Zn)	k_2	q_e(mg/g)	R^2
UMBC	0.076	0.56	0.999
SMBC	0.005	0.53	0.981
HMBC	0.010	0.48	0.993

K_2 is pseudo second order rate constant; q_e is the calculated equilibrium uptake capacities.

y = 0,07x + 1,5876
R² = 0,9723

y = 0,0556x + 0,9875
R² = 0,9952

y = 0,058x + 0,5274
R² = 0,9998
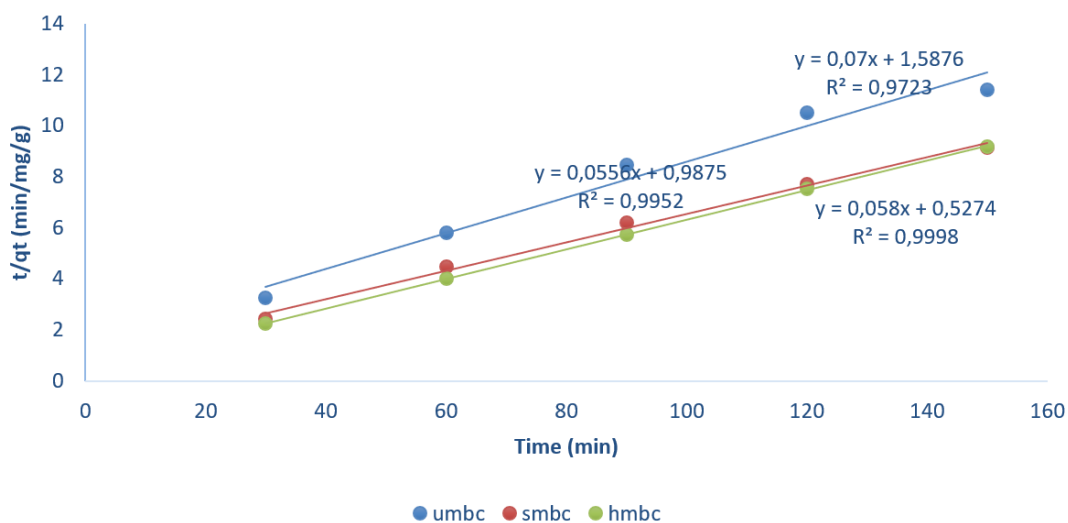
Figure 3c: Pseudo second order plot of UMBC//Fe, HMBC//Fe and SMBC//Fe.

y = 2,0984x + 21,255
R² = 0,9931

y = 1,8769x + 52,085
R² = 0,9816

y = 1,7912x + 4,0859
R² = 0,9993
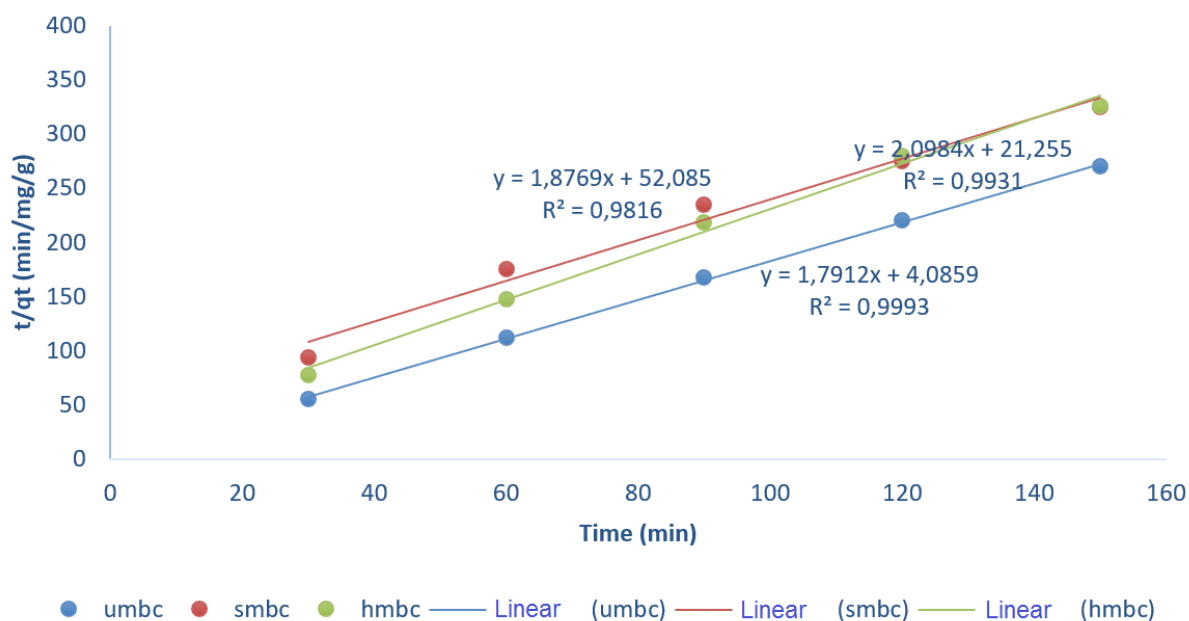
Figure 3d: Pseudo second order plot of UMBC//Zn, HMBC//Zn and SMBC//Zn

Adsorption Thermodynamics
Thermodynamic parameters can be useful in the evaluation of orientation of the adsorption process and which provide information regarding the mechanism of the process, structural changes, and energy due to molecular adsorption ion. All the thermodynamic parameters were determined using the system of equations shown in **Eqn. 6-9**.

$$\ln K = \frac{-\Delta H}{RT} + \frac{\Delta S}{R} \qquad \textbf{Eqn. 6,}$$

$$K = \frac{C_o - C_e}{C_o} \qquad \textbf{Eqn. 8}$$

$$\Delta G = -RT \ln K \qquad \textbf{Eqn. 7,}$$

$$\left|\ln \frac{K_{s1}}{K_{s2}}\right| = \frac{-E_a}{R}\left(\frac{T_2 - T_1}{T_1 T_2}\right) \qquad \textbf{Eqn. 9}$$

Where K represents the distribution coefficient, ΔH represents enthalpy, ΔS represents entropy change, and ΔG represents the free energy change of adsorption. T_1 and T_2 are the absolute temperatures, R is the gas constant, E_a is the activation energy of adsorption, K_{s1} and K_{s2} are distribution coefficient for adsorption at temperature T_1 and T_2 respectively. The thermodynamic plot obtained from the equation for the various sorption systems studied are depicted in **Figure 4,** and the thermodynamic parameters obtained from these plots are summarised in **Table 10**.
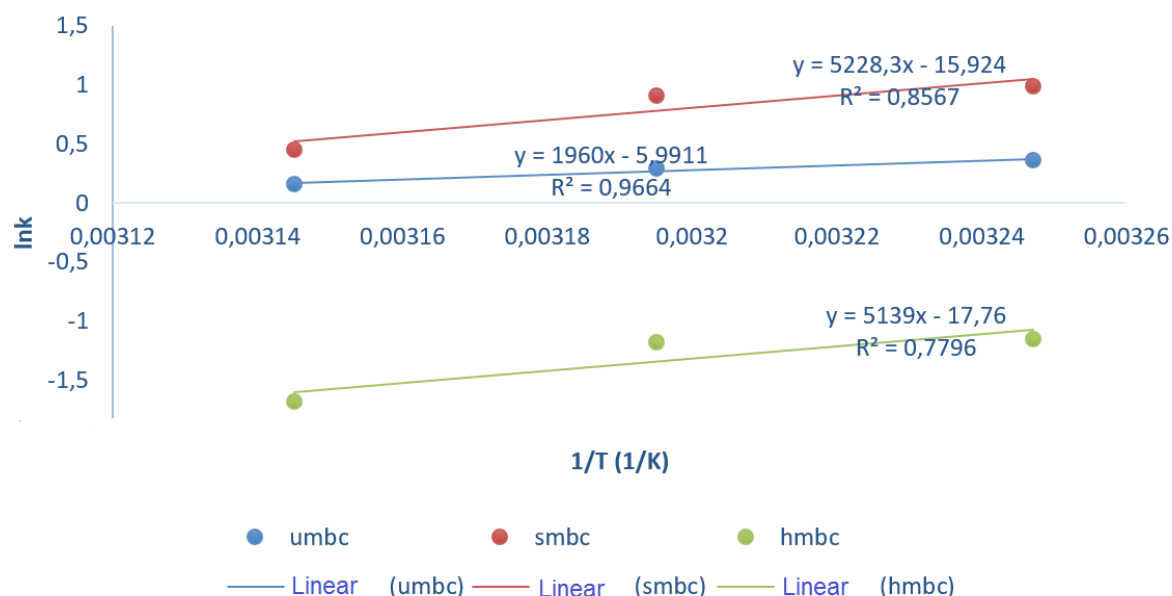
Figure 4: Thermodynamic plot of UMBC, HMBC and SMBC//Fe)

Table 10: Thermodynamic parameter for various adsorption systems of Fe(III)

SYSTEM(Fe)	T (K)	ΔG (KJ/mol)	ΔH (KJ/mol)	ΔS(J/mol/k)	R^2
Unmodified Bentonite Clay – type (UMBC//Fe)	308	-927.938	-235.61	-0.720	0.967
	313	-761.218			
	318	-428.398			
Sulphuric acid modified Bentonite Clay – type (SMBC//Fe)	308	-2536.61	-628.79	-1.914	0.858
	313	-2358.68			
	318	-1202.51			
Hydrochloric acid Modified Bentonite Clay – type (HMBC//Fe)	308	2952.444	618.21	2.136	0.781
	313	3071.783			
	318	4442.479			

The thermodynamic plot for the following adsorbents, namely, UMBC are plotted in **Figure 4** gave R^2 value of 0.967. The relatively high R^2 values can be attributed to the regular trends exhibited in their respective temperature profile diagram except for SMBC and HMBC with 0.858 and 0.781 respectively of R^2 value, which exhibited irregular trends in his temperature profile diagram. From **Table 10**, it was observed that all the ΔG values in the

Abdullahi AA et al. JOTCSA. 2020; 7(3); 727-744.

RESEARCH ARTICLE

adsorption system are negative, which suggested that the process of adsorption is spontaneous over the range of temperature studied except for HMBC and HMKC in which ΔG values are positive which indicate that the process of adsorption is not spontaneous. The ΔS values of -0.720 J/mol/k, -1.914 J/mol/k and 2.136 J/mol/K for UMBC, SMBC, and HMBC, respectively, which indicate that there is decrease and increase in randomness at the solid/solution interface during the adsorption. The ΔH values were found to be -235.61 KJ/mol, and -628.79 KJ/mol, for UMBC, SMBC respectively suggest that the process is exothermic while ΔH values were found to be 618.21 KJ/mol for HMBC which indicate that the process is endothermic.

CONCLUSION

From this study, acid-modified adsorbents were successfully prepared from Bentonite clays. Physicochemical properties of modified and unmodified adsorbents were observed to have significant differences in all parameters. Adsorbent dosage of 0.05 g and pH values of 8 were found to be the optimal value. The adsorption data in this study were best explained using the Langmuir isotherm model. Sulfuric acid-modified bentonite clay (SMBC) performs best among all the adsorbents. The kinetic data in this study was best explained by the pseudo-second-order kinetic model implying the physisorption process. The thermodynamic data show that HMBC showed that the process is endothermic and non-spontaneous. Negative of ΔS values indicated that there is a decrease in randomness except for HMBC at the solid/solution interface during the adsorption. Furthermore, it was observed that acid modification was helped to increase the sorption capacity of the clay to the heavy metals studied.

DISCLOSURE STATEMENT

Conflict of Interest: The authors declare that there are no conflicts of interest.
Compliance with Ethical Standards: This article does not contain any studies involving human or animal subjects.

REFERENCES

1. Adeniyi, A.G. and J.O. Ighalo, Biosorption of Pollutants by Plant Leaves: An Empirical Review. Journal of Environmental Chemical Engineering, 2019. 7(3): p. 103100 DOI: http://dx.doi.org/10.1016/j.jece.2019.103100.

2. Aziz, H.A., M.N. Adlan, and K.S. Ariffin, Heavy metals (Cd, Pb, Zn, Ni, Cu and Cr (III)) removal from water in Malaysia: Post treatment by high quality limestone. Bioresources Technology, 2008. 99(6): p. 1578-1583.

3. Landrigan, P.J., R. Fuller, N.J. Acosta, O. Adeyi, R. Arnold, A.B. Balde, R. Bertonllini, S. Bose-O'Reilly, J.I. Boufford, P.N. Breysse, and T. Chiles, The Lancet commission on pollution and health. The lancet, 2018. 391: p. 462-512.

4. Mohammed, A.-A. and Z. Al-Anber, Utilization of natural zeolite as ion-exchange and sorbent material in the removal of iron. Desalination, 2008. 255: p. 70-81.

5. Akpor, O.B., G.O. Ohiobor, and T.D. Olaolu, Heavy metal pollutants in wastewater effluents: sources, effects and remediation. Advances in Bioscience and Bioengineering, 2014. 2(4): p. 37-43.

6. Harvey, A.L., R. Edrada-Ebel, and R.J. Quinn, The re-emergence of natural products for drug discovery in the genomics era. . Natural reviews drug discovery, 2015. 14(2).

7. Ahmadi, M., H. Elmongy, T. Madrakian, and M. Abdel-Rehim, Nanomaterials as sorbents for sample preparation in bioanalysis: a review. Analytica Chimica Acta, 2017. 958: p. 1-21.

8. Nwosu, F.O., O.J. Ajala, R.M. Owoyemi, and G.B. Raheem, Preparation and characterization of adsorbents derived from Bentonite and kaolin clays. Applied Water Science, 2018. 8(195) DOI: http://doi.org/10.1007/s13201-018-0827-2.

9. Ajala, O.J., F.O. Nwosu, and R.K. Ahmed, Adsorption of Atrazine from aqueous solution using Unmodified and Modified Bentonite clays. Applied water science, 2018. 8(214): p. 1-11 DOI: http://dx.doi.org/10.1007/s13201-018-0855-y.

10. Heydari, S., L. Zare, and H. Ghiassi, Plackett–Burman experimental design for the removal of diazinon pesticide from aqueous system by magnetic bentonite nanocomposites. Journal of Applied Research in Water and Wastewater, 2019. 6(1): p. 45-50.

11. De Souza, F.M., O.A.A. dos Santos, and M.G.A. Vieira, Adsorption of herbicide 2, 4-D from aqueous solution using organo-modified bentonite clay. Environmental Science and

Pollution Research, 2019: p. 1-14.

12. Murrey, H.H., Applied Clay Mineralogy, Occurrences, Processing and Application of Kaolins, Bentonites, Palygorskite-Sepiolite, and Common Clays. Applied Clay Mineralogy. Vol. 2. 2007: Elsevier, .

13. Schütz, T., S. Dolinská, P. Hudec, A. Mockovčiaková, and I. Znamenáčková, Cadmium adsorption on manganese modified bentonite and bentonite–quartz sand blend. International Journal of Mineral Processing, 2016. 150: p. 32-38.

14. Tohdee, K. and L. Kaewsichan, Enhancement of adsorption efficiency of heavy metal Cu (II) and Zn (II) onto cationic surfactant modified bentonite. Journal of Environmental Chemical Engineering, 2018. 6(2): p. 2821-2828.

15. Yan, L., S. Li, H. Yu, R. Shan, B. Du, and T. Liu, Facile solvothermal synthesis of Fe3O4/bentonite for efficient removal of heavy metals from aqueous solution. Powder Technology, 2016. 301: p. 632-640.

16. Cantuaria, M.L., A.F. de Almeida Neto, E.S. Nascimento, and M.G. Vieira, Adsorption of silver from aqueous solution onto pre-treated bentonite clay: complete batch system evaluation. Journal of cleaner production, 2016. 112: p. 1112-1121.

17. Alduaij, O.K., M.I. Attia, L. Khezami, and K.K. Taha, Removal of cobalt (II) from aqueous solution by local Saudi bentonite: Kinetic and equilibrium investigations. Macedonian Journal of Chemistry and Chemical Engineering, 2016. 35(1): p. 87-96.

18. Hanafiah, M.A., W.S. Ngah, S. Ibrahim, H. Zakaria, and W.A. Ilias, Kinetics and thermodynamic study of lead adsorption from aqueous solution onto rubber (Hevea brasiliensis) leaf powder. Journal of Applied Sciences, 2006. 6(13): p. 2762-2767.

19. Nwosu, F.O., O.J. Ajala, F.O. Okeola, S.A. Adebayo, O.K. Olanlokun, and O.A.A. Eletta, Adsorption of chlorotriazine herbicide onto unmodified and modified kaolinite: Equilibrium, kinetic and thermodynamic studies. Egyptian Journal of Aquatic Research, 2019 DOI: http://dx.doi.org/10.1016/j.ejar.2019.05.005.

20. Atsar, F.S., D.T. Kukwa, R.L. Tyohemba, E. A., and R.A. Wuana, Cleaning of heavy metals from Spent Lubrication Oil (SLO) by adsorption process using acid modified clay. International Journal of Chemical Science and Technology, 2013. 3(4): p. 71-75.

21. Ademoroti, M.A., Standard Methods for Water and Effluent Analysis. 1st ed, ed. E.M.a.M.S.o. Bioremediation. Vol. 2. 1996.

22. Olaniyi, I., O. Raphael, and J.O. Nwadiogbu, Effect of Industrial Effluent on the Surrrounding Environment. Scholars Research Library, 2012. 4(1): p. 406-413.

23. ASTM, Standard methods for acidity or alkalinity of water, in American Society Testing and materials. 1982: Philadelphia, USA.

24. APHA, Standard Methods for the Examination of Water and Wastewater. 2005, American Public Health Association: Washington, DC.

25. Ahmad, M. and W. Wan Zainal, Adsorption of malachite green onto cocoa pod husk-based activated carbon: Kinetics and equilibrium studies. Malaysian Cocoa Journal, 2010. 6: p. 41-47.

26. Baysal, Z., E. Cinar, Y. Buluk, H. Alkan, and M. Dogru, Equilibrium and thermodynamic studies of Biosorption of Pb (II) onto Candida albicans biomass. Journal of hazardous material, 2009. 161: p. 62 – 67.

27. Onyeji, L.I. and A.A. Aboje, Removal of Heavy Metals from Dye Effluent using Activated Carbon Produced from Coconut Shell. International Journal of Engineering Science and Technology, 2011. 3(12): p. 8240-8243.

28. Ostroski, I.C., M.A.S.D. Barros, E.A. Silvab, J.H. Dantas, P.A. Arroyo, and O.C.M. Lima, A comparative study for the ion exchange of Fe(III) and Zn(II) on zeolite NaY. Journal of Hazardous Material, 2009. 161: p. 1404-1412.

29. Ozer, A. and H.B. Pirincci, Physical Adsorption of Cd (II) ions on sulphuric acid treated Wheat brain. Journal of Hazard and Material, 2006. 137: p. 849 – 855.

30. Ajayi, O., Kinetics and Thermodynamics of biosorption of copper, cadium and lead using water hyacinth and rice husk. 2013, University of Ilorin: Ilorin, Nigeria.

RESEARCH ARTICLE

New distribution areas of Angelica tatianaeBordz and study of their coumarin derivatives

Husniya Mammadova Gara[1]* ✉ iD **and Mashayeva Sevil Saleh[2]** ✉ iD

[1]Department of Chemistry and Biology, Sumgait State University,Sumgait, Azerbaijan
[2]Azerbaijan National Academy of Sciences, Institute of Polymeric Materials, Sumgait, Azerbaijan

Abstract: The Angelica L. genus belongs to Umbelliferae family. *Angelica tatianae*is very rare in Azerbaijan. In Azerbaijan so far, there has been no research about phytochemistry of *A. tatianae*. In the present study, phytochemicals of the plant have been isolated and their structures have been elucidated. The roots of *Angelica tatianae* Bordz were extracted with 95% alcohol and the contents were extracted of a total of 3 individual substances by chromatography in a glass column filled with Al_2O_3, (1.$C_{13}H_{10}O_5$, m.p. 148.0°C; 2. $C_9H_6O_2$, m.p. 67.0-68.0 °C; 3. $C_{12}H_8O_4$, m.p. 145.0-146.0 °C).Based on chemical and spectral results (FTIR, ^1H NMR, ^{13}C NMR), the obtained substances were identified with isopimpinellin, coumarin, and xanthotoxin, respectively.

INTRODUCTION

There are nearly 4500 kinds of plants in the flora of Azerbaijan. Among these plants, Apiaceae Lindl's family takes a special place. This family is represented in the world with 400 genders. Among the genders including this family, Angelica L. Gender attracts attention for its specific features. There are 115 types of this gender in the world (plant list 2013, 115), (plant list 2018, 116) (1).

There are more than 50 types of Angelica species in the Caucasus. In the floraof Azerbaijan, Angelica L. gender is represented with 3 types: *A.sachokiana*, *Angelica purpurascens* and *Angelica tatianae* Bordz (2,3). The first of them,*A. sachokiana*, is described in Azerbaijan (Ismailly, Nialdag, Kuzun village of Gusar region) (4, 5). It is encountered in the middle and upper mountain ranges of Greater Caucasus region on the rocks, on the banks of mountain rivers. The second *A. purpurascens* is the subalpine meadows plant of Nakhchivan and the Small Caucasus region) (6). The third type *A.tatianae* is

encountered in the forest areas upper mountain ranges of the Small Caucasus region (Gadabay region). It is also encountered in the western part of the Greater Caucasus region (Zakhatala region) in upper mountain ranges. On our part, we found that in the small and medium range of the Lesser Caucasus (Gadabay region) is distributed in a limited range of forest areas.

A.tatianae is a rare species in the flora of Azerbaijan. This species is a remarkable perennial plan. The lifespan of the plant is 7 years. It is a monocarpous plant. It blooms in the last year, forms seeds and dies.

A.tatianae is a very valuable medicinal plant with 1-1,5m height and an empty stem. It passes to the blooming phase in July with white flowers. The length of the petals is about 1-2mm. The columns are short cone-shaped. The column is much longer than under columns and they are folded.The flowers turn whitish-yellow as they grow.

The length of the umbrellas consists of various, roughly 25-35 rays. The petals are white and are gathered in the umbrella flower group. The sizes of the edge and middle flowers are different. The grown seeds are wide oval-shaped, backbones are narrow, from sides are large winged, above is naked. The length of the seed is 10 mm; the width is 5-6mm and consists of ribs. The seed has a specific dark smell.
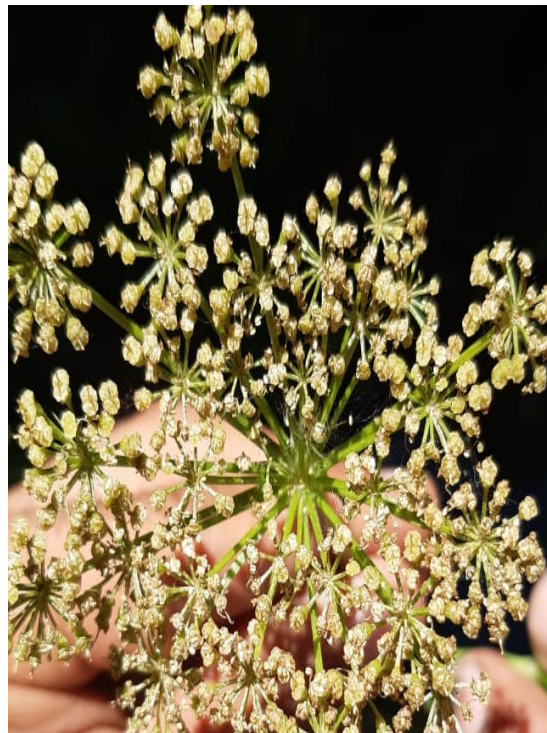
Picture 1-2. *A.tatianae flowering phase (July).*

The leaf limb is wide triangle-shaped, consists of 3 parts, it is feather-like, the length is about 30-40 cm, initial slices of a leaf are wide egg-shaped and the length is 20-25cm. The deep feather-like cut sharply pointed part is 6-8cm. The edges are unequal sharp cogged; the veinlet is short-hairy especially at the bottom part. Inside the stem is empty. It has a bitter taste.

The seeds of the plant were planted in special conditions and vegetation was observed for 9 years. Sown seeds begin to ripen in the second year. Development is slow.

As a result of literature research, it is known that the phytochemistry of the plant A.tatianae has been little studied. In previous studies, the surface part (seeds) of the plant was used.

According to the literature in the fruit of Xanthogalum (Angelica) tatianae (Bordz.) Schischk., collected in the Gordzhomi region (Adjar ASSR) they had established the presence of 2.2% of lactones of the coumarin group consisting of a mixture of four substances: bergapten, isooxypeucedanin, bergaptol, b-sitosterol (A. I. Sokolo and G. K. Nikonov, 1969) (13,14).

The phytochemistry of *A. tatianae* has not been studied in Azerbaijan. We first obtained isopimpinellin, coumarin and xanthotoxin from the roots of the plant. Isopimpinellin and xanthotoxin derived from plant roots belong to the class of furanocoumarins (8,9,24, 25).

MATERIALS AND METHOD

A. tatianae was collected from the Gadabay region in July 2013 and was assigned to the Institute of Botany of the Azerbaijan National Academy of Sciences (compared to herbariums in the herbarium fund). On July 28, 2018, the plant was re-collected from a forest area at an altitude of 2000m above sea level and phytochemical studies were conducted.The bio-ecological features of the species have been studied by us. In addition, we studied the antimicrobial activity of *A. tatianae* and the repellent effect of the extract of *A. tatianae* on the mosquito *Culex pipiens molestus* (15-17).

Coumarins are widely spread in types of Apiaceae, especially in the genus Angelica L. (18-23).

Picture 3. Seeds of *A.tatianae*

Picture 4. Photo from the herbarium fund of the Institute of Botany (*A.tatianae*)

Picture 5. *A. tatianae* (root).

Picture 6. *A. tatianae* (surface part).

After the root of the plant was finely chopped and dried (120 g), it was extracted 3 times (each time for three days) in alcohol. Obtained the substance mixture (extract) (17g) was used. Thus, substance mixture was chromatographed in a glass column (h=100cm, d=3cm) that was filled with Al_2O_3. The mixture of substances we mean benzene + n-hexane (3: 1), chloroform + ethanol (4: 1), and other mixtures used in chromatography.

The volume of each fraction is 100 mL. Chromatography column was digitalized with n-hexane (46 fractions), n-hexane+benzene (42), benzene (20 fractions), benzene+chloroform (23 fractions), chloroform+benzene (20 fractions), chloroform (28 fractions), chloroform+alcohol (6 fractions). The individuality of the substances was determined by using a thin layer chromatography method (Silifol UV254, solvent-benzene+chloroform, 1:1), the melting temperature was defined on Boytius table. IG spectrums were recorded by the UR-20 spectrophotometer in Vaseline oil and the chemical structure of coumarin derivatives was defined on the base of the results obtained from the detection of NMR spectra.

RESULTS AND DISCUSSION

Three substances were extracted from chromatography of extracts from the root system of

A.tatianae. The structures of matter are determined chemically and spectrally.

The thin layer chromatography method was used to determine the individuality of the substances derived from the root of the plant, which has been identified as substances isopimpinellin, coumarin, xanthotoxin. All 3 substances were identified with based on the results of the detection of IR and NMR spectra (7).

Coumarin and its derivatives were obtained from the roots of the plant and identified (Table 1). As can be seen from the table, the roots of the studied plant contained the amount of coumarin derivatives - isopimpinellin (1.356%), xanthotoxin (1.809%) and coumarin (3.310%).

Substance 1. Composition of the element $C_{13}H_{10}O_5$, m.p. 148⊕C, **(Figure1).** In the IR spectrum, there are absorption peaks that characterize the carbonyl (1714 cm^{-1}) and double bonds (1600, 1649 cm^{-1}) of the lactone cycle. UV spectrum: λ_{max} 224 (logε 4.40), 241 (logε 4.16), 268 (logε 4.26), 312 nm (logε 4.11).Signals detected in the 1H NMR are as follows: δ 3,96 (s, 3H, OCH$_3$); 5,23 (s, 1H, H3); 5,99 (s, 1H, H13); 6,13 (s, 1H, H6); 6,80 (d, 1H, $J_{11,12}$= 8,1 Hz; H11), e 7,13 (dd, H1, $J_{12,11}$=8,1 Hz e $J_{12,8}$ =1,8Hz; H12), e 7,40 (d, 1H, $J_{8,12}$ =1,8Hz; H8). It is established that the substance obtained in item 1 generally refers to linear coumarin and identified as Isopimpinellin **(Table 1, A)** (8).
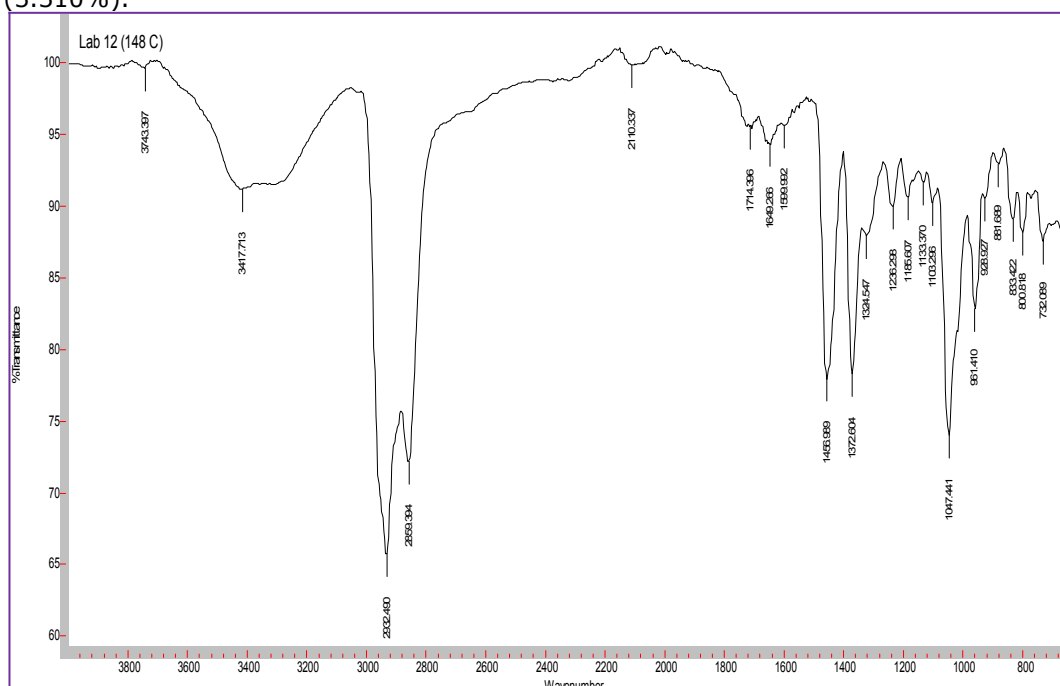
Figure 1. Composition of the element $C_{13}H_{10}O_5$, m.p. 148⊕C.

Substance 2. The crystalline substance was extracted from the 12–16 fraction fractionated by chloroform in the chromatographic column **(Figure 2).** After crystallizing with ethanol + water, the elemental composition of the substance is $C_9H_6O_2$. It was 67.0 - 68.0⁰C. UV-spectrum: λ_{max} 275 (logε 3.9), 325 nm (logε 3.75) In the FTIR spectrum of the substance, the v_{max} is 1723 (CO-δ-lactone cycle), and 1610 cm^{-1} (C = C benzene cycle) for double bonds. Signals detected in the ^{1}H NMR spectrum of the compound: δ: 7.65 (1H, d, J = 9.0 Hz H-4), 7.50 (2H, m, H-6, H7), 7.48 (1H, d, J = 8.5 Hz, H-8), 7.20 (1H, d, J = 8.5 Hz, H-5), 6.40 (1H, d, J = 9.4 Hz H-3).The obtained formula 2 proves that the structural formula of coumarin is the same as the structure formula were identified**(Table 1, B)**(8).

f.44
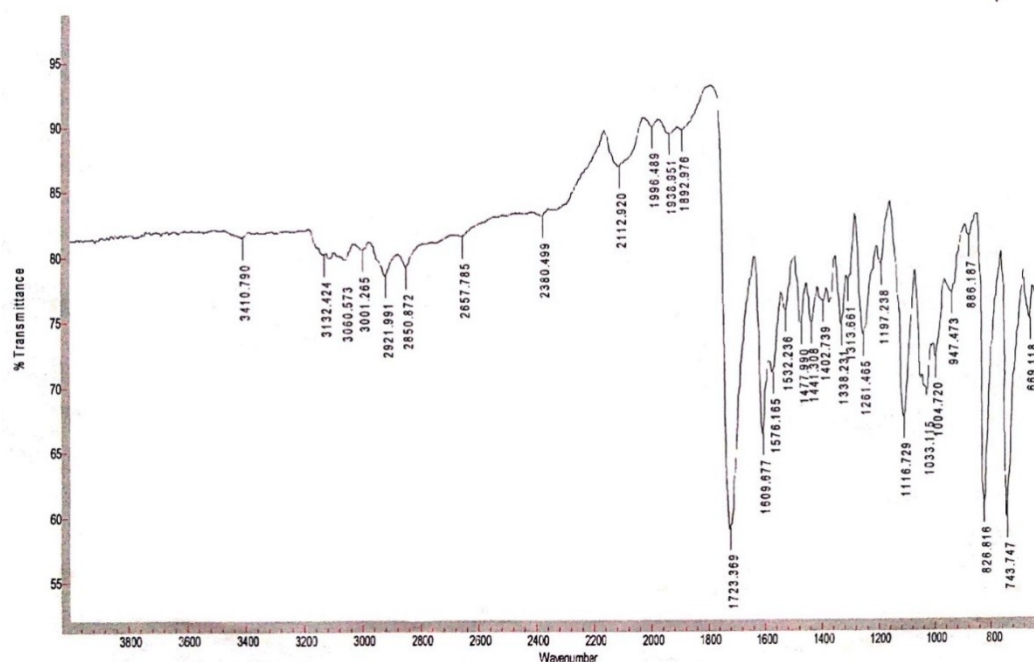
Figure 2. Composition of the element $C_9H_6O_2$, m.p.67.0 – 68.0 °C.

Substance 3. Composition of the element $C_{12}H_8O_4$ 145.0-146.0 °C **(Figure 3).** In the IR spectrum, the absorption peaks of the δ-lactone cycle C = O group (1726 cm^{-1}) and the double bonds of the aromatic system (1624, 1594, 1550 cm^{-1}) indicate that the compound belongs to the furocoumarin group. Signals detected in the ^{1}H NMR spectrum of matter: 7.73 (d, J = 9.65 Hz, 1H, CH =, H-4) , 7.60 (d. J = 2,00 Hz, 1H, CH =, H-3 ') 7.32 (s., 1H, CH =, H-5), 6.80 (d., J = 2,00 Hz, 1H, CH =, H-2 '), 6.30 (d., J = 9.65 Hz, H-3), and 3,4m singlet proves the presence of methoxy (−OCH$_3$) group in the molecule. The substance obtained was identified as xantotoxin**(Table 1, C)**(9).
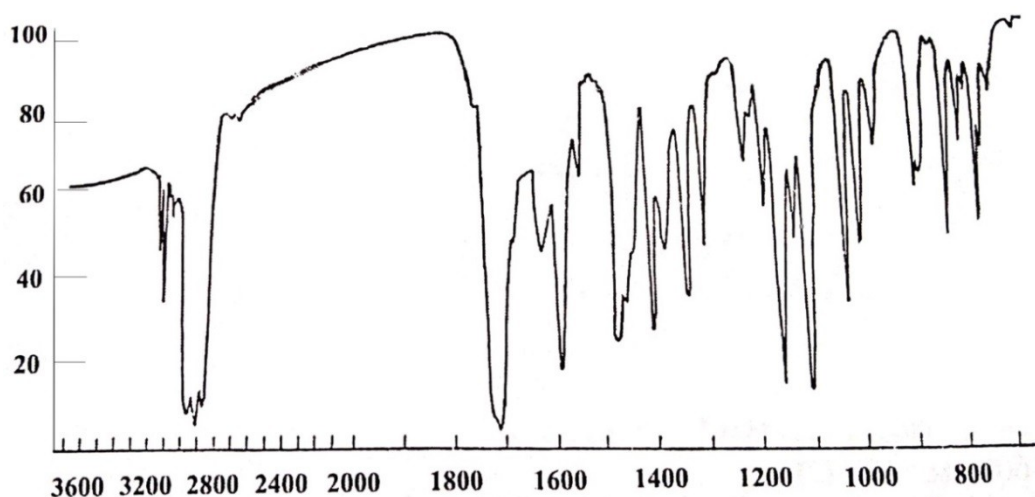
Figure 3. Composition of the element $C_{12}H_8O_4$, 145.0-146.0 °C.

749

Table 1. *Angelica tatianae* Bordz. chemical composition of the species.
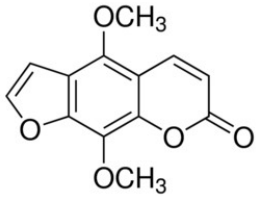
Coumarin	Amount, %
A. Isopimpinellin, $C_{13}H_{10}O_5$	1.356
B. Coumarin, $C_9H_6O_2$	3.310
C. Xanthotoxin, $C_{12}H_8O_4$	1.809
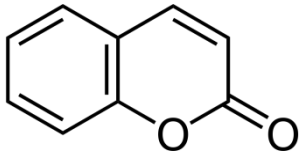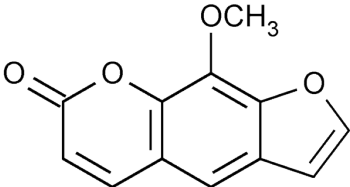
Isopimpinellin possibly inhibits 7,12-dimethylbenz(a)anthracene, which is the initiator of skin tumors. Evidence has also been reported that links these compounds to the inhibition of breast cancers. Isopimpinellin has inhibitory activity against the enzyme adenine phosphoribosyltransferase (APRT) from Leishmania, a tropical parasite causing endemic disease in poor countries (10).

The coumarins are of great attention due to their therapeutic property. Their physiological, bacteriostatic and anti-tumor activity marks coumarins as novel ones for therapeutic applications. Several researchers have reported the clinical applications of coumarins and their derivatives in the treatment of several diseases. Several studies have proven multiple potential roles of coumarins which include disease spread and prevention, growth modulation, antioxidant and anti-tumor effects (12).

Xanthoxin belongs to the group of medicines called psoralens. It is used along with ultraviolet light (found in sunlight and some special lamps) in a treatment called PUVA to treat vitiligo, a disease in which skin color is lost, and psoriasis, a skin condition associated with red and scaly patches (11). Xanthoxin is also used with ultraviolet light in

the treatment of white blood cells. This treatment is called photopheresis and is used to treat the skin problems associated with mycosis fungoides, which is a type of lymphoma.

Isopimpinellin, coumarin, and xanthotoxin were first extracted from the substances investigated in the root of the Angelica tatianae plant; need further research and investigations to find out new areas of application.

REFERENCES

1. www.theplantlist.org,The Plant List, 115 (2013), The Plant List, 116 (2018).

2. Askerov AM. Higher plants of Azerbaijan. Abstract flora of Azerbaijan. 2005;1.

3. I. I. Karyagin, Flora of Azerbaijan, Genus Heracleum L., Vol. 6, 1953, p. 495.

4. H.A. Imanli, S.V. Serkerov Study of coumarin derivatives of roots and overground Parts Of Angelica Sachokiana by the Chromato-Mass-Spectroscopy Method. News of ANAS (biology and medical scienses), Vol.70, 2015, p.15-20. Bio və Tibb Elmləri [Internet]. [cited 2020 Jul 19].

Available from:http://www.jbio.az/en/journal/article/241

5. Azimova SS, Yunusov MS, editors. Natural Compounds: Alkaloids [Internet]. New York: Springer-Verlag; 2013 [cited 2020 Jul 19]. Available from: https://www.springer.com/gp/book/978146140559 7

6.Geidarov I, Serkerov S. Coumarins from Roots of Angelica purpurascens. Chemistry of Natural Compounds. 2017;53.

7. Razavi SM, Nazemiyeh H, Hajiboland R, Kumarasamy Y, Delazar A, Nahar L, et al. Coumarins from the aerial parts of Prangos uloptera (Apiaceae). Revista Brasileira de Farmacognosia. 2008;18:1–5.

8. G. A. Kuznetsova, Natural Coumarins and Furocoumarins [in Russian], Leningrad (1967), p. 248.

9. Kuznetsova GA, Markelova EV, Perelson ME, Klein E, Pavlović S. (−)-3'(R)-hydroxy-4'(S)-methoxy-3'4'-dihydroxanthyletin from the roots of Peucedanum arenarium. Phytochemistry. 1978 Jan 1;17(10):1805–6.

10.Prince M, Campbell CT, Robertson TA, Wells AJ, Kleiner HE. Naturally occurring coumarins inhibit 7,12-dimethylbenz[a]anthracene DNA adduct formation in mouse mammary gland. Carcinogenesis. 2006 Jun;27(6):1204–13.

11. Fulton JE Jr, Leyden J, Papa C. Treatment of Vitiligo With Topical Methoxsalen and Blacklite. Archives of Dermatology. 1969;100(2):224–9.

12. Lacy A, O'Kennedy R. Studies on coumarins and coumarin-related compounds to determine their therapeutic role in the treatment of cancer. Curr Pharm Des. 2004;10(30):3797–811.

13. Sokolo AI, Nikonov GK. Furocoumarins of the fruit ofXanthogalum (Angelica) tatianae. Chem Nat Compd. 1969 Jul 1;5(4):268–268.

14. Zorin EB, Ivashenko NV, Perelson ME, Pimenov MG. Coumarins from the roots of Angelica komarovii. KHIMIYA PRIRODNYKH SOEDINENII. 1984 ;(3):388–388.

15.H.G.Mammadova, Q.M.Verdiyeva, Bioecological features the genus Angelica tatianae of species Angelica L. spread in Dashkasan–Gadabay. Actual problems of the modern nature sciences. Vol. 2,2017May 4,(5): 63-65.

16. H.G.Mammadova, Studying of antimicrobial effect of Angelica tatianae plant extract, Azerbaijan

pharmaceutical and pharmacotherapy journal.2019, :30-32.

17. H.G.Mammadova, M.I.Aliev, A.N.Aleskerova, P.A.Cafarova, The repellent effect of the extract of the plant Angelica tatianae Bordz on mosquitoes Culex pipiens molestus. Biology science Kazakhstan No 1, 2020, :12-17.

18. Kurbanova F, Serkerov S. A new psoralenic methoxyfurocoumarin from fruit of Heracleum transcaucasicum. Chemistry of Natural Compounds. 2012;48.

19. Lemmich J, Lemmich E, Nielsen BE. Constituents of umbelliferous plants. 8. Coumarins from the root of Seseli libanotis (L.) Koch. The structure of three new coumarins. Acta Chem Scand. 1966;20(9):2497–507.

20. Analysis, isolation and insecticidal activity of linear furanocoumarins and other coumarin derivatives fromPeucedanum (Apiaceae: Apioideae) - PubMed [Internet]. [cited 2020 Jul 19]. Available from: https://pubmed.ncbi.nlm.nih.gov/24242727/

21. K R, Ps S. Therapeutic Role of Coumarins and Coumarin-Related Compounds. Journal of Thermodynamics & Catalysis. 2014;5(2):1–3.

22. Abyshev A.Z., Nguyen C.B. SYNTHETIC COVALENTLY COMBINED DERIVATIVES OF 2H-1-BENZOPYRAN-2-ONE. Drug development & registration. 2017;(4):132-138. (In Russ.)

23. Yuldashev MP, Batirov EKh, Malikov VM. Coumarin glycosides ofHaplophyllum perforatum. Chem Nat Compd. 1980 Mar 1;16(2):125–8.

24. 1987 – Volume 12, Issue 2 – FABAD Journal of Pharmaceutical Sciences [Internet]. [cited 2020 Jul 19]. Available from: http://dergi.fabad.org.tr/1987-volume-12-issue-2/

25. Murray, R. D. H., J. Mendez, and S. A. Brown, The Natural Coumarins: Occurrence, Chemistry, and Biochemistry, Wiley, New York, 1982.Google Scholar

RESEARCH ARTICLE

Synthesis of Novel Oxadiazole Derivatives, Molecular Properties Prediction, and Molecular Docking Studies

Zühal KILIC-KURT* ✉ iD

Ankara University, Faculty of Pharmacy, Department of Pharmaceutical Chemistry, Tandogan, Ankara, Turkey

Abstract: In this work, the synthesis of novel 1,3,4-oxadiazole derivatives was reported. A good molecular properties profile was predicted for the target compounds. In drug-likeness prediction, compound **4b** and **8b** possess the highest score of 0.31 and 0.33, respectively. Since the compounds have good bioactivity scores as a kinase inhibitor, possible interactions of compounds with VEGFR-2 kinase and probable binding conformations were evaluated by molecular docking. All compounds formed hydrogen bonding interactions with Asp1046 amino acid of key residues.

INTRODUCTION

The 1,3,4-oxadiazole ring is often used in drug design research due to its effect on the ADME properties of the compounds. It has a better metabolic and solubility profile. Oxadiazole ring can interact with ligand via its hydrogen bond acceptor properties. It has been used instead of ester and amide functional groups for bioisosteric replacements. Moreover, to provide an appropriate orientation of the molecule, an oxadiazole ring can be used as a flat aromatic linker (1-2). To date, several compounds based on oxadiazole moiety have been reported with different pharmacological activities such as antibacterial, antifungal, antiviral, antitubercular (3), anticancer (4) as well as other biological activities. 1,3,4-Oxadiazole-based compounds such as **Zibotentan** (ZD4054) and **Ataluren** (Figure 1) are in the late-stage clinical trial for prostate cancer and cystic fibrosis, respectively (5-6). Moreover,

several oxadiazole derivatives were reported to have potential anticancer activity through a different mechanism (7-9). Compound **I** (Figure 1) exhibited significant inhibition on tubulin polymerization and caused mitotic arrest in A431 human epidermoid cells (10). Compound **II** (Figure 1) displayed the inhibitory effect on the proliferation of SMMC-7721 cell line (11). 1,3,4-Oxadiazole based compound **III** (Figure 1) combined with alanine amino acid was found as a selective inhibitor of histone deacetylase-8 (HDAC-8) and showed inhibition on proliferation of breast cancer cell lines (12). Another 1,3,4-oxadiazole based compound **IV** (Figure 1) inhibited NF-κB signaling pathway. It also induced antiproliferative effect and apoptosis in hepatocellular carcinoma (13). Compound **V** (Figure 1) exhibited potent anticancer activity towards MCF-7 cells and significant EGFR tyrosine inhibition (14). Compound **VI** (Figure 1) showed strong inhibitory activity against focal adhesion kinase (FAK) and unusual

antiproliferative activity related to the 5-Fluorouracil (15). Oxadiazole derivative bearing ((pyridin-4-yl)ethyl)pyridine moiety (**VII**) was reported as a selective and competitive inhibitor of VEGFR-2 with IC_{50} value of 31 nM (16). Oxadiazole derivative combined with pyrrolotriazine scaffold (**VIII**) exhibited potent enzymatic (IC_{50} = 11 nM) and VEGF-stimulated HUVEC cellular inhibitory activity against VEGFR-2 (IC_{50} = 11 nM) (17). Another oxadiazole based compound **IX** demonstrated nanomolar inhibitory potency toward VEGFR-2 in both enzymatic and cellular phosphorylation assays. It also showed strong activity in tubulin cellular G2M block assay in the nanomolar range (18).

Based on the above-mentioned findings, in this work, novel 1,3,4-oxadiazole derivatives bearing benzo[*b*]thiophen (**4a-c**) and thiophene (**8a-c**) scaffolds were designed and synthesized. All the synthesized compounds have been subjected to the prediction of molecular properties, bioactivity, and drug-likeness scores. Bioactivity score prediction results suggest that synthesized compounds can be active (**4a-c**; >0) or moderate active (**8a-c**; -0.5-0) against kinases. It is reported that oxadiazole derivatives have strong inhibitor activity on kinases such as EGFR (19-21), FAK (15, 22) and VEGFR-2 (16-18,23,24) proteins. So, to make target prediction for designed compounds, molecular docking studies of compounds in EGFR, FAK, and VEGFR-2 kinases were performed using Autodock Vina, and results were discussed.

MATERIALS AND METHODS

Synthesis of methyl esters (1 and 5)
Carboxylic acids (1 eq) and a catalytic amount of concd. H_2SO_4 (0.1 mL) were refluxed in MeOH (5 mL) overnight. Then, the solvent was evaporated and satd. $NaHCO_3$ (aq) was added. The white precipitate was filtered, then washed with water, and dry to obtain the methyl esters **1** and **5** (25).

Synthesis of carbohydrazide derivatives (2-6)
Methyl esters (**1** and **5**, 1 eq) were dissolved in methanol (15 mL), hydrazine hydrate (10 eq) was added and heated at reflux for 3 hours,

cooled and the precipitate filtered to afford hydrazide derivatives **2** and **6** (26).

Synthesis of 2-(benzo[*b*]thiophen-2-yl)-5-(chloromethyl)-1,3,4-oxadiazole (3) and 2-(chloromethyl)-5-(thiophen-2-yl)-1,3,4-oxadiazole (7)
A mixture of chloroacetic acid (1.2 eq) and an appropriate acid hydrazide (1 eq, **2** or **6**) in 7-8 mL of $POCl_3$ was refluxed for 5-6 h. Then, to the mixture, ice was added, and 2 M NaOH solution was added until pH=6-7. The white precipitate was filtered and washed with water. Purification was performed by column chromatography using n-hexane:EtOAc (7:1) mixture to afford pure compounds **3** and **7** in moderate yields.

2-(Benzo[b]thiophen-2-yl)-5-(chloromethyl)-1,3,4-oxadiazole (3)
CAS number:1250681-18-5. Mp: 175 °C. Proton NMR (DMSO-d_6) δ: 5.15 (s, 2H, CH_2), 7.46-7.54 (m, 2H), 8.03 (d, 1H, J=6.8 Hz), 8.11 (d, 1H, J=8.4 Hz), 8.25 (s, 1H). Carbon NMR (DMSO-d_6, 100 MHz) δ: 33.08, 122.89, 123.43, 125.42, 125.46, 127.09, 127.81, 138.72, 140.07, 161.31, 162.85. Mass (ESI) *m/z*: 251.78 [M+H].

2-(Chloromethyl)-5-(thiophen-2-yl)-1,3,4-oxadiazole (7)
Mp: 91 °C. Proton NMR (DMSO-d_6) δ: 5.09 (s, 2H, CH_2), 7.29 (dd, 1H, J= 6.8 Hz, 4 Hz), 7.85 (dd, 1H, J=4 Hz, 1.2 Hz), 7.97 (dd, 1H, J=4 Hz, 1.2 Hz). Carbon NMR (DMSO-d_6, 100 MHz) δ: 33.13, 123.65, 128.90, 130.85, 132.20, 161.27, 162.26. (27).

Synthesis of 2-(benzo[*b*]thiophen-2-yl)-5-((4-substituted-piperazin-1-yl) methyl)-1,3,4-oxadiazole (4a-c) and 2-((4-substituted-piperazin-1-yl)methyl)-5-(thiophen-2-yl)-1,3,4-oxadiazole derivatives (8a-c)
The intermediates **3** or **7** (1 eq), appropriate piperazine (2 eq), potassium carbonate (2 eq) and potassium iodide (1 eq) were refluxed in acetone (30 mL) for 5-6 h. Then, acetone was evaporated to dryness, and water was added. Ethyl acetate extraction was done, and purification was performed by silica gel column chromatography with dichloromethane: methanol or n-hexane: ethyl acetate to give the compounds **4a**-**c** and **8a**-**c** in 40–60% yields.

Zibotentan   **Ataluren**   **I**

II   **III**   **IV**

V   **VI**

VII   **VIII**   **IX**
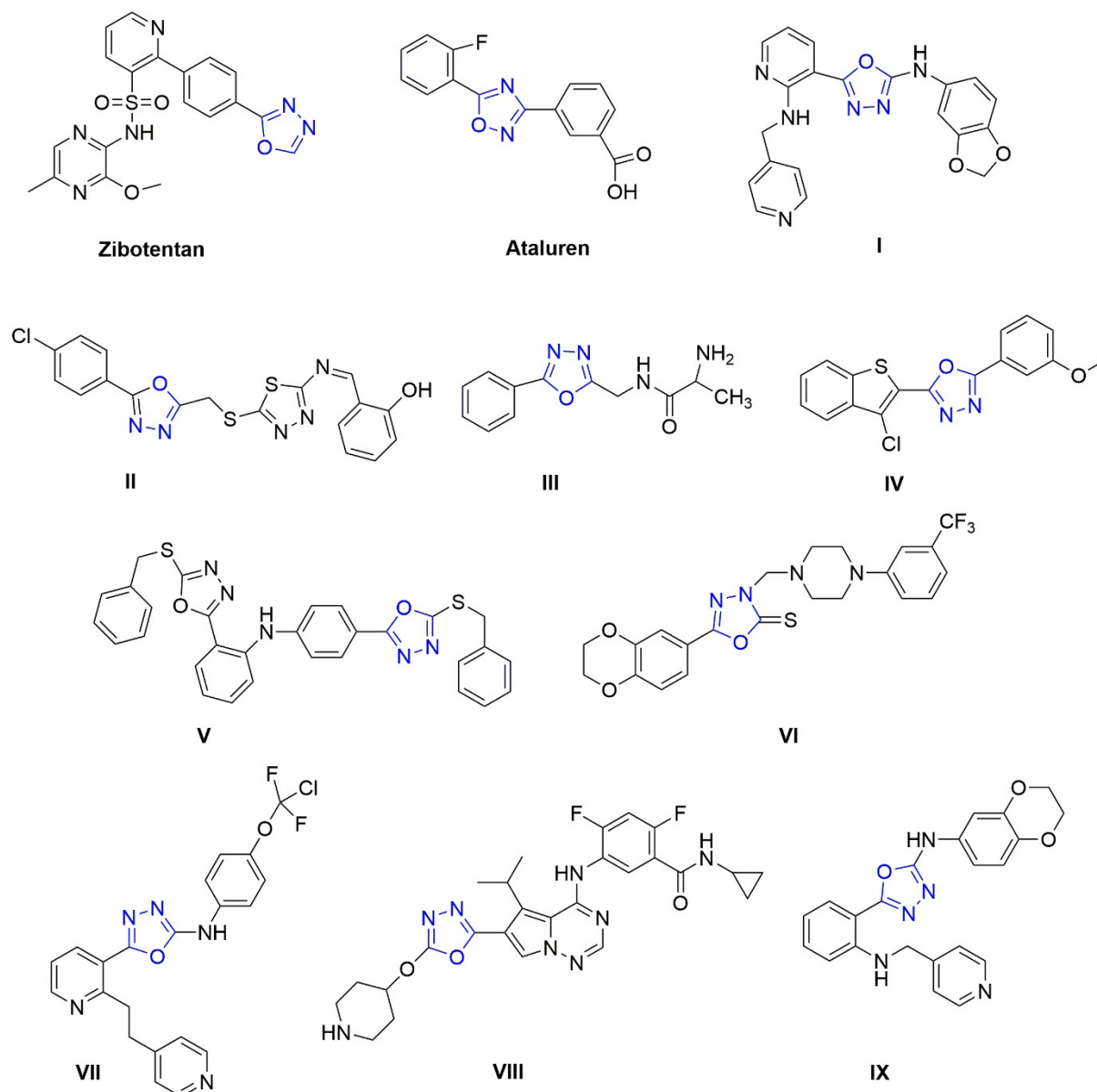
Figure 1. 1,3,4-Oxadiazole compounds having anticancer activity.

2-(Benzo[b]thiophen-2-yl)-5-((4-methylpiperazin-1-yl)methyl)-1,3,4-oxadiazole (4a)

Yield: 45%. Mp: 128 °C. Proton NMR (DMSO-d_6) δ: 2.19 (s, 3H, CH$_3$), 2.30 (bs, 4H, H-a), 2.51 (bs, 4H, H-b), 3.86 (s, 2H, CH$_2$), 7.44-7.52 (m, 2H, H-5,6), 8.01 (dd, 1H, J=6.8 Hz, 1.6 Hz, H-4), 8.08 (d, 1H, J=7.6 Hz, H-7), 8.19 (s, 1H, H-3). Carbon NMR (DMSO-d_6, 100 MHz) δ: 45.57 (CH$_3$), 50.97 (CH$_2$), 51.97 (piperazine-b), 54.40 (piperazine-a), 122.83, 124.04, 125.26, 125.37, 126.86, 127.18, 138.78, 139.89, 160.76, 163.78. Mass (ESI) *m/z*: 315.55 [M+H].

2-(Benzo[b]thiophen-2-yl)-5-((4-(3-methoxyphenyl)piperazin-1-yl)methyl)-1,3,4-oxadiazole (4b)

Yield: 76%. Mp: 165 °C. Proton NMR (DMSO-d_6) δ: 2.68 (t, 4H, H-b), 3.15 (t, 4H, H-a), 3.69 (s, 3H, OCH$_3$), 3.97 (s, 2H, CH$_2$), 6.36 (dd, 1H, J=8.4 Hz, 2.4 Hz, H-4'), 6.44 (t, 1H, H-2'), 6.51 (dd, 1H, J=8.4 Hz, 2 Hz, H-6'), 7.09 (t, 1H, H-5'), 7.47-7.54 (m, 2H, H-5,6), 8.03 (dd, 1H, J=6.8 Hz, 2 Hz, H-4), 8.11 (d, 1H, J=7.6 Hz, H-7), 8.22 (s, 1H, H-3). Carbon NMR (DMSO-d_6, 100 MHz) δ: 48.09 (piperazine-a), 51.02 (OCH$_3$), 52.05 (piperazine-b), 54.83 (CH$_2$),

101.61, 104.21, 108.12, 122.90, 124.11, 125.33, 125.44, 126.94, 127.28, 129.57, 138.83, 139.97, 152.24, 160.15, 160.88, 163.73. Mass (ESI) *m/z*: 408.10 [M+H+1].

2-(Benzo[b]thiophen-2-yl)-5-((4-(2-fluorophenyl)piperazin-1-yl)methyl)-1,3,4-oxadiazole (4c)
Yield: 40%. Mp: 175 °C. Proton NMR (DMSO-*d₆*) *δ*: 2.72 (t, 4H, H-b), 3.04 (t, 4H, H-a), 3.99 (s, 2H, CH₂), 6.92-7.13 (m, 4H, aromatic protons), 7.47-7.55 (m, 2H, H-5,6), 8.03 (dd, 1H, J=6.8 Hz, 1.6 Hz, H-4), 8.11 (d, 1H, J=8 Hz, H-7), 8.23 (s, 1H, H-3). Carbon NMR (DMSO-*d₆*, 100 MHz) *δ*: 49.96 (piperazine-a), 51.02 (CH₂), 52.11 (piperazine-b), 115.88, 119.26, 122.36, 122.90, 124.12, 124.78, 125.39, 126.94, 127.29, 138.84, 139.68, 139.97, 153.70, 156.13, 160.88, 163.73. Mass (ESI) *m/z*: 396.0 [M+H+1].

2-((4-Methylpiperazin-1-yl)methyl)-5-(thiophen-2-yl)-1,3,4-oxadiazole (8a)
Yield: 81%. Mp: 75 °C. Proton NMR (DMSO-*d₆*) *δ*: 2.13 (s, 3H, CH₃), 2.32 (bs, 4H, H-a), 2.49 (t, 4H, H-b), 3.83 (s, 2H, CH₂), 7.28 (dd, 1H, J=4.8 Hz, 3.2 Hz), 7.82 (dd, 1H, J=4 Hz, 1.2 Hz), 7.94 (dd, 1H, J=4 Hz, 1.2 Hz). Carbon NMR (DMSO-*d₆*, 100 MHz) *δ*: 45.80 (CH₃), 50.25 (CH₂), 52.02 (piperazine-b), 54.20 (piperazine-a), 124.0, 128.25, 130.25, 131.85, 160.50, 163.10. Mass (ESI) *m/z*: 265.46 [M+H].

2-((4-(3-Methoxyphenyl)piperazin-1-yl)methyl)-5-(thiophen-2-yl)-1,3,4-oxadiazole (8b)
Yield: 30%. Mp: 100 °C. Proton NMR (DMSO-*d₆*) *δ*: 2.65 (t, 4H, H-b), 3.14 (t, 4H, H-a), 3.69 (s, 3H, CH₃), 3.92 (s, 2H, CH₂), 6.35 (dd, 1H, J=8 Hz, 2 Hz, H-4'), 6.43 (t, 1H, H-2'), 6.50 (dd, 1H, J=8 Hz, 2 Hz, H-6'), 7.08 (t, 1H, H-5'), 7.29 (dd, 1H, J=4.4 Hz, 4 Hz), 7.83 (dd, 1H, J=3.6 Hz, 1.2 Hz), 7.94 (dd, 1H, J=4.8 Hz, 1.2 Hz). Carbon NMR (DMSO-*d₆*, 100 MHz) *δ*: 48.08 (piperazine-a), 50.96 (OCH₃), 52.05 (piperazine-b), 54.83 (CH₂), 101.61, 104.22, 108.13, 124.25, 128.75, 129.57, 130.32, 131.56, 152.25, 160.15, 160.76, 163.01. Mass (ESI) *m/z*: 357.63 [M+H].

2-((4-(2-Fluorophenyl)piperazin-1-yl)methyl)-5-(thiophen-2-yl)-1,3,4-oxadiazole(8c)
Yield: 45%. Mp: 127 °C. Proton NMR (DMSO-*d₆*) *δ*: 2.67 (t, 4H, H-b), 3.00 (t, 4H, H-a), 3.91 (s, 2H, CH₂), 6.91-7.11 (m, 4H), 7.27 (dd, 1H, J=4.8 Hz, 4 Hz), 7.81 (dd, 1H, J=4 Hz, 1.2 Hz), 7.93 (dd, 1H, J=4 Hz, 1.2 Hz). Carbon NMR (DMSO-*d₆*, 100 MHz) *δ*: 49.86 (piperazine-a), 50.88 (CH₂), 52.04 (piperazine-b), 115.80, 119.18, 122.28, 124.18, 124.70, 128.66, 130.24, 131.47, 139.61, 153.63, 156.05, 160.67, 162.92. Mass (ESI) *m/z*: 345.57 [M+H].

Molecular properties prediction
Molecular properties of the synthesized compounds and bioactivity scores were predicted by the Mol inspiration online tool (28). Druglikeness scores were calculated by the molsoft program (29).

Molecular Docking
The X-ray crystallographic structures of the target proteins EGFR (PDB ID: 1xkk), FAK (PDB ID: 2etm), and VEGFR-2 (PDB ID: 3VHE) were retrieved from the Protein Database (PDB, http://www.rcsb.org). The chemical structures of the compounds were constructed, then they were energetically minimized. Native ligand and waters were extracted from the protein, and the polar hydrogen was added to the proteins. The grid boxes of EGFR and FAK, VEGFR-2 were created with spacing 48x40x48 and 30x30x30, respectively. The docking study was performed using AutoDock vina 1.1.2 (30). The binding energy of the compounds and interactions with protein were evaluated.

RESULT AND DISCUSSION

Chemistry
Synthesis of the target compounds (**4a-c**, **8a-c**) derivatives is depicted in Scheme 1. Firstly, the methyl esters (**1** and **5**) were prepared by esterification of appropriate carboxylic acid in the presence of H₂SO₄ in methanol (31). Hydrazide derivatives (**2** and **6**) were obtained by the reaction of esters (**1** and **5**) with hydrazine hydrate in methanol (32). Hydrazides were refluxed with chloroacetic acid in phosphorous oxychloride to afford 2-(benzo[*b*]thiophen-2-yl)-5-(chloromethyl)-1,3,4-oxadiazole (**3**) and 2-(chloromethyl)-5-(thiophen-2-yl)-1,3,4-oxadiazole (**7**). Final products (**4a-c**, **8a-c**) were prepared by the alkylation reactions of compound **3** and **7** with appropriate piperazine derivatives in the presence of K₂CO₃ and KI (33).
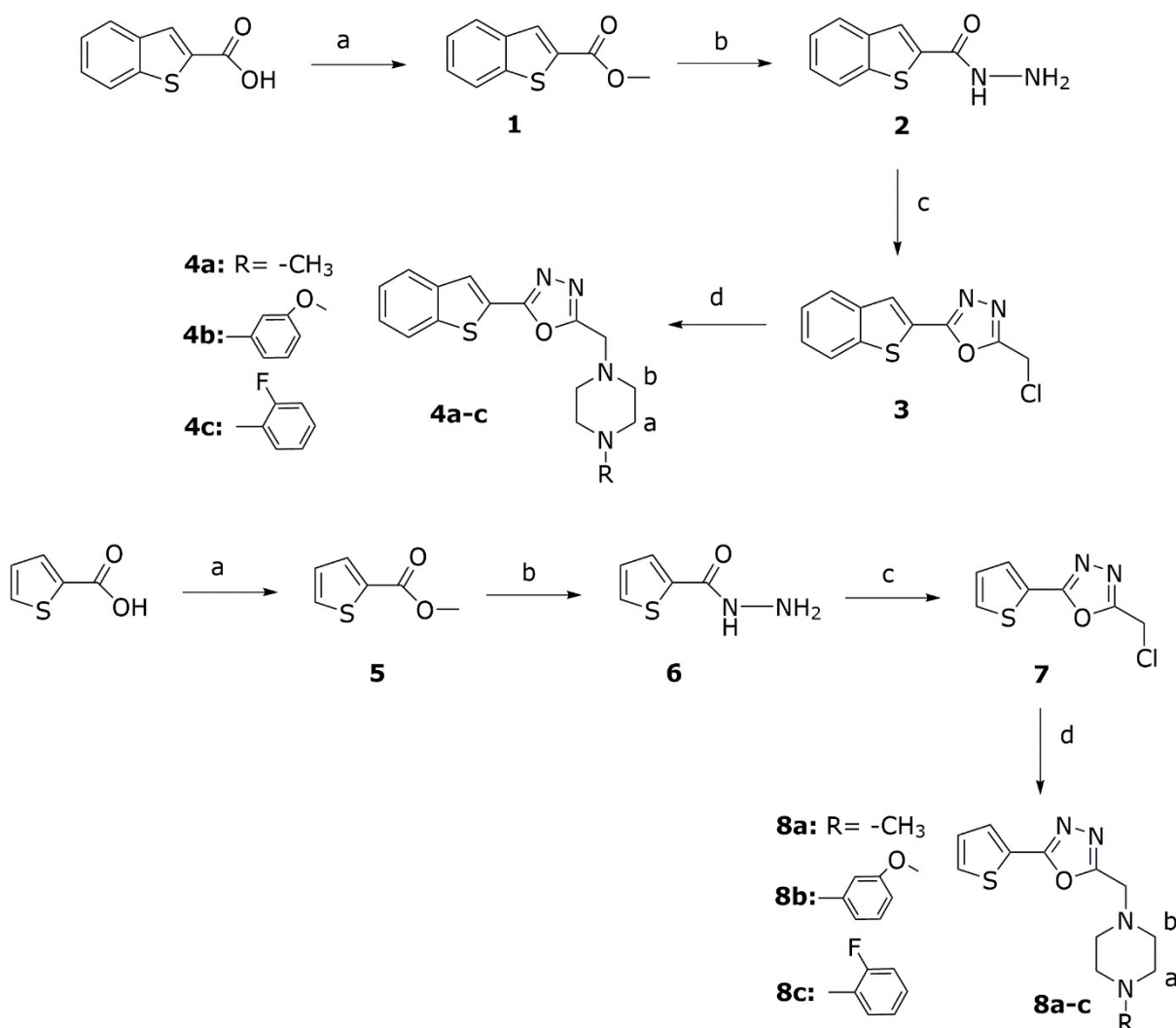
Scheme 1. A synthesis method of compounds **4a-c** and **8a-c**. Reaction conditions: (a) methanol, concd. H_2SO_4 (0.1 mL) (b) hydrazine hydrate, methanol, reflux (c) chloroacetic acid, phosphoryl chloride, reflux (d) K_2CO_3, KI, appropriate piperazine derivatives, acetone, reflux.

^{1}H NMR, ^{13}C NMR, and MS analysis were performed to characterize the compounds. ^{1}H NMR spectra of the compounds containing phenylpiperazine derivatives (**4b-c**, **8b-c**) showed a triplet at δ 2.65-2.72 and 3.0-3.15 ppm indicating the presence of piperazine protons–b and –a, respectively. In the compounds bearing *N*-methylpiperazine moiety (**4a** and **8a**), piperazine protons-a showed the peak in the upfield region (2.30-2.32 ppm) due to the shielding effect of the methyl group. Chemical shift between δ 3.83 to 3.99 ppm showed by all compounds represent the protons of CH_2. Compound **4a-c** exhibited multiplet at δ 7.44-7.55 and singlet peak at δ 8.19-8.23 ppm due to H-5,6 and H-3 protons of benzo[*b*]thiophene ring, respectively. Chemical shift between δ 8.01-8.03 ppm showed by

compounds **4a-c** represents the H-4 proton. The peak belonging H-7 proton of benzo[*b*]thiophene ring was observed in the downfield region (8.08-8.11 ppm) due to nearby sulfur atom of thiophene ring. Compound **8a-c** showed three double doublets peak between δ 7.27-7.94 ppm due to the presence of the thiophene ring. ^{13}C NMR spectra of the target compounds (**4b-b**, **8b-c**) displayed peaks at δ 48.08-54.40, and δ 51.97-52.11 ppm representing piperazine carbon–a and –b. The peaks between δ 50.88-54.83 ppm indicate the presence of CH_2 carbons. Compound **4a** and **8a** with *N*-methylpiperazine moiety showed peaks at δ 45.75 and 45.80 ppm due to CH_3 carbon, respectively. Compound **4b** and **8b** displayed peaks at δ

51.02 and 50.96 ppm, indicating the presence of OCH_3, respectively.

Molecular properties prediction and drug-likeness

Some molecular properties, which are shown in Table 1, were calculated using Molinspiration online calculation software (28). The predicted values are given in Table 1. All the compounds meet the LogP criteria. Calculation of %ABS was done with equation %ABS = 109 − (0.345 x TPSA) (34). All synthesized compounds possess the good %ABS value of 90.15 and 93.33% and acceptable nOHNH (≤5) and nON (≤10) number. Also, NROTB (≤10) of the compounds were found as 3-5, providing moderate flexibility to the compounds (35). MW of the compounds was found less than 500. Druglikeness model score was predicted by MolSoft software (29) and shown in Table 1. Drug-like candidate compounds should have a value of more than zero. Compounds **4b** and **8b** possess the highest drug-likeness score of 0.31 and 0.33, respectively.

Table 1. Predicted molecular properties and drug-likeness scores of the target compound (**4a-c**, **8a-c**).

Cpd	MW[a]	Volume	%ABS[b]	TPSA[c]	NROTB[d]	nON[e]	nOHNH[f]	LogP[g]	nviolations	Drug likeness score
Rule	>500	-	-	-	-	≤10	≤5	≤5	≥1	-
4a	314.41	278.71	93.33	45.40	3	5	0	2.15	0	0.14
4b	406.51	359.10	90.15	54.63	5	6	0	3.88	0	0.31
4c	394.48	338.49	93.33	45.40	4	5	0	3.96	0	0.15
8a	264.35	234.72	93.33	45.40	3	5	0	0.84	0	0.07
8b	356.45	315.11	90.15	54.63	5	6	0	2.57	0	0.33
8c	344.42	294.49	93.33	45.40	4	5	0	2.65	0	0.14

[a] MW: Molecular weight; [b] %ABS: Percentage absorption; [c] TPSA: Topological polar surface area; [d] NROTB: Number of rotatable bonds; [e] nON: Number of hydrogen acceptors; [f] nOHNH: Number of hydrogen donors; [g] LogP: Log octanol/water partition coefficient.

Bioactivity score prediction and molecular docking

Bioactivity scores, which are given in Table 2, were predicted by Molinspiration online calculation software (28). If the bioactivity score of the compound is >0 or -0.5-0 or <0, it can be active or moderate or inactive, respectively (36). Synthesized compounds showed the acceptable kinase inhibitor scores (>0 or -0.5-0) with compound **4a-c**; **8a-c** suggested that these compounds might possess kinase inhibitor activity. So, EGFR, FAK, and VEGFR-2 kinases, which are reported as targets for many oxadiazole derivatives (21-24), were selected as putative targets for synthesized compounds. Molecular docking studies were performed using Autodock vina to present the binding interactions between synthesized compounds and the active site of EGFR, FAK, and VEGFR-2 kinases.

Table 2. Bioactivity scores prediction of the target compounds (**4a-c**, **8a-c**).

Cpd	GPCRL	ICM	KI	NRL	PI	EI
4a	-0.02	-0.37	0.14	-0.44	-0.11	-0.03
4b	-0.07	-0.41	0.05	-0.37	-0.16	-0.14
4c	-0.05	-0.35	0.08	-0.40	-0.10	-0.11
8a	-0.42	-0.53	-0.35	-1.04	-0.54	-0.27
8b	-0.24	-0.53	-0.19	-0.65	-0.33	-0.30
8c	-0.22	-0.46	-0.15	-0.70	-0.27	-0.27

GPCRL: G protein-coupled receptor ligand; ICM: ion channel modulator; KI: kinase Inhibitor; NRL: nuclear receptor ligand; PI: protease inhibitor; EI: enzyme inhibitor.

The docking method was optimized by re-docking of co-crystallized ligands into the binding site of target proteins. The re-docked ligands of EGFR, FAK, and VEGFR-2 kinases were superimposed on native ligands with RMSD values of 1.42, 0.7, and 0.5 Å, respectively. According to docking results, all compounds occupied into the binding site of VEGFR-2 and formed the hydrogen bond between oxadiazole ring and Asp1046 amino acid. The docking results, binding free energy, hydrogen bond distance, and angles were shown in Table 3. The binding model of compound **4b**, which has the lowest binding

free energy (ΔGb=-11.2 kcal/mol) in the active site of VEGFR-2 was depicted in Figure 2. Otherwise, compounds did not show interaction with the key residue of EGFR (Met793 and Thr854) and FAK kinase (Cys502) active sites. Docking results of compounds with EGFR and FAK kinases were given in supplementary material (Figure S1, Table S1-S2).
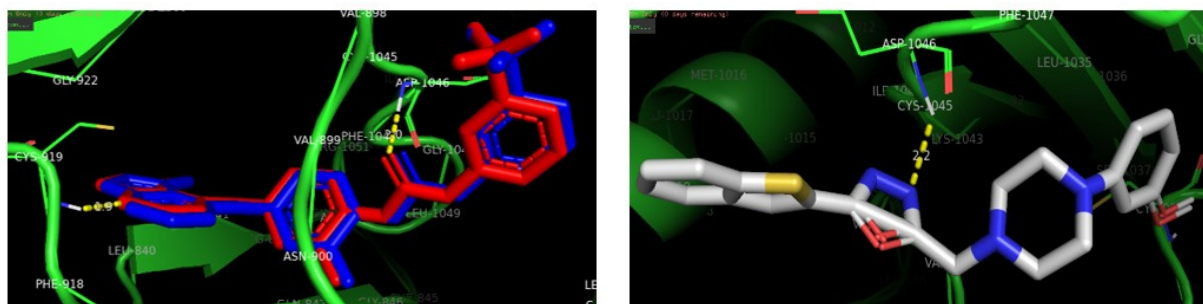
Figure 2. Superposition of co-crystallized (blue) and docked (red) conformations of the reference ligand (left). Predicted binding mode of compound **4b** in the active site of VEGFR-2 (PDB code: 3VHE) (right). Hydrogen bonds were shown as yellow dashed lines. Figure was generated using PyMOL.

Table 3. The docking results of the compounds.

Compound	ΔGb[a] (kcal/mol)	Hydrogen bonds			
		Atom of compound	Amino acid	Distance (Å) D-H.....A	Angle (°)
4a	-9.1	Oxadiazole-O	Asp1046-NH	1.9	163.7
4b	-11.2	Oxadiazole-N4	Asp1046-NH	2.2	136.3
4c	-11.0	Oxadiazole-O	Asp1046-NH	2.2	148.4
8a	-6.9	Oxadiazole-N3	Asp1046-NH	2.2	128.4
8b	-8.7	Oxadiazole-N4	Asp1046-NH	2.2	140.3
8c	-9.4	Oxadiazole-O	Asp1046-NH	2.2	151.0
Native ligand		Urea-N	Glu885-O		
		PP-N4	Cyc919-NH		
		Urea-O	Asp1046-NH		
Docked ligand	-12.6	Urea-O	Asp1046-NH	2.0	161.9
	RMSD[b]:0.5	PP-N4	Cyc919-NH	1.9	162.4

[a]Binding free energy, [b]root-mean-square deviation

CONCLUSION

In this study, 2-(benzo[*b*]thiophen-2-yl)-5-((4-substituted-piperazin-1-yl)methyl)-1,3,4-oxadiazole (**4a-c**) and 2-((4-substituted-piperazin-1-yl)methyl)-5-(thiophen-2-yl)-1,3,4-oxadiazole derivatives (**8a-c**) were synthesized and molecular properties and bioactivity score were predicted. All compounds obeyed the Lipinski's rules and showed good drug-likeness scores. The best bioactivity prediction scores of compounds were found as a kinase inhibitor. Moreover, hydrogen bonding interactions of the compounds with VEGFR-2 kinase active site were found by molecular docking study, suggesting possible *in vitro* inhibitor activities of these compounds towards VEGFR-2 kinase.

REFERENCES

1. Glomb T, Szymankiewicz K, S´wiatek P. Anti-cancer activity of derivatives of 1,3,4-oxadiazole. Molecules. 2018;23,33-61. Doi:10.3390/molecules23123361.

2. Boström J, Hogner A, Llinàs A, Wellner E, Plowright AT. Oxadiazoles in Medicinal Chemistry. Journal of Medicinal Chemistry. 2012;55:1817−1830. Doi:10.1021/jm2013248.

3. Zhang HZ, Zhao ZL, Zhou CH. Recent advance in oxazole-based medicinal chemistry.

European Journal of Medicinal Chemistry. 2018;144:444-492. Doi:10.1016/j.ejmech.2017.12.044.

4.   Akhtar J, Khan AA, Ali Z, Haider R, Shahar Yar M. Structure-activity relationship (SAR) study and design strategies of nitrogen-containing heterocyclic moieties for their anticancer activities. 2017;125:143-189. Doi: 10.1016/j.ejmech.2016.09.023.

5.   James ND, Growcott JW. Zibotentan. Drugs of the Future. 2009;34(8):624-633. Doi:10.1358/dof.2009.34.8.1400202.

6.   Jones AM, Helm JM. Emerging treatments in cystic fibrosis. Drugs. 2009;69:1903−1910. Doi:10.2165/11318500-000000000-00000.

7.   Rasool I, Ahmad M, Khan ZA, Mansha A, Maqbool T, Zahoor AF, Aslam S. Recent advancements in oxadiazole-based anticancer agents. Tropical Journal of Pharmaceutical Research.2017;16:723-733. Doi:10.4314/tjpr.v16i3.30.

8.   Khan I, Ibrar A, Abbas N. Oxadiazoles as Privileged Motifs for Promising Anticancer Leads: Recent Advances and Future Prospects. Archiv der Pharmazie. 2014;347:1-20. Doi:10.1002/ardp.201300231.

9.   Bajaj S, Asati V, Singh J, Roy PP. 1,3,4-Oxadiazoles: An emerging scaffold to target growth factors, enzymes and kinases as anticancer agents. European Journal of Medicinal Chemistry. 2015;97:124-141. Doi:10.1016/j.ejmech.2015.04.051.

10.   Ouyang X, Piatnitski EL, Pattaropong V, Chen X, Hai-Ying H, et al. Synthesis, inhibition of tubulin polymerization, and activity in tumor cell lines. Bioorganic and Medicinal Chemistry Letters. 2006;16:1191-1196. Doi:10.1016/j.bmcl.2005.11.094.

11.   Zhang K, Wang P, Xuan LN, Fu XY, Jing F, Li S, Liu YM, Chen BQ, Synthesis and antitumor activities of novel hybrid molecules containing 1,3,4-oxadiazole and 1,3,4-thiadiazole bearing Schiff base moiety. Bioorganic and Medicinal Chemistry Letters. 2014;24:5154-5156. Doi:10.1016/j.bmcl.2014.09.086.

12.   Pidugu VR, Yarla NS, Pedada SR, Kalle AM, Satya AK. Design and synthesis of novel hdac8 ınhibitory 2,5-disubstituted-1,3,4-oxadiazoles containing glycine and alanine hybrids with anti cancer activity. Bioorganic Medicinal Chemistry. 2016;24:5611−5617. Doi:10.1016/j.bmc.2016.09.022.

13.   Mohan CD, Anilkumar NC, Rangappa S, Shanmugam MK, Mishra S, Chinnathambi A, Alharbi SA, Bhattacharjee A, Sethi G, Kumar AP, Rangappa KS. Novel 1,3,4-oxadiazole induces anticancer activity by targeting nf-κb in hepatocellular carcinoma cells. Frontiers in Oncology. 2018;8:42. Doi:10.3389/fonc.2018.00042.

14.   Abou-Seri SM. Synthesis and biological evaluation of novel 2,4'-bis substituted diphenylamines as anticancer agents and potential epidermal growth factor receptor tyrosine kinase inhibitors. European Journal of Medicinal Chemistry. 2010;45:4113−4121. Doi:10.1016/j.ejmech.2010.05.072.

15.   Sun L, Ren SZ, Lu XY, Li JJ, Shen FQ, Xu C, Zhu HL. Discovery of a series of 1,3,4-oxadiazole-2(3h)-thione derivatives containing piperazine skeleton as potential Fak inhibitors. Bioorganic Medicinal Chemistry. 2017;25:2593−2600. Doi:10.1016/j.bmc.2017.03.038.

16.   Kiselyov AS, Semenova M, Semenov VV, Milligan D. Inhibitors of VEGF receptors-1 and -2 Based on the 2-((pyridin-4-yl)ethyl)pyridine Template. Bioorganic Medicinal Chemistry Letters. 2006;16:1913−1919. Doi:10.1016/j.bmcl.2005.12.090.

17.   Cai Z-W, Wei D, Borzilleri RM, Qian L, Kamath A, Mortillo S, Wautlet B, Henley BJ, Jeyaseelan R, Tokarski J, Hunt JT, Bhide RS, Fargnoli J, Lombardo LJ. Synthesis, SAR, and Evaluation of 4-[2,4-Difluoro-5-(cyclopropylcarbamoyl) phenylamino] pyrrolo[2,1-f][1,2,4]triazine-based VEGFR-2 Kinase Inhibitors. Bioorganic Medicinal Chemistry Letters. 2008;18:1354−1358. Doi:10.1016/j.bmcl.2008.01.012.

18.   Piatnitski Chekler EL, Kiselyov AS, Ouyang X, Chen X, Pattaropong W, Wang Y, Tuma MC, Doody JF. Discovery of dual VEGFR-2 and tubulin inhibitors with in vivo efficacy. ACS Medicinal Chemistry Letters. 2010;1:488-492. Doi:10.1021/ml1001568.

19.   Hughes TV, Xu G, Wetter SK, Connolly PJ, Emanuel SL, Karnachi P, Pollack SR, Pandey N, Adams M, Moreno-Mazza S, Middleton SA, Greenberger LM. A novel 5-[1,3,4-oxadiazol-2-yl]-N-aryl-4,6-pyrimidine diamine having dual

EGFR/HER2 kinase activity: Design, synthesis, and biological activity. Bioorganic Medicinal Chemistry Letters. 2008;18:4896–4899. Doi:10.1016/j.bmcl.2008.07.057.

20.   Dokla EME, Fang C-S, Abouzid KAM, Chen CS. 1,2,4-Oxadiazole derivatives targeting EGFR and c-Met degradation in TKI resistant NSCLC. European Journal of Medicinal Chemistry. 2019;182:111607. Doi:10.1016/j.ejmech.2019.111607

21.   Fathi MA, Abd El-Hafeez AA, Abdelhamid D, Abbas SH, Montano MM, Abdel-Aziz M. 1,3,4-oxadiazole/chalcone Hybrids: Design, synthesis, and ınhibition of leukemia cell growth and egfr, src, IL-6 and stat3 activities. Bioorganic Chemistry. 2019;84:150–163. Doi:10.1016/j.bioorg.2018.11.032.

22.   Altıntop MD, Sever B, Çiftçi GA, Turan-Zitouni G, Kaplancıklı ZA, Özdemir A. Design, synthesis, in vitro and in silico evaluation of a new series of oxadiazole-based anticancer agents as potential Akt and Fak ınhibitors. European Journal of Medicinal Chemistry. 2018;155:905–924. Doi:10.1016/j.ejmech.2018.06.049.

23.   Ruel R, Thibeault C, L'Heureux A, Martel A, Cai ZW, Wei D, Qian L, Barrish JC, Mathur A, D'Arienzo C, et al. Discovery and preclinical studies of 5-isopropyl-6-(5-methyl-1,3,4 -oxadiazol-2-yl)-N-(2-methyl-1H-pyrrolo[2,3-b]pyridin-5-yl)pyrrolo [2,1-f][1,2,4]triazin-4-amine (BMS-645737), an in vivo active potent VEGFR-2 inhibitor. Bioorganic Medicinal Chemistry Letterrs. 2008;18:2985–2989. Doi:10.1016/j.bmcl.2008.03.057

24.   Bhanushali U, Kalekar-Joshi S, Kulkarni-Munshi R, Yellanki S, Medishetty R, Kulkarni P, Chelakara RS. Design, synthesis and evaluation of 5-pyridin-4-yl-2-thioxo-[1,3,4] oxadiazol-3-yl derivatives as anti-angiogenic agents targeting VEGFR-2. Anticancer Agents Medicinal Chemistry. 2017;17:67–74. Doi:10.2174/1871520615666160504094222

25.   Feinstein A, Gore PH, Reed, GL. Alkaline hydrolysis of the methyl esters of benzo[b] furan-2- and 3-carboxylic acid, benzo[b]thiophene-2- and 3-carboxylic acid, and indole-2- and 3-carboxylic acid. Journal of the Chemical Society [Section] B: Physical Organic. 1969;3:205-207.

26.   Kovalenko SI, Antypenko LM, Bilyi AK, Kholodnyak SV, Karpenko OV, Antypenko OM, Mykhaylova NS, Los TI, Kolomoets OS. Synthesis and anticancer activity of 2-(alkyl-, alkaryl-, aryl-, hetaryl-)[1,2,4]triazolo[1,5-c]quinazolines. Scientia Pharmaceutica. 2013;81(2):359-391. Doi:10.3797/scipharm.1211-08.

27.   Guo Y, Xu T, Bao C, Liu Z, Fan J, Yang R, Qin S. Design and synthesis of new norfloxacin-1,3,4-oxadiazole hybrids as antibacterial agents against methicillin-resistant Staphylococcus aureus (MRSA). European Journal of Pharmaceutical Sciences. 2019;136:104966. Doi:10.1016/j.ejps.2019.104966.

28.   Molinspiration Cheminformatics, Bratislava, Slovak Republic, Available from: http://www.molinspiration.com/services/properties.html

29.   Drug-likeness and molecular property prediction, available from: http://www.molsoft.com/mprop/

30.   Trott O, Olson AJ. AutoDock Vina: improving the speed and accuracy of docking with a new scoring function, efficient optimization and multithreading, Journal of Computational Chemistry. 2010;31:455-461. Doi: 10.1002/jcc.21334.

31.   Mistry SN, Shonberg J, Draper-Joyce CJ, Herenbrink CK, Michino M, Shi L, Christopoulos A, Capuano B, Scammells PJ, Lane JR. Discovery of a novel class of negative allosteric modulator of the dopamine d2 receptor through fragmentation of a bitopic ligand. Journal of Medicinal Chemistry. 2015;58:6819-6843. Doi: 10.1021/acs.jmedchem.5b00585.

32.   Almutairi MS, Zakaria AS, Ignasius PP, Al-Wabli RI, Joe IH, Attia MI. Synthesis, spectroscopic investigations, DFT studies, molecular docking and antimicrobial potential of certain new indole-isatin molecular hybrids: Experimental and theoretical approaches. Journal of Molecular Structure. 2018;1153:333-345. Doi:10.1016/j.molstruc.2017.10.025.

33.   Wei Z-Y, Chi K-Q, Wanga K-S, Wub J, Liu L-P, Piao H-R. Design, synthesis, evaluation, and molecular docking of ursolic acid derivatives containing a nitrogen heterocycle as anti-inflammatory agents. Bioorganic and Medicinal Chemistry Letters. 2018;28:1797-1803. Doi:10.1016/j.bmcl.2018.04.021.

34.   Zhao YH, Abraham MH, Le J, Hersey A, Luscombe CN, Beck G, Sherborne B, Cooper Rate-limited steps of human oral absorption and QSAR studies. I. Pharmaceutical Research. 2002;19:1446-1457. Doi:10.1023/A:1020444330011

35.   Veber DF, Johnson SR, Cheng HY, Smith BR, Ward KW, Kopple KD. Molecular properties that influence the oral bioavailability of drug candidates. Journal of Medicinal Chemitry.

2002;45:2615-2623. Doi:10.1021/jm020017n

36.   Jain NK, Chourasia MK, Jain S, Jain SK. Development and characterization of engineered commensal bacteria for the delivery of enzymes. Indian Journal of Pharmaceutical Sciences. 2003;65:113-121.

SUPPLEMENTARY DATA

Synthesis of Novel Oxadiazole Derivatives, Molecular Properties Prediction and Molecular Docking Studies

Zühal KILIC-KURT*

Ankara University, Faculty of Pharmacy, Department of Pharmaceutical Chemistry, Tandogan, Ankara, Turkey

*Corresponding author. E-mail: zkurt@ankara.edu.tr

NMR and mass spectral analysis of the target compounds

2-(Benzo[b]thiophen-2-yl)-5-((4-methylpiperazin-1-yl)methyl)-1,3,4-oxadiazole (4a)
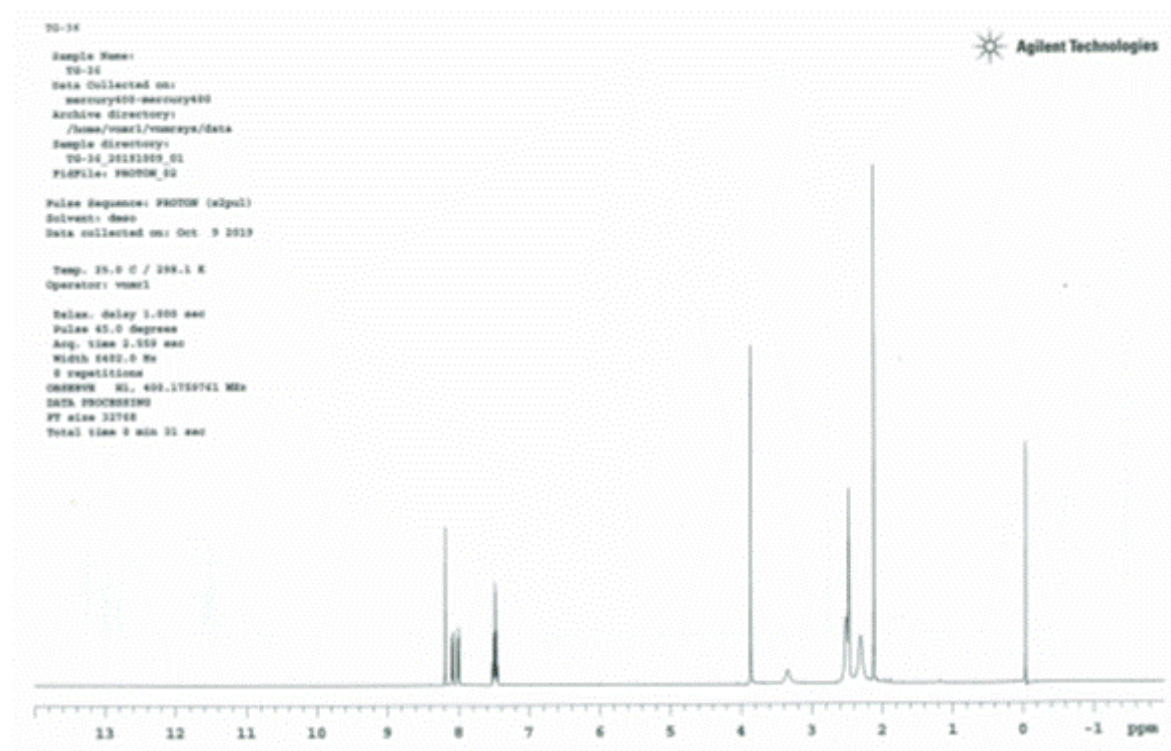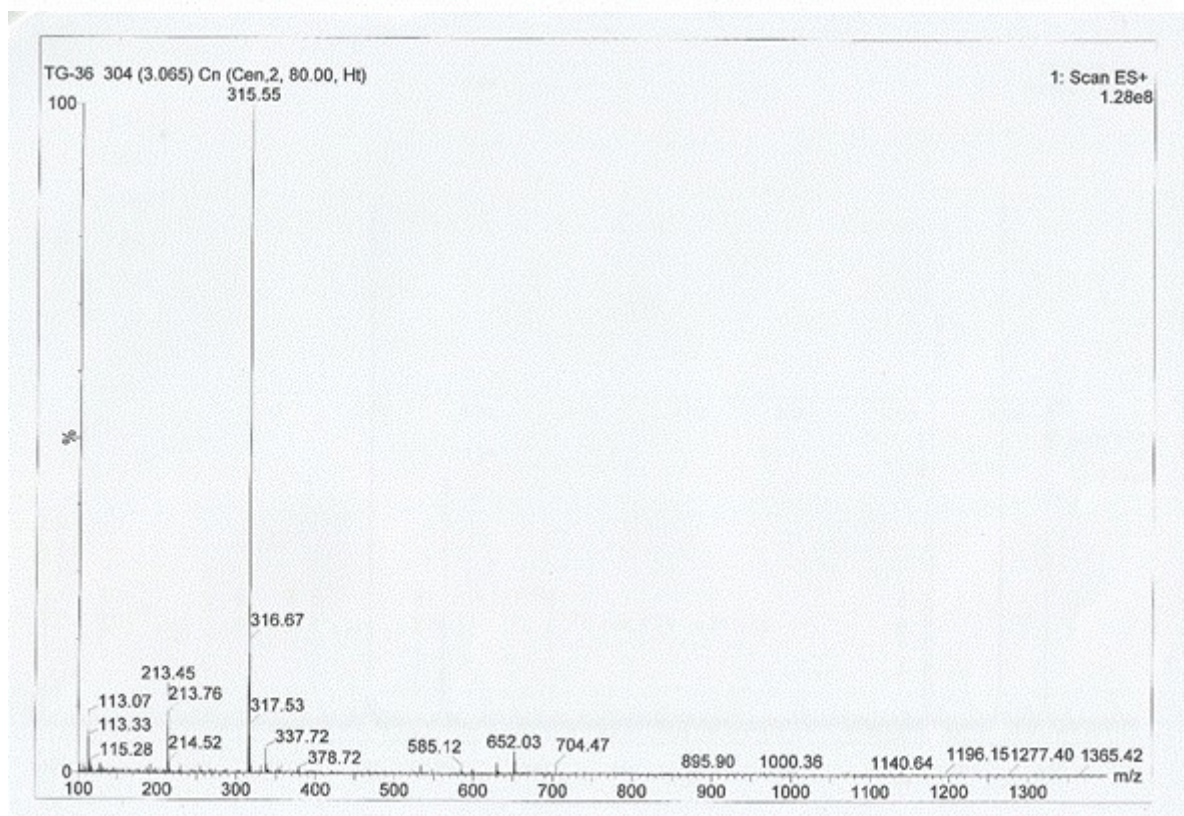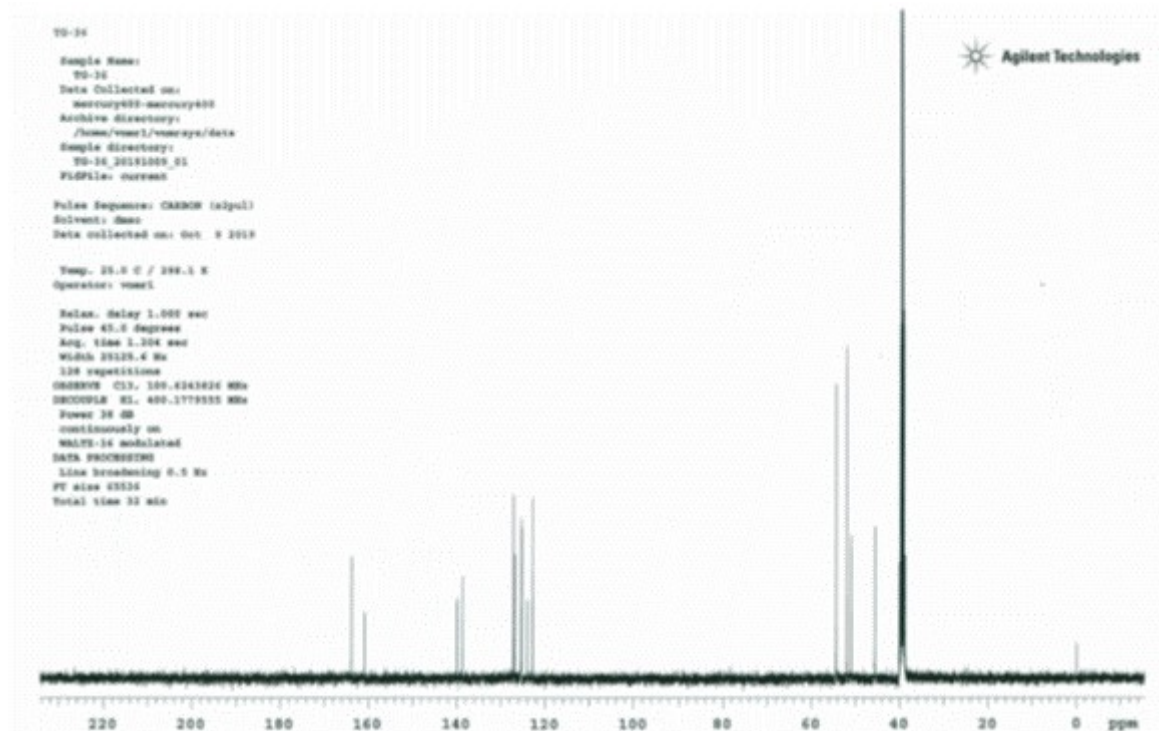
2-(Benzo[b]thiophen-2-yl)-5-((4-(3-methoxyphenyl)piperazin-1-yl)methyl)-1,3,4-oxadiazole (4b)

TG-38 256 (5.162)

1: Scan ES+
1.14e8
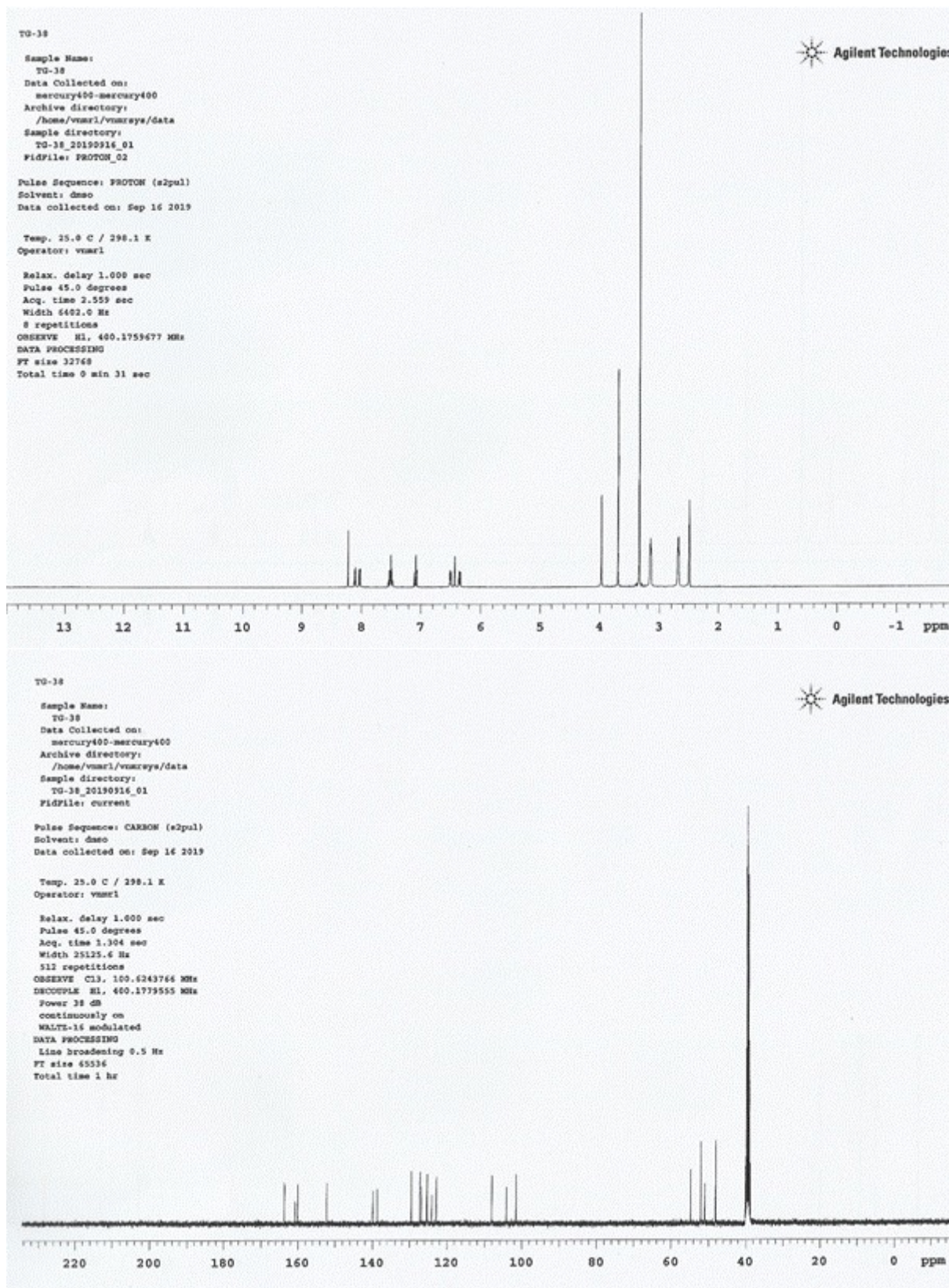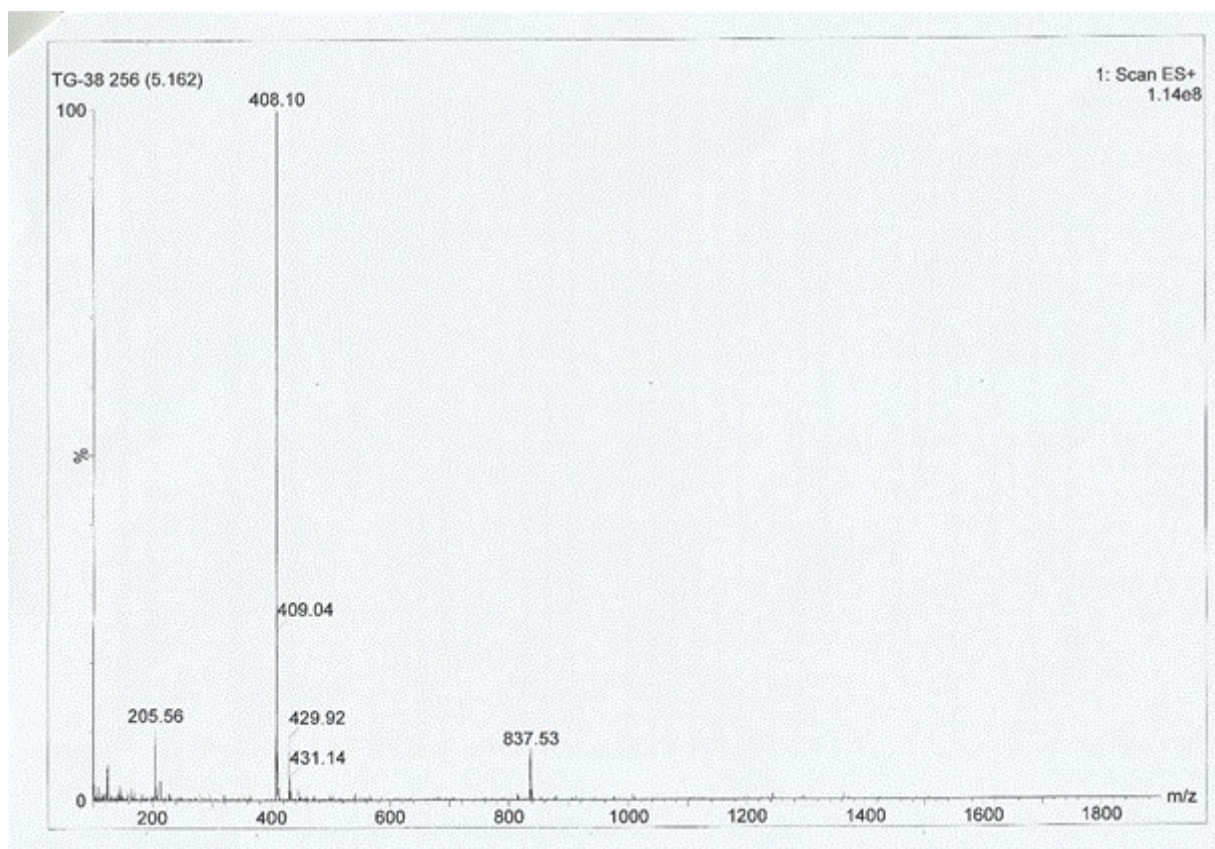
2-(Benzo[b]thiophen-2-yl)-5-((4-(2-fluorophenyl)piperazin-1-yl) methyl)-1,3,4-oxadiazole (4c)
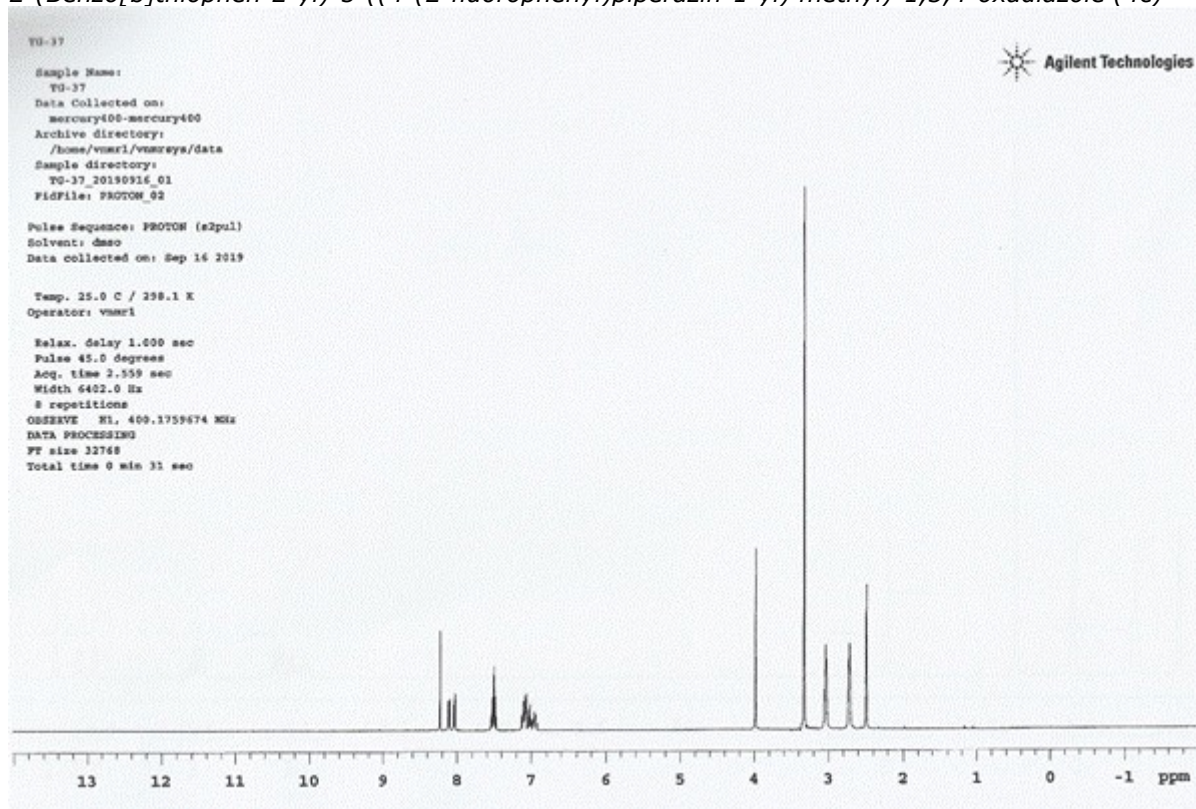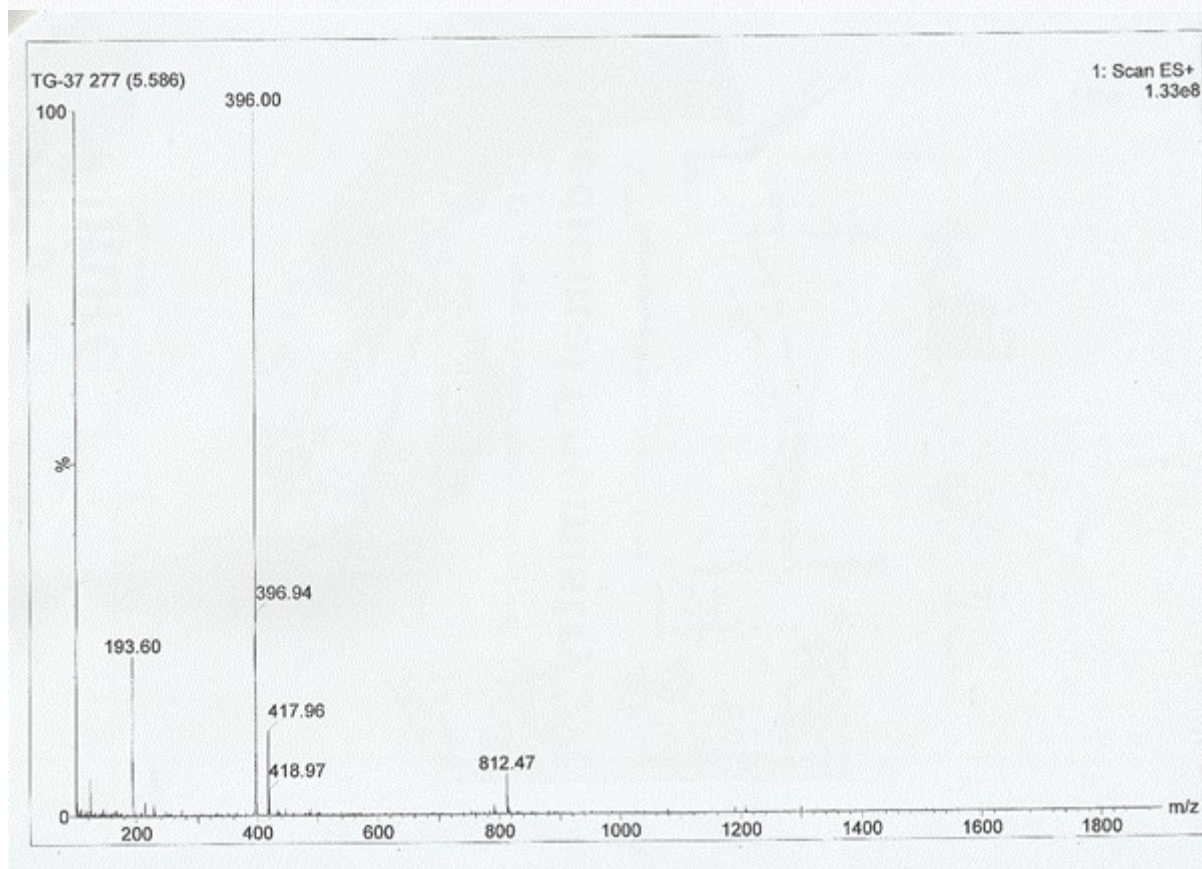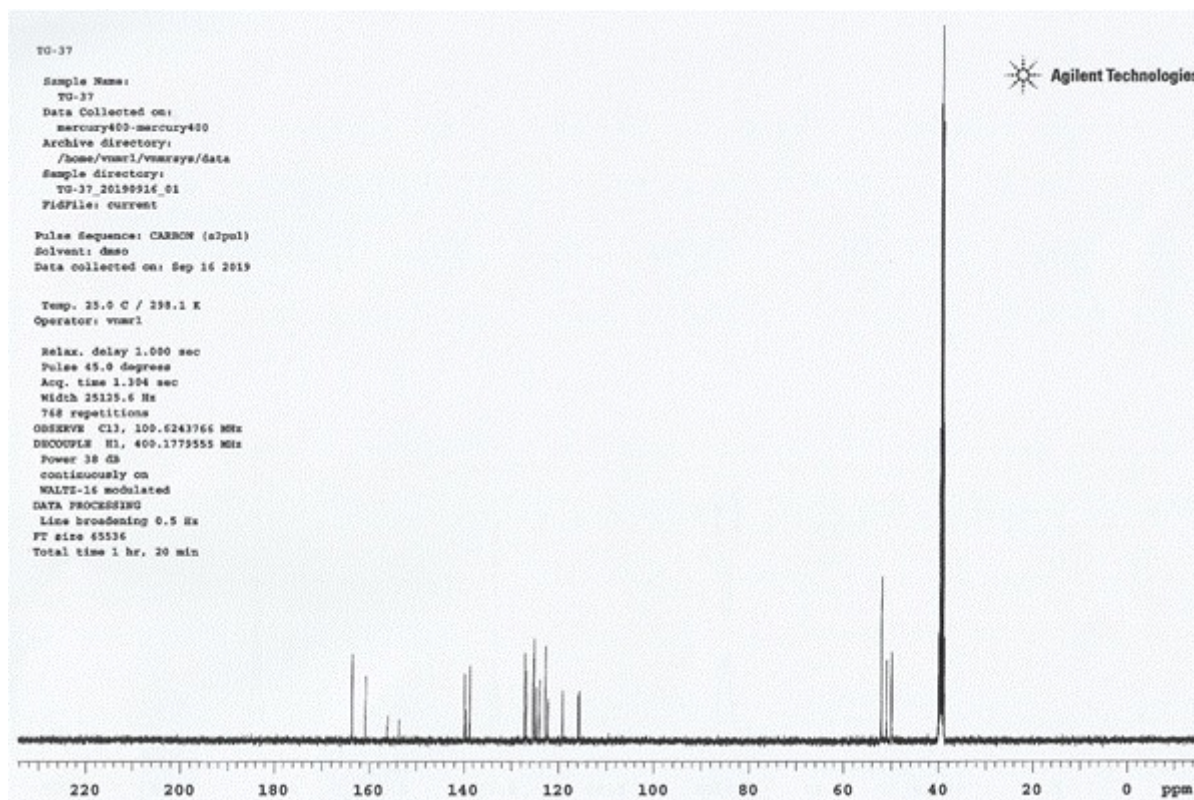
2-((4-Methylpiperazin-1-yl)methyl)-5-(thiophen-2-yl)-1,3,4-oxadiazole (8a)
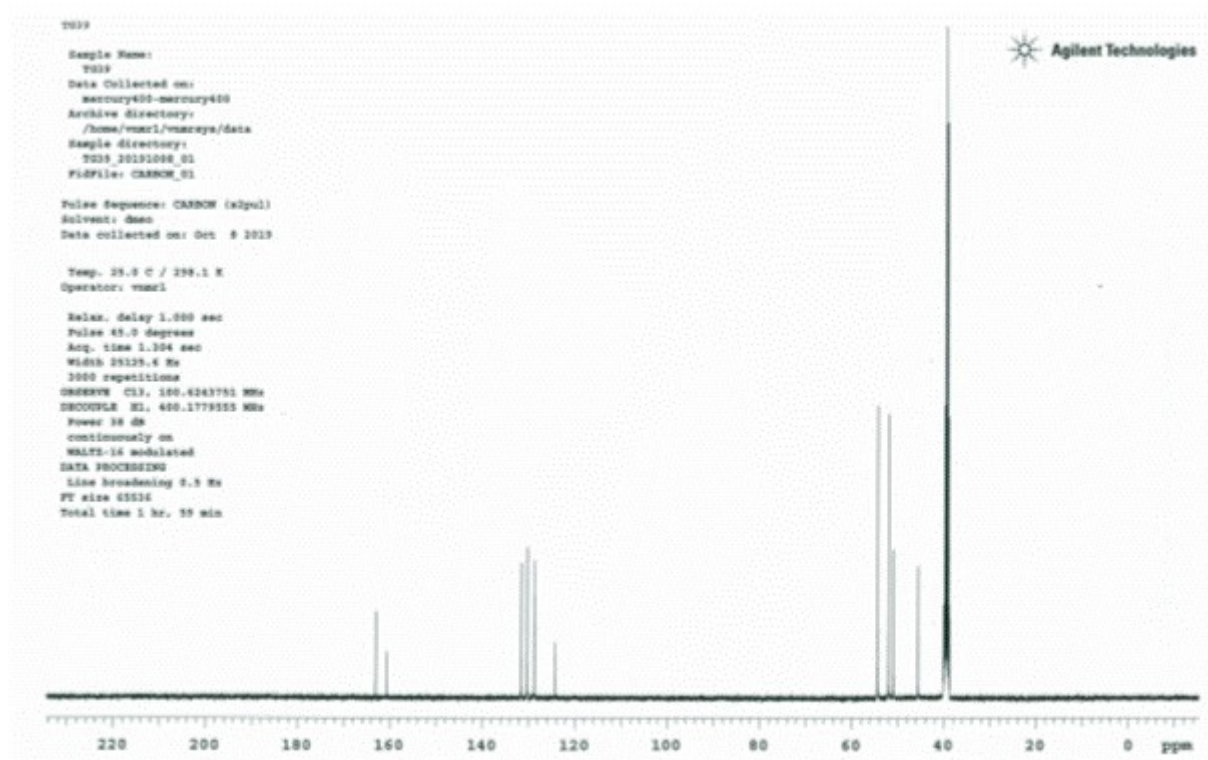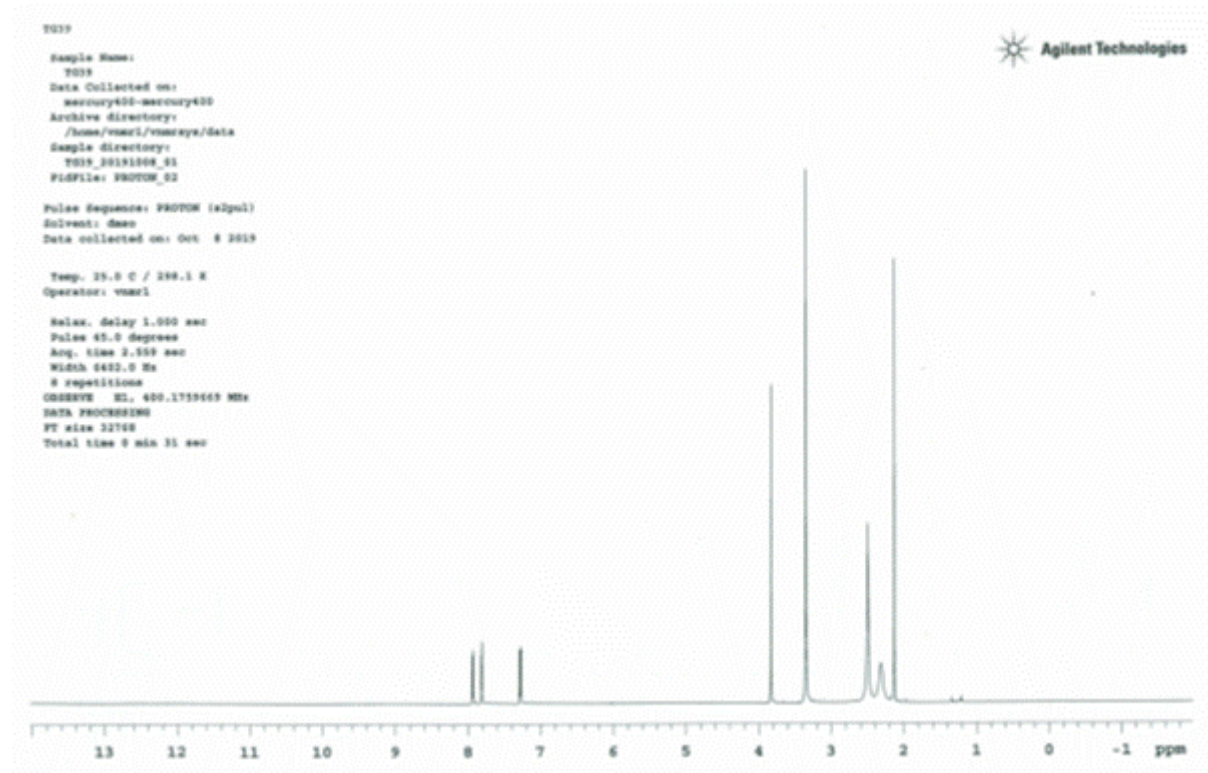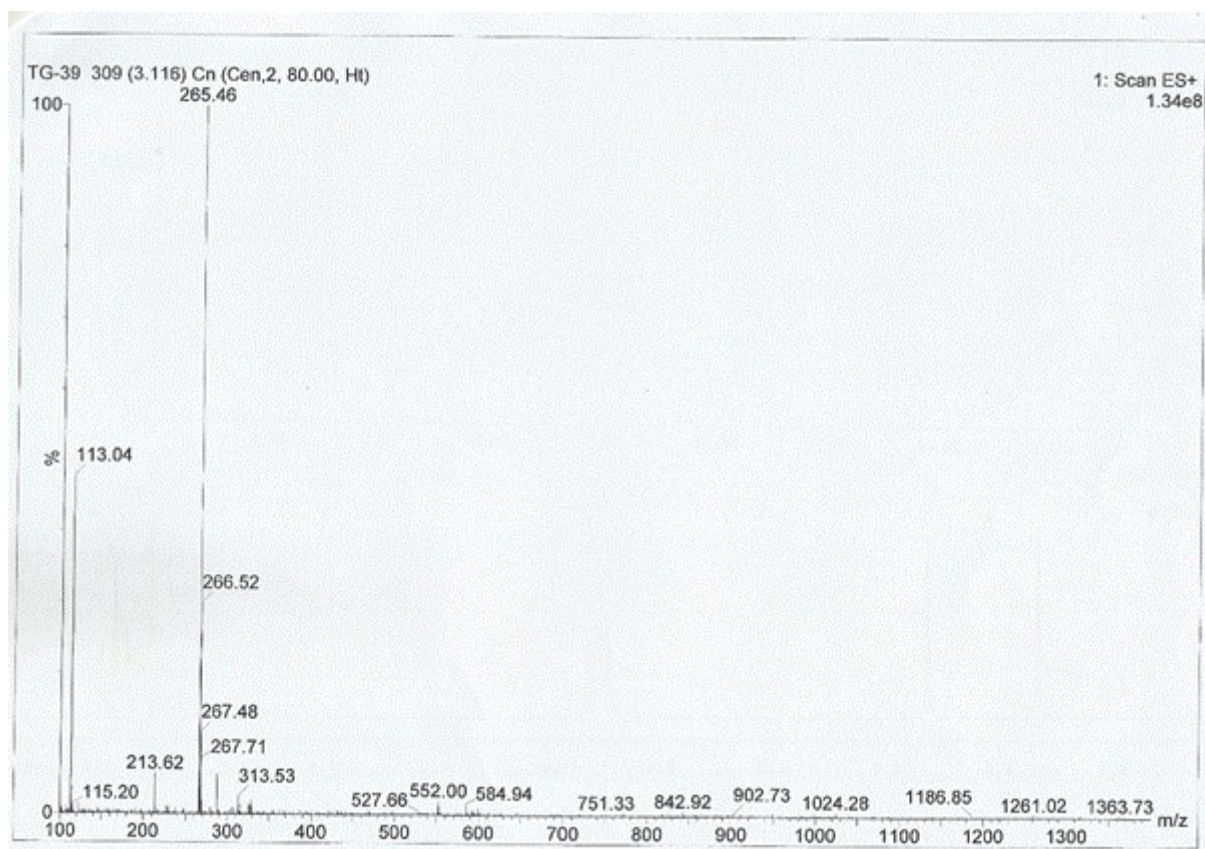
2-((4-(3-Methoxyphenyl)piperazin-1-yl)methyl)-5-(thiophen-2-yl)-1,3,4-oxadiazole (8b)
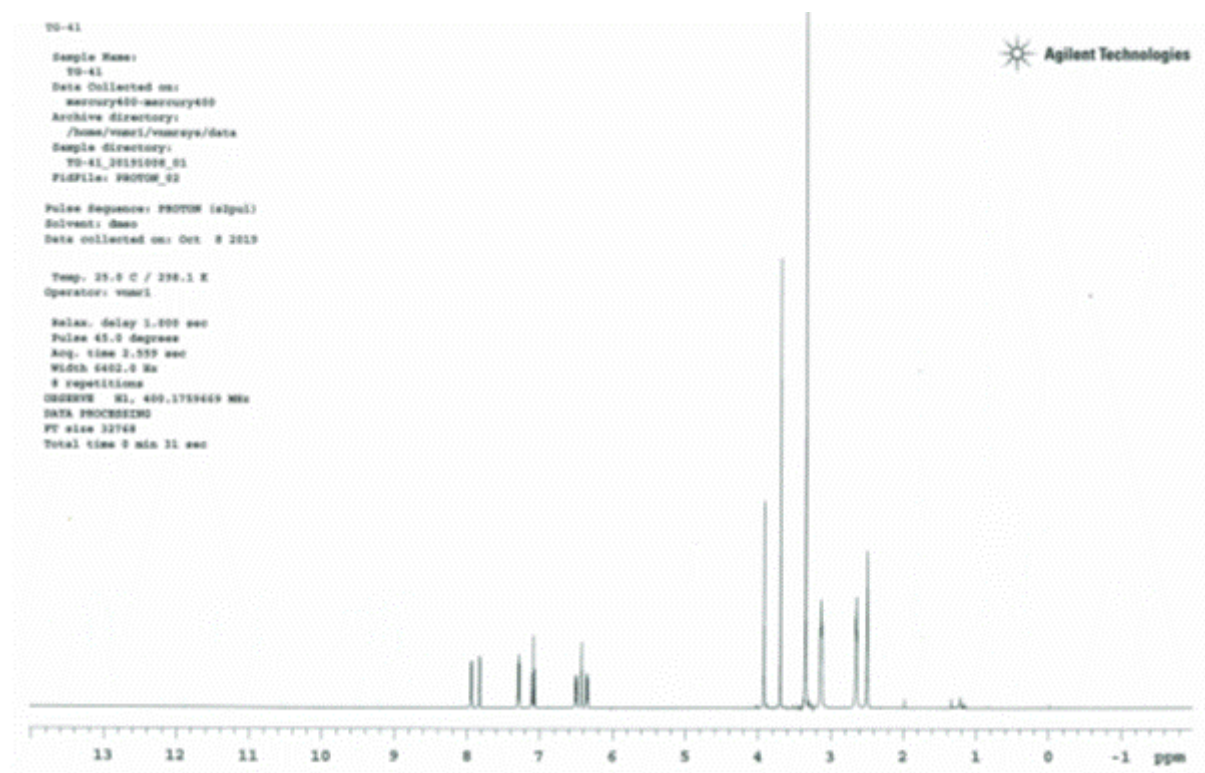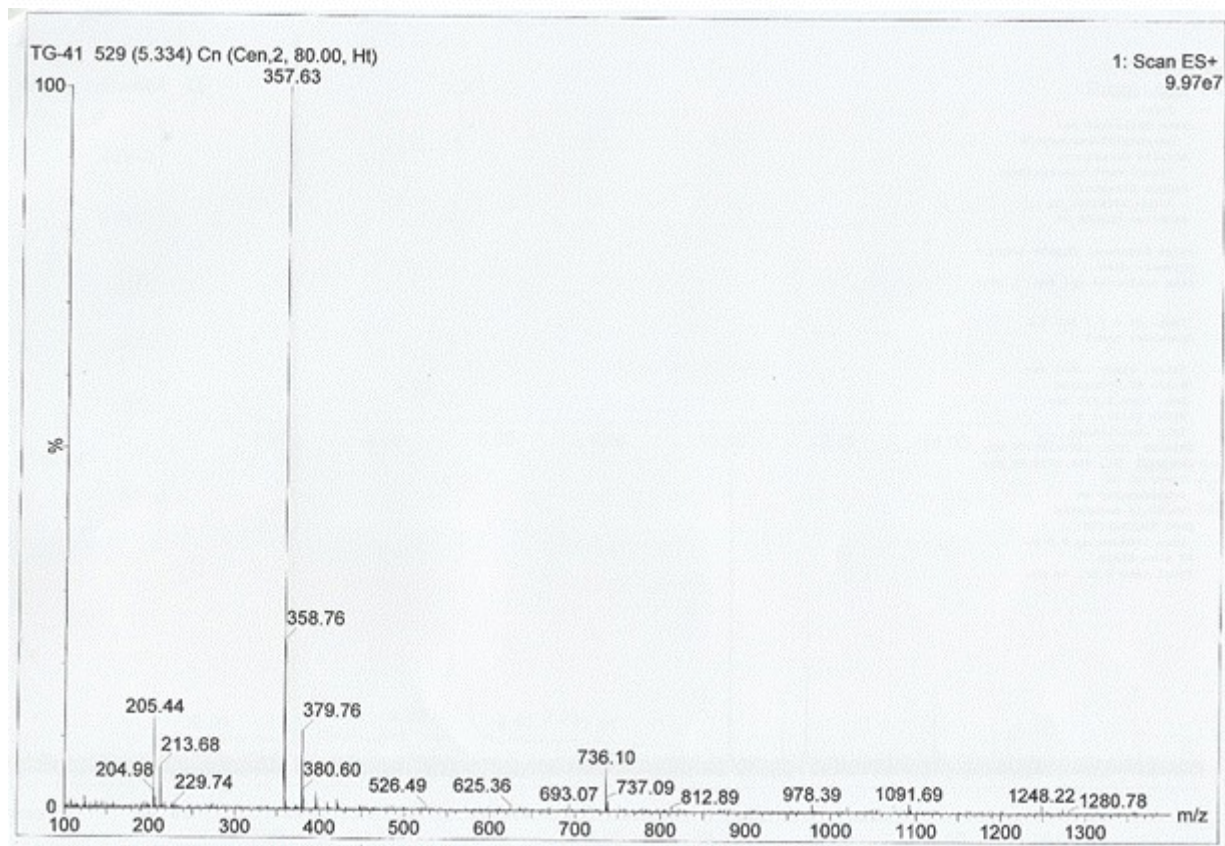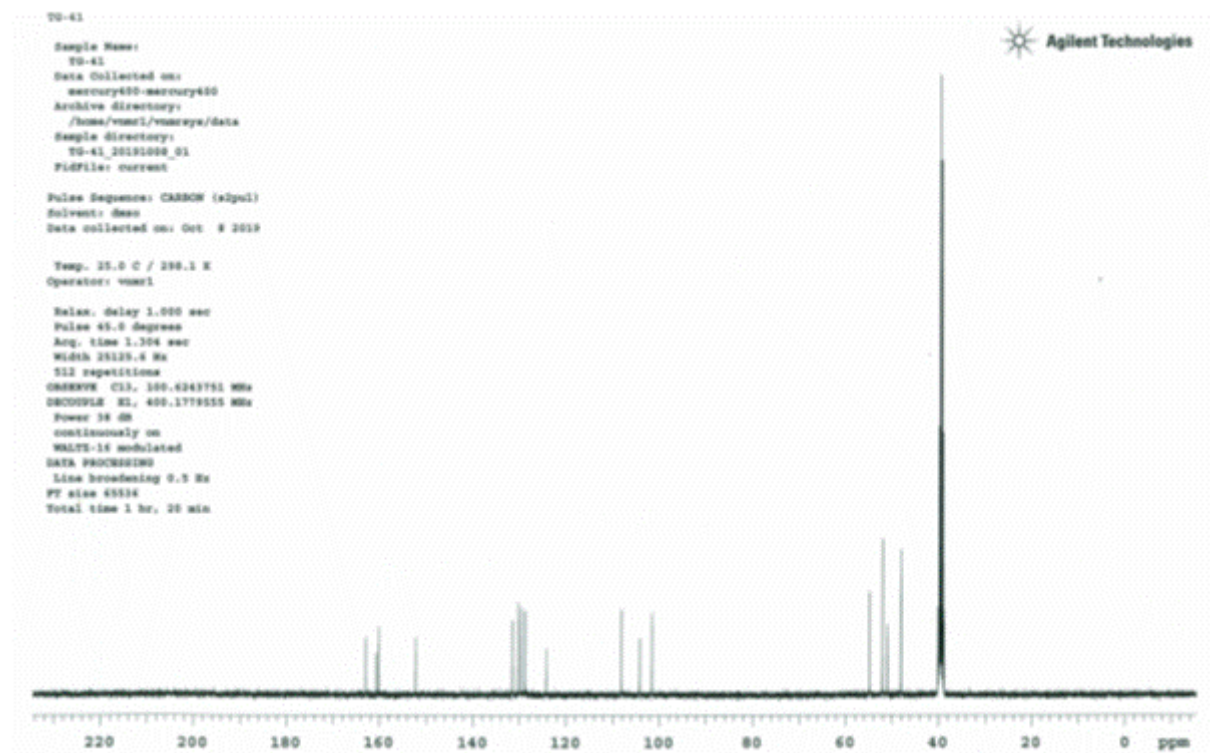
TG-41 529 (5.334) Cn (Cen,2, 80.00, Ht)   1: Scan ES+
357.63   9.97e7

2-((4-(2-Fluorophenyl)piperazin-1-yl)methyl)-5-(thiophen-2-yl)-1,3,4-oxadiazole(8c)

TG-40 557 (5.616) Cn (Cen,2, 80.00, Ht)
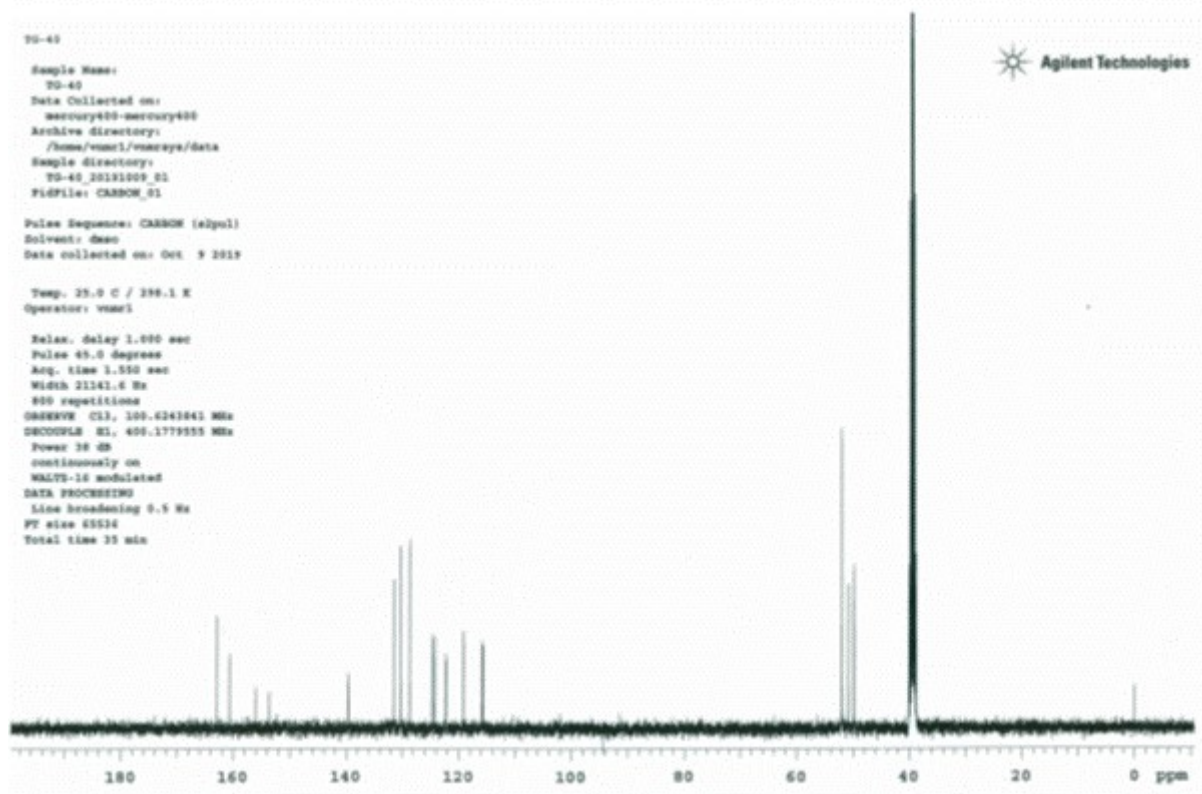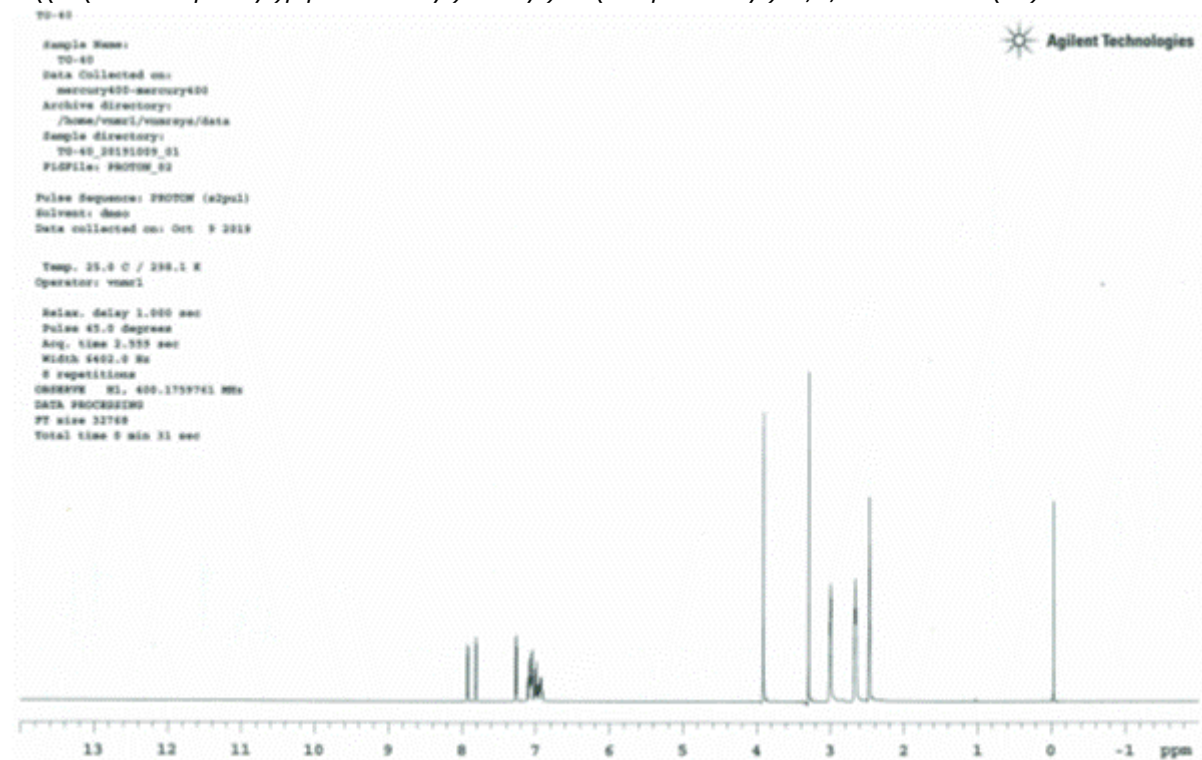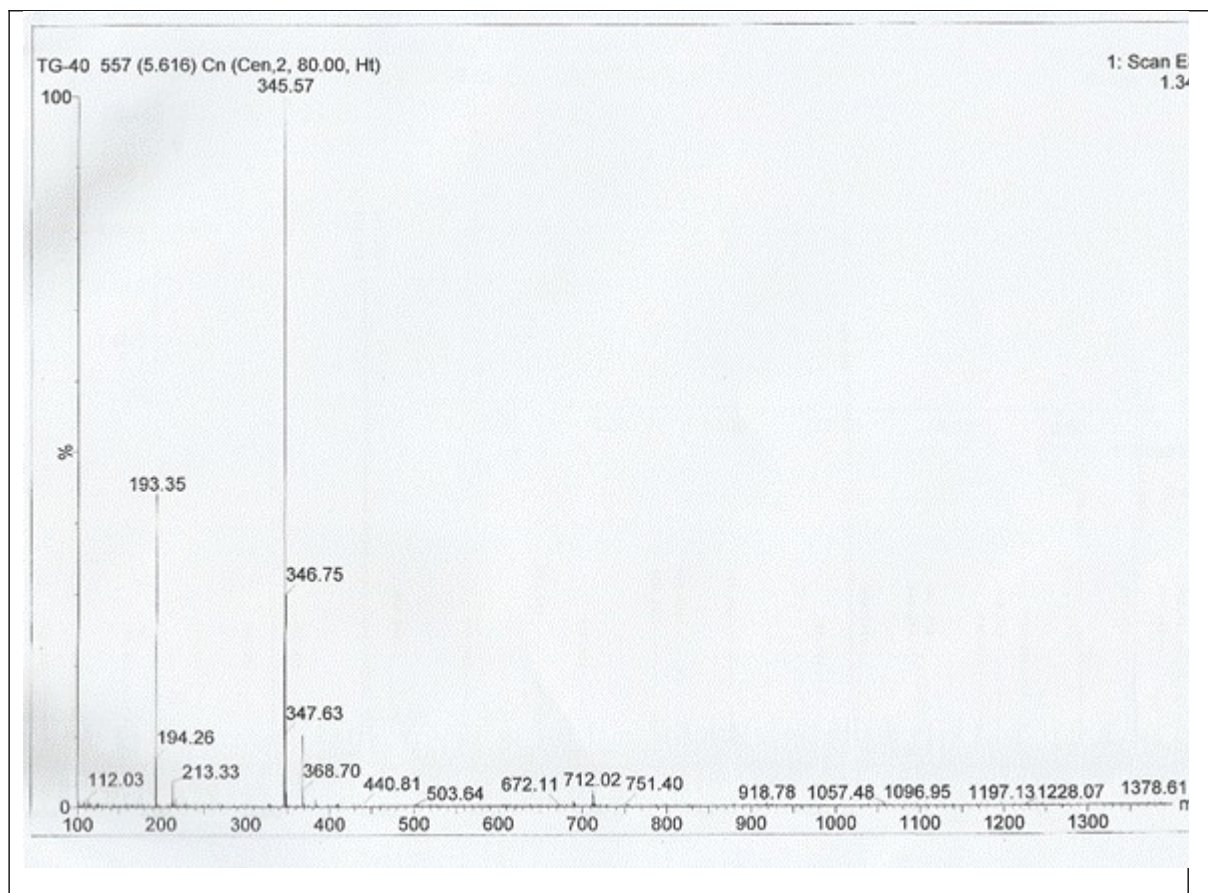
Docking results of compounds in active sites of EGFR and FAK kinases.

Figure S1. Superposition of native (blue) and docked ligand (magenta) of EGFR (1xkk, RMSD:1.42) (left). Superposition of native (blue) and docked ligand (magenta) of FAK (2etm, RMSD: 0.7) (right).

Table S1. The docking results of compounds with EGFR kinase

Compound	ΔGb[a] (kcal/mol)	Hydrogen bonds between atoms of compounds and amino acids	
		Atom of compound	**Amino acid**
4a	-9.0	-	-
4b	-9.4	O of oxadiazole	NH of Lys745
4c	-9.4	-	-
8a	-7.2	-	-
8b	-7.9	-	-
8c	-9.0	-	-
Native ligand		N-1 of quinazoline ring N-3 of quinazoline ring	NH of Met793 Thr854
Docked ligand	-11.2 RMSD[b]: 1.42	N-1 of quinazoline ring	NH of Met793

[a]Binding free energy, [b]root-mean-square deviation. −No interaction.

Table S2. The docking results of compounds with FAK kinase

Compound	ΔGb[a] (kcal/mol)	Hydrogen bonds between atoms of compounds and amino acids	
		Atom of compound	**Amino acid**
4a	-6.9	-	-
4b	-8.0	N3 of Oxadiazole	NH of Arg550
4c	-8.2	N3 of Oxadiazole N4 of Oxadiazole	NH of Arg550 OH of Ser568
8a	-6.1	N3 of Oxadiazole	NH of Gln432
8b	-7.6	N3 of Oxadiazole	NH of Gln432
8c	-7.6	N3 of Oxadiazole	NH of Gln432
Native ligand		N-3 of pyrimidine ring Exocyclic N	NH of Cys502 CO of Cys502
Docked ligand	-8.7 RMSD:0.7	N-3 of pyrimidine ring Exocyclic N	NH of Cys502 CO of Cys502

[a]Binding free energy, [b]root-mean-square deviation. −No interaction.

EQUILIBRIUM STUDIES ON Ni(II) and Cu(II) COMPLEXES with 4,7-DIMETHYL-1,10-PHENANTHROLINE and ACIDIC AMINO ACIDS in AQUEOUS SOLUTION

Duygu İNCİ¹* ✉ iD

¹ Department of Chemistry, Faculty of Arts and Sciences, Kocaeli University, 41380 Kocaeli, Turkey.

Abstract: The aim of this study is to determine the protonation constants of selected ligands {4,7-dimethyl-1,10-phenanthroline (4,7-dmphen), aspartic acid (asp), and glutamic acid (glu)} and their stability constants of (1:1) and (1:1:1) complexes with Ni(II) and Cu(II) ion have been determined I = 0.1 M KCl and T = 298.15 K. The protonation constants of the 4,7-dmphen, asp, and glu and their stability constants of the (1:1) and (1:1:1) Ni(II) and Cu(II) complexes have been computed performing BEST program. Moreover, SPE program has been used to determine the distribution of the species occurred in aqueous solution medium. The stability constants of the (1:1:1) Ni(II) and Cu(II) complexes are compared with those of the corresponding to the stability of the (1:1) Ni(II) and Cu(II) complexes with regard to Δlog K values.

INTRODUCTION

Research on the acidity constants of molecules and their stability constant of metal ions are increasingly becoming more significant and could give an idea about the role of metal ions in biological systems (1). Investigation on the stability of the ternary metal complexes could help against figuring out the driving forces which induced complex formation in biological systems (2-4). As known, the interactions of peptides, proteins, and enzymes with metal ions are of biochemical significance on the other hand they are yet to be entirely understood. For this reason, explanation of this situation in the biological systems could be likely by the determination of acidity constants of the molecules along with their stabilities of metal complexes (5).

4,7-Dimethyl-1,10-phenanthroline (4,7-dmphen) is a chelating agent and has structural features such as being a rigid planar and hydrophobic molecule.

Aspartic acid (asp) and glutamic acid (glu), being acidic amino acids, play significant roles in the enzyme active centers, along with in sustaining the solubility and ionic character of proteins. Many studies in the literature have focused on experimentally and computationally determining the protonation constant of ligands and their stability constants of the complexes formed with metal ions (6-8). Recently, we have reported that (1:1) and (1:1:1) palladium(II) and copper(II) complexes of amino acids, 1,10-phenanthroline, and derivatives in aqueous solution (9-14). As a continuation of these studies, the protonation constants of the 4,7-dmphen, asp and glu (Figure 1) and their stability constants of (1:1) and (1:1:1) Ni(II) and Cu(II) complexes have been computed by potentiometric titration methods (T = 298.15 K and I = 0.1 M KCl). The protonation constants of 4,7-dmphen, asp, and glu and their stability constants of the (1:1) and (1:1:1) Ni(II) and Cu(II) complexes have been computed with the BEST program (15) and the

species distribution of (1:1) and (1:1:1) Ni(II) and Cu(II) complexes in these systems was assessed using the SPE program (15). Thus, the tendency of Ni(II) and Cu(II) ions and 4,7-dmphen, asp, and glu

to form the (1:1) and (1:1:1) Ni(II) and Cu(II) complexes was identified by calculating their $\log_{10}K$ values.

a)

b)   **c)**
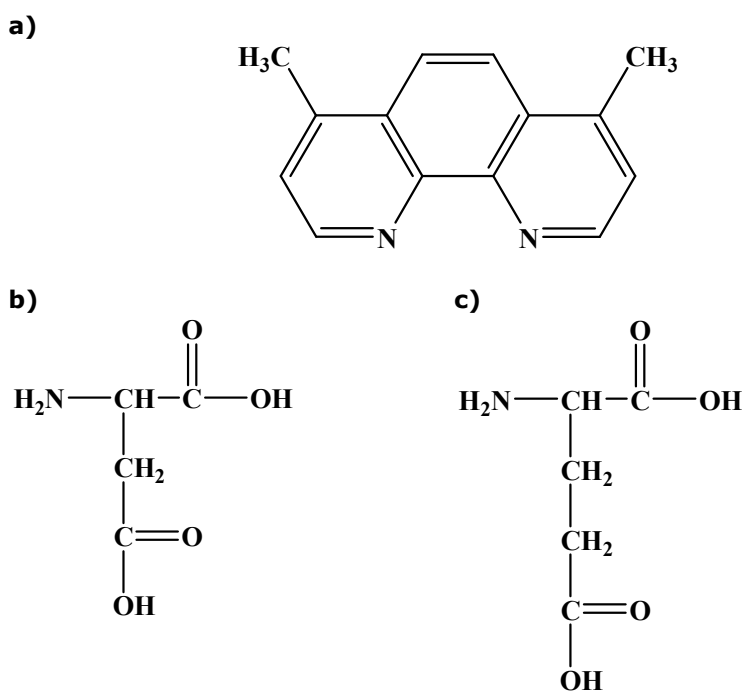
Figure 1. The structures of the ligands used in this study: **a)** 4,7-dimethyl-1,10-phenanthroline (4,7-dmphen) **b)** aspartic acid (asp) **c)** glutamic acid (glu)

EXPERIMENTAL

All ligands and Ni(II) chloride and Cu(II) chloride utilized in this experimental study were purchased from Sigma-Aldrich and the aqueous solution was treated with excess HCl to obtain protonated species. The all experimental details such as instruments, electrode calibration, and data

processing were similar to those described in our previous studies (9-14).

The stability constant of the (1:1) and (1:1:1) Ni(II) and Cu(II) complexes, β_{pqrs}, is defined by equations 1 and 2, where *p, q, r,* and *s* are the moles of M(II), 4,7-dmphen, asp/glu and proton (H), respectively, M_p(4,7-dmphen)$_q$(asp/glu)$_r$H$_s$ (charges are neglected for clarity).

$$\text{pM} + q(4,7\text{-dmphen}) + r(\text{asp/glu}) + s\text{H} \xrightleftharpoons{\beta_{\text{pqrs}}} \text{M}_p(4,7\text{-dmphen})_q(\text{asp/glu})_r\text{H}_s \tag{1}$$

$$\beta_{\text{pqrs}} = \frac{[\text{M}_p(4,7\text{-dmphen})_q(\text{asp/glu})_r\text{H}_s]}{[\text{M}]^p[4,7\text{-dmphen}]^q[\text{asp/glu}]^r[\text{H}]^s} \tag{2}$$

RESULTS AND DISCUSSION

Protonation constants of 4,7-dmphen/acidic amino acids

The protonation constant of 4,7-dmphen was previously reported our research group under the same conditions (10). The values of protonation constants for acidic amino acids (asp and glu) were also determined under the same experimental conditions. In these measurements, experimental results are compatible with the literature values

(Table 1), according to the differences such as in ionic strength, ionic medium, temperature, etc. (14, 16-17). Potentiometric titration curves of the 4,7-dmphen, asp, and glu are illustrated in Figures 2 and 3, where m is base moles added per mole of ligand. The BEST program, which could be one of the most useful computer programs for detection of the acidity constants of molecules and stability constant of the metal complexes from potentiometric data, was used to detect the protonation constants of the 4,7-dmphen, asp, and glu from potentiometric titration data (15).

Table 1. Protonation constants of the selected ligands.

Ligands	$\log_{10}K_1$	$\log_{10}K_2$	Ref
4,7-dmphen	5.89	0.61	(10), 5.95 (16), 5.94 (17)
Asp	9.64 ± 0.02*	3.73 ± 0.04*	9.66; 3.70 (14)
Glu	9.51 ± 0.02*	4.23 ± 0.03*	9.58; 4.16 (14)

*This work. Refs (10) and (14) are our previous studies.

(1:1) complexes of Ni(II) and Cu(II) with 4,7-dmphen/acidic amino acids

The titration curves of Ni(II):(4,7-dmphen) systems are illustrated in Figures 2 and 3. The observed decline in the (1:1) [Ni(4,7-dmphen)]$^{2+}$ curve in comparison to the 4,7-dmphen solution curve alone displays the formation of the (1:1) [Ni(4,7-dmphen)]$^{2+}$. Furthermore, the point of inflection

observed at m = 2.0 demonstrated that [Ni(4,7-dmphen)]$^{2+}$ was formed. [Ni(4,7-dmphen)(OH)]$^{+}$ starts to occur after m = 2.0 and is illustrated by the dashed line in Figures 2 and 3. The equilibrium in the Ni(II):(4,7-dmphen) systems could be defined by the following equations (the overall stability constant of the [Ni(4,7-dmphen)]$^{2+}$ is β, the stepwise stability constant is K).

$$\text{Ni}^{2+} + \text{H}_2(4,7\text{-dmphen})^{2+} \xrightleftharpoons{\quad} [\text{Ni}(4,7\text{-dmphen})]^{2+} + 2\text{H}^+ \tag{3}$$

$$[\text{Ni}(4,7\text{-dmphen})]^{2+} + \text{H}_2\text{O} \xrightleftharpoons{K_{[\text{Ni}(4,7\text{-dmphen})(\text{OH})]^+}} [\text{Ni}(4,7\text{-dmphen})(\text{OH})]^+ + \text{H}^+ \tag{4}$$
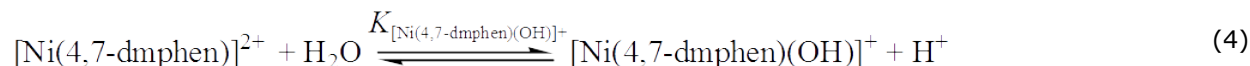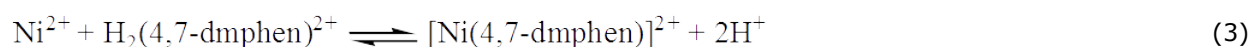
$$K_{[\text{Ni}(4,7\text{-dmphen})(\text{OH})]^+} = \frac{[\text{Ni}(4,7\text{-dmphen})(\text{OH})][\text{H}^+]}{[\text{Ni}(4,7\text{-dmphen})^{2+}]}$$

$$\text{Ni}^{2+} + 4,7\text{-dmphen} \xrightleftharpoons{\beta^{\text{Ni}}_{\text{Ni}(4,7\text{-dmphen})}} [\text{Ni}(4,7\text{-dmphen})]^{2+} \tag{5}$$
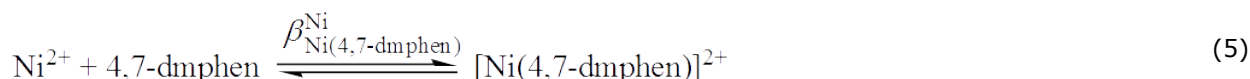
$$\beta^{\text{Ni}}_{\text{Ni}(4,7\text{-dmphen})} = \frac{[\text{Ni}(4,7\text{-dmphen})^{2+}]}{[\text{Ni}^{2+}][4,7\text{-dmphen}]}$$

The stability constant of the (1:1) [Ni(4,7-dmphen)]$^{2+}$ was computed using the BEST program (12). The experimental results were compared with the literature data and the stability constant of the binary [Ni(4,7-dmphen)]$^{2+}$ is given in Table 2. Potentimetric titrations of the Cu(II):(4,7-dmphen) system was previously reported our research group under the same conditions (10).

The potentimetric titrations of the (1:1) molar ratios M(II):(asp/glu) {M: Ni(II) or Cu(II)} systems were performed (Figures 2 and 3). The observed decline in the (1:1) [M(asp/glu)]$^+$ curve in comparison to

the alone acidic amino acids (asp and glu) solution curve demonstrates the formation of the (1:1) [M(asp/glu)]$^+$. This could be clarified by the release of proton from the coordinated acidic amino acids. The inflection point, at $m = 2.0$, demonstrated that the (1:1) [M(asp/glu)]$^+$ was formed. After formation of the [M(asp/glu)]$^+$, the titration curve shifting because of the formation of the [M(asp/glu)(OH)] complex. This complex starts to occur after $m = 2.0$ and is illustrated by the dashed line in Figures 2 and 3. The equilibria contained in the M(II):(asp/glu) systems could be defined by the following equations.

$$M^{2+} + H_2(asp/glu)^+ \rightleftharpoons [M(asp/glu)]^+ + 2H^+ \tag{6}$$

$$[M(asp/glu)]^+ + H_2O \xrightarrow{K^{[M(asp/glu)]-}_{[M(asp/glu)(OH)]}} [M(asp/glu)(OH)] + H^+ \tag{7}$$

$$K^{[M(asp/glu)]-}_{[M(asp/glu)(OH)]}{}^+ = \frac{[M(asp/glu)(OH)][H^+]}{[M(asp/glu)^+]}$$
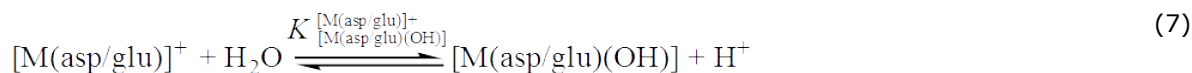
$$M^{2+} + (asp/glu)^- \xrightarrow{\beta^M_{M(asp/glu)}} [M(asp/glu)]^+ \tag{8}$$

$$\beta^M_{M(asp/glu)} = \frac{[M(asp/glu)^+]}{[M^{2+}][(asp/glu)^-]}$$

Taking the likely species into consideration, the stability constants of the (1:1) [M(II):(asp/glu)]$^+$ complexes were computed performing the BEST program (15). Table 2 compares the stability

constant of the (1:1) [M(II):(asp/glu)]$^+$ with literature displaying a good agreements [14,16, 18-20].
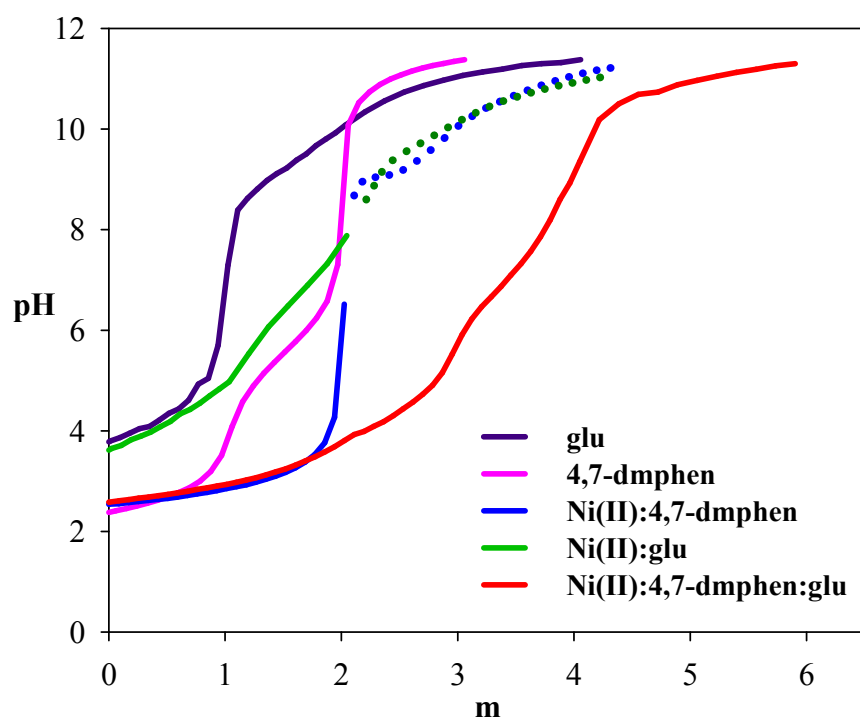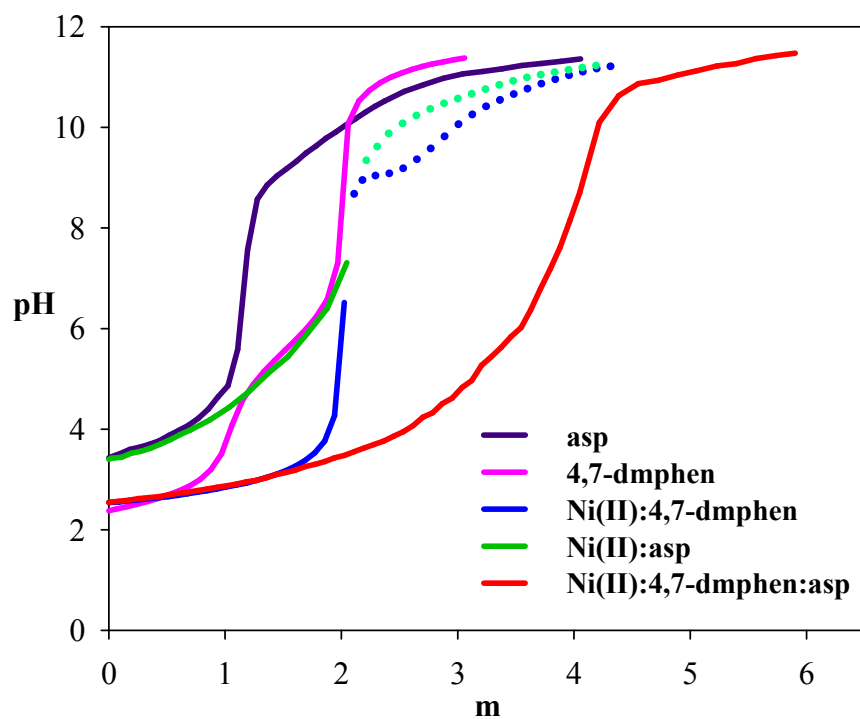
Figure 2. Potentiometric titration curves of the Ni(II):(4,7-dmphen):(asp) and Ni(II):(4,7-dmphen):(glu) systems.
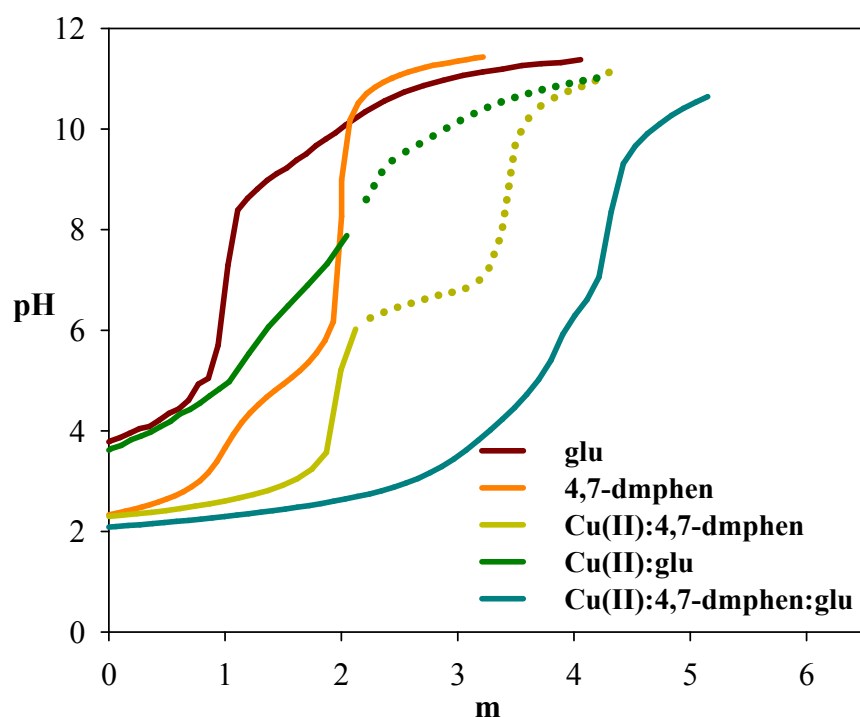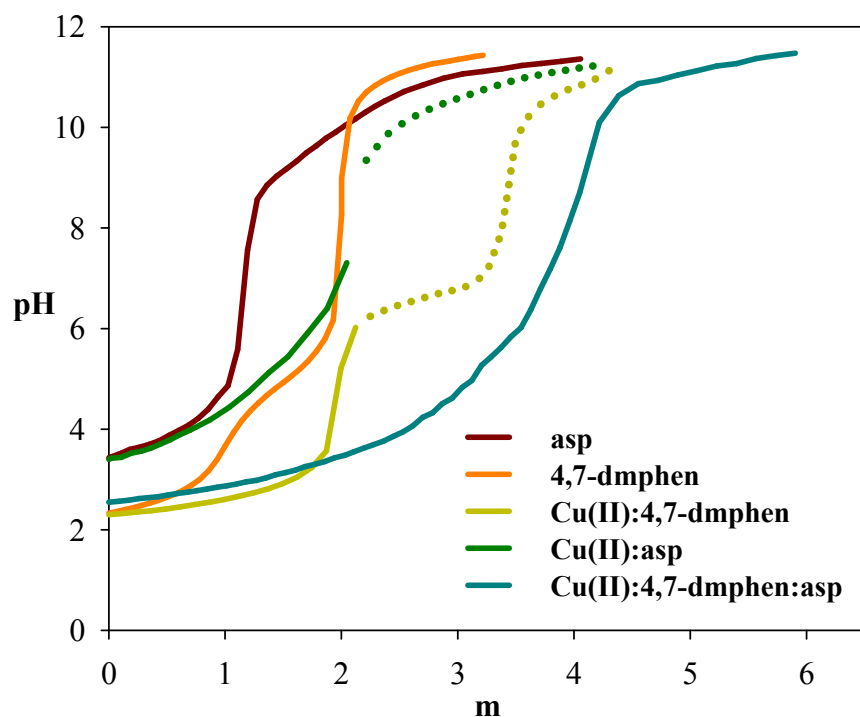
Figure 3. Potentiometric titration curves of the Cu(II):(4,7-dmphen):(asp) and Cu(II):(4,7-dmphen): (asp)systems.

Table 2. Stepwise and overall stability constants of the binary Ni(II) and Cu(II) complexes

Metal	Ligands	$\log_{10}\beta$ ML	Refs
Ni(II)	4,7-dmphen	6.64 ± 0.04*	8.44 (16)
	Asp	7.28 ± 0.04*	7.16 (18), 7.20 (19), 7.35 (14)
	Glu	6.02 ± 0.02*	5.90 (20), 5.95 (19), 6.09 (14)
Cu(II)	4,7-dmphen	7.57	(10), 8.76 (16)
	Asp	8.89 ± 0.03*	8.92 (14), 8.83 (19)
	Glu	8.31 ± 0.04*	8.22 (14), 8.50 (19)

*This work. Ref (10) and (14) is in our previous studies.

(1:1:1) complexes of Ni(II) and Cu(II) with 4,7-dmphen/acidic amino acids

The potentiometric titration curves of the M(II): (4,7-dmphen):(asp/glu) systems were given in Figures 2 and 3. In the Ni(II):(4,7-dmphen):(asp/glu) systems, two inflection points were seen at $m = 3.0$ and $m = 4.0$. It was observed that the 4,7-dmphen and acidic amino acids had a buffer region at a lower pH than [Ni(4,7-dmphen)(asp/glu)]$^+$ titration curve and a total of four protons were titrated. This experimental result demonstrates that the 4,7-dmphen and acidic amino acids are bound to the Ni(II) ion in the aqueous solution. Additionally, the potentiometric titration curve of [Ni(4,7-dmphen) (asp/glu)]$^+$ overlaps with binary [Ni(4,7-dmphen)]$^{2+}$ curve in the $m = 0.0$-2.0 buffer region. In this buffer region, firstly, [Ni(4,7-dmphen)]$^{2+}$ is formed. This is followed by the ligation of acidic amino acids occupying the remaining coordination positions. When overlooking at the potentiometric titration curves of Cu(II):(4,7-dmphen):(asp/glu) systems, it was observed that the 4,7-dmphen and acidic amino acids had a buffer region at a lower pH than [Cu(4,7-dmphen)(asp/glu)]$^+$ titration curve and a total of four protons were titrated. This experimental result demonstrates that the 4,7-dmphen, asp, and glu are bound to the Cu(II) ion in aqueous solution. The equilibria contained in the M(II):(4,7-dmphen):(asp/glu) systems could be defined by the following equations.

$$M^{2+} + H_2(4,7\text{-dmphen})^{2+} + H_2(asp/glu)^+ \rightleftharpoons [M(4,7\text{-dmphen})(asp/glu)]^+ + 4H^+ \tag{9}$$
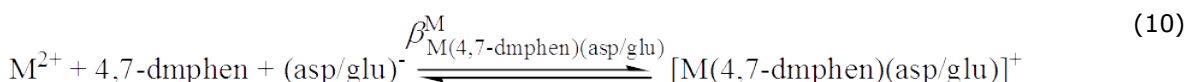
$$M^{2+} + 4,7\text{-dmphen} + (asp/glu)^- \xrightleftharpoons{\beta^M_{M(4,7\text{-dmphen})(asp/glu)}} [M(4,7\text{-dmphen})(asp/glu)]^+ \tag{10}$$

$$\beta^M_{M(4,7\text{-dmphen})(asp/glu)} = \frac{[M(4,7\text{-dmphen})(asp/glu)^+]}{[M^{2+}][4,7\text{-dmphen}][(asp/glu)^-]}$$

The obtained protonation constants of the 4,7-dmphen and acidic amino acids, as well as their the stability constants with metal(II) in the (1:1) systems were performed the BEST program (15). These experimental results are given in Table 3.

The relative stability of the (1:1:1) complexes compared to those of the corresponding (1:1) species might be assessed in distinct ways. In most cases $\Delta\log_{10}K$ values are employed (9-11). The $\Delta\log_{10}K$ values have been computed with the Equation 11 and given in Table 3. An example is given for M(II):(4,7-dmphen):(asp/glu) system.

$$\Delta\log_{10}K = \log_{10}K^{M(4,7\text{-dmphen})}_{M(4,7\text{-dmphen})(asp/glu)} - \log_{10}K^M_{M(asp/glu)} = \log_{10}K^{M(asp/glu)}_{M(4,7\text{-dmphen})(asp/leu)} - \log_{10}K^M_{M(4,7\text{-dmphen})} \tag{11}$$

For experimental systems in this study, the $\Delta\log_{10}K$ values were found negative in [Ni(4,7-dmphen)(asp/glu)]$^+$ complexes (Table 3). The negative $\Delta\log_{10}K$ values of this results demonstrates that the (1:1:1) Ni(II) complexes are less stable than the (1:1) Ni(II) complexes. These values of $\Delta\log_{10}K$ do not mean that the (1:1:1) Ni(II) complexes are not formed. It could be owing to the higher stability of its (1:1) Ni(II) complexes, with a reduced number of geometric structure, coordination sites, steric hindrance (21-22), electrostatic interaction (23-24), different bond type (25). The steric hindrance is one

of the most remarkable parameter due to the fact that the entry of the secondary ligands (asp and glu) faces steric hindrance because of bigger size of the [Ni(4,7-dmphen)(asp/glu)]$^+$ complexes as compared to aqua ion, which restrict the entry of the secondary ligands in the coordination sphere of the Ni(II) ion and thereof declines the stability of the (1:1:1) [Ni(4,7-dmphen)(asp/glu)]$^+$ complexes. The $\Delta\log_{10}K$ values of [Cu(4,7-dmphen)(asp/glu)]$^+$ complexes were found positive (Table 3). The positive $\Delta\log_{10}K$ values of [Cu(4,7-dmphen)(asp/glu)]$^+$ complexes demonstrate that the (1:1:1) Cu(II) complexes are more stable than the (1:1) Cu(II) complexes.

Table 3. Stepwise and overall stability constants of the ternary Ni(II) and Cu(II) complexes.

Metal	Ligand	Amino acids	$\log_{10} \beta_{MAB}$	$\log_{10} K_{MAB}^{MA}$	$\log_{10} K_{MAB}^{MB}$	$\Delta\log_{10}K$
Ni(II)	4,7-dmphen	Asp	13.98 ± 0.02*	7.34	6.70	-0.06
		Glu	12.82 ± 0.03*	6.18	6.80	-0.16
Cu(II)		Asp	15.44 ± 0.03*	7.87	6.55	1.02
		Glu	15.01 ± 0.04*	7.44	6.70	0.87

*This work.

Distribution diagrams of the (1:1:1) complexes of Ni(II) and Cu(II) with 4,7-dmphen/acidic amino acids

Species distribution diagrams have been utilized to define the types of equilibria. Stability of the (1:1:1) Ni(II) and Cu(II) complexes have been computed performing the SPE program (15). The species distribution diagrams of the (1:1:1) Ni(II) and Cu(II) complexes are illustrated in Figures 4-7.

The species distribution curves of Ni(II):(4,7-dmphen):(asp/glu) systems are illustrated in Figures 4 and 5. The [Ni(4,7-dmphen)(asp/glu)]$^+$ begins to occur at pH = 4.0 and, with rising pH, its concentration reaches 97.0% at pH = 8.0. H(asp/glu), H$_2$(asp/glu)$^+$, H(4,7-dmphen)$^+$, H$_2$(4,7-dmphen)$^{2+}$, Ni^{2+}, [Ni(4,7-dmphen)]$^{2+}$ at pH = 2.0; [Ni(4,7-dmphen)]$^{2+}$ and H(asp/glu) at pH = 4.0; [Ni(4,7-dmphen)(asp/glu)]$^+$, [Ni(4,7-dmphen)]$^{2+}$, H(asp/glu) at pH = 6.0; and [Ni(4,7-dmphen)(asp/glu)]$^+$ at pH = 8.0 are the predominant species.

The species distribution curves for Cu(II):(4,7-dmphen):(asp/glu) systems are displayed in Figures 6 and 7. In the Cu(II):(4,7-dmphen):(asp) and Cu(II):(4,7-dmphen):(glu) systems at pH 2.0, the concentrations of [Cu(4,7-dmphen)]$^{2+}$ are ca. 76.52 and 71.31 %, respectively. [Cu(4,7-dmphen)(asp/glu)]$^+$ begins to occur at pH = 5.0 and with rising pH, its concentration reaches $\sim$ 98.0 % at pH = $\sim$6.0-10.0. [Cu(4,7-dmphen)(asp/glu)]$^+$ is the predominant species.

a)
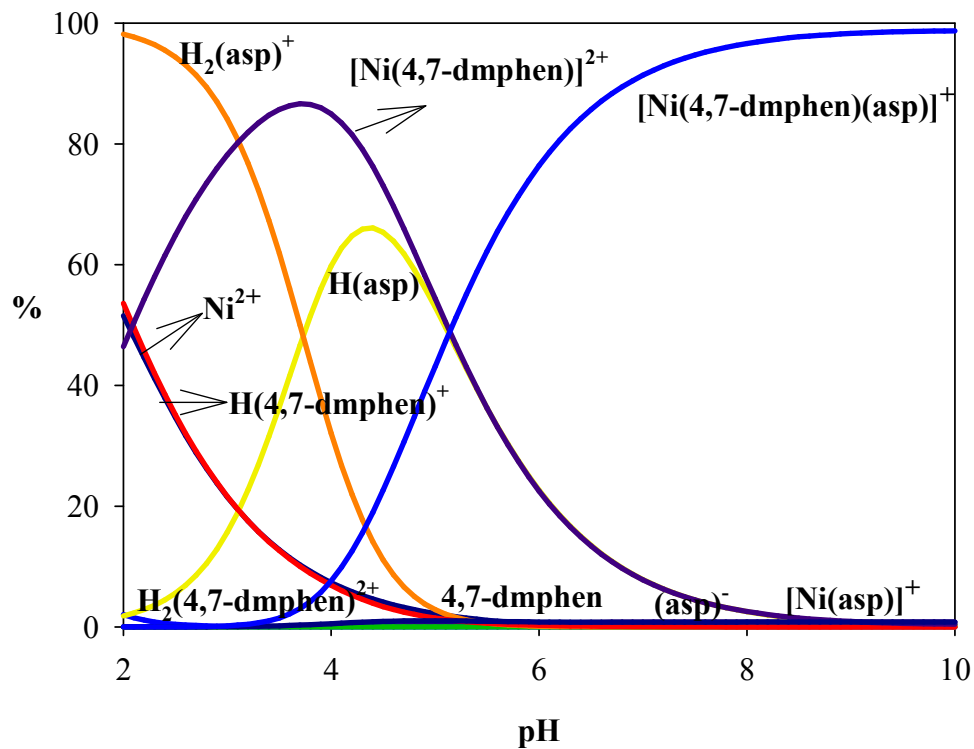
b)
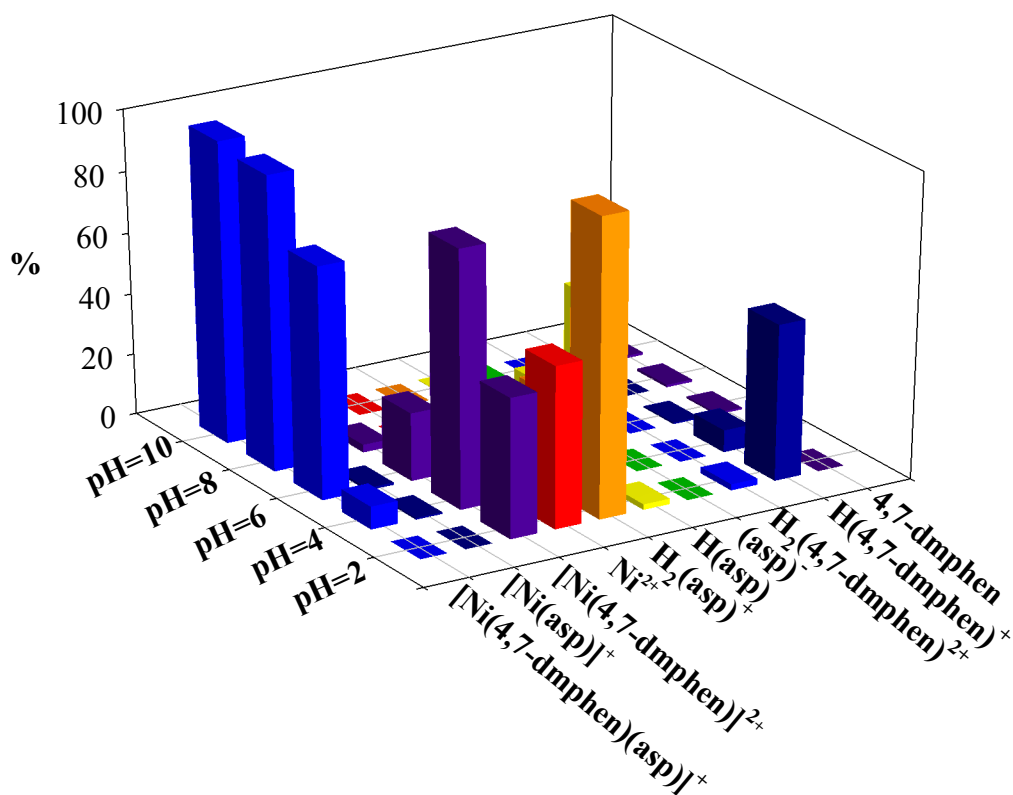
Figure 4. (a) Distribution of species as a function of pH in Ni(II):(4,7-dmphen):(asp) system **(b)** A bar chart of the percentage distribution of the species in aqueous solutions.

a)
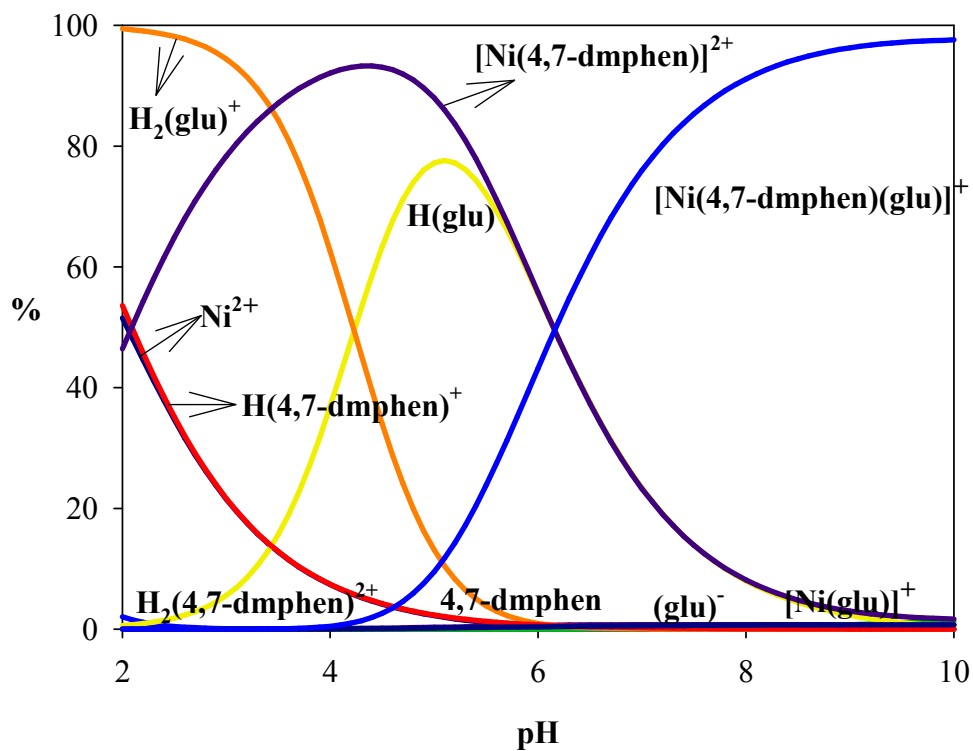
b)
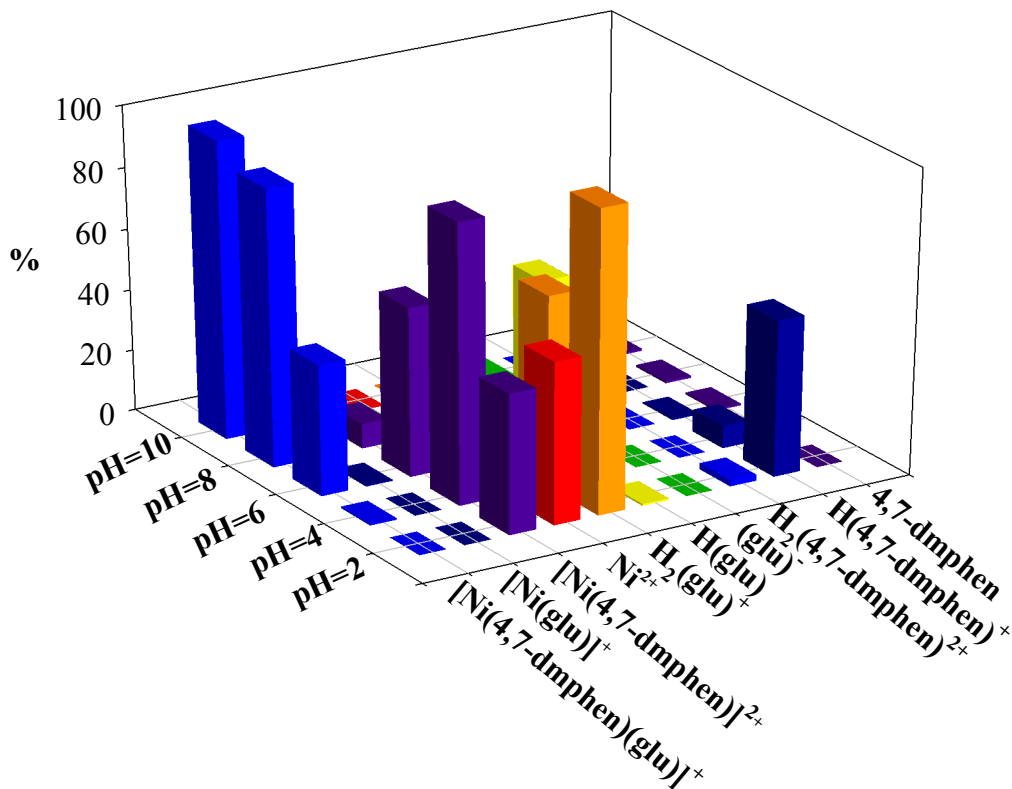
Figure 5. (a) Distribution of species as a function of pH in Ni(II):(4,7-dmphen):(glu) system **(b)** A bar chart of the percentage distribution of the species in aqueous solutions.

a)
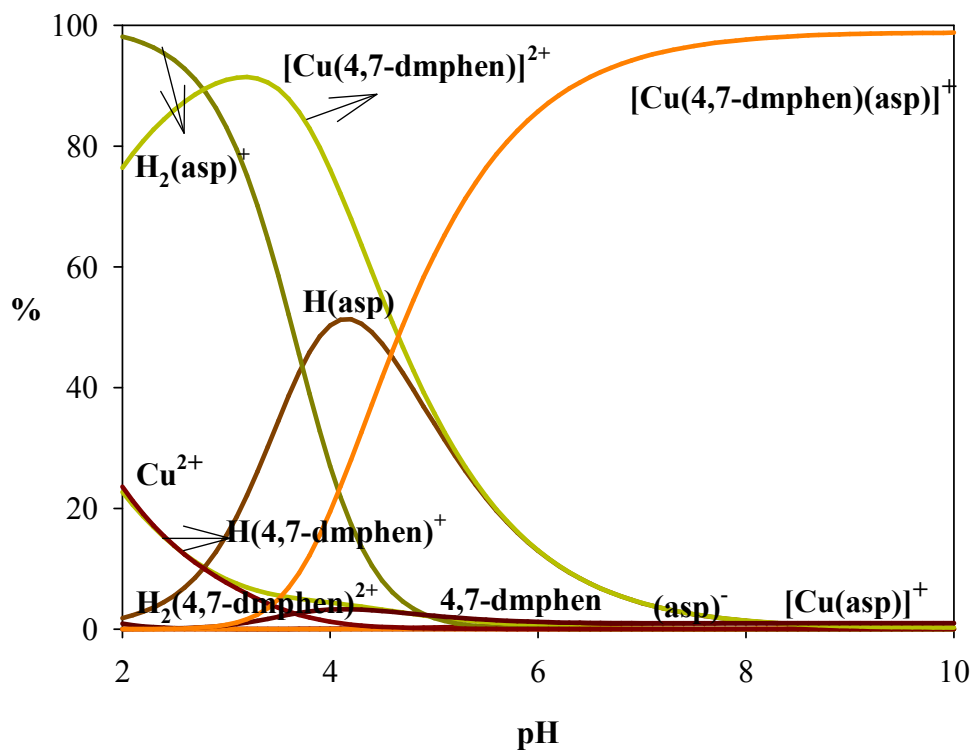
b)
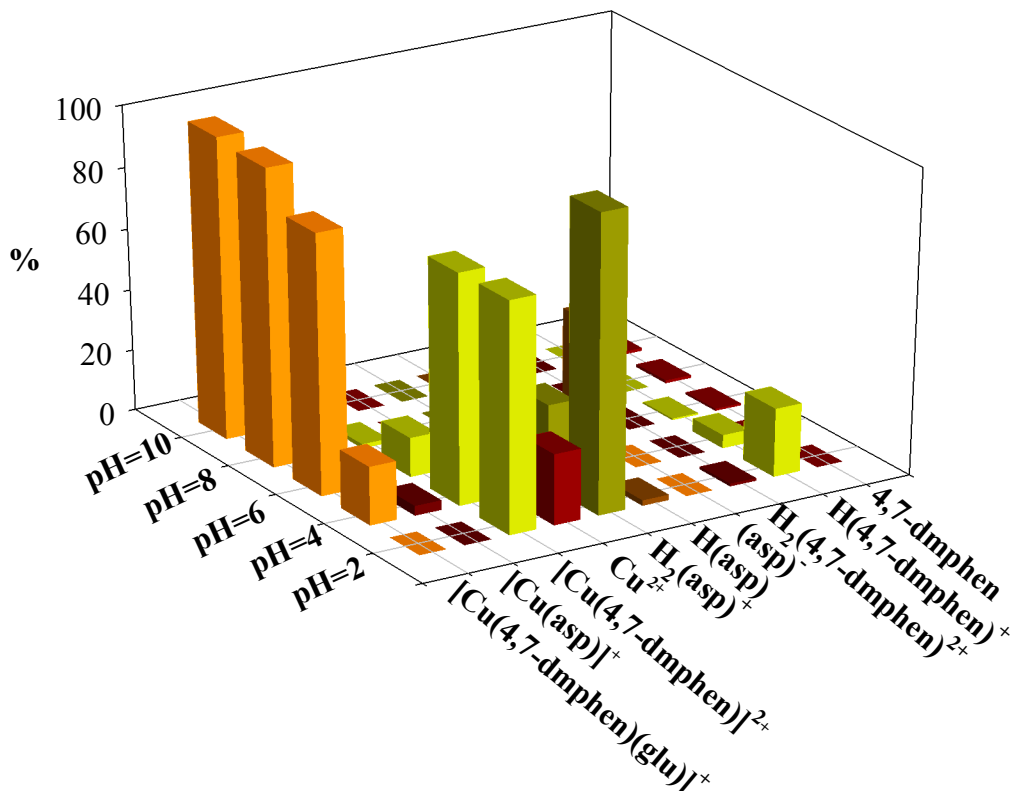
Figure 6. (a) Distribution of species as a function of pH in Cu(II):(4,7-dmphen):(asp) system **(b)** A bar chart of the percentage distribution of the species in aqueous solutions.

a)
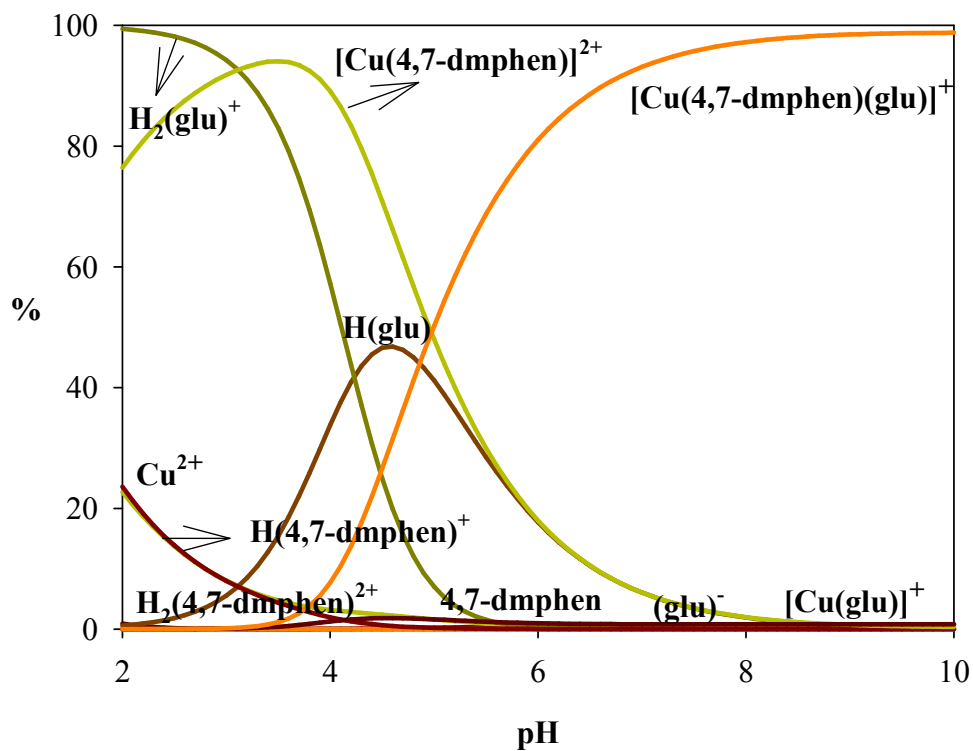
b)
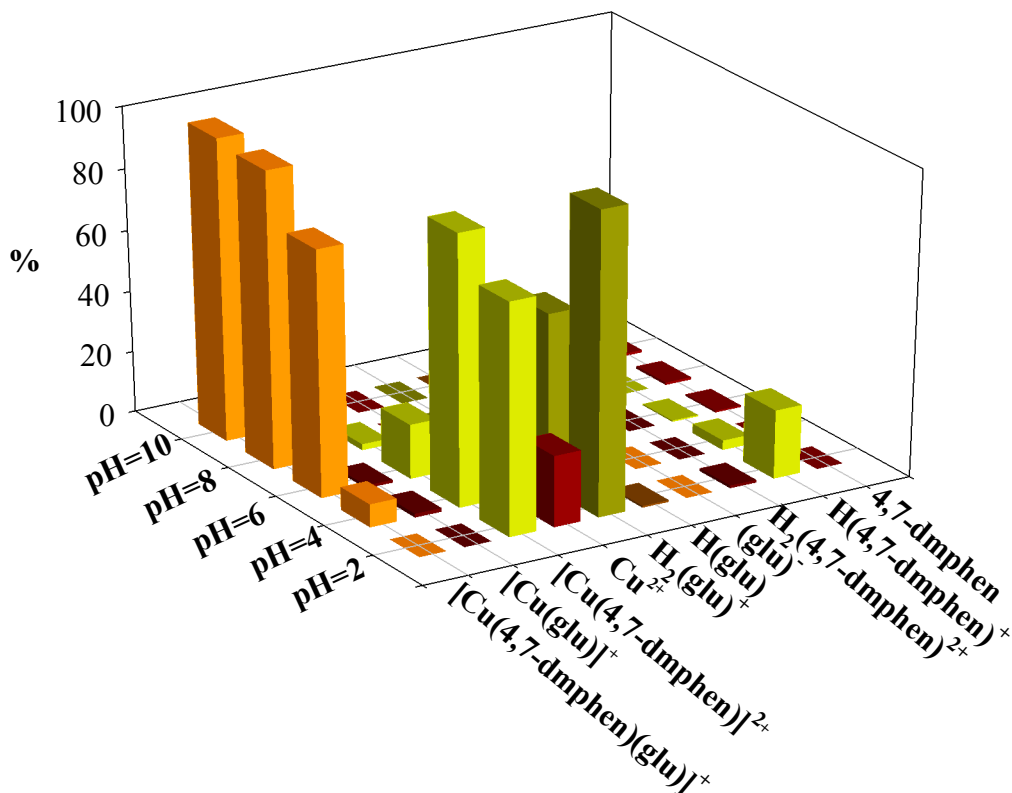
Figure 7. (a) Distribution of species as a function of pH in Cu(II):(4,7-dmphen):(glu) system **(b)** A bar chart of the percentage distribution of the species in aqueous solutions.

CONCLUSIONS

The formation of the (1:1:1) Ni(II) and Cu(II) complexes involving 4,7-dmphen and acidic amino acids using potentiometric titration methods were investigated. Compared to metal(II) ions, the stability constant of the [Cu(4,7-dmphen)(asp/glu)]$^+$ complexes were found higher than [Ni(4,7-dmphen)(asp/glu)]$^+$ complexes which were accordance with Irving-Williams series. Furthermore, glutamic acid complexes were found lower than aspartic acid complexes because of has one additional methylene group in its side chain. The above mentioned parameters and experimental results could be beneficial in understanding the biological behavior of the (1:1:1) Ni(II) and Cu(II) complexes in the biological implementations.

ACKNOWLEDGEMENTS

CONFLICT OF INTEREST

No conflict of interest was declared by the author.

REFERENCES

1. Agrawal BR, Magare BK, Farooqui MN, Janrao DM, Ubale MB. Stability Constants of Cu(II), Ni(II) and Mn(II) Metal Complexes with Cetrizine and Benzoic Acid. Int J Chem Sci. 2009;7(3):2169-72.

2. Nakon R, Rechani PR, Angelici RJ. Copper(II) complex catalysis of amino acid ester hydrolysis. A correlation with complex stability. J Am Chem Soc. 1974;96(7):2117-20.

3. Ullah MR, Bhattacharya PK. Study of the effect of nature of ligand on reproportionation constants of ternary complexes. Proc Indian Acad Sci Chem Sci. 1990:102(4):513-19.

4. Reddy PR, Rao KS. Ternary nickel(II) complexes as hydrolytic DNA-cleavage agents. Chem Biodivers. 2006;3(2):231-44.

5. Wyatt KS, Harrison KN, Jensen CM. Release of platinum from cysteine residues induced by N,S-donor chelation. Inorg Chem. 1992;31(18):3867-8.

6. Nural Y. Synthesis and Determination of Acid Dissociation Constants in Dimethyl Sulfoxide–Water Hydro-organic Solvent of 5,5- Diphenylpyrrolidine N-aroylthiourea Derivatives. JOTCSA. 2017; 4(3): 841-54.

7. Berber H, Uysal UD. Calculation of Acidity Constants of Azo Dyes Derived 4-(phenyldiazenyl)benzene-1,3-diol by DFT Method. JOTCSA. 2015; 2(2): 74-7.

8. Ersen D, Gemili M, Sarı H, Nural Y . Acid Dissociation Constants of 5,5-Diphenylpyrrolidine N-Aroylthioureas and Stability Constants of their Pt(II) and Ni(II) Complexes in Acetonitrile-Water Hydroorganic Solvent. Celal Bayar University Journal of Science. 2017; 13(1): 125-38.

9. İnci D, Aydın R. Structures, hydrolysis, stabilities of palladium(II) complexes containing biologically active ligands and species distribution in aqueous solution. Journal of Molecular Structure. 2019;1187:23-37.

10. İnci D, Aydın R. Stabilities of the Ternary Complexes of Copper(II) with Substituted 1,10-Phenanthrolines and Some Amino Acids in Aqueous Solution. J Solution Chem. 2014;43(4):711-26.

11. İnci D, Aydın R. Potentiometric Studies on Complexation of Cu(II) Ion with Methyl/Nitro-Substituted 1,10-Phenanthrolines and Selected Amino Acids. J Solution Chem. 2017;46(1):124-38.

12. Şenel P, Inci D, Aydın R. Temperature and methyl substitution effect on copper(II) complexes with biorelevant ligands and species distribution in aqueous solution. Physics and Chemistry of Liquids. 2019;1-15.

13. Kiraz S, İnci D, Aydın R, Vatan Ö, Zorlu Y, Cavaş T. Antiproliferative activity of copper(II) glutamine complexes with N,N-donor ligands: Synthesis, characterization, potentiometric studies and DNA/BSA interactions. Journal of Molecular Structure. 2019;1194:245-55.

14. Aydin R, Yirikogullari A. Potentiometric Study on Complexation of Divalent Transition Metal Ions with Amino Acids and Adenosine 5'-Triphosphate. J Chem Eng Data. 2010;55(11):4794-800.

15. Martell AE, 1916-, Motekaitis RJ. Determination and use of stability constants [Internet]. VCH Publishers; 1992. Available: https://agris.fao.org/agris-search/search.do?recordID=US201300727267

16. Brisbin DA, Mcbryde WAE. THE stability of metallic complexes of two dimethylphenanthrolines. Can J Chem. 1963;41(5):1135-41.

17. Yasuda M, Sone K, Yamasaki K. Stability of Zinc and Cadmium Complexes with Some Methyl Derivatives of 1,10-Phenanthroline and 2,2'-Bipyridine. J Phys Chem. 1956;60(12):1667-8.

18. Makar GKR, Touche MLD, Williams DR. Thermodynamic considerations in co-ordination. Part XXIII. Formation constants for complexes of

protons, zinc(II), and acid anions and their use in computer evaluation of a better zinc therapeutical. J Chem Soc, Dalton Trans. 1976;(11):1016-9.

19. Boraei AAA, Ibrahim SA, Mohamed AH. Solution Equilibria of Binary and Ternary Systems Involving Transition Metal Ions, Adenosine 5'-Triphosphate, and Amino Acids. J Chem Eng Data. 1999;44(5):907-11.

20. Erçag A, Sismanoglu T, Pura S. Thermodynamics of binary and ternary complexes of 3-amino-1, 2, 4-triazole and aminoacids with Ni(II) and Co(II) metal ions. Journal of the Serbian Chemical Society. 2005;70(8-9):1057-66.

21. Shoukry MM, Shehata MR, Mohamed MMA. Binary and ternary complexes of Cd(II) involving triethylenetetramine and selected amino acids and DNA units. Mikrochim Acta. 1998;129(1):107-13.

22. Abdel Gaber AA, Farghaly OA, Ghandour MA, El-Said HS. Potentiometric Studies on SomeCephalosporin Complexes. Monatshefte für Chemie. 2000;131(10):1031-8.

23. Chikira M, Tomizawa Y, Fukita D, Sugizaki T, Sugawara N, Yamazaki T, vd. DNA-fiber EPR study of the orientation of Cu(II) complexes of 1,10-phenanthroline and its derivatives bound to DNA: mono(phenanthroline)-copper(II) and its ternary complexes with amino acids. Journal of Inorganic Biochemistry. 2002;89(3):163-73.

24. Su C-C, Tai T-Y, Wu S-P, Wang S-L, Liao F-L. Spectroscopic and electronic properties of mixed ligand aminoacidatocopper(II) complexes: Molecular structure of [Cu(4,7-dimethyl-1,10-phenanthroline)(l-phenylalaninato)](ClO$_4$). Polyhedron. 1999;18(18):2361-8.

25. Kamecka A, Kurzak B. Review: Solution equilibria of ternary complexes formed from copper(II), aliphatic amines, and bioligands. Journal of Coordination Chemistry. 2014;67(15):2497-529.

The Syntheses and Characterization of New Dithiophosphonates derived from Novel 2,4-Bis(methoxytolyl)-1,3-dithia-2,4-diphosphetane 2,4-disulfides and Their Ni(II) Complexes

Ertuğrul Gazi Sağlam[1]* ✉ iD **, Elif Bulat[1]** ✉ iD **and Hamza Yılmaz[2]** ✉ iD

[1] Yozgat Bozok University, Department of Chemistry, 66900, Yozgat, Turkey
[2] Ankara University, Department of Chemistry, 06100 Tandoğan, Ankara, Turkey

Abstract: Two novel perthiophosphonic acid anhydrides, 2,4-bis($R^{x,y}$)-1,3-dithia-2,4-diphosphetane 2,4-disulfide [($R^{x,y}$-P(S)S)$_2$; R^x=3-methoxytolyl (**SAV-B1**) and R^y=2-methoxytolyl (**SAV-B2**)] were synthesized. From the reaction of **SAV-B1** and **SAV-B2** with alcohols, four new dithiophosphonic acids [HS$_2$P($R^{x,y}$)(ORn)] (Rn; R1=ethyl R2=2-propyl) were prepared. These acids were converted to corresponding ammonium salts, [NH$_4$][S$_2$P($R^{x,y}$)(ORn)]. The ammonium salts were further reacted with NiCl$_2$.6H$_2$O to prepare four new dithiophosphonato nickel(II) complexes, [Ni(S$_2$P($R^{x,y}$)(ORn))$_2$]. The ligands and complexes were characterized by elemental analyses, IR, ESI-MS, 1D ^{1}H, ^{13}C, ^{31}P NMR and 2D HSQC techniques. Complementary structural information was provided by the HSQC spectrum of the [NH$_4$][S$_2$P($R^{x,y}$)(OR2)]. The structure of the perthiophosphonic acid anhydrides was deduced from the structures of dithiophosphonates thereof.

INTRODUCTION

Perthiophosphonic acid anhydrides (PTPA) are called as 2,4-diorganyl-1,3,2,4-dithiadiphosphetane-2,4-disulfides and known to be the starting materials in the synthesis of phosphorus-1,1-dithiolates. For example, dithiophosphonates, dithiophosphinates, and amidodithiophoshonates were obtained through the reactions of PTPAs with alcohols (1), Grignard compounds (2,3), and amines (4), respectively (Scheme 1).
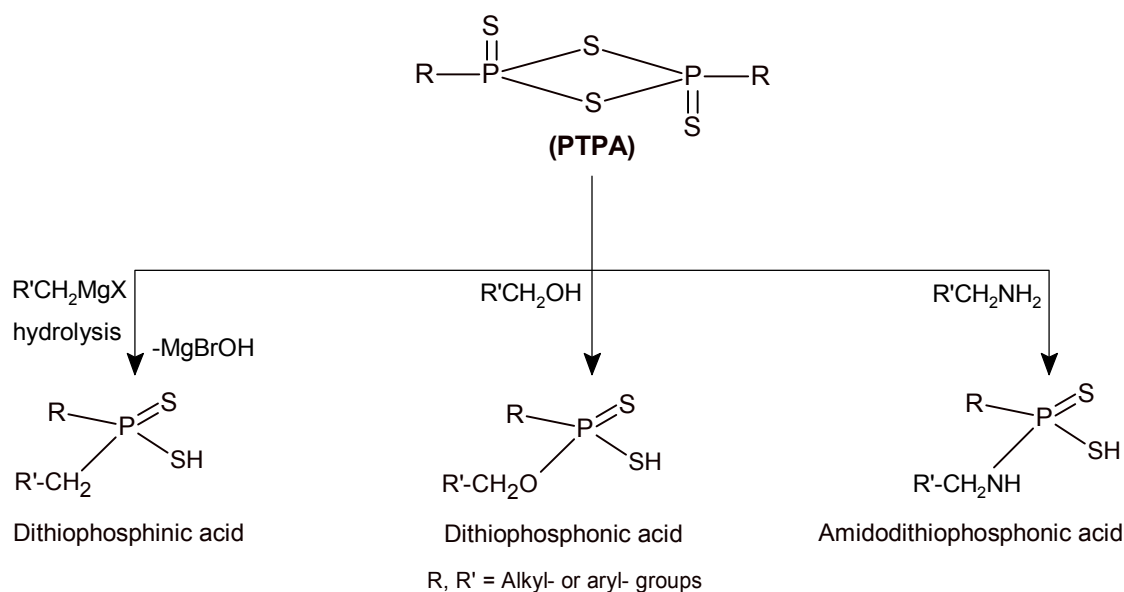
Scheme 1. Synthesis pathways through the reaction of perthiophosphonic acid anhydrides and nucleophiles to obtain phosphorus-1,1-dithiolates.

The first example of PTPA-type compounds was cyclohexyl-PTPA reported by Fay and co-workers (5). They reacted P_4S_{10} and cyclohexane directly. This procedure has been used ever since with various aromatic and aliphatic hydrocarbons instead of cyclohexane (6). In fact, there are two other routes to prepare PTPA compounds (7,8), but they are relatively more difficult and tiresome, not to mention a number of side-products.

Among commercially available PTPAs [R=-PhOPh (Belleu's reagent), -SCH₃ (Davy's reagent), -SPh (Yokoyama's reagent), etc.] (9), Lawesson's reagent (R=-PhOCH₃) (LR) has proven to be the most widely used (10). Ferrocenyl group can also be linked to the phosphorus-1,1-dithiolate group, and the resultant, so-called Ferrocenyl-Lawesson reagent (Fc-LR), 2,4-diferrocenyl-1,3-dithiadiphosphetane 2,4-disulfide is known for three decades, although not commercially available (11).

Phosphorus-1,1-dithiolates obtained from a PTPA and a nucleophile are soft base-type, bidentate ligands, and they find some use in industry (12, 13), agriculture (14), biochemistry (15), and metallurgy (16). The metal-complexing ability of phosphorus-1,1-dithiolates are based on sulfur donor groups that form four-membered chelate rings with metal cations (17). Dithiohosphonic acids, in particular, were reported to form complexes with transition metal cations like Ni(II), Cu(II), Zn(II), Cd(II), etc. (18,19). Among these, dithiohosphonato Ni(II) complexes possessing four-coordinate square-planar geometry (20).

In this work, first of all, we have prepared two novel PTPAs [$R^{x,y}$-P(S)S)₂], that is, 2,4-bis(3-methoxytolyl)-1,3-dithia-2,4-diphosphetane 2,4-disulfide [(R^x-P(S)S)₂] (**SAV-B1** reagent) and 2,4-bis(2-methoxytolyl)-1,3-dithia-2,4-diphosphetane 2,4-disulfide [(R^x-P(S)S)₂] (**SAV-B2** reagent) (Scheme 2).
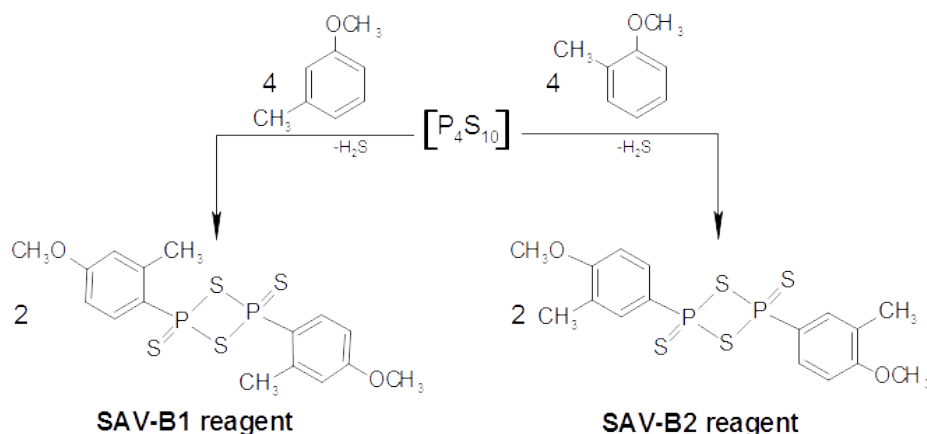
Scheme 2. Synthesis of novel PTPAs [$R^{x,y}$-P(S)S)₂] (**SAV-B1** and **SAV-B2**).

The reaction of **SAV-B1** and **SAV-B2** reagents with ethanol and 2-propanol and then dry ammonia gas furnished the four new alkyl dithiophosphonate ligands, O-ethyl-(3-methoxytolyl)dithiophosphonate, O-2-propyl-(3-methoxytolyl)dithiophosphonate, O-ethyl-(2-methoxytolyl)dithiophosphonate, and O-2-propyl-(2-methoxytolyl)dithiophosphonate in the form of their ammonium salts $[NH_4][S_2P(R^{x,y})(ORn)]$. The ligands were reacted with $NiCl_2.6H_2O$ to

produce the complexes $[Ni(S_2P(R^{x,y})(ORn))_2]$, *trans*-bis-[O-ethyl-(3-methoxytolyl)]nickel(II), *trans*-bis-[O-propyl-(3-methoxytolyl)]nickel(II), *trans*-bis-[O-ethyl-(2-methoxytolyl)]nickel(II), *trans*-bis-[O-propyl-(2-methoxytolyl)]nickel(II) (Scheme 3). The ligands and their Ni(II) complexes were elucidated by elemental analyses, IR, ESI-MS, 1D ^1H, ^{13}C, ^{31}P NMR, and 2D HSQC techniques.
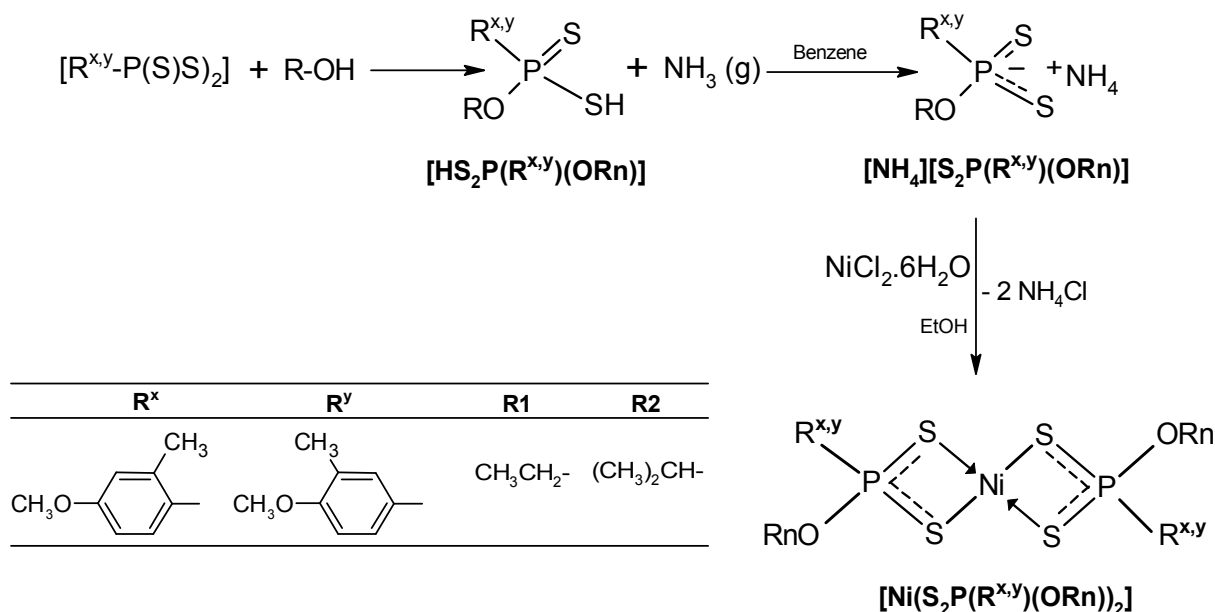
Scheme 3. Syntheses of the ligands and Ni(II) complexes.

EXPERIMENTAL

Materials and Instruments
Methanol, ethanol, 2-propanol, benzene, chloroform, 3-methoxytoluene, 2-methoxytoluene, P_4S_{10}, and $NiCl_2.6H_2O$ were purchased from Sigma-Aldrich and used without further purification. Diethyl ether was also provided by Sigma-Aldrich but re-distilled and then dried with sodium wire.

Microanalyses were carried out on a LECO CHNS-932 CHNS-O elemental analyzer. Melting points were measured with an Electrothermal 9200 apparatus. IR spectra were run on a Perkin Elmer Spectrum Two Model FT-IR instrument (ATR method) with a wavenumber range of 200–4000 cm^{-1}. The MS spectra were run on a Waters Micromass ZQ, with an ESI(+) ionizer.

^1H (500 MHz), ^{13}C (125 MHz), and ^{31}P NMR (202.4 MHz) spectra were recorded on a Bruker FT spectrometer at 298 K. ^1H and ^{13}C NMR chemical shifts (δ) are given in ppm and referenced to the internal signal of TMS. 85% H_3PO_4 was used as the external standard for ^{31}P NMR. D_2O was the solvent of choice for the ligand-ammonium salts and $CDCl_3$ for Ni(II) complexes. Diagnostic correlations which

are based on Heteronuclear Single Quantum Coherence (HSQC) experiments were also performed on a Bruker FT spectrometer at 298 K.

Preparation of SAV-B1 [(R^x-P(S)S)$_2$] and SAV-B2 [(R^y-P(S)S)$_2$]
In a fume hood with an inert (argon) atmosphere, 4.00 g (9.0 mmol) of P_4S_{10} and an excess (90 mmol, 11.00 g) of either 3-methylanisole or 2-methylanisole (the same molar mass) were mixed in a three-necked, round-bottomed flask mounted to a dropping funnel in one neck. Our experience proved that 2-methylanisole should be added dropwise. Adding in one batch leads to side reactions and low yield. 3-methylanisole, however, does not appear to be as reactive and could be added in one portion. The mixture was heated to 165°C (with 3-methylanisole) or 130°C (with 2-methylanisole), and kept as such for three hours. The PTPA derivative of 3-methylanisole precipitated in the third hour whereas the 2-methylanisole analog appeared to have formed within the first hour. The mixture was left to cool down to ambient temperature, then poured into 30 mL of dry ether, filtered, washed with ether, dried and kept in water-tight, amber-colored bottles under argon atmosphere. The PTPA compounds are stable for weeks if handled like this.

Characteristics:
SAV-B1
Yield: 4.3 g (55%). Yellow. m.p. 257-260°C. Anal. Calcd. for: $C_{16}H_{18}O_2P_2S_4$ (432.52 g.mol^{-1}): C, 44.43; H, 4.19; S, 29.65; found: C, 44.53; H, 4.23; S, 29.72 %.

SAV-B2
Yield: 5.7 g (73%). Yellow. m.p. 230-232°C. Anal. Calcd. for: $C_{16}H_{18}O_2P_2S_4$ (432.52 g.mol^{-1}): C, 44.43; H, 4.19; S, 29.65; found: C, 44.49; H, 4.20; S, 29.75 %.

General Procedure for the ammonium salts of dithiophosphonic acids [NH₄][S₂P(Rˣ,ʸ)(ORn)]
1.00 g (2.3 mmol) of the PTPA reagent [(Rˣ,ʸ-P(S)S)₂] was taken into a three-necked flask, and onto it, a 4.6 mmol of one of the alcohols (0.21 g of ethanol; 0.28 g of 2-propanol) was added dropwise. The mixture was heated to 50-60⁰C, kept at this temperature range until complete dissolution, and then left aside to cool. The crude dithiophosphonic acid (an oily, viscous mixture), was poured into 50-60 mL of benzene. The benzene solution was filtered (filter paper) and cooled to 0⁰C. Through this solution, dry gaseous ammonia was bubbled at a rate of 20 mL/min until the precipitation was complete. The white, amorphous precipitate was filtered (filter paper), washed with benzene, and dried in a vacuum desiccator.

General Procedure for the synthesis of the complexes [Ni(S₂P(Rˣ,ʸ)(ORn))₂]
A 2 mmol sample of the ammonium salt of interest (0.56 g [NH₄][S₂P(Rˣ)(OR1)] or [NH₄][S₂P(Rʸ)(OR1)] and 0.59 g [NH₄][S₂P(Rˣ)(OR2)] or [NH₄][S₂P(Rʸ)(OR2)]) was dissolved in 20-30 mL ethanol. Onto this, a solution of 1 mmol (2.4 g) NiCl₂.6H₂O in the same solvent was added dropwise. The mixture was heated to 50-60⁰C; kept as such for 5-10 min and filtered through filter paper without letting excess cooling. Tiny, violet crystals formed upon cooling. This compound was recrystallized from ethanol.

Characteristics:
[NH₄][S₂P(Rˣ)(OR1)]
Yield: 0.89 g (69%). White. m.p. 102-105°C, (decomposition). LC/MS: m/z 261.65 ([M-NH₄]$^+$, 100%). Anal. Calcd. for: $C_{10}H_{18}NO_2PS_2$ (279.36 g.mol^{-1}): C, 43.00; H, 6.49; N, 5.01; S, 24.35; found: C, 43.13; H, 6.62; N, 5.05; S, 24.75 %.

[NH₄][S₂P(Rˣ)(OR2)]
Yield: 1.19 g (87%). White. m.p. 195-198°C, (decomposition). LC/MS: m/z 275.69 ([M-NH₄]$^+$, 100%). Anal. Calcd. for: $C_{11}H_{20}NO_2PS_2$ (293.38 g.mol^{-1}): C, 45.03; H, 6.82; N, 4.77; S, 21.86; found: C, 45.15; H, 6.98; N, 4.85; S, 21.98 %.

[NH₄][S₂P(Rʸ)(OR1)]
Yield: 1.11 g (85%). White. m.p. 158-160°C. LC/MS: m/z 261.72 ([M-NH₄]$^+$, 100%). Anal. Calcd. for: $C_{10}H_{18}NO_2PS_2$ (279.36 g.mol^{-1}): C, 43.00; H, 6.49; N, 5.01; S, 24.35; found: C, 43.20; H, 6.55; N, 5.10; S, 24.38%.

[NH₄][S₂P(Rʸ)(OR2)]
Yield: 1.11 g (82%). White. m.p. 153-155°C. LC/MS: m/z 275.68 ([M-NH₄]$^+$, 100%). Anal. Calcd. for: $C_{11}H_{20}NO_2PS_2$ (293.38 g.mol^{-1}): C, 45.03; H, 6.82; N, 4.77; S, 21.86; found: C, 45.23; H, 7.01; N, 4.92; S, 21.89 %.

[Ni(S₂P(Rˣ)(OR1))₂]
Yield: 4,9 g (84%). Violet. m.p. 190-193°C, (decomposition). LC/MS: m/z 581.93 ([M-H]$^+$, 100%). Anal. Calcd. for: $C_{20}H_{28}NiO_4P_2S_4$ (581.34 g.mol^{-1}): C, 41.31; H, 4.85; S, 22.06; found: C, 41.52; H, 5.01; S, 22.15 %.

[Ni(S₂P(Rˣ)(OR2))₂]
Yield: 4,7 g (77%). Violet. m.p. 205-207°C. LC/MS: m/z 151.98 ([P(C₆H₃-(CH₃)(OCH₃)]$^+$, 100%), 610.04 ([M]$^+$, 93%). Anal. Calcd. for: $C_{22}H_{32}NiO_4P_2S_4$ (609.39 g.mol^{-1}): C, 43.35; H, 5.25; S, 21.04; found: C, 43.42; H, 5.45; S, 21.18 %.

[Ni(S₂P(Rʸ)(OR1))₂]
Yield: 5,1 g (87%). Violet. m.p. 165-168°C. LC/MS: m/z 151.98 ([P(C₆H₃-(CH₃)(OCH₃)]$^+$, 100%), 610.04 ([M]$^+$, 32%). Anal. Calcd. for: $C_{20}H_{28}NiO_4P_2S_4$ (581.34 g.mol^{-1}): C, 41.31; H, 4.85; S, 22.06; found: C, 41.40; H, 4.93; S, 22.13%.

[Ni(S₂P(Rʸ)(OR2))₂]
Yield: 5,1 g (88%). Violet. m.p. 128-130°C. LC/MS: m/z 610.00 ([M]$^+$, 100%). Anal. Calcd. for: $C_{22}H_{32}NiO_4P_2S_4$ (609.39 g.mol^{-1}): C, 43.35; H, 5.25; S, 21.04; found: C, 43.48; H, 5.38; S, 21.11 %.

RESULTS AND DISCUSSION

Spectroscopic studies
IR spectra
IR spectra were inspected to find evidence about the existence of PS and Ni-S bonds. The modes v(PS)$_{asym}$ and v(PS)$_{sym}$ as well as a couple of bands relating to the Ni-S coordination namely, v(Ni-S)$_{asym}$ and v(Ni-S)$_{sym}$ are visible as listed in Table 1.

Table 1: Selected IR data (v, cm^{-1}) assignment of vibrational bands for the compounds.

Compounds	v(Ni-S)$_{sym}$	v(Ni-S)$_{asym}$	v(PS)$_{sym}$	v(PS)$_{asym}$	v(N-H)
[(R^x-P(S)S)$_2$]	-	-	583	663	-
[(R^y-P(S)S)$_2$]	-	-	577	687	-
[NH$_4$][S$_2$P(R^X)(OR1)]	-	-	540	747	2945
[NH$_4$][S$_2$P(R^X)(OR2)]	-	-	556;544	743	2973
[NH$_4$][S$_2$P(R^y)(OR1)]	-	-	559	752	2977
[NH$_4$][S$_2$P(R^y)(OR2)]	-	-	584;567	738	2970
[Ni(S$_2$P(R^X)(OR1))$_2$]	275	325	553	670	-
[Ni(S$_2$P(R^X)(OR2))$_2$]	271	322	553	666	-
[Ni(S$_2$P(R^y)(OR1))$_2$]	277	327	573	665	-
[Ni(S$_2$P(R^y)(OR2))$_2$]	283	329	557	663	-

The N-H stretching signal, v(N-H), observed in the spectra of the ammonium salts at 2945 and 2977 cm^{-1} disappears in the spectra of the complexes. IR data reported for similar compounds agree well with the signals (19-22).

Mass Spectra
The structure of the peaks in the mass spectra reflects the natural abundance of nickel and sulfur isotopes. The molecular ion peaks are clearly visible and in fact, they are either the main peak or comparable in intensity for the mass spectra of the complexes. Mass spectral data reported for similar compounds agree well (23-26) with the signals we observed.

NMR Spectroscopy
The PTPA acids are insoluble in the NMR solvents available, so no NMR data were provided for them. The numbering scheme for carbon and hydrogen atoms is given in Figure 1.
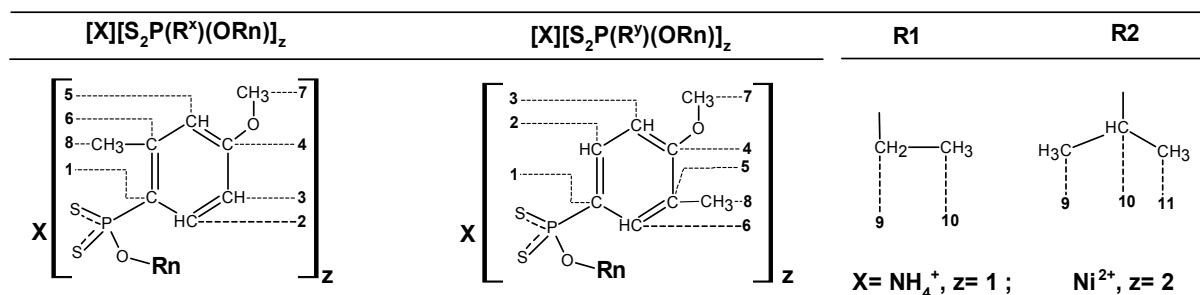
Figure 1. Numbering scheme for the ligands [NH$_4$][S$_2$P(R^{x,y})(ORn)] and complexes [Ni(S$_2$P(R^{x,y})(ORn))$_2$].

The ^{31}P NMR data of the ligands and complexes are presented in Table 2. No general relation was observed between the ^{31}P chemical shifts of the complexes and of the ligands. All these values are in agreement with the literature (3,19,20).

Table 2: ^{31}P NMR data of the ligands and the corresponding complexes.

[NH$_4$][S$_2$P(R^{x,y})(ORn)]	δ (ppm)		[Ni(S$_2$P(R^{x,y})(ORn))$_2$]
[NH$_4$][S$_2$P(R^X)(OR1)]	102.6	102.0	[Ni(S$_2$P(R^X)(OR1))$_2$]
[NH$_4$][S$_2$P(R^X)(OR2)]	100.2	99.2	[Ni(S$_2$P(R^X)(OR2))$_2$]
[NH$_4$][S$_2$P(R^y)(OR1)]	67.5	101.7	[Ni(S$_2$P(R^y)(OR1))$_2$]
[NH$_4$][S$_2$P(R^y)(OR2)]	103.8	98.6	[Ni(S$_2$P(R^y)(OR2))$_2$]

The ^{13}C NMR data are listed in Table 3 and 4. Remarkably, the strong, single-bond P-C coupling constants in the complexes is somewhat greater (~112.5 Hz) than those in the ligands (109.6 Hz).

In the spectra of the ligands ([NH$_4$][S$_2$P(R^x)(ORn)]), the signals of the neighboring carbons C_2 and C_3 give rise to the *doublets* with two ($^2J_{PC}$) and three ($^3J_{PC}$) bond couplings to the P-atom of *ca.* 11 and

14.5 Hz, respectively. These values compare well with the literature reports for similar structures (19,20). Interestingly, the three-bond coupling of the phosphorus atom to C_8 is not observable whereas, again, the three-bond coupling to C_5 (7.4 Hz) and the four-bond coupling to C_4 are (2.9 Hz). Presumably, the electron delocalization in the aromatic ring facilitates somewhat stronger coupling relative to aliphatic carbons. As a general trend, the ^{13}C NMR signals of all the complexes show up at higher fields relative to the corresponding signals in the spectra of the ligands. Similar trends were reported for structurally related compounds (26-32).

As to the ^{13}C NMR spectra of ligand $[NH_4][S_2P(R^y)(ORn)]$, two-bond P-C couplings to $C2_{ar}$ and $C6_{ar}$ are the same with $^2J_{PC}$= 12.0 Hz. It is noteworthy to state that P-C three-bond coupling constants ($^3J_{PC}$) are 15.6 Hz for C_3 and 14.7 Hz for C_5. In addition, the P-C two- and three-bond coupling constants can be put into order as; $^3J_{PC}>^2J_{PC}$. This observation has been reported in the literature for similar structures (19,20). No general trend was observed in the ^{13}C NMR spectral data of the complexes with respect to these ligands.

Table 3: ^{13}C NMR data of $[NH_4][S_2P(R^x)(ORn)]$ (D$_2$O) and $[Ni(S_2P(R^x)(ORn))_2]$ (CDCl$_3$) (δ in ppm, J in Hz).

	$[NH_4][S_2P(R^x)(OR1)]$	$[NH_4][S_2P(R^x)(OR2)]$	$[Ni(S_2P(R^x)(OR1))_2]$	$[Ni(S_2P(R^x)(OR2))_2]$
C_1	127.8, $^1J_{PC}$=109.4	128.4, $^1J_{PC}$=109.7	120.8, $^1J_{PC}$= 112.0	121.0, $^1J_{PC}$=113.2
C_2	135.8, $^2J_{PC}$=11.3	136.0, $^2J_{PC}$=11.8	132.4, $^2J_{PC}$=13.5	132.5, $^2J_{PC}$=13.3
C_3	123.5, $^3J_{PC}$=14.5	123.2, $^3J_{PC}$=14.5	121.1, $^3J_{PC}$=16.2	120.9, $^3J_{PC}$=16.0
C_4	162.0, $^4J_{PC}$=2.9	162.2, $^4J_{PC}$=2.8	160.5	160.4
C_5	115.8, $^3J_{PC}$=7.4	115.6, $^3J_{PC}$=7.4	112.6, $^3J_{PC}$=7.2	112.5, $^3J_{PC}$=7.4
C_6	147.5, $^2J_{PC}$=2.5	147.4, $^2J_{PC}$=2.5	145.4	145.4
C_7	58.2	57.9	55.9	55.7
C_8	23.5	23.5	21.9	21.9
C_9	64.3, $^2J_{PC}$=7.4	-	62.5, $^2J_{PC}$=5.6	-
C_{10}	18.3, $^3J_{PC}$=8.7	73.7, $^2J_{PC}$=7.4	16.3, $^3J_{PC}$=7.1	71.7, $^2J_{PC}$=6.0
$C_{9,11}$	-	26.1, $^3J_{PC}$=4.1	-	24.1, $^3J_{PC}$=3.7

Table 4: ^{13}C NMR data of $[NH_4][S_2P(R^y)(ORn)]$ (D$_2$O) and $[Ni(S_2P(R^y)(ORn))_2]$ (CDCl$_3$) (δ in ppm, J in Hz).

	$[NH_4][S_2P(R^y)(OR1)]$	$[NH_4][S_2P(R^y)(OR2)]$	$[Ni(S_2P(R^y)(OR1))_2]$	$[Ni(S_2P(R^y)(OR2))_2]$
C_1	129.7, $^1J_{PC}$=144.8	133.8, $^1J_{PC}$=114.4	128.0, $^1J_{PC}$=115.6	128.2, $^1J_{PC}$=116.5
C_2	129.7, $^2J_{PC}$=12.0	129.3, $^2J_{PC}$=13.2	129.4, $^2J_{PC}$=14.6	129.4, $^2J_{PC}$=14.5
C_3	110.2, $^3J_{PC}$=15.6	109.9, $^3J_{PC}$=15.7	109.4, $^3J_{PC}$=17.4	109.4, $^3J_{PC}$=17.4
C_4	159.4, $^4J_{PC}$=3.5	159.3, $^4J_{PC}$=3.0	161.2, $^4J_{PC}$=1.4	161.1
C_5	126.4, $^3J_{PC}$=14.7	126.1, $^3J_{PC}$=14.6	127.2, $^3J_{PC}$=15.7	127.1, $^3J_{PC}$=15.7
C_6	132.3, $^2J_{PC}$=12.1	132.0, $^2J_{PC}$=13.0	131.6, $^2J_{PC}$=14.1	131.6, $^2J_{PC}$=14.2
C_7	55.5	55.6,	55.6	55.6
C_8	15.5	15.5	16.3	24.3
C_9	61.4, $^2J_{PC}$=6.2	-	62.6, $^2J_{PC}$=5.9	-
C_{10}	15.6, $^3J_{PC}$=7.3	70.7, $^2J_{PC}$=7.3	16.2, $^3J_{PC}$=3.7	72.1, $^2J_{PC}$=5.5
$C_{9,11}$	-	23.4, $^3J_{PC}$=3.8	-	16.3

The ^1H NMR data of the ligands [NH$_4$][S$_2$P(R^x)(OR1)], [NH$_4$][S$_2$P(R^x)(OR2)], [Ni(S$_2$P(R^x)(OR1))$_2$] and [Ni(S$_2$P(R^x)(OR2))$_2$] are given in Table 5. As seen in the Table 5, the signals of the aromatic protons are virtually the same for the ligand salts [NH$_4$][S$_2$P(R^x)(OR1)] and [NH$_4$][S$_2$P(R^x)(OR2)]. The proton C$_2$-**H** appears at about 8 ppm as *doublet of doublets* with $^3J_{HH}$= 7.8 Hz and $^3J_{PH}$= ~17.1 Hz. On the other hand, C$_3$-**H** appears at 6.9 ppm with $^3J_{HH}$= 7.8 Hz. The four-bond coupling to phosphorus is barely appreciable as the *doublet* is slightly broadened. Phosphorus does not also split the signal of the C$_8$-C**H**$_3$ protons that show up at 2.4 ppm. However, the four-bond coupling between phosphorus and C$_5$-**H** is notable with a $^4J_{PH}$ of 6.0 Hz.

Similar trends in the coupling patterns of the aromatic protons are observed in the ^1H NMR spectra of [Ni(S$_2$P(R^x)(OR1))$_2$] and [Ni(S$_2$P(R^x)(OR2))$_2$].

The ^1H NMR data of [NH$_4$][S$_2$P(R^y)(OR1)] and [NH$_4$][S$_2$P(R^y)(OR2)] ligands and [Ni(S$_2$P(R^y)(OR1))$_2$] and [Ni(S$_2$P(R^y)(OR2))$_2$] complexes are listed in Table 6. The signals of the aromatic protons are again, almost the same for the two ligands, [NH$_4$][S$_2$P(R^y)(OR1)] and [NH$_4$][S$_2$P(R^y)(OR2)]. Here the proton C$_2$-**H** appears at about 8 ppm as a *doublet of doublets* with $^3J_{HH}$= 8.4 Hz and $^3J_{PH}$= 12.8 Hz (for [NH$_4$][S$_2$P(R^y)(OR1)]) and $^3J_{PH}$= 14.1 Hz (for [NH$_4$][S$_2$P(R^y)(OR2)]). In these compounds, the four-bond couplings between phosphorus and C$_3$-**H** is read as $^4J_{PH}$= ~3 Hz. On the other hand, phosphorus splits C$_2$-**H** (δ= 7.6 ppm) and C$_6$-**H** (δ= 7.5 ppm) by $^3J_{HH}$= 12.8 Hz (for [NH$_4$][S$_2$P(R^y)(OR1)]) and $^3J_{HH}$= 14.0 Hz (for [NH$_4$][S$_2$P(R^y)(OR2)]). All the ^1H NMR shifts are in agreement with findings in the literature for similar compounds (3,19,20).

Similar trends are also observed in the coupling patterns of the aromatic protons of the ^1H NMR spectra of [Ni(S$_2$P(R^y)(OR1))$_2$] and [Ni(S$_2$P(R^y)(OR2))$_2$].

Table 5: ^1H NMR data of [NH$_4$][S$_2$P(R^x)(ORn)] (D$_2$O) and [Ni(S$_2$P(R^x)(ORn))$_2$] (CDCl$_3$) (δ in ppm, *J* in Hz, s: *singlet*, d: *doublet*, dd: *doublet of doublets*, t: *triplet*, and m: *multiplet*).

	[NH$_4$][S$_2$P(R^x)(OR1)]	[NH$_4$][S$_2$P(R^x)(OR2)]	[Ni(S$_2$P(R^x)(OR1))$_2$]	[Ni(S$_2$P(R^x)(OR2))$_2$]
C$_2$-**H**	8.0 (dd,1H) $^3J_{PH}$=17.0 $^3J_{HH}$=7.8	8.1 (dd,1H) $^3J_{PH}$=17.3 $^3J_{HH}$=7.8	7.9 (dd,2H) $^3J_{PH}$=18.1 $^3J_{HH}$=7.5	7.9 (dd,2H) $^3J_{PH}$=18.3 $^3J_{HH}$=7.7
C$_7$-**H**	3.9(s,3H)	3.9 (s,3H)	3.9 (s,6H)	3.9 (s,6H)
C$_3$-**H**	6.9 (d,1H) $^3J_{HH}$=7.8	6.9 (d,1H) $^3J_{HH}$=7.8	6.8 (d,2H) $^3J_{HH}$=5.1	6.7 (d, 2H) $^3J_{PH}$=5.8
C$_8$-**H**	2.4 (s,3H)	2.4 (s, 3H)	2.4 (s,6H)	2.4 (s,6H)
C$_5$-**H**	7.0 (d,1H) $^4J_{PH}$=6.0	7.0 (d,1H) $^4J_{PH}$=6.0	6.9 (d,2H) $^4J_{PH}$=6.5	6.9 (d,2H) $^4J_{PH}$=7.7
C$_9$-**H**	δ= 3.9 (m,2H)	-	4.4 (m,4H)	-
C$_{10}$-**H**	1.3 (t,3H) $^3J_{HH}$=7.1	4.7 (m,1H)	1.4 (t,6H) $^3J_{HH}$=6.9	5.1(m,2H)
C$_{9,11}$-**H**	-	1.2 (d,6H) $^3J_{HH}$=6.2	-	1.3 (d,12H) $^3J_{HH}$=6.2

Table 6: ^1H NMR data of [NH$_4$][S$_2$P(R^y)(ORn)] (D$_2$O) and [Ni(S$_2$P(R^y)(ORn))$_2$] (CDCl$_3$) (δ in ppm, *J* in Hz, s: *singlet*, d: *doublet*, dd: *doublet of doublets*, t: *triplet*, and m: *multiplet*).

	[NH$_4$][S$_2$P(R^y)(OR1)]	[NH$_4$][S$_2$P(R^y)(OR2)]	[Ni(S$_2$P(R^y)(OR1))$_2$]	[Ni(S$_2$P(R^y)(OR2))$_2$]
C$_2$-**H**	7.6 (dd,H) $^3J_{PH}$=12.8 $^3J_{HH}$=8.4	7.8 (dd,1H) $^3J_{PH}$=14.1 $^3J_{HH}$=8.5	7.9 (dd,2H) $^3J_{PH}$=13.5 $^3J_{HH}$=9.4	7.9 (dd,2H) $^3J_{PH}$=12.8 $^3J_{HH}$=8.6
C$_7$-**H**	3.8 (s,3H)	3.8 (s,3H)	3.9 (s,6H)	3.9 (s,6H)
C$_3$-**H**	6.9 (dd,1H) $^4J_{PH}$=3.1 $^3J_{HH}$=8.4	7.0 (dd,H) $^4J_{PH}$=3.0 $^3J_{HH}$=8.5	6.9 (dd, 2H) $^4J_{PH}$=3.1 $^3J_{HH}$=8.4	6.9 (dd,2H) $^4J_{PH}$=3.0 $^3J_{HH}$=8.4
C$_8$-**H**	2.1 (s,3H)	2.2 (s,3H)	2.3 (s,6H)	2.3 (s, 6H)
C$_6$-**H**	δ=7.5 (d,1H)	7.8 (d,1H)	7.8 (d,2H)	7.8 (d,2H)

	$^3J_{PH}=12.8$	$^3J_{PH}=14.0$	$^3J_{PH}=13.3$	$^3J_{PH}=13.5$
C$_9$-**H**	3.8 (m,2H)	-	4.5 (m,4H)	-
C$_{10}$-**H**	1.1 (t,3H) $^3J_{HH}=7.1$	4.6 (m,1H)	1.5 (t,6H) $^3J_{HH}=7.1$	5.3 (m,2H)
C$_{9,11}$-**H**	-	1.2 (d,6H) $^3J_{HH}=6.3$	-	1.4 (d,12H) $^3J_{HH}=6.2$

The unambiguous assignments of ^1H and ^{13}C NMR data of the ligands and complexes are made by HSQC spectra. The HSQC spectra of the ligands [NH$_4$][S$_2$P(R^x)(OR2)] and [NH$_4$][S$_2$P(R^y)(OR2)] are given as examples in Figures 2 and 3, respectively. The HSQC spectra of [NH$_4$][S$_2$P(R^{x,y})(OR2)] are also depicted in the Supplementary Material.
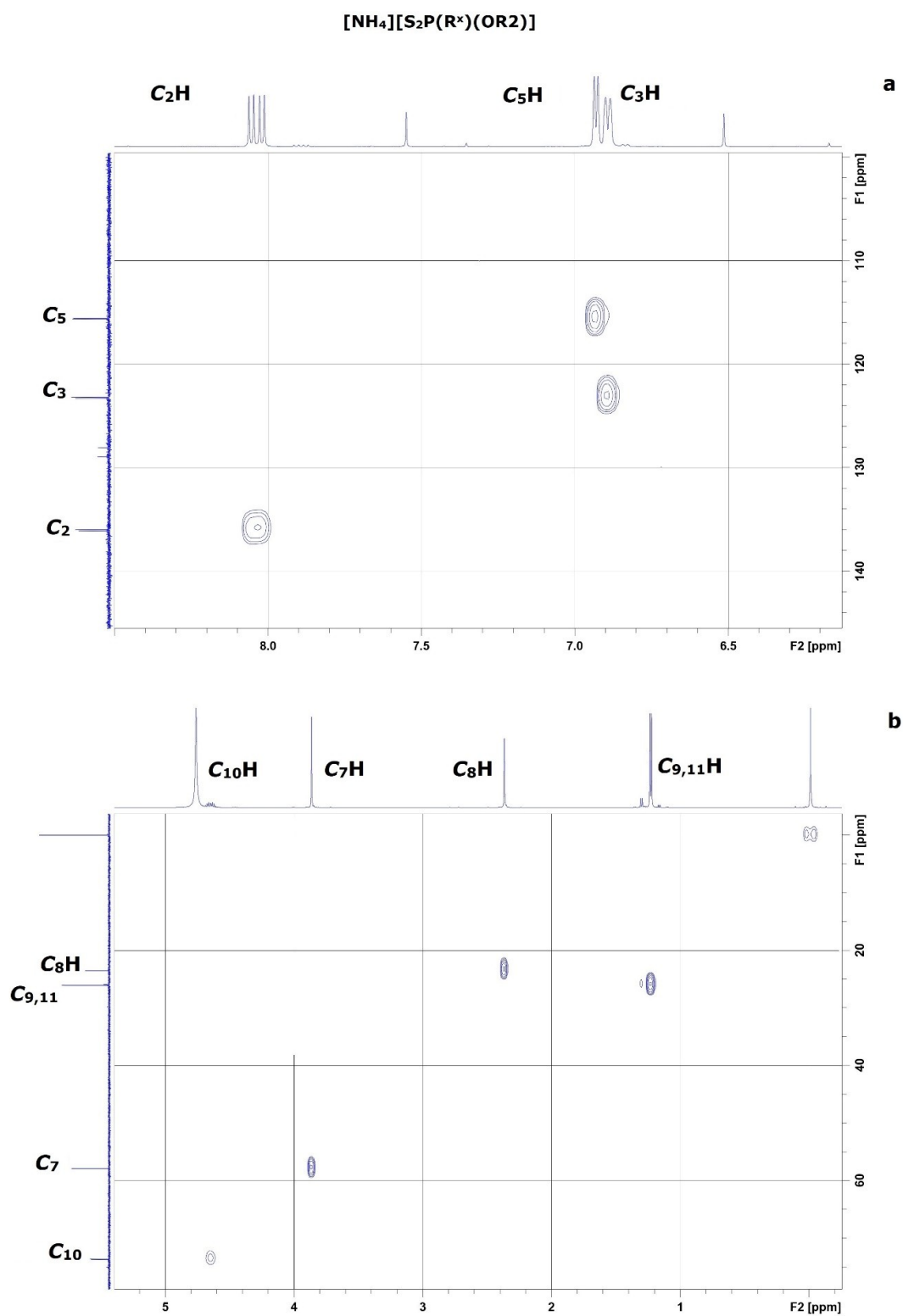
[NH₄][S₂P(Rˣ)(OR2)]

Figure 2. HSQC spectrum (**a**) for the aromatic region and (**b**) for the aliphatic region of [NH₄][S₂P(Rˣ)(OR2)].

[NH$_4$][S$_2$P(R$^\gamma$)(OR2)]
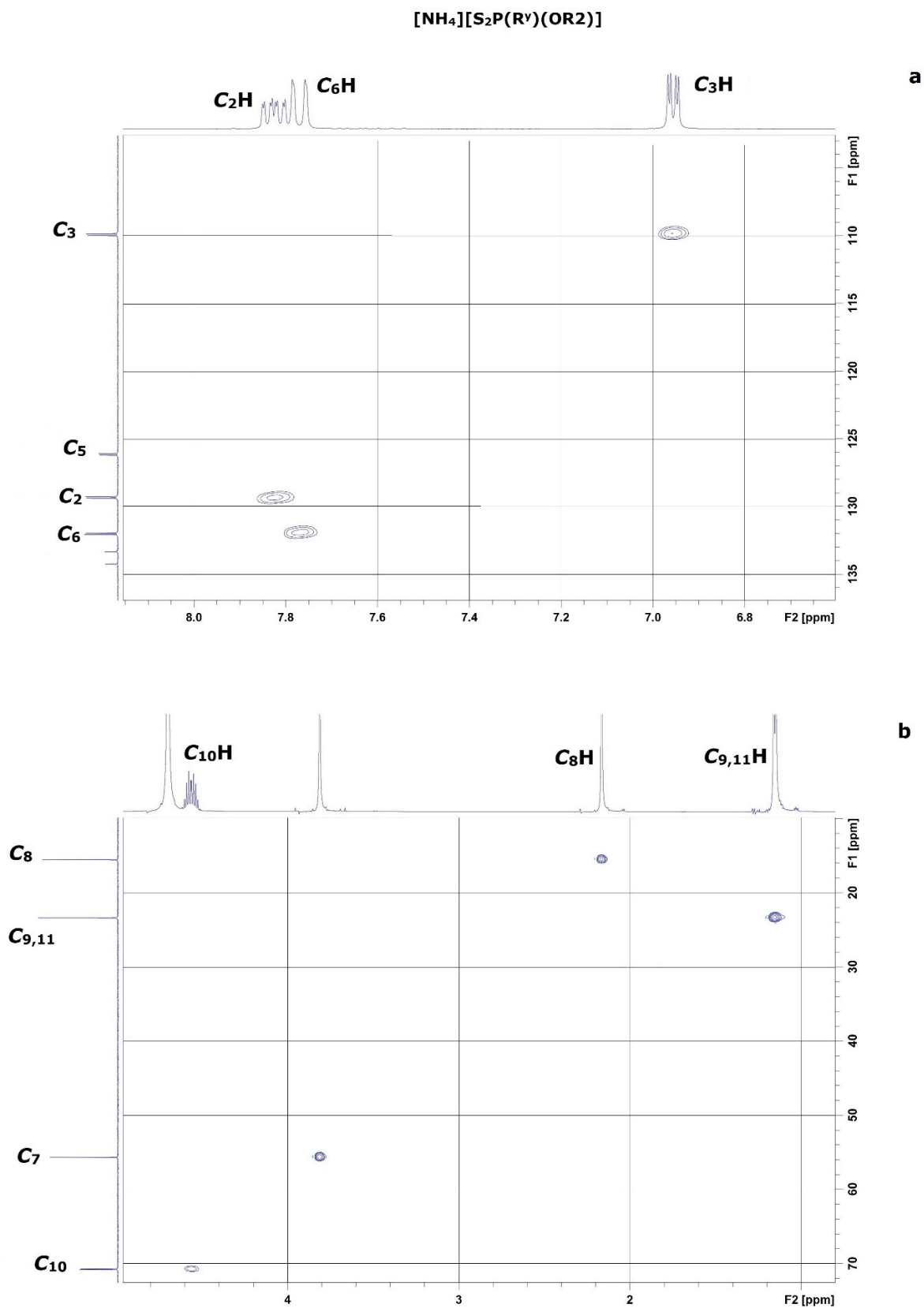
Figure 3. HSQC spectrum (**a**) for the aromatic region and (**b**) for the aliphatic region of [NH$_4$][S$_2$P(R$^\gamma$)(OR2)].

CONCLUSIONS

As an approach to create more alternatives to the well-known Lawesson's reagent, an easy procedure for the synthesis of two new perthiophosphonic acid anhydrides were described. These compounds were used in the synthesis of structurally different organo- dithiophosphonic acid ammonium salts, and the anions of these salts were used in the preparation of new dithiophosphonato Ni(II) complexes. The structures of the ligands and the complexes were determined by spectroscopic techniques. The ^{13}C NMR spectra of the aromatic parts of the compounds display interesting features. Three-bond P-C couplings, for example, are bigger than the two-bond P-C couplings.

ACKNOWLEDGEMENTS

REFERENCES

1. Van Zyl WE, Fackler JP. A General and Convenient Route to Dithiophosphonate Salt Derivatives, Phosphorus, Sulfur Silicon Relat. Elem. 2000; 167(1): 117-32.

2. Diemert K, Kuchen W. Zur Kenntnis der Organophosphorverbindungen XVII, Dithiophosphinsauren RR'P(S)SH, Ihre Synthese, Derivate und MetallKomlexe", Phosphorus, Sulfur Silicon Relat. Elem. 1977; 3: 131-6.

3. Sağlam EG, Acar N. Syntheses and characterization of new dithiophosphinato zinc complexes. J. Turkish Chem. Soc. A. 2018; 5(2): 931-40.

4. Aydemir C, Solak S, Acar Doğanlı G, Şensoy T, Arar D, Bozbeyoglu Mercan Dogan N, Lönnecke P, Hey-Hawkins E, Şekerci M, Karakuş M, Synthesis, Characterization, and Antibacterial Activity of Dithiophosphonates and Amidodithiophosphonates. Phosphorus, Sulfur Silicon Relat. Elem. 2015; 190(3): 300–9.

5. Fay P, Lankelma HP. The Reaction of Cyclohexene with Phosphorus Pentasulfide. J. Am. Chem. Soc. 1952; 74: 4933-5.

6. Lecher HZ, Greenwood RA, Whitehouse KC, Chao TH. The Phosphonation of Aromatic compounds with Phosphorus Pentasulfide. Am. Chem. Soc. 1956; 78: 5018–22.

7. Newallis PE, Chupp JP, Groenweghe CD. Thionophosphine Sulfides. I. Preparation and Use in the Friedel-Crafts Reaction. J. Org. Chem. 1962; 27: 3829–83.

8. Maier L. Organische Phosphorverbindungen VII. Zur Kenntnis der Reaktion von Phenylphosphin mit Schwefell. Helv. Chim. Acta. 1963; 46(5): 1812–8.

9. Thomsen I, Clausen K, Scheibye S, Lawesson S-O. Thiation with 2,4-bis(4-Methoxyphenyl)-1,3,2,4-Dithiadiphosphetane 2,4-disulfide: N-methylthiopyrrolidone. Organic Syntheses, Coll. 1990; 7: 372.

10. Avelino C-S, Alejandra MN-L, Rubicelia V, Jorge G. Dissociation energy for the P_2S_2 ring in a family of thionation reagents and the corresponding chemical reactivity of separated species: a density functional theory analysis. J. Phys. Org. Chem. 2016; 1–9.

11. Foreman MRStJ, Slawin AMZ, Woollins JD. 2,4-Diferrocenyl-1,3,dithiadiphosphetane 2,4 disulfide; structure and reactions with catechols and [PtCl$_2$(PR$_3$)$_2$] (R = Et or Bu^n). J. Chem. Soc., Dalton Trans. 1996; 3653–7.

12. Ziyatdinova GK, Budnikov GK, Samigullin AI, Gabdullina GT, Sofronov AV, Al'metkina LA, Nizamov IS, Cherkasov RA. Electrochemical Determination of Synthetic Antioxidants of Bisdithiophosphonic Acids. J Anal Chem. 2010; 65: 1273-9.

13. Mc.Cleverty JA, Rick SZ, Kowalski N, Bailey A, R Mulvaney, O'Cleirigh DA. Aspects of the inorganic chemistry of rubber vulcanisation. Part 4. Dialkyl- and diaryl-dithiophosphate and -dithiophosphinate complexes of zinc: phosphorus-31 nuclear magnetic resonance spectral studies and structures of [NMe$_4$][Zn{S$_2$P(OC$_6$H$_4$Me-p)$_2$}$_3$] and [NEt$_4$][Zn(S$_2$PPh$_2$)$_3$]. J. Chem. Soc. Dalton Trans. 1983; 627-34.

14. Kabra V, Mitharwal S, Singh S. Synthesis and Insecticidal Activity of Novel Dithiophosphonates. Phosphorus, Sulfur Silicon Relat. Elem. 2009; 184(9): 2431-42.

15. Banaei A, Saadat A, McArdle P, Goli MM. Crystal structure, antibacterial activity and nanoparticles of Cd(II) complex derived from dithiophosphonate ligand. Phosphorus, Sulfur Silicon Relat. Elem. 2018; 193(6): 369-74.

16. Xihong H, Guoxin T, Jing C, Linfeng R. Characterization of the extracted complexes of trivalent lanthanides with purified cyanex 301 in comparison with trivalent actinide complexes. J. Chem. Soc., Dalton Trans. 2014; 43: 17352-7.

17. Haiduc I. 1,1-Dithiolato Ligands in Comprehensive Coordination Chemistry II Edited by McCleverty JA, Meyer TJ. 2004; 1: 349-76.

18. Van Zyl WE, Woollins J D. The coordination chemistry of dithiophosphonates: An emerging and versatile ligand class. Coord. Chem. Rev. 2013; 257: 718–73.

19. Sağlam EG, Bulat E, Acar N, Demirel İ. New Homodinuclear Alkyl- and Aryl- Dithiophosphonato Cd(II) and Hg(II) complexes: Syntheses and Characterizations. J. Turk. Chem. Soc. A. 2020; 7(1): 49-64.

20. Sağlam EG, Ebinç A. Syntheses and Spectroscopic Characterization on New [O-3-phenyl-1-propyl-(4-methoxyphenyl)dithiophosphonato] Ni(II), Cd(II) and Hg(II) Complexes. J. Turk. Chem. Soc. A. 2018; 5(3): 1239-48.

21. Sunder S, Hanlan L, Bernstein HJ. Resonance Raman Spectra of Metal Complexes of Substituted Dithiophospinic Acids. Inorg. Chem. 1975; 14(8): 2012-3.

22. Aragoni MC, Arca M, Demartin F, Devillanova FA, Graiff C, Isaia F, Lippolis V, Tiripicchio A, Verani G. Reactivity of phosphonodithioato Ni^{II} complexes: solution equilibria, solid state studies and theoretical calculations on the adduct formation with some pyridine derivatives. J. Chem. Soc., Dalton Trans. 2001; 18: 2671-7.

23. Chakravarty M, Pailloux S, Ouizem S, Smith KA, Duesler EN, Paine RT, Williams NJ, Hancock RD. Synthesis and metal coordination chemistry of (phenyl)(pyridine-2-ylmethyl)phosphinodithioic acid. Polyhedron [2-C_5H_4N]CH_2P(S)(SH)(Ph). 2012; 33: 327-35.

24. Heinz S, Keck H, Kuchen W. Mass spectrometric studies of dithiophosphinato metal complexes. Org. Mass Spectrom. 1984; 19: 82-6.

25. Karakuş M, Yılmaz H. Synthesis and Characterization of Ni(II), Zn(II), and Cd(II) Complexes with Dithiophosphonate Derivatives. Russ. J. Coord. Chem. 2006; 32(6): 437–43.

26. Keck H, Kuchen W. Massenspektrometrische Untersuchungen An Organophosphorverbindungen IV. Über den massenspektrometrischen Zerfall von Dithiophosphinsären. Phosphorus, Sulfur Silicon Relat. Elem. 1983; 14: 225-8.

27. Kallinowski G, Vogt W. ^{13}C Nuclear Magnetic Resonance Study of Some Phosphinolipids: Assignments and Conformational Studies. Magn Reson Chem. 1989; 27: 647-52.

28. Gray GA, Cremer SE. Carbon-13 nuclear magnetic resonance of organophosphorus compounds. III. Phosphorus heterocycles. J. Org. Chem. 1972; 37(22): 3458-69.

29. Al-Rawi JMA, Sheat MA, Ayed N. Carbon-13 NMR of some organophosphorus compounds. 2—chemical shifts and P-C coupling constants of diaryl-, dialkoxy- and diaryloxy-phosphine amines with general formula Y_2PNRR', Magn Reson Chem. 1984; 22(5): 336-39.

30. Grossmann G, Beckmann H, Rademacher O, Krüger K, Ohms G. Crystal structure, nuclear magnetic resonance spectroscopy and individual gauge for localised orbitals (IGLO) calculations of $C_6H_4P_2S_6$, a new tetrathiadiphosphorinane, and comparison with related P–S compounds. J. Chem. Soc., Dalton Trans. 1995; 2797-2803.

31. Beckmann H, Ohms G, Großmann G, Krüger K, Klostermann K, Kaiser V. Synthesis, crystal structure, and NMR spectroscopy of a 1,3,2λ5,4λ5-oxathiadiphosphetane. Heteroat. Chem. 1996; 7(2): 111-18.

32. Ernst L. ^{13}C n.m.r. spectroscopy of diethyl alkyl- and benzyl-phosphonates. A study of phosphorus–carbon spin–spin coupling constants over one to seven bonds. 1977; 9(1): 35-43.

NMR (1H, 13C, 31P) HSQC SPECTRA of the LIGANDS and COMPLEXES

[NH4][S2P(RX)(OR1)] 1H-NMR

$^1J_{HH}$ = 7.82 Hz

$^1J_{PH}$ = 16.97 Hz

C2H (dd)
7.99

C5H (d)
6.96

C3H (d)
6.92

$^3J_{HH}$ = 7.83 Hz

$^4J_{PH}$ = 6.02 Hz

C7H (s)
3.89

C9H (m)
3.94

C8H (s)
2.38

C10H (t)
1.27

$^3J_{HH}$= 7.09 Hz

[NH4][S2P(RX)(OR2)] 1-HNMR

C2H (dd) 8.05
$^3J_{HH}$ = 7.81 Hz
$^3J_{PH}$ = 17.29 Hz
8.08 f1 (ppm)
3234.47 3226.65 3217.17 3209.37

C5H (d) 6.95 | C3H (d) 6.91
$^4J_{PH}$ = 6.04 Hz
$^1J_{HH}$ = 7.80 Hz
6.96 6.92 f1 (ppm)
2782.76 2776.72 2767.78 2759.98

C7H (s) 3.87
C8H (s) 2.38

C10H (m) 4.68
1879.37 1873.07 1866.81 1864.61 1858.37
4.68 f1 (ppm)

C9H and C11H (d) 1.24
$^3J_{HH}$ = 6.24 Hz
500.47 494.23
1.26 f1 (ppm)

NH4+

8.08 8.06 8.04 8.02
6.95 6.94 6.92 6.90
4.74 4.73 4.71 4.70 4.68 4.66 4.66 4.64 4.63
3.88
2.38
1.25 1.24

f1 (ppm)

[Ni(S2P(RX)(OR1))2] 1-HNMR

C2H (dd) 7.88
$^3J_{HH}$ = 7.54 Hz
$^3J_{PH}$ = 18.14 Hz

C5H (d) 6.90
$^4J_{PH}$ = 6.47 Hz

C3H (d) 6.76
$^1J_{HH}$ = 5.05 Hz

C7H (s) 3.88

C8H (s) 2.42

C9H (m) 4.37

C10H (t) 1.37
$^3J_{HH}$ = 6.86 Hz

[Ni(S2P(RX)(OR2))2] 1-HNMR

7.91, 7.89, 7.86, 7.84

6.89, 6.87, 6.73, 6.72

5.19, 5.18, 5.16, 5.15, 5.14, 5.12, 5.11, 5.09

3.85

2.39

1.35, 1.33

3156.20, 3145.64, 3137.89

C2H (dd)
7.87

$^3J_{HH}$ = 7.75 Hz

$^3J_{PH}$ = 18.31 Hz

2756.72, 2750.05, 2693.25, 2687.41

C5H (d)
6.88

C3H (d)
6.72

$^4J_{PH}$ = 7.66 Hz

$^3J_{HH}$ = 5.84 Hz

2065.33, 2050.10

C10H (m)
5.14

C7H (s)
3.85

C8H (s)
2.39

539.36, 533.16

C9H and C11H (d)
1.34

$^1J_{HH}$ = 6.20Hz

7.88

6.9 6.8

5.1

1.36

1.83

1.93 1.84

1.95

6.14

6.08

11.53

8.0 7.5 7.0 6.5 6.0 5.5 5.0 4.5 4.0 3.5 3.0 2.5 2.0 1.5 1.0 0.5

[NH4][S2P(RY)(OR1)] 1H NMR

7.58 7.57 7.56 7.54 7.53 7.50
6.94 6.93 6.92 6.92
3.82 3.81 3.81 3.80 3.79 3.79 3.79 3.78 3.78 3.77
2.12
1.14 1.12 1.11

C7H (s)
3.77

C8H (s)
2.12

3792.76 3784.69 3779.64 3771.61 3763.78 3750.97

C2H (dd)
7.56

C6H (d)
7.51

$^3J_{HH} = 8.38\ Hz$

$^3J_{PH} = 12.81\ Hz$

$^3J_{PH} = 12.76\ Hz$

3470.70 3467.62 3462.28 3459.20

C3H (dd)
6.93

$^4J_{PH} = 3.08\ Hz$

$^3J_{HH} = 8.43\ Hz$
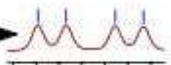
1897.01 1895.90 1888.77

C9H (m)
3.80
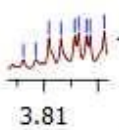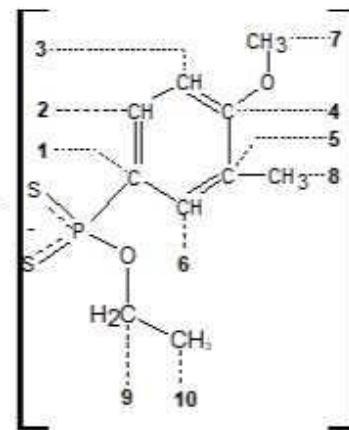
568.95 561.86 554.76

C10H (t)
1.12

$^3J_{HH} = 7.09\ Hz$

NH_4^+

7.55   7.50

6.94

3.81

1.14

0.97 0.98   0.96   1.74 3.12   3.05   2.97

[NH4][S2P(RY)(OR2)] 1H NMR

C2H (dd) 7.82
C6H (d) 7.77
$^3J_{PH}$ = 13.70 Hz
$^3J_{HH}$ = 8.47 Hz
$^3J_{PH}$ = 14.06 Hz

C3H (dd) 6.96
$^4J_{PH}$ = 3.03 Hz
$^3J_{HH}$ = 8.49 Hz

C7H (s) 3.81

C10H (m) 4.56

C8H (s) 2.16

C9H and C11H (d) 1.15
$^3J_{HH}$ = 6.25 Hz

[Ni(S2P(RY)(OR1))2] 1H NMR

7.93, 7.91, 7.90, 7.88, 7.83, 7.81

6.94, 6.94, 6.93, 6.92

4.49, 4.47, 4.46, 4.44, 4.43

3.92

2.31

1.47, 1.45, 1.44

3957.28, 3953.15, 3942.97, 3917.69, 3904.38

3473.34, 3470.26, 3464.92, 3461.86

2230.39, 2227.50

733.97, 726.88, 719.74

C2H (dd) 7.91 C6H (d) 7.82

$^{3}J_{PH}$ = 13.31 Hz

$^{3}J_{HH}$ = 9.39 Hz

$^{3}J_{PH}$ = 13.52 Hz

C3H (dd) 6.93

$^{4}J_{PH}$ = 3.07 Hz

$^{3}J_{HH}$ = 8.41 Hz

C9H (m) 4.46

C7H (s) 3.92

C8H (s) 2.31

C10H (t) 1.45

$^{3}J_{HH}$ = 7.12 Hz

7.91

6.94

1.46

1.89, 1.73

2.02

3.58

5.88

5.92

6.43

[Ni(S2P(RY)(OR2))2] 1H NMR

[NH4][S2P(RX)(OR1)] 13C-NMR
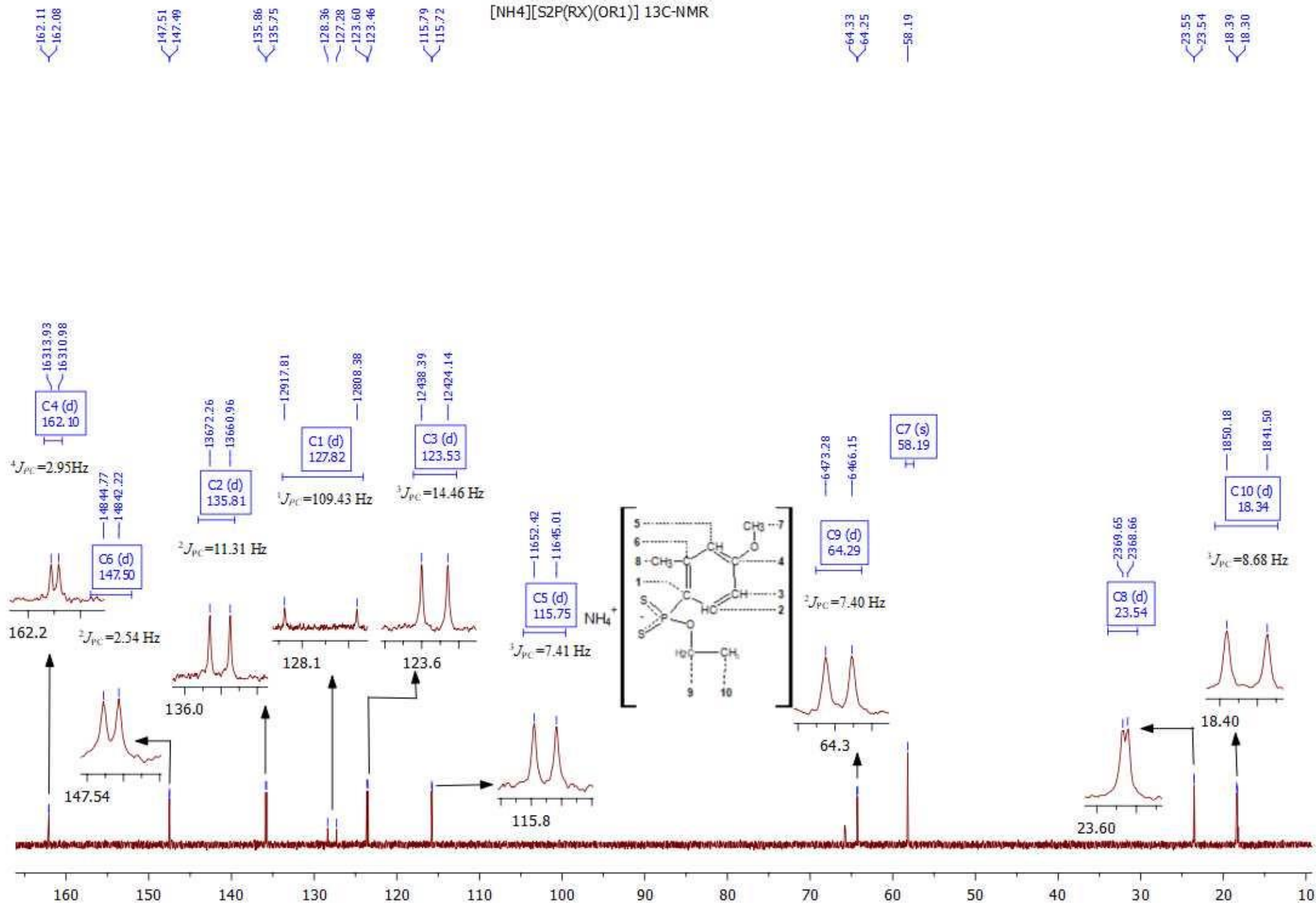
[NH4][S2P(RX)(OR2)] 13C-NMR

[Ni(S2P(RX)(OR1))2] 13C-NMR

[Ni(S2P(RX)(OR2))2] 13C-NMR

[NH4][S2P(RY)(OR1)] 13C NMR

[NH4][S2P(RY)(OR2)] 13C NMR

[Ni(S2P(RY)(OR1))2] 13C NMR

[NH4][S2P(RX)(OR1)] 31P-NMR

102.59

[NH4][S2P(RX)(OR2)] 31P-NMR
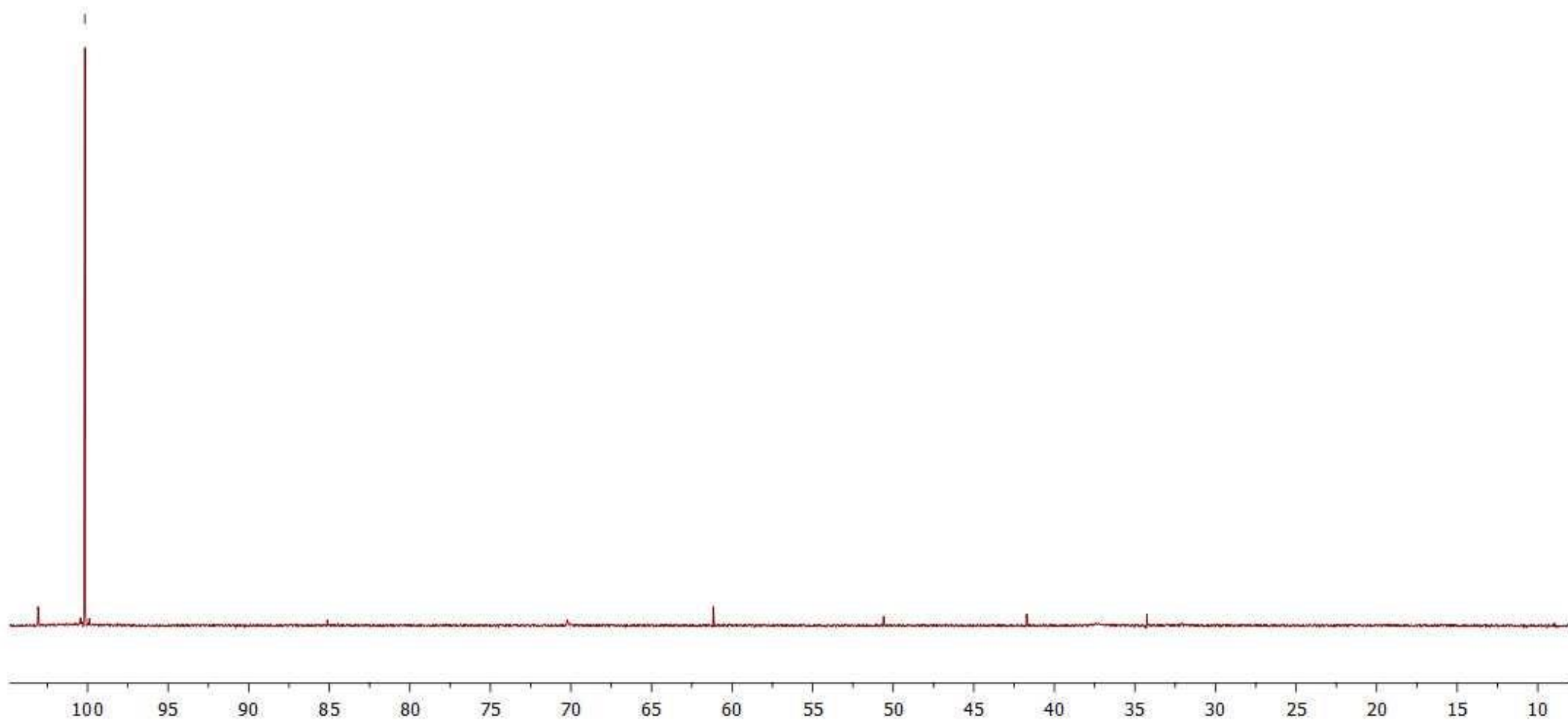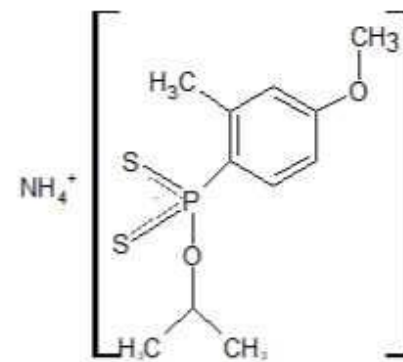
[Ni(S2P(RX)(OR1))2] 31P-NMR
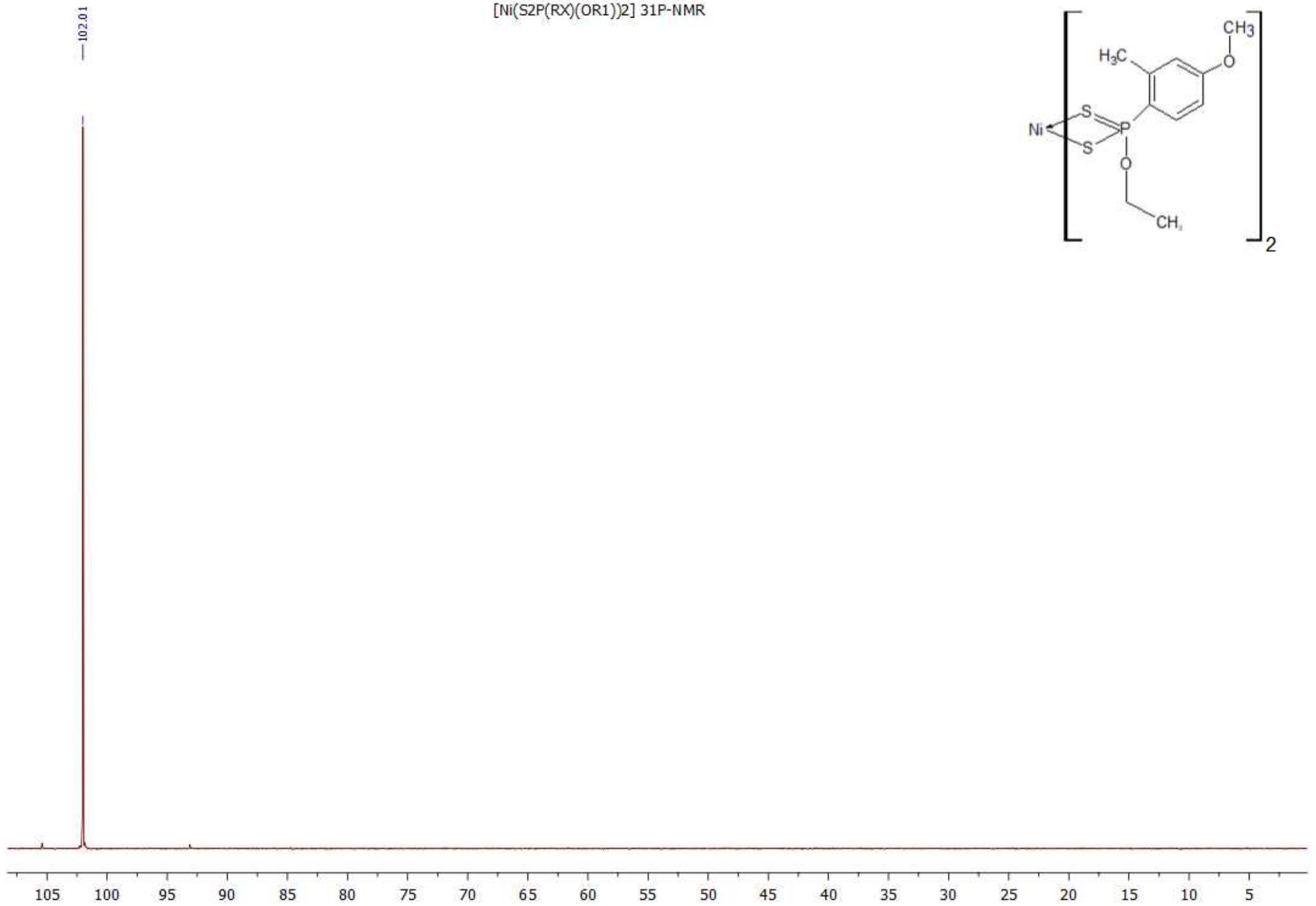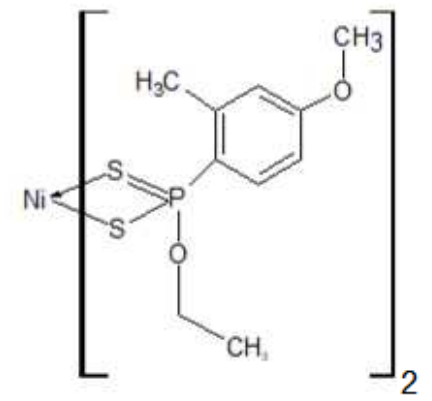
[Ni(S2P(RX)(OR2))2] 31P-NMR

[NH4][S2P(RY)(OR1)] 31P NMR

67.51
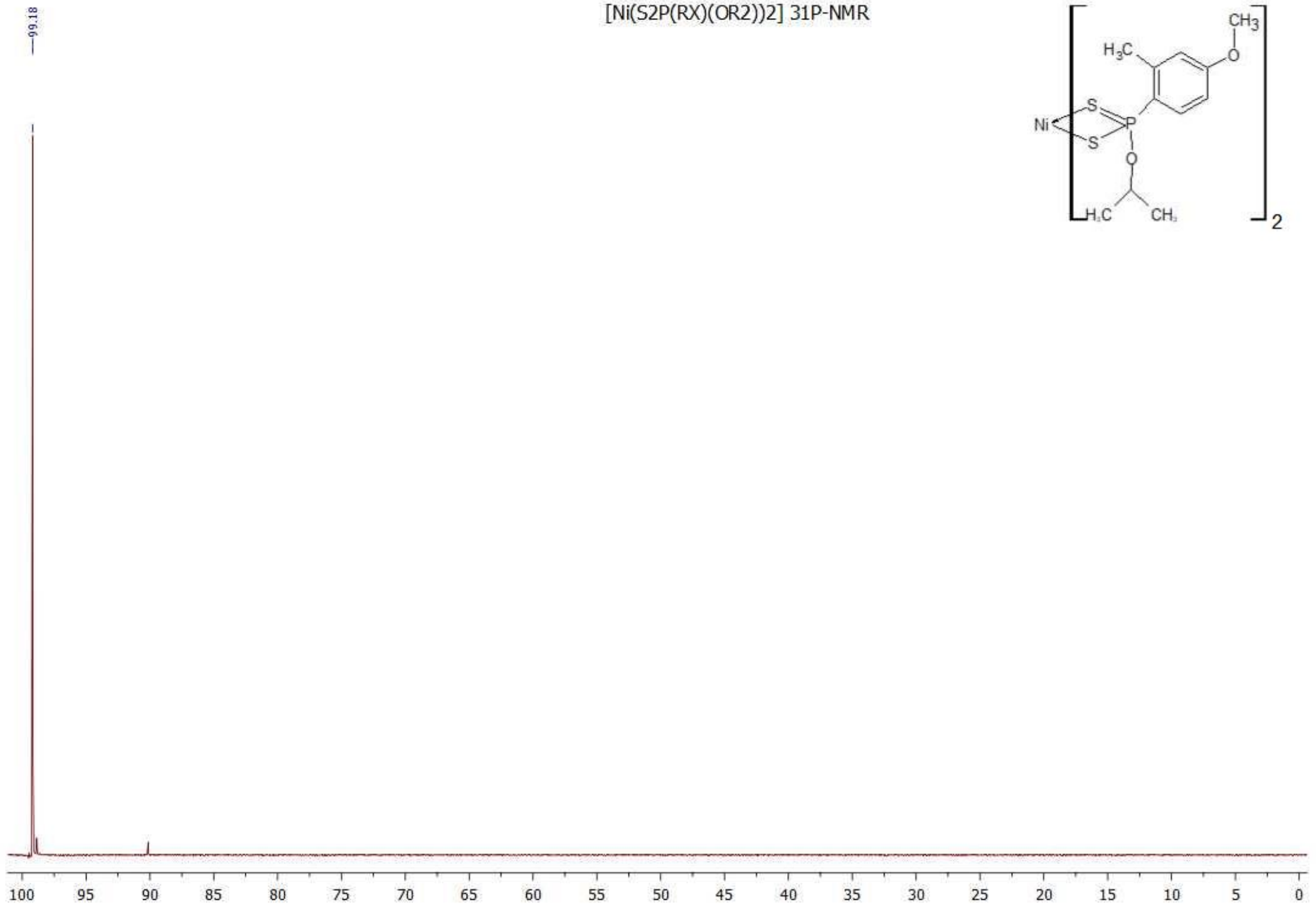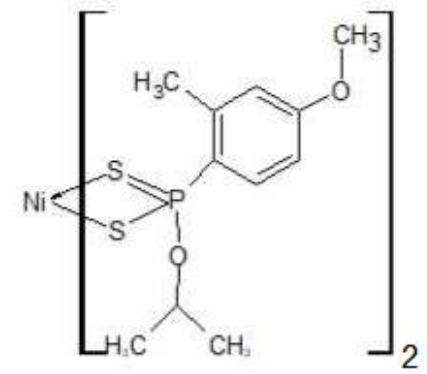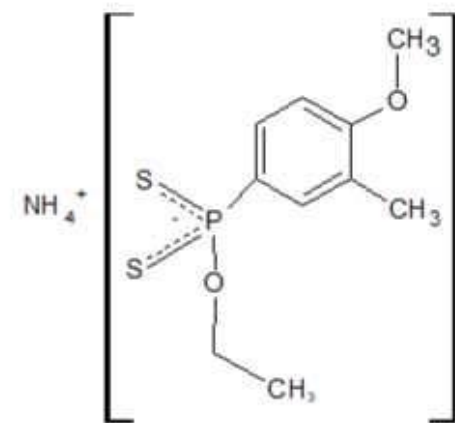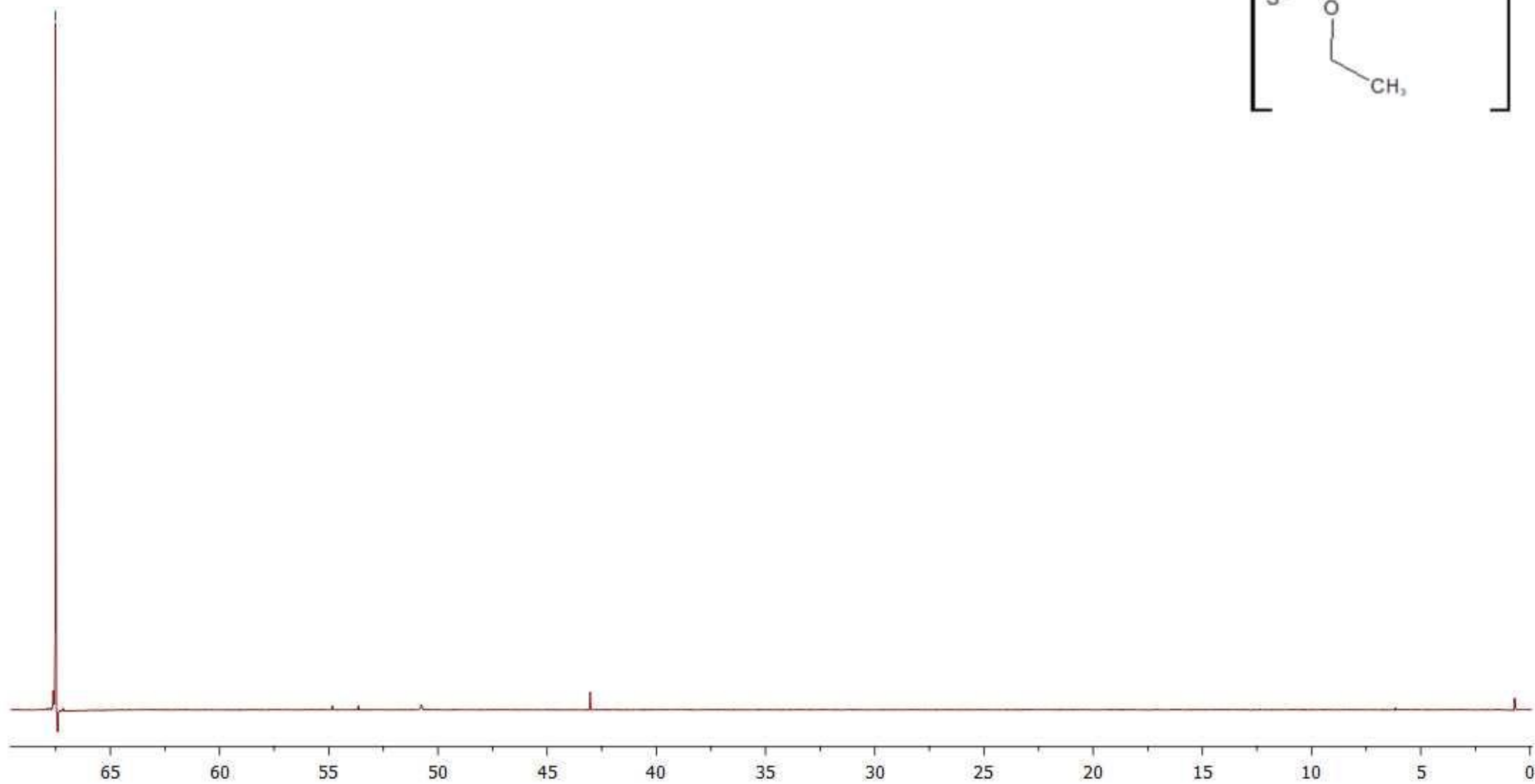
[NH4][S2P(RY)(OR2)] 31P NMR

103.81
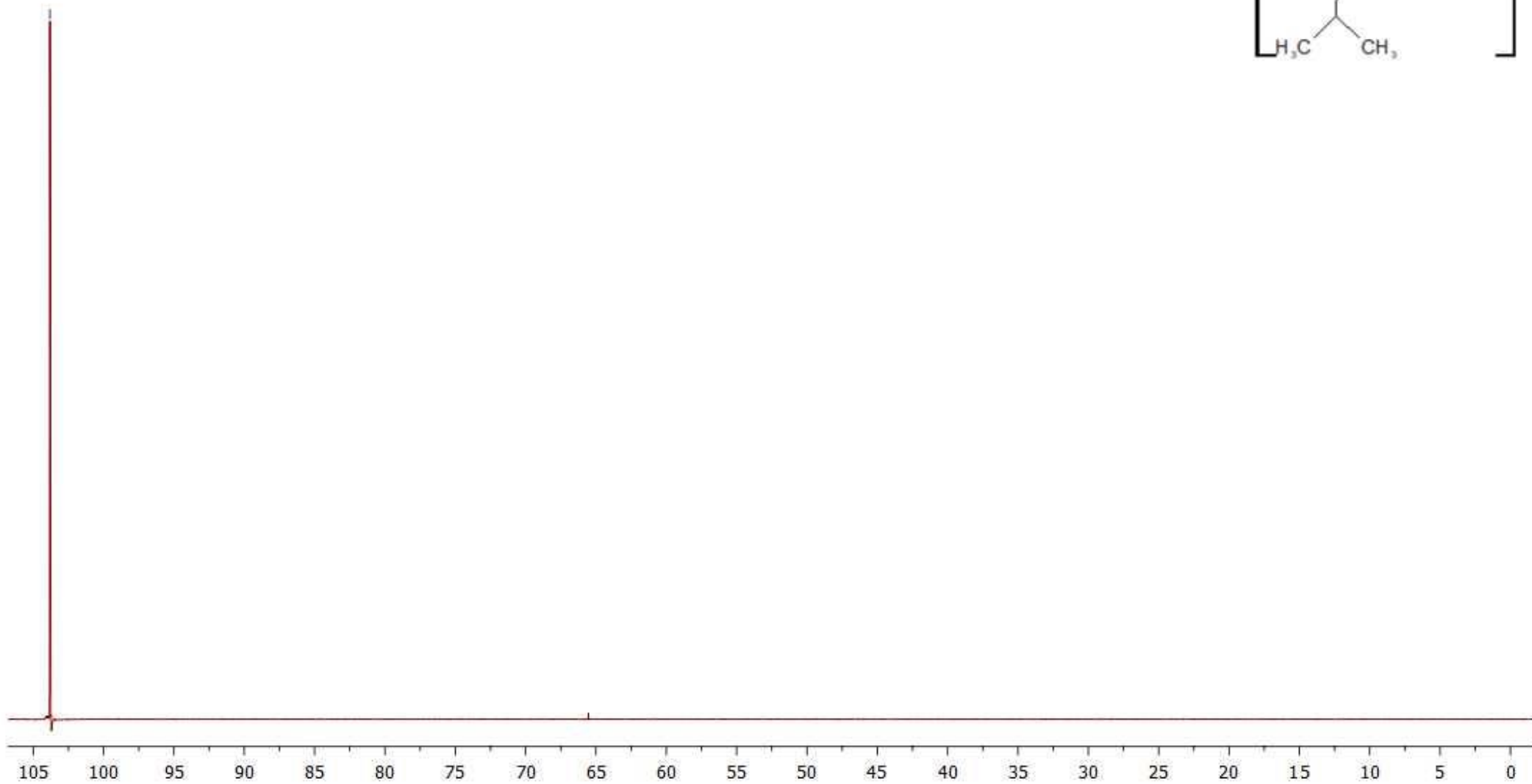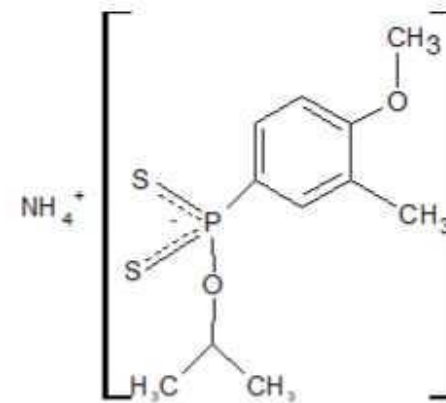
[Ni(S2P(RY)(OR1))2] 31P NMR
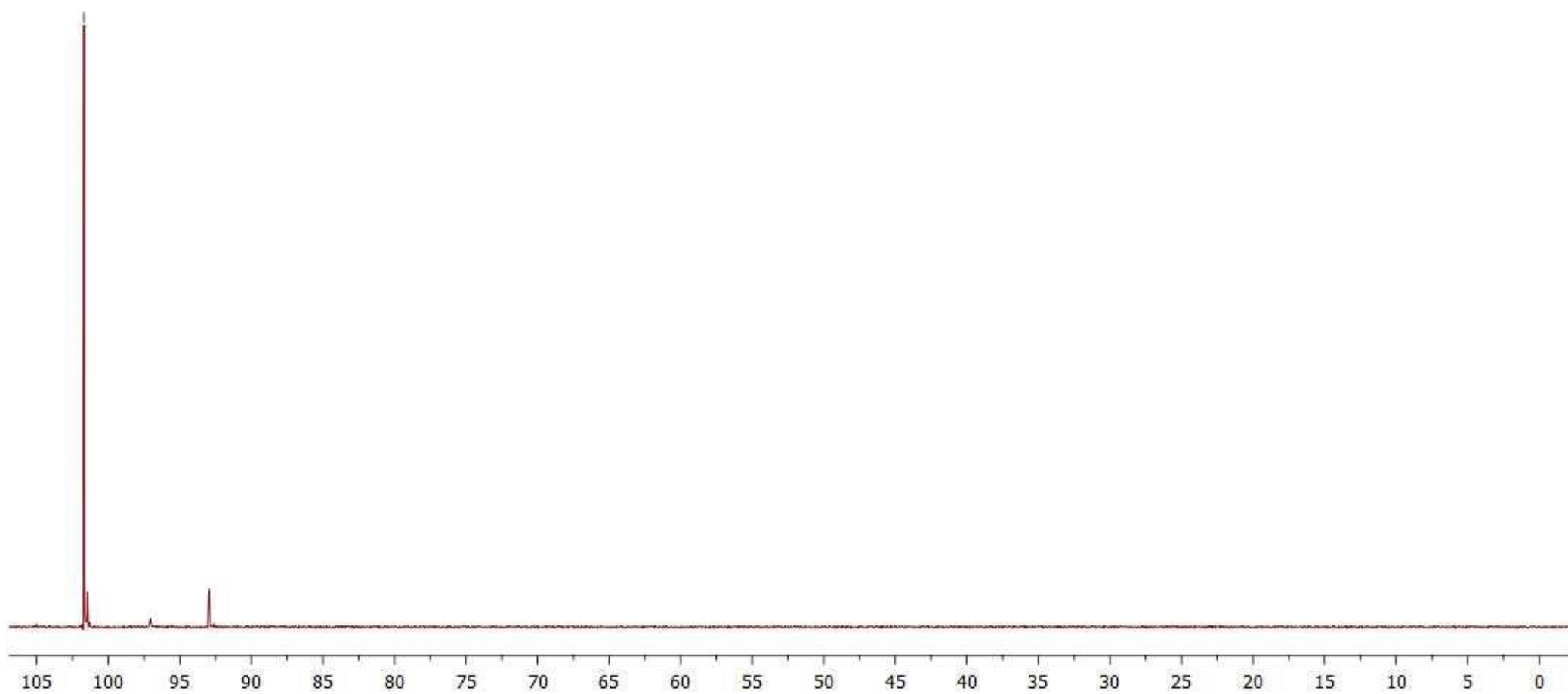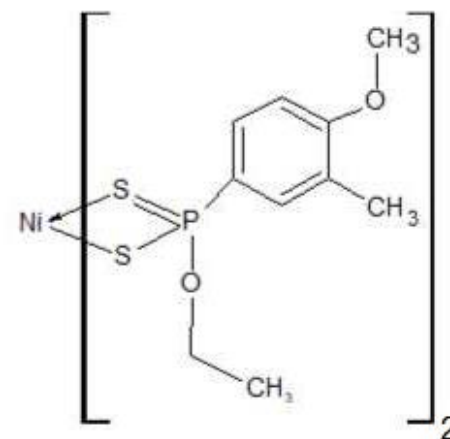
[Ni(S2P(RY)(OR2))2] 31P NMR
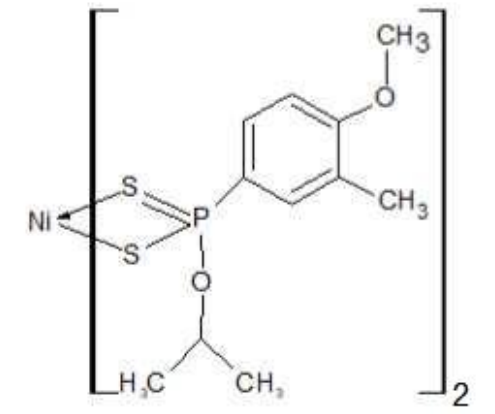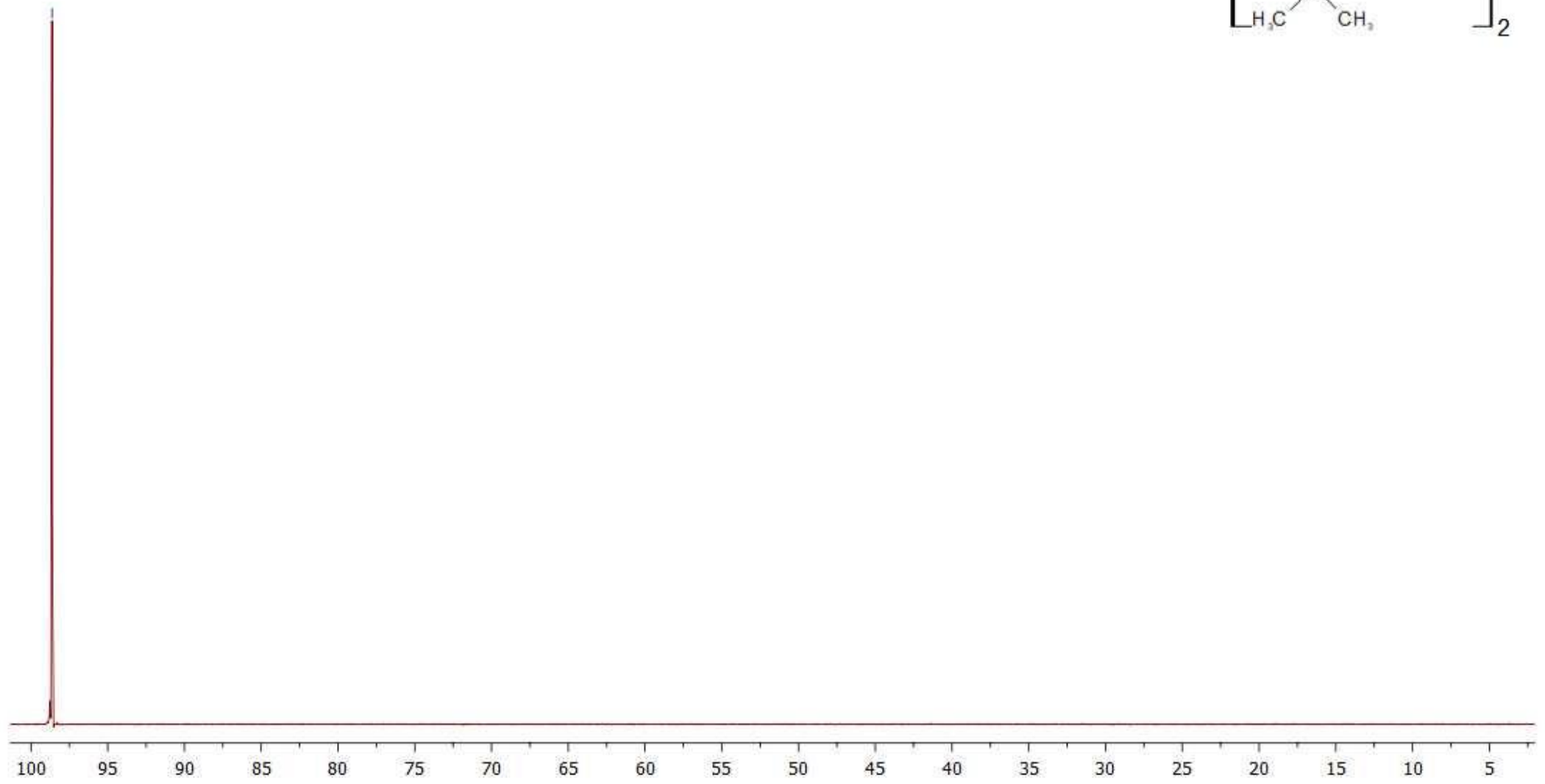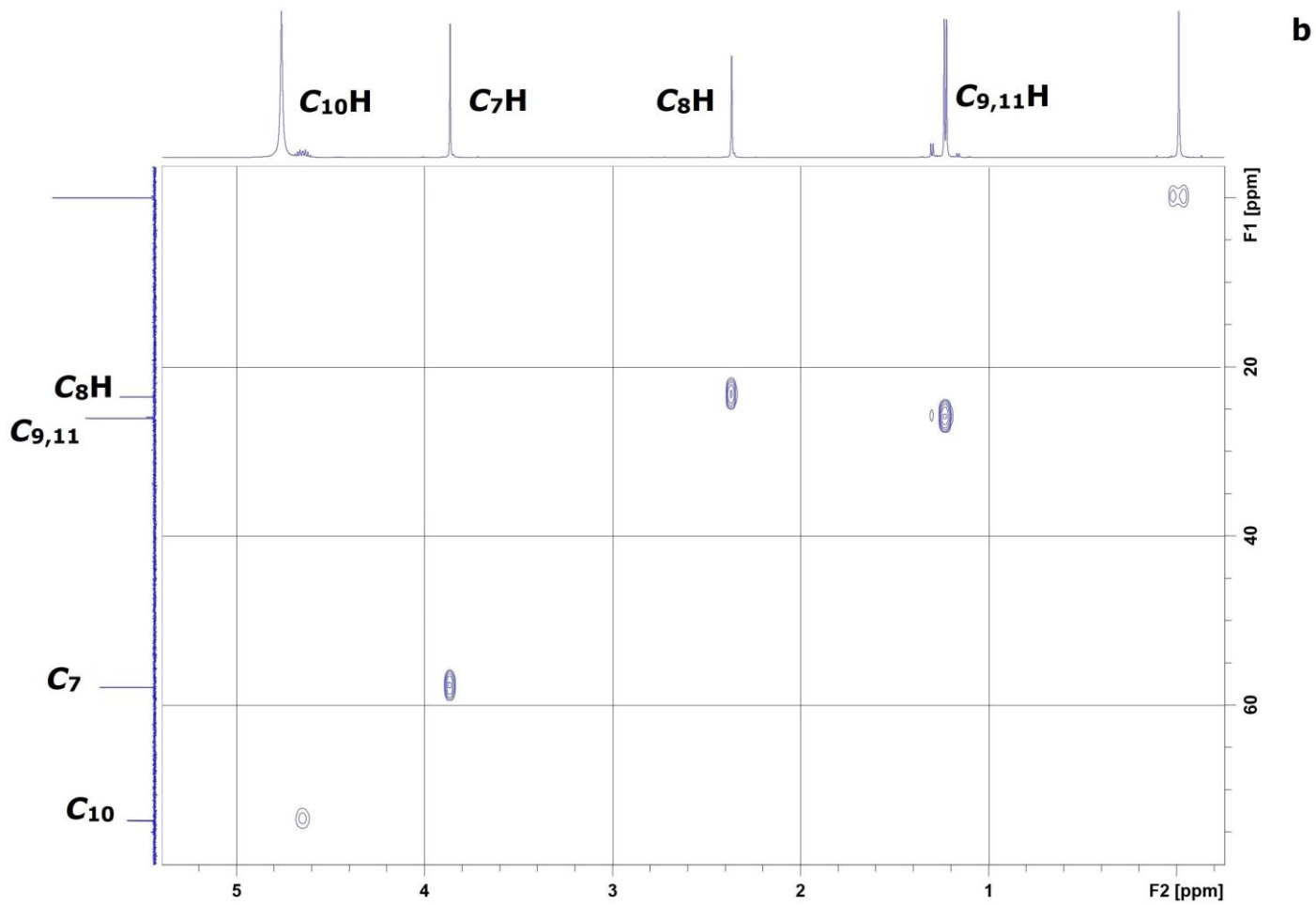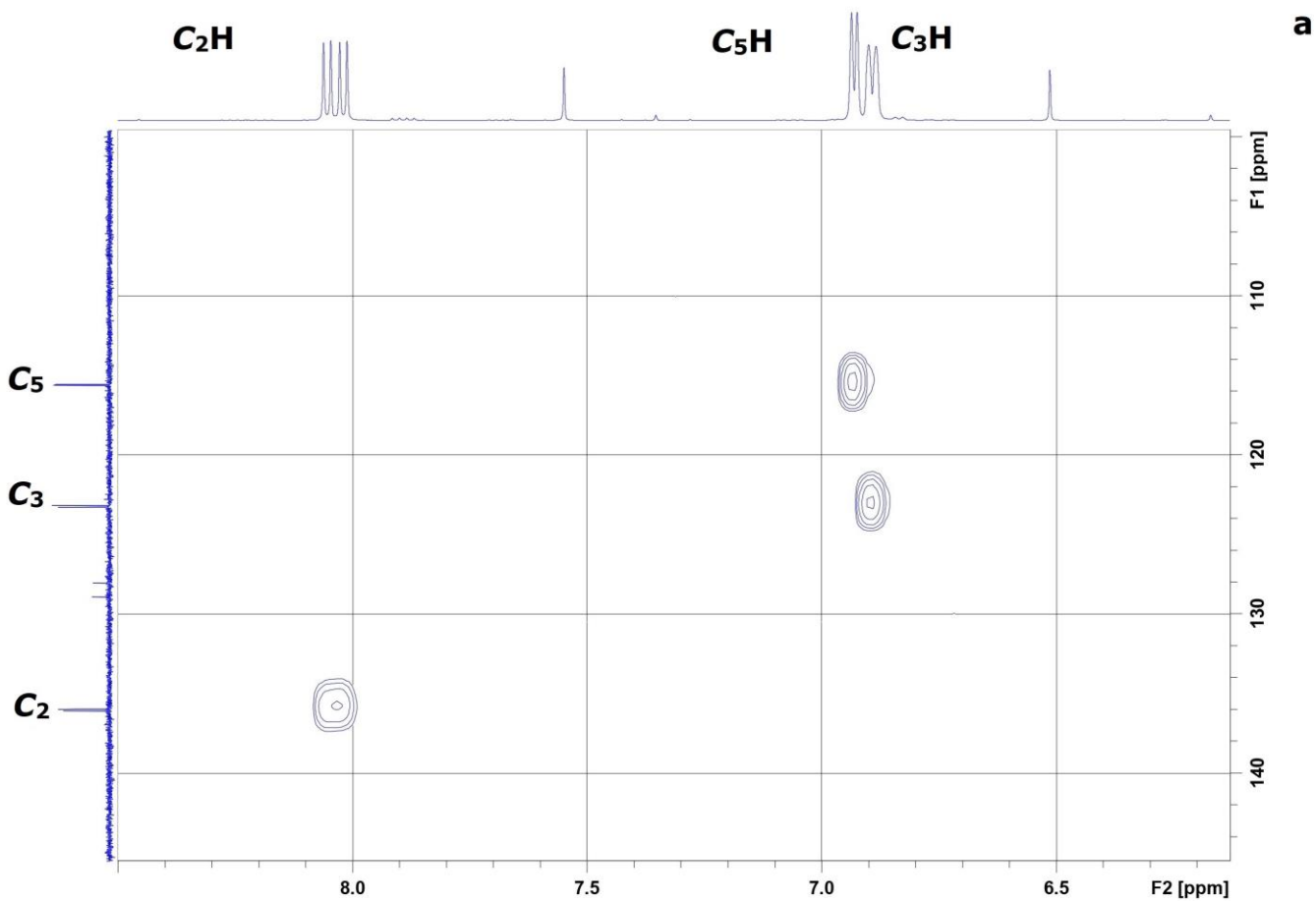
$[NH_4][S_2P(R^x)(OR2)]$

[NH₄][S₂P(Rʸ)(OR2)]

MASS SPECTRA OF THE LIGANDS and Ni(II) COMPLEXES
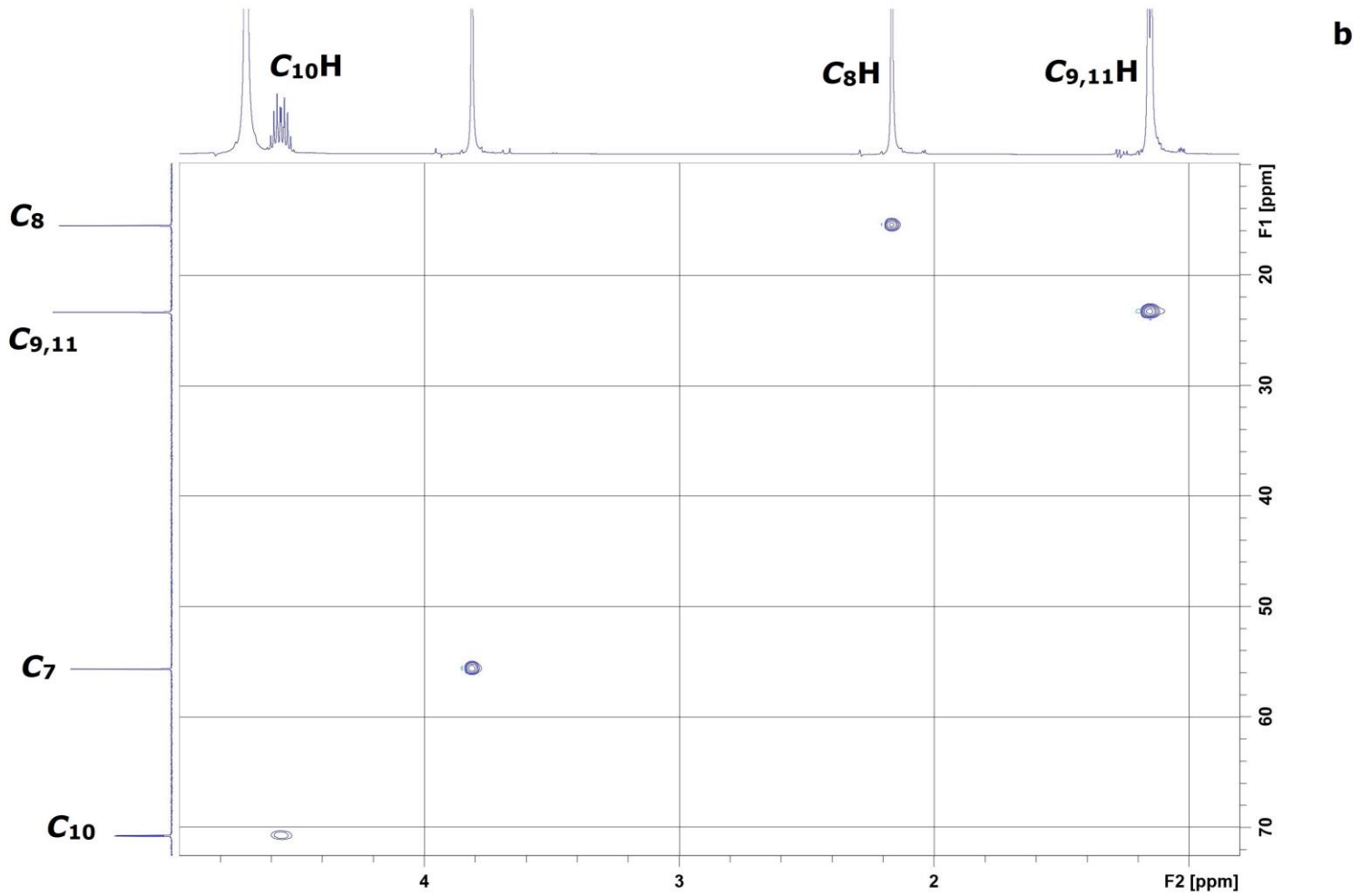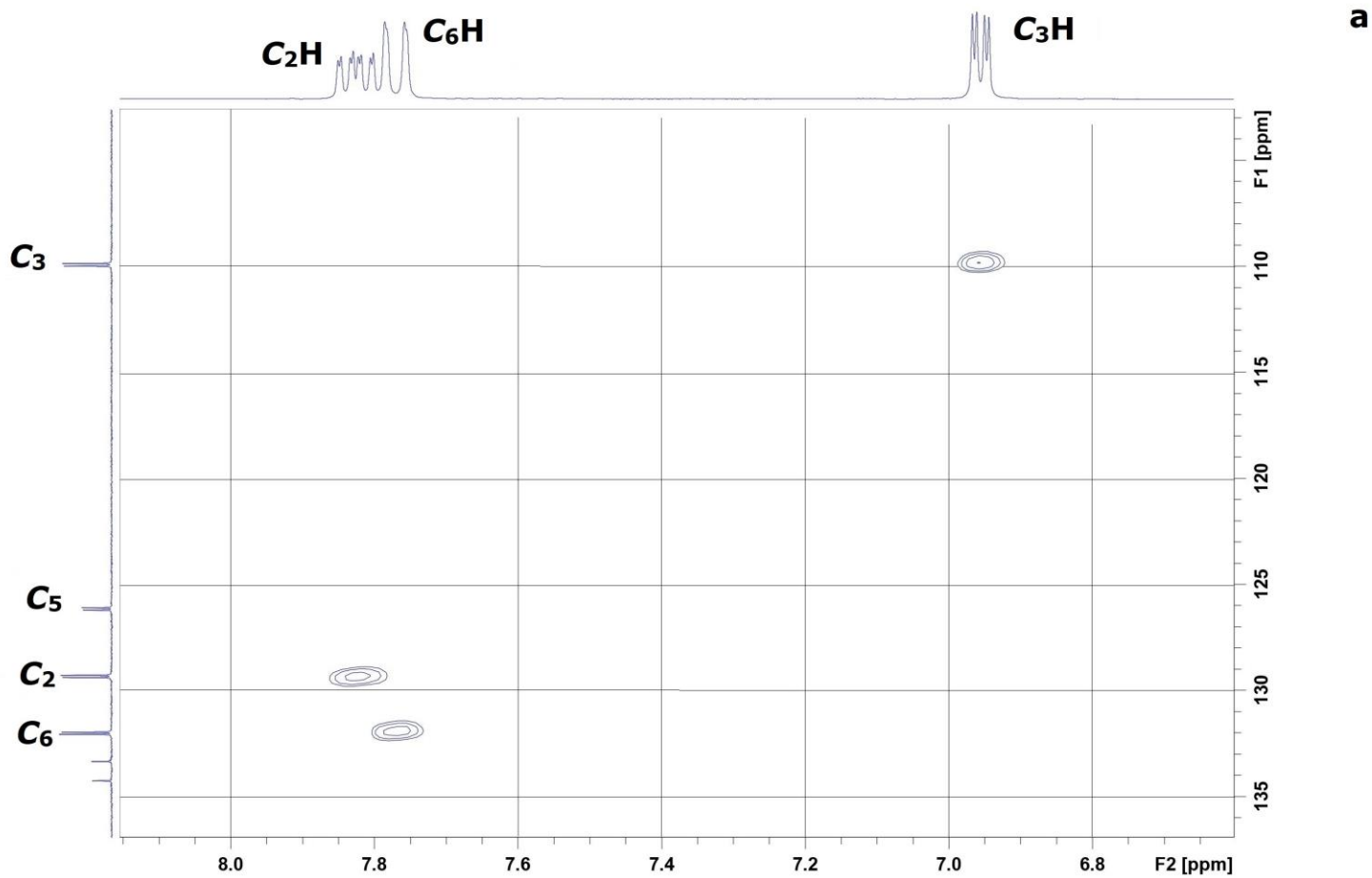
SAV3-Et 12 (0.232) Cn (Cen,2, 80.00, Ht)

[NH₄][S₂P(Rˣ)(OR1)]
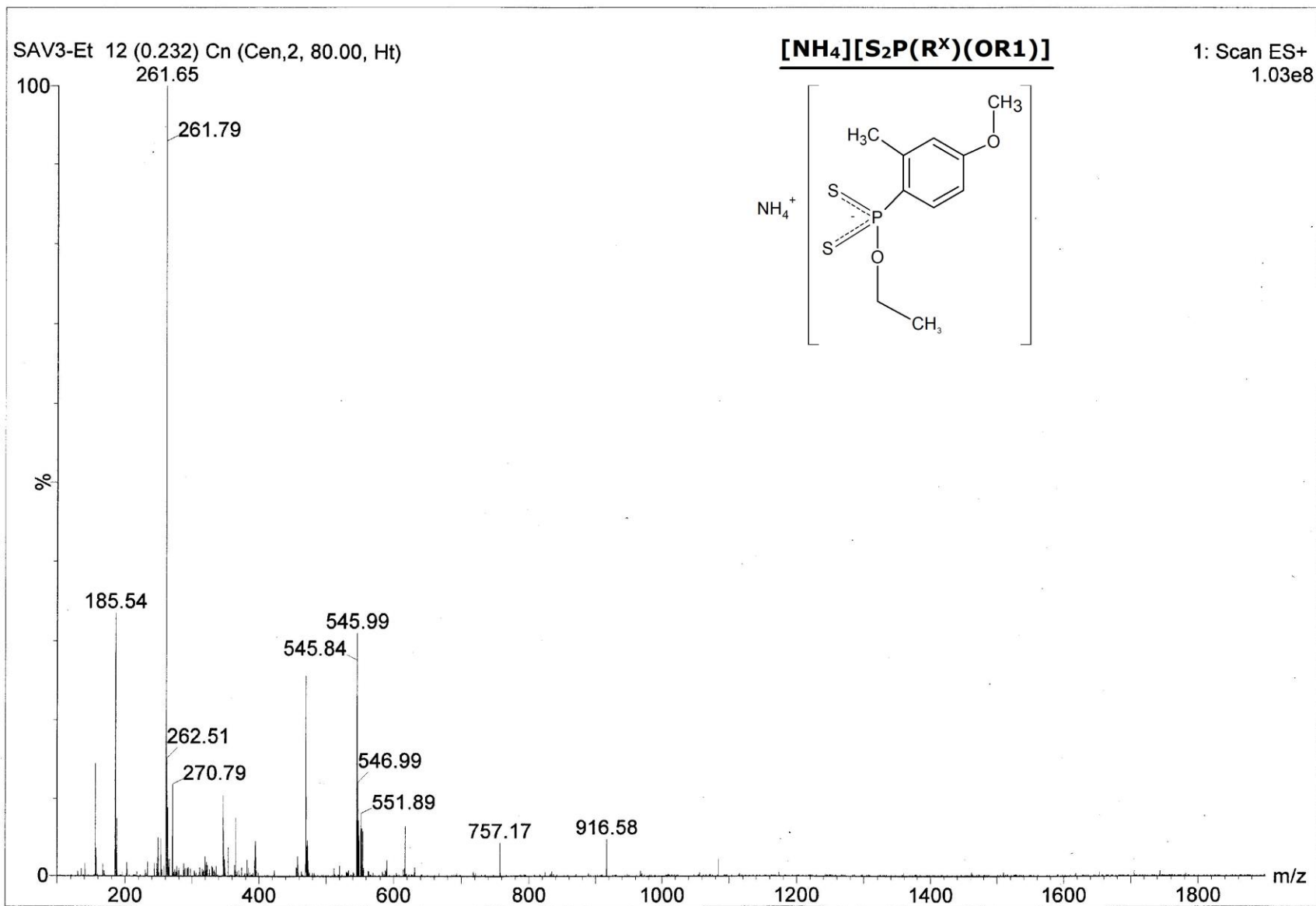
1: Scan ES+
1.03e8

SA3-2-Pr 13 (0.252) Cn (Cen,2, 80.00, Ht)

1: Scan ES+
3.59e7

$[NH_4][S_2P(R^X)(OR2)]$

100 -

%

0 -

275.69

213.56

512.11

573.93
574.28

511.78

276.55

574.96

195.69

276.78   449.79

576.00

360.94

663.93

837.96   872.25

1083.85 1167.23

1353.43 1506.94   1698.03   1854.13

m/z

200   400   600   800   1000   1200   1400   1600   1800
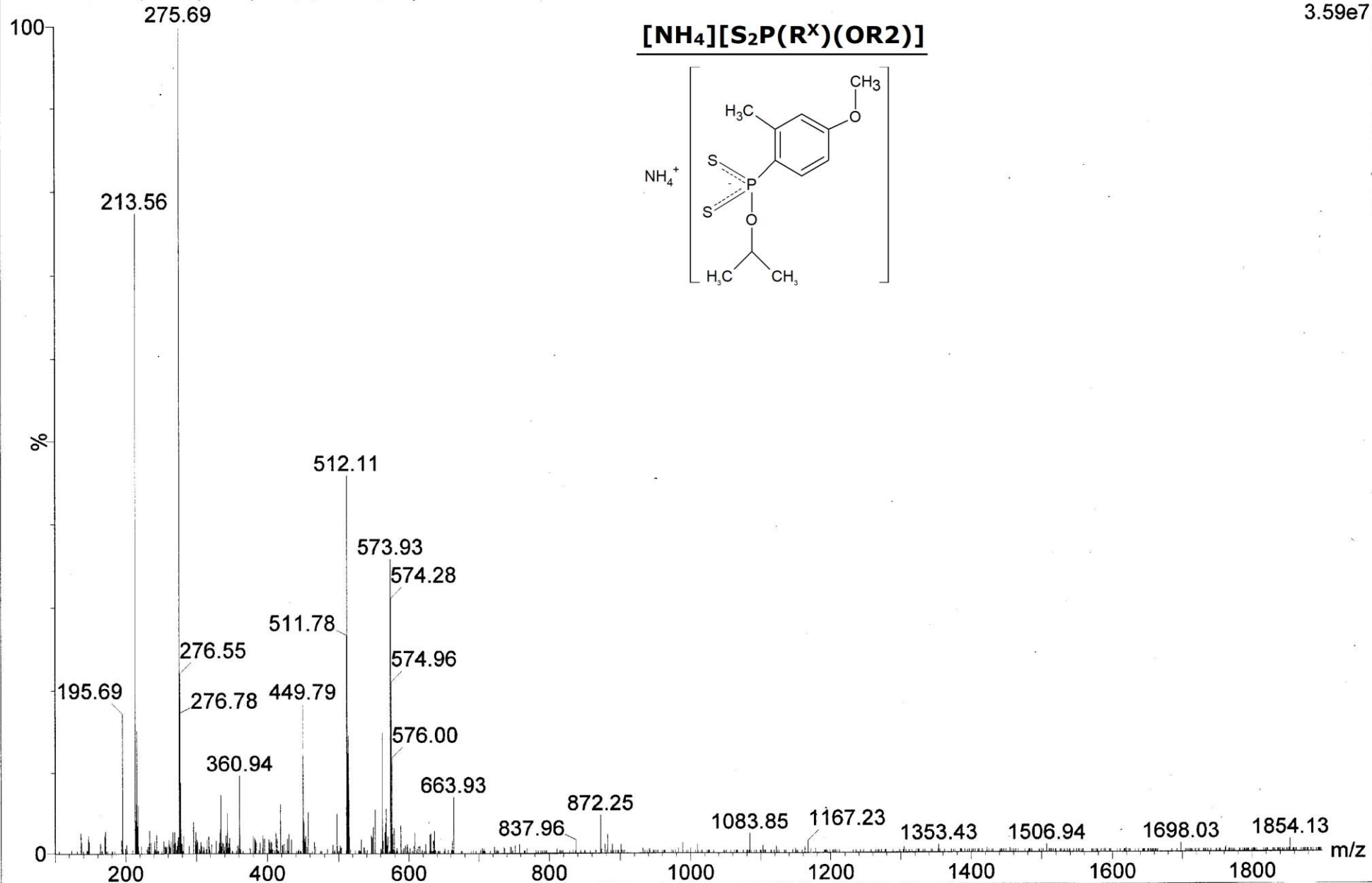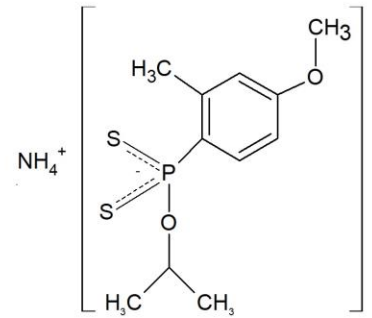
SAV4-Et 10 (0.192)

1: Scan ES+
1.34e8
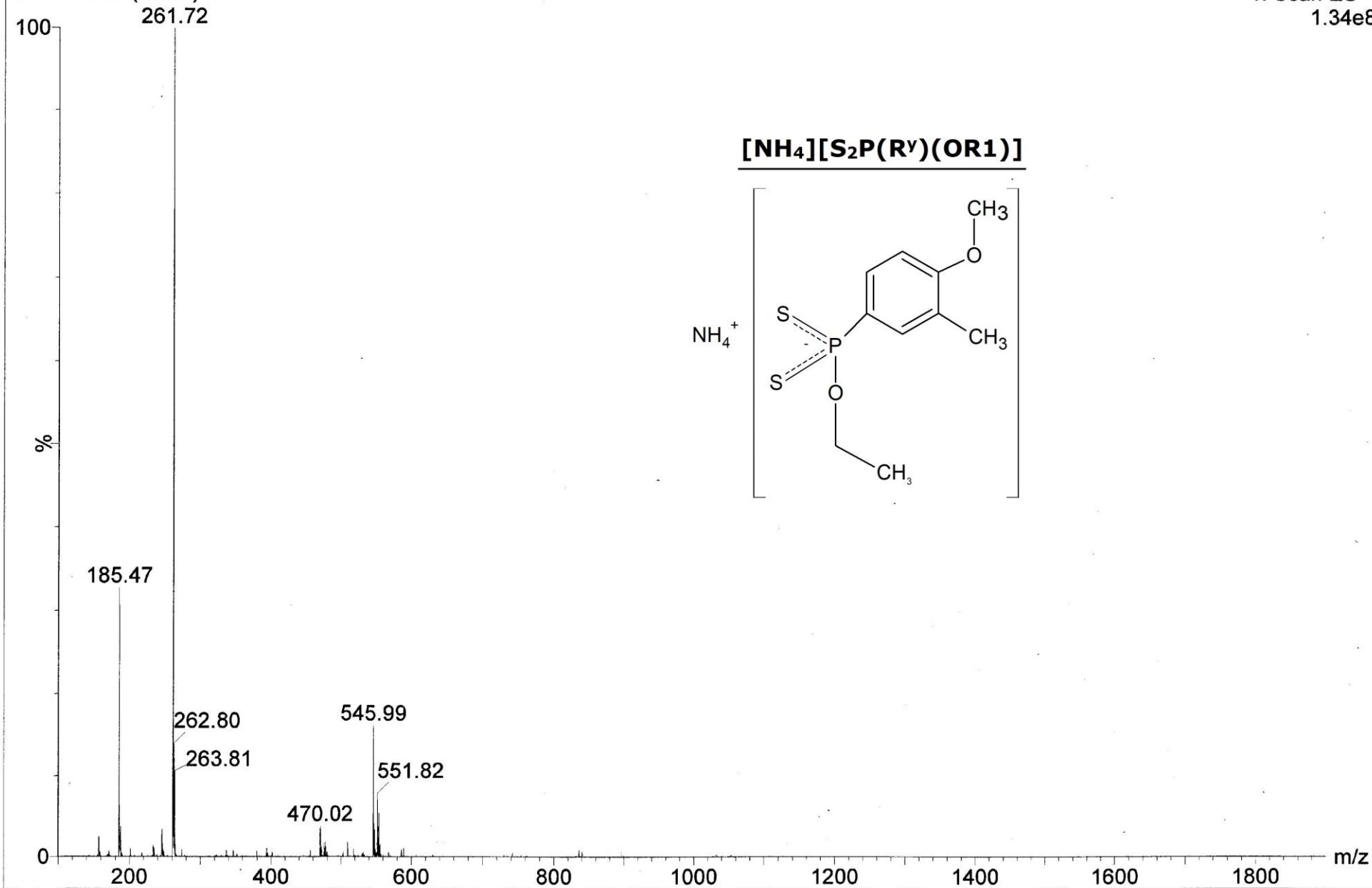
$[NH_4][S_2P(R^y)(OR1)]$
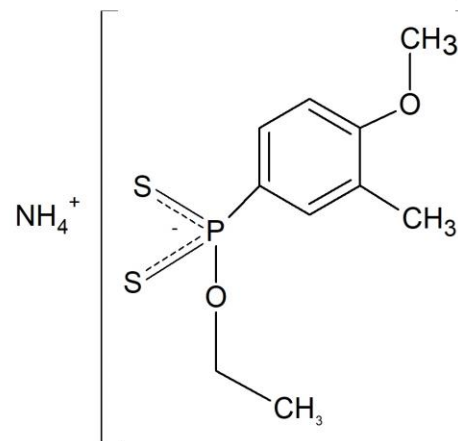
SAV4-2pr 10 (0.192)

1: Scan ES+
2.11e7
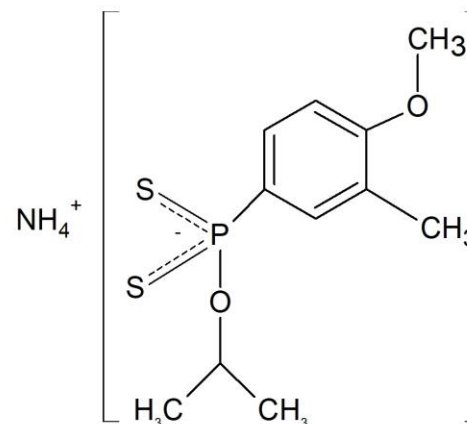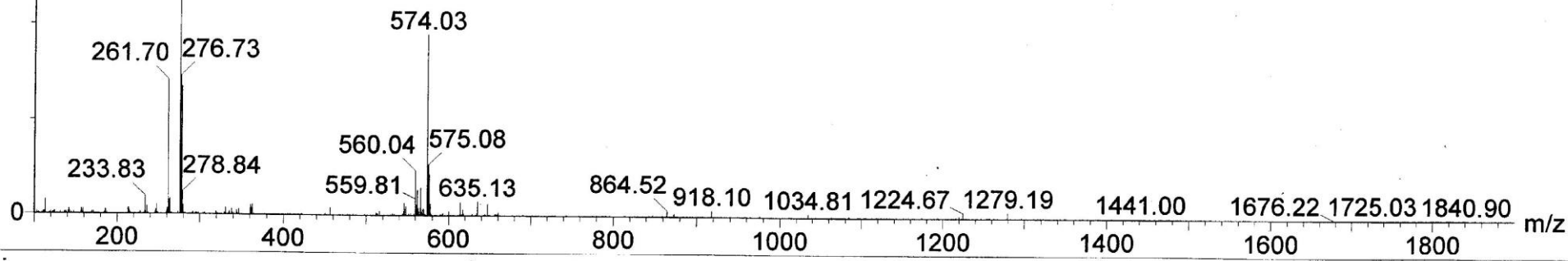
$[NH_4][S_2P(R^y)(OR2)]$

SAV3-Et-Ni 9 (0.172) Cn (Cen,2, 80.00, Ht)

1: Scan ES+
9.39e6

[Ni(S₂P(Rˣ)(OR1))₂]

100 — 581.93

152.63

581.63
584.08
604.02

902.17
900.10
1181.43
1181.63

153.42

536.05
606.02
1179.35

%

360.78
903.14
905.06

229.41
362.95
1190.28

229.70
401.57
611.25
686.08 745.58
908.07
1179.04 1190.63

406.66
986.36
1301.51 1427.52 1548.66 1762.94 1889.99

0
200   400   600   800   1000   1200   1400   1600   1800   m/z
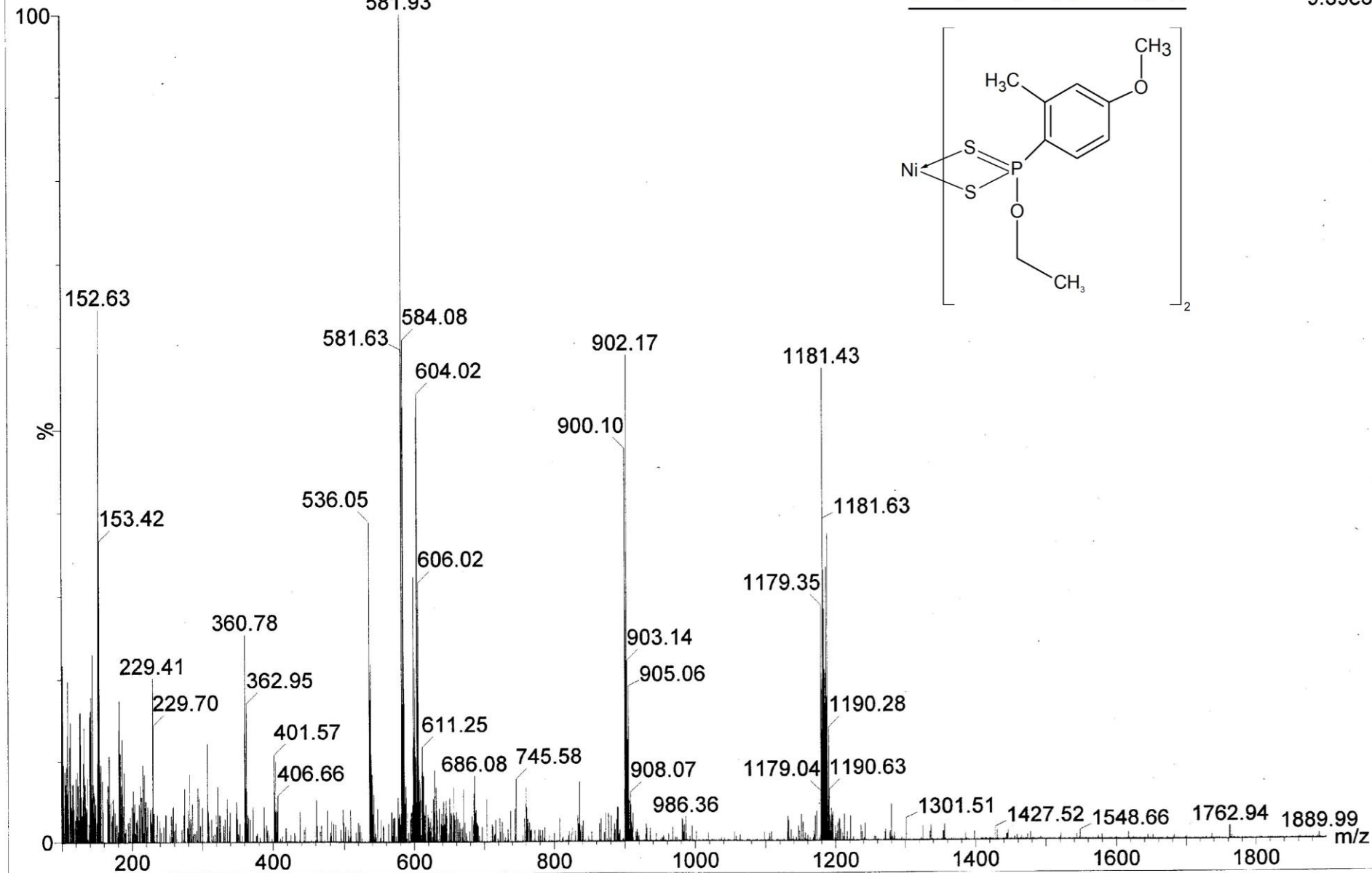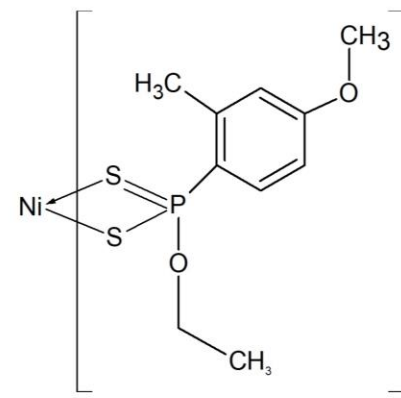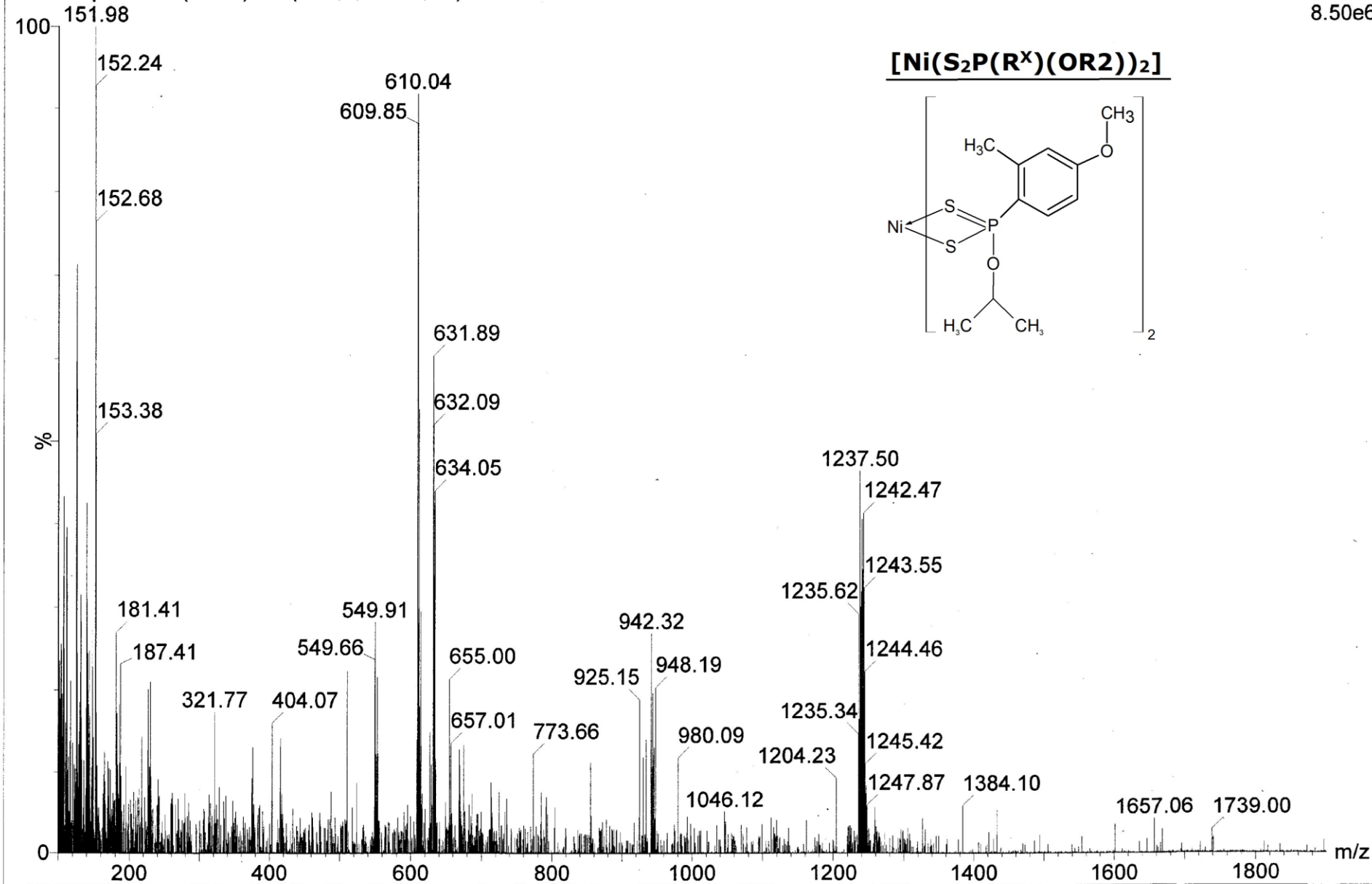
SAV4-Et-Ni 9 (0.172) Cn (Cen,2, 80.00, Ht)

1: Scan ES+
3.81e7

$[Ni(S_2P(R^y)(OR1))_2]$

100 — 152.34

152.63

%

153.28

153.64

581.93

582.13

583.72

599.03

902.13

904.08

904.27

906.07

906.53

185.39

360.77

535.79

508.33

627.03

825.93

1183.44

1299.21

1408.36

1718.70

1799.24

0

200   400   600   800   1000   1200   1400   1600   1800   m/z
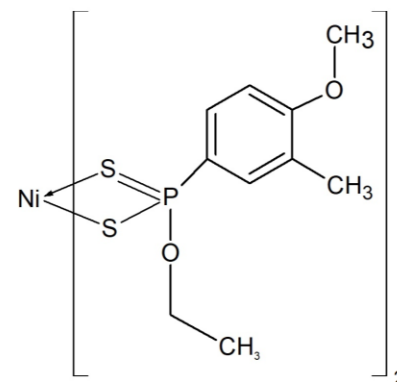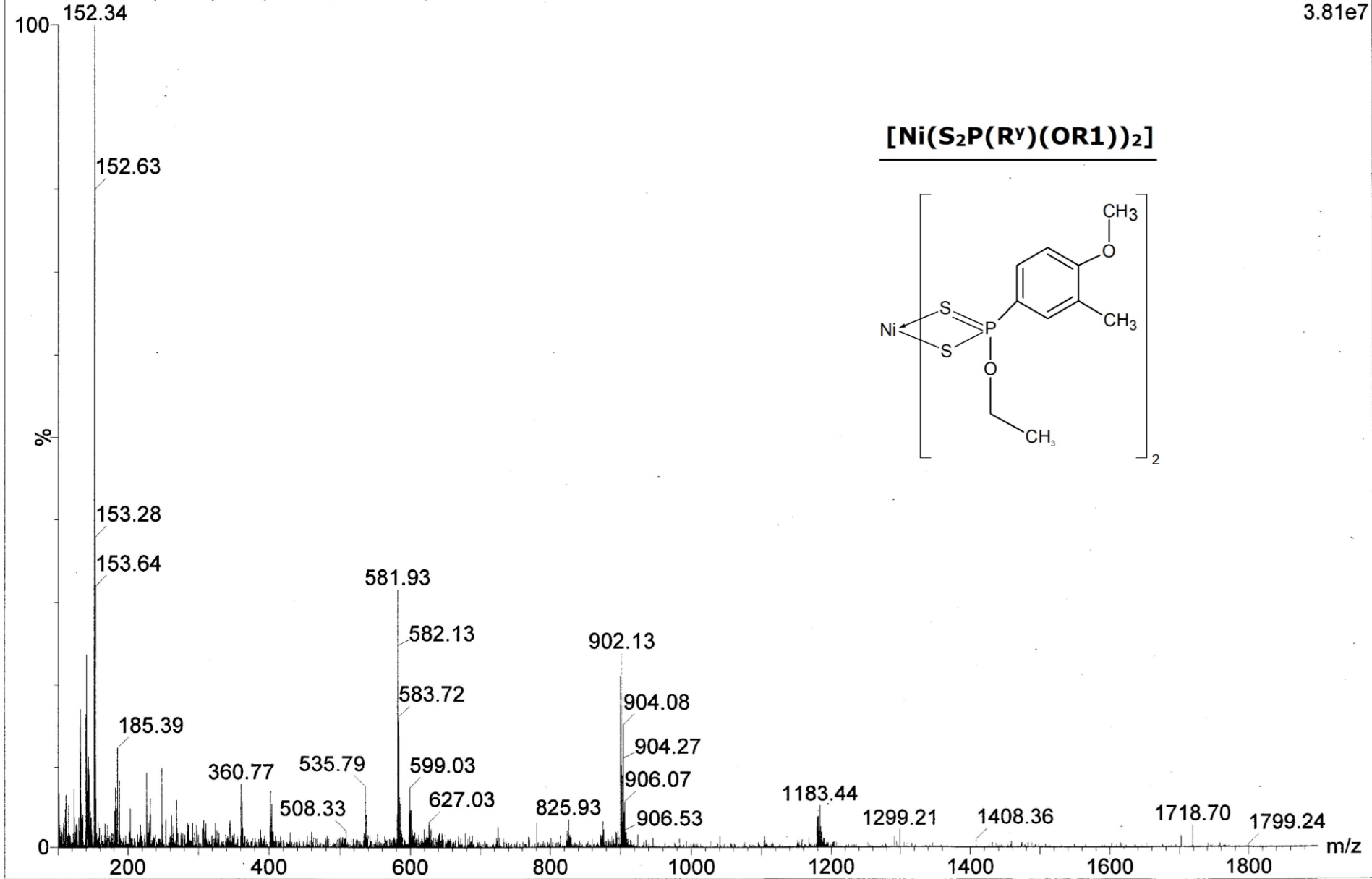
SAV4-2-Pr-Ni 12 (0.232)

1: Scan ES+
1.08e7

100

%

0

$[Ni(S_2P(R^y)(OR2))_2]$

610.00
609.85
611.94
612.95
614.03
944.16
944.31
942.15
946.32
947.11
235.73
321.91
374.69
416.02
417.82
418.97
139.89
595.96
685.24
760.27
890.09
930.19
948.12
949.13
1235.56
1237.43
1235.41
1243.91
1244.56
1223.97
1221.52
1245.71
1258.53
1462.29
1869.76

200   400   600   800   1000   1200   1400   1600   1800   m/z
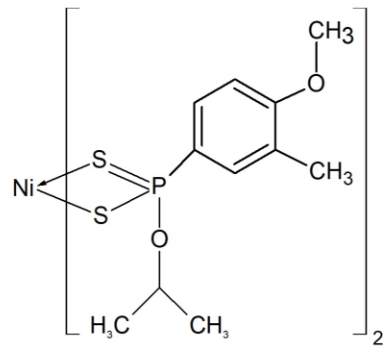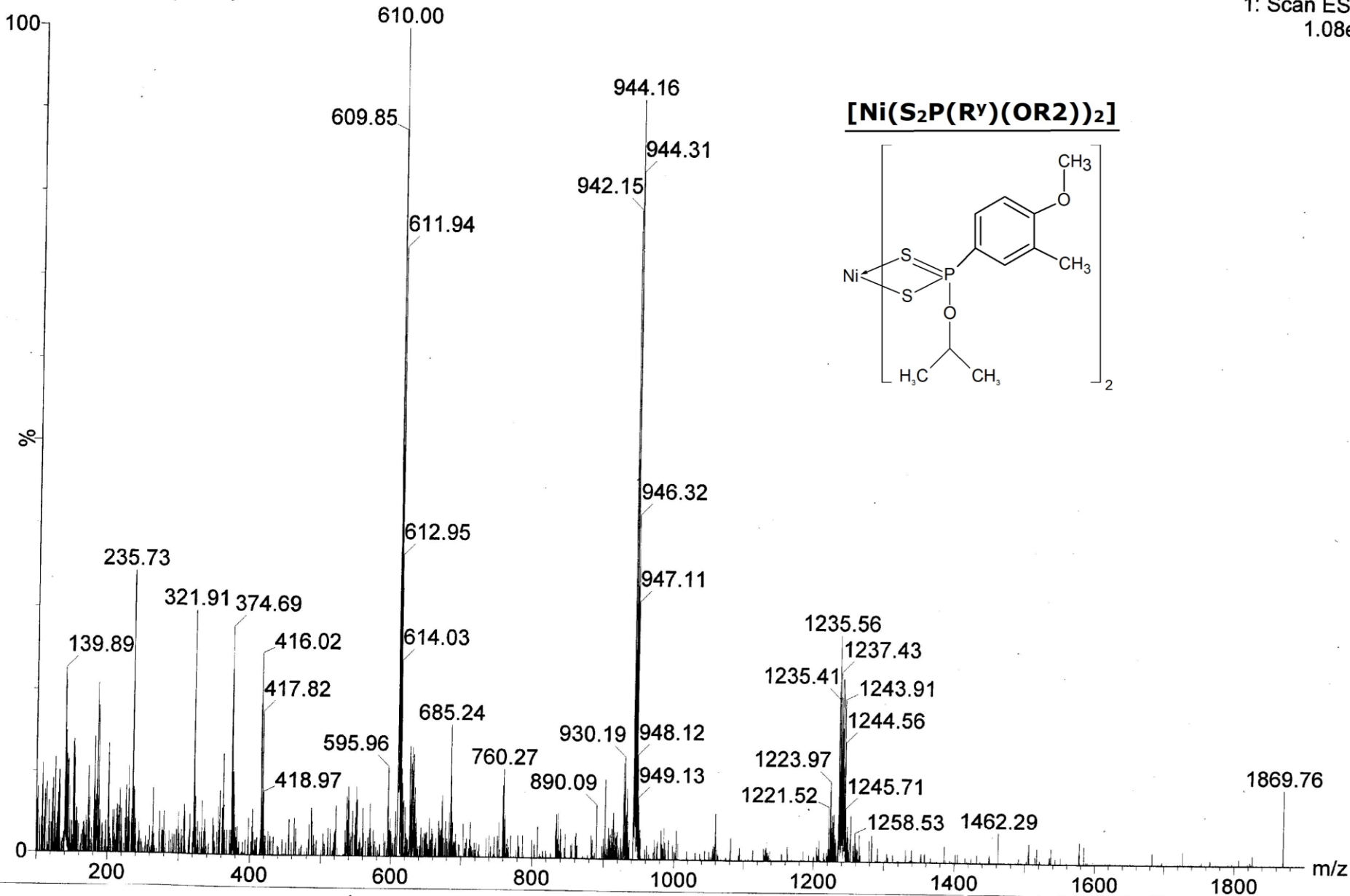
Determination of Some Pesticides Harmful To Environment and Human Health in Bogazköy (Turkey) Dam Water by LC-MS/MS

İbrahim Yılmaz[1] ✉ iD **, Gülbin Erdoğan[2]*** ✉ iD

[1]University of Marmara, Institute of Health Sciences, 34854-Maltepe, Istanbul, Turkey.
[2]University of Marmara, Faculty of Pharmacy, 34854-Maltepe, Istanbul, Turkey.

Abstract: Pesticides are the most dangerous organic pollutants for human and environmental health. These are substances that are harmful to health, the use of which has increased in recent years, to kill pests in agricultural production. The areas of use of pesticides, apart from agricultural activities, are in the fight against mosquitoes, which cause malaria, which creates a significant health problem for human health in the landscape, construction industry, timber protection, forestry, control of aquatic organisms, industrial insect control, food storage, transportation, and community hygiene there are multiple uses such as. Excessive intake of the body leads to many diseases, cancer formation, even death. In this study, it was aimed to analyze the pesticides Atrazine, Chlorfenvinfos, Chlorpyrifos, Diuron, Isoproturon, and Simazine simultaneously with LC-MS/MS, in Boğazköy Dam in Bursa(Turkey) and the branches that feed the dam in Bursa, İnegöl district. The samples were taken from 12 locations and were given to the device by direct injection. Environmental Quality Standards were taken as reference for the calibration of the method. Validation studies such as LOD, LOQ, linearity, and recovery have been performed for the accuracy of the method. As a result, it has been determined that the pesticide derivatives examined in the waters feeding the Boğazköy Dam and the dam itself do not exceed the Environmental Quality Standards limit values and do not pose a risk in irrigation of agricultural areas and surface waters.

INTRODUCTION

Controlling the environment has been the common goal of people for centuries. But day by day, it has reached incredible dimensions in terms of population growth, quality of life, purchasing, unplanned settlement. Accordingly, its impact on the environment has increased over time, putting life in danger(1). Organic pollutants pose a great danger to the environment and health as they remain active in the environment for a long time. For this reason, the determination of these pollutants is necessary for human health and pollution control. Measuring the concentrations of the priority substances mentioned in the above-

ground water resources legislation of the Ministry of Forestry and Water Affairs is important for the control and prevention of existing and potential new pollution. Biological or chemical products used to control these pests that carry infectious diseases to foodstuffs, humans, and animals, used to remove or destroy microorganisms that damage the products during consumption, production, and storage of foodstuffs, in addition to ensuring proper growth of plants. It is called "pesticide" (2). In addition, agricultural activities, the use of pesticides in the fight against mosquitoes that cause malaria to create an important health problem for human health (3,4). There are multiple uses such as landscape, construction industry, timber protection,

forestry, aquatic organism control, industrial insect control, food storage, storage, transportation, and community hygiene. The majority of these pesticides that have been used in these areas for many years are dangerous substances in the hazardous class and are widely spread around the environment (5). Pesticides are among the most commonly used chemicals in the world and are also one of the most dangerous for human health. In order to protect human health and the environment, there are limit values that should not be exceeded in the legislation for priority substances and specific pollutants in water, soil, and biota samples. These limit values that should not be exceeded are expressed as an Environmental Quality Standard (6).

Pesticides are classified according to their molecular structure, appearance, and formulations, as well as their classification according to the active ingredient, toxicity effects, and usage patterns. The common classification is the classification made according to the active ingredient and the harmful substance groups in which it is used (7).

1. Classification by Effective Groups
a. Insecticides (insecticides)
b. Molluscides (molluscicidal)
c. Herbicides (herbicide)
d. Algicides (algae killer)
e. Rodenticides (rodent killer)
f. Nematocytes (killing roundworms)
g. Acaricides (mite killer)
h. Fungicides (fungicide)
I. Avicides (kills birds)
j. Actresses (tractors)
k. Bactericide (which kills bacteria)

2. Classification According To The Effective Substance Group In Its Composition.
This classification is the most scientific one (8).

A. Inorganic pesticides
I. Arsenic-containing pesticides
ii. Copper-containing pesticides
iii. Mercury-containing pesticides
iv. Elementary sulfur-containing pesticides
vi. Fluoride-containing pesticides

B. Synthetic organic-containing pesticides
I. Organophosphate pesticides
ii. Organochlorines
iii. Organosulfurs
iv. Carbamates

C. Natural organic-containing pesticides
I. Allethrin
ii. Pyrethrum
iii. Rotenone
iv. Nicotine

The direct harmful effect of the pesticides on the human body occurs when it enters the metabolism as a result of drinking or eating a pesticide-contaminated food. Pesticides have many negative effects on both human health and the health of other living bodies (9). Different results occur depending on age, race, and gender, as well as diet, economic status, disease status, exposure time, and pesticide concentration. Improper use of drugs in the fight against insects and some carelessly applied pesticides have caused and brought down the number of bird species that can be fed with seeds, predatory bird species, and the number of insect-eating birds. Although songbirds, heron species, and a strong structure, eagles are one of the bird species affected by pesticides (5).

The first used pesticides were sulfur and arsenic. Nicotine was the first plant-derived pesticide used. Pyrethrin, which is naturally found in chrysanthemum flowers and considered as an organic insecticide, has been used since the 19th century. Until the 1860s, copper-containing arsenic compounds called Paris green were used for potato beetle, which was common in the state of Colorado, USA. By the time, lead and mercury compounds started to be used (1). The use of pesticides against insects has increased since the mid-1940s. The Swiss chemist Paul Mueller described the properties of the pesticide known as DDT dichlorodiphenyltrichloroetamine in 1939 and was introduced to the market. In 1979, DDT was banned due to its accumulation in the living organism and its passage into the food chain. German scientists studied nerve gases during World War II and discovered the insecticide parathion, an organophosphate compound. In 1943, parathion was put on the market as an insecticide. USA and other countries, during World War II, turned to synthetic organic chemicals due to the difficulty of supplying the country with botanical based pesticides (5). The first use of pesticides in Turkey began in 1965. Great progress has been made in harvesting crops due to their use. According to the statistics of the Ministry of Agriculture and Forestry, approximately 30,000 to 35,000 tons of pesticides are used every year in our country (10). The first law on pesticides was enacted in the USA in 1947 and the Environmental Protection Agency (EPA) was established in 1970 (2).

Çağdar (11) aimed to make pesticide analysis in the soil in Amik Plain using QuEcheRs method and GC/MS and LC/MS/MS devices. As a result of the analysis, he found 10 different pesticide derivatives in soil samples. These are imidacloprid, dimethomorph, metolachlor, epoxiconazole, tebuconazole, acetochlor, clothianidin, captan, triflualin, and 4,4-DDT. It drew attention to the significant presence of the 4,4-DDT pesticide, although it was banned in 1985. He emphasized that the results are between the limit values required in the Water Regulation for Human

Consumption and the Regulation on Natural Mineral Water (11). Baloglu et al. developed a method for direct injection, LC-MS/MS device for drinking, using, and determination of pesticides in natural waters. In this method, they determined the recoveries as 84.6% to 109.2% and their precision values as 2.2% to 10.5%. They compared their results with the residual limit values required in the Regulation on Water for Human Consumption and the Regulation on Natural Mineral Waters, and found that the results were among these limit values (12). The levels of some organochlorine pesticides was investigated in the tap water samples taken from Asartepe Dam Lake and its vicinity in Ayas district of Ankara. In the analysis, GC-ECD device was used and liquid-liquid extraction. As a result of the analysis, they determined, α-BHC, β-BHC, γ-BHC, δ-BHC, DDD, DDE, DDT, heptachlor, heptachlorperoxide, aldrin, dieldrin, endosulfan-I, endosulfan-II, endrin, and aldehyde pesticides were determined. It has been determined that the amount of organochlorine pesticides in dam and drinking water exceeds the limits specified in the European Union's directive 76/464 / EEC 2006/11 / EC "Pollution caused by the discharge of hazardous substances to the aquatic environment" and "80/778 / EEC drinking water" directive (5,13).

Kapsi Tsoutsi et al. aimed to measure the residual levels of 3 different pesticides (fungicides, herbicides and insecticides) derivatives in samples taken from 3 different points of the Lourus River in Greece. They performed extraction before they introduced the samples to the device. They used the solid-phase extraction (SPE) method as the extraction method. They made the analysis using GC / MS and LC / MS device. As a result of the analyses, 25 pesticide derivatives were identified. The most common pesticide derivatives are quizalofop-ethyl, pendimethalin and trifluralin pesticides. They stated that the tebufenpyrad pesticide is found everywhere (14). Another revealed methods for measuring and identifying agricultural chemicals in the Jucar River basin of Spain. They took samples from 15 different points of the river. Samples were extracted with SPE cartridge and made the analysis using LC-MS / MS device. 20 of the 50 pesticide derivatives analyzed exceeded the detection limit. The concentrations determined were terbuthylazine-2-hydroxide in chlorfenvinphos: 0.05 ng/L, terbuthylazine diethyl: 13.0 ng/L, diazinone: 0.2 ng/L, and 0.66 ng/L. They found chlorpyrifos in all samples, etion in 87%, chlorfenvinphos and tolklofos-methyl pesticides in 80% (15). It was aimed to analyze the distribution of atrazine and simazine using different organic solvents in the study on residue determinations on foods. Shaking, microwave irradiation, ultrasonic assisted extraction, and soxhlet extraction were employed as extraction methods. The solvents used are acetone, chloroform, n-hexane, methanol, and acetonitrile. Following the extraction process, they

aimed to develop a method for the determination of atrazine and simazine derivatives using the HPLC device In this method they developed, LOD and LOQ values for atrazine and simazine, respectively, LOD 0.2 μg/mL – 0.3 μg/mL, LOQ: 0.73 μg/mL – 1.12 μg/mL. In the soil samples examined, they determined the concentration of atrazine and simazine in the range of 3.45–8.60 μg/g, 11.9–13.03 μg/g, respectively (16). Mualefe Torto et al. (17) investigated pesticide derivatives with GC/ECD and GC-TOF/MS methods in water samples taken from Okavango delta in Botswana. As a result of the analyses, they detected 4,4'-DDD and 4,42-DDE pesticide derivatives from hexachlorobenzene, and t-chlorine. They found the pesticide concentration to be 61.4 μg/L, 3.2 μg/L, 2.4 μg/L and 5.3 μg/L, respectively. According to the results of the analysis, they concluded that the pesticide derivatives were far above the European Union Drinking Water Directive Limit (0.1 μg/L). Poolpak et al. analyzed 20 organochlorine pesticide derivatives in the sediment samples using a GC device in Mae Klong Creek in the center of Thailand between 2003-2005. They used solid-liquid extraction as the extraction method. In the sediment samples, the total organochlorine pesticide concentration was 4.12-214.9 μg/g and 3.26-215 μg/g. In the summer season, they detected organochlorinated pesticide residue at high concentrations in both periods. The most common pesticide derivative was heptachlor epoxide. Dieldrin and aldrin, the concentrations of which were found to be 0.001-0.17 μg/g, 0.001-2.38 μg/g, respectively (18). Sun et al.(19) investigated 13 organochlorine pesticide derivatives by taking samples from the sediment and surface waters of the Qiantang Creek in China in all seasons. They used a GC/ECD device after solid phase extraction as the method of analysis. They found the total organochlorinated pesticide concentration to be 7.68-269.4 ng/L in water samples and 23.11-1616.5 ng/L in sediment samples. Among the organochlorine pesticides, lindane and heptachlor were common in water samples, while HCH, DDT, and heptachlor were common in widespread samples. They observed that pollution was common in the summer and autumn seasons. They found that DDT concentration in water samples was 8.11 ng/L and HCH 75.2 ng/L. As a result of their study, they showed that pesticide residues with organochlorine exist in water and sediment. Aybala investigated the responsibilities brought by the relevant legal regulations to the countries, the Environmental Quality Statement examined national and international regulations that may be relevant and made a general evaluation. With the Directive 2013/39 / EU, the annual average (AA-EQS) and maximum (MAX-EQS) values of 45 priority substances, freshwater and saltwater related to these substances have been determined. However, they also developed CCT values in biota for 11 items, which are among 45 priority items. In order

to protect and maintain the environment and human health, the Environmental Quality Standard (CCS), which is named as the concentrations that the pollutant and pollutant groups should not reach in the samples of water, soil, or biota, basically refers to the quality status that should be provided in the receiving environments. In the water regulation, the EQS determines the limit values that should be taken into account when evaluating the water quality monitoring data, it is used in determining the quality to control the pollution in the water resources, and reveals the necessity of the protection and improvement studies needed in order to achieve environmental targets (6). Beale David et al. have presented a simple and relatively inexpensive method for detecting Atrazine, Simazine and Hexazinone pesticides in natural waters. In the method used, samples were injected directly into High Performance Liquid Chromatography (HPLC) device. They obtained the best results for this method in the mobile phase consisting of acetonitrile and water in the ratio of (30:70, (v/v). They were found the results as Atrazine: 5.7 µg/L, Simazine: 4.7 µg/L and Hexazinone: 4.0 µg/L (20). Diaz Llorca-Pórcel et al. have implemented a new method for the determination of pesticides in tap and treated wastewater using liquid chromatography-tandem mass spectrometry (LC-MS/MS). The method used has been validated according to ISO / IEC 17025: 1999. The most important feature of this method is detecting pesticides by separating them in a short time with electrospray ionization (ESI) MS-MS. They found the detection limits below 15 and the correlation coefficients of the calibration curves drawn between 30-2000 ng/L concentrations higher than 0.99. They determined LOD values of Atrazine 2 µg /L, Diuron 8 µg/L, Isoproturon 3 µg/L, Simazine 4 µg/L, Alaklor 6 µg/L, Chlorfenvinfos 4 µg/L and Chlorpyrifos 7 µg/L. Accuracy was verified by external evaluation and precision was found always under 20% (21).

Limit values for Environmental Quality Standards have been determined for Atrazine, Chlorfenvinfos, Chlorpyrifos, Diuron, Isoproturon and Simazine, which are included in the Surface Water Quality Regulation published by the Ministry of Forestry and Urbanization in 2016, which are certain pollutants for surface water resources. Information containing priority substances and environmental quality standards limit values for surface water resources is given in Table 1 (22).

Table 1. Priority Substances and Environmental Quality Standards Limit Values for Surface Water Resources.

Pesticide's Name	CAS No	AA-EQS Rivers/Lakes (µg/L)	MAX- EQS Rivers/Lakes (µg/L)	AA-EQS Coastal and Transitional Waters (µg/L)	MAX-EQS Coastal and Transitional Waters (µg/L/)
Atrazine	1912-24-9	0.6	2.0	0.6	2.0
Chlorfenvinfos	470-90-6	0.1	0.3	0.1	0.0
Chlorpirifos	2921-88-2	0.03	0.1	0.03	0.1
Diuron	330-54-1	0.2	1.8	0.2	1.8
Isoproturon	34123-59-6	0.3	1.0	0.3	1.0
Simazine	122-34-9	1.0	4.0	1.0	4.0

AA-EQS: Annual Average-Environmental Quality Standards
MAX-EQS: Maximum-Environmental Quality Standards

With the increasing use of pesticides in the world in recent years, a lot of studies have been started on pesticide analysis. The use of pesticides in agriculture is also of great importance in our country. Boğazköy Dam is a basin of Sakarya Region where this study will be carried out. Boğazköy Dam was built to irrigate agricultural lands and started to hold water since 2010. This dam is located on Göksu Stream, one of the side branches of Sakarya River in Northwest Anatolia. Within the boundaries of the basin, there is İnegöl District and villages connected to Bursa Province. In our study, it was aimed to identify some pesticide derivatives from the priority substances in the Surface Water Quality Regulation by taking samples from different parts of the Boğazköy Dam and the branches that feed the dam in Bursa İnegöl region. In addition, these pesticides will be compared with the Environmental Quality Standard values determined in the legislation. In the method, simple and cheap methods will be tried to measure potentially harmful permanent pesticides in order to reduce time, chemical and consumable expenses in pesticide determinations.

MATERIAL AND METHOD

Material
Samples of water were used in the determination of pesticide amounts for the thesis work; Samples were taken from Boğazköy Dam Basin and the feeding branches of the Basin in İnegöl Region, which is given from satellite in Figure 1, and 12 different locations (3 samples from one point). Water samples were taken in 250 mL glass bottles and stored at +4 °C until analysis.
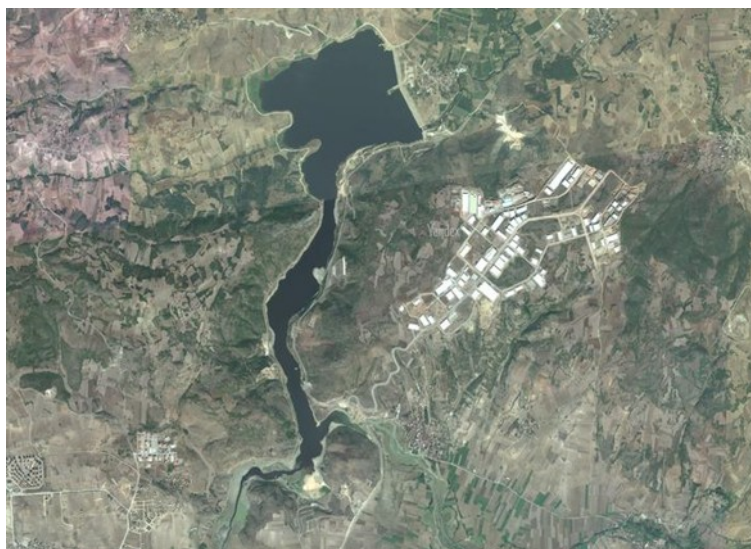
Figure 1. Boğazköy Dam Basin, satellite view.
Source: https://images.app.goo.gl/NjQ8ceDuzc9KP3GK8

Method
Liquid Chromatography-Tandem Mass Spectrometry LC-MS/MS (Shimadzu (LC/MS-8040)) device was used to determine pesticides in aqueous samples and to determine the quantities. MS/MS device working method is given in Figure 2. The Chromatography Column is Restek (Biphenyl 2.7 µm 100 x 2.1 mm). Depending on the sample to be analyzed, ESI (Electrospray Ionization) or APCI (Atmospheric Pressure Ionization Source) ionization techniques were used. In general, the analysis of polar compounds such as amines, pesticides and proteins uses the ESI technique, and the APCI technique is used for apolar compounds such as steroids.
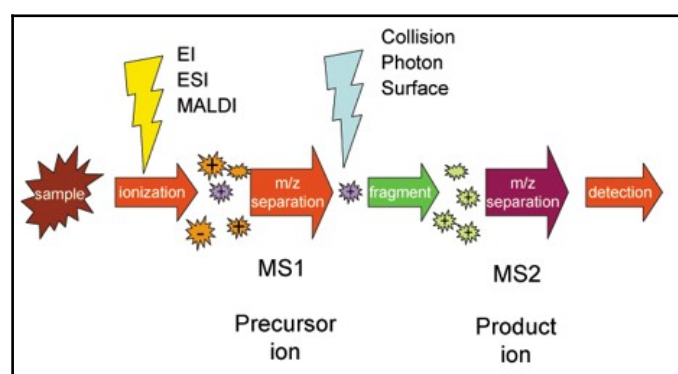
Figure 2. MS / MS Sequential Mass Analyzer.
https://images.app.goo.gl/2cQhe6ENzSmMu3W8A

Chemical and Materials
The chemicals and consumables used during the analysis are given respectively methanol (99 %w/w) and formic acid(>%98) were of high purity and of HPLC grade from Merck. Other pesticide standards; chlorpyrifos was 200 µg/mL n-hexane/acetone (80/20:w/w) from Restek, atrazine (100 µg/mL in methanol), klorfenvinfos (1000 µg/mL n-hexane/acetone (97.5/2.5:w/w), diuron (100 µg/ mL in methanol), isoproturon (100 µg/mL in methanol), simazine (100 µg/mL in methanol) and they were Certified Reference Materials from AccuStandard (New Haven, CT 06513 USA). 0.22 µm 13 mm PTFE filter was provided from ChromXpert. The chromatographic conditions determined for the analysis in Table 2 and the other liquid chromatography flow chart is given in Table 3.

Table 2. Chromatographic Conditions for LC/MS-MS.

Parameter	Chromatographic conditions
Flow Rate	0.4 mL/min
Injecting Volume	20.0 µL
Column Temperature	35 °C
Analysis Time	15.0 minutes
Mode	Gradient Flow
Ion Source	ESI
Dry Gas Flow Rate	15.0 L/min
Initial Temperature	250°C
Block Temperature	400°C
Nitrogen Gas Flow Rate	3 L/min
Mobile Phase A	Water 98%+Methanol 2%+Formic Acid 0.1%
Mobile Phase B	100 % Methanol+Formic Acid 0.1%

Table 3. Chromatographic Flow Table for LC-MS/MS.

t (min)	Flow Rate (mL/min)	Mobile Phase A %	Mobile Phase B %
1	0.4	90	10
3	0.4	45	55
10,5	0.4	0	100
12	0.4	0	100
12.01	0.4	97	3
15	0.4	100	0

MRM optimization

The optimum values were obtained as a result of the study with 98% water + 2% methanol containing 0.1% formic acid for mobile phase A, and 100% methanol containing 0.1% formic acid for mobile phase B. The Q1 and Q3 ions were determined by solving the pure standards to be analyzed in methanol and using MRM (multiple reaction monitoring) optimizations in a Shimadzu LC-MS 8040 Liquid Chromatography Triple Quadrupole Mass Spectrometer. For improving the SRM technique, mass spectra of the $[M+H]^+$ ions obtained by MS and MS/MS were registered in order to find convenient daughter ions for all the pesticides studied. The highest intensity Q1 and Q3 ions are given in Table 4.

Table 4. Optimization values and SRM parameters of the pesticide derivatives.

Pesticides	Retention time (min)	Molecular weight (g/mol)	Precursor ion (m/z)	Daughter ion, (m/z)
Atrazine	5.54	215.68	216.10[M+H]$^+$	174.10
Chlorfenvinfos	8.16	359.56	359.00[M+H]$^+$	169.50
Chlorpyrifos	9.37	350.59	350.00[M+H]$^+$	197.95
Diuron	5.50	231.10	233.00[M+H]$^+$	72.10
Isoproturon	5.65	206.30	207.20[M+H]$^+$	72.15
Simazine	4.96	201.65	202.10[M+H]$^+$	124.20

Preparation of the calibration standard solutions

The main stock solution concentration was 20.0 µg/L. To generate the calibration curves of Atrazine, Chlorfenvinfos, Chlorpyrifos, Diuron, Isoproturon, and Simazine, standard pesticide solutions at concentrations of (0.1 µg/L; 0.3 µg/L; 0.5 µg/L; 0.8 µg/L; 1.0 µg/L; 2.0 µg/L; 5.0 µg/L; 10.0 µg/L) were prepared from the main stock solution (20.0 µg/L) diluted with 99.0% methanol, respectively.

Preparation of Samples

For the analysis, water samples kept at + 4 °C in a refrigerator were taken into vials by filtering through a 0.2 micron filter without any extraction. Then, these samples were prepared in 3 replicates and introduced to the LC/MS-MS by direct injection method for measurement.

RESULTS AND DISCUSSIONS

In this study, pesticide analysis (Atrazine, Chlorfenvinfos, Chlorpyrifos, Diuron, Isoproturon and Simazine) was carried out in the Bogazkoy Dam Basin in the Inegol District of Bursa Province and its feeding branches. While determining the pesticide derivatives that need to be analyzed, priority substances were taken as reference for the Surface Water Resources mentioned in the Surface Water Quality Regulation (2016).

Validation Parameters

Six pesticides were selected for analysis under optimum conditions. In validation studies, the linearity of parameters, selectivity, detection limits (LOD), quantification limits (LOQ), accuracy (recovery), precision, and sensitivity parameters

were carefully made and the results were given.

Linearity

The linear range is the range over which the relationship between the signal and analyte concentration in the sample medium of analysis results is proportional. Calibration curves are used to determine the linear range. The linear range was made to determine the concentration range at which the method quantitatively showed correct results. For this purpose, 6 pesticides prepared in the given concentration ranges (Atrazine 1.0-20.0 µg/L; Chlorfenvinfos and Chlorpyrifos 0.3-20.0 µg/L; Diuron 0.5-20.0 µg/L; Isoproturon 1.0-20.0 µg/L; Simazine 0.8-20.0 µg/L) were analyzed and calibration curves were drawn. Analysis was performed by making three measurements at each concentration level. While determining the calibration sub-points, environmental quality standards to be evaluated were taken as reference. Linearity was determined from the calibration curves drawn at the end of the analysis. The slope equation, Area and R^2 values of the calibration curves obtained as a result of the calibration studies are given in Table 5.

Table 5. Calibration Information of Pesticides.

Pesticide's Name	R^2	Equation of the curve
Atrazine	0.9996	y=75442x+12541
Chlorfenvinfos	0.9996	y=29408x-5714
Chlorpyrifos	0.9999	y=10937x+2524
Diuron	0.9998	y=21915x-2384
Isoproturon	0.9996	y=4352x+12528
Simazine	0.9997	y=19445x+2598

Selectivity(Specificity)

Selectivity is the ability of the analytical method to accurately measure only the intended component or components in the presence of expected physical/chemical interferences. Therefore, blind water samples were analyzed by LC-MS/MS in order to observe possible noise from interference the

studied water samples. According to the chromatograms examined, no interference originating from the matrix has been found for pesticide derivatives in the retention times determined. Blind sample chromatogram and standard sample chromatogram (10 µg/L) are given in Figures 3 and 4, respectively.
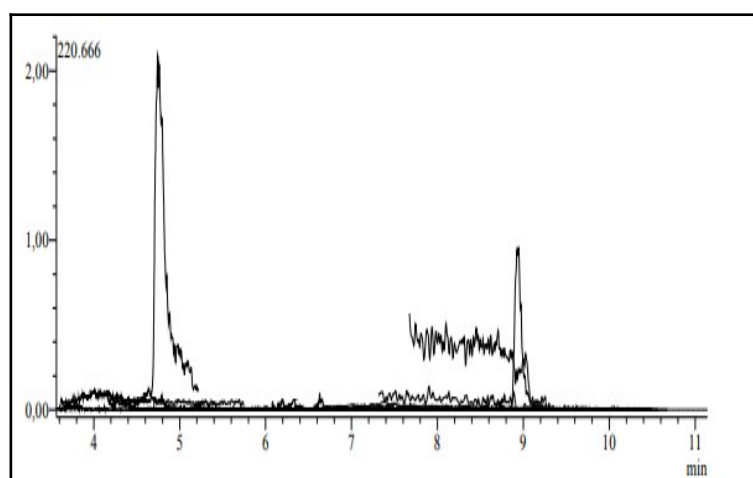
Figure 3. Blind Sample Chromatogram.
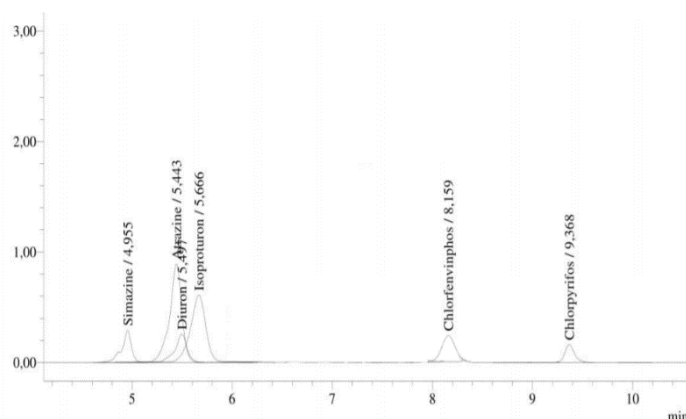
Figure 4. Standard Sample Chromatogram (10 µg/L).

The limits of detection (LOD) and limits of quantification (LOQ)

The lowest amount that the analyte signal that can be determined by the detector can be distinguished from the noise that can interfere with the background analysis is the diagnostic limit (LOD) of that substance. The lowest concentration value at which the reliable quantitative result for the substance analyzed can be obtained is the lower limit of the determination of that substance (LOQ). Calculation of diagnosis and detection lower limit

values;
LOD = Xbl + 3 Sbl
LOQ = Xbl + 10 Sbl
Xbl = Average of analyte-free measurements
Sbl = Standard deviation of analyte-free measurements
(LOD) the limits of detection and (LOQ) limits of quantification were calculated by considering the average and standard deviation measurements. LOD and LOQ studies the results of standard solutions (2 µg/L) for n=7 are given in Table 6.

Table 6. The limits of detection(LOD)and limits of quantification(LOQ) values

n=7	Atrazine	Chlorfenvinfos	Chlorpyrifos	Diuron	Isoproturon	Simazine
LOD(µg/L)	0.25	0.23	0.28	0.45	0.22	0.31
LOQ(µg/L)	0.86	0.79	0.96	1.51	0.75	0.89

Accuracy (Recovery %)

In determining the correctness of a method, a recovery study is required. It shows the closeness of the data to be obtained from the experiments to the correct value. The % recovery value rates should be between 70-120% according to the SANCO document (23). To determine the recovery values, 2 µg/L value of standard solution was added to the blind sample and chromatograms were taken, and the recovery was calculated. The accuracy (Recovery %) results studied are given in Table 7. Recovery rates were found in accordance with the 70-120% range specified for validation studies.

Precision

Precision shows the repeatability (closeness to each other) of experimental data. Precision is expressed

in relative standard deviation. In the SANCO document published by the "General Directorate of Health and Consumer Protection of the European Commission" on November 19, 2013, the repeatability and reproducibility suitability is performed through SD and RSD% results (23). According to the same SANCO document, according to the acceptability criteria of the performance of a method, the relative standard deviation (%RSD) value should be ≤20. In experimental studies, depending on the conditions under which the experiment was performed, standard deviation (SD) and percent relative standard deviation (%RSD) values were calculated for the performance, that is, the repeatability of the method. It is given in Table 7.

Table 7. Pesticide Derivatives's Accuracy (Recovery%) and Precision results.

Pesticides	Recovery %	SD	RSD %
Atrazine	91.17	3.37×10^3	4.3
Chlorfenvinfos	91.53	3.38×10^3	21.2
Chlorpyrifos	84.95	5.28×10^3	26.6
Diuron	101.2	2.36×10^3	13.5
Isoproturon	84.85	2.37×10^3	11.7
Simazine	84.70	8.28×10^3	8.7

Analysis of Dam Water Samples
Following the validation studies, the samples were analyzed in 3 replicates on the same day, and the average of the data obtained from the studies was obtained. After the study was completed, it was observed that the pesticide amounts in the samples remained below the LOQ level. The analysis results of the samples are given in Table 8. Column charts including peak areas of pesticides with error bars represented (n=7) replicates in Figure 6.

Table 8. Quantities of pesticide samples determined in dam waters and their status according to the values given in the regulation.

Water Samples	Atrazine (µg/L)	Chlorfenvinfos (µg/L)	Chlorpyrifos (µg/L)	Diuron (µg/L)	Isoproturon (µg/L)	Simazine (µg/L)
B1	<1	<0.3	<0.3	<0.5	<1	<0.8
B2	<1	<0.3	<0.3	<0.5	<1	<0.8
B3	<1	<0.3	<0.3	<0.5	<1	<0.8
B4	<1	<0.3	<0.3	<0.5	<1	<0.8
B5	<1	<0.3	<0.3	<0.5	<1	<0.8
B6	<1	<0.3	<0.3	<0.5	<1	<0.8
B7	<1	<0.3	<0.3	<0.5	<1	<0.8
B8	<1	<0.3	<0.3	<0.5	<1	<0.8
B9	<1	<0.3	<0.3	<0.5	<1	<0.8
B10	<1	<0.3	<0.3	<0.5	<1	<0.8
B11	<1	<0.3	<0.3	<0.5	<1	<0.8
B12	<1	<0.3	<0.3	<0.5	<1	<0.8

The analysis results of the chromatograms of the samples were given as follows in Figure 5.
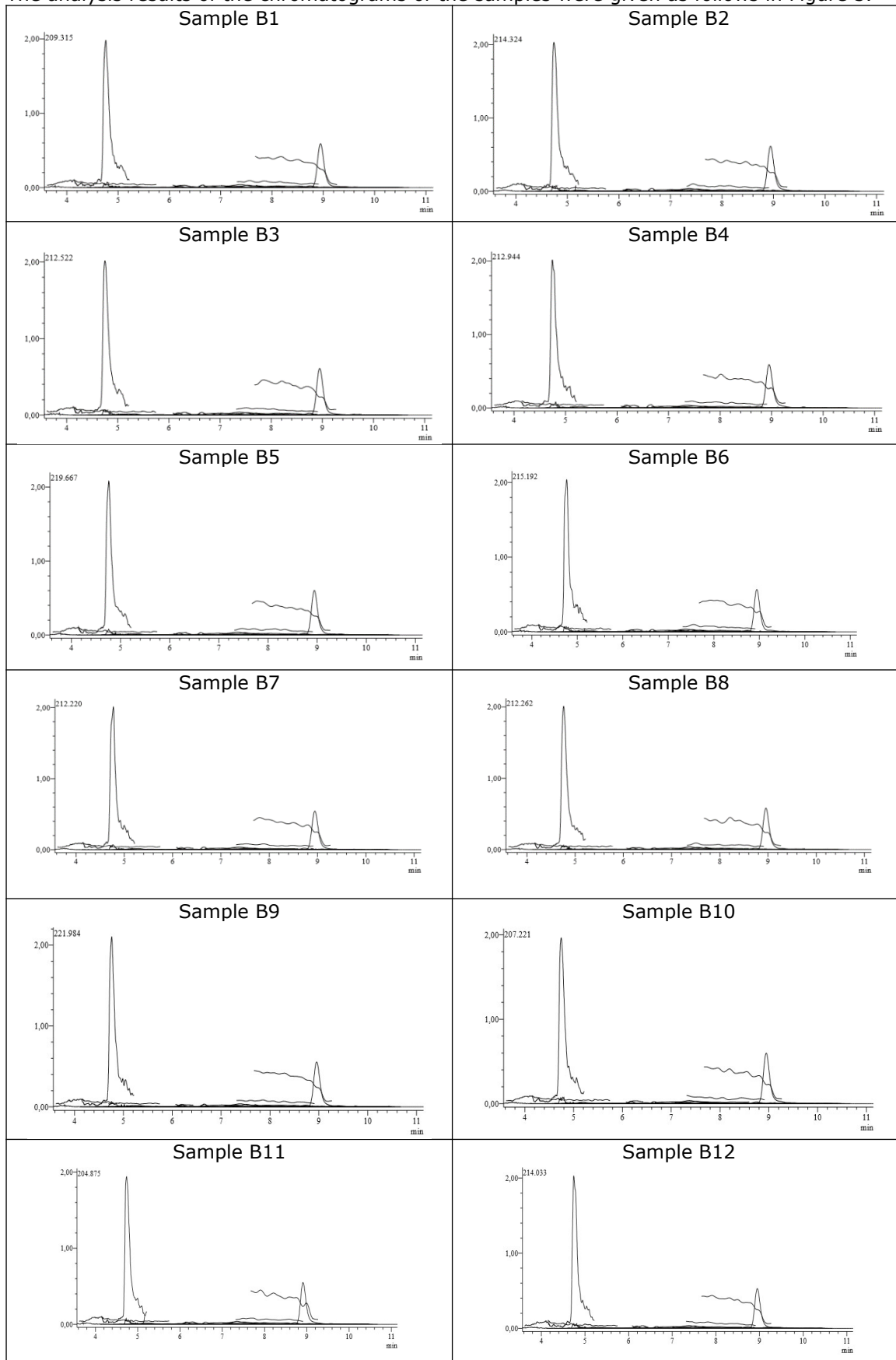
Figure 5. The chromatograms of the samples taken from dam water.
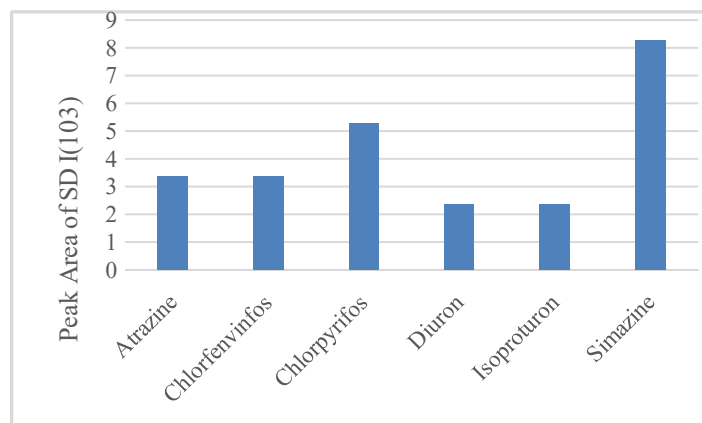
Figure 6. Column charts including peak areas of pesticides with error bars represented for n=7 replicates.

Calibration curves for pesticide derivatives were drawn first in the study. Limit values were taken as reference when drawing the calibration curves. For atrazine: 1 µg/L, for chlorfenvinfos: 0.3 µg/L, for chlorpyrifos: 0.3 µg/L, for diuron: 0.5 µg/L, for isoproturon: 1 µg/L, and for simazine: 0.8 µg/L values were determined. The correlation coefficients close to 1 proved that the linear relationship of the experimental data was strong. Calibration information and correlation coefficients are given in Table 5, respectively.

In the other part of the statistical calculations, the detection (LOD) and determination limits (LOQ) of the pesticides in the samples were made in the laboratory (see Table 6). The 20% RSD values, which should be according to the SANCO document, were below 20% in the calculations, as shown in Table 5. These results also prove the accuracy of the method. Each pesticide has been calculated and evaluated within its own area. Since the results (see Table 8) were below our LOD values, pesticides were not evaluated as quantitative analysis and were expressed as smaller (<) than the limit values (see Table 1).

When the results for the accuracy of the method were compared with SANCO documents, the recovery of pesticide derivatives was between 84% and 101%. It has been determined that it is compatible with the recovery values that should be between 70-120% according to SANCO Document (see Table 5).

Samples taken from 12 points were filtered through microfilters without extraction and were introduced to LC-MS/MS device. The analyzed pesticide derivatives were found below the Environmental Quality Limit Values. The analysis results of the samples are given in Table 8.

CONCLUSION

As a result, it was observed that the pesticide derivatives (atrazine, klorfenvinfos, chlorpirifos, diuron, isoproturon, and simazine) analyzed in the waters taken from the Boğazköy Dam and the waters that feed the dam do not exceed the Environmental Quality Standards limit values in the Surface Water Regulation. It has been determined that Boğazköy Dam will not pose a risk in irrigation of agricultural lands and its use in surface waters in this region, considering agricultural products and human health, and therefore it can be easily used as irrigation and groundwater. Only in the region, the continuous production and continuation of agricultural production will bring pesticide use with it. Therefore, it should be remembered that periodic continuous monitoring of the region should not be ignored in terms of protecting agricultural products and human health.

ACKNOWLEDGEMENTS

CONFLICTS OF INTEREST

There is no potential or existing conflict of interest between our scientific work and our personal situation.

REFERENCES

1. Güler Ç, Çobanoğlu Z. Pesticides. Environmental Health Basic Resource Series, 52, (1 st Edition), Ilkoz Printing Press (1997) Ankara.

2. Açar ÖÇ. Pesticide analysis training note T. C. Ministry of Food, Agriculture and Livestock National Food Reference Laboratory Residue/Pesticide Unit, (2015) Ankara.

3. Lari SZ, Khan NA, Gandhi KN, Meshram TS, Thacker NP. Comparison of pesticide residues in surface water and ground water of agriculture intensive areas. J Envîron Heal Sci Eng. 2014; 12(11): 1-7. Doi; 10.1186\2052-336X-12-11

4. Masiá A, Ibáñez M, Blasco C, Sancho V, Picó Y, Hernández F. Combined use of liquid chromatography triple quadrupole mass spectrometry and liquid chromatography quadrupole time-of-flight mass spectrometry in systematic screening of pesticides and other contaminants in water samples, Anal Chim Acta. 2013; 761: 117–127. Doi: 10.1016/j.aca.2012.11.032

5. Erdem Ö. Chromatographic Determination of Organochlorinated Pesticides in Drinking and Using Water in Ayas District [Master Thesis]. [Ankara]: Institute of Science, Gazi University; 2010.

6. Aybala OK. Methodology for the Development of Environmental Quality Standards Related to Hazardous Substances in Surface Waters. Ministry of Forestry and Water Management [Master Thesis]. [Ankara]: T. C. Ministry of Forestry and Water Management;2015.

7. Tiryaki O, Canhilal R, Horuz S. Pesticides Use and Risks. J Inst Sci and Tech. 2010; 26(2): 154-169.

8. Kuş FS. Determination of Organochlorinated Pesticide Residues in Afyonkarahisar Province Drinking Water and Eber and Karamık Lake Water [Master Thesis]. [Afyon]: Afyon Kocatepe University Institute of Science; 2007.

9. Almeida TB, Madeira LS, Watanabe PC, Melettib PC, Nixdorf SC. Pesticide Determination in Water Samples from a Rural Area by Multi-Target Method Applying Liquid Chromatography-Tandem Mass Spectrometry. J Brazil Chem Soc. 2019; 30(8): 1657-1666. Doi: 10.21577/0103-5053.20190066

10. Çakmak Z. Examination and determination of aclonifen pesticide with electrochemical techniques [Master Thesis]. [Ankara]:Institute of Science, Gazi University; 2013.

11. Çağdar MG. Pesticide Analysis in Amik Plain Soils with GC-MS and LC-MS / MS Device [Master Thesis]. [Hatay]: Institute of Science, Mustafa Kemal University; 2014.

12. Baloglu Z, Bozkurt EN, Binici A. Determination of pesticides in waters by LC-MS / MS. Turk Hij Den Biyol Derg 2017; 74(1):41-48. Doi: 10.5505/TurkHijyen.2017.09798

13. Regulation on Control of Pollution Caused by Hazardous Substances in Water and its Environment (76/464/ AB) (26/11/2005 R.G.No: 26005) Ministry of Forestry and Water Management, Ankara.

14. Kapsi, M., Tsoutsi, C., Paschalidou, A., Albanis, T., Environmental monitoring and risk assessment of pesticide residues in surface waters of the Louros River (N.W. Greece). Sci. Tot. Environ. 2019; 650: 2188–2198. Doi: 10.1016/j.scitotenv.2018.09.185

15. Aguilar JAP, Andreu V, Campo J, Picó Y, Masiá A. Pesticide occurrence in the waters of Júcar River, Spain from different farming landscapes. Sci Tot Environ. 2017; 607-608: 752–760. Doi: 10.1016/j.scitotenv.2017.06.176

16. Barchaska H. Baranowska I. Procedures for analysis of atrazine and simazine in environmental matrices. Rev Environ Contam T, Berlin: Springer, 2019; 53-84. Doi:10.1007/978-1-4419-0028-9_3

17. Mmualefe LC, Torto N, Huntsman-Mapila P. Mbongwe B. Headspace solid phase microextraction in the determination of pesticides in water samples from the Okavango Delta with gas chromatography-electron capture detection and time-of-flight mass spectrometry. Microchem J. 2009; 91(2): 239–244. Doi: 10.1016/j.microc.2008.12.005

18. Poolpak T, Pokethitiyook P, Kruatrachue M, Arjarasirikoon U, Thanwaniwat N. Residue analysis of organochlorine pesticides in the Mae Klong river of Central Thailand. J Hazard Mater. 2008; 156(1-3): 230–239. Doi:10.1016/j.jhazmat.2007.12.078

19. Sun K, Zhao Y, Gao B, Liu X, Zhang Z, Xing B. Organochlorine pesticides and polybrominated diphenyl ethers in irrigated soils of Beijing, China: Levels, inventory and fate. Chemosphere. 2009; 77(9): 1199-1205. Doi: 10.1016/j.chemosphere.2009.09.016

20. Beale DJ, Kaserzon SL, Porter NA, Roddick FA, Carpenter Peter D. Detection of s-triazine pesticides in natural waters by modified large-volume direct injection HPLC. Talanta. 2010; 82(2): 668–674. Doi: 10.1016/j.talanta.2010.05.030

21. Diaz L, Llorca-Pórcel J, Valor I. Ultra trace determination of 31 pesticides in water samples by direct injection–rapid resolution liquid chromatography-electrospray tandem mass spectrometry. Anal Chim Acta 2008; 624(1):90–96. Doi: 10.1016/j.aca.2008.06.053

22. Aboveground Water Quality Management Regulation Number:29797 (10.08.2016) Ministry of Forestry and Water Affairs, Ankara.

23. SANCO/12571/2013. Guidance Document on analytical quality control and validation procedures for pesticide residues analysis in food and feed.

Chemical Composition and Antioxidant Activities of Leaf and Flower Essential Oils of *Origanum onites* L. (Lamiaceae) Growing in Mount Ida-Turkey

Züleyha Özer[1]* ✉ iD

[1] University of Balıkesir, Altınoluk Vocational School, Programme of Medicinal and Aromatic Plants, 10870 Balıkesir, TURKEY

Abstract: The chemical composition of leaf and flower essential oils of *Origanum onites* L. were analyzed using Thermo Scientific TSQ GC-MS/MS. Also, antioxidant activities of the leaf and flower essential oils were investigated by using DPPH (1,1-diphenyl-2-picrylhydrazyl) free radical scavenging activity and β-carotene linoleic acid assays. BHA (Butylated hydroxyanisole) and BHT (Butylated hydroxytoluene) were used as standards. The essential oil yields of *O. onites* were 1.75% for leaves and 4.25% for flowers. A total of twenty-three compounds representing 99.9% of leaf oil and twenty-four compounds constituted 99.6% of the flower oil were determined. Oxygenated monoterpenes were detected at a high percentage (69.2%) in leaf essential oil, and carvacrol (64.9%) was determined as the main compound. Also, flower essential oil was dominated by sesquiterpene hydrocarbons (73.5%), and α-cubebene (36.4%) was determined as a primary compound. For leaf oil, a high antioxidant capacity was determined, primarily due to carvacrol and *p*-cymene.

INTRODUCTION

Plants have been one of the necessary, indispensable resources of life since ancient times. People have used plants not only for nutrition but also for the treatment of various diseases (1). Nowadays, medicinal and aromatic plants are used in food, cosmetics, paint, textile, medicine, and agriculture (2).

Lamiaceae (Labiatae) family, which is rich in medicinal plants, is usually one or perennial herbaceous plants containing essential oil. Turkey is an important center in terms of gene Lamiaceae plants (3, 4). The genus *Origanum* L. is one of the most widely used genera of the Lamiaceae family. The genus *Origanum* has 21 species (24 taxa) and 13 hybrids in Turkey (5-7). The pharmacological and biological activities of *Origanum* species mostly due to the antioxidant, antimicrobial, anticancer, analgesic, antiradical, antibacterial, cytotoxic, antifungal, and insecticidal activities of their essential oils (8-14).

O. onites L. (Turkish oregano), leaves, flowers, and essential oils of this plant are used in herbal tea, medicine, food, cosmetics, and perfumery industries. It is also named as 'kırkbas kekik', 'bilya kekik', 'tokalı kekik', 'koca lealı kekik', 'arı kekiği' in vernacular (15). The infusion prepared from the above-ground parts of this species is used in the treatment of diseases and symptoms such as gastrointestinal diseases, diabetes, dyspepsia, carminative, bronchitis, respiratory tract diseases, cold & flu, hypertension, and tachycardia by the local people (1, 15, 16). *O. onites* is abundantly present in the natural habitat of the Mediterranean coastline (17). The essential oil compounds of *O.*

onites have been researched earlier from diverse places in the world. The essential oil was comprised of carvacrol as a major compound, followed by thymol, linalool, α-pinene, *p*-cymene, sabinene hydrate, γ-terpinene, α-terpinene (17-23). The essential oil of *O. onites* has antioxidant (23-26), antimicrobial, antifungal (27), insecticidal (28), larvicidal (29), antidiabetic (30), and cholinesterase inhibitory (31) activities.

The literature abounds with reports regarding the detection of chemical components of the essential oil of *O. onites* aerial parts, and no studies differentiating the essential oils of leaf and flower have been reported to date. Although the essential oils are usually procured from the aerial parts of the herb, this report gives us to see the variation among the components of both parts of the herb. Hence, this report was aimed to identify chemical components and antioxidant activities of leaf and flower essential oils of *O. onites*.

EXPERIMENTAL SECTION

Plant material
The aerial parts of *O. onites* (300 g) were collected from Balıkesir, (Edremit, Altınoluk, Kaz Dağı, Bent Picnic Area) 39°34'51.4"N, 26° 45'26.4"E, 100 m, in July 2016. The investigated species was identified by Prof. Dr. Selami Selvi at Balıkesir University. The voucher specimens were deposited at the Herbarium of the Altınoluk Vocational School, Balıkesir University, Balıkesir, Turkey (Herbarium number SV 1567).

Essential oil
Fresh leaves and flowers (40 g each) were dried in the shade, chopped into small pieces, and subjected to hydrodistillation with a Clevenger-type apparatus for 4 h. The yields of essential oils are 1.75% and 4.25% from leaf and flower, respectively. They were

stored in amber vials at 4 °C for further analyses.

GC-MS experiments
GC-MS was conducted on Thermo Scientific TSQ GC-MS/MS. The column used was Rtx-5Sil MS, 30 m, 0.25 mm ID, 0.25 μm (32). A detailed procedure was given in the supplementary material.

Antioxidant activity
The antioxidant activities were measured based on DPPH (1,1-diphenyl-2-picrylhydrazyl) free radical scavenging activity (33-36) and β-carotene linoleic acid (34-36) assays. The activity tests were carried on at 10, 25, 50, 100 μg/mL concentrations. BHA and BHT were used as standards. IC_{50} values of all samples were calculated. A detailed procedure was given in the supplementary material.

Statistical analysis
Antioxidant activity results were evaluated using a One-way ANOVA test (GraphPad, Software version is 8.4.2). $P < 0.05$ was accepted as the minimum level of significance.

RESULTS AND DISCUSSION

Essential oil
Higher essential oil yield was obtained from the flower (4.25%) compared to the leaf (1.75%) essential oil. Altogether, twenty-three compounds representing 99.9% of leaf essential oil and twenty-four compounds constituted 99.6% of the flower essential oil were determined. The components of essential oils were classified into 4 based on their chemical structures: monoterpene hydrocarbons, oxygenated monoterpenes, sesquiterpene hydrocarbons and oxygenated sesquiterpenes. The essential oil components of leaves and flowers of *O. onites* are summarized in Table 1.

Table 1: Essential oil compositions of leaf and flower of *O. onites.*

No	Compounds	RT[a]	KI[b]	Leaf (%)	Flower (%)
1	α-thujene	5.25	930	1.5	0.5
2	α-pinene	5.37	939	0.5	0.2
3	camphene	6.08	954	0.3	t[c]
4	sabinene	14.48	975	t[c]	t[c]
5	*β*-pinene	6.70	979	0.1	-
6	α-phellandrene	7.85	1003	1.3	0.7
7	α-terpinene	8.30	1017	2.4	0.9
8	*p*-**cymene**	8.53	1025	**11.2**	3.9
9	*β*-phellandrene	8.70	1030	0.6	0.3
10	(E)-*β*-ocimene	9.28	1050	9.1	2.7
11	γ-terpinene	9.39	1060	0.4	0.3
12	sabinene hydrate-cis	17.25	1070	0.4	0.1
13	sabinene hydrate-trans	11.41	1098	0.2	0.1
14	*β*-cis-terpineol	13.20	1144	1.2	0.1
15	camphor	18.22	1146	0.8	0.1
16	carvacrol, ethyl ether	20.10	1298	2.1	-
17	**carvacrol**	20.14	1299	**64.5**	16.0
18	**δ-elemene**	21.77	1338	-	**34.6**
19	**α-cubebene**	22.33	1351	-	**36.4**
20	α-copaene	23.49	1377	0.4	-
21	*β*-bourbonene	24.05	1388	-	0.1

22	aromadendrene	26.27	1441	1.1	1.2
23	Z-β-farnesene	26.33	1443	0.1	0.1
24	α-humulene	26.82	1455	0.2	-
25	E-β-farnesene	26.92	1457	-	0.1
26	allo-aromadendrene	27.07	1460	1.3	1.0
27	spathulenol	31.96	1578	0.2	0.1
28	α-cadinol	34.93	1654	-	0.1
Monoterpene hydrocarbons				27.4	9.5
Oxygenated monoterpenes				69.2	16.4
Sesquiterpene hydrocarbons				3.1	73.5
Oxygenated sesquiterpenes				0.2	0.2
Total (%)				99.9	99.6

[a] RT: Retention time
[b] KI: Kovats indices
[c] t: trace (<0.1%)

The main components of leaf essential oil were carvacrol (64.5%), *p*-cymene (11.2%), and (E)-β-ocimene (9.1%), while α-cubebene (36.4%), δ-elemene (34.6%), and carvacrol (16.0%) were determined as the main compounds in the flower essential oil (Figure 1). The leaf essential oil was qualified by the high content of monoterpenes (96.6%), including hydrocarbons (27.4%) and their oxygenated derivatives (69.2%), while sesquiterpenes (3.3%) were detected in very low amounts.

Sesquiterpene hydrocarbons (73.5%) composed the primary class of compound determined in the flower essential oil with α-cubebene (36.4%) and δ-elemene (34.6%). Oxygenated monoterpenes and monoterpene hydrocarbons were also detected at an average percentage in flower essential oil (16.4% and 9.5%, respectively).

The results indicate that the essential oil content of leaf and flower were dissimilar. For example, carvacrol was found mainly in leaf essential oil at 64.5% against 16.0% in the flower essential oil. In contrast, α-cubebene (36.4%) and δ-elemene (34.6%), significant compounds of flower essential oil were not detected in leaf essential oil. Also, β-pinene, carvacrol ethyl ether, α-copaene, and α-humulene were detected only in the leaf essential oil. Also, *p*-cymene and (E)-β-ocimene were found to be significant compounds in leaf essential oil at 11.2 and 9.1% against 3.9 and 2.7% in the flower essential oil, respectively. It is well known that different parts of the same plant may include different phytochemicals (37, 38). This variation can be elucidated by the presence of different secretory structures in different plant parts. Dissimilar phytochemicals are available in each of the parts of the plant may explanation for the variation in the pharmacological and biological properties.

Carvacrol, the most abundant compound of the leaf essential oil, was reported in the essential oils of aerial parts of *O. onites* from Turkey (18, 24, 29, 39, 40) and Greece (22, 23, 41, 42). However, α-cubebene and δ-elemene were not reported previously as significant components of *O. onites*. α-Cubebene was detected in low quantities of aerial parts of *O. onites* from Greece (42). Also, Figuérédo et al. reported that *O. onites* was the linalool types (42). Ceylan et al. (2003) reported the essential oil compounds of *O. onites* from eighteen different localities of Turkey, while generally, carvacrol was found to be a significant compound, and only one locality had linalool-rich (43). Lukas et al. (2010) reported that chemotypes of *O. onites* from ten different locations of Turkey and Greece. In Greece location of *O. onites* was found to be "cymyl"-chemotypes. In Turkey location of *O. onites* was characterized by linalool and "cymyl"-chemotypes (44). These differences in the chemical composition of essential oil may be due to the environmental, climate conditions, drying methods, harvest period, extraction methods, extraction time, and temperature. These variables affect the vegetative cycle of the herb and subscribe to the chemical variations of its essential oil.
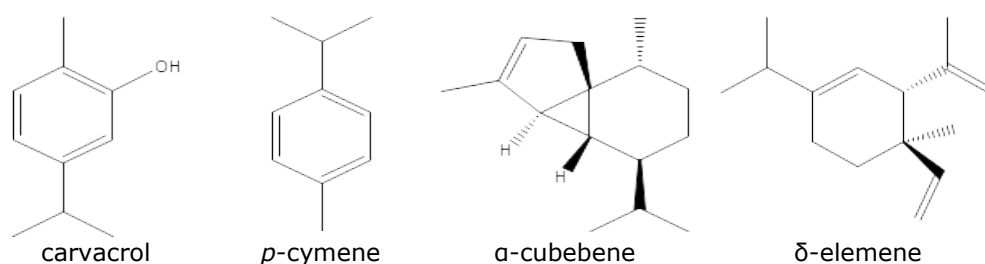
Figure 1: Chemical structures of the main compounds of leaf and flower essential oils.

Antioxidant activity

DPPH free radical scavenging activity and β-

carotene linoleic acid assays were used to determined antioxidant activities of leaf and flower essential oils of *O. onites*. The 50% inhibition concentrations (IC$_{50}$) results are given in Table 2. Leaf and flower essential oils have an excellent antioxidant capacity for both tested assays. IC$_{50}$ values for the DPPH of leaf and flower essential oils were found to be 19.05 ± 3.96 µg/mL and 29.95 ± 5.86 µg/mL, respectively. Besides, BHA and BHT IC$_{50}$ values were found to be 11.73 ± 2.27 µg/mL and 17.22 ± 1.55 µg/mL. IC$_{50}$ values of leaf and flower essential oil were found to be 22.39 ± 3.88 µg/mL and 30.29 ± 0.84 µg/mL in the *β*-carotene linoleic acid assay, respectively. None of the leaf and flower essential oils showed higher antioxidant activity than BHA or BHT. Low IC$_{50}$ values reflect a high antioxidant activity. These results revealed that leaf essential oil showed better antioxidant capacity when compared to flower essential oil. Carvacrol and *p*-cymene were reported to play a important role in antioxidant capacity (45, 46).

Table 2: Antioxidant capacity of leaf and flower essential oils (IC$_{50}$).

	β-carotene	DPPH
Leaf	22.39 ± 3.88	19.05 ± 3.96
Flower	30.29 ± 0.84	29.95 ± 5.86
BHA	14.21 ± 1.16	11.73 ± 2.27
BHT	17.73 ± 2.43	17.22 ± 1.55
IC$_{50}$ values are mean ± SD (n = 3).		

CONCLUSION

The chemical contents of leaf and flower essential oils of *O. onites* were investigated. Also, the antioxidant activity of the essential oils was determined. In this study, it was found that the leaf essential oil was found as carvacrol type, and flower essential oil was the α-cubebene type. It can be said that the quantitative and qualitative differences of essential oils depend on different secretory structures in different plant parts. To the best of our knowledge, this is the first report on the chemical components and antioxidant activities of leaf and flower essential oils of *O. onites*. The leaf and flower essential oils of *O. onites* have the good antioxidant capacity. Thus, the essential oils from both parts of *O. onites* may be regarded as possible natural antioxidant agents for cosmetic, food and pharmaceutical industries.

Supplementary data
Inhibition (%) of lipid peroxidation and DPPH free radical scavenging activity, Gas chromatography-Mass spectrometry conditions and antioxidant activities procedures were given in supplementary material.

REFERENCES

1.   Baytop T. Türkiye'de Bitkiler İle Tedavi, Geçmişte ve Bugün. İstanbul: İstanbul Üniversitesi, Eczacılık Fakültesi; 1999. 550s p.

2.   Vergine M, Nicolì F, Negro C, Luvisi A, Nutricati E, Accogli RA, Sabella E, Miceli A. Phytochemical Profiles and Antioxidant Activity of *Salvia* Species from Southern Italy. Rec Nat Prod. 2019;13(3):205-15.

3.   Mokhtarzadeh S, Demirci B, Ağalar HG, Khawar KM, Kırımer N. In vitro Propagation and Volatile Compound Characterization of *Lavandula stoechas* L. subsp. *stoechas*-An Economically Important Source of Essential Oil. Rec Nat Prod. 2019;13(2):121-8.

4.   Davis PH. Flora of Turkey and The East Agean Islands. Labiatae. University. Edinburg; 1982. 462–463 p.

5.   Arabaci T, Dirmenci T, Yıldız B. *Origanum* L. (Ballıbabagiller/Lamiaceae) Cinsine Ait Yeni Bir Melez: *Origanum× malatyanum* Yıldız, Arabacı & Dirmenci. Bağbahçe Bilim Dergisi. 2020;7(1):10–5.

6.   Özer Z, Gören AC, Kılıç T, Öncü M, Çarıkçı S, Dirmenci T. The Phenolic Contents, Antioxidant and Anticholinesterase Activity of Section *Amaracus* (Gled.) Vogel and *Anatolicon* Ietsw. of *Origanum* L. Species. Arab J Chem. 2020;13(4):5027–39.

7.   Dirmenci T, Yazici T, Özcan T, Çelenk S, Martin E. A New Species and a New Natural Hybrid of *Origanum* L. (Lamiaceae) from the West of Turkey. Turk J Botany. 2018;42(1):73–90.

8.   Fotakis C, Tsigrimani D, Tsiaka T, Lantzouraki DZ, Strati IF, Makris C, et al. Metabolic and Antioxidant Profiles of Herbal Infusions and Decoctions. Food Chem [Internet]. 2016;211:963–71. Available from: http://dx.doi.org/10.1016/j.foodchem.2016.05.124

9.   Hajlaoui H, Mighri H, Aouni M, Gharsallah N, Kadri A. Chemical Composition and in vitro Evaluation of Antioxidant, Antimicrobial, Cytotoxicity and Anti-acetylcholinesterase Properties of Tunisian *Origanum majorana* L. Essential Oil. Microb Pathog. 2016;95:86–94.

10.   Yan F, Azizi A, Janke S, Schwarz M, Zeller S, Honermeier B. Antioxidant Capacity Variation in the Oregano (*Origanum vulgare* L.) Collection of the German National Genebank. Ind Crops Prod

[Internet]. 2016;92:19–25. Available from: http://dx.doi.org/10.1016/j.indcrop.2016.07.038

11. Aykac A, Becer E, Özbeyli D, Şener G, Başer KHC. Protective Effects of *Origanum onites* Essential Oil in the Methotrexate-Induced Rat Model: Role on Apoptosis and Hepatoxicity. Rec Nat Prod. 2020;14(6):395-404.

12. Sivropoulou A, Papanikolaou E, Nikolaou C, Kokkini S, Lanaras T, Arsenakis M. Antimicrobial and Cytotoxic Activities of *Origanum* Essential Oils. J Agric Food Chem. 1996;44(5):1202–5.

13. Hanana M, Mansour MB, Algabr M, Amri I, Gargouri S, Romane A, ... & Hamrouni L. Potential Use of Essential oils from Four Tunisian Species of Lamiaceae: Biological Alternative for Fungal and Weed Control. Rec Nat Prod. 2017;11(3):258-69.

14. Pavela R. Insecticidal Activity of Certain Medicinal Plants. Fitoterapia. 2004;75(7–8):745–9.

15. Sargin SA, Akçicek E, Selvi S. An Ethnobotanical Study of Medicinal Plants Used by the Local People of Alaşehir (Manisa) in Turkey. J Ethnopharmacol. 2013;150(3):860–74.

16. Selvi S, Dağdelen A, Kara S. Kazdağlarından (Balıkesir-Edremit) Toplanan ve Çay Olarak Tüketilen Tıbbi ve Aromatik Bitkiler. Journal of Tekirdag Agricultural Faculty. 2013;10(2):26-33.

17. Tepe B, Cakir A, Sihoglu Tepe A. Medicinal Uses, Phytochemistry, and Pharmacology of *Origanum onites* (L.): A Review. Chem Biodivers. 2016;13(5):504–20.

18. Korukluoglu M, Gurbuz O, Sahan Y, Yigit A, Kacar O. Rouseff R. Chemical Characterization and Antifungal Activity of *Origanum onites* L. Essential Oils and Extracts. J Food Saf. 2008;29(2009):144–61.

19. Ozkan G, Baydar H, Erbas S. The Influence of Harvest Time on Essential Oil Composition , Phenolic Constituents and Antioxidant Properties of Turkish Oregano (*Origanum onites* L .). J Sci Food Agr. 2010;90(2):205–9.

20. Vokou D, Kokkini S, BessiÈRe JM. *Origanum onites* (Lamiaceae) in Greece: Distribution, Volatile Oil Yield, and Composition. Econ Bot. 1988;42(3):407–12.

21. Spyridopoulou K, Fitsiou E, Bouloukosta E, Tiptiri-Kourpeti A, Vamvakias M, Oreopoulou A, et al. Extraction, Chemical Composition, and Anticancer Potential of *Origanum onites* L. Essential Oil. Molecules. 2019;24(14):2612.

22. Stefanakis MK, Touloupakis E, Anastasopoulos E, Ghanotakis D, Katerinopoulos HE, Makridis P. Antibacterial Activity of Essential Oils from Plants of the Genus *Origanum*. Food Control [Internet]. 2013;34(2):539–46. Available from: http://dx.doi.org/10.1016/j.foodcont.2013.05.024

23. Lagouri V, Blekas G, Tsimidou M, Kokkini S, Boskou D. Composition and Antioxidant Activity of Essential Oils from Oregano Plants Grown Wild in Greece. Z Lebensm Unters Forsch. 1993;197(1):20–3.

24. Özkan A, Erdoğan A. A Comparative Evaluation of Antioxidant and Anticancer Activity of Essential Oil from *Origanum onites* (Lamiaceae) and its Two Major Phenolic Components. Turkish J Biol. 2011;35(6):735–42.

25. Ozdemir N, Ozgen Y, Kiralan M, Bayrak A, Arslan N, Ramadan MF. Effect of Different Drying Methods on the Essential Oil Yield, Composition and Antioxidant Activity of *Origanum vulgare* L. and *Origanum onites* L. J Food Meas Charact [Internet]. 2018;12(2):820–5. Available from: http://dx.doi.org/10.1007/s11694-017-9696-x

26. Semiz G, Semiz A, Mercan-Doğan N. Essential Oil Composition, Total Phenolic Content, Antioxidant and Antibiofilm Activities of Four *Origanum* Species from Southeastern Turkey. Int J Food Prop [Internet]. 2018;21(1):194–204. Available from: https://doi.org/10.1080/10942912.2018.1440240

27. Altintas A, Tabanca N, Tyihák E, Ott PG, Móricz ÁM, Mincsovics E, et al. Characterization of Volatile Constituents from *Origanum onites* and Their Antifungal and Antibacterial Activity. J AOAC Int. 2013;96(6):1200–8.

28. Yildirim E, Kordali S, Yazici G. Insecticidal Effects of Essential Oils of Eleven Plant Species from Lamiaceae on *Sitophilus granarius* (L.) (Coleoptera: Curculionidae). Rom Biotechnol Lett. 2011;16(6):6702–9.

29. Erler F, Cetin H. Components from the Essential Oils from Two *Origanum* Species as Larvicides against Euproctis chrysorrhoea (Lepidoptera: Lymantriidae). J Agric Urban Entomol. 2009;26(1):31–40.

30. Lermioglu F, Bagci S, Onderoglu S, Ortac R, Tugrul L. Evaluation of the Long-term Effects of Oleum Origani on the Toxicity Induced by Administration of Streptozotocin in Rats. J Pharm Pharmacol. 1997;49(11):1157–61.

31. Orhan I, Şener B, Kartal M, Kan Y. Activity of Essential Oils and Individual Components against Acetyl-and Butyrylcholinesterase. Zeitschrift fur Naturforsch - Sect C J Biosci. 2008;63(7–8):547–

53.

32.   Özer Z, Kiliç T, Selvi S, Pasa C. Effect of Different Drying Methods and Development Stages on the Essential Oil Chemical Composition of Aerial Parts of *Origanum vulgare* L. subsp. *hirtum* (link) Letsw. J Essent Oil-Bearing Plants. 2018;21(5):1403-09.

33.   Blois MS. Antioxidant Determinations by the Use of A Stable Free Radical. Nature. 1958;181:1199–2000.

34.   Miller H.E. A Simplified Method for the Evaluation of Antioxidants. J Am Oil Chem Soc. 1971;48(2):91.

35.   Özer Z. Investigation of Phenolic Compounds and Antioxidant Activity of *Mentha spicata* subsp. *spicata* and *M. longifolia* subsp. *typhoides* (briq.) Harley Decoction and Infusion. J Turkish Chem Soc Sect A Chem. 2018;5(2):445-56.

36.   Özer Z. The Phenolic Compounds, Antioxidant and Anticholinesterase Activities of *Cyclotrichium origanifolium* (Labill.) manden & scheng and *Thymus sipyleus* Boiss Teas from Turkey. Stud Univ Babes-Bolyai Chem. 2019;64(3):217–28.

37.   Liang X, Bi D, Li F, Wang L. Chemical Compounds from the Twigs and Leaves of *Caesalpinia cucullata* Roxb. Rec Nat Prod. 2019;13(6):462-7.

38.   Trung HD, Thang TD, Khôi NK, Dai DN, Ogunwande IA. Chemical Constituents of Essential Oils from the Leaf, Flower and Fruit of *Zanthoxylum avicenna* (Lam.) DC. (Rutaceae) from Vietnam. J Essent Oil-Bearing Plants. 2016;19(4):1019–24.

39.   Arslan M, Uremis I, Demirel N. Effects of Sage Leafhopper Feeding Damage on Herbage Colour, Essential Oil Content and Compositions of Turkish and Greek Oregano. Exp Agric.

2012;48(3):428–37.

40.   Bostancioĝlu RB, Kürkçüoĝlu M, Başer KHC, Koparal AT. Assessment of Anti-Angiogenic and Anti-Tumoral Potentials of *Origanum onites* L. Essential Oil. Food Chem Toxicol. 2012;50(6):2002–8.

41.   Kokkini S, Karousou R, Hanlidou E, Lanaras T. Essential Oil Composition of Greek (*Origanum vulgare* ssp. *hirtum*) and Turkish (*O. onites*) Oregano: A Tool for Their Distinction. J Essent Oil Res. 2004;16(4):334–8.

42.   Figuérédo G, Cabassu P, Chalchat JC, Pasquier B. Studies of Mediterranean Oregano Populations. VII: Chemical Composition of Essential Oils of Carvacrol-rich Oregano of Various Origins. J Essent Oil Res. 2006;18(3):244–9.

43.   Ceylan, A., Bayram, E., Sahbaz, N., Otan, H., Karaman S. Yield Performance and Essential Oil Composition of Individual Plants and Improved Clones of *Origanum onites* L. Grown in the Aegean region of Turkey. Isr J Plant Sci. 2003;51(4):285–90.

44.   Lukas, B., Samuel, R., Novak J. Oregano or Marjoram? The Enzyme γ-terpinene Synthase Affects Chemotype Formation in the Genus *Origanum*. Isr J Plant Sci. 2010;58(3–4):211–20.

45.   Sarikurkcu C, Zengin G, Oskay M, Uysal S, Ceylan R, Aktumsek A. Composition, Antioxidant, Antimicrobial and Enzyme Inhibition Activities of Two *Origanum vulgare* Subspecies (subsp. *vulgare* and subsp. *hirtum*) Essential Oils. Ind Crops Prod [Internet]. 2015;70:178–84. Available from: http://dx.doi.org/10.1016/j.indcrop.2015.03.030

46.   De Oliveira TM, De Carvalho RBF, Da Costa IHF, De Oliveira GAL, De Souza AA, De Lima SG, et al. Evaluation of *p*-cymene, A Natural Antioxidant. Pharm Biol. 2015;53(3):423–8.

SUPPLEMENTARY DATA

Chemical Composition and Antioxidant Activities of Leaf and Flower Essential Oils of *Origanum onites* L. (Lamiaceae) Growing in Mount Ida-Turkey

Züleyha Özer[1*]

[1] University of Balıkesir, Altınoluk Vocational School, Programme of Medicinal and Aromatic Plants, 10870 Balıkesir, TURKEY
*Corresponding author. E-mail: zuleyhaozer@balikesir.edu.tr, Tel: +90 266 3961552
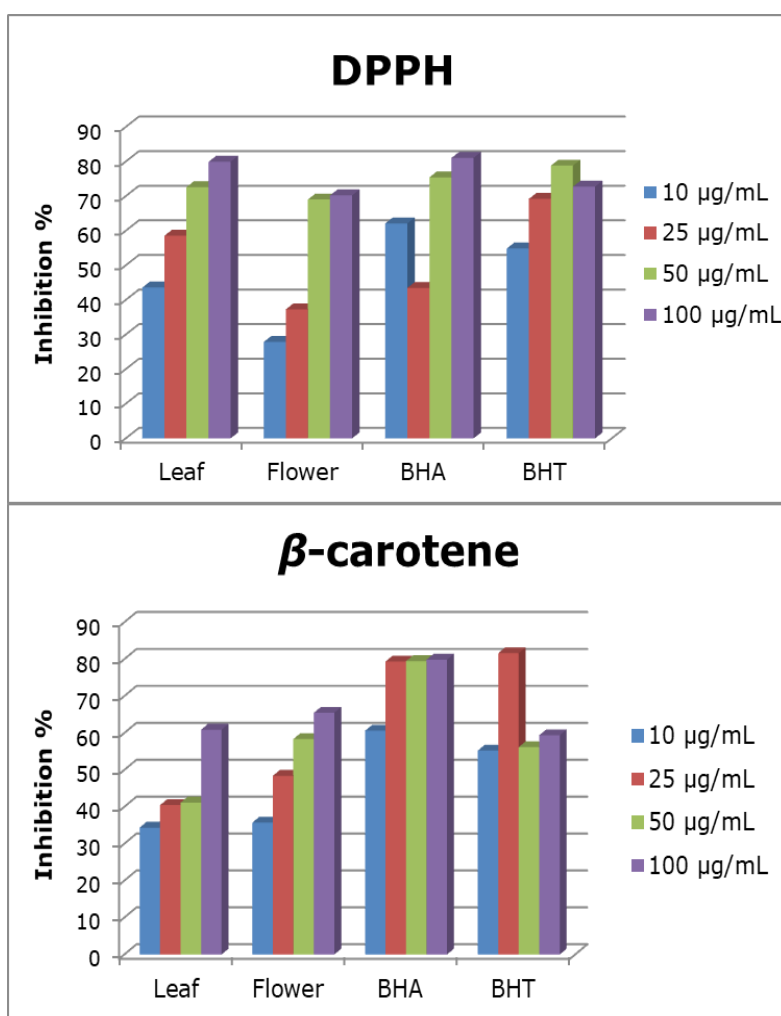
Figure S1. Inhibition (%) of lipid peroxidation and DPPH free radical scavenging activity of essential oils.

Gas chromatography-Mass spectrometry (GC-MS) conditions

Helium was used as carrier gas at a constant flow rate of 1 mL/min (20 psi). 1 µL of the sample was injected (100 µL of essential oil dissolved in 1900 µL of dichloromethane). The GC temperature program was set as follows; 150 °C hold for 5 min, ramp to 250 °C at 3 °C/min, and hold for 10 min. The temperature of the MS transfer line was set at 230 °C. A mass range from 50 to 650 *m/z* was scanned.

The column used was an Rtx-5Sil MS, 30 m, 0.25 mmID, 0.25 µm. Thermo Scientific TSQ GC-MS/MS was used in this study. A homologous series of n-alkanes was used as a reference in the calculation of Kovats Indices (KIs). Identification of the compounds was based on the comparison of their relative retention indices and mass spectra with those obtained from authentic samples and the NIST and Wiley spectra as well as the literature data (1).

Antioxidant activity

DPPH free radical scavenging method
The free radical scavenging activity of the extracts was determined spectrophotometrically by the DPPH (1,1-diphenyl-2-picrylhydrazyl) assay (2-5). In its radical form, DPPH absorbs at 517 nm, but upon reduction by an antioxidant or a radical species its absorption decreases. Briefly, 0.1 mM solution of DPPH in methanol was prepared and 160 µL of this solution was added to 40 µL of sample solutions in methanol at different concentrations (10, 25, 50, and 100 µg/mL). These tubes were left in the dark for 30 min. The measurements were made at 517 nm. BHA and BHT were used as standard compounds.

β-carotene bleaching method
The antioxidant activity was evaluated using β-carotene-linoleic acid model system (3-5) β-carotene (0.5 mg) in 1 mL of chloroform was added to 25 µL of linoleic acid, and 200 mg of Tween 40 emulsifier mixture. After evaporation of chloroform under vacuum, 100 mL of distilled water saturated with oxygen, was through vigorous shaking. A mixture of 4000 µL was transferred into different test tubes containing different concentrations of the sample (10, 25, 50, and 100 µg/mL). As soon as the emulsion was added to each tube, the zero time absorbance was measured at 470 nm using a spectrophotometer. The emulsion system was

incubated for 2 h at 50 °C. A blank, devoid of β-carotene, was prepared for background subtraction. BHA and BHT were used as standard compounds.

REFERENCES

1.   Özer Z, Kiliç T, Selvi S, Pasa C. Effect of Different Drying Methods and Development Stages on the Essential Oil Chemical Composition of Aerial Parts of *Origanum vulgare* L. subsp. hirtum (link) Letsw.   J   Essent   Oil-Bearing   Plants. 2018;21(5):1403-09.

2.   Blois MS. Antioxidant Determinations by the Use   of   A   Stable   Free   Radical.   Nature. 1958;181:1199–2000.

3.   Miller H.E. A Simplified Method for the Evaluation of Antioxidants. J Am Oil Chem Soc. 1971;48(2):91.

4.   Özer   Z.   Investigation   of   Phenolic Compounds and Antioxidant Activity of *Mentha spicata* subsp. *spicata* and *M. longifolia* subsp. *typhoides* (briq.) Harley decoction and infusion. J Turkish Chem Soc Sect A Chem. 2018;5(2):445-56.

5.   Özer   Z.   The   Phenolic   Compounds, Antioxidant and Anticholinesterase Activities of *Cyclotrichium originafolium* (Labill.) manden & scheng and *Thymus sipyleus* Boiss Teas from Turkey.   Stud   Univ   Babes-Bolyai   Chem. 2019;64(3):217–28.

The production of antiviral - breathing mask against SARS-CoV-2 using some herbal essential oils

Adem Önal[1]* ✉ iD, **Oguz Özbek[2]** ✉ iD, **Sama Nached[3]** ✉ iD

[1]University of Tokat Gaziosmanpaşa, Natural Dyes Application and Research Center, 60250, Tokat, Turkey.
[2]University of Zonguldak Bülent Ecevit, Science and Technology, Application and Research Center, 67600, Zonguldak, Turkey.
[3]University of Tokat Gaziosmanpaşa, Faculty of Science and Arts, Department of Molecular Biology and Genetics, 60250, Tokat, Turkey.

Abstract: In the fight against the new type of coronavirus (SARS-CoV-2 causing Covid-19), which emerged in China in 2019 and caused the illness and death of many people all over the world, preventive measures come to the fore as vaccines have not yet been produced. These are physical distance, mask use, and hygiene. The use of masks has become mandatory all over the world and the production of alternative masks continues uninterruptedly. In this study, we aimed to produce an effective and breathing mask against the virus using antiviral and aromatic vegetable oils. As a result of the study, 100% cotton fabrics dyed with anti-microbial effective herbal dyes were treated with anti-viral, breathable vegetable oils, and new types of protective masks against coronavirus were produced, and odor emission times of the produced masks were determined.

INTRODUCTION

Coronaviruses (Latin: Orthocoronavirinae) are viruses that cause diseases in birds and mammals and are one of the two subfamilies of the Coronaviridae family. These viruses can cause respiratory infections in humans with several members, including MERS-CoV, SARS-CoV, and SARS-CoV-2 (causing COVID-19 (2019-nCoV)), along with a pathway compiled by common cold cases. Coronaviruses cause diarrhea in cows and pigs and respiratory diseases in chickens. They contain positive-polar, single-stranded RNA as their genetic material (genome). They are the viruses with the largest RNA genome detected to date, over 30 kilobases in length. The most distinctive feature of the virus, which has a size of 125 nanometers, is a similar protrusion around it. With this feature, it has been named coronavirus; because it resembles the crown of the sun (Latin: corona) under microscopy. No vaccine or specific antiviral drug has yet been developed against coronaviruses yet, including SARS-CoV-2. Symptomatic treatment, isolation, and various experimental applications are involved in the control of the disease. Hand washing, keeping distance, and not touching the face can be used to limit the spread of coronavirus infections (1–2).

Coronavirus and Plants

Starting at the end of 2019, herbal components effective on the new Coronavirus (SARS-CoV-2 (again an RNA virus) causing the disease named Covid-19), which peaked in 2020 and affected the whole world, has not been sufficiently studied since it is fairly new. For this

reason, it is necessary to test the effectiveness of these components in the control of SARS-CoV-2 infections. According to the new study of Vietnamese scientists published in March 2020, garlic 'oil' has proven to be effective (natural antivirus) against SARS-CoV-2. This method which has been tested and yielded good results in the laboratory conditions is not yet available in the clinic. However, any herbal ingredient that relieves the symptoms of this viral infection has not yet been studied (3-8).

However, there are other scientific studies (also applied studies) effective against SARS (Severe Acute Respiratory Syndrome) virus (SARS-CoV), which is one of the old coronavirus varieties and some herbal essential oils have proven to be effective. One of these is a study by Lebanese scientists in 2008. According to this study, laurel (Laurus nobilis) oil, which is an important Mediterranean plant, was found to be effective against SARS-CoV. (In different scientific studies, other than laurel; indigo -*Isatis indigotica* with its new name *Isatis tinctoria*-, speedwell -*Artemisia annua*-, *Lycoris radiata*, *Pyrrosia lingua* (a type of fern), *Lindera aggregate*, licorice root are effective for SARS).

All of these studies are based on antiviral effectiveness. Antiviral extracts are known to not kill viruses but only inhibit them. However, it should be kept in mind that virucidal ingredients can be fully effective in viruses. In this sense, it should be stated again that there is no scientific applied study about any virucidal herbal component (number of *in vitro*-laboratory environment- virucidal studies is very small-). Viruses studied in most of these studies are viruses that mostly cause skin disorders (for example; Herpes simplex virus) rather than respiratory tract infecting-viruses (9-10).

Essential oils have been used in traditional medicine for many years to relieve viral respiratory symptoms in many parts of the world (11). In recent years, with the increase of publications examining the antiviral properties of essential oils, the mechanism of action of viruses affecting the upper respiratory tract such as influenza, SARS, and MERS has been revealed and the way for evidence-based applications is opened (12). Vimalanathan *et al.* conducted an *in vitro* study and the results of which show the efficacy of 10 minutes of vapor of eucalyptus (*Eucalyptus globulus*) and bergamot (*Citrus bergamia*) essential oils against virus infection. It was determined that the vapor of essential oils of cinnamon (*Cinnamomum zeylanicum*), lemongrass (*Cymbopogon flexuosus*), lavender (*Lavandula officinalis*), and geranium

(*Pelargonium graveolens*) showed a very strong antiviral effect against influenza (H1N1) virus within 30 minutes (13, 14).

What are the standards of respirators?
The US Centers for Disease Control (CDC) specifies the N95 respirators as part of the personal protective equipment (PPE) recommended in the Covid-19 and SARS guidelines. Europe, on the other hand, preferred the "Filtered face part" score (FFP) from EN standard 149:2001.

The features of known respirators are as follows;
• FFP2 filters have 94% filter capacity
• N95 filters have 95% filter capacity
• FFP3 and n99 filters have 99% filter capacity
• N100 filters have 99.7% filter capacity
"Filter capacity" refers to what percentage of particles 0.3 micron or larger filters out (15).

EXPERIMENTAL SECTION

Reagents and equipment
Terry Cotton mask fabric was purchased from Toga Textile Company, Tokat-Turkey. Essential oils were provided from Cemre Herbal Company in 2020, Tokat, Turkey. These fabrics are light, durable, washable, do not cause sweating, and have air permeability. It is mostly used in the health sector. Distilled water was used for all steps. Extraction was performed using soxhlet apparatus. Color codes were determined by Pantone Color Guide. The wash-, crock- (wet, dry), and light- fastnesses of all dyed samples were established according to ISO 105-C06 and to CIS, and fastness values were determined by Atlas Weather-ometer, a Launder-ometer, and a 255 model crock-meter, respectively.

Extraction of dyestuff
Curcumin powder (50 g) was extracted in 5 liters of distilled water until colorlessness and used for dyeing of cotton fabric. Onion shells (250 g) was extracted in 5 liters of distilled water until colorlessness and then used for dyeing of cotton fabric (16).

Dyeing of mask fabric
Unmordanting dyeing method was applied for the dyeing of mask fabrics. For this purpose, Cotton (1 m^2) fabric was dyed in the 5 liters of dye bath solution for 30 min. at 70 °C at medium pH, At the end of the dyeing period, the dyed fabric was removed, rinsed with distilled water, and dried.

Dyeing mechanism
The dyestuff in *Allium cepa* is Quercetin and the dyestuff in *Curcumin longa* is Curcumin as seen below (17) (Figure 1).

R' = R'' = H: Curcumin
R = OMe; R' = H; R'' = H: dimethoxycurcumin
R = R' = R'' = OMe: 5-methoxycurcumin

Quercetin   **Curcumin**
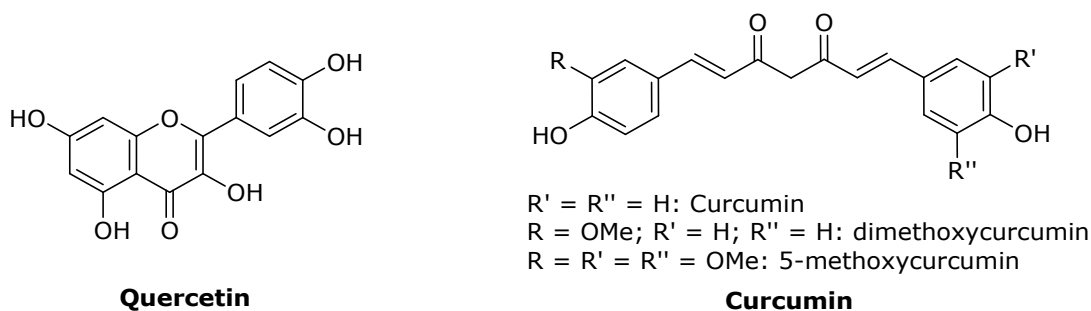
Figure 1: Structure of Quercetin and Curcumin.

Quercetin and curcumin are bonded with hydrogen bonds to the oxygen atoms in the –OH groups of the cellulose molecules (Figure 2) and provide the fabric to be dyed.
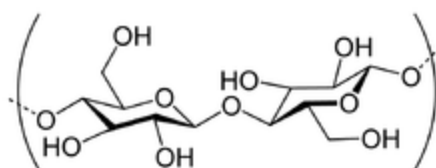
Figure 2: Structure of Cellulose.

Treatment of mask fabric with essential oil
For this purpose, the dyed fabrics using *Curcumin longa* and *Allium cepa* extracts were soaked with distilled water and treated with essential oils as given in Table 1. They were left to dry at room temperature. Later, odor emission times were determined (Table 2).

Table 1. Fastness values and color codes of dyed cotton mask fabric for *Curcumin Longa* and *Allium Cepa.*

Method	Plant/dye	pH	Light	Wash	Rubbing (wet/dry)	Color code
Unmordanting	*Curcumin Longa* (Curcumin)	7.0	6/7	5	5/5	Pantone Yellow CS C:0 M:2 Y:100 K:6
Unmordanting	*Allium cepa* (Quercetin)	6.8	5/6	4/5	5/5	Pantone 1235 CS C:0 M: 27 Y:93 K:0

The odor emission times of mask fabrics dyed with onion shell and *curcumin longa* are given in Table 2.

Table 2. Odor emission times of dyed mask fabrics.

Dye plant	Plant oil	Number of oil drops	Odor emission period (h)
Onion Shell/Curcumin	Lavender + clove	3 + 3	48
Onion Shell/Curcumin	Lavender + Thymus	4 + 4	288
Onion Shell/Curcumin	Mint + Thymus	2 + 2	120
	Mint + Thymus	3 + 3	160
Onion Shell/Curcumin	Clove + Thymus	2 + 2	288
	Clove + Thymus	3 + 3	288
Onion Shell/Curcumin	Juniper	4	24
	Juniper	6	24
Onion Shell/Curcumin	Rosemary	6	24
Onion Shell/Curcumin	Mint	6	24
Onion Shell/Curcumin	Thymus	6	288
Onion Shell/Curcumin	Clove	6	288
Onion Shell/Curcumin	Rosemary	4	24
Onion Shell/Curcumin	Mint	4	24
Onion Shell/Curcumin	Thymus	4	288
Onion Shell/Curcumin	Clove	4	288

When the results are examined in Table 2, it is seen that the vegetable oils with the longest odor emission time are thyme and clove oils for each dyed cotton fabrics with both onion (*Allium Cepa*)

and curcumin (*Curcumin Longa*). A single and double mixture of thyme and clove oil mixtures have 288 h of odor emissions. This result can be considered as an advantage pointing to the higher antiviral properties of thyme oil. The odor emission time was determined as 48h for a mixture of (lavender + clove) oil. Mint, rosemary, and juniper oils provide odor emission for 24h only. Masks dyed with *Curcumin Longa* and *Allium Cepa* extracts are given in Figure 3.

Figure 3: Masks dyed with *Curcumin Longa* **(a)** *and Allium Cepa* **(b)** extracts.

CONCLUSION

In this study, terry cotton fabric following the medical standards was dyed with antimicrobial *Curcumin Longa* and *Allium Cepa* extracts to protect against the highly contagious, and a new, lethal type of coronavirus (SARS-CoV-2 causing the disease termed Covid-19), which emerged in China in 2019 and soon caused a pandemic. Later, antiviral and breath-opening properties were provided by interacting with antiviral and breath-opening vegetable oils. The odor emission times of the masks were determined. The longest odor emission was achieved with the combination of thyme and clove oil. The masks we produced are wired, washable and rechargeable with vegetable oils.

In some countries, different masks are produced to protect against coronavirus infection. Some of these masks contain photocatalytic titanium dioxide, and also silver nitrate is added to some. Some entrepreneurs have produced 3-layer masks coated with herbal solutions. It has been featured in the media that self-cleaning masks are produced from carbon fibers. We aimed to contribute to the pandemic period by producing a new type of mask that is protective against SARS-CoV-2 infection. After this stage, it is necessary to examine the effects of these masks on patients in an interdisciplinary study. Further investigations are still going on.

REFERENCES

1. Yücel B, Görmez A. Sars–Corona Virus Overview. Turkish Journal of Applied Sciences and Technology. 2019;2(1):32–9.

2. Bozler MA. Recommendation of uygur medicine products for novel coronavirus (COVID-19). Journal of Integrative and Anatolia Medicine. 2020;1(2):21–8.

3. Astani A, Reichling J, Schnitzler P. Comparative study on the antiviral activity of selected monoterpenes derived from essential oils. Phytotheraphy Research. 2009;24(5):673–9. Doi: 10.1002/ptr.2955.

4. Brochot A, Guilbot A, Haddioui L, Roques C. Antibacterial, antifungal, and antiviral effects of three essential oil blends. Microbiologyopen. 2017;6(4):e00459. Doi: 10.1002/mbo3.459.

5. Cinatl J, Morgenster B, Bauer G, Chandra P, Rabenau H, Doerr HW. Glycyrrhizin, an active component of liquorice roots, and replication of

SARS-associated coronavirus. Lancet. 2003;361:2045–6. Doi: 10.1016/S0140-6736(03)13615-X.

6. Elaissi A, Rouis Z, Salem NAB, Mabrouk S, Salem YB, Salah KBH, Aouni M, Farhat F, Chemli R, Harzallah-Skhiri F, Khouja ML. Chemical composition of 8 eucalyptus species' essential oils and the evaluation of their antibacterial, antifungal and antiviral activities. BMC Complementary and Alternative Medicine. 2012;12:81. Doi: 10.1186/1472-6882-12-81.

7. Garozzo A, Timpanaro R, Bisignano B, Furneri PM, Bisignano G, Castro A. In vitro antiviral activity of melaleuca alternifolia essential oil. Letters in Applied Microbiology. 2009;49:806–8. Doi: 10.1111/j.1472-765X.2009.02740.x.

8. Li S, Chen C, Zhang H, Guo H, Wang H, Wang L, Zhang X, Hua S, Yu J, Xiao P, Li R, Tan X. Identification of natural compounds with antiviral activities against sars-associated coronavirus. Antiviral Research. 2005;67:18–23.

9. Lin C, Tsai F, Tsai C, Lai C, Wan L, Ho T, Hsieh C, Chao PL. Anti-SARS coronavirus 3C-like protease effects of ısatis indigotica root and plant-derived phenolic compounds. Antiviral Research. 2005;68:36–42. Doi: 10.1016/j.antiviral.2005.07.002.

10. Loizzo M, Saab A, Tundis R, Statti G, Menichini F, Lampronti I, Gambari R, Cinatl J, Doerr H. Phytochemical analysis and in vitro antiviral activities of the essential oils of seven lebanon species. Chemistry & Biodiversity. 2008;5(3):461–70. Doi: 10.1002/cbdv.200890045.

11. Minami M, Kita M, Nakaya T, Yamamoto T, Kuriyama H, Imanishi J. The inhibitory effect of essential oils on herpes simplex virus type-1 replication in vitro. Microbiology Immunology. 2003;47(9):681–4. Doi: 10.1111/j.1348-0421.2003.tb03431.x.

12. Thuy BTP, My TTA, Hai NTT, Hieu LT, Hoa TT, Loan HTP, Triet NT, Anh TTV, Quy PT, Tat PV, Hue NV, Quang DT, Trung NT, Tung VT, Huynh LK, Nhung NTA. Investigation into SARS-CoV2 resistance of compounds in garlic essential oil. ACS Omega. 2020;5(14):8312–20. Doi: 10.1021/acsomega.0c00772.

13. Usachev EV, Pyankov OV, Usacheva OV, Agranovski IE. Antiviral activity of tea tree and eucalyptus oil aerosol and vapour. Journal of Aerosol Science. 2013;59:22–30. Doi: 10.1016/j.jaerosci.2013.01.004.

14. Vimalanathan S, Hudson J. Anti-influenza virus activity of essential oils and vapor. American Journal of Essential Oils and Natural Products. 2014;2(1):47–53.

15. MacIntyrea CR, Chughtai AA. A rapid systematic review of the efficacy of face masks and respirators against coronaviruses and other respiratory transmissible viruses for the community, healthcare workers and sick patients. International Journal of Nursing Studies. 2020;108:103629. Doi: 10.1016/j.ijnurstu.2020.103629.

16. Onal A, Eser F, Bayrak S. Investigation of dyeing properties of different fabric species with alkanna orientalis root extract. Journal of Food Science and Engineering. 2017;7:213–20. Doi: 10.17265/2159-5828/2017.04.006.

17. Onal A, Yilmaz M, Eser F. Use of fermented dough extract in the dyeing of wool fabrics. Indian Journal of Fibre & Textile Research. 2018;43:132–5.

Simultaneous determination of 4F-MDMB BINACA, a new synthetic cannabinoid, and its metabolites in human blood samples by LC-MS/MS

Oya Yeter* ✉ iD

Council of Forensic Medicine, Department of Chemistry, Istanbul, Turkey.

Abstract: Methyl 2-(1-(4-fluorobutyl)-1H-indazole-3-carboxamide)-3,3-dimethylbutanoate), also referred to as 4F-MDMB BINACA (**M0**), is a recently introduced synthetic cannabinoid (SC) that was identified in herbal blends submitted to the Istanbul Narcotics Laboratory of Council of Forensic Medicine (CFM), in March 2019. A sensitive analytical method was developed to be able to detect and quantify 4F-MDMB BINACA (**M0**) and its two metabolites, 4F-MDMB BINACA {3,3-dimethylbutanoic acid ((S)-2-(1-(4-fluorobutyl)-1H-indazole-3-carboxamido)-3, 3-dimethylbutanoic acid)} (**M1**), and 4F-MDMB BINACA-*N*-4-hyroxybutyl (methyl (S)-2-(1-(4-hydroxybutyl)-1H-indazole-3-carboxamido)-3,3-dimethylbutanoate) (**M2**) in blood samples by liquid chromatography-tandem mass spectrometry (LC-MS/MS). The samples were prepared using a solid-phase extraction method. The method validation was performed in terms of linearities, limits of detection (LODs), limits of quantification (LOQs), recoveries, matrix effects, process efficiencies, accuracies, and precisions, was also applied to six blood samples from cases of autopsy in the CFM, Istanbul.

INTRODUCTION

SCs are produced to imitate the effects of THC (Tetrahydrocannabinol, the major alkaloid of cannabis) in illegal laboratories and marketed as legal marihuana. According to the European Monitoring Centre for Drugs and Drug Addiction (EMCDDA), they are the largest New Psychoactive Substance (NPS) group and they have been traded by street names such as "K2", "Bonsai", and "Spice" since 2004 and labeled with "research chemical", "not for human consumption", and "fertilizer" to circumvent the laws since 2004 (1). SCs are often highly potent substances and have been reported to have additional negative effects. Although the pharmacokinetic and pharmacodynamic properties of synthetic cannabinoids are not fully known, most synthetic cannabinoids are strong CB1 agonists, and their affinity for cannabinoid receptors is known to

be higher than cannabis, thereby producing longer-lasting, stronger side effects. Among the acute effects of SC, agitation, anxiety, confusion, hypertension, sedation, psychosis, hallucination, and tachycardia have been reported. Fatal and/or nonfatal SC intoxication of cases have been reported (2–10).

4F-MDMB BINACA (**M0**) is a newly appearing synthetic cannabinoid in the drug market. This compound is structurally similar to 5F-ADB (5F-MDMB PINACA), differing by the removal of one-carbon (-CH₂) linkage from the carbon tail of the molecule. After the first report of 4F-MDMB BINACA to the Early Warning System of the EMCDDA, it was added to the European information system and database on new drugs (EDND) in November 2018 (11). Although no detailed information about the toxicological effect of 4F-MDMBBINACA (**M0**), drug-

users report it that (**M0**) causes SCRA (synthetic cannabinoid receptor agonist)-like effects (12).

Krotulski et al. identified (**M0**) in herbal samples. They also detected (**M0**) and/or its metabolites in human blood and urine samples collected from toxicology cases (13). The metabolism of (**M0**) was reported by Haschimi et al. They identified in vivo and in vitro metabolites of (**M0**) using authentic samples of human urine and an assay of pooled human hepatic microsomes (pHLM) (14).

After the identification of the (**M0**) in an herbal

sample, analyzed by Istanbul Narcotics Laboratory of the CFM, a sensitive analytical method is needed to identify (**M0**) in human blood specimens to monitor its consumption. The main objective of the study was to develop and validate a liquid chromatography-tandem mass spectrometric method for simultaneous detection and quantification of (**M0**) and its metabolites, namely 4F-MDMB BINACA 3,3-dimethylbutanoic acid (**M1**), and 4F-MDMB BINACA-*N*-4-hydroxybutyl (**M2**) in blood samples (Figure 1). This method was also applied to the postmortem blood samples taken from cases of autopsy submitted to the CFM.

4F-MDMB BINACA   4F-MDMB BINACA 3,3-dimethylbutanoic acid   4F-MDMB BINACA *N*-4-hyroxybutyl
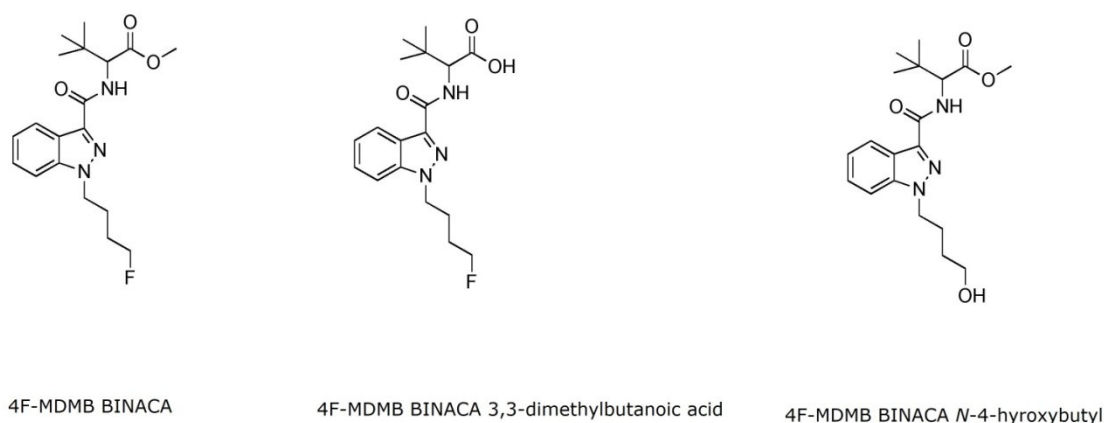
Figure 1: Chemical structure of 4F-MDMB BINACA (**M0**) and its two metabolites, (**M1**) and (**M2**).

MATERIALS AND METHODS

Chemicals and reagents
4F-MDMB BINACA (**M0**), 4F-MDMB BINACA 3,3-dimethylbutanoic acid (**M1**), and 4F-MDMB BINACA *N*-4-hyroxybutyl (**M2**) metabolites were procured from Cayman Chem. (AnnArbor, Michigan, USA). All the organic solvents and water were of LC-MS grade; they were provided by Merck (Darmstadt, Germany) and formic acid (≥98.0%) and ammonium acetate (≥99.0%) were used in the chromatographic analysis, supplied by Sigma-Aldrich (Steinheim, Germany); lastly, OASIS HLB cartridges were obtained from Waters (Milford, MA, USA).

Liquid chromatography-tandem mass spectrometry
LC-MS/MS system consisted of an ultra high-performance liquid chromatography (Shimadzu Nexera X2 LC-30AD) coupled with Shimadzu 8050 triple quadrupole mass spectrometer (Shimadzu,

Kyoto, Japan). The analytes were separated using an Agilent Poroshell 2.7-μm (150 × 4.6 mm) column (Agilent, CA, USA)at 40 °C using 15 min gradient elution with 0.6 mL/min flow rate. The mobile phase consisted of 5 mM ammonium acetate containing 0.1% formic acid in water (mobile phase A) and methanol (mobile phase B). The initial mobile phase composition was 10% B (0-0.3 min), increasing to 80% B (0.3 to 3 minutes), increasing to 95% B (3 to 7 minutes), held constant at 95% B for 4 min (7 to 11 minutes), decreasing back to 10% B (11 to 11.1 minutes) and held constant at 10 % (11.1-15 min). All analytes were analyzed using the positive ESI-multiple reaction monitoring (MRM) mode, with the following source parameters: heating gas: 250 °C, heat block temperature:400 °C, interface temperature: 300 °C, heating and drying gas flow: 10 L/min and nebulizing gas flow: 3 L/min. The MRM transitions with the corresponding collision energies for all the analytes and IS are presented in Table 1.

Table 1: LC-MS/MS parameters for (M0), (M1), (M2), and AB PINACA-d$_9$.

Analytes	Parent ions (m/z)	Product ions (m/z)	Collision energy (eV)
4F-MDMB-BINACA	364.00	219.20*	-27
		145.10	-42
		304.20	-17
4F-MDMB-BINACA 3,3-dimethylbutanoic acid	350.00	219.10*	-25
		145.10	-40
		304.20	-15
4F-MDMB BINACA *N*-4-hyroxybutyl	362.00	145.10*	-40
		217.10	-25
		224.20	-28
AB PINACA-d$_9$	340.00	295.30	-16
		146.10	-40

*Quantitative ion.

Standard solutions

The main analyte stock solutions of (**M0**), (**M1**), and (**M2**) were prepared at 1000 µg/mL in methanol. The working solutions, at 0.1–500 ng/mL concentration, were prepared by proper dilution from the primary stock solutions in a daily manner. The IS solution was 500 ng AB PINACA-d$_9$/mL methanol. All standard and IS solutions were stored at -20 °C and waited for 20 min at ambient temperature before use.

Sample preparation

All blood samples were prepared using solid-phase extraction (OASIS HLB 3 cc, 60 mg). Blood samples were added with 10 µL of the IS solution and diluted with 2 mL of water. After vortexing the samples, they were centrifuged at 5000 rpm for 10 min. The SPE was performed as follows: conditioning: 2 mL X 2 ethyl acetate, 2 mL x 2 methanol, and 2 mL X 2 distilled water, sample loading onto the cartridge, washing: 2 mL of 5% methanol (in water,v/v), drying for 10 min using nitrogen stream, and elution: 2 x 0.5 mL methanol and 2 x 0.5 mL ethyl acetate. All eluates were evaporated at 40 °C using nitrogen stream, reconstituted in 0.5 mL of the mobile phase A/B (80:20 v/v) mixture, and 5 µL of aliquot was injected to LC-MS/MS.

Validation of the analytical method

The method validation was carried out using drug-free human blood samples spiked with analytes according to international guidelines (15,16). Validation parameters were studied as follows: selectivity, linearity, detection, and quantification limits (LOD, LOQ), intra- and inter-day accuracy and precision, recovery, matrix effect, and process efficiency. Selectivity was performed by analyzing of drug-free blood from five different sources and any interferences at the retention times of analytes and IS were checked. To assess the linearity, seven calibration standards (0.05, 0.1, 0.5, 1.0, 2.5, 5.0, and 10.0 ng/mL) were analyzed in triplicate at each concentration in the blood samples.

The calibration curves of analytes were required to correlation coefficient (R^2) of 0.995 and calibrators were± 15% deviation from the nominal value. LOD and LOQ were calculated by analyzing the spiked blood samples at the lowest concentrations (n=10). The precision and accuracy of the method were determined through the analysis of low (0.05 ng/mL), medium (2.5 ng/mL), and high (10 ng/mL) level quality control samples prepared in from drug-free blood, with ten replicates per level. Inter-assay precision and accuracy were calculated from triplicates per run on five days in a consecutive manner. Recovery, matrix effect, and process efficiency were estimated at low, medium, and high concentrations (n=6) using Matuszewski's approach (17).

Application to real samples

The regional blood donation center provided blank human blood samples. Postmortem blood samples were collected from the cases of autopsy performed in CFM, Istanbul, according to 5271/87-89 (Turkish Criminal Procedure). No blood samples were taken specifically for the study. Blank and postmortem blood samples were stored at -20 °C until the time of analysis. In this analysis, postmortem blood samples of cases containing (**M0**) and/or its metabolites (**M1**, **M2**) (n=6) were used.

Table 2: Validation data of the developed method.

Parameter	4F-MDMB BINACA	4F-MDMB-BINACA butanoic acid	4F-MDMB BINACA N-4-hyroxybutyl
Intra-assay precision (RSD %)			
0.05 ng/mL	2.1	2.9	2.9
2.5 ng/mL	1.4	3.3	3.5
10.0 ng/mL	2.9	2.3	1.9
Intra-assay accuracy (%)			
0.05 ng/mL	99.6	99.4	99.6
2.5 ng/mL	91.6	98.1	95.6
10.0 ng/mL	107.1	101.3	98.6
Inter-assay precision (RSD %)			
0.05 ng/mL	2.1	8.7	7.9
2.5 ng/mL	6.4	8.5	7.7
10.0 ng/mL	3.5	5.8	3.6
Inter-assay accuracy (%)			
0.05 ng/mL	99.7	94.8	96.3
2.5 ng/mL	93.6	96.5	94.1
10.0 ng/mL	102.5	99.8	99.9
Matrix effect (%)			
0.05 ng/mL	91.1	105.2	113.7
2.5 ng/mL	100.3	102.1	107.2
10.0 ng/mL	104.9	99.7	109.4
Recovery (%)			
0.05 ng/mL	95.7	97.5	93.3
2.5 ng/mL	86.6	84.1	87.1
10.0 ng/mL	83.1	87.3	85.9
Process efficiency (%)			
0.05 ng/mL	87.2	100.1	106.1
2.5 ng/mL	86.9	85.8	93.3
10.0 ng/mL	87.2	87.0	94.6
LOD	0.02	0.05	0.02
LOQ	0.05	0.1	0.05

RESULTS and DISCUSSION

Analytical Method Validation

Table 2 shows the method validation parameters. Selectivity was studied by analyzing the blank blood samples, and any interfering peaks were not detected at the retention times for the analytes and IS. 4F-MDMB BINACA (**M0**), 4F-MDMB BINACA 3,3-dimethylbutanoic acid (**M1**), 4F-MDMB BINACA N-4-hyroxybutyl (**M2**), and AB PINACA-d$_9$ (IS) were eluted at 8.0, 7.1, 7.4, and 8.0 minutes, respectively (Figure 2). The matrix-matched calibration standards were prepared in the range 0.05–10.0 ng/mL, with a coefficient of determination (R^2) that was greater than 0.995. The

calibration curves were established with (1/x) linear regression model for all analytes. The intra- and inter-assay precisions and accuracies of the method were within the range of 1.4-3.5% and2.1–8.5% and 91.6–107.1% and 93.6–102.5%, respectively. The LOD and LOQ values were at the range of 0.02–0.05 ng/mL, and 0.05–0.1 ng/mL, respectively. The intra- and inter-day precision and accuracy of the method were acceptable with CV values below 10% and bias values below 10%. The recovery (83.1–97.5%), matrix effect (91.1-109.4%), and process efficiency (85.8–106.1%) are presented in Table 2. These findings suggest that the internal standard provides appropriate matrix match compensation and remarkable extraction recovery.

AB PINACA-d9   4F-MDMB BINACA   4F-MDMB BINACA   4F-MDMB BINACA
                                               3,3 butanoic acid   *N*-4-hydroxybutyl
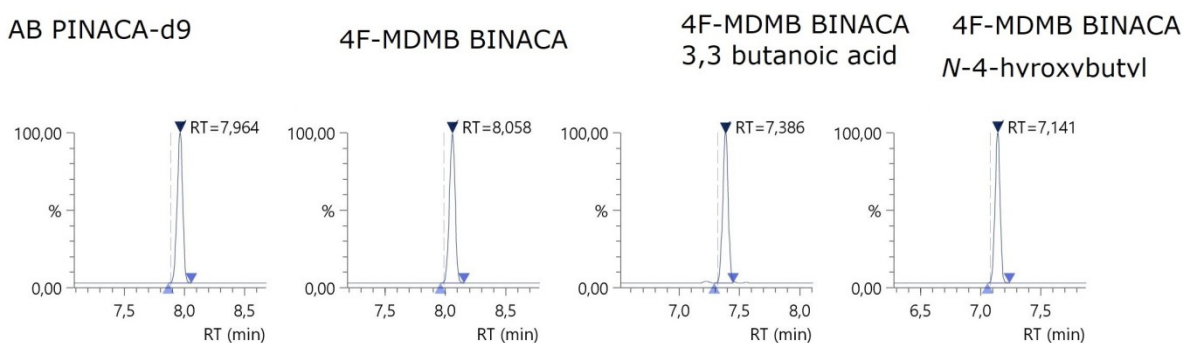
Figure 2: MRM chromatograms of (**M0**), (**M1**), (**M2**), and AB PINACA-d$_9$ for spiked matrix blank blood with 0.05 ng / mL concentration.

Application to real samples

The developed method was applied to the identification and quantification of (**M0, M1, and M2**) in postmortem blood samples collected from the cases of autopsy. We detected and quantified the (**M0**) and/or its metabolites (**M1**) and (**M2**) and in blood samples taken from six cases of autopsy. All of the cases were male and aged from 21 to 39 (mean: 31); (**M0**) was detected in 3 of 6 blood, with the concentration ranged from 0.10 to 2,90 ng/mL (mean: 0.42 ng/mL).(**M2**) was detected in 1 of 6 blood samples (0.21 ng/mL). (**M1**) was detected in all blood samples with a range of 0.12-9.05 ng/mL and a mean of 3.15 ng/mL. In this study, detecting and quantification of (**M0**) and its two metabolites (**M1, M2**) in postmortem blood samples is reported.

A few reports were published about 4F-MDMB BINACA and its metabolites and their identification in biological samples. Krotulski et al. reported the identification of (**M0**) and/or its metabolites in blood and urine samples (13). According to their study, (**M1**) was the most significant metabolite in blood and urine addition to (**M2**). (**M1**) was found to be a sensitive and specific urinary marker (14). However, blood concentration levels of (**M0**) and its metabolites were not reported in either of these studies.

CONCLUSIONS

The detection of (**M0**) in postmortem cases indicates a significant worrying alarm about the emergence of this substance. A sensitive LC-MS/MS method was developed and validated for the detection and quantitation of (**M0**), and its two metabolites (**M1**), and (**M2**) in the blood. The method was applied to six postmortem blood samples collected from the cases of autopsy. According to the results obtained, the method can be considered to be sensitive, reliable, and suitable for the analysis of postmortem blood samples. To the best of the author's knowledge, this is one of the first reports of quantification of the (**M0, M1, M2**) in postmortem blood samples.

REFERENCES

1. European Monitoring Centre for Drugs and Drug Addiction (EMCDDA), Perspectives on Drug: Synthetic Cannabinoids in Europe, (2017) . Available at https://www.emcdda.europa.eu/system/files/publications/2753/POD_Synthetic %20cannabinoids_0.pdf(Accessed 20 June 2020)

2. Schaefer N, Peters B, Bregel D, Kneisel S, Schmidt PH, Ewald AH. A fatal case involving several synthetic cannabinoids. Toxichem Krimtech. 2013;80(Special Issue):248

3. Cooper ZD. Adverse Effects of Synthetic Cannabinoids: Management of Acute Toxicity and Withdrawal. Curr Psychiatry Rep. 2016;18(5):52. doi:10.1007/s11920-016-0694-1

4. Adamowicz P. Fatal intoxication with synthetic cannabinoid MDMB-CHMICA. Forensic Sci Int. 2016;261:e5-10. https://doi.org/10.1016/j.forsciint.2016.02.024

5. Giorgetti A, Mogler L, Halter S, Haschimi B, Alt A, Rentsch D. Four cases of death involving the novel synthetic cannabinoid 5F-Cumyl-PEGACLONE. Forensic Toxicol. 2020;38(2):314-26. https://doi.org/10.1007/s11419-019-00514-w

6. Dogan H, Ozucelik D, Aciksari K, Avci A, Yazicioglu M, Celikmen M. New synthetic cannabinoid intoxications in emergency department (It's grass, Its no sin). Anatol J Psychiatry. 2016;17(1):18-25.

7. Lovett C, Wood DM, Dargan PI. Pharmacology and toxicology of the synthetic cannabinoid receptor agonists. Réanimation. 2015;24(5):527-41. DOI 10.1007/s13546-015-1104-4

8. Giorgetti A, Busardò FP, Tittarelli R, Auwärter V, Giorgetti R. Post-Mortem Toxicology: A Systematic Review of Death Cases Involving Synthetic Cannabinoid Receptor Agonists. Front Psychiatry. (Accessed 20 Hune 2020) https://www.ncbi.nlm.nih.gov/pmc/articles/PMC7261860/

9. Kronstrand R, Roman M, Andersson M, Eklund A.

Toxicological Findings of Synthetic Cannabinoids in Recreational Users. J Anal Toxicol. 2013;37(8):534-41. doi:10.1093/jat/bkt068

10. Assi S, Marshall D, Bersani F, Corazza O. Uses, Effects and Toxicity of Synthetic Cannabinoids from the Perspective of People with Lived Experiences. J Psychoactive Drugs. 2020; doi:10.1080/02791072.2020.1723748

11. European Monitoring Centre for Drugs and Drug Addiction. European information system and database on new drugs, early warning system reports. Available at https://ednd.emcdda.europa.eu. (Accessed May 20, 2020)

12. World Health Organisation (WHO).Critical review report: 4F-MDMB BINACA. 2019. GenavaAvailable at https://www.who.int/medicines/access/controlled-substances/Final_4F-MDMB-BINACA.PDF?ua=1 (Accessed May 25, 2020)

13. Krotulski AJ, Mohr ALA, Kacinko SL, Fogarty MF, Shuda SA, Diamond FX.4F-MDMBBINACA: A New Synthetic Cannabinoid Widely Implicated in Forensic Casework. J Forensic Sci. 2019;64(5):1451-61.

14. Haschimi, B, Mogler, L, Halter, S, Giorgetti, A, Schwarze, B, Westphal, F, Fischman, S, Auwarter, V. Detection of the recently emerged synthetic cannabinoid 4F-MDMBBINACA in "legal high" products and human urine specimens. Drug Test Anal. 2019; 11: 1377– 86. https://doi.org/10.1002/dta.2666

15. Scientific Working Group for Forensic Toxicology (SWGTOX) Standard Practices for Method Validation in Forensic Toxicology. J Anal Toxicol. 01 Eylül 2013;37(7):452-74.

16. Peters FT, Drummer OH, Musshoff F. Validation of new methods. Forensic Sci Int. Ocak 2007;165(2-3):216-24.

17. Matuszewski BK, Constanzer ML, Chavez-Eng CM. Strategies for the assessment of matrix effect in quantitative bioanalytical methods based on HPLC-MS/MS. Anal Chem. 01 Temmuz 2003;75(13):3019-30.

Effect of Inorganic Components of Fire Foaming Agents on the Aquatic Environment

Maya Gurbanova[1] ✉ iD **, Valentyna Loboichenko[2]*** ✉ iD **, Nataliia Leonova[3]** ✉ iD **,
Victor Strelets[4]** ✉ iD

[1]Academy of Ministry of Emergency Situations of the Azerbaijan Republic, AZ1089, Baku, Azerbaijan Republic
[2]Department of Occupational, Technogenic and Environmental Safety, National University of Civil Defense of Ukraine, 61023, Kharkiv, Ukraine
[3]Chemical Metrology Department, Kharkiv National University Named by V.N. Karazin, 61022, Kharkiv, Ukraine
[4]Scientific Department on Problems of Civil Protection and Technogenic and Ecological Safety, National University of Civil Defence of Ukraine, 61023, Kharkiv, Ukraine

Abstract: Impact on the aquatic medium of the number of inorganic additives that are part of the foaming agents for firefighting is investigated in paper. The influence of the most widespread inorganic components on aquatic organisms was analyzed. Significant variability of data was noted. It is proved that the magnesium and sodium chlorides are the safest for the environment and the most dangerous ones are aluminum compounds and sulfamic acid. Inorganic additives based on aluminum, sulfamic acid, and sodium bicarbonate are the most dangerous for aquatic living organisms, in the short and long term, and the safest compounds are magnesium and sodium chlorides.

INTRODUCTION

Today's environment is often subject to anthropogenic impact. Apart from the work of industrial enterprises, agricultural facilities, housing and communal sector, the influence of various types combustion that turn into fires is also negative. Fires often acquire catastrophic scale affecting individual technogenic objects (1) and the planet as a whole (2, 3) despite the preventive measures (4, 5, 6).

Today, one of the most effective means for localizing and extinguishing fires of various types, including oil products, is foam. During the fire both

firemen (7) and environmental objects are exposed to dangerous thermal effects. At the same time, the environment is negatively affected both by the fire itself (8) and the ingress of combustion products and components of fire extinguishing mixtures into the air, water, and soil (9, 10). As the latter ones, apart from foams (11), the water (12) and fire extinguishing powders (13) often act.

According to the composition, foaming agents are divided into synthetic, protein, fluorosynthetic, and fluoroprotein ones (14). They are a mixture of organic and inorganic compounds of natural or artificial origin. In addition to identifying (15, 16) and evaluating the content of these compounds

and their decomposition products in the environment using various laboratory (17) and express physical and chemical methods of analysis (18, 19), it is important to study their ecological properties.

Detergents (20), alkyl sulfonates (21), fatty acids (22), natural compounds (23), and fluorinated derivatives (24) are used as the main active ingredients.

The influence of the main substances, which are present in the foaming agents, on the environment, mainly, aquatic environment, has been sufficiently studied (25, 26). As ecological and ecotoxicological characteristics, experimental or calculated bioindication parameters appear in this case.

On the contrary, it should be noted that in addition to the main substance, various additives are also included in the foams, which affect on the properties of the foams such as multiplicity, viscosity, stability, frost resistance, etc. These additives are organic (alcohols, acids, and their salts) or inorganic compounds. When extinguishing the fires, these additives also enter the environment and have a negative impact on it.

The policy of developers and manufacturers to replace the precise composition of the foaming agent with a trade name, brand or generic name, including the Safety Data Sheets (27), greatly complicates the assessment of the environmental characteristics and environmental impact of individual components of the foaming agents. The information about the environmental impact of individual components of the foaming agents can be useful while developing new, more environmentally friendly compounds of the foaming agents. It will also allow potential buyers to make more environmentally conscious choices when purchasing these products.

The aim of this paper is a comparative study of the impact on the environment, in particular, the aquatic environment of the individual inorganic components of the foaming agents.

MATERIAL AND METHODS

The well-known analytical methods of processing the data are used in the paper by applying the information about chemicals presented in the literature and on the website of European Chemicals Agency (28). As the parameters of research, the values PNEC - predicted no effect concentration, LC - Lethal concentration, NOEC - no observed effect concentration, LOEC - lowest observed effect concentration, ECx the effect

concentration associated with x% response (27, 29) are selected.

RESULTS AND DISCUSSION

In the paper, the approach proposed in (13, 30) was used. The essence of the proposed assessment is to study the environmental characteristics of inorganic salts which are used to improve the extinguishing properties of foaming agents. Their composition can vary from a few thousandths to tens of percent of the total mass of the substance (0.005 - 40%).

The best known (31-40) additives are compounds such as magnesium chloride and its natural analogue, bischofite ($MgCl_2$), basic aluminum chloride ($Al_2(OH)_5Cl$), sulfamic acid (NH_2SO_3H), sodium bicarbonate ($NaHCO_3$), calcium chloride ($CaCl_2$), sodium chloride ($NaCl$), sodium carbonate (Na_2CO_3), ammonium sulfate ($(NH_4)_2SO_4$), aluminum sulfate ($Al_2(SO_4)_3$), sodium hydroxide ($NaOH$), and sodium hexametaphosphate ($Na_6P_6O_{18}$).

With the temperature factor (since extinguishing the fires involves a high ambient temperature) and the presence of several components in the mixture, for example (36, 37, 39), some products may also be released into the environment:

$$3Al_2(OH)_5Cl \rightarrow AlCl_3 + 5Al(OH)_3 \quad (1)$$

in turn, when exposed to heat:

$$2Al(OH)_3 \rightarrow Al_2O_3 + 3H_2O_{(g)} \quad (2)$$

Also, the temperature factor can lead to the formation of such products for the mixture:

$$3Al_2(OH)_5Cl + 6(NH_4)_2SO_4 \rightarrow 2Al_2(SO_4)_3 + Al_2O_3 + 12NH_{3\,(g)} + 3HCl_{\,(g)} + 12H_2O_{(g)} \quad (3)$$
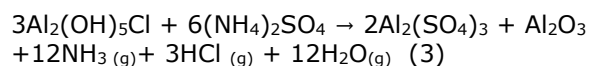
In the composition of foams, these compounds can be found mainly in aquatic and soil ecosystems. The paper examined the effect of inorganic components of foaming agents on aquatic ecosystems. Since sodium hexametaphosphate is a more branched structure of sodium metaphosphate, the main analysis can be done by using EXA data on sodium metaphosphate.

The data on the predicted safe concentration (PNEC) of a substance for organisms living in marine and freshwater ecosystems are presented in Table 1.

It was concluded that the lower the PNEC value, the unsafer the substance for organisms, so aluminum and ammonium sulfates are more dangerous to get into fresh water, and aluminum sulfate and sulfamic acid to get into the sea water,

periodic discharges, containing in the fresh water, sulfamic acid and ammonium sulfate are unsafer. In sediments, the accumulation of ammonium sulfate (fresh water) and sulfamic acid (seawater) is unsafe. That is, as seen from the presented PNEC values, sulfonated inorganic compounds have a greater negative effect on aquatic organisms.' Thus, the comparative analysis of the environmental hazard of the tested inorganic additives of foaming agents showed that the most dangerous for the environment are aluminum compounds and sulfamic acid, and the safest are magnesium and sodium chlorides.

To assess the environmental hazard to aquatic organisms data, obtained in the same conditions, were used.

For a comparative analysis of inorganic additives of foaming agents according to their short-term toxicity the parameter LC50 (4 days) is the most suitable for fish. Table 2 shows sodium, calcium and magnesium chlorides, as well as sodium bicarbonate in the short term are the least toxic for fish. It is difficult to name the most toxic substance for fish, since there is data variability. If we accept that in the case of variable data, we follow the lowest value, then the most dangerous compounds are aluminum-based compounds for fish. If we take the maximum values of LC50 (4 days), then sulfamic acid, ammonium sulfate, and sodium hexametaphosphate are more toxic in the short term for fish.

Values of long-term toxicity of substances for fish also vary greatly, and the data themselves are incomplete. So, NOEC for the studied compounds is presented to the fullest extent possible (Table 2). It can be noted that sodium chloride is the safest for freshwater fish in terms of long-term toxicity, and the most dangerous is basic aluminum chloride and, as a possible reaction product, aluminum sulfate.

Table 1. PNEC for Aquatic Organisms, mg/L (mg/kg sediment dw)

Substance	PNEC					
	Freshwater	**Intermittent releases (freshwater)**	**Marine water**	**Sewage treatment plant**	**Sediment (freshwater)**	**Sediment (marine water)**
Magnesium chloride	3.21 mg/L	5.48 mg/L	320 µg/L	90 mg/L	288.9 mg/kg sediment dw	28.89 mg/kg sediment dw
Sodium chloride	5 mg/L	No data	aquatic toxicity unlikely	aquatic toxicity unlikely	No exposure of sediment expected	No exposure of sediment expected
Calcium chloride	No data	No data	No data	No data	No data	No data
Basic Aluminum chloride	No hazard identified	No hazard identified	No hazard identified	No hazard identified	No hazard identified	No hazard identified
Sodium hydroxide	No data	No data	No data	No data	No data	No data
Sulfamic acid	1.8 mg/L	480 µg/L	180 µg/L	No data	8.36 mg/kg sediment dw	840 mg/kg sediment dw
Ammonium sulfate	312 µg/L	530 µg/L	31.2 µg/L	16.18 mg/L	63 mg/kg sediment dw	No data
Sodium bicarbonate	No data	No data	No data	No data	No data	No data
Sodium carbonate	aquatic toxicity unlikely	aquatic toxicity unlikely	aquatic toxicity unlikely	aquatic toxicity unlikely	No data	No data
Sodium hexametaphosphate	No hazard identified	No hazard identified	No hazard identified	No hazard identified	No hazard identified	No hazard identified
Aluminum chloride	No hazard identified	No hazard identified	No hazard identified	No data	No data	No data
Aluminum sulfate	300 – 4 500 000 ng/L	30.11 mg/L	30 – 64 000 000 ng/L	No hazard identified	10 mg/kg sediment dw	31.4 mg/kg sediment dw
Aluminum oxide	aquatic toxicity unlikely	aquatic toxicity unlikely	aquatic toxicity unlikely	aquatic toxicity unlikely	No data	No data
Aluminum hydroxide	No hazard identified	No hazard identified	No hazard identified	No hazard identified	No data	No data

Table 2. Data on toxicity of test substances for aquatic organisms

Substance	Short–term toxicity to fish	Long–term toxicity to fish	Short–term toxicity to aquatic invertebrates	Long–term toxicity to aquatic invertebrates	Toxicity to aquatic algae and cyanobacteria	Toxicity to microorganisms
1	**2**	**3**	**4**	**5**	**6**	**7**
Magnesium chloride	LC50 (4 days) 541 – 2 119.3 mg/L Summaries:	No data	LC50 (48 h) 140 - 548.4 mg/L Summaries:	EC10 (21 days) 82 - 321 mg/L Summaries:	EC50 (72 h) 100 mg/L NOEC (72 h) 100 mg/L	EC50 (3 h) 900 mg/L Summaries:

1	2	3	4	5	6	7
	LC50 for freshwater fish 2,119 g/L LC50 for marine water fish 10,968 g/L		EC50/LC50 for freshwater invertebrates 548,4 mg/L EC50/LC50 for marine invertebrates 3,259 g/L	EC10/LC10 or NOEC for freshwater invertebrates 321 mg/L	Summaries: EC10 or NOEC for freshwater algae 100 mg/L	EC10 or NOEC for microorganisms 900 mg/L
Sodium chloride	LC50 (4 days) 5.84 g/L Summaries: LC50 for freshwater fish 5.84 g/L	NOEC (33 days) 252 - 533 mg/L LOEC (33 days) 352 - 734 mg/L Summaries: EC10/LC10 or NOEC for freshwater fish 252 mg/L	LC50 (48 h) 4.136 g/L LC50 (24 h) 874 mg/L Summaries: EC50/LC50 for freshwater invertebrates 1.9 g/L	NOEC (21 days) 314 mg/L LOEC (21 days) 441 mg/L Summaries: EC10/LC10 or NOEC for freshwater invertebrates 314 mg/L	EC50 (5 days) 2.43 g/L Summaries: EC50 for freshwater algae 2.43 g/L	EC50 (4 days) 6.87 g/L Summaries: EC10 or NOEC for microorganisms 5 g/L

1	2	3	4	5	6	7
Calcium chloride	LC50 (4 days) 4.63 g/L LC50 (48 h) 6.56 g/L LC50 (24 h) 6.66 g/L	No data	LC50 (48 h) 2.4 - 2.77 g/L NOEC (48 h) 2 g/L	EC50 (21 days) 610 mg/L LC50 (21 days) 330 - 920 mg/L	EC50 (72 h) 2.9 - 27 g/L EC20 (72 h) 1 g/L	No data
Basic aluminum chloride	LC50 (4 days) 1.39 - 186 mg/L LC10 (4 days) 580 - 142 000 µg/L EC50 (4 days) 156 µg/L NOEC (4 days) 156 - 1 000 000 µg/L	NOEC (60 days) 13 - 26 µg/L NOEC (7 days) 752 - 56 480 µg/L LOEC (7 days) 831 - 91 420 µg/L LC50 (42 days) 15 µg/L LC50 (28 days) 19 µg/L	EC50 (48 h) 214 - 200 000 µg/L EC10 (48 h) 2.8 - 42 mg/L NOEC (48 h) 160 mg/L	NOEC (7 days) 15 mg/L LOEC (7 days) 15 mg/L	EC50 (72 h) 75 - 14 000 µg/L NOEC (72 h) 20 - 1 000 µg/L EC10 (72 h) 15 - 3 100 µg/L	EC50 (3 h) 4.4 - 1 000 mg/L EC10 (3 h) 4.4 – 1 000 mg/L
Sodium hydroxide	No data	No data	EC50 (48 h) 40.4 mg/L	No data	No data	No data
Sulfamic acid	LC50 (4 days) 70.3 mg/L Summaries: LC50 for freshwater fish	NOEC (65 days) 25 µg/L NOEC (34 days) 60 mg/L	EC50 (48 h) 71.6 mg/L EC50 (24 h) 71.6 mg/L	NOEC (35 days) 150 µg/L NOEC (21 days) 19 mg/L	EC50 (72 h) 33.8 - 48 mg/L NOEC (72 h) 18 mg/L	EC50 (3 h) 200 mg/L NOEC (3 h) 200 mg/L

1	2	3	4	5	6	7
	70.3 mg/L	Summaries: EC10/LC10 or NOEC for freshwater fish 60 mg/L	Summaries: EC50/LC50 for freshwater invertebrates 71.6 mg/L	LOEC (21 days) 34 mg/L EC50 (21 days) 60 mg/L Summaries: EC10/LC10 or NOEC for freshwater invertebrates 19 mg/L	EC10 (72 h) 13.3 - 29.5 mg/L Summaries: EC50 or freshwater algae 48 mg/L EC10 or NOEC for freshwater algae 18 mg/L	Summaries: EC50 for microorganisms 200 mg/L EC10 or NOEC for microorganisms 200 mg/L
Ammonium sulfate	LC50 (4 days) 53 - 57.2 mg/L Summaries: LC50 for freshwater fish 53 mg/L	EC10 (30 days) 5.29 mg/L Summaries: EC10/LC10 or NOEC for freshwater fish 5.29 mg/L	EC50 (48 h) 121.7 - 169 mg/L Summaries: EC50/LC50 for freshwater invertebrates 169 mg/L	EC10 (70 days) 3.12 mg/L Summaries: EC10/LC10 or NOEC for freshwater invertebrates 3.12 mg/L	EC50 (18 days) 2.7 g/L EC50 (5 days) 1.605 g/L	EC50 (30 min) 1.618 g/L
Sodium bicarbonate	LC50 (4 days) 7.1 g/L NOEC (4 days) 5.2 g/L Summaries: LC50 for freshwater fish 7.1 g/L	No data	EC50 (48 h) 4.1 g/L NOEC (48 h) 3.1 g/L Summaries: EC50 / LC50 for freshwater invertebrates 4.1 g/L	NOEC (21 days) 576 mg/L	No data	No data
Sodium carbonate	LC50 (4 days) 300 mg/L Summaries: LC50 for freshwater fish 300 mg/L	No data	EC50 (48 h) 200 - 227 mg/L Summaries: EC50/LC50 for freshwater invertebrates 200 mg/L	No data	No data	No data

1	2	3	4	5	6	7
Sodium hexametaphosphate	LC50 (4 days) 100 mg/L NOEC (4 days) 100 mg/L Summaries: LC50 for freshwater fish 100 mg/L	No data	EC50 (48 h) 485 mg/L Summaries: EC50/LC50 for freshwater invertebrates 100 mg/L	No data	EC50 (72 h) 100 mg/L NOEC (72 h) 32 mg/L LOEC (72 h) 100 mg/L Summaries: EC50 for freshwater algae 100 mg/L	EC50 (3 h) 1 g/L NOEC (3 h) 1 g/L Summaries: EC50 for microorganisms 1 g/L EC10 or NOEC for microorganisms 1 g/L
Aluminum chloride	LC50 (16 days) 430 - 3 910 µg/L LC50 (8 days) 22.4 mg/L LC50 (4 days) 78 - 218 640 µg/L LC50 (72 h) 10 - 19.3 mg/L LC50 (48 h) 11.5 mg/L	NOEC (60 days) 88 - 350 µg/L NOEC (30 days) 57 - 88 µg/L NOEC (28 days) 4.7 - 23.1 mg/L NOEC (7 days) 160 - 56 480 µg/L LOEC (60 days) 169 - 350 µg/L	EC50 (48 h) 1.5 - 27.3 mg/L LC50 (4 days) 22 - 30.6 mg/L LC50 (48 h) 71 - 99 600 µg/L NOEC (4 days) 22.6 mg/L NOEC (48 h) 5 - 672 µg/L	NOEC (28 days) 1.89 mg/L NOEC (21 days) 76 - 137 µg/L NOEC (8 days) 4.9 mg/L NOEC (7 days) 1.1 - 1.4 mg/L NOEC (6 days) 340 - 1020 µg/L	EC50 (4 days) 24 - 570 µg/L EC50 (72 h) 200 - 4 980 µg/L NOEC (72 h) 4 - 600 µg/L LOEC (72 h) 1 mg/L EC10 (72 h) 51 - 3 155 µg/L	No data

1	2	3	4	5	6	7
Aluminum sulfate	LC50 (8 days) 122.17 - 161.4 mg/L LC50 (7 days) 430 – 4 270 µg/L LC50 (6 days) 560 – 6 650 µg/L LC50 (5.833 days) 22.74 mg/L LC50 (5 days) 1.05 - 20.8 mg/L Summaries: LC50 for freshwater fish	NOEC (60 days) 13 - 1 670 µg/L NOEC (33 days) 71.5 - 558.1 µg/L NOEC (30 days) 250 - 1 670 µg/L NOEC (28 days) 29.8 - 44.9 mg/L NOEC (15 days) 1.67 mg/L Summaries: EC10/LC10 or NOEC for freshwater fish 44.9 mg/L	EC50 (4 days) 5.9 - 58.2 mg/L EC50 (72 h) 27.7 mg/L EC50 (48 h) 1.4 - 200 mg/L LC50 (7 days) 11.2 mg/L LC50 (72 h) 1.52 - 19.5 mg/L Summaries: EC50/LC50 for freshwater	NOEC (42 days) 232.6 - 453.8 µg/L NOEC (30 days) 1.092 - 2.099 mg/L NOEC (28 days) 53.1 - 12 000 µg/L NOEC (17 days) 962.5 µg/L NOEC (10 days) 1.1 - 4.282 mg/L Summaries: EC10/LC10 or NOEC for freshwater invertebrates	EC50 (30 days) 1.767 g/L EC50 (5 days) 3.011 - 19.091 g/L EC50 (4 days) 460 - 570 µg/L EC50 (72 h) 40 - 100 000 µg/L EC50 (22 h) 25 mg/L Summaries: EC50 for freshwater	EC50 (1.084 years) 500 - 3 100 µg/L EC50 (22 days) 114 - 512 µg/L EC50 (5 days) 3.011 - 19.091 g/L EC50 (24 h) 6 mg/L EC50 (3 h) 200 - 1 000 mg/L Summaries:

	122.17 mg/L LC50 for marine water fish 12.2 mg/L	EC10/LC10 or NOEC for marine water fish 4.5 mg/L	invertebrates 242 mg/L EC50/LC50 for marine invertebrates 19.5 mg/L	12 mg/L EC10/LC10 or NOEC for marine invertebrates 41.2 mg/L	algae 3.011 g/L EC50 for marine algae 302 mg/L EC10 or NOEC for freshwater algae 602 mg/L EC10 or NOEC for marine algae 30 mg/L	EC50 for microorganisms 3.011 g/L EC10 or NOEC for microorganisms 200 - 602 mg/L
1	**2**	**3**	**4**	**5**	**6**	**7**
Aluminum oxide	LC50 (16 days) 430 - 3 910 µg/L LC50 (8 days) 22.4 mg/L LC50 (4 days) 78 - 218 644.1 µg/L LC50 (4 days) 2.9 µmol/L LC50 (72 h) 10 - 19.3 mg/L	NOEC (60 days) 88 - 350 µg/L NOEC (33 days) 71.5 - 558.1 µg/L NOEC (30 days) 57 - 88 µg/L NOEC (28 days) 4.7 - 23.1 mg/L NOEC (7 days) 25.1 - 56 480 µg/L	EC50 (48 h) 1.5 - 2.56 mg/L LC50 (4 days) 22 - 30.6 mg/L LC50 (48 h) 5.7 - 99 600 µg/L NOEC (4 days) 22.6 mg/L NOEC (48 h) 5 - 672 µg/L	NOEC (42 days) 232.6 - 453.8 µg/L NOEC (30 days) 1.092 - 2.099 mg/L NOEC (28 days) 53.1 - 4 281.8 µg/L NOEC (21 days) 76 - 600 µg/L NOEC (17 days) 962.5 µg/L	EC50 (4 days) 5.4 - 570 µg/L EC50 (72 h) 16.9 - 4 980 µg/L NOEC (72 h) 4 - 600 µg/L LOEC (72 h) 400 - 1 000 µg/L EC10 (72 h) 203 - 3 155 000 ng/L	No data
Aluminum hydroxide	LC50 (16 days) 430 - 3 910 µg/L LC50 (8 days) 22.4 mg/L LC50 (4 days) 570 - 218 644.1 µg/L LC50 (4 days) 2.9 µmol/L LC50 (72 h) 10 - 19.3 mg/L	NOEC (60 days) 88 - 350 µg/L NOEC (33 days) 71.5 - 558.1 µg/L NOEC (30 days) 57 - 88 µg/L NOEC (28 days) 4.7 - 23.1 mg/L NOEC (7 days) 25.1 - 56 476.6 µg/L	EC50 (48 h) 1.5 - 2.56 mg/L LC50 (4 days) 22 - 30.6 mg/L LC50 (48 h) 5.7 - 99 600 µg/L NOEC (4 days) 22.6 mg/L NOEC (48 h) 5 - 671.2 µg/L	NOEC (42 days) 232.6 - 453.8 µg/L NOEC (30 days) 1.092 - 2.099 mg/L NOEC (28 days) 53.1 - 4 281.8 µg/L NOEC (21 days) 76 - 600 µg/L NOEC (17 days) 962.5 µg/L	EC50 (4 days) 5.4 - 570 µg/L EC50 (72 h) 16.9 - 1 799 µg/L NOEC (72 h) 4 - 600 µg/L LOEC (72 h) 400 - 1 000 µg/L EC10 (72 h) 203 – 3 155 000 ng/L	No data

For invertebrates, the smallest effect of short-term toxicity is sodium bicarbonate, and the greatest one is chloride, oxide and aluminum hydroxide.

Analysis of the long-term toxicity of substances for aquatic invertebrates shows a significant variation in data and the difficulty in evaluating them. The most fully presented are the final values of EC10 / LC10 or NOEC for freshwater invertebrates. As one can see, the most dangerous compound is ammonium sulfate. At the same time, the lowest NOEC values, obtained for a different period (6-42 days) (Table 2), are characteristic of aluminum compounds. However, these data have a significant scatter, which complicates the objectivity of their comparison.

The toxicity of the tested compounds for algae and cyanobacteria is most fully characterized by EC50 values (72 h). As can be seen, toxicants such as aluminum compounds are the most dangerous for these organisms.

When analyzing the toxic effects of the tested inorganic compounds on aquatic microorganisms, the EC50 parameter was used (3 h). As can be seen (Table 2), the most dangerous compounds are sulfonic compounds and aluminum compounds, in particular sulfamic acid, basic aluminum chloride and aluminum sulfate. Based on scattered data, it can be assumed that magnesium and sodium chlorides, as well as ammonium sulfate, have the least toxic effect on aquatic microorganisms.

It can be said that in the short and long term, inorganic compounds based on aluminum, sulfamic acid and sodium bicarbonate are the most dangerous for aquatic living organisms. And the safest ones are magnesium and sodium chlorides. Incomplete data and their significant variability greatly complicate data processing.

Thus, despite the fragmentation and incompleteness of the available data, and their significant variability, including the parameters themselves and the conditions for obtaining them, for aquatic living organisms in the short and long term, the most dangerous are inorganic compounds based on aluminum, sulfamic acid and sodium bicarbonate, and the safest are magnesium and sodium chlorides.

CONCLUSIONS

It is advisable to analyze the effect of inorganic additives of foaming agents on the environment by studying the ecological, ecotoxicological and toxicological characteristics of inorganic salts, which are used to improve the extinguishing properties of foaming agents, taking into account

their effect on living organisms and the environment.

A comparative analysis of the environmental hazards of the tested inorganic additives of foaming agents showed that the most dangerous for the environment are aluminum compounds and sulfamic acid, and the safest are magnesium and sodium chlorides.

Despite the fragmentation and incompleteness of the available data, and their significant variability, including the parameters themselves and the conditions for obtaining them, for aquatic living organisms in the short and long term, the most dangerous are inorganic compounds based on aluminum, sulfamic acid and sodium bicarbonate, and the safest are magnesium and sodium chlorides.

REFERENCES

1. Abramov YA, Basmanov OE, Salamov J, Mikhayluk AA Model of thermal effect of fire within a dike on the oil tank. Naukovyi Visnyk Natsionalnoho Hirnychoho Universytetu. 2018 2:95-100 DOI: 10.29202/nvngu/2018-2/12.

2. The race to decipher how climate change influenced Australia's record fires. Available at: https://www.nature.com/articles/d41586-020-00173-7.

3. World Fire Statistics. Available at: https://www.ctif.org/world-fire-statistics.

4. Dubinin D, Korytchenko K, Lisnyak A, Hrytsyna I, Trigub V. Numerical simulation of the creation of a fire fighting barrier using an explosion of a combustible charge. EasternEuropean Journal of Enterprise Technologies. 2017 6(10-90):11-16 DOI: 10.15587/1729-4061.2017.114504

5. Andronov V, Pospelov B, Rybka E, Skliarov S. Examining the learning fire detectors under real conditions of application. EasternEuropean Journal of Enterprise Technologies. 2017 3(9-87):53-59 DOI: 10.15587/1729-4061.2017.101985.

6. Mygalenko K, Nuyanzin V, Zemlianskyi A, Dominik A, Pozdieiev S. Development of the technique for restricting the propagation of fire in natural peat ecosystems. EasternEuropean Journal of Enterprise Technologies. 2018 1(10-91):31-37 DOI: 10.15587/1729-4061.2018.121727.

7. Kostenko V, Kostenko T, Zemlianskiy O, Maiboroda A, Kutsenko S. Automatization of individual anti-thermal protection of rescuers in the

initial period of fire suppression. EasternEuropean Journal of Enterprise Technologies. 2017 5(10-89): 4-11 DOI: 10.15587/1729-4061.2017.109484.

8. Vasiliev MI, Movchan IO, Koval OM. Diminishing of ecological risk via optimization of fire-extinguishing system projects in timber-yards. Naukovyi Visnyk Natsionalnoho Hirnychoho Universytetu. 2014 5:106-113.

9. Holemann H. Environmental Problems Caused by Fires and Fire-Fighting Agents. Available at: http://www.iafss.org/publications/fss/4/61/view.

10. Loboichenko V, Strelets V, Gurbanova M, Morozov A, Kovalov P, Shevchenko R, Kovalova T and Ponomarenko R. Review of the Environmental Characteristics of Fire Extinguishing Substances of Different Composition used for Fires Extinguishing of Various Classes. Journal of Engineering and Applied Sciences. 2019 14: 5925-5941.

11. Tureková I & Balog K. The Environmental Impacts of Fire-Fighting Foams. Research Papers Faculty of Materials Science and Technology Slovak University of Technology. 2011 18(29):111-120 doi:10.2478/v10186-010-0033-z.

12. Dubinin D, Korytchenko K, Lisnyak A, Hrytsyna I, Trigub V. Improving the installation for fire extinguishing with inelydispersed water. EasternEuropean Journal of Enterprise Technologies. 2018 2(10-92):38-43 DOI: 10.15587/1729-4061.2018.127865.

13. Loboichenko V, Leonova N, Strelets V, Morozov A, Shevchenko R, Kovalov P, Ponomarenko R and Kovalova T Comparative Analysis of the Influence of Various Dry Powder Fire Extinguishing Compositions on the Aquatic Environment. Water and Energy International. 2019 62/RNI(7):63-68.

14. Sharovarnikov AF, Sharovarnikov SA. Penoobrazovateli i peny dlya tusheniya pozharov. Sostav, svoystva, primeneniye. M: Pozhnauka. 2005 335 p (in Russian).

15. Vasyukov A, Loboichenko V, Bushtec S. Identification of bottled natural waters by using direct conductometry. Ecology, Environment and Conservation. 2016 22 (3):1171-1176.

16. Loboichenko V, Andronov V, Strelec V. Evaluation of the metrological characteristics of natural and treated waters with stable salt composition identification method. Indian Journal of Environmental Protection. 2018 38(9):724-732.

17. Osnovy analiticheskoy khimii. V 2 kn. Kn. 2. Metody khimicheskogo analiza. Ucheb. dlya vuzov / Zolotov YuA (Ed.). 2004 M: «Vysshaya shkola», 503 p. (in Russian)

18. Loboichenko VM, Tishakova TS, Vasyukov AE. Application of direct coulometry for rapid assessment of water quality in Krasno-Oskol Reservoir (Kharkiv Region, Ukraine). Der Pharma Chemica. 2016 8 (19):27-34.

19. Loboichenko VM, Vasyukov AE, Tishakova TS. Investigations of Mineralization of Water Bodies on the Example of River Waters of Ukraine. Asian Journal of Water, Environment and Pollution. 2017 14 (4):37-41 DOI: 10.3233/AJW-170035.

20. Kawahara T, Hatae Sh, Kanyama T, Ishizaki Y, Uezu K. Development of Eco-Friendly Soap-Based Firefighting Foam for Forest Fire. Environ. Control Biol. 2016 54(1):75-78 DOI: 10.2525/ecb.54.75/.

21. Kawano T, Otsuka K, Kadono T, Inokuchi R, Ishizaki Y, Dewancker B and Uezu K. Eco-Toxicological Evaluation of Fire-Fighting Foams in Small-Sized Aquatic and Semi-Aquatic Biotopes. Advanced Materials Research. 2014 875-877:699-707.

22. Levterov AM, Levterov AA. Thermodynamic properties of fatty acid esters in some biodiesel fuels. Functional Materials. 2018 25(2):308-312 DOI: 10.15407/fm25.02.308.

23. Chirkina M, Saveliev D, Pitak O. Possibility of using eco-friendly foams for fire suppression. Problems of fire safety. 2017 42:176 -180 (in Russian)

24. Korolchenko DA, Volkov AA. Extinguishing of flammable liquids by film forming foaming agents. Pozharovzryvobezopasnost/Fire and Explosion Safety. 2017 26(8):45-55. https://doi.org/10.18322/PVB.2017.26.08.45-55 (in Russian)

25. Seow J. Department of Environment and Conservation Western Australia, 2013, Fire Fighting Foam with perfluorochemical environmental review. Available at: http://www.hemmingfire.com/news/fullstory.php/aid/1748/The_final_definitive_version_of__91Fire_Fighting_Foams_with_Perfluorochemicals__96_Environmental_Review_92,_by_Dr_Jimmy_Seow,_Manager,_Pollution_Response_Unit,_Department_of_Environment_and_Conservation_Western_Australia.html.

26. Goto K, Takaichi H and Kawano T. Learning from the Eco-Toxicology of Fire-Fighting Foams in Aquatic Organisms: Altered Eco-Toxicity of Sodium Alkyl Sulfonates on Green Paramecia and Medaka

Fish Maintained in Different Waters. J. Disaster Res. 2015 10(4):604-612.

27. Globally harmonized system of classification and labelling of chemicals (GHS). United Nations, New York, USA. Available at: http://www.unece.org/ru/trans/danger/publi/ghs/ghs_rev07/07files_e0.html.

28. Database of the European Chemicals Agency. Available at: https://echa.europa.eu/home.

29. GOST R 53857-2010: Classification of chemicals for environmental hazards. General principles. 2011.

30. Dadashov I, Loboichenko V and Kireev A. Analysis of the ecological characteristics of environment friendly fire fighting chemicals used in extinguishing oil products. Pollution Research. 2018 37:63-77.

31. Patent RU 2403935. Foaming composition of heat-resistant foam to extinguish fires at subzero temperatures. Taysumov HA. 2010. Bul. № 32. (in Russian)

32. Patent RU 2457879. Foaming composition of heat-resistant foam for the fuel tank safety cover. Taysumov HA. 2012. Bul. № 22. (in Russian)

33. Patent RU 2418611C1. Fire extinguishing composition for fire fighting. Garavin VYu, Tretyakov AV. 2011. Bul. № 14. (in Russian)

34. Patent RU 2290240. Fire extinguishing composition. Dushkin AL., Karpyshev AV. 2006. Bul. № 36. (in Russian)

35. Patent SU 865303. The composition of the foaming agent to extinguish fires. Kazakov MV., Bilkun DG., Peshkov VV, Puzako M.V. 1981. Bul. № 35. (in Russian)

36. Patent US 3554912. Basic Aluminum Salt Fire Extinguishing compositions. EP Moore Jr. Patented Jan. 12, 1971.

37. Patent RU 2465028. Environmentally friendly foaming composition of heat-resistant foam. Taysumov HA. 2010. Bul. № 32. (in Russian)

38. Patent RU 2452544. Foaming composition of heat-resistant hop-based foam. Taysumov HA. 2012. Bul. № 16. (in Russian)

39. Patent RU 2328325. Concentrated stabilizer of heat-resistant foam to extinguish fires. Taysumov HA. 2008. Bul. № 19. (in Russian)

40. GB 748931A. United Kingdom. Improvements in or relating to the production of foam for fire-fighting purposes. John Kerr and Co Manchester ltd. Published 1956-05-16.

STABILITY INDICATING ANALYTICAL METHOD DEVELOPMENT AND VALIDATION OF ELTROMBOPAG OLAMINE IN TABLET DOSAGE FORM BY RP-UPLC

Dr. Ajay I. Patel[1] ✉ iD, Shweta Gosai*[1] ✉ iD, Kajal Jadav[1] ✉ iD, Dr. Amit J. Vyas[1] ✉ iD, Dr. Ashok B. Patel[1] ✉ iD, Dr. Nilesh K. Patel[1] ✉ iD

1- B. K. Mody Government Pharmacy College, Rajkot-360003, Gujarat, India.

Abstract: A simple, precise, and accurate stability indicating isocratic Reverse Phase Ultra-Performance Liquid Chromatographic (RP-UPLC) method was developed for quantitative determination of Eltrombopag olamine in the presence of degradant products. The method was developed using Acquity UPLC BEH C_{18} (50 × 2.1 mm, 1.7 μm) column with mobile phase containing water (adjusted to pH 3 with formic acid) and acetonitrile in the ratio of 30:70. The eluted compound was monitored at 244 nm and run time was within 2 min. Eltrombopag olamine was subjected to the stress condition of oxidative, acid, base, thermal, and photolytic degradation. The drug was found to degrade significantly in acid, base, and oxidative stress condition and stable in thermal and photolytic degradation conditions. The degradation products were well resolved from the main peak, providing stability indicating power of the method. The developed method was validated as per ICH Q2(R1) guideline with linearity range was between 25-75 μg/mL,% recovery range was found as 99.8-101.9 and precision was found as RSD less than 2.

INTRODUCTION

Eltrombopag is formulated as Eltrombopag olamine salt with the chemical name of 3- {(2Z)-2- [1- (3, 4-dimethylphenyl) -3-methyl-5-oxo-1, 5-dihydro-4H-pyrazol-4-ylidene] hydrazine}-2-hydroxy-3-biphenylcarboxylic acid-2-aminoethanol (1:2) (1). Eltrombopag olamine is a thrombopoeitin receptor agonist used in idiopathic thrombocytopenic purpura

(2). Eltrombopag olamine is a member of biphenylhydrazone class which stimulates activation of the cytoplasmic tyrosine kinases Janus kinase (JAK)2 and tyrosine kinase 2 and signal transducers and activators of transcription five (STAT)5 by activating thrombopoeitin receptor, resulting in megakaryocyte proliferation and differentiation into platelets. The structure of Eltrombopag olamine is given in Figure 1.
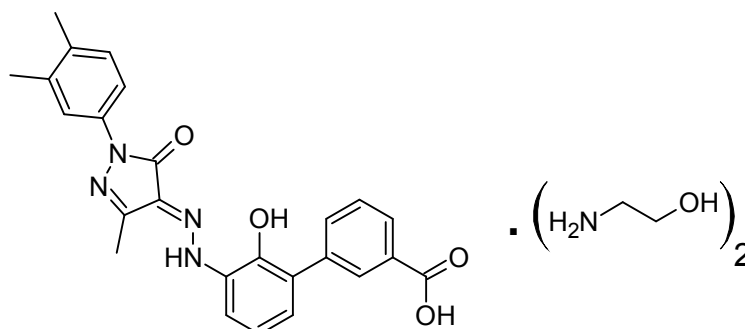
Figure 1. Structure of Eltrombopag olamine.

Forced degradation is degradation of drug substance and drug product at conditions more harsh than accelerated conditions. It is required to exhibit specificity of stability indicating methods to solve stability related problems and it also provides an insight into degradation pathways and degradation products which helps in elucidation of the structure of degradation products. The drug is exposed to various stress conditions, which are acidic, basic, oxidative, thermal, and photolytic degradation with degradation between 5-20% acceptance range (3-5).

Literature review revealed that there is no any pharmacopeial method available and various methods available are HPLC (6-7), HPLC stability (8-10), UV method (11), RP-UPLCMS (12) and LC-MS\MS (13), but there is no single method available for stability indicating method for the estimation of Eltrombopag olamine by RP-UPLC. Ultra-performance liquid chromatography (UPLC) provides significant increase in resolution, sensitivity, and speed of analysis. As compared to HPLC, RP-UPLC takes less run time and less solvent consumption, so it lowers the cost and makes the technology eco-friendly. Thus, it is worthwhile to develop stability indicating analytical method for estimation of Eltrombopag olamine tablet dosage form by RP-UPLC, which can be employed for routine analysis.

MATERIAL AND METHOD

Chemicals and Reagents
Eltrombopag olamine was kindly provided as a gift sample from Piramal Discovery Solution, Ahemdabad. Promacta tablet (75 mg) was purchased from the market. HPLC grade acetonitrile, Milli Q water, AR grade formic acid, AR grade hydrochloric acid, AR grade sodium hydroxide, and hydrogen peroxide were used.

Chromatographic Condition
UPLC (Acquity UPLC, Waters) used, data were processed using Empower software. Chromatographic separation was performed using UPLC BEH C_{18} (50 mm × 2.1 mm, 1.7 µm) column. The mobile phase consists of water pH 3 with formic acid and acetonitrile in ratio of 30:70. The flow rate was set to be 0.5 mL/min. The injection volume was

3 µL. The detection was carried out at 244 nm at column temperature 30 °C within run time of 2 min.

PREPARATION OF THE STANDARD SOLUTION

A standard solution of Eltrombopag olamine (50 µg/mL) was prepared by dissolving an 25.6 mg (equivalent to 20 mg of Eltrombopag) of Eltrombopag olamine in acetonitrile : water 70:30 (v/v) (diluent).

Preparation of Stock Solution
A standard stock solution of 200 µg/mL for Eltrombopag olamine was prepared by using acetonitrile : water 70:30 (v/v) as a diluent.

Preparation of Sample Solution
20 tablets of Promacta (75 mg of Eltrombopag) were weighed and finely powdered. About 97 mg (equivalent to 20 mg of Eltrombopag) of tablet powder was weighed and diluted to obtain 50 µg/mL solution of Eltrombopag olamine.

FORCED DEGRADATION STUDIES

The study was carried out to specify the method by ensuring the separation of degradant's peaks and standard drug peak. Acidic degradation was carried out using 1 N HCl at 60 °C for 2.5 h and alkaline degradation was performed with 0.05 N NaOH at room temperature for 24 h and then the mixture was neutralized, diluted, and filtered. Oxidation studies were conducted using 0.3% H_2O_2 for 1 h. Thermal degradation was carried out 60 °C for 1 h. For photolytic degradation, the powdered drug was exposed to UV light for 1 ICH cycle.

Preparation of force degradation solution

About 97 mg of tablet powder was used to perform force degradation, which was, after neutralization, diluted to obtain 50 µg/mL solution of Eltrombopag.

METHOD VALIDATION (14)

Analytical validation parameters for this proposed method were determined according to ICH (Q2R1) guideline.

Linearity

The stock solution of 200 µg/mL was diluted appropriately to obtain a concentration range of 50-150% i.e; 25-75 µg/mL of working sample i.e; 50 µg/mL of Eltrombopag olamine.

a) 50%: 2.5 mL of stock solution was diluted up to 20 mL to obtain 25 µg/mL.

b) 75%: 3.5 mL of stock solution was diluted up to 20 mL to obtain 35 µg/mL.

c) 100%: 5 mL of stock solution was diluted up to 20 mL to obtain 50 µg/mL.

d) 120%: 6 mL of stock solution was diluted up to 20 mL to obtain 60 µg/mL.

e) 150%: 7.5 mL of stock solution was diluted up to 20 mL to obtain 75 µg/mL.

LOD and LOQ

The limit of detection (LOD) and limit of quantification (LOQ) were calculated by Calibration curve method.

$LOD = 3.3 \times SD/slope$

$LOQ = 10 \times SD/slope$

Specificity

Specificity was performed by injecting diluent, placebo and sample solution to check the interference of excipients.

Precision

Repeatability was performed under 6 replicates of Eltrombopag olamine (50 µg/mL). Intra-day and inter-day variations of Eltrombopag olamine was performed in triplicate at three different concentration levels 50, 100, 150% (25, 50 and 75 µg/mL).

Accuracy

The accuracy was carried out by spiking in triplicate of three different concentrations 50, 100 and 150% (25, 50 and 75 µg/mL of Eltrombopag olamine) of target concentration of drug to placebo and % recovery was calculated.

Robustness

The robustness of method was established by applying small deliberate changes in the experimental condition. The changes made in flow rate ± 0.05 (0.45 mL/min, 0.5 mL/min, 0.55 mL/min), Temperature ± 2 °C (28 °C, 30 °C, 32 °C) and pH ± 0.2 (2.8, 3, 3.2).

Assay of Tablet Dosage Form

Twenty tablets were weighed and powdered. The mass equivalent of 97 mg of sample (equivalent to 20 mg of Eltrombopag olamine) was taken into a 50 mL volumetric flask. The solution is further diluted to obtain concentration of 50 µg/mL.

RESULT AND DISCUSSION

Optimized Condition

Initially methanol, acetonitrile, and water were tried in different concentrations for mobile phase selection. The optimized mobile phase was water pH 3 with formic acid and acetonitrile (30:70% v/v). Chromatographic separation was performed using UPLC BEH C_{18} (50 mm × 2.1 mm) × 1.7 µm. The flow rate was set to be 0.5 mL/min. The injection volume was 3 µL with detection wavelength 244 nm. The optimized chromatogram is given in Figure 2.
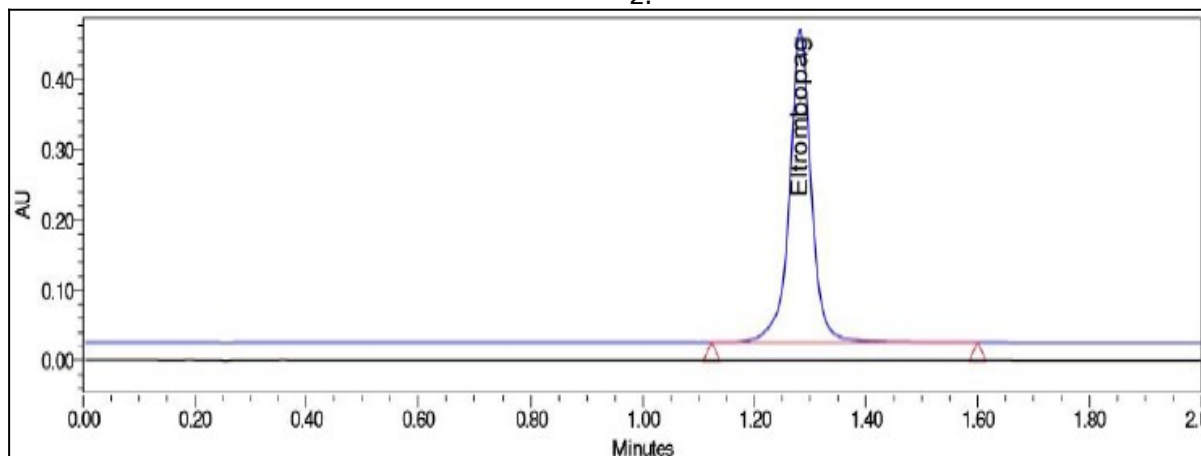
Figure 2. Chromatogram of optimized condition.

System Suitability Parameter

The system suitability parameter is shown in Table 1, which shows that all the parameters are within the acceptance limit i,e; Theoretical plates is greater than 2000 and tailing factor is less than 2.

Table 1. Summary of System Suitability Parameters

Drug	Retention Time	Area	Theoretical Plates	Tailing Factor
Eltrombopag olamine	1.30	1252210	6848	1

Forced degradation study

Force degradation study shows % degradation was obtained between 5-20% in acidic, basic, and oxidative stress condition and drug was stable in thermal and photolytic degradation. The degradation order was acidic > oxidative > basic > photolytic and thermal. Peak purity test passes as there was no any unknown peak get merged in API peak, which is also confirmed from purity angle is less than purity threshold. Force degradation data is given in Table 1 and chromatograms of different stress condition is given in Figure 3.

Table 2. Forced degradation summary.

Degradation Condition	Purity Threshold	Purity Angle	% Degradation
Acidic degradation	0.268	0.071	6
Basic degradation	0.314	0.149	4.8
Oxidative degradation	0.262	0.049	5.4
Photolytic degradation	0.262	0.049	0.2
Thermal degradation	0.271	0.080	0.3
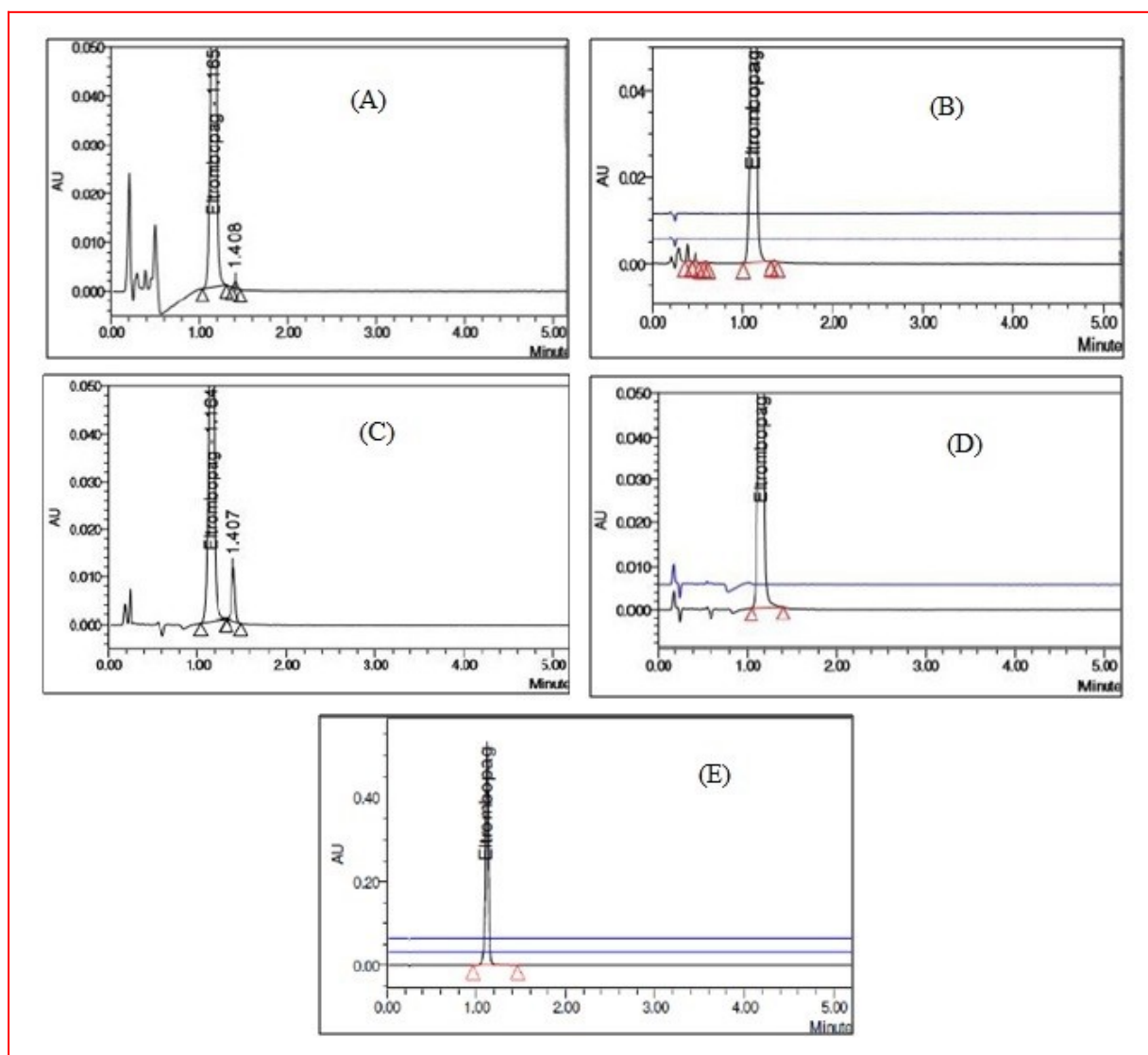
Figure 3. Force degradation chromatograms of A) Acidic condition B) Basic condition (Overlay of placebo, blank and sample) C) Oxidative condition D) Thermal condition (Overlay of placebo and sample) E) Photolytic condition (Overlay of placebo and sample).

METHOD VALIDATION

Linearity: The calibration curve obtained for Eltrombopag olamine in the range of 25-75 µg/mL and the correlation coefficient was found to be 0.999. Linearity spectra and graph is given in Figures 4 and 5.
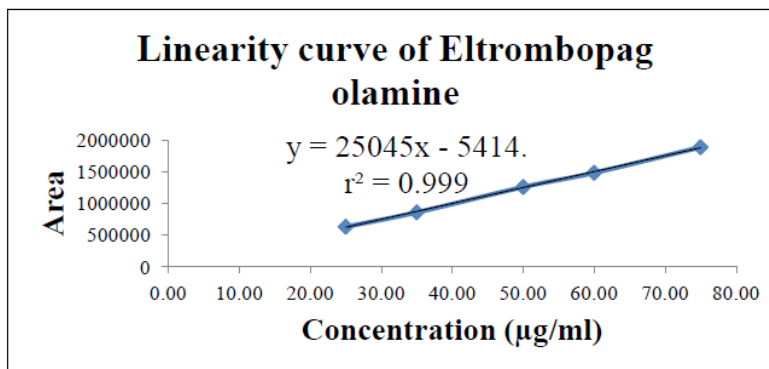
Figure 4. Linearity curve of Eltrombopag olamine.
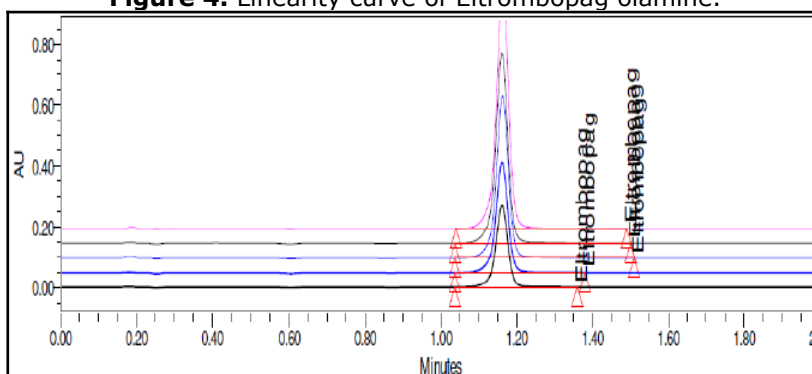
Figure 5. Linearity overlay chromatogram of Eltrombopag olamine.

LOD and LOQ: LOD and LOQ were found to be 1.19 µg/mL and 3.59 µg/mL.

Specificity: Specificity study shows that there no any interference of the diluents and placebo at the retention time of drug peak. Also purity angle is obtained less than purity threshold, so peak purity shows a positive result. Also % interference was found as 0.02%, thus the method is specific.

Precision: Repeatability and intraday, interday precision for RP-UPLC method was measured in terms of RSD and RSD was found to be less than 2.Thus, the method is precise. Results are shown in Table 2.

Table 3. Summary of intraday and interday precision and accuracy.

Precision			Interday Precision	Intraday Precision	Accuracy
Drug Name	Level (%) (n = 3)	Conc. (µg/mL) (n = 3)	%RSD (n = 3)	%RSD (n = 3)	%Recovery Range
Eltrombopag olamine	50	25	0.43	0.18	99.8-101.9
	100	50	0.09	0.06	
	150	75	0.03	0.05	

Accuracy:% recovery was found between 98-102% specify that method developed is accurate. Result for accuracy is tabulated in Table 2.

Robustness: Making deliberate changes in flow rate, temperature and pH, the RSD of peak area was found to be less than 2, specifying that the method is robust and results remained unaffected by small variations of these parameters.

Assay of tablet dosage form
% Drug content of tablet dosage form of Eltrombopag olamine was found between 99-100%. The data is given in Table 3. Thus, the method can be used for routine assay of tablet dosage form.

Table 4. Assay of Eltrombopag olamine.

Drug	CONC (µg/mL) (n=3)	CONC Mean ± SD	% Assay (n=3)
Eltrombopag olamine	50	50.98 ± 0.717	101.96

CONCLUSION

The developed stability indicating method for estimation of Eltrombopag olamine is simple and rapid. Data obtained from precision shows result in terms of RSD less than 2, which conclude that the method is reproducible and precise. Accuracy range is between 99.8-101.9% recovery ensure good accuracy and specificity shows no interference of diluent and placebo, indicating that the method is specific with good response for the estimation of Eltrombopag olamine. Deliberately changing the chromatographic conditions gives RSD less than 2 show developed method is robust in nature. Stress degradation carried out in acidic, basic, oxidative, thermal, and photolytic condition shows method was capable of quantifying drug in presence of degradants as peak purity of drug peak passes. Drug get degrade in acidic, basic, and oxidative condition indicate that drug is susceptible to these conditions and stable in thermal and photolytic degradation. From this, it is concluded that method is reliable for analysis of Eltrombopag olamine in tablet dosage form with its degradants.

ACKNOWLEDGMENTS

REFERENCES

1. Zhang Z and Kolesar JM. Eltrombopag: An Thrombopoietin Receptor Agonist for the Treatment of idiopathic Thrombocytopenic Purpura. Clinical Therapeutics. 2011; 33: 1560-76.

2. Gonzalez JR and Bastida JM. Eltrombopag in immune thrombocytopenia: efficacy review and update on drug safety. Therapeutic Advance in Drug Safety. 2018; 9: 263-85.

3. ICH – Harmonized Tripartite Guideline. Stability testing of New drug substance and products Q1A (R2). International Conference on Harmonization. IFPMA, Geneva, Switzerland, 2003.

4. Singh S and Bakshi M. Guidance on Conduct of Stress Tests to Determine Inherent Stability of Drugs. Pharmaceutical Technology. 2000; 1-14.

5. Blessy M, Patel RD, Prajapati PN and Agrawal YK. Development of forced degradation and stability indicating studies of drugs – A review. J. Phar. Anal. 2013; 4: 159- 65.

6. Pal N, Pravalika P, Bhavani DS, Geetha R, Afreen A and Rao AS. New method development and validation for the determination of Eltrombopag in bulk and tablet dosage form by HPLC. World journal of Pharmacy and Pharmaceutical science. 2018; 7: 1176-84.

7. Madasu RK, Isreal S and Rao NV. Development and validation for detection of DIC and IHC in Eltrombopag olamine tablet by RP-HPLC method. World journal of Pharmacy and Pharmaceutical science. 2018; 7: 744-62.

8. Sindhuriya M, Chaudhari GV, Shah P and Khoja SS. Development and validation of Stability indicating RP-HPLC method for estimation of Eltrombopag olamine in pharmaceutical dosage form. European journal of Biomedical and Pharmaceutical science. 2018; 5: 454-60.

9. Manoharan G. Development and validation of Stability indicating RP-HPLC method for estimation of the Eltrombopag in bulk and tablet formulation. Asian journal of Chemical science. 2018; 4(1): 1-9.

10. Mohan TSSJ, Khagga M and Jogia HA. Stability indicating UHPLC method development and validation for estimation of Eltrombopag and related impurities in tablet dosage form. Oriental journal of chemistry. 2018; 34: 1098-104.

11. Marakatham S, Vallikumari RV and Meruva SK. Spectrophotometric method for determination of Eltrombopag in bulk and pharmaceutical formulation. International journal of Research in Pharmacy and Biosciences. 2017; 4: 13-6.

12. Basha DM, Reddy GV, Rani TS, Susithra E and Chekkara R. RP-UPLC-MS assay method for Eltrombopag: application in pharmaceuticals, human plasma and urine samples. Asian J. Chem. 2015; 27: 4615-9.

13. Maddela R, Gajula R, Pilli NR, Siddiraju S, Maddela S and Makula A. Liquid chromatography-tandem mass spectrometric assay for Eltrombopag in 50 µl of human plasma: A pharmacokinetic study. J. Pharm. Biomed. Anal. 2014; 1-23.

14. ICH – Harmonized Tripartite Guideline. Validation of analytical procedures: text and methodology Q2 (R1). International Conference on Harmonization. IFPMA, Geneva, Switzerland, 2005.

Chitosan-drug encapsulation as a potential candidate for COVID-19 drug delivery systems: A review

Onome Ejeromedoghene [a1]* ✉ iD **, Olayinka Oderinde** [a1]* ✉ iD **, George Egejuru** [b] ✉ iD **, Sheriff Adewuyi** [c]* ✉ iD

a School of Chemistry and Chemical Engineering, Southeast University, Jiangning District, Nanjing, Jiangsu Province, 211189, PR China.
b School of Public Health, Southeast University, Jiangning District, Nanjing, Jiangsu Province, 211189, PR China.
c Department of Chemistry, College of Physical Sciences, Federal University of Agriculture, PMB 2240, Abeokuta, Ogun State, Nigeria.

[1] Authors OE and OO contributed equally to this work and should be regarded as the first author.

Abstract: Since the outbreak of COVID-19, the World Health Organization (WHO), Centre for Disease Control (CDC), and other health organizations around the world have coordinated the flow of information and given out preventive directives measures and guidelines to reduce the impact and spread of the disease. Meanwhile, bodies of scientists and researchers around the world are still working ceaselessly to study the virus, mode of transmission mechanisms, and are rapidly developing therapeutic antiviral drugs and vaccines. Thus, the urgent need for the fabrication of biocompatible and biodegradable composite materials as drug delivery vehicles for the efficient loading, targeted delivery, and controlled release of antiviral drugs to the target site is been inspired. Therefore, this review highlights the antimicrobial and antiviral activities of chitosan as well as the potency of a combined therapy via electrostatic/hydrogen bonding encapsulation onto the WHO suggested clinical trial drugs and possible chelation with metal ions to form new improved antiviral compounds as promising agents for targeted drug delivery.

INTRODUCTION

Since the outbreak of the novel coronavirus disease (COVID-19) which was first identified in December 2019 in China, the World Health Organization (WHO) has considered it as a global epidemic due to its current spread across different countries around the world (1,2). This infectious and deadly disease, formally referred to as Severe Acute Respiratory Syndrome-Coronavirus-2 (SARS-

CoV-2), is caused by a new virus possessing spherical particles resembling crown-shape and bearing proteins called spikes (see Figure 1), protruding from their surfaces that can cling and replicate on the host's cells, hence the general name, coronaviruses (3). The origin of COVID-19 is similar to SARS, also caused by a coronavirus (CoV) that occurred in the seafood and wet animal wholesale market in Wuhan, Hubei Province, China (4). The virus can easily be transmitted by close

contact between two or more people (via touching, handshake, and hugging), and aerosol transmission (i.e. respiratory droplets from the cough or sneezing of an infected person) (5,6). The clinical manifestation of the disease reported so far is a respiratory involvement, which is linked to mild flu-like illness, potential lethal acute respiratory distress syndrome, or fulminant pneumonia (7). However, other symptoms such as a cough, fever, sore throat, and in more severe cases, difficulty in breathing have also been reported to be attributed with early signs of the contraction of the disease which have an incubation period of about 5 to 14 days (see Figure 2) (8). Although the clinical manifestations of COVID-19 are subject to frequent changes, they include an asymptomatic carrier, ARD, and pneumonia of varying degrees of severity. However, the first asymptomatic cases were diagnosed based on positive viral nucleic acid test results, without any early COVID-19 symptoms, such as fever, gastrointestinal and respiratory symptoms, as well as no significant abnormalities on pulmonary radiograph (9,10).

The widespread of the disease with a corresponding daily increase in the number of confirmed cases and deaths globally have inspired the urgent quest for antiviral drugs to curb the menace. Several attempts are being made to treat and reduce severe infections. Chloroquine and other antiviral drugs which have been used globally for decades as an antimalarial drug and treatment of previous cases of viral infection respectively, and are enlisted as part of the WHO model list of potential medicines, have been suggested as potential candidates against the spread of the disease, however, their efficacy and safety concerns remain unclear (11,12). Also, the virtual screening and repurposing of some drugs such as Chromocarb, Ribavirin, Telbivudine, Vitamin B12, etc. approved by the Food and Drug Administrations (FDA), show a high docking score and high ligand efficiency and can be used to inhibit the COVID-19 main protease (13,14). Cortegiani et al. carried out a study using PubMed, EMBASE, and three trial registries to identify studies on the use of chloroquine in patients with COVID-19. The authors were able to unravel one narrative letter, one *in-vitro* study, one editorial, expert consensus paper, two national guideline documents, and 23 ongoing clinical trials. Early investigations inferred that chloroquine derivatives seem to be effective in limiting the replication of SARS-CoV-2 (the virus causing COVID-19) *in vitro* (15). Some other studies have proposed the efficacy of a single drug or combined drug therapy of Remdesivir, Lopinavir /Ritonavir, Favipiravir since they can interfere with the synthesis of viral mRNA targeting RdRp (16,17).

Experimental research is currently in top gear on the use of various antibiotics and antiviral agents, especially in combined therapy as a possible vaccine for COVID-19 (18). Herein, we project the potency of the combined therapy of encapsulating the clinical trial drugs with biocompatible and biodegradable chitosan (a biopolymeric cationic molecule with free OH and NH groups) as a potential drug delivery agent for COVID-19.
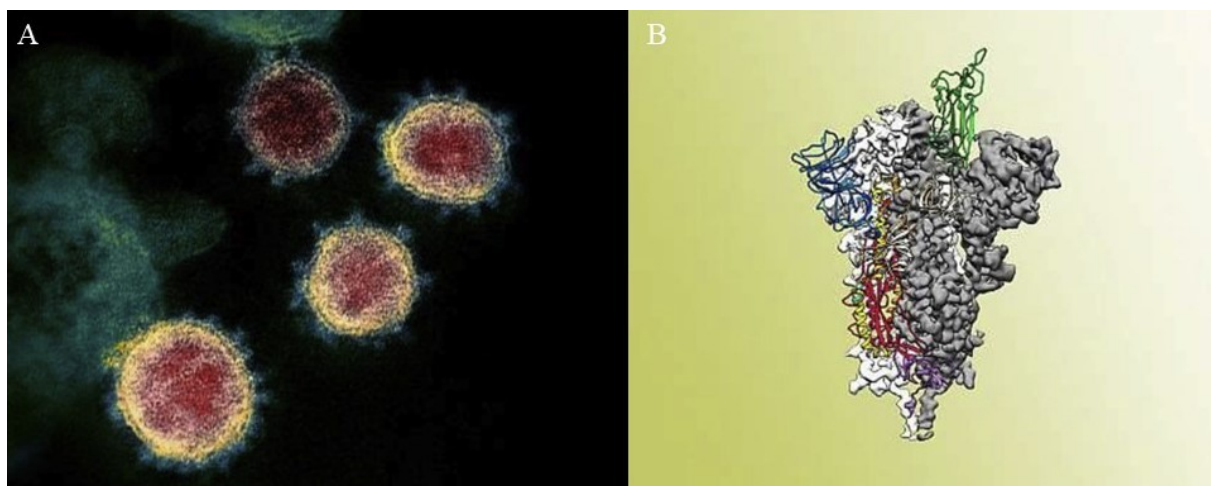
Figure 1. (A) The spikes on the outer edge of the virus particles give coronaviruses their name, crown-like, TEM image (B) Atomic-level structure of the SARS-CoV-2 spike protein. Reproduced with permission from Ref. (3). Copyright 2020 IMSS (Elsevier Inc.).
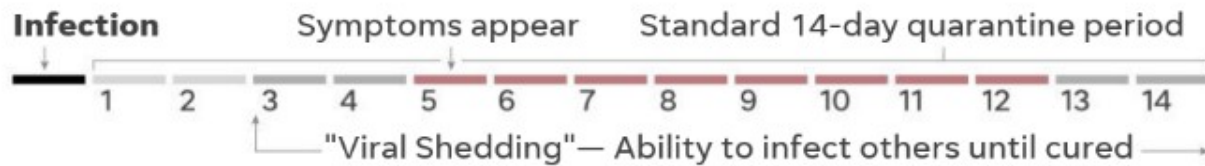
Figure 2. Incubation period of COVID-19 after an initial period of exposure to the virus to quarantine period. Reproduced from Ref. (8). Copyright USA Today.

MODE OF ACTION OF COVID-19

Coronaviruses (SARS-CoV) are single-stranded RNA viruses belonging to the family Coronaviridae, which can cause various diseases with enteric, respiratory, hepatic, and neurological symptoms with mild to serious infections in birds and mammals (19). Under an electron microscope, the coronaviruses were observed to be protruding to the periphery with a diameter of 60-160 nm. Each particle is enveloped containing a single-stranded positive-sense RNA (+ssRNA) genome of 27-32 kb with 5'-cap structure and 3'-poly A tail which interacts with the nucleoprotein (20). Thus, when the virus finds its way into the host, it infects the cells by binding to the angiotensin-converting enzyme 2 (ACE2) receptor on the surface of the cell through its envelope-spike glycoprotein domain (21–23).

The entry of SARS-CoV into cells was initially identified to be accomplished by direct membrane fusion between the virus and plasma membrane. Therefore, once inside the cells, the viral RNA genome is released into the cytoplasm and is translated into two polyproteins and structural proteins, after which the viral genome begins to replicate (see Figure 3) (24). The newly formed envelope glycoproteins are inserted into the membrane of the endoplasmic reticulum or Golgi, and the nucleocapsid is formed by the combination of genomic RNA and nucleocapsid protein. Then, viral particles germinate into the endoplasmic reticulum-Golgi intermediate compartment (ERGIC) (25). Eventually, the vesicles containing the virus particles fuse with the plasma membrane to release the virus (23).

Presently, nucleic acid testing and computed tomography (CT) scans are being used to diagnose and screen possible COVID-19 infected patients, with a number of reverse transcription polymerase chain reaction (RT-PCR) kits been designed to detect SARS-CoV-2 based on genes, with CT scans which involves many X-ray measurements taken at different angles at infected person's pulmonary region, are both used for accurate diagnoses as they can target as well as identify the specific viral agent (26–29).
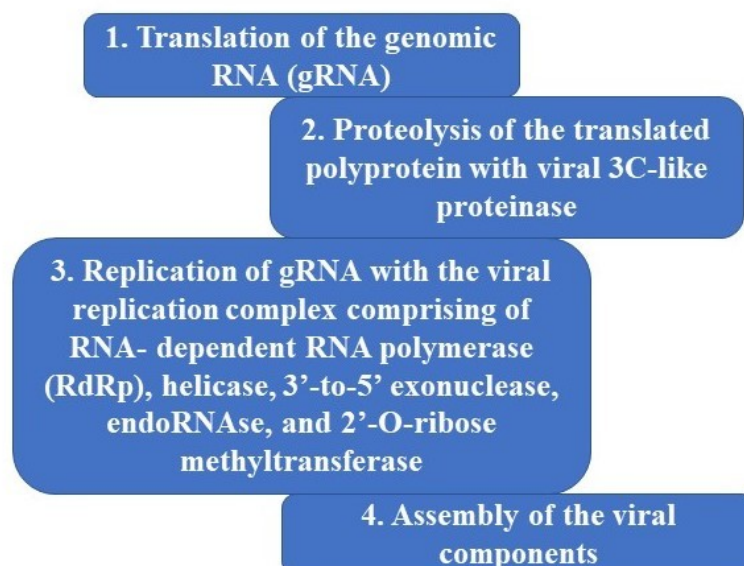
Figure 3. Replication processes involved in the life cycle of the coronavirus after entering the host cell. Adapted from Ref. (30,31) Copyright 2020 CC-BY-NC-ND 4.0 International license and 2015 Elsevier B.V.

ANTIVIRAL AGENTS FOR COVID-19

Chloroquine (see Figure 4a), also known as Resochin is a weak base that was first extracted from the bark of cinchona tree which had been used to treat fever and malaria. This compound, which is an amine acidotropic form of quinine is a lysosomotropic agent with rapid rate of absorption and distribution in bodily tissues; its metabolism is partially hepatic, giving rise to its main metabolite, desethylchloroquine and easily excreted in urine (32). Hydroxychloroquine (see Figure 4b) is the main derivative of chloroquine which differs by the presence of a hydroxyl group at the end of the side chain: the N-ethyl substituent is β-hydroxylated (33). Over the years, chloroquine and its derivatives have been used to treat autoimmune diseases, such as amebiasis that is occurring outside the intestines, rheumatoid arthritis, and systemic lupus erythematosus (34). More so, the sulfate and phosphate salts (see Figure 4c) of chloroquine have both been commercialized as antimalarial drugs (35). For example, Kashyap et al. formulated dextran nanoparticles bearing chloroquine diphosphate by solvent diffusion method yielding particle size below 70 nm with zeta-potential of −20.1±3.2 mV. This was successfully used for drug delivery and overwhelmed drug resistance in *Plasmodium falciparum* parasites (36).

Studies have shown that chloroquine or its derivatives possess a broad spectrum of antiviral effects as potent inhibitors on a variety of viruses including the Ebola virus, Zika virus, and SARS-CoV-1, etc. (37–39). They are deployed as an antiviral drug because it can affect virus infection in many ways depending on the part and extent to which the virus utilizes endosomes for entry (37). Thus, they can inhibit the *in vitro* replication of viruses which envelope and fuses with that of the acidified endosome (40), since the structure and mechanism of action is via acting as a weak base that can change the pH of acidic intracellular organelles including endosomes/lysosomes, essential for the membrane fusion (41,42). Additionally, since SARS-CoV-2 utilizes the similar surface receptor ACE2, it is believed that chloroquine can also interfere with ACE2 receptor glycosylation and prevents SARS-CoV-2 attachment to the target cells (43,44) The clinical safety profile of hydroxychloroquine is better compared with that of chloroquine (during long-term use) and allows higher daily dose with fewer concerns regarding drug-drug interactions (45). It also shows a high partitioning in tissue, including lung and brain, thus, offering a key clinical advantage in the case of COVID-19 (46).

Preliminary results from a small trial suggest that a combination of hydroxychloroquine and azithromycin is efficacious for reducing the viral load in patients with COVID-19 as tested on a 72-year-old woman admitted to a non-telemetry floor with a cohort of other COVID-19 patients (47). Meanwhile, Gautret et al. iterated that hydroxychloroquine treatment is significantly associated with viral load reduction/disappearance in COVID-19 patients and its effect is reinforced by azithromycin after an extensive study on 22 cases in France (48). Apart from chloroquine and derivatives, other therapeutic drugs reported for treating viral-related cases are listed in Table 1.
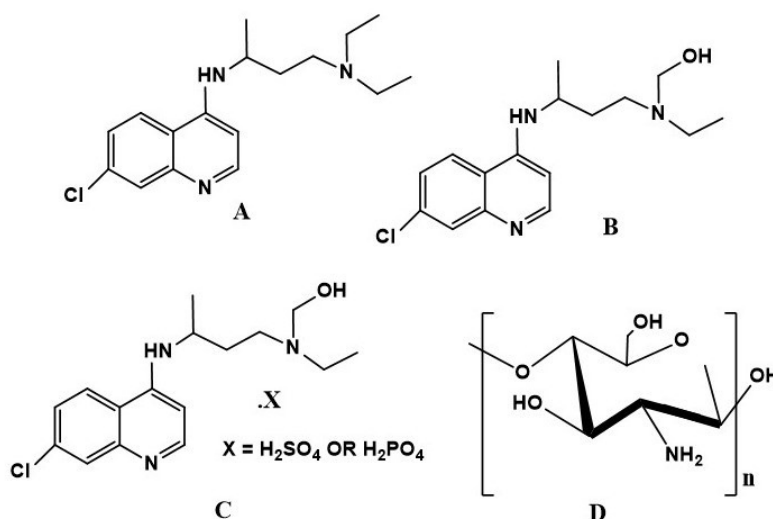
Figure 4. Structural formula of (A) chloroquine (B) hydroxychloroquine (C) hydroxychloroquine sulfate/phosphate (D) chitosan.

Table 1 Other therapeutic prospective antiviral drugs/treatments.

Drug	Chemical formula	Class of drug	Target	Ref.
Remdesivir	$C_{27}H_{35}N_6O_8P$	Adenosine analogue	Viral RNA chains	(49)
Lopinavir /Ritonavir	$C_{37}H_{48}N_4O_5/$ $C_{37}H_{48}N_6O_5S_2$	Protease inhibitors	HIV protease enzymes, SARS associated coronavirus	(50,51)
Favipiravir	$C_5H_4FN_3O_2$	Prodrug anti-influenza	Viral RNA-dependent RNA polymerase	(52)
Ribavirin	$C_8H_{12}N_4O_5$	Guanosine (ribonucleic) analog	Viral RNA synthesis and viral mRNA capping	(53,54)
Sofosbuvir	$C_{22}H_{29}FN_3O_9P$	HCV polymerase inhibitor	Inhibitor of viral RNA synthesis	
Galidesivir	$C_{11}H_{15}N_5O_3$	Nucleoside analog	Broad-spectrum of RNA virus families	
Tenofovir	$C_{19}H_{30}N_5O_{10}P$	Antiretroviral prodrug	Nucleotide reverse transcriptase inhibitor	
Triazavirin	$C_5H_4N_6O_3S$	Non-nucleoside antiviral drugs	Influenza strains such as H5N1	
Teicoplanin	$C_{88}H_{97}Cl_2N_9O_{33}$	Glycopeptide antibiotic	Viral spike protein	(55)
Atazanavir	$C_{38}H_{52}N_6O_7$	Protease inhibitor	Active viral proteins	(30)
Interferons		Signaling proteins (cytokines)	Viral infections	(56,57)
Convalescent plasma		Antibody titer	Inhibiting the formation of inflammatory cytokine storms	(58,59)

CHITOSAN-ENCAPSULATED DRUG AS DRUG DELIVERY VEHICLES

Chitosan (see Figure 4d) is a naturally occurring polysaccharide that has attracted lots of scientific interest over the years especially in the aspect of drug delivery systems which is considered to be a hopeful and viable strategy for improving infectious disease treatment (60). Chitosan is a biodegradable and biocompatible deacetylated derivative of chitin made up of randomly distributed β-(1→ 4)-2-amino-2-deoxy-D-glucopyranose which have been extensively exploited in bio-medical applications (61–63). The antimicrobial activity of chitosan has been extensively observed against a wide variety of microorganisms including fungal, algal, and bacterial strains (64–66). This has been achieved by taking advantage of the cationic charge and hydrogen bonding ability to stabilize biological structures such as DNA, RNA, and proteins in biological systems (67). Also, the higher antibacterial activity of chitosan over other types of disinfectants is demonstrated in its ability to chelate with metal ions to form new compounds and lower toxicity towards mammalian cells (68).

The skeletal framework of chitosan is made of free hydroxy and amine groups which can easily hydrogen-bond with other molecules, while the free amine groups can be protonated in acidic medium and ionically bind with the reactive sulfate or phosphate groups of the drug molecules (see Table 1) via an encapsulation strategy to form new compounds (see Figure 5) (30). Therefore, this cationic biopolymer can act as an effective viral drug delivery agent since it can enhance the loading efficiency of DNA/RNA binding electrostatically, thereby reduces the rate of diffusion and promoting a more sustained release to target sites (69,70). Additionally, the existence of the outer polymer encapsulate could protect the DNA/RNA from innate biological degradation systems allowing more-effective transport across the cellular membrane to reach the target site in the nucleus (see Figure 6) (71). Apart from the successful encapsulation of chitosan for enhanced drug delivery (72), chitosan and its derivatives have been successfully utilized *in vitro* and *in vivo* for DNA and siRNA delivery systems because of their cationic charge, biodegradability and biocompatibility, as well as mucoadhesive, and permeability-enhancing properties (73). Additionally, the encapsulation of chitosan with other bulk- or nano-materials have been achieved for the effective delivery of gene (74), nucleic acid, (75) and as a non-viral vector in different clinical applications.
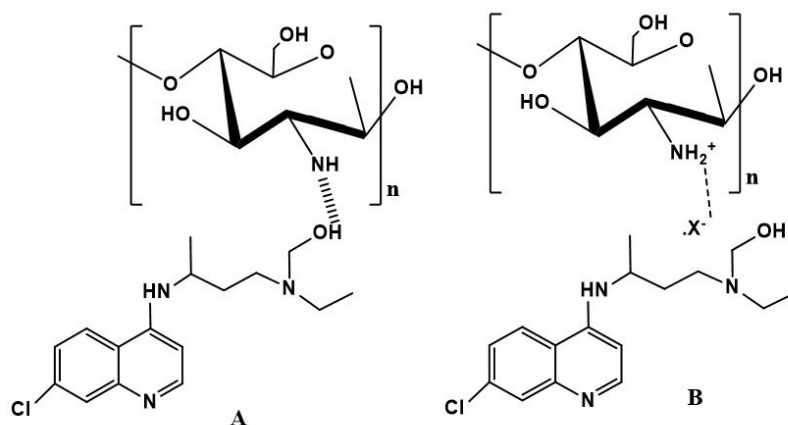
Figure 5. Possible interaction between chitosan and chloroquine or other drug molecules via (A) hydrogen bonding (B) ionic bonding with the available OH or ionic group in the drug's skeletal framework.

Existing studies have reported the efficacy of chitosan–tripolyphosphate conjugated chloroquine nanoparticle as an *in vivo* anti-malarial and anti-oxidant agent (76). For example, Magalhães et al. prepared chitosan (polycationic)/*Sterculia striata* (polyanionic) polysaccharides nanocomplex by polyelectrolyte complexation method and subsequently employed as a potential chloroquine drug release agent (77). Also, polymeric based iron nano-chloroquine phosphate was designed to encapsulate drug molecule for the delayed or slow release of drug in biological systems (78). These studies clearly show the potency of the nanodrug delivery technology as a more prospective treatments strategy than using only chloroquine or its derivatives alone to combat the parasite infection, oxidative stress as well as inflammation and DNA/RNA damage (60). However, using a combination of structural and molecular modeling approaches, Fantini et al. was able to show that chloroquine, which is one of the drugs currently under investigation for SARS-CoV-2 treatment, could bind sialic acids and gangliosides with high affinity. Thus, the team identified a new type of ganglioside-binding domain at the tip of the N-terminal domain of the SARS-CoV-2 spike (S) protein. This domain (aa 111-158), which is fully conserved among clinical isolates worldwide, may improve the attachment of the virus to lipid rafts and facilitate the contact with the ACE2 receptor, with an inference that in the presence of chloroquine or its derivate, the viral spike is no longer able to bind gangliosides (79). Moreover, hydroxychloroquine, being less toxic, has an N - hydroxyethyl side chain in place of the N -diethyl group of chloroquine. This modification makes hydroxychloroquine more soluble than chloroquine, making it more open for easy attachment with other compounds like chitosan. In the same vein, hydroxychloroquine encapsulated chitosan increases the pH and could confer antiviral effects (80), thereby offering a modulating effect on activated immune cells and altering the glycosylation of the cellular receptors of coronaviruses (81,82). Furthermore, very limited studies have reported the encapsulation of other viral drugs on polymeric substrates as drug delivery vehicles to target sites. The success of Ravi et al. on the oral delivery of Lopinavir loaded nanoparticles on a hydrophobic derivative of pullulan acetate with a nanoparticle size distribution of ~197 nm, high entrapment efficiency (~75%), monodispersive nature (PDI < 0.2) and stability for 3 months opens promising adventure for higher encapsulated drug delivery than a drug-free system (83).
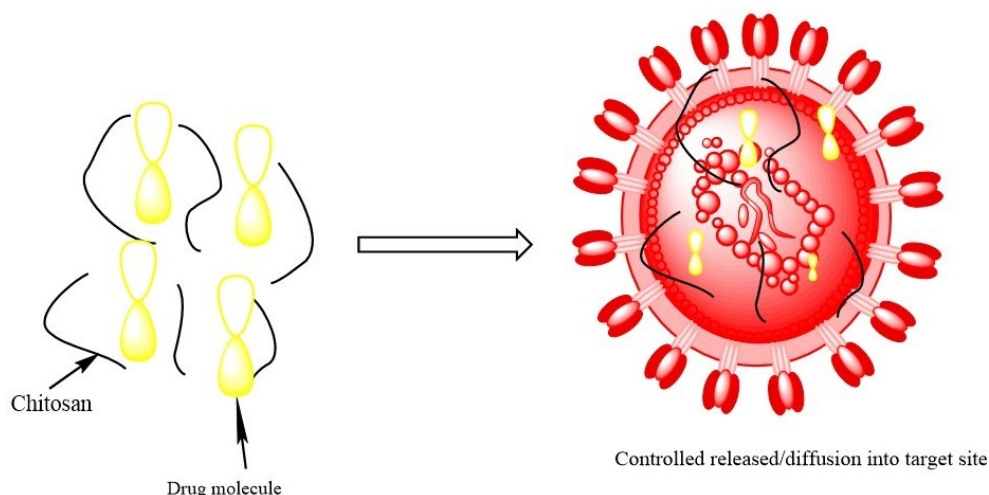
Figure 6. Controlled release of chitosan encapsulated drug and diffusion into the target site in the nucleus of the host.

Delivery of Chitosan Loaded Anti-Viral Drugs/ Vaccines

Antiviral drugs, either target specific or broad-spectrum are a class of drug molecules used for treating viral infections or inhibiting the development of a viral pathogen. Studies have shown that the pharmacokinetics of Triazavirin, $C_5H_4N_6O_3S$, can be improved via encapsulation with amino acids and quaternary amine compounds. Thus, Kozhikhova et al. (84) reported the stability and high mucoadhesive activity of charged liposome with modified chitosan coating as a nanocarrier for the delivery of Triazavirin via an underlying interaction between liposomes surface, positive chitosan coating, and negatively charged mucin secreted from epithelial cells, while Cánepa et al. (85) reported a novel chitosan-based nanocarrier for the oral delivery of interferon-α (IFNα-2b) prepared by ionotropic gelation and encapsulating approximately 100 % of the drug, with the antiviral potency of the nanocarrier showing maximum inhibitory efficiency against Human Lymphotropic-T Virus type 1 at 0.3 MIU to CF1 in mice. Also, Donalisio et al. (86) formulated chitosan nanosphere via a modified nanoemulsive template method for the delivery of acyclovir into Vero cell line infected with Herpesviruses, HSV-1, and HSV-2 strains. The acyclovir-loaded chitosan nanosphere displayed remarkable antiviral activity with no anti-proliferative activity, no signs of cytotoxicity and a drug loading capacity was recorded to be about 8.5 % with an *in vitro* release of approximately 30 % after 6 h. Additionally, Ulla et al. (87) examined the morphology and drug loading performance of a copolymerized chitosan and starch nanohydrogel functionalized with phthalic-anhydride and hexamethylenetetramine via 1-ethyl-3-(3-dimethylaminopropyl) carbodiimide catalyzed coupling, respectively. The promising antiviral and antimicrobial agents with flexible and biocompatible functionalities revealed an increased drug loading efficiency from 65% to 80 and 85% for hydrophobic- anionic drugs. Furthermore, a novel nanoparticulate system for based on foscarnet-chitosan nanoparticles was prepared by Russo et al. (88) for the delivery of foscarnet (antiviral agent for herpesvirus DNA polymerase). It was reported that the foscarnet released from nanoparticles was non-toxic and also maintained the antiviral activity of the free drug when tested *in vitro* against lung fibroblasts (HELF) cells infected with HCMV strain AD-169.

In an attempt to improve the antiviral effectiveness of nucleoside reverse transcriptase inhibitors (NRTIs) and lessen possible side effects, Yang et al. (89) developed a novel nanosized water-soluble chitosan-O-isopropyl-5'-O-d4T monophosphate conjugate. The *in vitro* drug release studies of the conjugate system at pH 1.1 and pH 7.4 in MT4 cell line show outstanding anti-HIV effect and low cytotoxicity. Yan et al. (90) explored the potentials of nanosized polyelectrolyte (PEC) complexes constructed by simple mixing of negatively charged curdlan sulfate (CRDS) into positively charged chitosan in aqueous solutions. The spherical PEC with negative zeta potential (-38 mV) were successfully loaded into zidovudine (an antiretroviral medication) and exhibited favorable drug loading efficiency at controlled pH. On another hand, Cazorla-Luna et al. (91) reported as-prepared chitosan-based mucoadhesive vaginal tablets in combination with pectin and locust bean gum, for the sustained release of tenofovir against HIV infection. The obtained results show that the tablet's formulation containing chitosan/pectin has the most homogeneous tenofovir dissolution profiles and stayed attached to the vaginal mucosa for up to 96 h, hence a promising self-protection choice for women against sexually-transmitted

HIV. Furthermore, Wu et al. (92) investigated the nanocomplexation of polyelectrolytes comprising of chitosan, chondroitin sulfate, and zinc(II) ions followed by encapsulation onto tenofovir, with the study revealing that the nanoparticles were noncytotoxic to human peripheral blood mononuclear cells and could reduce HIV-1 infection with an inhibitory concentration, IC_{50} of 4.35 µmol·L^{-1} to 1.95 µmol·L^{-1} when employed as drug carriers.

Vaccination is the most effective method of inhibiting and controlling viral infections. Viral infections can be mainly categorized into three based on the infection nature, namely: (a) acute infections caused by antigenically stable viruses, e.g. yellow fever, measles, mumps; (b) acute infections caused by rapidly mutating viruses e.g. influenza; and (c) chronic infections such as HIV and HCV. (93–95) Antiviral vaccines, on the other hand, are biological preparations containing an agent that mimics the viral pathogen, offering an active acquired immunity to a specific viral infection. Biopolymeric chitosan has shown the potentials of augmenting the immune responses with established safety and nontoxicity record in animals and humans as a vaccine against respiratory syncytial virus (RSV) infection (96). Spinner et al. (97) examined the sublingual vaccination of mice with split-flu vaccine formulated with methylglycol chitosan (MGC) and synthetic toll-like receptor 4 agonist (CRX-601) alone or in combination. The obtained results revealed that MGC and/or CRX-601 adjuvanted split-flu vaccines administered sublingually prompted a better mucosal and a corresponding systemic immune response to flu vaccine when delivered intramuscularly. Also, an adjuvanted influenza chitosan nanovaccine based on poly(I:C) could induce the proliferation of antigen-specific IFNγ secreting T-helper/memory and γδ T cells, have been developed and tested in young swine against swine influenza virus (98). In another approach, El-Sissi et al. (99) prepared an adjuvanted vaccine formulation based on chitosan (CS) or chitosan nanoparticles (CNP, prepared by ionic gelation technique) loaded with Rift Valley Fever Virus (RVFV) inactivated antigen. These formulations were observed to be superior to the RVFV-Alum vaccine as the former strongly boosted the phagocytic activity of peritoneal macrophage, neutralization of antibodies titer against RVFV and IgG values against RVFV nucleoprotein.

CONCLUSION

Chitosan is an abundant natural biopolymer that has been effective as an anti-microbial agent and has been successfully applied for the treatment of many ailments. Studies have shown that its effective application as a non-viral carrier for gene

delivery, nucleic acid, and drug delivery systems. The cationic biopolymer possesses free hydroxyl and amine functional groups that can easily be encapsulated to the existing antiviral agents via electrostatic interaction or hydrogen bonding to form new compounds with milder side effects and enhanced ability to be delivered to the target sites. The numerous binding sites and chelating ability of the polymer may also be exploited for the fabrication of organometallic complexes, coordination compounds, and nanocomposites for possible deployment as an effective drug delivery agent against the deadly COVID-19.

ACKNOWLEDGMENTS

CONFLICTS OF INTEREST

The authors hereby declare no conflicting interest.

AUTHORS' CONTRIBUTIONS

Onome Ejeromedoghene: Conceptualization, writing - original draft preparation, Funding acquisition; Olayinka Oderinde: Writing - original draft preparation, Funding acquisition; George Egejuru: Writing - review and editing; Sheriff Adewuyi: Supervision, critical review and editing.

REFERENCES

1.   Fang L, Karakiulakis G, Roth M. Antihypertensive drugs and risk of COVID-19? – Authors' reply. *Lancet Respir Med* [Internet] Elsevier Ltd; 2020;2600(20):19–20. Available from: http://dx.doi.org/10.1016/S2213-2600(20)30159-4

2.   Wu F, Zhao S, Yu B, et al. A new coronavirus associated with human respiratory disease in China. *Nature* 2020;579(7798):265–9.

3.   Das UN. Can Bioactive Lipids Inactivate Coronavirus (COVID-19)? *Arch Med Res* [Internet] Elsevier Inc; 2020; Available from: https://doi.org/10.1016/j.arcmed.2020.03.004

4.   Mackenzie JS, Smith DW. COVID-19: a novel zoonotic disease caused by a coronavirus from China: what we know and what we don't. *Microbiol Aust* 2020;

5.   Yang Y, Peng F, Wang R, et al. The deadly coronaviruses: The 2003 SARS pandemic and the 2020 novel coronavirus epidemic in China. *J Autoimmun* [Internet] Elsevier; 2020;102434. Available from: https://doi.org/10.1016/j.jaut.2020.102434

6.   McCuaig C. What We Know So Far (As of March 26, 2020) About COVID-19 – An MRT Point of View. *J Med Imaging Radiat Sci* [Internet] Canadian Association of Medical Radiation Technologists; 2020; Available from: http://www.sciencedirect.com/science/article/pii/S1939865420300394

7.   Driggin E, Madhavan M V., Bikdeli B, et al. Cardiovascular Considerations for Patients, Health Care Workers, and Health Systems During the Coronavirus Disease 2019 (COVID-19) Pandemic. *J Am Coll Cardiol* [Internet] American College of Cardiology Foundation; 2020;2019. Available from: https://doi.org/10.1016/j.jacc.2020.03.031

8.   Zarracina J, Rodriguez A. A visual guide of coronavirus infection, symptoms of COVID-19 and the effects of the virus inside the body, in graphics. *USA Today* [Internet] 2020 Mar 17; Available from: https://www.usatoday.com/in-depth/news/2020/03/13/what-coronavirus-does-body-covid-19-infection-process-symptoms/5009057002/

9.   Yan Bai, Yao L, Wei T, et al. Presumed Asymptomatic Carrier Transmission of COVID-19. *letters* 2020;382(13):1199–207.

10.   Lai CC, Liu YH, Wang CY, et al. Asymptomatic carrier state, acute respiratory disease, and pneumonia due to severe acute respiratory syndrome coronavirus 2 (SARS-CoV-2): Facts and myths. *J Microbiol Immunol Infect* [Internet] Elsevier Taiwan LLC; 2020;2(xxxx). Available from: https://doi.org/10.1016/j.jmii.2020.02.012

11.   World Health Organization (WHO). What is the WHO position on the use of chloroquine and hydroxylchloroquine in the context of the COVID-19 response? [Internet]. 2020 [cited 2020 Apr 13]. Available from: https://www.who.int/news-room/q-a-detail/malaria-and-the-covid-19-pandemic

12.   World Health Organization. 19th WHO Model List of Essential Medicines. *Http://WwwWhoInt/Medicines/Publications/Essentialmedicines/En* [Internet] 2015;1–43. Available from: http://www.who.int/medicines/organization/par/edl/expcom13/eml13%7B_%7Den.pdf

13.   Kandeel M, Al-Nazawi M. Virtual screening and repurposing of FDA approved drugs against COVID-19 main protease. *Life Sci* [Internet] Elsevier; 2020;251:117627. Available from: https://doi.org/10.1016/j.lfs.2020.117627

14.   Smith T, Bushek J, LeClaire A, Prosser T. COVID-19 Drug Therapy. *Elsevier - Nov Coronavirus Inf Cent* [Internet] 2020;(CDC):1–21. Available from: https://www.elsevier.com/connect/coronavirus-information-center#research

15.   Cortegiani A, Ingoglia G, Ippolito M, Giarratano A, Einav S. A systematic review on the efficacy and safety of chloroquine for the treatment of COVID-19. *J Crit Care* [Internet] Elsevier Inc.; 2020;3–7. Available from: https://doi.org/10.1016/j.jcrc.2020.03.005

16.   Duan Y, Zhu H-L, Zhou C. Advance of promising targets and agents against 2019-nCoV in China. *Drug Discov Today* [Internet] Elsevier Ltd; 2020;00(00):10–2. Available from: https://doi.org/10.1016/j.drudis.2020.02.011

17.   Choy K-T, Yin-Lam Wong A, Kaewpreedee P, et al. Remdesivir, lopinavir, emetine, and homoharringtonine inhibit SARS-CoV-2 replication in vitro. *Antiviral Res* [Internet] Elsevier B.V.; 2020;104786. Available from: http://www.ncbi.nlm.nih.gov/pubmed/32251767

18.   Smereka J, Szarpak L. COVID 19 a challenge for emergency medicine and every health care professional. *Am J Emerg Med* 2020; (xxxx):2–3.

19.   Lim YX, Ng YL, Tam JP, Liu DX. Human Coronaviruses : A Review of Virus – Host Interactions. *Diseases* 2016;4(26):1–28.

20.   Kang S, Peng W, Zhu Y, et al. Recent Progress in understanding 2019 Novel Coronavirus associated with Human Respiratory Disease: Detection, Mechanism and Treatment. *Int J Antimicrob Agents* [Internet] Elsevier B.V.; 2020;105950. Available from: https://doi.org/10.1016/j.ijantimicag.2020.105950

21.   Wu C-I, Postema PG, Arbelo E, et al. SARS-CoV-2, COVID-19 and inherited arrhythmia syndromes. *Hear Rhythm* [Internet] Heart Rhythm Society; 2020; Available from: http://www.sciencedirect.com/science/article/pii/S154752712030285X

22.   Simmons G, Reeves JD, Rennekamp AJ, Amberg SM, Piefer AJ, Bates P. Characterization of severe acute respiratory syndrome-associated coronavirus (SARS-CoV) spike glycoprotein-mediated viral entry. *Proc Natl Acad Sci U S A* 2004;101(12):4240–5.

23.   De Wit E, Van Doremalen N, Falzarano D, Munster VJ. SARS and MERS: Recent insights into emerging coronaviruses. *Nat Rev Microbiol* [Internet] Nature Publishing Group; 2016;14(8):523–34. Available from:

http://dx.doi.org/10.1038/nrmicro.2016.81

24.	Perlman S, Netland J. Coronaviruses post-SARS: Update on replication and pathogenesis. *Nat Rev Microbiol* 2009;7(6):439–50.

25.	Li X, Geng M, Peng Y, Meng L, Lu S. Molecular immune pathogenesis and diagnosis of COVID-19. *J Pharm Anal* [Internet] Elsevier Ltd; 2020;19(xxxx):1–7. Available from: https://doi.org/10.1016/j.jpha.2020.03.001

26.	Udugama B, Kadhiresan P, Kozlowski HN, et al. Diagnosing COVID-19: The Disease and Tools for Detection. *ACS Nano* 2020;

27.	Kageyama T, Kojima S, Shinohara M, et al. Broadly reactive and highly sensitive assay for Norwalk-like viruses based on real-time quantitative reverse transcription-PCR. *J Clin Microbiol* 2003;41(4):1548–57.

28.	Lee EYP, Ng MY, Khong PL. COVID-19 pneumonia: what has CT taught us? *Lancet Infect Dis* Elsevier Ltd; 2020;20(4):384–5.

29.	Bernheim A, Mei X, Huang M, et al. Chest CT Findings in Coronavirus Disease-19 (COVID-19): Relationship to Duration of Infection. *Radiology* 2020;1–8.

30.	Beck BR, Shin B, Choi Y, Park S, Kang K. Predicting commercially available antiviral drugs that may act on the novel coronavirus (2019-nCoV), Wuhan, China through a drug-target interaction deep learning model. *bioRxiv* [Internet] The Authors; 2020;18:2020.01.31.929547. Available from: https://www.biorxiv.org/content/biorxiv/early/2020/02/02/2020.01.31.929547.full.pdf

31.	Fung TS, Liu DX. Human Coronavirus: Host-Pathogen Interaction. *Annu Rev Microbiol* 2019;73(1).

32.	Srivastava V, Lee H. Chloroquine-based hybrid molecules as promising novel chemotherapeutic agents. *Eur J Pharmacol* [Internet] Elsevier; 2015;762:472–86. Available from: http://dx.doi.org/10.1016/j.ejphar.2015.04.048

33.	Devaux CA, Rolain J-M, Colson P, Raoult D. New insights on the antiviral effects of chloroquine against coronavirus: what to expect for COVID-19? *Int J Antimicrob Agents* [Internet] Elsevier B.V.; 2020;105938. Available from: https://doi.org/10.1016/j.ijantimicag.2020.105938

34.	Zhang W, Zhao Y, Zhang F, et al. The use of anti-inflammatory drugs in the treatment of

people with severe coronavirus disease 2019 (COVID-19): The experience of clinical immunologists from China. *Clin Immunol* [Internet] Elsevier; 2020;214:108393. Available from: https://doi.org/10.1016/j.clim.2020.108393

35.	Touret F, de Lamballerie X. Of chloroquine and COVID-19. *Antiviral Res* [Internet] Elsevier; 2020;177:104762. Available from: https://doi.org/10.1016/j.antiviral.2020.104762

36.	Kashyap A, Kaur R, Baldi A, Kumar U, Chandra R, Madan J. Chloroquine diphosphate bearing dextran nanoparticles augmented drug delivery and overwhelmed drug resistance in Plasmodium falciparum parasites. *Int J Biol Macromol* [Internet] Elsevier B.V.; 2018;114:161–8. Available from: https://doi.org/10.1016/j.ijbiomac.2018.03.102

37.	Vincent MJ, Bergeron E, Benjannet S, et al. Chloroquine is a potent inhibitor of SARS coronavirus infection and spread. *Virol J* 2005;10:1–10.

38.	Barnard DL, Day CW, Bailey K, et al. Evaluation of immunomodulators , interferons and known in vitro SARS-CoV inhibitors for inhibition of SARS-CoV replication in BALB / c mice. *Antivir Chem Chemother* 2006;275–84.

39.	Akpovwa H. Chloroquine could be used for the treatment of filoviral infections and other viral infections that emerge or emerged from viruses requiring an acidic pH for infectivity. *Cell Biochem Funct* 2016;191–6.

40.	Lecuit M. Chloroquine and COVID-19, where do we stand? *Médecine Mal Infect* [Internet] Elsevier Masson SAS; 2020;3–4. Available from: https://doi.org/10.1016/j.medmal.2020.03.004

41.	Colson P, Rolain JM, Lagier JC, Brouqui P, Raoult D. Chloroquine and hydroxychloroquine as available weapons to fight COVID-19. *Int J Antimicrob Agents* [Internet] Elsevier B.V.; 2020; (xxxx):105932. Available from: https://doi.org/10.1016/j.ijantimicag.2020.105932

42.	Singh AK, Singh A, Shaikh A, Singh R, Misra A. Chloroquine and hydroxychloroquine in the treatment of COVID-19 with or without diabetes: A systematic search and a narrative review with a special reference to India and other developing countries. *Diabetes Metab Syndr Clin Res Rev* [Internet] Elsevier Ltd; 2020;14(3):241–6. Available from: https://doi.org/10.1016/j.dsx.2020.03.011

43.	Colson P, Rolain J-M, Raoult D. Chloroquine for the 2019 novel coronavirus. *Int J Antimicrob*

Agents [Internet] Elsevier B.V.; 2020;105923. Available from: https://doi.org/10.1016/j.ijantimicag.2020.105923

44.	Lu H. Drug treatment options for the 2019-new coronavirus (2019- nCoV). *Biosci Trends* 2020;P1–3.

45.	Yao X, Ye F, Zhang M, et al. In Vitro Antiviral Activity and Projection of Optimized Dosing Design of Hydroxychloroquine for the Treatment of Severe Acute Respiratory Syndrome Main point : Hydroxychloroquine was found to be more potent than chloroquine at inhibiting SARS-CoV-2 in vit. *Clin Infect Dis* 2020;2:1–25.

46.	Picot S, Marty A, Bienvenu A-L, et al. Coalition: Advocacy for prospective clinical trials to test the post-exposure potential of hydroxychloroquine against COVID-19. *One Heal* [Internet] Elsevier B.V; 2020; Available from: https://doi.org/10.1016/j.onehlt.2020.100131

47.	Gabriels J, Saleh M, Chang D, Epstein LM. Inpatient Use of Mobile Continuous Telemetry for COVID-19 Patients Treated with Hydroxychloroquine and Azithromycin. *Hear Case Reports* [Internet] Heart Rhythm Society; 2020; (PG-). Available from: http://www.sciencedirect.com/science/article/pii/S2214027120300580 NS -

48.	Gautret P, Lagier J-C, Parola P, et al. Hydroxychloroquine and azithromycin as a treatment of COVID-19: results of an open-label non-randomized clinical trial. *Int J Antimicrob Agents* [Internet] Elsevier B.V.; 2020;105949. Available from: https://doi.org/10.1016/j.ijantimicag.2020.105949

49.	Wang M, Cao R, Zhang L, et al. Remdesivir and chloroquine effectively inhibit the recently emerged novel coronavirus (2019-nCoV) in vitro. *Cell Res* 2020;30(3):269–71.

50.	Meynard JL, Moinot L, Landman R, et al. Week 96 efficacy of lopinavir/ritonavir monotherapy in virologically suppressed patients with HIV: A randomized non-inferiority trial (ANRS 140 DREAM). *J Antimicrob Chemother* 2018;73(6):1672–6.

51.	Chu CM, Cheng VCC, Hung IFN, et al. Role of lopinavir/ritonavir in the treatment of SARS: Initial virological and clinical findings. *Thorax* 2004;59(3):252–6.

52.	Cai Q, Yang M, Liu D, et al. Experimental Treatment with Favipiravir for COVID-19: An Open-Label Control Study. *Engineering* [Internet] Chinese Academy of Engineering; 2020;(xxxx):4–

10. Available from: https://doi.org/10.1016/j.eng.2020.03.007

53.	Lythgoe MP, Middleton P. Ongoing Clinical Trials for the Management of the COVID-19 Pandemic. *Trends Pharmacol Sci* [Internet] Elsevier Ltd; 2020;xx(xx):1–20. Available from: https://doi.org/10.1016/j.tips.2020.03.006

54.	Elfiky AA. Ribavirin, Remdesivir, Sofosbuvir, Galidesivir, and Tenofovir against SARS-CoV-2 RNA dependent RNA polymerase (RdRp): A molecular docking study. *Life Sci* [Internet] Elsevier Inc; 2020;117592. Available from: https://doi.org/10.1016/j.lfs.2020.117592

55.	Baron SA, Devaux C, Colson P, Raoult D, Rolain J-M. Teicoplanin: an alternative drug for the treatment of COVID-19? *Int J Antimicrob Agents* [Internet] Elsevier B.V.; 2020;2(xxxx):105944. Available from: https://doi.org/10.1016/j.ijantimicag.2020.105944

56.	Sallard E, Lescure FX, Yazdanpanah Y, Mentre F, Peiffer-Smadja N. Type 1 interferons as a potential treatment against COVID-19. *Antiviral Res* 2020;178.

57.	Chan JFW, Yao Y, Yeung M-L, et al. Treatment with lopinavir/ritonavir or interferon-β1b improves outcome of MERS-CoV infection in a non-human primate model of common marmoset. *J Infecteous Dis* 2015;212(12):1904–13.

58.	Brown BL, Mccullough J. Treatment for emerging viruses: Convalescent plasma and COVID-19. *Transfus Apher Sci* [Internet] Elsevier Ltd; 2020;102790. Available from: https://doi.org/10.1016/j.transci.2020.102790

59.	Mohamed T, El-aziz A, Stockand JD. Recent progress and challenges in drug development against COVID-19 coronavirus (SARS-CoV-2) - an update on the status. *Infect Genet Evol* [Internet] Elsevier; 2020;83:104327. Available from: https://doi.org/10.1016/j.meegid.2020.104327

60.	Tripathy S, Kar S, Chattopadhyay S, Das S. A novel chitosan based antimalarial drug delivery against Plasmodium berghei infection. *Acta Trop* [Internet] Elsevier B.V.; 2013;128(3):494–503. Available from: http://dx.doi.org/10.1016/j.actatropica.2013.07.011

61.	Adewuyi S, Sanyaolu NO, Amolegbe SA, Sobola AO, Folarin OM. Poly[β-(1→4)-2-amino-2-deoxy-D-ghicopyranose] based zero valent nickel nanocomposite for efficient reduction of nitrate in water. *J Environ Sci (China)* 2012;24(9):1702–8.

62.   Ahmed F, Soliman FM, Adly MA, Soliman HAM, El-Matbouli M, Saleh M. Recent progress in biomedical applications of chitosan and its nanocomposites in aquaculture: A review. *Res Vet Sci* [Internet] Elsevier; 2019;126:68–82. Available from: https://doi.org/10.1016/j.rvsc.2019.08.005

63.   Chylińska M, Kaczmarek H, Burkowska-But A. Preparation and characteristics of antibacterial chitosan films modified with N-halamine for biomedical application. *Colloids Surfaces B Biointerfaces* 2019;176:379–86.

64.   Ejeromedoghene, Onome., Alayande, J. Olalekan., Olatunji, D. Emmanuel ., Alli , A. Yakubu., and Adewuyi S. Synthesis of Chitosan-Zirconium(IV) Complexes as an Antifungal Spraying Agent Against Tomato Infected Aspergillus Niger. *J Chem Soc Niger* [Internet] 2019;44(1):125–9. Available from: http://journals.chemsociety.org.ng/index.php/jcsn/article/view/253

65.   Wang X, Du Y, Fan L, Liu H, Hu Y. Chitosan- metal complexes as antimicrobial agent : Synthesis , characterization and Structure-activity study. *Polym Bull* 2005;113:105–13.

66.   Huang J, Cheng Y, Wu Y, Shi X, Du Y, Deng H. Chitosan/tannic acid bilayers layer-by-layer deposited cellulose nanofibrous mats for antibacterial application. *Int J Biol Macromol* [Internet] Elsevier B.V.; 2019;139:191–8. Available from: https://doi.org/10.1016/j.ijbiomac.2019.07.185

67.   Fotoran WL, Müntefering T, Kleiber N, et al. A multilamellar nanoliposome stabilized by interlayer
hydrogen bonds increases antimalarial drug efficacy. *Nanomedicine Nanotechnology, Biol Med* [Internet] Elsevier Inc.; 2019;22:102099. Available from: https://doi.org/10.1016/j.nano.2019.102099

68.   Adewuyi S, Kareem KT, Atayese AO, Amolegbe SA, Akinremi CA. Chitosan-cobalt(II) and nickel(II) chelates as antibacterial agents. *Int J Biol Macromol* [Internet] Elsevier B.V.; 2011;48(2):301–3. Available from: http://dx.doi.org/10.1016/j.ijbiomac.2010.12.004

69.   Loh XJ, Wu YL. Cationic star copolymers based on β-cyclodextrins for efficient gene delivery to mouse embryonic stem cell colonies. *Chem Commun* [Internet] Royal Society of Chemistry; 2015;51(54):10815–8. Available from: http://dx.doi.org/10.1039/C5CC03686K

70.   Loh XJ, Ong SJ, Tung YT, Choo HT. Co-delivery of drug and DNA from cationic dual-

responsive micelles derived from poly(DMAEMA-co-PPGMA). *Mater Sci Eng C* [Internet] Elsevier B.V.; 2013;33(8):4545–50. Available from: http://dx.doi.org/10.1016/j.msec.2013.07.011

71.   Xiang Y, Nwe N, Oo L, Lee JP, Li Z, Loh XJ. Recent development of synthetic nonviral systems for sustained gene delivery. *Drug Discov Today* [Internet] Elsevier Ltd; 2017;22(9):1318–35. Available from: http://dx.doi.org/10.1016/j.drudis.2017.04.001

72.   Ahsan SM, Thomas M, Reddy KK, Gopal S, Asthana A, Bhatnagar I. Chitosan as biomaterial in drug delivery and tissue engineering. *Int J Biol Macromol* [Internet] Elsevier B.V.; 2018;110:97–109. Available from: http://dx.doi.org/10.1016/j.ijbiomac.2017.08.140

73.   Mao S, Sun W, Kissel T. Chitosan-based formulations for delivery of DNA and siRNA. *Adv Drug Deliv Rev* [Internet] Elsevier B.V.; 2010;62(1):12–27. Available from: http://dx.doi.org/10.1016/j.addr.2009.08.004

74.   Mansouri S, Lavigne P, Corsi K, Benderdour M, Beaumont E, Fernandes JC. Chitosan-DNA nanoparticles as non-viral vectors in gene therapy : strategies to improve transfection efficacy. *Eur J Pharm Biopharm* 2004;57:1–8.

75.   Buschmann MD, Merzouki A, Lavertu M, Thibault M, Jean M, Darras V. Chitosans for delivery of nucleic acids. *Adv Drug Deliv Rev* [Internet] Elsevier B.V.; 2013;65(9):1234–70. Available from: http://dx.doi.org/10.1016/j.addr.2013.07.005

76.   Tripathy S, Das S, Prasad S, Kumar S, Pramanik P, Roy S. Synthesis , characterization of chitosan – tripolyphosphate conjugated chloroquine nanoparticle and its in vivo anti-malarial efficacy against rodent parasite : A dose and duration dependent approach. *Int J Pharm* [Internet] Elsevier B.V.; 2012;434(1–2):292–305. Available from: http://dx.doi.org/10.1016/j.ijpharm.2012.05.064

77.   Magalhães GA, Moura E, Sombra VG, et al. Chitosan / Sterculia striata polysaccharides nanocomplex as a potential chloroquine drug release device. *Int J Biol Macromol* [Internet] Elsevier B.V.; 2016;88:244–53. Available from: http://dx.doi.org/10.1016/j.ijbiomac.2016.03.070

78.   Usman M, Akhyar Farrukh M. Formulation of polymeric iron nano-chloroquine phosphate anti-malarial drug via polyol method. *Mater Today Proc* [Internet] Elsevier Ltd; 2018;5(7):15595–602. Available from: https://doi.org/10.1016/j.matpr.2018.04.168

79.   Fantini J, Scala C Di, Chahinian H, Yahi N. Structural and molecular modeling studies reveal a new mechanism of action of chloroquine and hydroxychloroquine against SARS-CoV-2 infection. *Int J Antimicrob Agents* [Internet] Elsevier B.V.; 2020;105960. Available from: http://www.ncbi.nlm.nih.gov/pubmed/32251731

80.   Sahraei Z, Shabani M, Shokouhi S, Saffaei A. Aminoquinolines Against Coronavirus Disease 2019 (COVID-19): Chloroquine or Hydroxychloroquine. *Int J Antimicrob Agents* [Internet] Elsevier B.V.; 2020;2019(xxxx):105945. Available from: https://doi.org/10.1016/j.ijantimicag.2020.105945

81.   Jorge AM, Melles RB, Zhang Y, et al. Hydroxychloroquine prescription trends and predictors for excess dosing per recent ophthalmology guidelines. *Arthritis Res Ther* 2018;20(1):4–11.

82.   Lim HS, Im JS, Cho JY, et al. Pharmacokinetics of hydroxychloroquine and its clinical implications in chemoprophylaxis against malaria caused by plasmodium vivax. *Antimicrob Agents Chemother* 2009;53(4):1468–75.

83.   Ravi PR, Vats R, Balija J, Adapa SPN, Aditya N. Modified pullulan nanoparticles for oral delivery of lopinavir: Formulation and pharmacokinetic evaluation. *Carbohydr Polym* [Internet] Elsevier Ltd.; 2014;110:320–8. Available from: http://dx.doi.org/10.1016/j.carbpol.2014.03.099

84.   Kozhikhova K V., Ivantsova MN, Tokareva MI, et al. Preparation of chitosan-coated liposomes as a novel carrier system for the antiviral drug Triazavirin. *Pharm Dev Technol* [Internet] Taylor & Francis; 2018;23(4):334–42. Available from: http://dx.doi.org/10.1080/10837450.2016.1242624

85.   Cánepa C, Imperiale JC, Berini CA, Lewicki M, Sosnik A, Biglione MM. Development of a Drug Delivery System Based on Chitosan Nanoparticles for Oral Administration of Interferon-α. *Biomacromolecules* 2017;18(10):3302–9.

86.   Donalisio M, Leone F, Civra A, et al. Acyclovir-loaded chitosan nanospheres from nano-emulsion templating for the topical treatment of herpesviruses infections. *Pharmaceutics* 2018;10(2):1–12.

87.   Ulla F, Javed F, Khan AN, et al. Synthesis and surface modification of chitosan built nanohydrogel with antiviral and antimicrobial agent for controlled drug delivery. *Biointerface Res Appl Chem* [Internet] 2019;9(6):4439–45. Available from: https://doi.org/10.33263/BRIAC96.439445

88.   Russo E, Gaglianone N, Baldassari S, et al. Preparation, characterization and in vitro antiviral activity evaluation of foscarnet-chitosan nanoparticles. *Colloids Surfaces B Biointerfaces* [Internet] Elsevier B.V.; 2014;118:117–25. Available from: http://dx.doi.org/10.1016/j.colsurfb.2014.03.037

89.   Yang L, Chen L, Zeng R, et al. Synthesis, nanosizing and in vitro drug release of a novel anti-HIV polymeric prodrug: Chitosan-O-isopropyl-5′-O-d4T monophosphate conjugate. *Bioorganic Med Chem* [Internet] Elsevier Ltd; 2010;18(1):117–23. Available from: http://dx.doi.org/10.1016/j.bmc.2009.11.013

90.   Yan JK, Wang YY, Qiu WY, Wu JY. Construction and characterization of nanosized curdlan sulfate/chitosan polyelectrolyte complex toward drug release of zidovudine. *Carbohydr Polym* [Internet] Elsevier Ltd.; 2017;174:209–16. Available from: http://dx.doi.org/10.1016/j.carbpol.2017.06.082

91.   Cazorla-Luna R, Notario-Pérez F, Martín-Illana A, et al. Chitosan-based mucoadhesive vaginal tablets for controlled release of the anti-HIV drug tenofovir. *Pharmaceutics* 2019;11(1).

92.   Wu D, Ensinas A, Verrier B, et al. Zinc-stabilized chitosan-chondroitin sulfate nanocomplexes for HIV-1 infection inhibition application. *Mol Pharm* 2016;13(9):3279–91.

93.   Graham BS. Advances in antiviral vaccine development. *Immunol Rev* 2013;255(1):230–42.

94.   Ellebedy AH, Ahmed R. Antiviral Vaccines: Challenges and Advances. *Vaccine B Second Ed* Second. Elsevier Inc.; 2016. p. 283–310.

95.   Ellebedy AH, Webby RJ. Influenza vaccines. *Vaccine* 2009;27(SUPPL. 4):65–8.

96.   Muralidharan A, Russell MS, Larocque L, et al. Chitosan alters inactivated respiratory syncytial virus vaccine elicited immune responses without affecting lung histopathology in mice. *Vaccine* [Internet] Elsevier Ltd; 2019;37(30):4031–9. Available from: https://doi.org/10.1016/j.vaccine.2019.06.003

97.   Spinner JL, Oberoi HS, Yorgensen YM, et al. Methylglycol chitosan and a synthetic TLR4 agonist enhance immune responses to influenza vaccine administered sublingually. *Vaccine* [Internet] Elsevier Ltd; 2015;33(43):5845–53. Available from:

http://dx.doi.org/10.1016/j.vaccine.2015.08.086

98.   Renu S, Feliciano-Ruiz N, Ghimire S, et al. Poly(I:C) augments inactivated influenza virus-chitosan nanovaccine induced cell mediated immune response in pigs vaccinated intranasally. *Vet Microbiol* [Internet] Elsevier; 2020;242(January):108611. Available from: https://doi.org/10.1016/j.vetmic.2020.108611

99.   El-Sissi AF, Mohamed FH, Danial NM, Gaballah AQ, Ali KA. Chitosan and chitosan nanoparticles as adjuvant in local Rift Valley Fever inactivated vaccine. *3 Biotech* [Internet] Springer International Publishing; 2020;10(3):1–11. Available from: https://doi.org/10.1007/s13205-020-2076-y

Stability-Indicating Liquid Chromatographic Method for the Simultaneous Determination of Rosuvastatin and Ezetimibe from Pharmaceuticals and Biological Samples

Sevinc Kurbanoglu[1] ✉ iD **, Ozgur Esim[2]** ✉ iD **, Cansel Kose Ozkan[2]** ✉ iD **, Ayhan Savaser[2]** ✉ iD **, Yalcin Ozkan[2]** ✉ iD **, Bengi Uslu[1]** ✉ iD **, Sibel A. Ozkan[1*]** ✉ iD

[1] Ankara University, Faculty of Pharmacy, Department of Analytical Chemistry, Tandogan, 06560 Ankara, Turkey
[2] University of Health Sciences, Gulhane Faculty of Pharmacy, Department of Pharmaceutical Technology, 06018, Ankara, Turkey

Abstract: Fixed dose combinations of ezetimibe and rosuvastatin are well known to provide significantly superior efficacy to rosuvastatin alone in lowering total cholesterol, and triglyceride levels. Therefore, in this recent work, we prepared fixed dose (10 mg/10 mg) ezetimibe and rosuvastatin tablet formulations, and a simple, selective and we established and validated rapid chromatographic method for the sensitive and simultaneous determination of rosuvastatin and ezetimibe. We performed the separation on Zorbax SB-C18 (100 mm x 4.6 mm, 3.5 μm particle size) column at 30 °C with a mobile phase that has a composition as water containing 0.1% H_3PO_4:methanol:acetonitrile (50:25:25 v/v/v) at 1.2 mL/min flow rate. We further performed validation studies according to ICH guidelines. Furthermore, we exposed rosuvastatin and ezetimibe to degradation conditions. We plotted peak area vs. concentration graphs for rosuvastatin and ezetimibe and used for defining the linearity of the detector response. In this suggested method, we observed linear relationships varying from 0.05 to 50 μg/mL for ezetimibe concentrations and from 0.05 to 25 μg/mL for rosuvastatin concentrations. We found the limit of detection values for rosuvastatin and ezetimibe as 0.006 and 0.008 μg/mL, respectively. Moreover, we further used the established method for to the analysis of ezetimibe and rosuvastatin from real spiked samples of rabbit serum.

Keywords: Rosuvastatin, Ezetimibe, Liquid Chromatography, Validation, Stability Indicating Methods.

INTRODUCTION

Atherosclerosis is the main aspect of coronary heart disease (CHD), the most important reason for death and the main reason of illness all over the world (1,2). The main factors of risk for CHD (3,4) are hypercholesterolemia and higher low density lipoprotein cholesterol (LDLC) levels. Statins are generally used for lowering the cholesterol level. They inhibit the biosynthesis of cholesterol source; reduce the intracellular pools, and results in a reduction of plasma LDLC. However, an effective response cannot be obtained from a considerable fraction of hypercholesterolemic subjects, in the treatment of statin. Dose escalation and combination therapy of hypolipidemic drugs may be necessary to arrange LDLC blood levels (5,6). In LDLC reduction, drug combinations are successful hence; they may have some other effects. Nevertheless, the negligible efficacy of dose increase and present combination treatments using statins are limited by tolerance and compliance (7).

Ezetimibe, (EZE) ((3R,4S)-1-(4-fluorophenyl)-3-[(3S)-3- (4-fluorophenyl)-3-hydroxyl propyl)] -4-(4-hydroxy phenyl)-2-azetidinone) blocks dietary and biliary cholesterol absorption by the small intestine. Hence, US Food and Drug Administration approved EZE in 2002 for the treatment of primary hypercholesterolemia. EZE is a lipid-lowering drug active compound, can selectively prevent the intestinal absorption of cholesterol and related phytosterols (7–9). Rosuvastatin, (ROS) bis((E)-7-(4-(4-flurophenyl)-6-isopropyl-2-(methyl(methylsulfonyl)amino)pyrimidin-5-yl)(3R,5S) -3,5-dihydroxyhept-6-enoic acid) calcium salt is used for the treatment of hyperlipidemia inhibiting 3-hydroxyl-3-methylglutaryl coenzyme A reductase (10,11). ROS is a cholesterol lowering agent, which used as precursor for cholesterol. In order to avoid cardiovascular disease, high cholesterol and associated situations ROS can be used for treatment (12, 13). In the market, ROS generally has dual combinations with other drug active compounds in pharmaceutical preparations such as amlodipine, fenofibric acid, salicyclic acid, olmesartan, etc. In the literature, high performance liquid chromatographic (HPLC) methods with UV detection exist for these combinations (14–17). As stated in the literature, the patients taking 5, 10, 20, or 40 mg rosuvastatin daily, mean plasma concentration of rosuvastatin was 1.6 ng/mL, 3.5 ng/mL, 6.3 ng/mL and 9.8 ng/mL, respectively (18). Moreover, after a single dose of 10 mg ezetimibe, mean ezetimibe peak plasma concentrations (C_{max}) of 3.4 to 5.5 ng/mL were obtained within 4 to 12 hours (19). Patients at risk of coronary CHD might not achieve the low-density lipoprotein cholesterol levels recommended in statin monotherapy. The usage of ROS/EZE combination therapy reduced LDL and enhanced other constituents of the lipid/lipoprotein profile more than ROS alone (−69.8% vs −57.1%, p <0.001) (6,20–22). in contrary, EZE does not affect the CYP enzyme system; the hydrophilic properties of ROS may reduce the need for extensive metabolism by CYP enzymes. Therefore, this overlaid pharmacokinetic effects, EZE and ROS combination is used in the therapy of LDLC (6). To identify, quantify, and separe the components, HPLC is the most widely used technique, which depends on high pressure to push solvents through the column. This method has some advantages towards other chromatographic methods such as reproducible response, high resolution, good peak shape, and high speed (23). HPLC methods are widely examined for the simultaneous determination of combined drug formulations in the biological matrix. Since routine analyses for clinical and pharmacological studies need fast and precise detection methods, in this research, determination of ROS and EZE using a stability indicated, fully validated method was provided to assay drugs in pharmaceutical dosage forms. Moreover, to demonstrate the applicability of the suggested chromatographic method, we detected EZE and ROS from prepared fixed dose combinations of EZE and ROS and spiked rabbit serum samples.
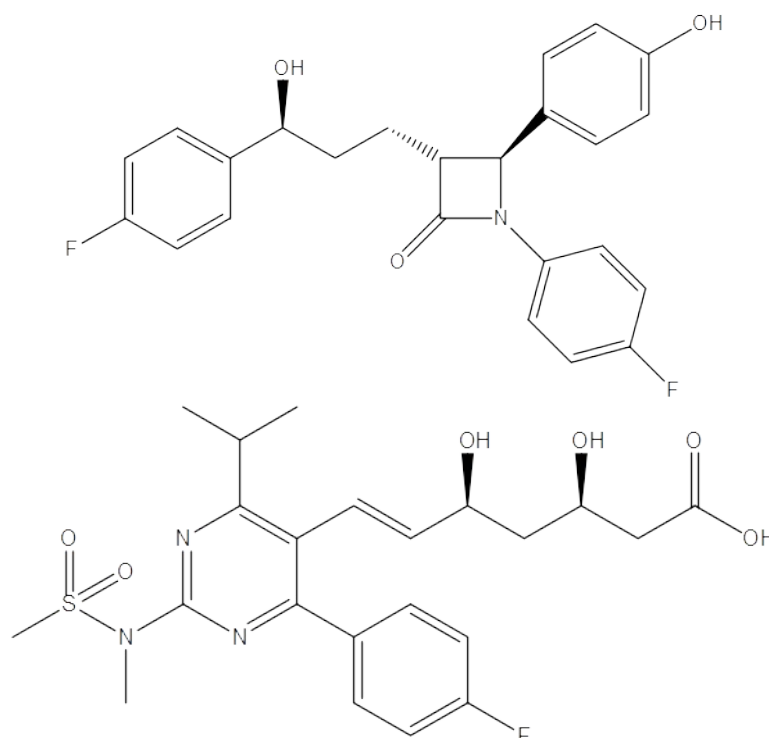
Scheme 1. Structures of Ezetimibe (top) and Rosuvastatin (bottom).

EXPERIMENTAL

Chemicals
We kindly obtained ROS and EZE from NUVOMED İLAÇ SAN. TİC. A.Ş. We received hydrogen peroxide, *o*-phosphoric acid, and microcrystalline cellulose from Sigma–Aldrich (St Louis, MO, USA). We purchased methanol, acetonitrile, sodium hydroxide, and hydrochloric acid, from Merck. To have ultra-pure water, we used Pure Flex water system (ELGA, Wycombe, UK). If not specified, all chemicals are of analytical reagent grade.

Instrumentation
We utilized the Agilent Hewlett-Packard 1100 HPLC system (Avondale, USA) consisting of DAD variable wavelength detector and data processing, which was supported with B.04.03 version of Chemstation®. We used Thermo Scientific Benchtop pH meter (Orion 3 Star™ Plus, USA) for the pH measurements. For the stationary phase, Zorbax SB-C18 (100 mm x 4.6 mm and 3.5 µm particle size), we purchased from Agilent Technologies (Agilent, USA)). For the preparation of pharmaceuticals, we used a tableting machine (Erweka EP-1, Germany).

MATERIAL AND METHODS

Chromatographic conditions
As the stationary phase, we used Zorbax SB-C18 (100 mm x 4.6 mm and 3.5 µm particle size (Agilent, USA)) column in isocratic mode at 30 °C and 1.2 mL/min flow rate with a mobile phase consisting of water containing 0.1% H_3PO_4:methanol:acetonitrile (50:25:25 v/v/v), with an injection volume of 10 µL. We used 5.0 M NaOH to adjust the pH of the mobile phase; we degassed and afterwards filtered the mobile phase. Prior to injections, we pre-conditioned the column for 30 min with the mobile phase. We washed the autosampler needle with mobile phase between each injection. We detected the samples at 242 nm.

Preparation of solutions
We prepared the stock solutions by dissolving ROS and EZE in methanol and diluted to desired concentrations with the mobile phase. We separated stock solutions of rabbit plasma using the solvent precipitation method. After addition of test solutions to the plasma, we mixed aliquots of 250 µL of plasma with 250 µL of cold acetonitrile and vortexed to precipitate the proteins. We then removed the precipitated proteins by centrifugation at 10000 rpm for 15 min. We withdrew 50 µL aliquots mixed with 950 µL mobile phase. We then placed aliquots of the resulting clear supernatants into the HPLC vials. We utilized KBr solution 0.01% (v/w) in water in chromatograms, to have the dead time (t_o).

Formulation and analyzing EZE–ROS tablets
We prepared tablets using direct compression method. Each tablet contained 10 mg of ROS and EZE as active substances and 230 mg of microcrystalline cellulose as the binder. Prior to compression, we screened granules using 300 µm sieve and then thoroughly blended in a mortar with pestle. For the preparation of tablets with an average weight of 250 mg, we utilized a single punch-tableting machine armed with flat-faced punches with a die, whose diameter was 11 mm.

System suitability test studies and validation of the method
We tested HPLC system using with USP criteria related to system suitability like capacity factor (from integrator), symmetry (at 10% height), tailing factor, and theoretical plate number. Subsequently, we achieved the validation of the proposed method and reported related to ICH guidelines and USP criteria (24–27). We injected different concentrations of ROS and EZE to the system to assess the linear range from triplicate injections. Thereafter, we accomplished the area of the detector response versus corresponding concentration to plot calibration graphs. We used least squares linear regression statistical analysis for the regression data analysis. Using the equations of $3.3 \times s/m$ and $10 \times s/m$, we calculated the limit of detection (LOD) and limit of quantification (LOQ), respectively. In these equations, (s) refers to the standard deviation of response and (m) to the slope of the calibration curve (25–27). We performed precision studies from averages of five measurements that were conducted in the same day and between days from 10 µg/mL for both standard and spiked rabbit serum samples. We confirmed the accuracy of the proposed method by recovery studies, which were performed using a standard addition procedure. We conducted recovery analysis by adding 5 µg/mL standard solutions of ROS and EZE on pharmaceutical dosage form to see the effect of ingredients. We expressed recovery studies in terms of the percent recovery, percent relative standard deviation and bias values. We performed recovery studies separately in mobile phase and serum samples.

According to ICH recommendations degradation studies consisted in terms of mild and drastic conditions (24,28). For thermal degradation of ROS and EZE, we located solid state of them in an oven at 75 ºC for 3 and 24 hours. We achieved acidic and oxidative degradation of 50 µg/mL ROS and EZE by exposing with hydrochloric acid (0.5 M HCl and 1 M HCl) and H_2O_2 (33% and 3%). We exposed these solutions for 3 hours under stress conditions. For alkaline hydrolysis, we exposed 50 µg/mL ROS and EZE to 0.5 M and 1 M NaOH for 3 hours.

RESULTS AND DISCUSSIONS

Method development
Prior to the validation studies, we improved the optimization of the HPLC detection parameters such as mobile phase composition in terms of % amount of H_3PO_4, methanol, and acetonitrile and pH; the flow rate and the temperature of the columns, (Data not shown) to have the optimum separation between ROS and EZE. Using Zorbax SB-C18 (100 mm x 4.6 mm, 3.5 µm particle size) column at 30 ºC with the mobile phase composition as water containing 0.1% H_3PO_4:methanol:acetonitrile (50:25:25 v/v/v) at 1.2 mL/min flow rate we obtained an acceptable separation.

Parameters of System Suitability Tests
Prior to the chromatographic analysis we performed system suitability tests related to USP criteria (25–27). We examined capacity factor (>2), symmetry at 10% height (<2), USP tailing (<2), theoretical plate number (>2000), resolution (>1.5) parameters which were all intolerable limits (24, 25). Moreover, the retention time of ROS was 2.80 min and EZE was 4.50 min. We found resolution between ROS and EZE as 10.58 and we calculated selective factor as 1.90 between ROS and EZE. We summarized all the parameters related to system suitability tests in Table 1.

Table 1: Parameters of System Suitability Tests.

Parameters	ROS	EZE	Recommended Value
Capacity Factor	2.05	3.90	>2
Selectivity to previous peak	-	1.90	>1
Resolution to previous peak	-	10.58	>2
Tailing Factor	1.21	1.17	<2
Symmetry at 10%height	1.09	1.16	<2
Theoretical number of plates	6904	9358	>2000

Method Validation

Linearity
The analytical performance of the method revealed by a linear relationship between ROS and EZE concentrations varying from 0.05 to 25 µg/mL for ROS, and 0.05 to 50 µg/mL for EZE. By means of the linearity equations, we obtained the LOD values as 0.006 µg/mL and 0.008 µg/mL for ROS and EZE,

respectively. Readers can also follow Table 2 that, we obtained the calibration curves between 0.25-10 µg/mL for ROS and 0.5-10 µg/mL for EZE in a biological sample, spiked rabbit serum. We reported all statistical assessment of the calibration data in Table 2 and we presented chromatograms of increasing concentrations of EZE and ROS in Figure 1 in mobile phase and in Figure 2 in a biological sample, spiked rabbit serum.
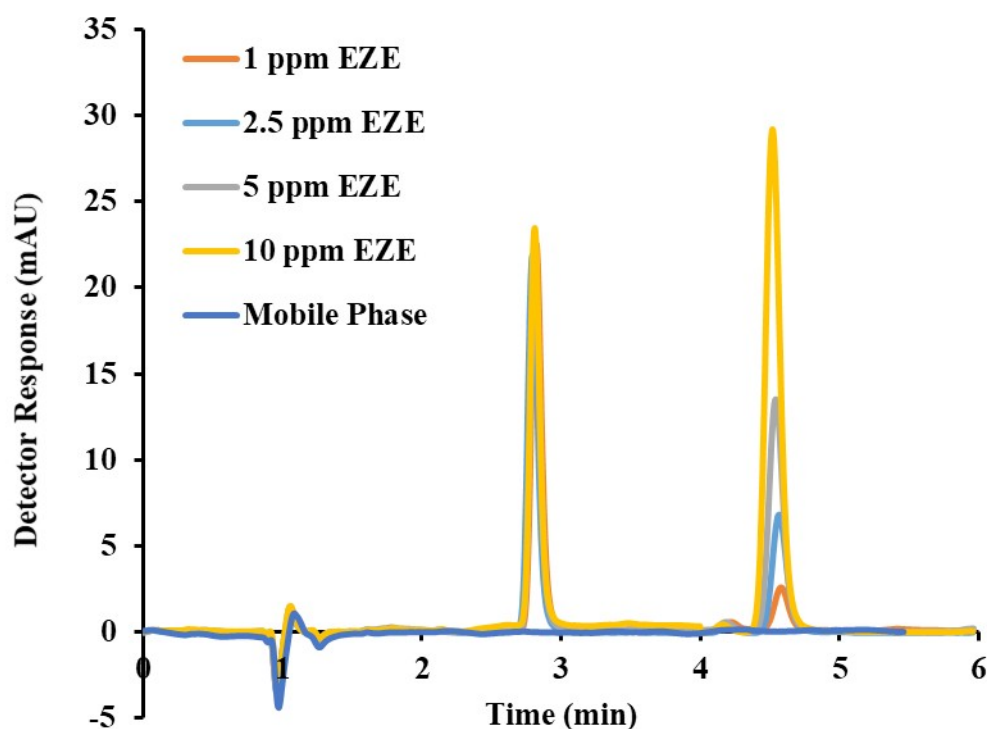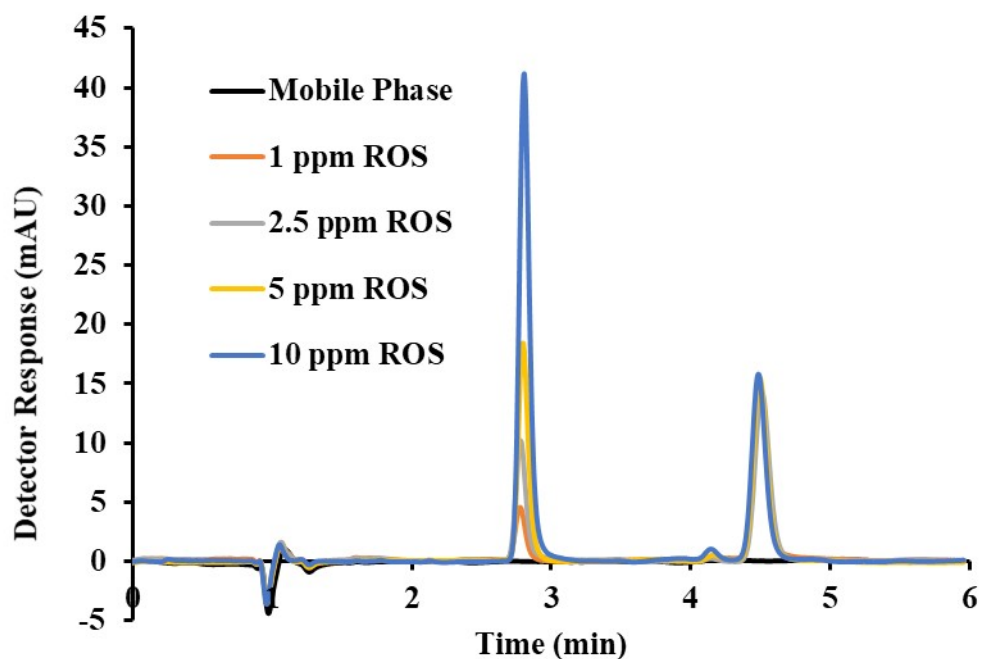
Figure 1: Chromatograms of increasing concentrations of EZE in the presence of 5 µg/mL ROS in mobile phase (top) and ROS in the presence of 5 µg/mL EZE in mobile phase (bottom).
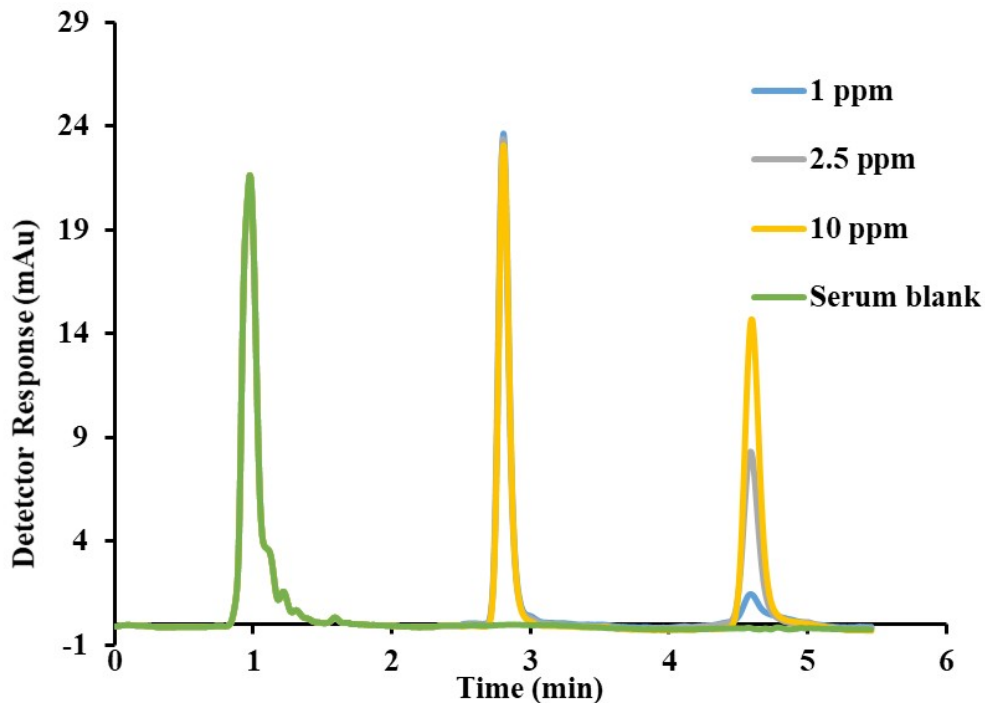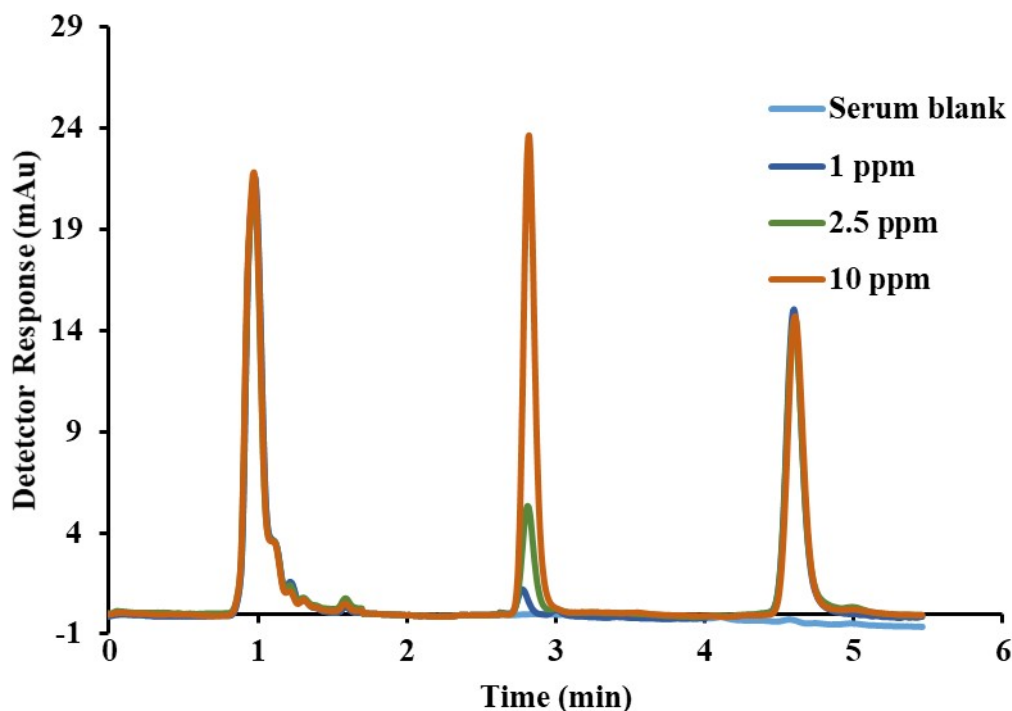
Figure 2: Chromatograms of increasing concentrations of EZE in the presence of 5 µg/mL ROS (top) and ROS in the presence of 10 µg/mL EZE (bottom) in spiked rabbit serum samples.

Precision: Repeatability studies

To have a precise method, we followed in day and between days repeatability studies and gave in terms of RSD %. It can be resulted from Table 2

that, low values of RSD % values indicate that the developed method is precise for the assay of both standard solutions and spiked rabbit serum samples of ROS and EZE.

Table 2: Statistical evaluation of the calibration data.

	Mobile Phase		Rabbit Serum	
Compounds	**ROS**	**EZE**	**ROS**	**EZE**
Linearity range (µg/mL)	0.05-25	0.05-50	0.25-10	0.5-10
Slope (mAU/µg.mL)	23.386	23.270	24.412	20.916
Intercept (mAU)	-3.362	-6.521	7.240	15.727
Correlation coefficient	0.999	0.999	0.999	0.999
LOD (µg/mL)	0.006	0.008	0.054	0.010
LOQ (µg/mL)	0.018	0.025	0.164	0.028
Within day Repeatability[a] (RSD %)	0.746	0.209	0.425	0.451
Between day Repeatability[a] (RSD %)	0.724	0.482	0.513	0.831

[a] Each value is the mean of five experiments.

Specificity: Degradation studies

We accomplished that degradation studies for 50 µg/mL ROS and EZE for specificity of the method. We designed degradation experiments at mild and drastic conditions with exposure to acidic and alkaline hydrolysis, hydrogen peroxide, UV, and

heat. We presented related results in Table 3. It can be resulted that, since we found the degradation percentage more than 90 in heating and UV exposure, the method and the drug active compounds especially ROS are very sensitive to heating and UV exposure.

Table 3: The results of hydrolytic, oxidizing, thermal, and photolytic stressed under drastic and mild conditions of ROS and EZE using developed HPLC method.

	Response Stress Conditions	Degradation of ROS%	Degradation of EZE%
Drastic Conditions	HCl (1 M)	85.63	25.90
	NaOH (1 M)	75.25	35.98
	H_2O_2 (30 %)	77.79	36.02
	Thermal (24 hours at 75 °C)	96.72	57.39
	UV light exposure (24 hours at 254 nm)	97.92	56.56
Mild Conditions	HCl (0.5 M)	70.82	15.90
	NaOH (0.5 M)	52.56	23.19
	H_2O_2 (3 %)	44.52	22.40
	Thermal (3 hours at 75 °C)	96.94	51.83
	UV light exposure (3 hours at 254 nm)	97.63	52.81

Accuracy: Pharmaceutical analysis and recovery studies

We realized the determination of ROS and EZE as pharmaceutical dosage form (see Figure 3) and recoveries from the pharmaceutical dosage form and rabbit serum samples to conduct accuracy studies. In account of that, we used the related obtained equations for the calibration curves for the simultaneous determination of ROS and EZE. We added known amounts of standard solutions (5 µg/mL) over pharmaceutical dosage form samples and serum samples for the recovery studies. The results of recovery %, RSD % and Bias % were shown in the Table 4. We found mean of the spike recoveries

between 99-101% for tablet and serum samples that specifies a tolerable accuracy of the method. Accordingly, it can be noticed that the developed method was not affected from the possible interferences in the tablet and rabbit serum.

As a result, we herein suggested a powerful, suitable, and valuable method for analysis of ROS and EZE with fully validated conditions. Since in our method, the organic solvent consumption is only 3 mL per injection and analysis time is 5 min, greener approach (29–32) shorter analysis time (29, 30) was investigated when we compare the results within the literature.
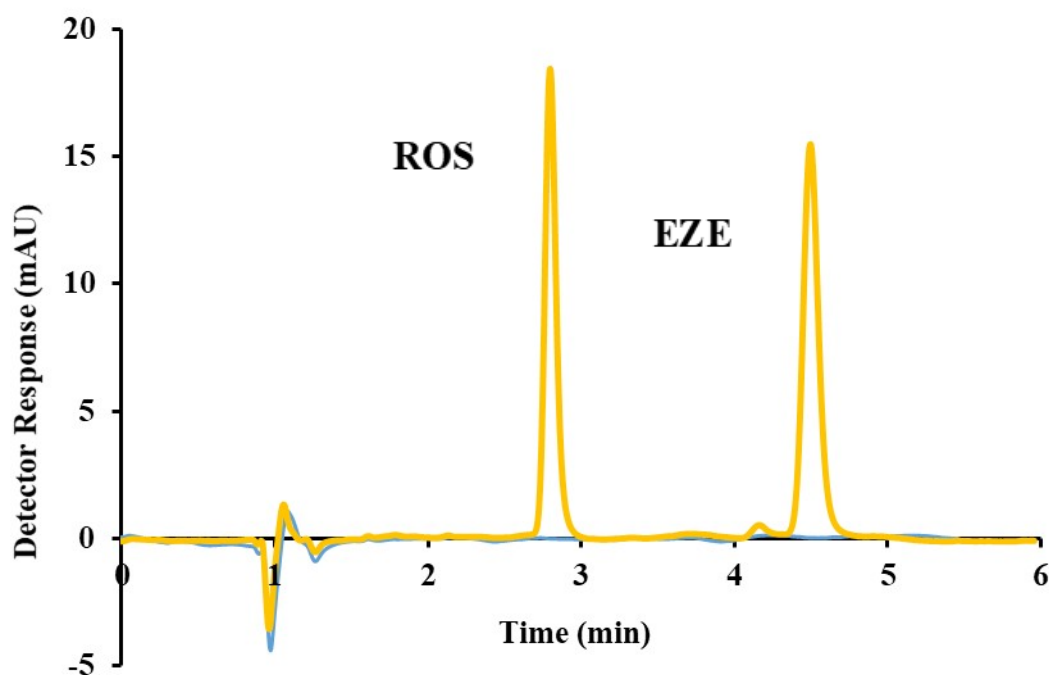
Figure 3: The chromatogram of 5 µg/mL Rosuvastatin and Ezetimibe from prepared tablet formulation.

Table 4: Results of tablet and recovery analysis.

	Mobile Phase		Rabbit Serum	
	ROS	**EZE**	**ROS**	**EZE**
Label Prepared (mg)	10.00	10.00	-	-
Found	10.06	10.07	-	-
RSD (%)	0.95	0.49	-	-
Bias (%)	-0.63	-0.71	-	-
Added (mg)	5.00	5.00	5.00	5.00
Found[a] (mg)	5.04	5.05	4.98	5.01
Recovery (%)	100.80	101.00	99.60	100.20
RSD of recovery (%)	0.82	0.25	0.93	0.85
Bias (%)	-0.80	-1.00	0.40	-0.20

[a]Each value is the mean of five experiments.

CONCLUSIONS

In this study, we achieved a simultaneous determination of ROS and EZE with optimization and validation studies via a selective, sensitive, precise, and accurate HPLC method. The system suitability test parameters were also reports as capacity factor (ROS:2.05; EZE:3.90), symmetry at 10% height (ROS:1.09; EZE:1.16), USP tailing (ROS:1.21; EZE:1.17), theoretical plate number (ROS:6904; EZE:9358), resolution (EZE:10.58), and selectivity (EZE:1.90) parameters. After having the optimum conditions for separation such as Zorbax SB-C18 (100 mm x 4.6 mm, 3.5 µm particle size) column at 30 ^{o}C with a mobile phase that has a composition as water containing 0.1% H_3PO_4:methanol:acetonitrile (50:25:25 v/v/v) at 1.2 mL/min flow rate; we followed the full validation parameters. In order to show that the method is suitable for the detection of ROS and EZE, we further achieved the detection of ROS- and EZE-spiked rabbit serum samples. Furthermore, we also accomplished degradation studies and we utilized the stability indicating method to analyze ROS and EZE in spiked rabbit serum samples.

ACKNOWLEDGEMENT

REFERENCES

1.   Schultheis A. Hypercholesterolemia: prevention, detection and management. Nurse Pract. 1990;15:40–6.

2.   Ross R. The Pathogenesis of Atherosclerosis — An Update. Vol. 314, New England Journal of Medicine. 1986. p. 488–500.

3.   Ornish D, Brown SE, Billings JH, Scherwitz LW, Armstrong WT, Ports TA, et al. Can lifestyle changes reverse coronary heart disease?. The Lifestyle Heart Trial. Lancet. 1990 Jul 21;336(8708):129–33.

4.   Ulbricht TLV, Southgate DAT. Coronary heart disease: seven dietary factors. Lancet. 1991 Oct 19;338(8773):985–92.

5.   Chapman MJ, McTaggart F. Optimizing the pharmacology of statins: Characteristics of rosuvastatin. In: Atherosclerosis Supplements. 2002. p. 33–7.

6.   Kosoglou T, Statkevich P, Yang B, Suresh R, Zhu Y, Boutros T, et al. Pharmacodynamic interaction between ezetimibe and rosuvastatin. Curr Med Res Opin. 2004;20(8):1185–95.

7.   Gagné C, Bays HE, Weiss SR, Mata P, Quinto K, Melino M, et al. Efficacy and safety of ezetimibe added to ongoing statin therapy for treatment of patients with primary hypercholesterolemia. Am J Cardiol. 2002;90(10):1084–91.

8.   Bays HE, Moore PB, Drehobl MA, Rosenblatt S, Toth PD, Dujovne CA, et al. Effectiveness and tolerability of ezetimibe in patients with primary hypercholesterolemia: pooled analysis of two phase II studies. Clin Ther. 2001;23(8):1209–30.

9.   Nutescu EA, Shapiro NL. Ezetimibe: A Selective Cholesterol Absorption Inhibitor. Pharmacotherapy. 2003;23(11):1463–74.

10.   McTaggart F. Comparative pharmacology of rosuvastatin. In: Atherosclerosis Supplements. Elsevier Ireland Ltd; 2003. p. 9–14.

11.   McTaggart F, Buckett L, Davidson R, Holdgate G, McCormick A, Schneck D, et al. Preclinical and clinical pharmacology of rosuvastatin, a new 3-hydroxy-3-methylglutaryl coenzyme A reductase inhibitor. In: American Journal of Cardiology. Elsevier Inc.; 2001. p. 28–32.

12.   Stein EA. Management of

hypercholesterolemia. Approach to diet and drug therapy. Am J Med. 1989;87(SUPPL. 4).

13.   Davidson MH. Rosuvastatin: A highly efficacious statin for the treatment of dyslipidaemia. Expert Opin Investig Drugs. 2002;11(1):125–32.

14.   Shah Y, Iqbal Z, Ahmad L, Khan A, Khan MI, Nazir S, et al. Simultaneous determination of rosuvastatin and atorvastatin in human serum using RP-HPLC/UV detection: Method development, validation and optimization of various experimental parameters. J Chromatogr B Anal Technol Biomed Life Sci. 2011 Mar 15;879(9–10):557–63.

15.   Nasir F, Iqbal Z, Khan A, Ahmad L, Shah Y, Khan AZ, et al. Simultaneous determination of timolol maleate, rosuvastatin calcium and diclofenac sodium in pharmaceuticals and physiological fluids using HPLC-UV. J Chromatogr B Anal Technol Biomed Life Sci. 2011;879(30):3434–43.

16.   Gomes FP, Garcia PL, Porto Alves JM, Singh AK, Kedor-Hackmann ERM, Santoro MIRM. Development and validation of stability-indicating hplc methods for quantitative determination of pravastatin, fluvastatin, atorvastatin, and rosuvastatin in pharmaceuticals. Anal Lett. 2009;42(12):1784–804.

17.   Sultana N, Arayne MS, Shah SN, Shafi N, Naveed S. Simultaneous determination of prazosin, atorvastatin, rosuvastatin and simvastatin in API, dosage formulations and human serum by RP-HPLC. J Chinese Chem Soc. 2010;57(6):1286–92.

18.   DeGorter MK, Tirona RG, Schwarz UI, Choi YH, Dresser GK, Suskin N, et al. Clinical and pharmacogenetic predictors of circulating atorvastatin and rosuvastatin concentrations in routine clinical care. Circ Cardiovasc Genet. 2013;6(4):400–8.

19.   Patel J, Sheehan V, Gurk-Turner C. Ezetimibe (Zetia): A New Type of Lipid-Lowering Agent. Baylor Univ Med Cent Proc. 2003;16(3):354–8.

20.   Kawashiri MA, Nohara A, Noguchi T, Tada H, Nakanishi C, Mori M, et al. Efficacy and safety of coadministration of rosuvastatin, ezetimibe, and colestimide in heterozygous familial hypercholesterolemia. Am J Cardiol. 2012;109(3):364–9.

21.   Ballantyne CM, Weiss R, Moccetti T, Vogt A, Eber B, Sosef F, et al. Efficacy and Safety of Rosuvastatin 40 mg Alone or in Combination With Ezetimibe in Patients at High Risk of Cardiovascular Disease (Results from the EXPLORER Study). Am J Cardiol. 2007;99(5):673–80.

22.   Yang YJ, Lee SH, Kim BS, Cho YK, Cho HJ, Cho KI, et al. Combination Therapy of Rosuvastatin and Ezetimibe in Patients with High Cardiovascular Risk. Clin Ther. 2017 Jan 1;39(1):107–17.

23.   Swartz ME, Murphy B. New frontiers in chromatography. Am Lab. 2005;37(3):22–7.

24.   Borman P, Elder D. Q2(R1) Validation of Analytical Procedures. In: ICH Quality Guidelines. John Wiley & Sons, Inc.; 2017. p. 127–66.

25.   Swartz ME, Krull IS. Analytical Method Development and Validation. 1997;3(4):96.

26.   The USP 40. The United States Pharmacopeia, The Official Compendia of Standards. MD, Rockville, USA.; 2017.

27.   Gumustas M, Kurbanoglu S, Uslu B, Ozkan SA. UPLC versus HPLC on drug analysis: Advantageous, applications and their validation parameters. Chromatographia. 2013;76(21–22):1365–427.

28.   Blessy M, Patel RD, Prajapati PN, Agrawal YK. Development of forced degradation and stability indicating studies of drugs - A review. J Pharm Anal. 2014;4(3):159–65.

29.   Swathi Sri D, Hemant Kumar T, Vara Prasada Rao K, Srinivasa Rao Y. Validated RP-HPLC method for simultaneous determination of Rosuvastatin Calcium and Ezetimibe in pharmaceutical dosage form. Int J Pharm Pharm Sci. 2015;7(4):209–13.

30.   Gajjar A, Gajjar AK, Shah VD. Development and Validation of a Stability-Indicating Reversed-Phase HPLC Method for Simultaneous Estimation of Rosuvastatin and Ezetimibe from Their Combination Dosage Forms Rational Drug Designing on Glycogen Synthase Kinase-3 beta View project Developme. Eurasian J Anal Chem. 2010;5(3):280–98.

31.   Mukthinuthalapati MA, Bukkapatnam V, Bandaru SPK. Stability indicating liquid chromatographic method for the simultaneous determination of rosuvastatin and ezetimibe in pharmaceutical formulations. Adv Pharm Bull. 2014;4(4):405–11.

32.   Varghese SJ, Ravi TK. Determination of rosuvastatin and ezetimibe in a combined tablet dosage form using high-performance column liquid chromatography and high-performance thin-layer chromatography. J AOAC Int. 2010;93(4):1222–7.

Some Properties of an Unmetalled Phthalocyanine Obtained by Chance at Low Temperature

Mevlude Canlica[1]* ✉ iD

[1]*Yildiz Technical University, Faculty of Science and Arts, Department of Chemistry, Davutpasa Campus, 34220 Esenler, Istanbul, Turkey.

Abstract: A novel tetrasubstituted metal-free phthalocyanine bearing phthalonitrile groups on the peripheral positions was synthesized accidentally by the cyclotetramerization reaction of the 4,4'-(1,3-phenylenebis(oxy))diphthalonitrile. For photodynamic therapy (PDT) application, photophysical properties including fluorescence quantum yield (Φ_F), fluorescence lifetime (τ_F), triplet state lifetime (τ_T), and triplet quantum yield (Φ_T) and photochemical properties including singlet oxygen quantum yield (Φ_Δ) and photodegradation quantum yield (Φ_d) as well as magnetic circular dichroism (MCD) properties were described. The Φ_T of the phthalocyanine was 0.81. The obtained lifetime (τ_T) was 40 μs for metal-free Pc.

INTRODUCTION

Phthalocyanines (Pcs) are macrocyclic compounds that consist of 4 pyrrolic subunits. The first synthesis of a Pc was found by accident in 1907, and it involves with low yield the reaction of o-cyanobenzamide in refluxing ethanol (1). However, nowadays a substituted phthalonitrile can be easily prepared by many different routes. Substituted Pcs can be formed from these phthalonitriles. The most commonly used method for the synthesis of Pc is cyclotetramerization of the phthalonitrile to form a Pc. A Pc offers 16 possible sites for peripheral and non-peripheral substitutions and a central cavity with metal ions and this makes them useful compounds in different fields and them are applied as dye, catalysis in a wide range of areas (2,3) non-linear optics (4), Langmuir-Blodgett thin films (5,6), chemical sensors (7), as photosensitizers in PDT (8-11) and as photocatalysts (12-14). On the other hand, ball-type structures of Pcs were first obtained as a new class of compound by Zefirova

in 2002 (15,16) and both Pcs and their ball-type derivatives (BPcs) have gained significance in a number of fields including their use as photosensitizers in photodynamic therapy (PDT) of cancer (17-20). In this study, a metal-free phthalocyanine, which was obtained accidentally during a reaction between 4-nitrophthalonitrile and resorcinol (1,3-dihydroxybenzene), was investigated photo-physico-chemical behaviors and MCD properties.

EXPERIMENTAL SECTION

Materials and methods
All equipments and chemicals that were used during all experimental and measurements are the same as the paper published earlier in the literature. The photophysical and photochemical properties of metal-free Pc were performed according to methods previously described in the literature (19,20).

Synthesis
Synthesis of 2(3), 9(10), 16(17), 23(24)-tetrakis-(4-(3-oxyphenoxy) phthalocyanine (**5**):
Compound **2** (1.272 g, 11.54 mmol) was dissolved in dry DMSO (25 mL) and compound 1 (3.98 g, 23.08 mmoL) was added under inert atmosphere. To this reaction mixture finely ground anhydrous potassium carbonate (4.00 g, 28.94 mmol) was added. The color of the mixture changed to the green from light brown while it was continued stirring at the end of 5 days at 70 °C. after a total of 6 days of stirring at this temperature, the entire green reaction mixture was then poured onto cracked ice to produce a precipitate, and the precipitate was washed sequentially with ethanol

and methanol resulting in the formation of a pure green precipitate. Finally, it was purified by silica gel column chromatography using gradient of chloroform, tetrahydrofuran as eluent and metal-free Pc was obtained as a green powder which has mp > 350 °C and is soluble in THF, DMSO, and DMF. Yield 0.069 g. UV-Vis (DMSO): λ_{max}/nm: 700, 668, 334. IR (ATR): (μ_{max}/cm^{-1}), 3296 (Ar-CH), 2238 (CN), 1717 (CO), 1596 (C=C), 1121/1083 (C-O-C). ^{1}H-NMR (DMSO-d_6): δ, ppm: 7.85–7.00 (40H, Ar-H). Anal. calcd. for $C_{88}H_{42}N_{16}O_8$: C, 72.82; H, 2.92; N, 15.44, found: C, 72.79; H, 2.88; N, 15.45 %. MALDI-TOF-MS: *m/z* calcd. 1451.4, found 1453.5 [M+2H]$^+$.
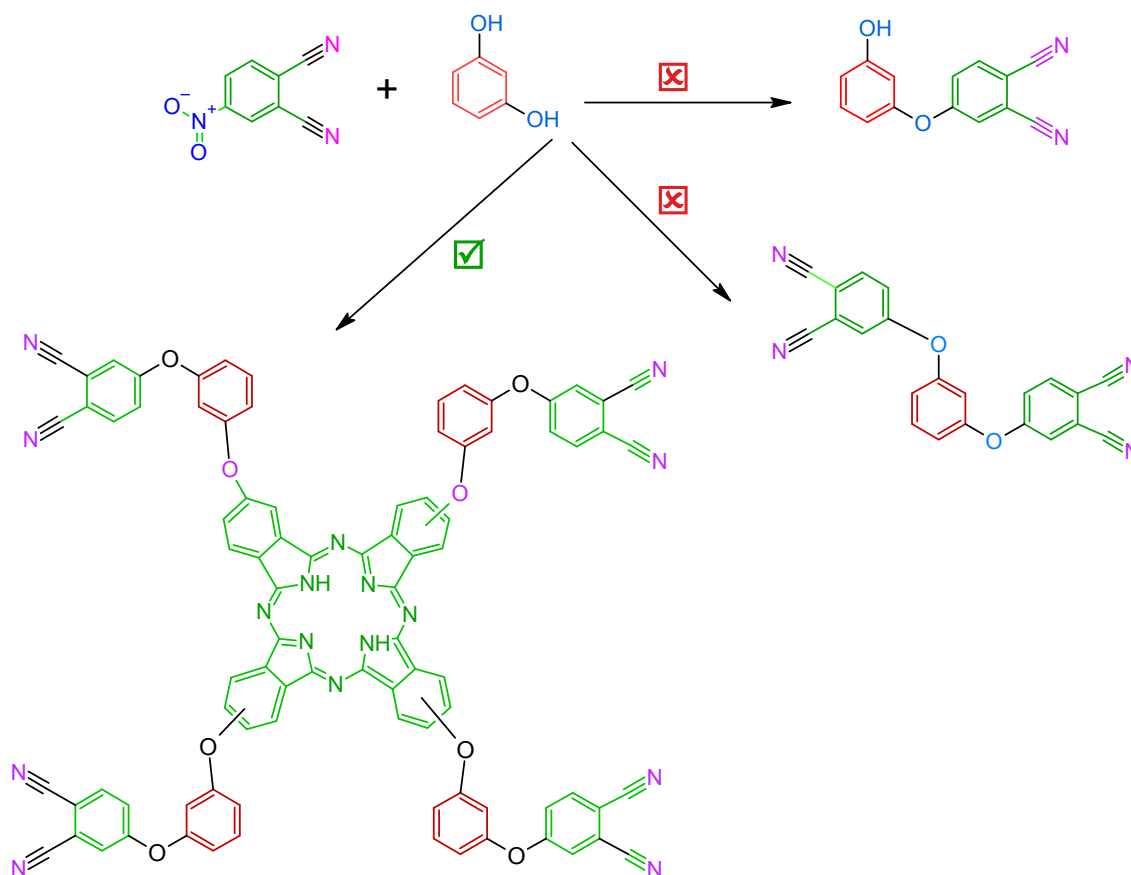
Scheme 1. Synthetic pathway for metal-free phthalocyanine (**5**) i: DMSO, 6 days, K$_2$CO$_3$.

RESULTS AND DISCUSSION

Synthesis and spectroscopic characterization
A reaction of 4,4'-(1,3-phenylenebis(oxy))diphthalonitrile (**3**) was started for the synthesis of the one which was intended for a BPc (Scheme 1). At the end of the fifth day, a green color was observed in the reaction tube. Metal-free phthalocyanine was obtained accidentally during a reaction which it give two possible products (**3** and **4**) between 4-

nitrophthalonitrile and resorcinol at low temperature. This showed that compound **3** gave quickly metal-free Pc (**5**) by self-condensation; it means that compound **5** occurred unexpectedly under the experimental conditions (21). So, compound **3** was not isolated and characterized (22).

After purification, the novel tetrakis (4-(3-oxyphenoxy) substituted Pc (5) was characterized by a handful of common spectroscopic techniques,

including FTIR, ^{1}H NMR, MALDI-TOF MS and UV-Vis, along with elemental analysis.

FT-IR spectrum of the H_2Pc was obtained with ATR and the spectrum showed -C≡N stretching at 2238 cm^{-1}. this value confirmed that compound **5** contains cyano end groups as determined by FT-IR spectroscopy. Aromatic C-H at 3296 cm^{-1}, aromatic C=C 1596 cm^{-1} and C–O–C vibrations at 1121/1083 cm^{-1} were observed. The ^{1}H NMR spectrum of (5) showed a multiplicity between 7.85 – 7.00 ppm in deuterated DMSO as the solvent. The inner core protons could not be observed. This may be due to the strong aggregation between the Pc rings. MALDI-TOF result showed the molecular peak of the compound **5** at m/z 1292.57, and also elemental analysis supported compound **5**.

The electronic absorption spectra for Pcs is generally characterized by two bands. One of both, the Q band is found in the longer wavelengths around 600-700 nm region were responsible for the green color of this complex. The other that are referred to as the B (Soret band). Figure 1 show the typical strong absorption bands. These transitions were assigned to π-π* transition between bonding and antibonding molecular orbitals.In the case of metal-free phthalocyanine, this band generally split into at two components. The B band is located at the shorter wavelengths around 300-400 nm region. B band arises mainly from the π to π* transition. The Q band results from π → π* transition that involves a_{1u} to e_g and the Soret band result from the π → π* transition that involves a_{2u} or b_{2u} to e_g. The non-degenerated e_g level leads to the observed split Q band in the UV-vis spectra for H_2Pc. On the other word, the splitting of the Q band is due to the splitting in the e_g level. In the spectrum of compound **5**, a loss was observed in the geometrically induced splitting between the Q_x and Q_y components (23).

Table 1: Photophysical and photochemical data of the Pc.

Compound	λAbs	λEms	λExc	λStokes	Φ_F	Φ_T	Φ_Δ	τ_T(ns)	τ_T(µs)	Φ_d(x10^{-6})
H_2Pc	668/700	709	701	9	0.06	0.81	0.19	4.65	40	1.959

MCD is used as an optical technique for the detection of the electronic structure of both ground and excited states (24). MCD can give information on the relative size of the ΔHOMO and ΔLUMO. Figure 1 shows the absorption and MCD spectra of compound **5** dissolved in DMSO. When the optical activity of compound **5** was investigated, a slight deviation was observed because its Q band showed less splitting, improved which this is attributed to its low symmetry as C_{2v} is isomer. The B_0 term appeared +320 nm and -370 nm. Faraday A term showed positive and negative sign since the excited state is orbitally degenerated. In the MCD spectrum, it was observed as a negative sign at -662 nm and -691nm.

Figure 2 shows the absorption, emission, and excitation spectra of compound **5** in DMSO. The spectral data are listed in Table 1. Fluorescence emission peaks was observed at 709 nm for **5**. The fluorescence quantum yield (Φ_F) value is 0.06 which is predicted for aggregated Pcs. Table 1 also shows Φ_T, Φ_d, τ_F and τ_T values of 5. The high triplet state quantum yield value (Φ_T) is 0.81. The Φ_T value suggests more efficient intersystem crossing (ISC), corresponding to low Φ_F values. The values of compound 5 are 0.75 for ISC, 4.65 ns for fluorescence lifetime and 40 µs for triplet lifetime. A triplet decay curve of change in absorbance (ΔA) versus time in seconds is obtained from the experiment and from this the triplet lifetime can be determined as shown in Figure 3. All this data may indicate metal-free structure including aggregations.

Figure 4 shows spectral changes obtained during photolysis of complexes with increasing time from 0 to 140 seconds in the presence of DPBF and the results are summarized in Table 1. DPBF degradation of the complexes 5 at 414 nm was monitored with UV-Vis spectrophotometry. There were no changes in the Q band intensities during these determinations, which is indicative of the fact that compound **5** is not degraded during singlet oxygen studies. The Φ_Δ value is 0.19. Although high triplet oxygen quantum yields of the phthalocyanine complex, accompany high singlet oxygen quantum yield, the compound gave a lower value of singlet oxygen quantum yield. This can be due to aggregation.

The photodegradation quantum yield value (Φ_d) of compound **5** was obtained by decrease in the intensities of the Q band under irradiation with increasing time from 0 to 60 minutes and the Φ_d was found as 1.959 x10^{-6}. This result showed that the Pc is of high stability in DMSO (Figure 5).
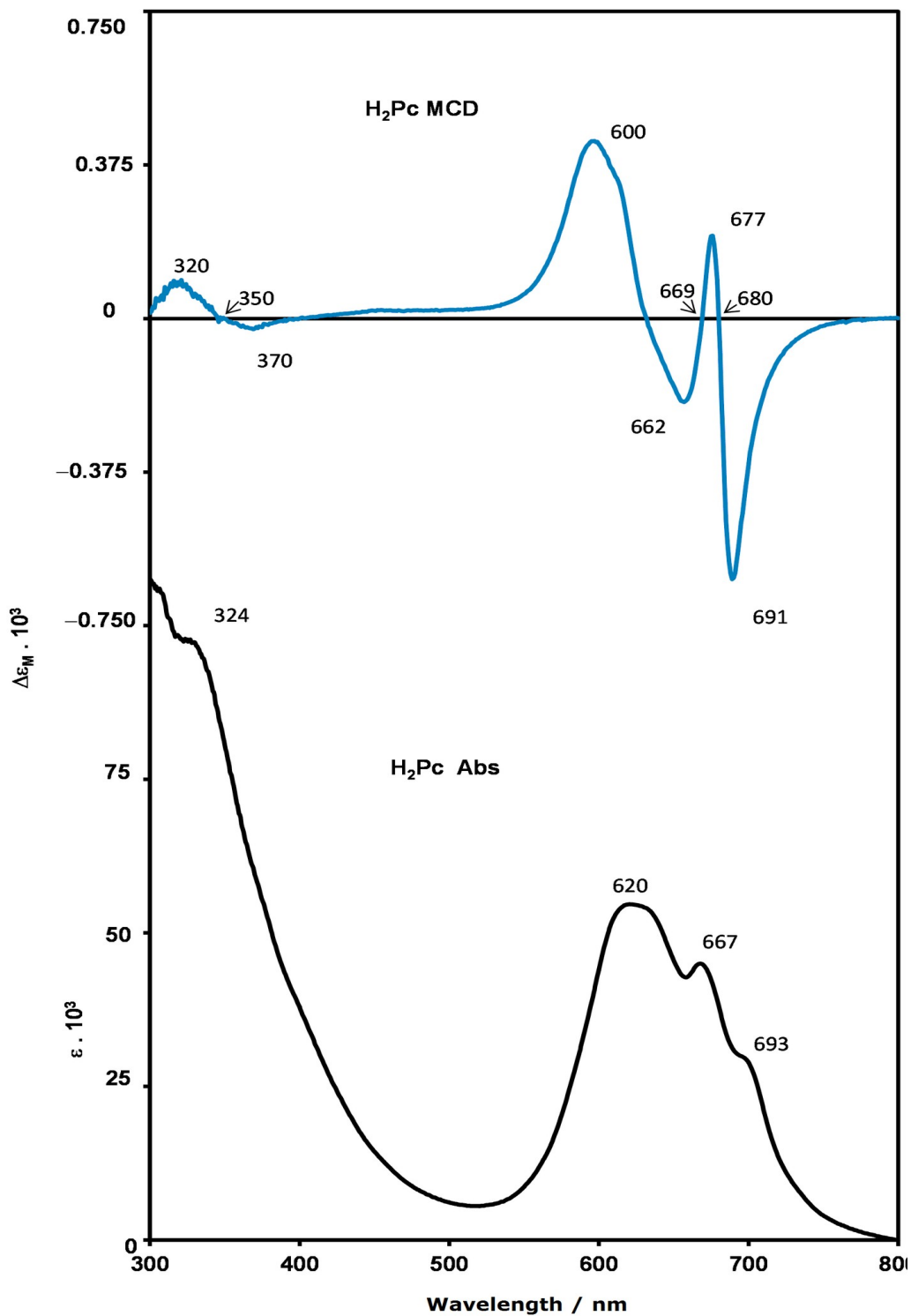
Figure 1. MCD (top) and UV-Vis (bottom) spectra for metal-free Pc.
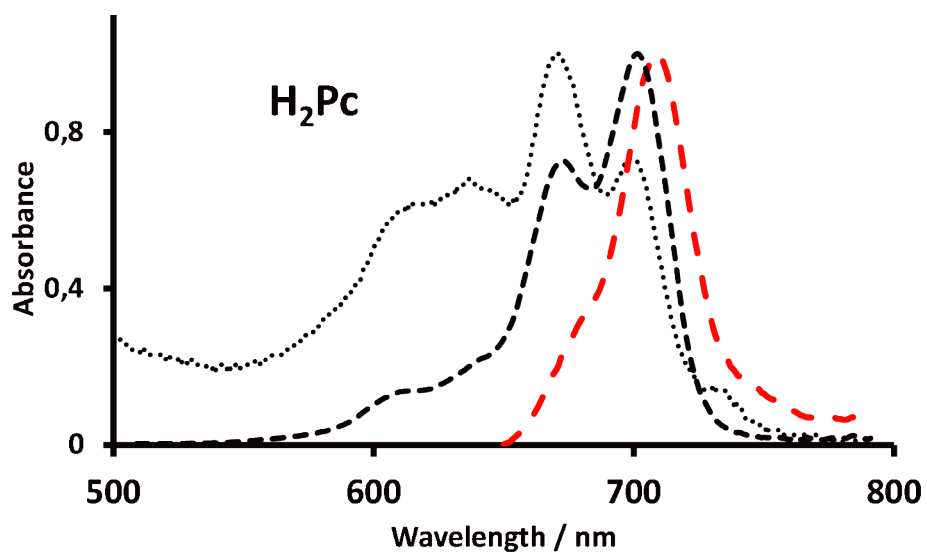
Figure 2. Absorption round dot line (black), excitation square dot line (black), and emission spectra dash line (red) of compound **5** λ_{exc} = 606 nm.
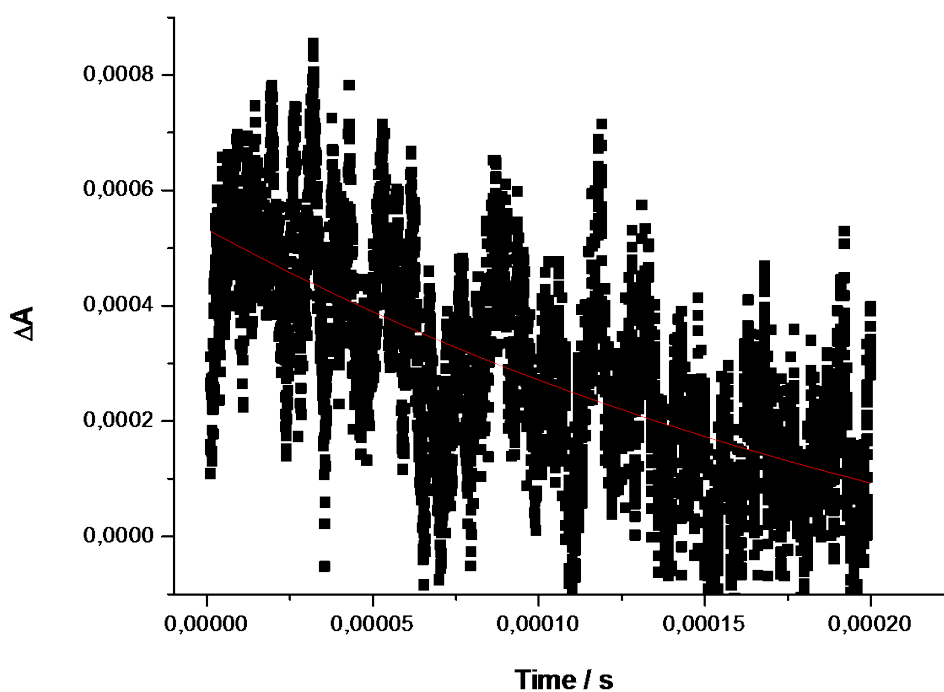
Figure 3. Triplet absorption decay curve for metal-free Pc.
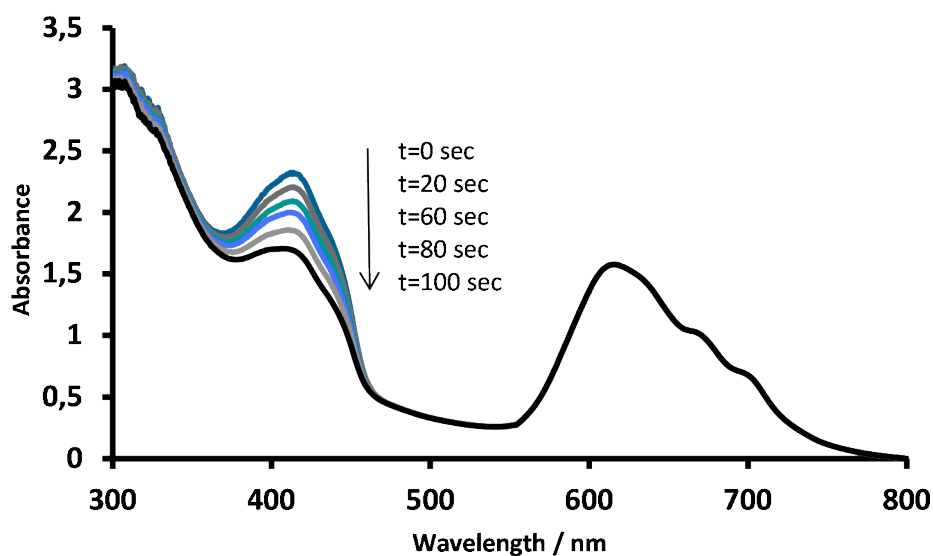
Figure 4. Time-dependent photobleaching of DPBF absorption in the presence of metal-free Pc in DMSO.
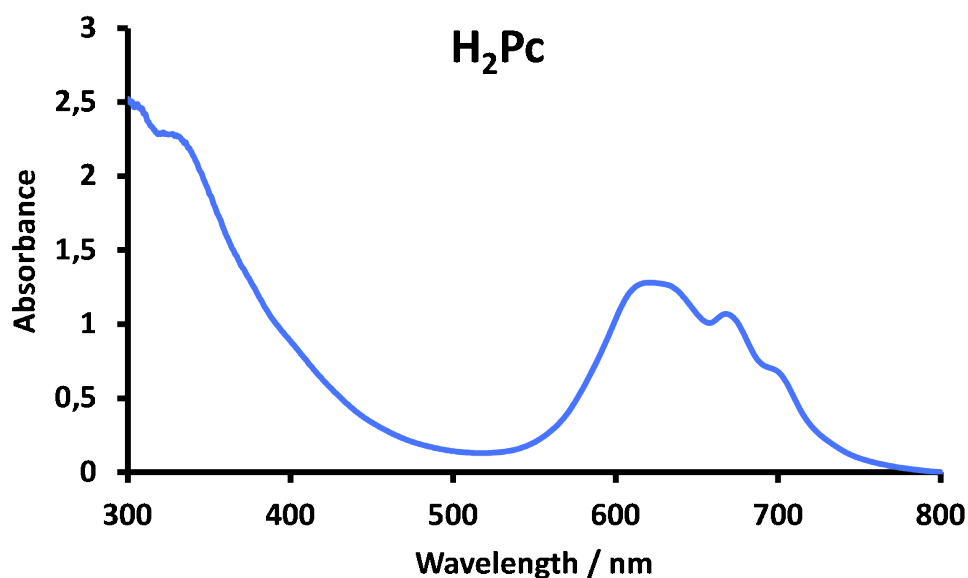
Figure 5: The spectra of photodegradation for metal-free Pc in DMSO.

CONCLUSION

β-substituted metal-free phthalocyanine which was obtained accidentally at 70 °C in DMSO was obtained. The molecules have high photostabilities. The photophysicochemical behavior was found suitable for photodynamic therapy activity of the unmetallated phthalocyanine. The reaction is rapid enough to proceed are very low temperatures for phthalocyanine formation. Unfortunately, formation of ide products leads to low yields. The Q band of metal free Pc displays a slight deviation showing less splitting, attributed to lower symmetry as well as is also attributed to aggregation.

880

REFERENCES

1. Braun A, Tcherniac J. Uber die Producte der Einwirkung von Acetanhydrid auf Phatalamid, Ber. Deutsch. Chem. Ges., 40, 1907; 40: 2709- 2714.

2. Leznoff CC, Lever ABP. (Eds.),Phthalocyanines: Properties and applications, C.C. VCH Publishers, New York, (1989, 1993, 1993, 1996); 1-4.

3. Kadish KM, Smith KM, Guilard R. (Eds.), The Porphyrin Handbook: Applications of Phthalocyanines, The Porphyrin Handbook, Academic Press, New York 2000; 19.

4. de la Torre G, Vásquez P, Agulló-López F, Torres T. Role of structural factors in the nonlinear optical properties of phthalocyanines and related compounds. Chem. Rev. 2004; 104**:** 3723.

5. Rella R, Serra A, Siciliano P, Tepore A, Troisi L, Valli L. Characterization of novel copper phthalocyanine Langmuir-Blodgett-films for NO_2 detection. Thin Solid Films. 1996; 284-285:870.

6. Armund F, Ferez H, Fouriaux S, Araspin O, Pradeau JP, Claessens CG, Maya EM, Vásquez P, Torres T. Tetraamidometallo-phthalocyanines Langmuir-Blodgett films: Morphology versus central metal effects on NO_2 detection. Synthetic Metals. 1999; 102: 1476.

7. Snow AW, Barger WR, Klusty M, Wohltjen H, Jarvis NL. Simultaneous electrical conductivity and piezoelectric mass measurements on iodine-doped phthalocyanine Langmuir-Blodgett films. Langmuir 1986; 2: 513.

8. Rosenthal I. Phthalocyanines as photodynamic sensitizers. Photochem. Photobiol. 1991; 53: 859.

9. Spikes JD. New trends in photobiology: Chlorins as photosensitizers in biology and medicine. J. Photochem. Photobiol. B 1990:6: 259.

10. Brown SG, Tralau CJ, Coleridge-Smith PD, Akdemir DT, Wieman TJ. Photodynamic therapy with porphyrin and phthalocyanine sensitisation: quantitative studies in normal rat liver. Br. J. Cancer. 1986; 54: 43.

11. Bonnett R, in *Chemical Aspects of Photodynamic Therapy*, D. Phillips (Ed.),Gordon and Breach Science, Canada, 2000.

12. Wöhrle D, Suvorova O, Gerdes R, Bartels O, Lapok L, Baziakina N, Makarov S, Slodek A. Efficient oxidations and photooxidations with molecular oxygen using metal phthalocyanines as catalysts and photocatalysts. *J. Porphyrins Phthalocyanines*. 2004*;* 8: 1020.

13. Mele G, Sole RD, Vasapollo G, García-López E, Palmisano L, Schiavello MJ. *Photocatalytic degradation of 4-nitrophenol in aqueous suspension by using polycrystalline TiO2 impregnated with functionalized Cu(II) -porphyrin or Cu(II)-phthalocyanine. Catalysis.* 2003*;* 217: 334.

14. Sehlotho N, Nyokong T. Catalytic activity of iron and cobalt phthalocyanine complexes towards the oxidation of cyclohexene using tert-butylhydroperoxide and chloroperoxybenzoic acid. *J. Mol. Catal. A: Chem.* 2004*;* 209: 51.

15. Tolbin AY, Ivanov AV, Tomilova LG, Zefirov NS. Preparation of 1,2-bis(3,4-dicyanophenoxymethyl)benzene and the binuclear zinc phthalocyanine derived from it. *Mendeleev Commun.* 2002; *12:* 96.

16. Tolbin AY, Ivanov AV, Tomilova LG, Zefirov NS. Synthesis of 1,2-bis(3,4-dicyanophenoxymethyl)benzene and binuclear zinc phthalocyanines of clamshell and ball types. *J Porphyr. Phtalocyan.* 2003; *7:* 162.

17. Canlica M. Photo-physico-chemical properties of 1,3-benzenediol-substituted face-to-face Phthalocyanines. Inorganica Chimica Acta 2020; 511: 119830.

18. Ali H, Van Lier JE. Rhodium-catalyzed modification of Phthalocyanines. Tetrahedron Lett. 2013; 54: 2956.

19. Canlica M. Synthesis, photophysics, and photochemistry of ball-type phthalocyanines. *J. Photochem. Photobiol. A Chem.* 2019; 384: 112043.

20. Canlica M, Omur BC, Salih B. Synthesis, photophysical, photochemical and SO2 sensing properties of ball-type phthalocyanines substituted with carboxyl groups. *Inorg. Chem. Comm*. 2019; 103: 75.

21. Greenberg S. Lever ABP, Lenoff CC. Approaches towards the synthesis of a 2,9,16,23-tetrasubstituted phthalocyanine as a pure isomer. Can. J. Chem. 1988; 66: 1059.

22. Keller TM, Dominguez DD. High temperature resorcinol-based phthalonitrile polymer. *Polymer.* 2005; 46: 4614.

23. Kobayashi N. Lever ABP. Cation or solvent-induced supermolecular phthalocyanine formation: crown ether substituted phthalocyanines. J. Am. Chem. Soc. 1987; 109: 7433.

24. Kobayashi N, Nakai K. Applications of magnetic circular dichroism spectroscopy to porphyrins and Phthalocyanines. Chem. Commun. 2007; 4077.

RESEARCH ARTICLE

Preparation, Characterization and Adsorption into Aqueous Solutions of Polyethyleneimine-Coated Silica Nanoparticles

Aslı Beyler-Çiğil[1] ✉ iD

[1] Amasya University Technical Sciences Vocational, Department of Chemistry and Chemical Process Technology School, Amasya, Turkey.

Abstract: In this study, polyethyleneimine-coated silica nanoparticles (PEI-SiNP) were used to prepare a polymeric material that can effectively and selectively adsorb Au(III) from aqueous solutions. For this purpose, silica nanoparticles were firstly reacted with (3-glycidyloxypropyl)trimethoxysilane (GPTMS) to achieve epoxy functionality. The structures of the silica nanoparticles (SiNP), silica nanoparticles with epoxy functionality (E-SiNP) and polyethyleneimine-coated silica nanoparticles were determined using ATR-FTIR (Attenuated Total Reflectance Fourier Transform Infrared) and XPS (X-Ray Photoelectron Spectroscopy), while their thermal properties were characterized using thermogravimetric analyses (TGA). The Au(III) ion-binding capacity of the PEI-SiNP adsorbent nanocomposite that contain high levels of imine was investigated. The effects of the interactions between pH, contact time, and foreign metal ions on adsorption were tested to determine the optimum conditions. The optimum contact time was 3 hours at pH 2. The adsorption capacity of the adsorbent nanocomposite prepared for Au(III) was found to be 116.27 mg/g. The Langmuir and Freundlich isotherms were used to determine the adsorption behaviors and the Langmuir isotherm model was selected as the best fit model (R^2: 0.997). The prepared PEI-SiNP adsorbent nanocomposite showed a high selectivity for the Au(III) ion even when different metal cations such as Cu(II), Cd(II), and Pb(II) were present.

INTRODUCTION

Gold is a valuable metal that is mostly found together with other metals such as silver, iron, and copper in nature (1). In addition to its appeal and shine, gold is well-known for its exceptional conductivity, ductility, malleability, and chemical stability (2,3). Thanks to its special physical and chemical properties, this valuable metal is widely used in jewelry production, production of electrical and electronic devices, aviation, and medical applications (4). Moreover, it exponentially gains value in human life due to the countless technological achievements and developments. Although gold is demanded in industrial activities,

its amount in Earth's crust is limited and its extraction from ore has various environmental impacts. Therefore, the investigation of cheap and productive separation methods for the recovery of gold is advantageous both in terms of environment and economy (5). Different methods including liquid-liquid extraction (6), ion exchange (7), solid phase extraction (8), cloud point extraction (9), sedimentation (10), electrodeposition, and adsorption (11) were used both for determining its amount in different environments and its recovery.

Compared with other separation methods, adsorption have attracted attention in recent years because of the ease of use, high efficiency, and low

cost of solid adsorbents and their suitability for use in the adsorption of Au(III) ions (12,13). In addition to their use in the recovery of valuable elements from aqueous solutions, adsorption is highly effective in the removal of toxic metal ions (14-16).

Various organic and inorganic adsorbents have been produced to remove Au(III) ions from aqueous solutions (17-19). In most studies, synthetic or bio-based polymeric resins or inorganic particles (silica, magnetite, etc.) were functionalized using ligands such as ethylenediamine, 2-mercaptobenzothiazole, guanyl thiourea, dithiooxamide, imidazole, 2-(diethylamino) or typically using organic molecules that have nitrogen and sulfur groups.

There have been extensive investigations for hybrid and composite materials because of their different properties (20-22). Their properties couple the advantages of inorganic materials (i.e. rigidity, thermal stability) with those of organic materials (i.e. flexibility, ductility, and processability). Therefore, organically modified silica nanoparticles are typically classified as hybrid materials (23). Modified silica nanoparticles have been extensively investigated in recent years because of their unique properties (24). Silica molecules have high-density hydroxyl groups and can be modified with specific functional groups such as carboxyl, amino, and chloro for various applications. Some studies have investigated the use of organically modified silicas in wastewater (25-27).

The study aims to prepare PEI-coated silica nanoparticles that can selectively and effectively adsorb Au(III) ions. For this purpose, the hard/soft acid/base (HSAB) theory of Pearson, who asserted that soft acids such as Au(III) ions had a strong interaction with soft bases such as nitrogen and sulfur-containing groups, was taken into consideration and polyethyleneimine that contains high levels of imine was selected as the polymeric surface.

EXPERIMENTAL SECTION

Materials
(3-Glycidyloxypropyl)trimethoxysilane (GPTMS), polyethyleneimine (PEI) (Mw ~10000 g/mol) and all solvents used were from Sigma Aldrich. Nanosilica (12 nm, AEROSIL®200, 200 m^2/g surface area) obtained from Evonik.

Preparation of the silica nanoparticles with epoxy end-groups (E-SiNP)
The procedure for the functionalization of the silicas with epoxy groups was adapted in a similar fashion to that of the procedures in the literature (28-30). Prior to use, AEROSIL®200 nanoparticles were firstly dried in a vacuum drying oven at 150 °C for 24 hours. Five-grams of silica nanoparticles were dispersed into 300 mL of toluene and 10-grams of

GPMTS were added. The mixture was kept in an ultrasonic bath for 30 minutes and, then kept in a condenser for 24 hours. Silica nanoparticles with epoxy end-groups were separated using centrifugation and purified for 48 hours using Soxhlet extraction with toluene. The particles were lastly dried in a vacuum drying oven at 100 °C.

Preparation of the adsorbent material (PEI-SiNP)
Five grams of the silica nanoparticles with epoxy end-groups were collected in a reaction flask and, then 15 mL of water and 6 g of PEI were added to the flask. The mixture was then kept in a shaking water bath at 65 °C for 24 hours. The prepared adsorbents were then rinsed with a NaCl solution and phosphate buffer at pH 5 and kept in a vacuum drying oven at 60 °C for 24 hours. Figure 1 shows all modifications made to the silica nanoparticles to obtain the adsorbent.

Characterization
The structure analyses of the silica nanoparticles with epoxy end-groups (E-SiNP) and PEI-coated silica nanoparticles (PEI-SiNP, adsorbent) were carried out using ATR-FTIR and XPS. The XPS analyses were performed using the Thermo Scientific K-Alpha X-ray Photoelectron Spectrophotometer in the Boğaziçi University Advanced Technologies Research and Development Center. The ATR-FTIR spectra were recorded using the Perkin Elmer Spectrum 100 ATR-FTIR spectrometer.

The thermogravimetric analyses of the silica nanoparticles, silica nanoparticles with epoxy end-groups, and PEI-coated silica nanoparticles were carried out using a model Pyris 1 TGA Perkin-Elmer Thermogravimetric analyzer. The measurements were made under nitrogen atmosphere and at temperatures between 30 and 750 °C at a heating rate of 20°C/minute.

An Analytic Jena Zeenit 700 flame atomic absorption spectrophotometer equipped with a deuterium lamp (Jena, Germany) was used to determine the amount of Au(III) ions.

Adsorption of Au(III) ions
The adsorption trials were carried out using 0.005 g PEI-coated silica nanoparticles and 50-mL glass jars that contained 15 mL Au(III) solutions at different concentrations. The jars were stirred at 250 rpm and room temperature. The effect of pH on the adsorption capacity of polymer-coated silica nanoparticles was examined at a constant Au(III) concentration of 10 mg/L and in the range of pH 1-5. The initial pH values were adjusted using HCl and NaOH and no significant pH change was observed throughout the contact time. To determine the intensity of the contact time, the adsorbents were immersed in a 50 mg/L Au(III) solution at pH 2 for

an interval of 30-400 minutes. The adsorption isotherms were obtained with a 3-hour contact time at pH 2 using the initial Au(III) solutions at different concentrations (5-500 mg/L). When the equilibrium was established, the aqueous solutions were separated from the adsorbent and final Au(III) ion concentrations were analyzed using flame atomic absorption spectrophotometry. All adsorption trials were repeated in triplicate and the mean values were recorded. The Au(III) ion concentrations per a unit mass of absorbent were calculated using the below equation:

$$q_e = \left(\frac{C_0 - C_e}{m} \right) \times V \qquad (1)$$

Here, C_0 and C_e represent the concentrations (mg/L) of Au(III) ions in the aqueous phase before and after adsorption time, respectively; V represents the volume of the aqueous phase (L); q_e represents the equilibrium adsorption capacity (mg/g) and m represents dry adsorbent amount (g) (31).

RESULTS AND DISCUSSION

XPS

XPS analysis was used to determine the element compositions of the silica nanoparticles with epoxy end-groups and PEI-coated silica nanoparticles. The surface analysis was carried out by examining the XPS spectra to evaluate the modification of imine and epoxy groups to silica nanoparticles. Figure 2 shows the XPS spectra of the silica nanoparticles and epoxy- and PEI-modified silica nanoparticles. Strong O 1s (533.2 eV) and Si 2p (103.5 eV) peaks are characteristic of silica nanoparticles. A Si and a few O peaks between the 25 and 104 eV energy interval are considered as the fingerprints of silica nanoparticles (32). Moreover, C 1s (283.8 eV) was observed due to hydrocarbon contamination residues that interacted during sample preparation for XPS. Carbon is found everywhere and, thus, it is detected in all samples exposed to the atmosphere (Figure 2a) (33-35). Table 1 shows the XPS element compositions of the non-modified silica nanoparticles and silica nanoparticles with a modified surface. Figure 2b shows the sweeping result after the reaction of silica nanoparticle and GPTMS. Here, when the spectrum of the non-modified silica nanoparticles was compared (Figure 2a), the increases in C and O indicated the presence of glycidoxypropyl and epoxy. In compliance with the ATR-FTIR spectrum below, it shows that the GPTMS was successfully grafted onto the silica nanoparticle. The peaks and element compositions found in the study agree with the literature (36). In addition, the C 1s and O 1s peaks in the PEI-silica nanoparticles were observed at near 284 eV and 532 eV, respectively. The C 1s peak at 285 eV generally corresponds to C-C and C-N bonds and, more importantly, as seen in Table 1, it contained 30.31% nitrogen after treatment with PEI in addition to all observed elements (37). This proves that there were nitrogen atoms on the surface that originated from PEI.
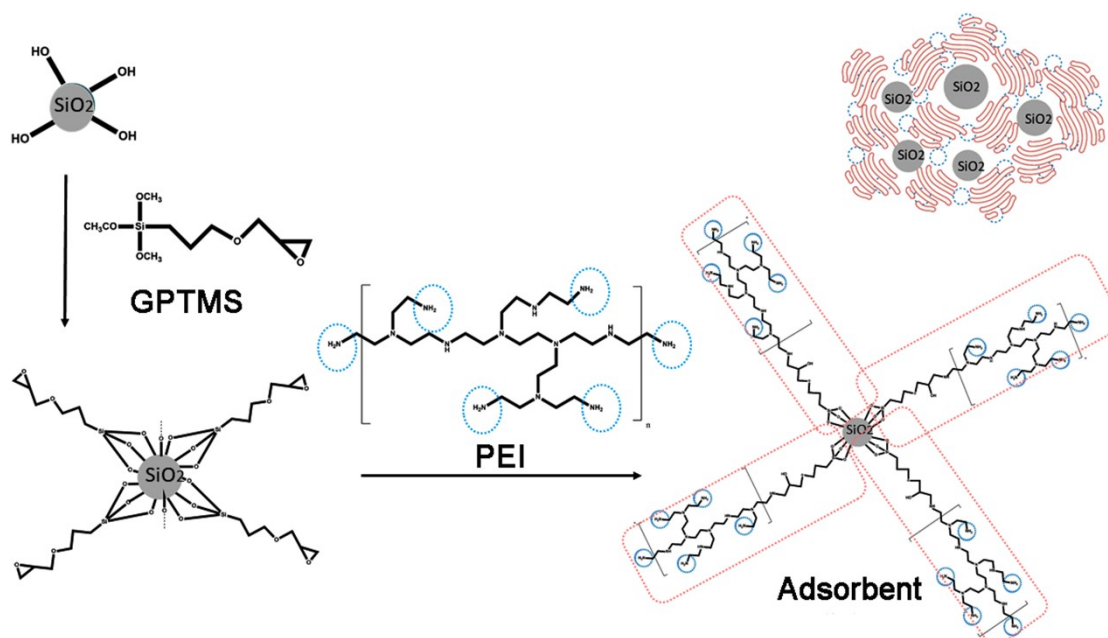
Figure 1: Preparation of the PEI-SiNP adsorbent.

Table 1: Elemental compositions of silica nanoparticles before and after surface modifications.

	C	O	Si	N
SiNP	8.06	55.41	36.53	-
E-SiNP	13.48	55.52	31.00	-
PEI-SiNP	24.15	36.56	28.99	30.31
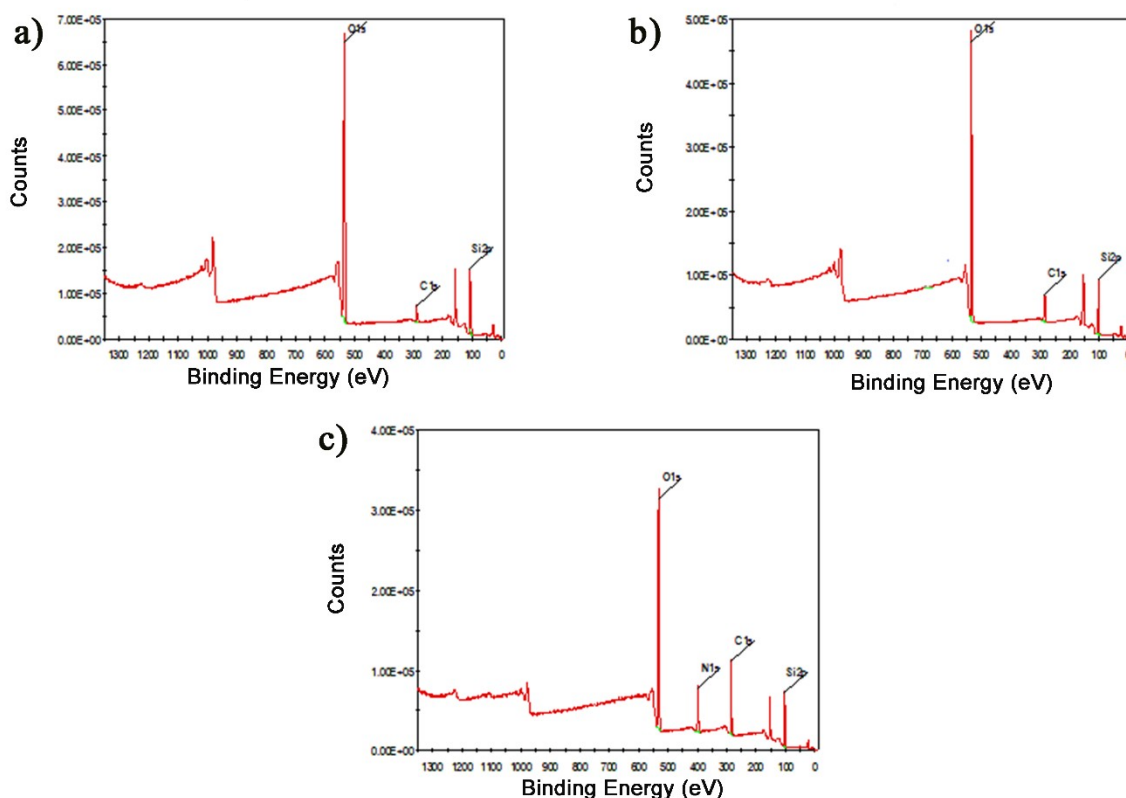
Figure 2: XPS spectra of a) Silica nanoparticles, b) epoxy modified silica nanoparticles and c) PEI coated silica nanoparticles.

ATR-FTIR

ATR-FTIR analysis was used to determine the functional groups of the silica nanoparticles, silica nanoparticles with epoxy end-groups, and PEI-coated silica nanoparticles. As seen in Figure 3, the peaks at 1087 cm^{-1}, 806 cm^{-1}, and 472 cm^{-1} are characteristic of SiO_2 (38). The weak peak at 1261 cm^{-1} is attributed to the stretching vibration of the epoxy group, indicating that the epoxy groups were successfully modified on the surface of the SiO_2 nanoparticle (Figure 3b) (39,40). Figure 3c shows the polyethyleneimine-treated silica nanoparticles. Here, an epoxide ring-opening occurs between polyethyleneimine and epoxy ring. This is confirmed by the decreased density of the characteristic bands of epoxide ring (i.e. 915 cm^{-1} and 831 cm^{-1}) and primary amine (i.e. 3206/3316 cm^{-1}) and the increased density of the -OH band (i.e. 3380 cm^{-1}) and secondary amine groups (i.e. 1573 cm^{-1}) (41,42). In the literature, similar peaks were observed in the triethylenetetramine treatment of epoxy-modified silica nanoparticles.
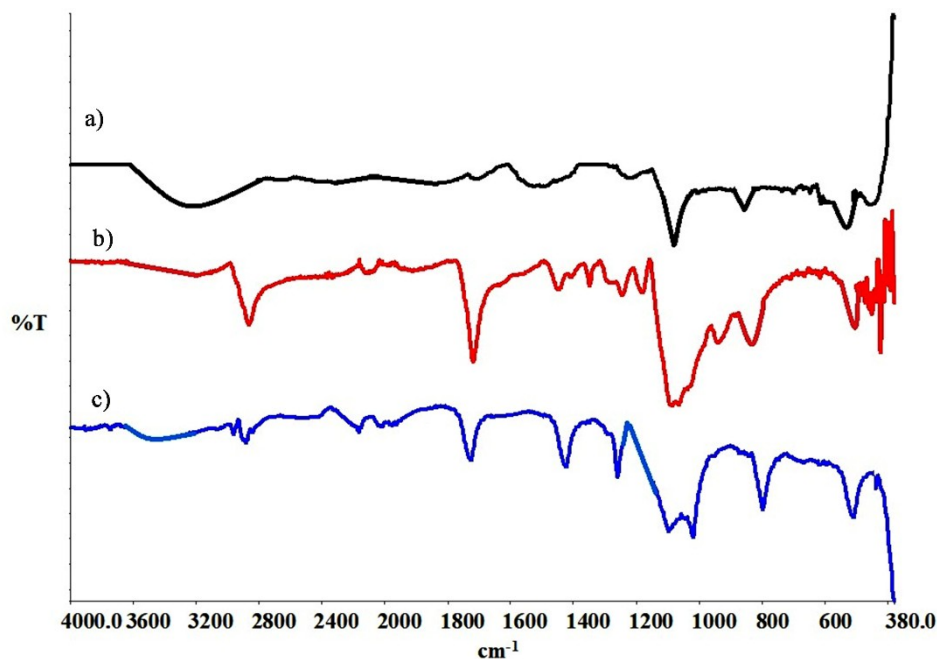
Figure 3: FTIR spectra of a) silica nanoparticles, b) epoxy modified silica nanoparticles, and c) PEI-coated silica nanoparticles.

TGA

Thermogravimetric analysis (TGA) was carried out to examine the thermal stability of the adsorbent and approximately determine the amount of modification occurring on the surface. Figure 4 shows the thermal degradation behaviors of the silica nanoparticle, epoxy-modified silica nanoparticle and adsorbent nanocomposite under nitrogen atmosphere. As seen in the figure, sample weight decreased by about 1% as temperature increased from 0 to 120 °C for the non-modified silica nanoparticles. Weight decreased from 99% to about 90% when temperature increased from 120 °C to 750 °C. The weight loss is associated with the loss of the condensation water that formed by the polycondensation of surface hydroxyl groups. Considering the SiO_2 nanoparticles that were functionalized with epoxy groups, a weight loss of about 27% occurs at temperatures between 300 °C and 750 °C in response to the thermal degradation of the functional groups on the surface (43). This can be explained by the loss of the epoxy group that was grafted onto the silica nanoparticle. In the case of the prepared adsorbent nanocomposite, actual degradation began at temperatures between 200 °C and 500 °C and weight loss reached around 40%. In conclusion, we are of the opinion that the epoxy groups and polyethyleneimine attached to the silica nanoparticle surface at a ratio of 17% and 30%, respectively.

Effect of pH on metal adsorption

The changes in the pH value of solutions affect the surface load of the adsorbent materials and, thus, the pH value of an aqueous solution is an important factor (44). The $-NH_2$ in the structure of the polymer-coated nanoparticle adsorbent is protonated to the NH_3^+ structure in an acidic environment. Adsorption considerably increases due to the electrostatic attraction between Au(III) ions, which are in the form of $AuCl_4^-$ in an acidic environment, and $-NH_3^+$ (45,46). The activity of the adsorbent at a pH range of 1-5 was investigated to find the most suitable pH value for the pH study carried out in an acidic environment. As seen in Figure 5, the most suitable pH for the polymer-coated nanoparticle adsorbent was determined to be pH 2.

Effect of contact time

Metal removal from wastewater sources is a time-consuming process. The amount of metal ions removed from aqueous solution gradually increases until saturation. Thus, contact time is an important parameter for applicable methods. The adsorbent was examined in the 30-400-minute interval to obtain maximum Au(III) ion adsorption with the prepared adsorbent. The maximum extraction performance for the adsorbent was obtained with 180 minutes (3 hours) (Figure 6). Insufficient space is left for adsorption after adsorbent reaches saturation. Hence, no increase in adsorption was observed after three hours.
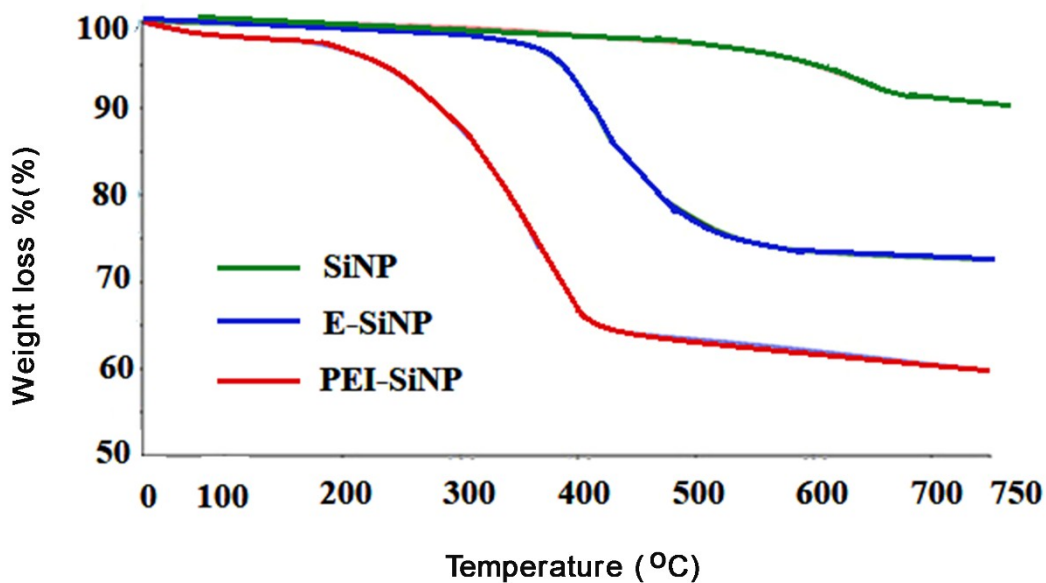
Figure 4: TGA thermograms.
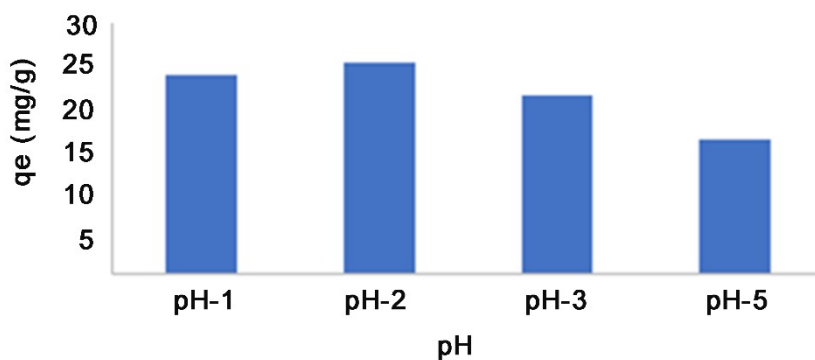
Figure 5: Effect of pH on the adsorption of Au(III) ions.
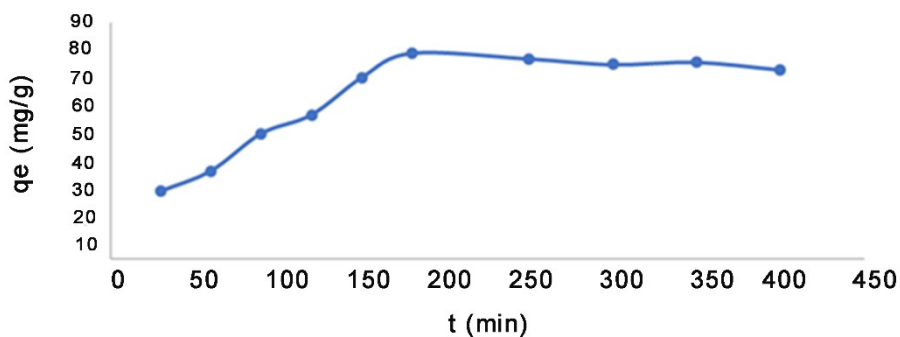
Figure 6: Effect of contact time on Au(III) ion adsorption.

Adsorption isotherms

Au(III) solutions of different concentrations ranging from 5 mg/L to 300 mg/L were used to investigate the affinity of the polymer-coated nanoparticle adsorbent to Au(III) ions. Adsorption capacity curve became relatively flattered at a higher concentration than the initial concentration of 200 mg/L, indicating that the adsorbent reached saturation (Figure 7).
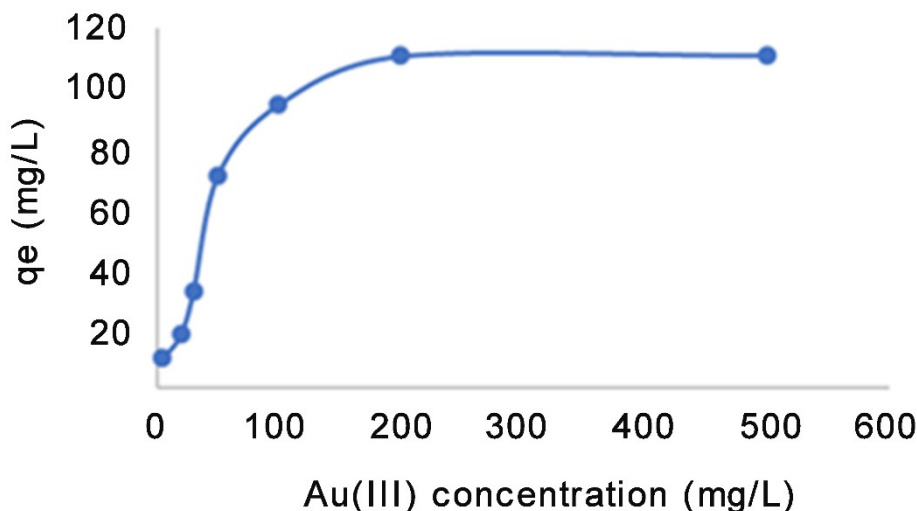
Figure 7: Effect of initial metal concentration on adsorption.

The adsorption performance of the PEI-SiNP prepared in this study was compared with the adsorbents used to some of the related studies in literature. As seen in Table 2, Au(III) was adsorbed in a very high amount compared to other similar work during the 3 hour adsorption period.

Table 2. Comparison of the adsorption performance of the PEI-SiNP with some recent adsorbent for uptake of Au(III) ions reported in literature

Adsorbent	pH	Contact time	Q_{max}(mg/g)	Reference
OSTE-IM	1.5	5 h	48.8	(46)
Amberlite XAD 7	< 4	1 h	1	(47)
Amberlite XAD 7-L-glutamic acid	< 4	1 h	14.2	(47)
Poly(acrylamide-1-allyl-2-thiourea) hydrogels	0.5	90 h	940	(48)
PEI-SiNP	2	3 h	116.27	This study

Equilibrium studies are required obtain the adsorption isotherms that are important in the determination of the capacity and especially the surface properties of the adsorbent. Information about the interaction between the polymer-coated nanoparticle absorbent and Au(III) ions are provided by isotherm studies. The Langmuir and Freundlich isotherms that are given below in respective order are used for this purpose (46,49).

$$\frac{C_e}{q_e} = \frac{1}{q_{max}} C_e + \frac{1}{K_L q_{max}} \quad (2)$$

q_{max}: Maximum adsorption capacity of the adsorbent K_L: Langmuir absorption constant

$$\ln q_e = \ln K_f + \frac{1}{n} \ln C_e \quad (3)$$

n: Constant, K_f = Freundlich constant

Table 3 shows a summary of the constants of the adsorption isotherms. The experimental data on the adsorption of Au(III) ions on the polymer-coated nanoparticle adsorbent had a high correlation coefficient of R^2: 0.9952 and was a good fit to the Langmuir model. The Langmuir isotherm indicates that a homogenous and single-layer surface adsorption occurred on the adsorbent surface.

Table 3. Isotherm parameters

	Q_{max} (mg/g)	K_L (L/mg)	R^2
Langmuir	116.27	0.052	0.9952
	n	**K_f**	**R^2**
Freundlich	2.36	11.56	0.6591

Effect of foreign ions

The absorbing capacity of the adsorbent in the presence of different ions was measured using 15 mL of synthetic wastewater containing different heavy metals and with a pH value of 2. Approximately 0.05 g of adsorbent material was immersed into 15 mL of synthetic wastewater for 3 hours. The initial concentration of all metal cations was 50 mg/L. The Au(III), Cu(II), Pb(II) and Cd(II) amounts absorbed by the material were 65, 1, 5, and 3 mg/g, respectively. Therefore, the Au(III) ions had a much higher binding capacity than that of the other ions. Higher affinity of Au(III) ions is attributable to the high amount of NH_2 groups in the structure.

CONCLUSIONS

The most appropriate pH value was 2 and adsorption time for Au(III) adsorption was 3 hours. The best fit for the adsorption was the Langmuir adsorption and thus, the adsorption in the study was determined to be a single-layer adsorption. Adsorption capacity was 116.27 mg/g, which is a considerably high value. The study showed that the polyethyleneimine-coated silica nanoparticles (PEI-SiNP) were effective adsorbents for the separation of Au(III) ions from aqueous solutions.

REFERENCES

1.   Souza C, Majuste D, Dantas MSS, Ciminelli VST. Selective adsorption of gold over copper cyanocomplexes on activated carbon. Hydrometallurgy. 2014;147-148:188-95.

2.   Sheel A, Pant D. Recovery of gold from electronic waste using chemical assisted microbial biosorption (hybrid) technique. Bioresour Technol. 2018;247:1189-92.

3.   Chen W, Geng Y, Hong J, Dong H, Cui X, Sun M, Zhang Q. Life cycle assessment of gold production in China. J. Clean Prod. 2018; 179:143-50.

4.   Syed S. Recovery of gold from secondary sources-A review. Hydrometallurgy. 2012;115-116:30-51.

5.   Cayumil R, Khanna R, Rajarao R, Mukherjee PS, Sahajwalla V. Concentration of precious metals during their recovery from electronic waste. Waste Manage. 2016;57:121-30.

6.   Papaiconomou N, Vite G, Goujon N, Lévêque JM, Billard I. Effient removal of gold complexes from water by precipitation or liquid–liquid extraction using ionic liquids. Green Chem. 2012;14:2050-6.

7.   Zhang H, Jeffry CA, Jeffey MI. Ion exchange recovery of gold from iodineiodide solutions. Hydrometallurgy. 2012;125–126:69–75.

8.   Xie RF, Hu QF, Yang GY, Chen J, Han YS, Zhao YH, Li Z. Solid-phase extraction gold from alkaline cyanide solution with quaternary ammonium surfactant. Rare Metals. 2016;35:282–8.

9.   Urucu OA, Gündüz ZY, Deniz S, Yetimoglu EK, Aydin A. A novel ligand for cloud point extraction to determine gold content in ore samples. Environ. Chem. Lett. 2014;12:449–53.

10. Kashefi K, Tor JM, Nevin KP, Lovley DR. Reductive precipitation of gold by dissimilatory Fe(III)-reducing bacteria and archaea. Appl Environ Microbiol. 2001;67:3275–9.

11.   Awual MR, Khaleque, MA, Ferdows M, Sarwaruddin-Chowdhury AM, Yaita T. Rapid recognition and recovery of gold(III) with functional ligand immobilized novel mesoporous adsorbent. Microchemical J. 2013;110:591–8.

12. Zhang Y, Xu Q, Zhang S, Liu J, Zhou J, Xu H, Xiao H, Li J. Preparation of thiolmodifid $Fe_3O_4@SiO_2$ nanoparticles and their application for gold recovery from dilute solution. Sep Purif Technol. 2013;116:391–7.

13. Villalobos LF, Yapici T, Peinemann KV. Poly-thiosemicarbazide membrane for gold recovery. Sep. Purif. Technol. 2014;136:94–104.

14. Moradi O, Zare K, Monajjemi M, Yari M, Aghaie H. The studies of equilibrium and thermodynamic adsorption of Pb(II), Cd(II) and Cu(II) ions from aqueous solution onto SWCNTs and SWCNT –COOH surfaces, fullerenes. Fuller. Nanotub. Carbon Nanostructures. 2010;18:285–302.

15. Moradi O, Aghaie M, Zare K, Monajjemi M, Aghaie H. The study of adsorption characteristics Cu^{2+} and Pb^{2+} ions onto PHEMA and P(MMA-HEMA) surfaces from aqueous single solution. J Hazard Mater. 2009;170:673-9.

16. Farghali AA, Abdel-Tawab HA, Abdel-Moaty SA, Khaled R. Functionalization of acidifid multi-walled carbon nanotubes for removal of heavy metals in aqueous solutions. J Nanostructure Chem. 2017;7:101–11.

17. Zhang G, Zhou Y, Ding Z, Fu L, Wang S. Nanosilica-supported thiosemicarbazide–glutaraldehyde polymer for selective Au(III) removal from aqueous solution. RSC Advances. 2017;7:55215-23.

18. Li H, Wang X, Cao L, Zhang X, Yang C. Gold recovery PVDF membrane functionalized with thiosemicarbazide. Chem Eng J. 2015;280:399-408.

19. Lin G, Wang S, Zhang L, Hu T, Peng J, Cheng S, Fu L. Synthesis and evaluation of thiosemicarbazide functionalized corn bract for selective and effient adsorption of Au(III) from aqueous solutions. J Mol Liq. 2018;258:235–43.

20. Mahdiani M, Soofivand F, Ansari F, Salavati-Niasari M. Grafting of $CuFe_{12}O_{19}$ nanoparticles on CNT and graphene: eco-friendly synthesis, characterization and photocatalytic activity. J Clean Prod. 2018;176:1185–97.

21. Ansari F, Sobhani A, Salavati-Niasari M. Simple sol–gel synthesis and characterization of new $CoTiO_3/CoFe_2O_4$ nanocomposite by using liquid glucose, maltose and starch as fuel, capping and reducing agents. J Colloid Interface Sci. 2018;514:723-32.

22. Naguib HM, Ahmed MA, Abo-Shanab ZL. Silane coupling agent for enhanced epoxy-iron oxide nanocomposite. J Mater Res Technol. 2018;7:21-8.

23. Sun Y, Zhang Z, Wong CP. Study on mono-dispersed nano-size silica by surface modification for underfill applications. J Colloid Interface Sci. 2005;292:436–44.

24. Moisala A, Li Q, Kinloch IA, Windle AH. Thermal and electrical conductivity of single-and multi-walled carbon nanotube-epoxy composites. Compos Sci Technol. 2006;66: 1285-92.

25. Lee JY, Chen C, Cheng H, Li SHY. Adsorption of Pb(II) and Cu(II) metal ions on functionalized large-pore mesoporous silica. Int J Environ Sci Technol. 2016;13:65-76.

26. Mansa RF, Sipaut CS, Rahman IA, Yusof NSM, Jafarzadeh M. Preparation of glycine-modified silica nanoparticles for the adsorption of malachite green dye. J Porous Mater. 2016;23:35–46.

27. Wang L, Cheng C, Tapas S, Lei J, Matsuoka M, Zhang J, Zhang F. Carbon dots modified mesoporous organosilica as an adsorbent for the removal of 2,4-dichlorophenol and heavy metal ions. J Mater Chem A. 2015;3:13357-64.

28. Zhuang M-Y, Jiang X-P, Ling X-M, Xu M-Q, Zhu Y-H, Zhang Y-W. Immobilization of glycerol dehydrogenase and NADH oxidase for enzymatic synthesis of 1,3-dihydroxyacetone with in situ cofactor regeneration. J Chem Technol Biotechnol. 2018;156:1-10.

29. Dixit CK, Bhakta S, Macharia J, Furtado J, Suib SL, Rusling JF. Novel Epoxy-Silica Nanoparticles to Develop Non-Enzymatic Colorimetric Probe for Analytical Immuno/Bioassays. Anal Chim Acta. 2018;1028:77-85.

30. Chruściel JJ, Leśniak E. Modification of epoxy resins with functional silanes, polysiloxanes, silsesquioxanes, silica and silicates. Prog Polym Sci. 2015;41:67-121.

31. Fırlak M, Kahraman MV, Yetimoğlu EK, Zeytuncu B. Adsorption of Ag (I) ions from aqueous solutions using photocured thiol-ene hydrogel. Sep Purif Technol. 2013;48:2860–70.

32. He X, Rytöluoto I, Anyszka R, Mahtabani A, Saarimäki E, Lahti K, Paajanen M, Dierkes W, Blume A. Surface Modification of Fumed Silica by Plasma Polymerization of Acetylene for PP/POE Blends Dielectric Nanocomposites. Polymers. 2019;11:1957-78.

33. Gruian C, Vanea E, Simon S, Simon V. FTIR and XPS studies of protein adsorption onto functionalized bioactive glass. BBA-Proteins Proteom. 2012;1824:873-81.

34. Michel R, Pasche S, Textor M, Castner DG. Influence of PEG architecture on protein adsorption and conformation. Langmuir. 2005;21:12327-32.

35. Zhao Y, Zou J, Shi W, Tang L. Preparation and characterization of mesoporous silica spheres with bimodal pore structure from silica/hyperbranched polyester nanocomposites. Micropor Mesopor Mat. 2006;92:251-8.

36. Nhavene EPF, Silva WM, Junior RRT, Gastelois PL, Venâncio T, Nascimento R, Batista RJC, Machado CR, Macedo WAA, Sousa EMB. Chitosan grafted into mesoporous silica nanoparticles as benznidazol carrier for Chagas diseases treatment. Micropor Mesopor Mat. 2018;272:265-75.

37. Yu JG, Le Y, Cheng B. Fabrication and CO_2 adsorption performance of bimodal porous silica hollow spheres with aminemodifed surfaces. RSC Advances. 2012;2:6784–91.

38. Feifel SC, Lisdat F. Silica nanoparticles for the layer-by-layer assembly of fully electro-active cytochrome c multilayers. J. Nanobiotechnology. 2011;9:59-71.

39. Ammar S, Ramesh K, Vengadaesvaran B, Ramesh S, Arof AK. Amelioration of anticorrosion and hydrophobic properties of epoxy/PDMS composite coatings containing nano ZnO particles. Prog Org Coat. 2016;92:54-65.

40. Li C, Wan J, Kalali EN, Fan H, Wang D-Y. Synthesis and characterization of functional eugenol derivative based layered double hydroxide and its use as a nanoflame-retardant in epoxy resin. J Mater Chem A. 2015;3:3471-9.

41. Chen F, Lu Y, Liu X, Song J, He G, Tiwari MK, Carmalt CJ, Parkin, IP. Table Salt as a Template to Prepare Reusable Porous PVDF–MWCNT Foam for Separation of Immiscible Oils/Organic Solvents and Corrosive Aqueous Solutions. Adv Funct Mater. 2017;27:1702926-37.

42. Lu L, Pan J, Li G. Recyclable high-performance epoxy based on transesterification reaction. J Mater Chem A. 2017;5:21505-13.

43. Omurlu C, Baran JR, Nguyen QP. Adsorption of Surface Functionalized Silica Nanoparticles onto Mineral Surfaces and Decane/Water Interface. J Nanopart Res. 2012;14:1246-56.

 44. Baghban N, Yilmaz E, Soylak M. Nanodiamond/ MoS_2 nanorod composite as a novel sorbent for fast and effective vortex-assisted micro solid phase extraction of lead(II) and copper(II) for their flame atomic absorption spectrometric detection. J Mol Liq. 2017;234: 260-7.

45. Ngatijo-Basuki R, Rusdiarso B, Nuryon N. Sorption-desorption profile of Au(III) onto silica modified quaternary amines (SMQA) in gold mining effluent. J Environ Chem Eng. 2020;8:103747- 87.

46. Aydın-Urucu O, Aracıer DE, Çakmakçi E. Allylimidazole containing OSTE based photocured materials for selective and efficient removal of gold from aqueous media. Microchem J. 2019;146:997-1003.

47. Mihăilescu M, Negrea A, Ciopec M, Davidescu CM, Negrea P, Narcis D, Rusu G. Gold (III) adsorption from dilute waste solutions onto Amberlite XAD7 resin modified with L-glutamic acid. Sci. Rep. 2019;9:8757-69.

48. Kılıc AG, Malcı S, Çelikbıçak Ö, Sahiner N, Salih B. Gold recovery onto poly(acrylamide-allylthiourea) hydrogels synthesized by treating with gamma radiation. Anal. Chim. Acta. 2005;547:18–25.

49. Beyler-Çiğil A, Aydın-Urucu O, Kahraman MV. Nanodiamond-containing polyethyleneimine hybrid materials for lead adsorption from aqueous media. J Appl Polym. 2019;136:48241-50.

RESEARCH ARTICLE

Vermicompost as a Potential Adsorbent for the Adsorption of Methylene Blue Dye from Aqueous Solutions

Zeynep CİĞEROĞLU[1] ✉ iD **and Eyup YILDIRIR[1]** ✉ iD

Uşak University, Department of Chemical Engineering, 64400 Uşak/Turkey

Abstract: Vermicompost (VC) as a low cost and waste-derived material was used as an adsorbent to remove textile dye effluents from the wastewater. Methylene blue (MB) was selected as a representative of dye effluents and its adsorption to VC was investigated. The effect of parameters such as pH, adsorption time, and the initial concentration of MB were determined via lab-scale batch experiments. The highest adsorption capacity of VC was reached when the pH of the solution was 4. The equilibrium was maintained after 90 minutes of operation since the removal percentage of MB was stabilized at 99%. The pseudo-second-order kinetic model described the most appropriate adsorption kinetic behavior. Both Langmuir (R^2=0.9891) and Freundlich isotherms (R^2=0.9895) fitted very well to the experimental data. Based on these results, vermicompost can be evaluated as an alternative adsorbent for the removal of dye effluents.

*Corresponding author. E-mail:zeynep.ilbay@usak.edu.tr, zilbay@gmail.com.
Tel: +90 276 221 2121/2774.

INTRODUCTION

Composting and vermicomposting are two biological processes to convert organic wastes such as sewage sludge, municipal solid waste, etc. into soil amendments (1). Composting is homogenization of mixed organic wastes by means of thermophilic process at a temperature range of 45 to 65 °C, while vermicomposting is the stabilizing the organic wastes or compost by the digestion of earthworms and micro-organisms at 35 °C (1,2). The final products after two processes have nutrients for the soil, humic acid, and metals together with high moisture contents; compost with 40 to 60 wt.% and vermicompost with 70 to 90 wt.% respectively (3).

Converting organic wastes into vermicompost is perceived as environmentally and economically sustainable since the product could be used as a promoter for plant growth and soil amendment.

However, there are reports in the literature criticizing the usage of compost and vermicompost as soil amendments since they may have pathogens and heavy metals which are hazardous for the human. Although vermicomposting reduce somewhat human pathogens, regulations by the governments limit the usage of compost and vermicompost due to their hazardous nature to human health (4). This situation influenced the researchers to investigate alternative usage areas for compost and vermicompost different from agricultural purposes. Vermicompost has gained attention to be used as an adsorbent to remove organic and inorganic contaminants in the wastewater and studies showed that due to its high surface area and functional groups existing naturally, making vermicompost an effective adsorbent (5). Especially the humic substances in the organic fraction of vermicompost provide the high surface area with high porosity, high density of

negative charges, and noticeable cationic exchange capacity.

Adsorption is a widely known technique applied to wastewater to remove organic and inorganic contaminants. Activated carbon is one of the most promising adsorbents according to the studies in the literature (6). However, its high cost limits its applicability therefore investigation of alternative adsorbents with low cost and appropriate characteristics is crucial. In this regard, compost, clays, chitosan, peats, biochar, etc. were utilized and a variety of contaminants tested in order to extract their potential as an effective adsorbent (7). Vermicompost, on the other hand, has proper physical and chemical properties to be evaluated as an absorbent, and its low cost attracts researchers to investigate its adsorption capability. Currently, vermicompost's price is around 20 TRY/kg and according to a recent report, its annual production rate was about 20,000 tonnes in 2017, in Turkey (8).

Early studies focused on the metal removal from the wastewater and the results were promising. Vermicompost produced from cattle manure was utilized in a glass column to determine its adsorption capability on Cu, Ni and Zn, and it was proven that higher adsorption rates were achieved compared to various adsorbents such as sewage sludge, apple residues, peat moss etc. (5). Zhu et al. reported that high removal efficiencies of Pb and Cd from wastewater stream were possible when cow manure and its vermicompost were used as adsorbent. They also determined that the performance of vermicompost was better and mainly the functional groups such as aliphatic alcohols, aromatic acids, carbonates, and phosphates contributed to the efficient removal of the metals (9). Pesticide methylparathion removal from water stream via adsorption onto vermicompost was studied as well and the results suggested that experimental data fitted to the Langmuir linear model yielding 0.17 mg/g of maximum adsorption capacity (10).

Apart from the metals and pesticide, dye effluents such as congo red, crystal violet, etc. were also adsorbed onto vermicompost and results looked promising (11,12). However, there is still more work to be carried out to figure out the optimum conditions for the process. Especially for Turkey, producing a versatile, low cost, and highly efficient adsorbent is important, as textile and leather industrial wastewater contains great amounts of dye effluents. In addition, only around 0.38% of 34.500 tonnes of MSW produced in Turkey is composted annually, according to TUIK (13). Since compost can be used for vermicompost production, Turkey has a great potential to reach vast production figures if alternative routes for vermicompost utilization could be established. In this study, vermicompost was

evaluated as a potential adsorbent for methylene blue adsorption as a model dye effluent. As a cationic dye, methylene blue could be contained in the textile and leather industrial wastewater since it is used in silk and wool dyeing processes. The high concentration of methylene blue is regarded as hazardous, and avoiding its leakage to soil and rivers is crucial (14).

The primary aim of this study was to examine the influences of the adsorption conditions such as the initial concentration of MB, pH of media on the adsorption capacity of MB onto VC. In addition, kinetic models (the first and second-pseudo-order, Intraparticular and Elovich models) and four isotherm models (Langmuir, Freundlich, Temkin and Dubinin-Radushkevich) were utilized to determine their compatibility with the experimental data.

MATERIALS AND METHODS

Materials
Sodium chloride, hydrochloric acid, sodium hydroxide, and methylene blue were purchased from Sigma Aldrich. Bidistilled water was used in the whole experimental process. Vermicompost (VC) was purchased from a local producer from İzmir, and it was produced from sewage sludge compost and sawdust. Initially, vermicompost was dried and sieved to yield a particle size of 0.125<Dp<0.600 [mm] for homogenization of the sample. Vermicompost sample was oxidized in a furnace at 500 °C for 6 hours and its ash content was determined as 31.05 wt.%.

Sorption Experiments
Methylene Blue (MB) solutions at various pH values were prepared and 10 mL of specified concentration of MB solutions were poured into an erlenmeyer flask along with 0.1 g of VC sample. The sorption experiments were carried out in an incubator shaker operating at 100 rpm and 25 °C temperature. After the sorption experiments were completed, the solutions in the Erlenmeyer flasks were pulled out and centrifuged at 400 rpm for 1 minute. The initial and the supernatant concentrations were read with the help of UV-Vis spectrophotometer (Perkin Elmer, Lambda 365) at λ max: 664 nm. Adsorption capacity (AC) and removal yield (R%) were determined according to equations 1 and 2, respectively.

$$AC = \frac{(C_i - C_e) * V}{m} \qquad (1)$$

$$R\% = \frac{(C_i - C_e) * 100}{C_i} \qquad (2)$$

C_i and C_e represent the initial and equilibrium concentration of the solution (mgL^{-1}), respectively. m denotes the mass of VC (g).

Determination of pHpzc

Slightly modified potentiometric titration method of Mohan et al. 2014 (15) was utilized to determine the point of zero charge. Briefly, 0.1 g of VC was added to 10 mL of 0,1 M NaCl solutions having pH values in the range of 2 to 12. The solutions were placed into the shaking water bath for 24 hours. After that, supernatant pH values were measured and a plot consisting of pH of initial solutions versus pH of final solutions was obtained.

Adsorption Kinetics
Batch kinetics were assessed with the help of appropriate kinetic models so that the adsorption rates and mechanism could be defined. In this research, the pseudo-first order (Eq. 3) (16), the pseudo-second-order (Eq. 4) (17), Intraparticular (Eq. 5) (18) and Elovich kinetic models (Eq. 6) (19) were applied to experimental data. The coefficient of determination (R^2) was calculated for each kinetic model to determine the best fit model.

$$\log(q_e - q_t) = \log q_e - \frac{k_p}{2.303} t \qquad (3)$$

$$\frac{t}{q_t} = \frac{1}{k_2 q_e^2} + \frac{t}{q_e} \qquad (4)$$

$$q_t = k_p t^{0.5} + c \qquad (5)$$

$$q_t = \frac{1}{\beta} \ln(\alpha\beta) + \frac{1}{\beta} \ln t \qquad (6)$$

Where q_e is the equilibrium adsorption capacity (mg/g), k_1 is pseudo-first-order constant (min⁻¹), k_2 is the pseudo-second-order constant (g/mg.min), β is the Elovich equation exponent (g/mg), k_p is diffusion constant.

Isotherm Models
In order to appraise the adsorption behavior, four isotherm kinetic models were utilized. Table 1 represents the Langmuir (20), Freundlich (21), Temkin (22), and Dubinin-Radushkevich (D-R)(23) isotherm models.

Table 1. Applied Isotherm Models with their equations and units.

Models	Equations	Units
Langmuir	$\frac{C_e}{q_e} = \frac{1}{q_{max} K_L} + \frac{C_e}{q_{max}}$	q_e: adsorbed amount (mgg⁻¹) C_e: adsorbed equilibrium (mgL⁻¹) K_L: Langmuir constant related to sorption energy (Lmg⁻¹) q_{max}: maximum adsorption capacity (mgg⁻¹) related to monolayer coverage
Freundlich	$\ln q_e = \ln(K_F) + \frac{1}{n} \ln C_e$	C_e: adsorbed equilibrium (mgL⁻¹) K_F: Freundlich constant (mgg⁻¹)(Lmg⁻¹)ⁿ $1/n$: intensity of adsorption
Temkin	$q_e = B \ln a_T + B \ln C_e$ $B = \frac{RT}{b_T}$	C_e: adsorbed equilibrium (mgL⁻¹) a_T: equilibrium bond constant B, b_T: Temkin constants
Dubinin-Radushkevich	$\ln q_e = \ln q_m - \beta \varepsilon^2$ $\varepsilon = RT \ln(1 + \frac{1}{C_e})$ $E = \frac{1}{\sqrt{2\beta}}$	C_e: adsorbed equilibrium (mgL⁻¹) q_m: maximum adsorption capacity (mgL⁻¹) ε: Polanyi potential β: activity coefficient (mol²J⁻²) R: gas constant (8.314 kJmol⁻¹K⁻¹) E: mean adsorption Energy (kJmol⁻¹)

RESULTS AND DISCUSSION

Effect of pH on methylene blue removal mechanisms
The impact of pH on the MB sorption was investigated with batch experiments performed in a pH range of 2-10 and the outcomes were shown in the Figure 1. The maximum MB removal was achieved when pH of the solution was 4. Therefore, all adsorption experiments were executed at pH 4.
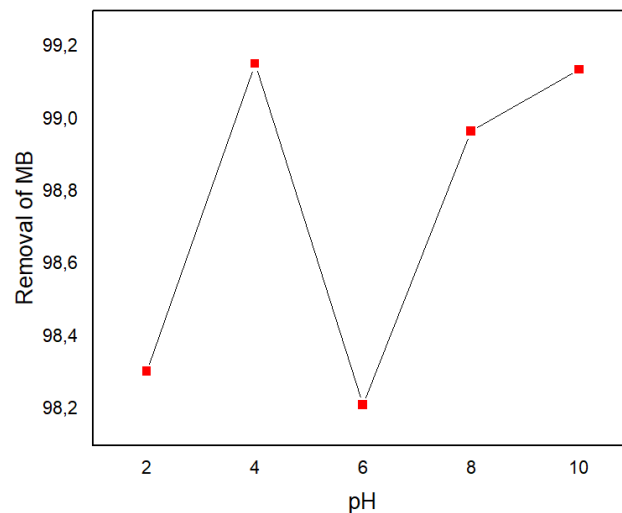
Figure 1. pH effect on the removal of MB.

Moreover, the point of zero charge (pHpzc) was measured as 8.51 as shown in Figure 2. At this pH, the surface charge of VC is zero. When pH<pHpzc, the surface of vermicompost has positive charge. In the opposite cases, the functional groups of vermicompost are negatively charged. MB is a cationic dye as it is known. Furthermore, the pKa of MB is 3.8; the cationic species of MB are dominant in the solutions above the value of pKa (24). The electrostatic adherence has occurred between the adsorbent and adsorbate at pH 4.
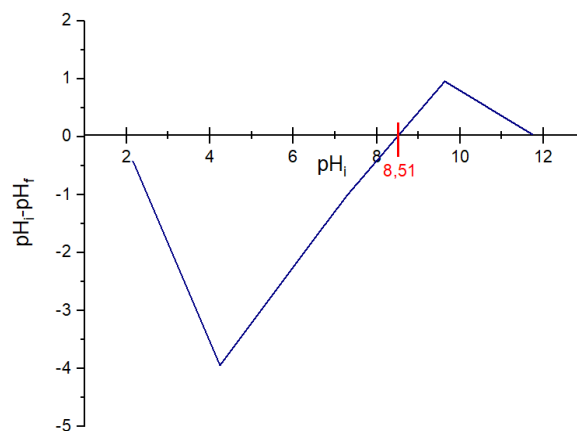
Figure 2. The point of zero charge of VC.

Effect of time and initial concentration of MB
The impact of time on MB adsorption onto VC was shown in Figure 3. Methylene blue adsorption onto VC was so rapid that adsorption equilibrium could be achieved within 60 minutes. As the vacant sites on the surface of VC were occupied with methylene blue, adsorption process happened very slowly by virtue of the small number of vacant sites and 99% removal of MB was achieved at 90 min. Besides, adsorption capacity enhanced with the higher initial concentration of MB, this phenomenon indicated in Figure 4. Initial concentration raises mass transfer between the adsorbate and the adsorbent owing to the driving force.

896
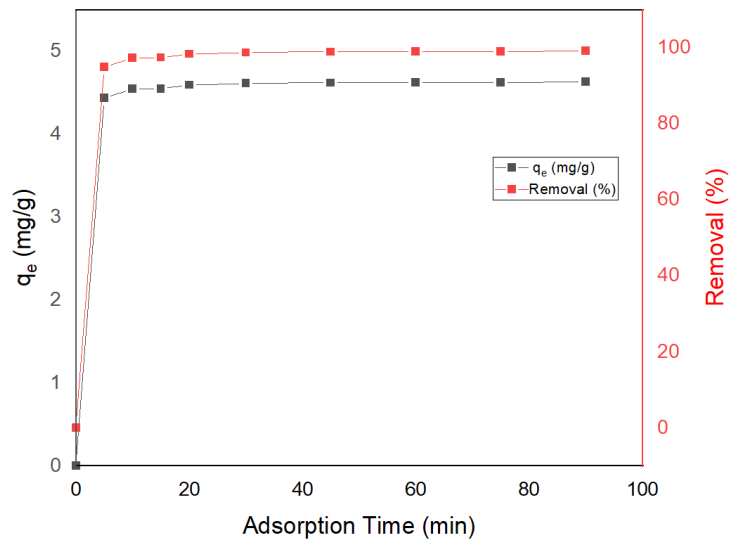
Figure 3. The effect of time on MB adsorption onto VC.
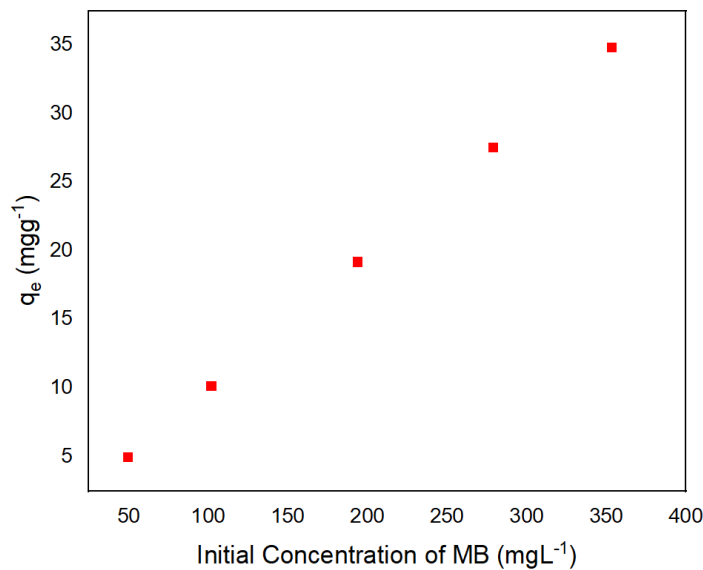
Figure 4. The effect of initial concentration on the adsorption capacity of MB onto VC.

Kinetic isotherm models

It can be deduced from Table 2 that chemisorption occurred according to the pseudo-second-order model. The first step of sorption was so fast owing to the large number of active sites of VC. With the increasing adsorption time, vacant sites of the surface were gradually decreased. As a result, all active surface was totally filled the adsorbate and adsorption process reached the equilibrium (25). The coefficients of determination of the kinetic models applied as shown in Figure 5 indicating that the pseudo-second-order model had the finest linear fit to the experimental data. Also, adsorption onto the VC comprised of two stages represented a multilinearity. Within the 5 min, the rapid MB adsorption took place. Then, the adsorption process has slightly risen. The boundary layer diffusion constitutes the first step, and the second stage was ascribed to the intraparticle diffusion (26).

Table 2. Kinetic parameters of applied kinetic models for MB adsorption onto VC at 298 K.

Models	Model parameter	VC
Pseudo-first-order kinetics	q_e	0.6760
	k_1	0.0914
	R^2	0.7571
Pseudo-second-order kinetics	q_e	4.63
	k_2	1.58
	R^2	1.0
Intraparticular	K_p	0.3846
	C_1	1.9457
	R^2	0.5208
Elovich	α	1.104
	β	3.758
	R^2	0.6887
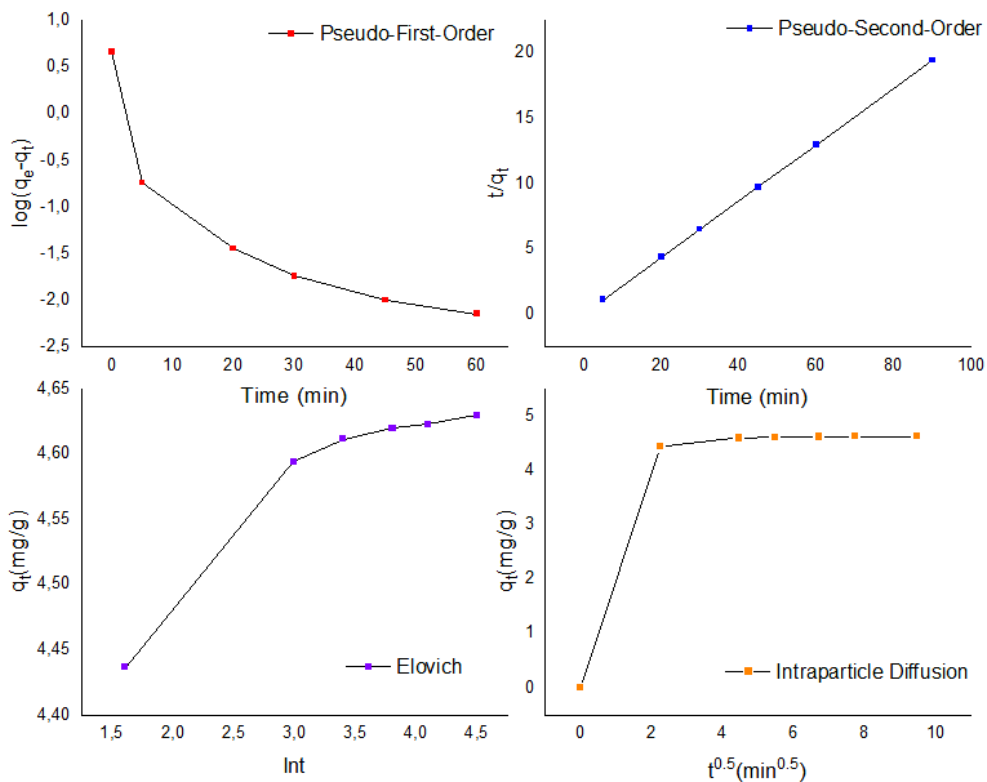
Figure 5. Applied kinetic models on the MB's adsorption onto the VC a) pseudo-first-order b) pseudo-second-order c) Elovich d) Intraparticle diffusion.

Adsorption isotherm models results

The calculated parameters for isotherm models applied in this research are summarized in Table 3. Furthermore, a plot was drawn by using nonlinear regression analysis showing the conformity of the isotherm models to experimental data in Figure 6. It can be said that both Langmuir and Freundlich isotherm models were excellent-fitted to empirical data. In fact, the coefficients of determination were so close to each other in all models. The Freundlich isotherm gave an idea that adsorption happened on the heterogeneous surface. Besides, there were no equal binding sites (27).

Table 3. The parameters of applied isotherm models for MB adsorption onto VC at 298 K.

Models	Model parameter	VC
Langmuir	qe(calculated)	34.7900
	qmax	58.4795
	K_L	0.2070
	R^2	0.9891
Freundlich	n	1.3077
	K_F	9.5410
	R^2	0.9895
Temkin	B	10.0620
	a_T	3.1760
	b_T	246.3545
	R^2	0.9832
Dubinin-Radushkevich	Qm	23.8456
	$\beta \times 10^7$	2.0000
	E	1581.1390
	R^2	0.9430
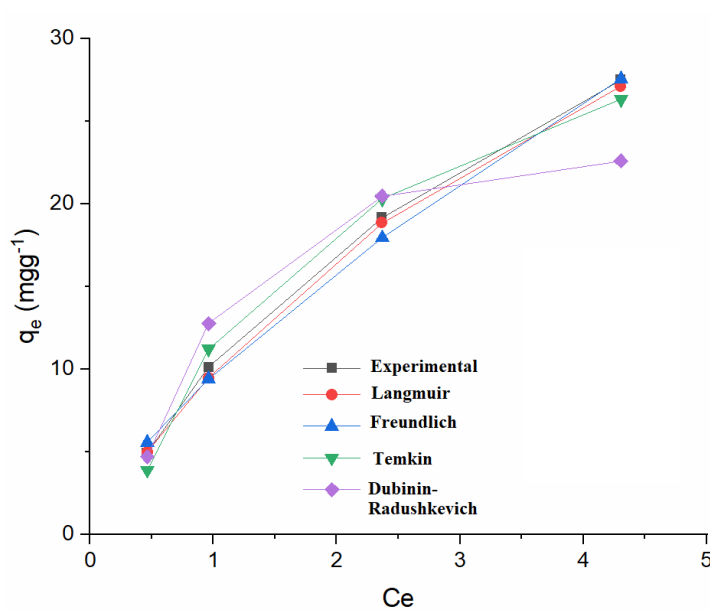
Figure 6. Adsorption isotherms of MB onto VC.

FTIR Analyses of the Adsorbent

FTIR analyses of raw vermicompost and vermicompost after MB adsorption were carried out and resulting spectra are shown in Figure 7. Raw vermicompost's broad peak seen at 3368 cm^{-1} is corresponding to the -OH band of hydroxyl groups which could belong to phenolic compounds. Furthermore, it can be inferred from the literature survey of vermicompost, N-H stretching band from amides and amines are observed in the range of 3300-3500 cm^{-1} (28). The sharp peak at 1634 cm^{-1} is attributed to -OH band. The intense peak at 1031 cm^{-1} may be assigned to stretching C-O group of polysaccharides. When the FTIR spectrum of vermicompost after MB adsorption was examined, the specific peak was detected at 1593 cm^{-1} corresponds to the C=C due to the aromatic rings. The two lower signal peaks were observed at 1323 cm^{-1} and 1384 cm^{-1} owing to the C–N stretching vibrations and -OH functional groups, respectively (29). Also, the symmetrical stretching C-H of CH$_2$ band appeared at 2928 cm^{-1} (28). The dramatic decrease on the magnitude of -OH peaks after the adsorption of MB onto VC could be evaluated to the chemisorption since the hydroxyl groups were neutralized.
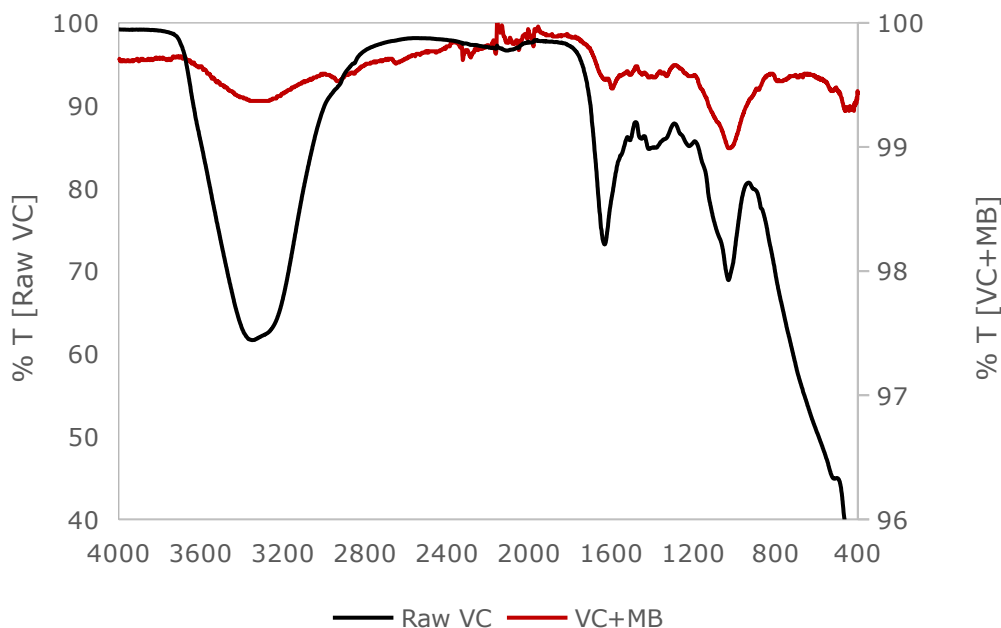
Figure 7. FTIR spectrum of Raw VC and MB adsorbed VC.

CONCLUSION

Vermicompost was evaluated as a cost-effective adsorbent in order to MB sorption from aqueous solution. The various kinetic models were applied to identify the reaction mechanism and the pseudo-second order kinetic model was matched with the experimental data, yielding the highest coefficient of determination (R^2=1.0). The nonlinear regression results of the isotherms pointed out that Langmuir model fitted the empirical results better than the other isotherm models. The maximum adsorption capacity value was calculated as 58.48 mgg^{-1} via the Langmuir isotherm. Furthermore, before and after the adsorption process, VC's functional groups were observed by FTIR. These results indicated the mechanism of the adsorption process between the VC and MB. Last but not the least, VC is a good candidate for the removal of MB.

REFERENCES

1.   Domínguez J, Edwards CA, Subler S. A comparison of vermicomposting and composting methods to process animal wastes. Biocycle. 1997;April(April):57–9.

2.   Zuccconi F, Bertoldi M. Compost pecification for the production and characterization of compost from municipal solid waste. Compost Prod Qual Use. 1987;

3.   Tognetti C, Laos F, Mazzarino MJ, Hernández MT. Composting vs. Vermicomposting: A Comparison of End Product Quality. Compost Sci Util [Internet]. 2005 Jan [cited 2020 Feb 20];13(1):6–13. Available from: http://www.tandfonline.com/doi/abs/10.1080/1065

657X.2005.10702212

4.   Eastman BR, Kane PN, Edwards CA, Trytek L, Gunadi B, Stermer AL, et al. The Effectiveness of Vermiculture in Human Pathogen Reduction for USEPA Biosolids Stabilization. Compost Sci Util [Internet]. 2001 Jan [cited 2020 Feb 21];9(1):38–49. Available from: https://www.tandfonline.com/action/journalInformation?journalCode=ucsu20

5.   Matos GD, Arruda MAZ. Vermicompost as natural adsorbent for removing metal ions from laboratory effluents. Process Biochem. 2003 Sep 30;39(1):81–8.

6.   Paradelo R, Vecino X, Moldes AB, Barral MT. Potential use of composts and vermicomposts as low-cost adsorbents for dye removal: an overlooked application. Vol. 26, Environmental Science and Pollution Research. Springer Verlag; 2019. p. 21085–97.

7.   Crini G. Non-conventional low-cost adsorbents for dye removal: A review. Vol. 97, Bioresource Technology. Elsevier; 2006. p. 1061–85.

8.   Bellitürk K. Vermicomposting in Turkey: Challenges and opportunities in future. Eurasian J For Sci [Internet]. 2018 [cited 2020 Jul 7];6(4):32–41. Available from: http://dergipark.gov.tr/ejejfs

9.   Zhu W, Du W, Shen X, Zhang H, Ding Y. Comparative adsorption of Pb2+ and Cd2+ by cow manure and its vermicompost. Environ Pollut. 2017 Aug 1;227:89–97.

10. Mendes CB, Lima GDF, Alves VN, Coelho NMM, Dragunski DC, Tarley CRT. Evaluation of vermicompost as a raw natural adsorbent for adsorption of pesticide methylparathion. Environ Technol [Internet]. 2012 Jan [cited 2020 Feb 28];33(2):167–72. Available from: https://www.tandfonline.com/action/journalInformation?journalCode=tent20

11. De Godoi Pereira M, Korn M, Santos BB, Ramos MG. Vermicompost for tinted organic cationic dyes retention. Water Air Soil Pollut. 2009 Jun 20;200(1–4):227–35.

12. Yang G, Wu L, Xian Q, Shen F, Wu J, Zhang Y. Removal of Congo Red and Methylene Blue from Aqueous Solutions by Vermicompost-Derived Biochars. Singer AC, editor. PLoS One [Internet]. 2016 May 4 [cited 2019 Nov 17];11(5):e0154562. Available from: https://dx.plos.org/10.1371/journal.pone.0154562

13. TÜİK. Türkiye İstatistik Kurumu [Internet]. Tarımsal Gübre İstatistikleri. 2019 [cited 2020 May 27]. Available from: http://www.tuik.gov.tr/PreTablo.do?alt_id=1001

14. Ciğeroğlu Z, Haşimoğlu A, Özdemir OK. Synthesis, characterization and an application of graphene oxide nanopowder: methylene blue adsorption and comparison between experimental data and literature data. J Dispers Sci Technol [Internet]. 2020 [cited 2020 Jul 20]; Available from: https://www.tandfonline.com/doi/abs/10.1080/01932691.2019.1710526

15. Mohan D, Kumar H, Sarswat A, Alexandre-Franco M, Pittman CU. Cadmium and lead remediation using magnetic oak wood and oak bark fast pyrolysis bio-chars. Chem Eng J [Internet]. 2014 [cited 2020 Jul 20];236:513–28. Available from: https://www.sciencedirect.com/science/article/pii/S1385894713012503

16. Lagergren S. Zur Theorie der sogenannten Adsorption gelöster Stoffe. Zeitschrift für Chemie und Ind der Kolloide [Internet]. 1907 Jul [cited 2020 Jul 22];2(1):15–15. Available from: https://www.sid.ir/en/journal/ViewPaper.aspx?ID=263167

17. Ho YS, McKay G. Sorption of dye from aqueous solution by peat. Chem Eng J [Internet]. 1998 Jun [cited 2020 Jul 22];70(2):115–24. Available from: https://linkinghub.elsevier.com/retrieve/pii/S0923046798000761

18. Weber W. Kinetics of Adsorption on Carbon from Solution. J Sanit Eng Div [Internet]. 1963 [cited 2020 Jul 22];89(2):31–60. Available from: https://cedb.asce.org/CEDBsearch/record.jsp?dockey=0013042

19. Wu F, Tseng R, Journal RJ-CE, 2009 undefined. Characteristics of Elovich equation used for the analysis of adsorption kinetics in dye-chitosan systems. Elsevier [Internet]. [cited 2020 Jul 22]; Available from: https://www.sciencedirect.com/science/article/pii/S1385894709000163

20. Langmuir I. The adsorption of gases on plane surfaces of glass, mica and platinum. J Am Chem Soc [Internet]. 1918 Sep 1 [cited 2020 Jul 22];40(9):1361–403. Available from: https://pubs.acs.org/doi/pdf/10.1021/ja02242a004.

21. Chemie HF-Z für physikalische, 1907 U. Über die adsorption in lösungen. degruyter.com [Internet]. [cited 2020 Jul 22]; Available from: https://www.degruyter.com/downloadpdf/j/zpch.1907.57.issue-1/zpch-1907-5723/zpch-1907-5723.xml

22. Tempkin MI, Pyzhev V. Kinetics of ammonia synthesis on promoted iron catalyst. Acta Phys Chim USSR [Internet]. 1940 [cited 2020 Jul 22];12:327–56. Available from: https://ci.nii.ac.jp/naid/20000744365/

23. Dubinin MM, Radushkevich LV. The equation of the characteristic curve of activated charcoal. , 55, 331 (1947). Proc Acad Sci USSR Phys Chem Sect [Internet]. 1947 [cited 2020 Jul 22];55:327–9. Available from: https://ci.nii.ac.jp/naid/10028158033/

24. Sousa HR, Silva LS, Sousa PAA, Sousa RRM, Fonseca MG, Osajima JA, et al. Evaluation of methylene blue removal by plasma activated palygorskites. J Mater Res Technol. 2019;8(6):5432–42.

25. Wang SY, Tang YK, Li K, Mo YY, Li HF, Gu ZQ. Combined performance of biochar sorption and magnetic separation processes for treatment of chromium-contained electroplating wastewater. Bioresour Technol. 2014;174:67–73.

26. Mezenner NY, Bensmaili A. Kinetics and thermodynamic study of phosphate adsorption on iron hydroxide-eggshell waste. Chem Eng J. 2009;147(2–3):87–96.

27. Farouq R, Yousef NS. Equilibrium and Kinetics Studies of adsorption of Copper (II) Ions on Natural Biosorbent. Int J Chem Eng Appl. 2015;6(5):319–24.

28. Subhash Kumar M, Rajiv P, Rajeshwari S, Venckatesh R. Spectroscopic analysis of vermicompost for determination of nutritional

quality. Spectrochim Acta - Part A Mol Biomol Spectrosc [Internet]. 2015 [cited 2020 Jul 22];135:252–5. Available from: https://www.sciencedirect.com/science/article/pii/S1386142514010786

29.   Wu Z, Zhong H, Yuan X, Wang H, Wang L, Chen X, et al. Adsorptive removal of methylene blue by rhamnolipid-functionalized graphene oxide from wastewater. Water Res [Internet]. 2014 [cited 2020 Jul 22];67:330–44. Available from: https://www.sciencedirect.com/science/article/pii/S0043135414006563

Investigation of Triamcinolone-Bovine Serum Albumin (BSA) Interaction by Spectroscopic Methods

Sabriye Aydinoglu ✉ iD

Çukurova University, Faculty of Pharmacy, Department of Analytical Chemistry, 01330, Adana, Turkey

Abstract: The aim of the present study was investigate the interaction between bovine serum albumin and triamcinolone. For this purpose, the interaction between BSA and triamcinolone was evaluated by UV–Vis and fluorescence spectroscopy under different temperatures and different salt concentrations at physiological pH (7.4). The binding constant of BSA-Triamcinolone system were evaluated different temperature at constant (pH=7.4) and ionic strength (0.01 M). The binding constant dependence of binding constant on temperature was analyzed by Van't Hoff equation. The standard enthalpy change (ΔH) was 9.0 kcal/mol and standard entropy change (ΔS) was 54.1 cal/mol K. In addition, the effect of salt concentration investigated for BSA-Triamcinolone system at constant temperature (T=25 °C) and increasing salt concentration lead to decrement on the binding constant value. The obtained thermodynamic parameters indicate hydrophobic forces take major role in BSA-Triamcinolone interaction. The arousal of salt concentration prompted to diminution on affinity between Triamcinolone and BSA.

INTRODUCTION

Endogeneous ligands and drugs are mostly bound to plasma proteins in the blood. Because of unbound drug freely penetrates to target organs and elimination organs drug-plasma protein interaction determines pharmacokinetics and pharmacodynamics properties of drugs. The drug binding to plasma proteins could cause to alteration on drug half-life time and drug blood concentration (1-3).

Albumin is the most abundant protein in plasma and it is bound reversibly various drugs including anticoagulants, antidiabetics, antineoplastic, and steroids (4-6). The importance of interaction between ligand and albumin or other plasma protein is well recognized (7). The interaction between plasma protein and drugs has significant value in order to understand behavior of drugs in biological systems (8, 9). Bovine Serum albumin (BSA) has similarities with Human Serum Albumin (HSA) from the point of structure, properties and functionalities. BSA is widely used to investigate drug-protein interaction because of its similarity with HAS (9-13). Experimental studies with serum albumin is represented a model for in vitro drug plasma protein interaction.

Triamcinolone is a synthetic corticosteroid drug used in the treatment of various inflammatory conditions such as dermatitis, allergic rhinitis, allergic asthma, rheumatoid arthritis and acute exacerbations of multiple sclerosis (14). The aim of present study is estimate the type of interaction between BSA and triamcinolone by thermodynamic approach. The thermodynamic parameters as like, standard enthalpy change (ΔH°) and standard entropy change (ΔS°), could offer an important evidence about interaction type which force binding between protein and drug molecule (15). For instance, in the case of the hydrophobic interaction both of

mentioned parameters result positive value (16). On the other hand, if ΔH and ΔS are negative, it means that the interaction occurs by Van der Waals interactions and hydrogen binding (14). In the case of negative ΔH with positive ΔS is demonstrate interaction cause by electrostatic interaction (8).

MATERIAL AND METHODS

All the chemicals were analytical grade and were employed without further purification. Triamcinolone and Bovine Serum Albumin (BSA, ≥98), and hydrochloric acid (HCl) were purchased from Sigma-Aldrich (Germany). Ethanol HPLC grade, Sodium hydroxide (NaOH), Sodium Chloride (NaCl), sodium dihydrogen phosphate (NaH_2PO_4), and disodium hydrogen phosphate (Na_2HPO_4) were purchased from Merck (Germany). The water used as a reaction medium and to prepare the solutions was ultrapure water was purchased from Tekkim (Turkey). Triamcinolone stock solution ($4.5×10^{-3}$ mol/L) was prepared by directly dissolution of weighed amount of drug in 100% ethanol. BSA stock solution ($1.0×10^{-4}$ mol/L) was prepared by dissolving known amount of lyophilized powder in ultrapure water, than stock solution was standardized spectrophotometrically,using ε =45000 L/mol.cm at 278 nm. [27]. A Oheaus Starter 5000 pH meter equipped with a combined glass electrode was used to perform pH measurements.

The absorbance spectra of triamcinolone with BSA were recorded by Agilent Cary 100 double beam spectrophotometer equipped with quartz cells (1 cm path length) with jacketed cell holders, with temperature control within ± 0.1 °C. In order to evaluate the equilibrium constants of Triamcinolone-BSA interaction reaction spectrophotometric titrations were performed as follows: increasing volumes of BSA solution were added with a Hamilton microsyringe (Mitutoyo) to the dye solution directly in the spectrophotometric cell. During spectrophotometric titration, the salt concentration was kept at constant value and after each addition of BSA standard solution the spectra of the solution was recorded. The titrations were repeated for different temparatures and salt concentrations.

On the other hand, spectrofluorometric measurements were done by Cary Eclipse Fluorescence Spectrophotometer at room temperature. In order to perform fluorescent measurements, a serial of drug-protein solutions were prepared with a constant protein concentration and different drug concentrations at constant pH and salt concentration. Then, the spectrum of each solution were recorded.

RESULTS AND DISCUSSION

UV-Vis absorbance measurements
The absorbance spectrum of triamcinolone was taken between 200-400 nm with gradually increased drug amount and the spectrum is given Figure 1. A. Lambert-Beer plot of triamcinolone at 242 nm is demonstrated Figure 1.B.
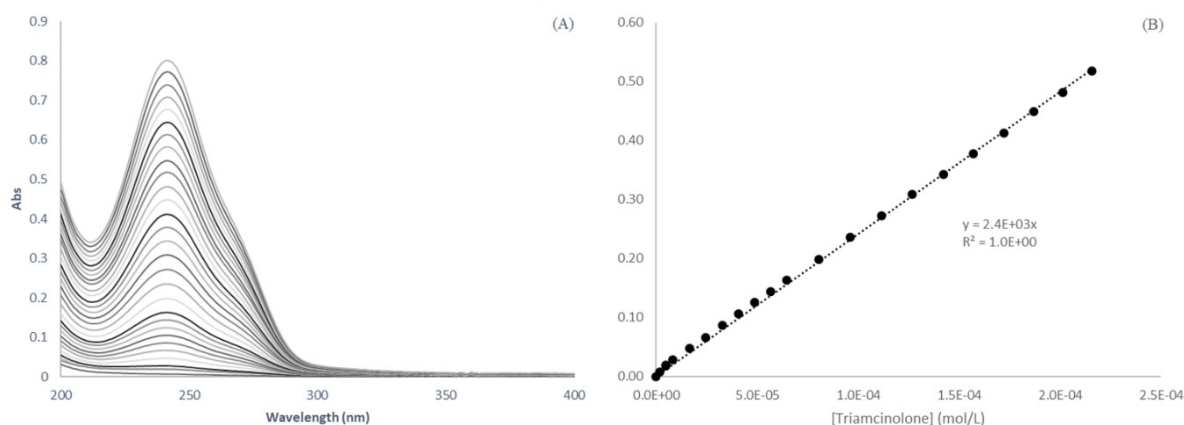
Figure 1. (A) The absorbance spectrum of triamcinolone; (B) The absorbance dependence on drug concentration at 242 nm; [Triamcinolone] =0 – 2.2 × 10^{-4} mol/L, pH =7.4 (PBS), [NaCl] = 0 mol/L, I = 0.01 mol/L, T = 25 °C.

In order to evaluate binding constant of Triamcinolone-BSA complex formation reaction, spectrophotometric titrations were performed. The absorbance spectrum was recorded with protein addition into drug solution and absorbance spectrum is given in Figure 2.
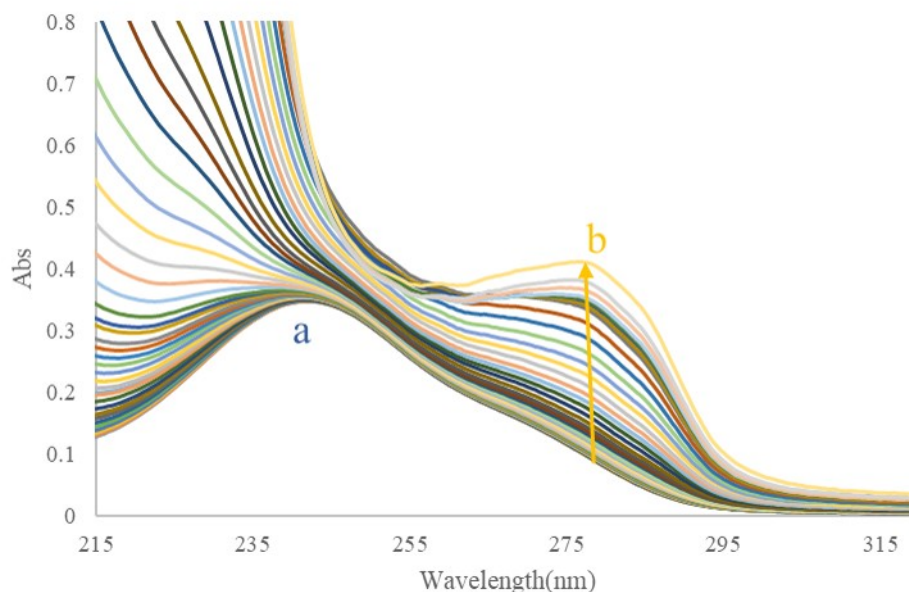
Figure 2. Normalized UV-Vis Spectrum of Triamcinolone-BSA Titration; [triamcinolone]= 2.2 × 10^{-5} a) [BSA] =0 mol/L, b)[BSA] = 4.8×10^{-5} mol/L, pH =7.4 (phosphate buffer), [NaCl] = 0.75 mol/L, T = 25 °C. After titration, the binding constant of studied system was determinated by Equation 1. (17)

$$\frac{C_D}{\Delta A} = \frac{\dfrac{1}{K\,\Delta\varepsilon}\times 1}{C_P} + \frac{1}{\Delta\varepsilon} \qquad (1)$$

In Eq. 1 C_D and C_P are respectively, analytical concentration of drug and protein while ΔA is the difference between after each protein addition measured Absorbance value to initial absorbance value of drug absence of protein, A_0, ΔA=A-A_0. The binding isotherm of spectrophotometric titration is given Figure 3.A. and analyses of binding isotherm according equation 1 is given Figure 3.B.
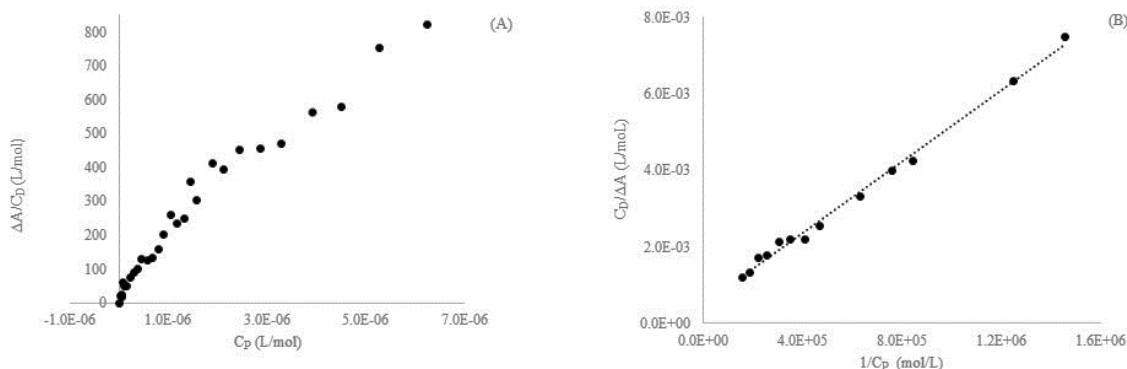
Figure 3. (A) The Binding isotherm for a spectrophotometric titration of Triamcinolone-BSA System; (B) Relevant Data Analysis according Eq. 1 ; [triamcinolone] = 2.2 × 10^{-5} [BSA] = 0-4.8 × 10^{-5} mol/L, pH = 7.4 (phosphate buffer), [NaCl] = 0.5 mol/L, T = 25 °C, λ = 250 nm.

In order to evaluate thermodynamic parameters as Standard Enthalpy change (ΔH°) and Standard Entropy change (ΔS°), for BSA-Triamcinolone interaction, the binding constants were evaluated at four different temperatures by performing spectroscopic titrations. The observed binding constant values analyzed according to Van't Hoff (Equation 2) in order to evaluate thermodynamic parameters as ΔH° and ΔS° (16).

$$ln\,K = \frac{-\Delta H°}{RT} + \frac{\Delta S}{R} \qquad (2)$$

The Van't Hoff diagram is given in Figure 4. In addition, free energy change is calculated by Equation 3 (5);

905

$$\Delta G\degree = \Delta H\degree - T\Delta S\degree \qquad (3)$$
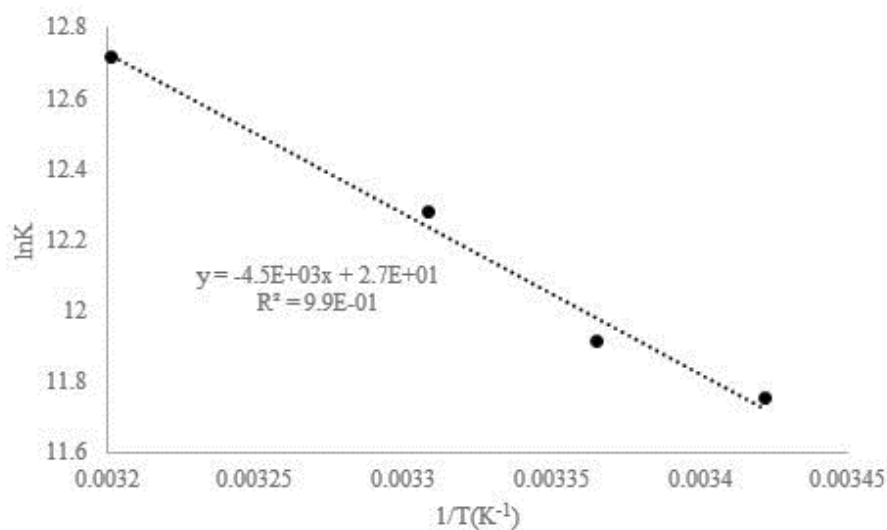
Figure 4. The Van't Hoff plot of BSA-triamcinolone system; pH = 7.4, I = 0.01 mol/L (PBS), [NaCl] = 0 mol/L.

The obtained binding constant values and thermodynamic parameters are presented in Table 1.

Table 1. Thermodynamic parameters for BSA-triamcinolone system at pH = 7.4 (PBS), I=0.01 L/mol.

T(K)	K(L/mol)	ΔG°(kJ/mol)
	1.27×10^5	
292.25		-28.4846
	1.49×10^5	
297.15		-29.5938
	2.15×10^5	
302.25		-30.7483
	3.33×10^5	
312.35		-33.0347
ΔH° (kJ/mol)		37.7
ΔS° (J/mol K)		226.4

The positive value of ΔH° and ΔS° parameters indicate hydrophobic interaction lead to complex formation between BSA-triamcinolone. Moreover, binding constant of BSA-triamcinolone system was determinated at constant temperature different salt concentration. The dependence of binding constant on salt concentration is given Table 2.

Table 2. Binding constant of BSA-Triamcinolone system by spectrophotometric titrations; pH =7.4(PBS), [NaCl]=0 – 0.76 mol/L, T=25°C.

[NaCl]	I	logI	K	logK
0	0.01	2.00	1.49×10^5	5.17
0.1	0.11	0.96	9.99×10^4	4.99
0.25	0.026	0.58	7.04×10^4	4.85
0.5	0.51	0.29	6.46×10^4	4.81
0.75	0.076	0.12	6.03×10^4	4.78

As seen from Table 2, augmentation of salt concentration caused a reduction in the binding constant of BSA-Triamcinolone system. The reason of this behavior could be explain with in the presence of chloride ions drug affinity to BSA decreases (4,8).

Fluorimetric Study
Triamcinolone - BSA interaction was also analyzed in a fluorimetric approach. The fluorescence spectrum of BSA solutions in the presence of different concentration of Triamcinolone was recorded at room temperature and the obtained spectrum is given in Figure 5.
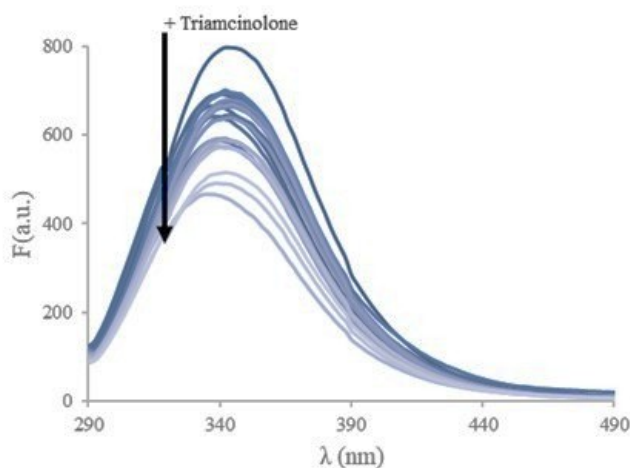
Figure 5. The fluorescence spectra of BSA - triamcinolone system C(BSA) = 5.0 × 10^{-7} mol.L^{-1}, C(triamcinolone) = 0 mol.L^{-1}-6 × 10^{-6} mol.L^{-1}, pH = 7.4 (Phosphate Buffer), I = 0.01 mol.L^{-1}, T = 25 °C, λ_{exc}=280 nm.

The emission intensity of BSA was diminished noticeably with gradually addition of drug solution which indicates triamcinolone binding to BSA. Also, with addition drug molecule in BSA cause to small blue shift of maximum fluorescence intensity of BSA from 342 nm to 338 nm. This behavior could explain assuming drug chromophore group movement in more hydrophobic zone.

The binding parameter of BSA-triamcinolone system was analyzed according to Benesi-Hildebrand equation (Equation 4) (18);
.

$$\frac{C_D \times C_P}{\Delta F} + \frac{\Delta F}{(\Delta \varphi)^2} = \frac{1}{K \Delta \varphi} + (C_D + C_P)\frac{1}{\Delta \varphi} \qquad (4)$$

In Equation 4, C_D is total analytical protein concentration and C_P is total analytical drug concentration. In order to calculate the binding constant by Eq. 4 iterative procedure was

performed. The binding isotherm and Benesi-Hildebrand diagrams are given respectively in Figure

6.A and Figure 6.B.
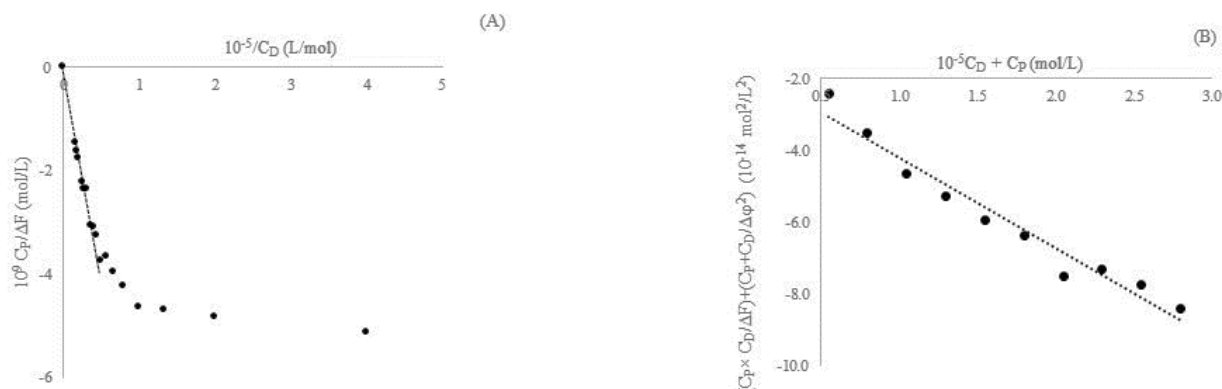
Figure 6. (A) The binding isotherm of spectrofluorometric measurements of BSA-triamcinolone system; (B) Benesi-Hildebrand diagrams for BSA-triamcinolone system; C(BSA) = 5.0×10^{-7} mol.L^{-1}, C(Triamcinolone)=0 mol.L^{-1} – 6×10^{-5} mol.L^{-1}, pH = 7.4 (phosphate buffer), I = 0.01 mol.L^{-1}, T = 25 °C, λ_{exc} = 280 nm.

The binding constant value was evaluated as K=1.47×10^5 L/mol by spectrofluorometric measurement good agreement with K=1.49×10^5 L/mol obtained by spectrophotometric measurement under same experimental conditions (T=25°C, I=0.01 M, pH=7.4).

On the other hand, BSA quenching by drug molecule was evaluated by using Equation 5 (13);

$$\frac{F_0 - F}{F} = \frac{1}{f K_{SV}(Q)} + \frac{1}{f} \tag{5}$$

where, K_{SV} is Stern-Volmer constant of BSA-Triamcinolone system, where F_0 is intensity of BSA absence of drug while F is intensity of BSA in the presence of drug. Q is drug concentration and f is the fractional maximum fluorescence intensity of protein. The Stern-Volmer plot is given Figure 7.
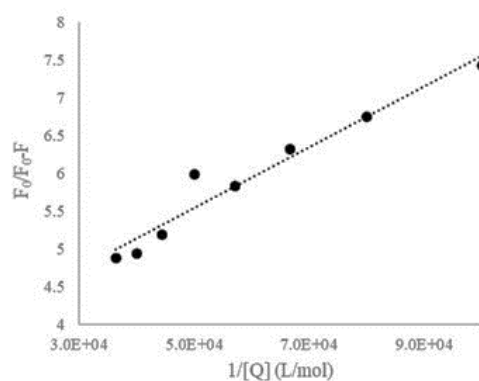
Figure 7. Stern-Volmer Plot for BSA-triamcinolone system obtained by fluorescence measurement. C(BSA) = 5.0×10^{-7} mol.L^{-1}, pH=7.4 (phosphate buffer), I = 0.01 mol.L^{-1}, T = 25 °C, λ_{exc}=280 nm.

The Stern-Volmer constant being equal to the binding constant causes when BSA-Triamcinolone complex does not fluoresce (16). Therefore, Stern-Volmer constant determined different from binding constant as 8.8×10^4 L/mol. Even if thermodynamic results were pointed hydrophobic interactions as a main force of binding, increase of salt concentration caused negative effect on binding constant. This

effect might explain with Triamcinolone displacement with chloride ions (4,8).

CONCLUSION

In the present study, BSA-Triamcinolone interaction was investigated by spectrophotometric and spectrofluorometric measurement. The binding

constant of system was determined for both methods in to order of 10^5 which indicate binding affinity of Triamcinolone to BSA is quite high. Moreover, the obtained positive thermodynamic parameters as like $\Delta H°$ and $\Delta S°$ indicate BSA-Triamcinolone interaction occurs due to hydrophobic forces. On the other hand, negative free energy change point to spontaneity of studied reaction. The interaction studies were repeated at different salt concentration to understand salt effect on studied system.

REFERENCES

1. Fasano M, Curry S, Terreno E, Galliano M, Fanali G, Narciiso P, Notari S, Ascenzi P. The extraordinary ligand binding properties of human serum albumin. IUBMB, Life. 2005; 57: 787 – 96. Doi: 10.1080/15216540500404093.

2. Rizzuti B, Bartucci R, Pey AL, Guzzi R. Warfarin increases thermal resistance of albumin through stabilization of the protein lobe that includes its binding site. Archives of Biochemistry and Biophysics. 2019; 676:(108123) 1-8. Doi: 10.1016/j.abb.2019.108123.

3. Pilati D, Kenneth A. Howard Albumin-based drug designs for pharmacokinetic modulation. Expert Opinion on Drug Metabolism & Toxicology. 2020; Doi: 10.1080/17425255.2020.1801633.

4. Wilting J, Van Der Giesen WF, Janssen LHM. The effect of chloride on the binding of warfarin to albumin as a function of pH. Biochemical Pharmacology. 1981:1025-31. Doi:10.1016/j.proeng.2010.09.152.

5. Kandagal PB, Ashoka S, Seetharamappa J, Shaikh SMT, Jadegoud Y, Ijare OB. Study of the interaction of an anticancer drug with human and bovine serum albumin spectroscopic approach. Journal of Pharmaceutical and Biomedical Analysis. 2006; 41: 393–9. Doi: 10.1016/j.jpba.2005.11.037.

6. Fender AC, Dobrev D. Bound to bleed: How altered albumin binding may dictate warfarin treatment outcome. IJC Heart & Vasculature. 2019; 22: 214-5.

7. Al-Harthi S, Lachowicz JI, Nowakowski ME. Towards the functional high-resolution coordination chemistry of blood plasma human serum albumin. Journal of Inorganic Biochemistry. 2019; 198: (110716) 1-15.

8. Seedher N, Bhatia S. Mechanism of interaction of the non-steroidal antiinflammatory drugs meloxicam and nimesulide with serum albumin. Journal of Pharmaceutical and Biomedical Analysis. 2005; 39: 257-69.

9. Sharifi M, Dolatabadi JEN, Fathi F, Rashidi M, Jafari B, Tajalli H, Rashidi MR. Kinetic and thermodynamic study of bovine serum albumin interaction with rifampicin using surface plasmon resonance and molecular docking methods. Journal of Biomedical Optics. 2017; 22: (037002)1-6. Doi: 10.1117/1.JBO.22.3.037002.

10. Raghav D, Mahanty S, Rathinasamy K. Characterizing the interactions of the antipsychotic drug trifluoperazine with bovine serum albumin: Probing the drug-protein and drug-drug interactions using multi-spectroscopic approaches. Spectrochimica Acta Part A: Molecular and Biomolecular Spectroscopy. 2020; 226: (117584) 1-14. doi: 10.1016/j.saa.2019.117584.

11. Chakraborty B, Basu S. Interaction of BSA with proflavin: A spectroscopic approach. Journal of Luminescence. 2009; 129: 34-9. Doi: 10.1016/j.jlumin.2008.07.012.

12. Jha NS, Kishore N. Thermodynamic studies on the interaction of folic acid with bovine serum albumin. The Journal of Chemical Thermodynamics. 2011; 43: 814-21. Doi: 10.1016/j.jct.2010.12.024.

13. Tian J, Liu J, Hu Z, Chen X. Interaction of wogonin with bovine serum albumin. Bioorganic & Medicinal Chemistry. 2005; 13: 4124–9. Doi: 10.1016/j.bmc.2005.02.065.

14. Goyal RN, Gupta VK, Chatterjee S. A sensitive voltammetric sensor for determination of synthetic corticosteroid triamcinolone abused for doping. Biosensors and Bioelectronics. 2009; 3562-8. Doi: 10.1016/j.bios.2009.05.016.

15. Chaires JB. Energetics of Drug–DNA. Current Opinion in Structural Biology. 1998; 8:314-20.

16. Macii F, Salvadori G, Bonini R, Giannarelli S, Mennucci B, Biver T. Binding of model polycyclic aromatic hydrocarbons andcarbamate-pesticides to DNA, BSA, micelles and liposomes. Spectrochimica Acta Part A: Molecular and Biomolecular Spectroscopy. 2019; 223: (117313)1-9. Doi: 10.1016/j.saa.2019.117313.

17. Aydinoglu S, Biver T, Figuccia S, Fiore T, Montanaro S, Pellerito C. Studies on DNA interaction of organotin(IV) complexes of meso-tetra(4-sulfonatophenyl)porphine that show cellular activity. Journal of Inorganic Biochemistry. 2016; 163: 311–7. Doi: 10.1016/j.jinorgbio.2016.06.030

18. Beccia MR, Biver T, Pardini A, Spinelli J, Secco F, Venturini M, , Jacopo Spinelli, Fernando Secco, Marcella Venturini, Vázquez Busto N, Cornejo Lopez MP, Martin Herrera VI, Gotor RP. The

fluorophore 4',6-diamidino-2-phenylindole (DAPI) induces DNA folding in long double-stranded DNA. Chemistry - An Asian Journal. 2012; 7; 1803-10. Doi: 10.1002/asia.201200177.

Physicochemical Properties and Fatty Acids Composition of Sudanese *Moringa oleifera* Seed Oil

Abeer A. Idris[1] ✉ iD, **Azhari H. Nour[1]*** ✉ iD, **Omer A. Omer Ishag[1]** ✉ iD,
Mahmoud M. Ali[1] ✉ iD, **Ibrahim Y. Erwa[1]** ✉ iD, **Abdurahman H. Nour[2]** ✉ iD

[1] International University of Africa (IUA), Department of Applied and Industrial Chemistry, Faculty of Pure and Applied Sciences, 12223, Khartoum, Sudan.
[2] Universiti Malaysia Pahang (UMP), Faculty of Chemical and Process Engineering Technology, College of Engineering Technology,26300, Gambang, Malaysia.

Abstract: *Moringa oleifera* is a robust and fast-growing tree considered as one of the most beneficial trees worldwide since almost all parts of it are used as food, medicine, and for industrial purposes. This study aimed to investigate the physicochemical properties and fatty acid composition of *M. oleifera* seed oil. The oil was extracted by Soxhlet using n-hexane; the physicochemical properties of the seed oil were assessed by standard and established methods, as well, the fatty acid composition of the seed oil was determined by GC-MS. The golden yellow oil with characteristic odor obtained from the seeds had the following physicochemical properties: yield, 42.87%; freezing point, 0 °C; melting point, 21 °C; boiling point, 225 °C; refractive index (25 °C), 1.447; iodine value, 96.6 g/100g of oil; peroxide value, 7.6 meq.O_2/kg of oil; free fatty acids, 0.07%; acid value, 1.4 mg of KOH/g of oil; saponification value, 185.2 mg KOH/g of oil; unsaponifiable matter, 3.2; moisture and volatile value, 4.91 (wt.%); density, 0.900 g/cm^3; viscosity, 60.99 mm^2/s; specific gravity, 0.907. The fatty acids composition showed that oleic-acid (51.74%) was the major fatty acid and followed by behenic- (10.54%), palmitic- (9.20%), stearic- (8.46%), arachidic- (6.41%), gondic- (4.88%), lignoceric- (3.08%) and palmitoleic acid (2.85%). Therefore, more and advanced research should be undertaken for this abundant source of natural oil for edible oil and possible industrial applications.

INTRODUCTION

Moringa oleifera Lamarck (fam. *Moringaceae*) tree is considered as one of the most beneficial trees in the world since all parts of this plant exploited as food, medicine, and for industrial purposes (1). *M. oleifera* is a fast-growing softwood tree native to sub-Himalayan tracts of Northern India and is one of 13 species within the same genus, and has become the most spread in tropical and subtropical regions at up to 2000 m (1). Furthermore, it is widely cultivated due to its high adaptability to environmental conditions (1,2). *M. oleifera* seed oil is a sustainable source of renewable energy for biodiesel production (3) due to its high content of monounsaturated fatty acids (4). There are enormous efforts to spread the use and cultivation of *M. oleifera* in many countries since it is a significant source of fats, proteins, β-carotene, vitamin C, iron, potassium and other nutrients with low toxicity of seeds and leaves (5). Some parts of this plant have drawn much attention and been studied for its various biological activities, including anti-atherosclerotic, immune-boosting, anti-

cardiovascular diseases, antiviral, antioxidant, antimicrobial, anti-inflammatory properties, and tumor-suppressive effects in skin papillomagensis, hepatocarcinoma, colon cancer, and myeloma (5). *M. oleifera* oil is high in oleic acid (>70%) and commercial common as "ben oil" or "behen oil" due to its content of behenic acid (6). Therefore, this study is aimed to investigate the physicochemical properties and fatty acid composition of Sudanese *M. oleifera* seed oil to increase the economic feasibility of future commercial cultivation and products of this tree.

MATERIALS AND METHODS

M. oleifera Seeds sample
M. oleifera seeds were obtained on 15 October 2017 from College of Forestry and Range Science, Sudan University of Science and Technology, Khartoum, Sudan. The seeds were dried and ground into coarse powder by using an electrical blender (Panasonic, Japan). Before grinding, the percentage moisture content of the plant materials was analyzed via a moisture content analyzer. The samples were sealed and kept in a desiccator to avoid any fungal activities.

Seeds Oil Extraction
The fixed oil (seed oil) was extracted via Soxhlet by using n-hexane and a mild extraction temperature was chosen to avoid thermal degradation (7). The crushed seeds were placed in the drying oven at 40 °C for 30 min prior to extraction. Constant heat was applied through the heating mantle and the extraction was conducted for a minimum extraction of 6 h. After complete extraction and cooling, the obtained oil was filtered through filter paper. The solvent was evaporated via a rotary evaporator, further dried under open air in a dark area. The yield of the oil was calculated and stored in

hermetically closed dark bottles and kept in a refrigerator for further physicochemical study.

Determination of the Lipid Content
The lipid content of the oil was calculated as based on dry seed weight (50 g) that were used in the extraction and expressed in percentage. The mass (g) of the acquired oil was obtained by an experimental balance Mettler Toledo (Switzerland) with ± 0.001 g accuracy and the lipid content was determined according to the following (Equation 1).

$$\%Lipid = \frac{weight\ of\ oil\,(g)}{weight\ of\ sample\,(g)} \times 100 \quad (1)$$

Physical State, Color, Odor, Freezing, Melting and Boiling Points Determination
Physical state determined at 25 °C and color of the oil was determined visually whereas odor was determined using sensation through volatilized smell. For freezing point, a clear glass vial was filled with oil, a thermometer was immersed into the oil and the oil was solidified through the usage of ice blocks. The solidification temperature was recorded as the freezing point. While for melting point, the solidified oil was melted over a water bath (29 °C) and the melting point was recorded. Once more, a clear glass vial was filled with 10 mL of the oil and a thermometer was inserted, then the vial exposed to heat on a heating mantle and the oil was observed, where it starts circulating leading to boiling; the temperature at this point was recorded as the boiling point (8).

Density and Refractive Index Determination
The small empty vial was weighed and was filled with a known amount of oil up to the brim. The vial was weighed once more and the density was determined as follows (Equation 2):

$$Density,\ \rho = \frac{\left[weight\ of\ vial-oil\,(g)\right]-\left[weight\ of\ empty\ vial\,(g)\right]}{volume\ of\ oil} \quad (2)$$

The refractive index (RI) of the oil was determined according to standard method described by Jessinta et al., and Ustun-Argon et al. (9,10) with slight modifications. This index was determined at 25 °C by Pen Refractometer (Atago, Japan) with resolution and accuracy value of 0.1%, and ± 0.2% in 10-60 °C. The pen tip was dipped into the sample and the start key was pressed to obtain the reading. The measurement was repeated in triplicate and the average value was calculated.

Acid Value Analysis

The AV was calculated through direct titration methods of oil against standard potassium hydroxide in an alcoholic medium according to the method described by Jessinta et al. (9) with some modifications. A mass of 0.5 g of oil was weighed into a 250 mL conical flask and 50 mL of freshly neutralized hot ethyl alcohol and 1 mL of phenolphthalein indicator solution were added. The mixtures were boiled around 5 min and titrated against standardized potassium hydroxide (0.24 M). The AV was then calculated according to the following (Equation 3).

$$AV = \frac{\left[56.1\right]\left[titration\ of\ standard\,(mL)\right]\left[molarity\ of\ standard\,(M)\right]}{weight\ of\ sample\,(g)} \quad (3)$$

Fatty Acids Composition Analysis
The crude oil was analyzed as methyl ester to determine the fatty acid composition; where the oil was converted into fatty acid methyl ester via a transesterification reaction. A solution of (2 M) KOH (methanolic potassium hydroxide) was prepared. An amount of 2 mL of oil sample was dissolved in 10 mL of n-hexane in a test tube. About 1 mL of KOH was added into the same test tube and vortexed.

The n-hexane layer was collected, washed twice with 4 mL of water after 15 min, and further dried over anhydrous sodium sulfate. The fatty acids composition analysis performed using a GC system coupled with an MS detector as method described by Jessinta et al, Yabalak and Tegın et al. with slight modification (9,11,12). The chromatography equipment and settings details are tabulated in Table 1.

Table 1: Chromatographic settings for the analysis of *M. oleifera* oil methyl ester.

Parameters	Settings
Chromatograph	Agilent Technologies 7890A GC Systems coupled with MS detector
Auto-sampler	GC autosampler
Column	Nonpolar capillary DB-1 of 100% dimethyl-polysiloxane (30 m, 0.25 mm i.d, film thickness 0.25 µm)
Carrier gas	Helium
Gas flow rate	1 mL/min
Injector mode	Splitless mode
Injector temp.	250 °C
Inject volume	1 µL
Temp. program	60 °C for 3 min, 240 °C at the rate of 3 °C/min and held for 10 min
Runtime	93 min
Lab data system	NIST Library Chem Station software

The composition of individual fatty acid was stated as a percentage. The percentages of saturated and unsaturated fatty acids were calculated by totaling the percentage of fatty acids detected via the analysis of fatty acid composition. The sum percentage of saturated fatty acids represented as total saturated fatty acids, whereas the sum of all unsaturated (mono- and polyunsaturated) represented as total unsaturated fatty acids (9).

Free Fatty Acid Analysis
The method described by Ouilly et al. (13), with slight modifications was adapted to determine the free fatty acids. An amount of 0.2 g of sample was weighed in 250 mL erlenmeyer flask with the addition of 50 mL of hot neutralized alcohol and 2 mL of phenolphthalein indicator. The solution was swirled to dissolve and titrated with standard sodium hydroxide (0.24 M) until the first permanent pink color that persists for 30 s. The volume of titration required for the changes was recorded and the free fatty acid (FFA) percentage was calculated as follows (Equation 4):

$$FFA\ as\ oleic(\%) = \frac{\left(Titration\ volume\ of\ standard\ (mL)\right)(28.2)}{Weight\ of\ Sample\ (g)} \quad (4)$$

Iodine Value Analysis
The Iodine Value (IV) was determined through the method described by Jessinta et al. (9), with a slight modification via the Wijs reagent. An amount of sample was filtered through a dry filter paper and 0.35 g of sample was transferred into a clean, dry, 500 mL glass-stoppered flask containing 20 mL of carbon tetrachloride, and 25 mL of the Wijs solution was pipetted into the flask. The mixture was swirled and allowed to stand in the dark for 30 min. Potassium iodide solution (20 mL) and recently boiled and cooled water (100 mL) were added and the mixture was titrated with sodium thiosulfate (0.11 M) until the yellow color almost disappears. Starch was added and the titration was continued until the blue color disappears entirely. At the end of the titration, the stoppered container was shaken vigorously therefore any iodine remaining in solution may be absorbed by the potassium iodide to for the triiodide. Blank determination conducted in the same manner and condition and the IV calculated by (Equation 5).

$$Iodine\ Value = \frac{\left(Titration\ of\ blank - sample\ (mL)\right)\left(Molarity\ of\ standard\ (M)\right)(12.69)}{Weight\ of\ Sample\ (g)} \quad (5)$$

Peroxide Value Analysis
The method described by Jessinta et al. (9), with slight modification applied to determine the Peroxide Value (PV). An amount of 0.50 g of sample was weighed into 250 mL of stoppered conical flask together with 30 mL of acetic acid-chloroform mixture and swirled to dissolve. The mixture was then added to 0.5 mL saturated potassium iodide

and allowed to stand in the dark with occasional shaking for 1 min and 30 mL of water were added. The liberated iodine in the mixture was titrated with sodium thiosulfate (0.11 M) with vigorous shaking until the yellow color almost disappeared. Then, 0.5

mL of starch indicator was added and titration was continued until the blue color disappears. The PV was expressed as milliequivalent of peroxide oxygen per kg sample (meq/kg) via the following (Equation 6).

$$Peroxide\ value = \frac{(Titration\ of\ standard\ (mL))(Molarity\ of\ standard\ (M))(100)}{Weight\ of\ Sample\ (g)} \quad (6)$$

Moisture and Volatile Matter Analysis
Moisture and volatile matter were analyzed according to air oven method of AOCS and the method described by Jessinta et al. (9). About 5 g of oil was weighed on a previously dried and tarred dish. The dish was covered with a loose lid and was heated in the oven at 105±1 °C for 1 h. The dish

was removed from the oven, cooled in a desiccator, and weighed. The plate was re-heated for the period of 1 h and the cooling and weighing process was repeated. The process was repeated until the weight change between two observations does not exceed 1 mg. The following equation 7, used to calculate the observations.

$$Moisture\ and\ volatile\ matter\ (\%) = \frac{(Loss\ of\ material\ on\ dry\ (g))(100)}{Weight\ of\ material\ taken\ for\ test\ (g)} \quad (7)$$

Saponification Value Analysis
The saponification value of the oil sample was estimated using the Official Method of AOCS (9). Accurately, 2 g of the oil sample was weighed into a 250 mL conical flask. A volume of 25 mL of potassium hydroxide (1 N) was added, and then the flask and the content was refluxed for one hour. Simultaneously, another conical flask containing only 25 mL of potassium hydroxide (1 N) was prepared which served as a blank. The condenser connected and the content heated gently, but

steadily for one hour. After the condenser and the flask have cooled, but not sufficiently to forming a gel, the content washed with a small amount of water and the condenser was removed. Then a few drops of phenolphthalein solution added to the flask and the sample was titrated with hydrochloric acid, (0.5 N) HCl until the pink color disappeared. The volume of the hydrochloric acid was recorded and the saponification value expressed as follows (Equation 8):

$$Saponification\ value\ (SV) = \frac{(56.1)(B-S)(C)(N\ of\ HCl)}{Weight\ of\ Sample\ (g)} \quad (8)$$

where, B and S are the volumes of hydrochloric acid required by blank and sample, respectively, and N is the concentration of hydrochloric acid.

Unsaponifiable Matter Analysis
The unsaponifiable matter analysis performed according to the method described by Jessinta et al. (9), with some modification. A volume of 50 mL of alcoholic potassium hydroxide was added into a conical flask containing 5 g of oil sample and was boiled under reflux conditions for one hour until a transparent medium is formed. The medium was then transferred into a separating funnel and was washed with petroleum ether allowing the layer to

separate. The lower layer was collected and the top layer was continued washing for another 3 times with around 50 mL of solvent per wash. The etheric extracts were combined and further washed with alcohol and water, 25 mL each. The etheric solution was concentrated to 5 mL; then 2 mL of acetone was added with some heat under the water bath to remove the solvent and further dried at 100 °C for 30 min until a constant weight is obtained. Then the residue was dissolved in 50 mL of warm neutralized ethanol with phenolphthalein indicator and titrated with sodium hydroxide (0.02 M). The weight of FFA and unsaponifiable matter values were calculated according to the following Equations 9 and 10.

$$Weight\ of\ FFA\ in\ the\ extract = (0.282 \times Titration\ of\ standard\ (mL)(Molarity\ of\ standard\ (M)) \quad (9)$$

$$Unsaponifiable\ matter = \frac{100((Weight\ of\ residue) - (Weight\ of\ FFA\ in\ the\ extract))}{Weight\ of\ Sample\ (g)} \quad (10)$$

Statistical Analysis
The Statistical analysis of the results was done using MS Excel (2007) – version 12.0.4518.1014. The results performed in three repetitions and expressed as mean ± standard deviation.

RESULTS AND DISCUSSION

Lipid Content, Physical State, Color, and Odor
Table 2 shows various physicochemical properties of the *M. oleifera* seed oil. In general, the results showed that *M. oleifera* seed was found to be rich in oil with an average yield of 42.87% (w/w); and this

value is represented in terms of lipid content, and the oil was highly unsaturated with a high FFA. The obtained oil is liquid at room temperature of 25 °C, golden yellow in color with a nutty odor. The freezing, melting, boiling points, specific gravity and viscosity were 0 °C, 21 °C, 225 °C, 0.9070 and 60.99 mm^2/s, respectively.

The obtained yield is agreeable with the literature stating that this plant's seed contains 26.2-40.90% oil on dry matter basis. Previously (1,7,14), a yellow color was reported for *M. oleifera* seed oil and researchers showed that the variation in the color intensity of oil from the same plant species, but from diverse location might be attributed due to the existence of various pigments such as the chlorophyll content (15). The green color of the immature seeds vanishes subsequent maturation resulting in chlorophyll retention. Besides, there is also a report stated that the presence of moisture contents at greater levels affects the color of the oil, whereby the moisture raises the chlorophyll content and thus contribute in an increment of color intensity (15). The normal and thermal oxidation process of oil can also contribute towards the deterioration of lipids, and thus it might influence the color changes of the oil (15,16). From Table 2 it

can be seen that the viscosity of *M. oleifera* seed oil is 60.99 mm^2/s which is considered high viscosity oil and it slightly lower than crude rubber seed oil (40.86 mm^2/s) and crude palm oil (38.1 mm^2/s). Therefore, it is not advisable to use *M. oleifera* seed oil directly as a fuel, because viscosity is an essential property that has to be monitored in vegetable oil to meet the gasoline standard.

Generally, vegetable oil is highly viscous. Even though there are suggestions made by some authors reporting the viability of running raw vegetable oil as an alternative fuel in compression-ignition engines with slight modification and maintenance, but this will create problems related to long-term durability test due to high viscosity and low volatility of such oils. Particularly at low temperatures, viscosity increases influence the fuel's fluidity, which result in disruption of the injection of the fuel operation equipment. Furthermore, high viscosity also promotes soot formation and deposition on the engines due to poor fuel atomization. In contrast, high viscous oil has also its advantages. They afford additional lubrication of the injector and avoid leakage and exhaustion generated by fuel injection pumps that fits inaccurately resulted from low viscous oil (17).

Table 2: Physicochemical properties of *M. oleifera* seed oil.

Components	Units	Experimental Values*
Yield	%	42.87
Color	-	Golden yellow
Odor	-	Nutty smell
Freezing point	°C	0
Melting point	°C	21
Boiling point	°C	225
Density point at 25 °C	g/cm^3	0.90052
Viscosity	mm^2/s	60.99
Specific gravity		0.9070
Refractive index at 25 °C	-	1.44732
Acid value (% FFA as oleic)	mg KOH/g of oil	1.4
FFA		
Oleic	%	50.74
Behenic	%	10.54
Palmitic	%	9.20
Stearic	%	8.46
Arachidic	%	6.41
Gondic	%	4.88
Iodine value (IV)		96.6
Peroxide value	meq.O$_2$/kg of oil	7.6
Unsaponifiable matter	wt. %	3.2
Saponification value	mg KOH/g of oil	185.2
Moisture and volatile matter	wt. %	4.91
Total Saturated Fatty Acid	wt. %	38.76
Total Unsaturated Fatty Acid	wt. %	61.17

* Values recorded as mean average

Density, Viscosity, and Specific Gravity
The density recorded for the oil in this study is 0.90052 g/cm^3. The literature had reported value ranged from 0.195 to 1.024 g/cm^3 that is agreeable to the obtained result (18). The density differs as

the concentration of the wall material varies at which more heavy material fits into spaces between the particles and causes an increase in mass and thus contribute towards high density (19).

Idris AA et al. JOTCSA. 2020; 7(3): 911-920.

RESEARCH ARTICLE

Refractive Index

The RI value is acceptable according to the amount of unsaturated fatty acids and long-chain hydrocarbon. The RI of the *M. oleifera* oil is 1.447 and this attributed by the amount of unsaturated fatty acid, length of the hydrocarbon chain, molecular weight and degree of unsaturation as well as conjugation (20). Previously, Chatepa et al. (14) reported the RI for *M. oleifera* seed oil is in the range of 0.60-1.47, which closed to our obtained result.

Acid Value

Besides, the acid value (AV) is the relative measure of rancidity as FFAs that are formed during decomposition or hydrolysis of oil glycerides due to the action of moisture, temperature and/or lipolytic enzyme lipase. The AV obtained in this study is 1.4 mg KOH/g and this result is in the range when compared to the study recorded by Adegbe et al. (21) and Chatepa et al. (14) their reported values were 6.73 and 9.46 ± 0.02 mg KOH/g, respectively. Oxidation and hydrolysis processes are also factors that led towards increment in AV as the percentage of unsaturated fatty acids increase (7).

Iodine Value

Among various factors of oil classification, the drying quality of the oil can be considered as one of the factors of oil classification; it could be non-drying, semi-drying or drying oil through the analysis of the IV (22). The IV for the current study was 96.6 g/100 g, and it suggests that it is a non-drying oil and it is comparable to the standard IV of less than 100 g of I_2/100 g as per its physical state of remaining liquid at 25 °C, low aeration (23). The low IV represents the fewer amounts of unsaturated bonds and thus the oil has fewer tendencies to go through oxidative rancidity (7). Ogunsina et al. (24) reported that the iodine value for cold-pressed and n-hexane-extracted *Moringa* seed oils (CPMSO and HEMSO) were found to be 67.8 and 68.5 g of I_2/100 g oil, our obtained results for IV was found higher than their results. Furthermore, in general, researchers reported IV for *M. oleifera* ranged from 34.11-252.34 g I_2/100 g (5,14,25).

Peroxide Value

The oil had also undergone some chemical decomposition process whereby the obtained PV is 7.6 meq O_2/kg; and was determined immediately after the extraction of the oil. PV indicates the rancidity process whereby the higher the PV, the higher is the oxidation level and the deterioration of lipids (26). Theoretically, oil that shows a high amount of PV is more prone to undergo rancidity that affects the total quality of the oil (20). A low peroxide value increases the appropriateness of the oil for long storage because of low level of oxidative and lipolytic activities. Adegbe et al. (21) reported that the PV 2.60 meq/kg for this oil which is lower than our result. Generally, many previous studies

reported that the PV was found to between range from 1.67-10.47 meq/kg (5,14).

Moisture and Volatile Matter

Besides, the moisture and volatile matter analysis prove that the oil contains a low amount of moisture and volatile matter, whereby the value recorded is 4.91 wt.% thus, the low moisture content of the oil serves as an indication that the activities of the micro-organisms would be reduced and thereby increases the shelf life of the oil. The presence of water or moisture contributes towards hydrolysis in breaking up of triglycerides into glycerol and FFAs. Therefore, both oxidation and hydrolysis reduce the amount of unsaturated FFA and thus contributing towards the reducing of IV and average molecular weight and increasing in the AV (7). The moisture content reported previously, Abiodun et al. (27), Adejumo et al. (28), Leone et al. (1) and Orhevba et al. (6) reported that the moisture has range 0.60-20%.

Saponification Value and Unsaponifiable Matter

The saponification value (SV) used to know the amount of free fatty acid present in the oil, and amount of free fatty acid estimated by determining the quantity of alkali that should be added to the fat to make it neutral. The SV for studied oil 185.2 mg KOH/g and it is agreeable to that reported in literature, which is 55.91-230.81 (1,5,7,14,25,27–30). The unsaponifiable matter is that portion of oils and fats which is soluble in conventional fat solvents but is unsaponified via caustic alkali. Unsaponifiable matter does not react with bases during the formation of soap such as hydrocarbon, pigments, waxes, higher molecular weight alcohols, and sterols (AOCS Ca 6a-40, 1998). The unsaponifiable matter value for *M. oleifera* seed oil was 3.2 wt.%. Previously reported unsaponifiable matter *M. oleifera* seed oil which is determined by titration with sodium hydroxide solution in alcoholic, found to in a range between 0.60-0.83 (5, 27). The current studied oil showed higher unsaponifiable matter than the reported value. Therefore, due to the small value of unsaponifiable matter (< 2 wt.%), *M. oleifera* could be suitable in the application of biodiesel production (31). From the current study, it could be said that the oil had undergone some oxidation and hydrolysis process as indicated by the value of unsaturated fatty acids. This oxidation process might be influenced by storage of the oil whereby the presence of air in the bottle is in contact with the oil surface. Thus, the oxidation process converts the triglycerides into peroxides and hydroperoxides.

Free Fatty Acids, Fatty Acid Composition, Percentage of Saturated and Unsaturated Fatty Acid

Acids with long hydrocarbon chains; which is the main constituent of seed oil and known to be a

major parameter that differentiates the physicochemical properties of the seed oils. In this study, twenty-one different fatty acids were detected and include both saturated and unsaturated. The sequence arrangement according to the increasing percentage (>1%) of fatty acid is oleic-, behenic-, palmitic-, stearic-, arachidic-, gondic-, lignoceric- and palmitoleic acid; their percentage were 51.74, 10.54, 9.20, 8.46, 6.41, 4.88, 3.08 and 2.85%, respectively, in addition to kovats index for each as shown in Table 3.

The total percentage of fatty acids chains were 99.93 wt.%. All the values are represented as the relative percentage area from the sum of all identified peaks. The overall results of this analysis showed that the unsaturated fatty acid (UFA) makes 61.17 wt.% of the compositions, whereby the monounsaturated fatty acids (MUFA) are 60.31wt. %, polyunsaturated fatty acids (PUFA) are 0.86 wt. %; and the saturated fatty acids (SFA) were 38.76 wt.%, as shown in Figure 1. In general, our obtained results agreed to the results obtained by Lalas and Tsaknis (32) who claimed that oleic acid (71.60%) was a major component of *M. oleifera* seed oil, in addition to present of palmitic and behenic acid both up to 6.4%. Also, the results obtained by Adegbe et al. (21) mainly oleic acid (22.51%) and erucic acid (1.98%), palmitic (10.64%), stearic acid (6.07%), arachidic acid

(2.21%) and docosanoic (behenic acid) (1.03%); confirmed the presences of the same acid, but the percentage of acids were slightly different from our obtained results.

Pereira et al. (25) results were also agreed our obtained results, as oleic acid was the major component in the extracted oil; but there was a slight difference in the percentage of these acids with our obtained results. Janaki (35) obtained results showed oleic acid, palmitic acid, stearic acid, linoleic acid, margaric acid, and α-linolenic acid. The percentages were 77.40 ± 0.40, 12.97 ± 0.15, 2.95 ± 0.04, 1.40 ± 0.01, 1.40 ± 0.15 and 1.39 ± 0.01, respectively. Where these results agreed our obtained results for oleic acid as major components, palmitic closed to and stearic acid was lower than our results, but for margaric acid and linoleic acid, results were very low, while linolenic acid not detected in our obtained results. The differences in the results obtaining by the researchers can be attributed to many factors, like environmental conditions, geographical origin, soil, cultivation climate, harvesting time, maturity, and the drying process (9,36).

Fatty acid composition of *M. oleifera* seed oil reported in the literature is shown in Table 4; our results agreed with many previously reported results.

Table 3: Fatty acid composition of *M. oleifera* seed oil.

Fatty acid	Formula	Structure	%	KI
Myristic	$C_{14}H_{28}O_2$	C14:0	0.23	1750[a]
5-Octadecenoic	$C_{18}H_{34}O_2$	C18:1	0.02	2383[a]
Pentadecylic	$C_{15}H_{30}O_2$	C15:0	0.02	1843[a]
Palmitoleic	$C_{16}H_{30}O_2$	C16:1	2.85	1936[a]
Palmitic	$C_{16}H_{32}O_2$	C16:0	9.20	1965[a]
Margaric	$C_{17}H_{34}O_2$	C17:0	0.19	2039[a]
Linoleic	$C_{18}H_{32}O_2$	C18:2	0.86	2109[a]
Oleic	$C_{18}H_{34}O_2$	C18:1	51.74	2115[a]
Stearic	$C_{18}H_{36}O_2$	C18:0	8.46	2170[a]
Arachidic	$C_{20}H_{40}O_2$	C20:0	6.41	2380[a]
Heneicosylic	$C_{21}H_{42}O_2$	C21:0	0.15	2463.2[a]
Behenic	$C_{22}H_{44}O_2$	C22:0	10.54	2569[a]
Tricosylic	$C_{23}H_{46}O_2$	C23:0	0.23	2668.1[a]
Cerotic	$C_{26}H_{52}O_2$	C26:0	0.23	2962[b]
Lignoceric	$C_{24}H_{48}O_2$	C24:0	3.08	2685[a]
Lauric	$C_{12}H_{24}O_2$	C12:0	0.02	1567[a]
Cis-10-Heptadecenoic	$C_{17}H_{32}O_2$	C17:1	0.12	2073.2[a]
Cis-10-Nonadecenoic	$C_{19}H_{36}O_2$	C19:1	0.09	2256 [a]
Erucic acid	$C_{22}H_{42}O_2$	C22:1	0.32	2572[b]
Paullinic	$C_{20}H_{38}O_2$	C20:1	0.29	2374[b]
Gondic	$C_{20}H_{38}O_2$	C20:1	4.88	2374[b]

* The obtained results in terms of fatty acid methyl esters from GC-MS library data system reviewed and the results listed out in the form of fatty acid chains. KI: kovats index, a: NIST (33) , b: Chemspider (34).
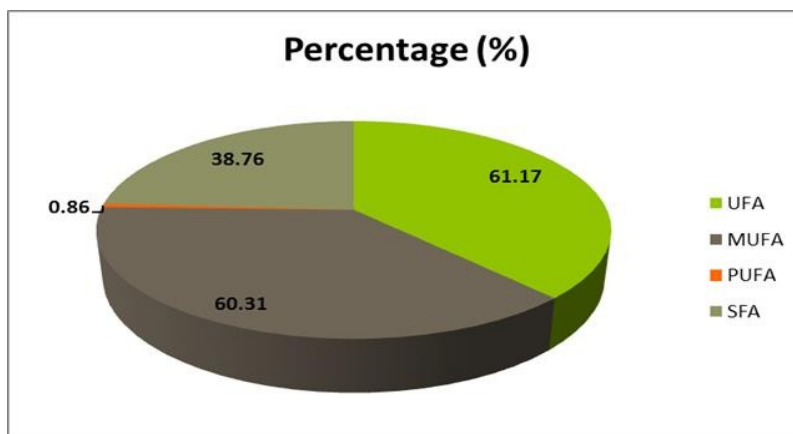
Figure 1: Types of fatty acids present in *M. oleifera* seed oil.

CONCLUSION

In this study, the physicochemical properties and fatty acid composition of the Sudanese *M. oleifera* seed oil assessed by standard and established methods. Based on the results of the study, the oil properties are interesting and promising for several applications. The overall results of this analysis show that the oil content was 42.87%; major fatty acid compositions were oleic acid (51.74%) and followed by behenic acid (10.54%), palmitic acid (9.20%), stearic acid (8.46%) and gondic acid (4.88%). The unsaturated fatty acid makes 61.17% of the compositions, whereby the MUFA, PUFA and SFA were 60.31, 0.86 and 38.76 wt.%. Most of the obtained results in this study were acceptable and similar to previous studies. Thus, the Sudanese *M. oleifera* seed oil which does not contain linolenic acid could not be suitable for several applications such as paint, varnish, and ink industries, but it might be suitable for other industrial aspects such as pharmaceutical, cosmetic, and food industries, due to its fatty acid content. Therefore, further studies on Sudanese *M. oleifera* are needed to investigate their potential as raw materials for new industrial products and applications to increase the economic feasibility of future commercial cultivation of the tree.

ACKNOWLEDGEMENTS

AUTHORS CONTRIBUTION STATEMENT

Abeer A. Idris and Azhari H. Nour conceptualized and gathered the data with regard to this work. Mahmoud M. Ali, Ibrahim Y. Erwa, Omer A. Omer Ishag and Abdurahman H. Nour analyzed these data and necessary inputs were given towards the designing of the manuscript. All authors discussed the methodology and results and approved the final manuscript.

CONFLICT OF INTEREST

Authors declare no conflict of interest exists.

Table 4: Fatty acid composition of *M. oleifera* seed oil reported in literature.

Fatty acids			Composition (%)*				
Lauric	C12:0	N/A	0-0.3	N/A	N/A	N/A	N/A
Myristic	C14:0	0.78	0.3-1.5	0.2	0.72	N/A	0.13
Palmitic	C16:0	10.64	25-46	7.8	6.1	5.66-6.46	6.46
Palmitoleic	C16:1	N/A	0.82–3.44	2.9	1.2	1.43-1.92	0.09
Stearic	C18:0	6.07	2.68–6.00	7.6	4.6	4.79-7.94	5.88
Oleic	C18:1	22.51	67.79–79.50	70	78.7	73.30-79.58	71.21
Linoleic	C18:2	N/A	0.83	0.9	N/A	0.58-0.59	0.06
Linolenic	C18:3	N/A	0.36	0.5	1.8	0.15-0.17	0.18
Arachidic	C20:0	2.21	2.14-4.08	4.2	2.3	1.57-5.1	3.62
Behenic	C22:0	1.03	4.57–7.10	6.2	4.5	2.62-3.62	6.41
Lignoceric	C24:0	N/A	0.54	N/A	N/A	N/A	N/A
Gondic	C20:1	N/A	N/A	N/A	N/A	N/A	N/A
	SFA	N/A	17.24–23.79	49.1	18.3	15.00-22.83	N/A
	MUFA	N/A	71.71–80.70	N/A	79.9	N/A	N/A
	PUFA	N/A	0.41–2.20	N/A	1.8	N/A	N/A
	UFA	N/A	N/A	50.9	79.9	77.14-84.98	N/A
References	(a)	(b)		(c)	(d)	(e)	(f)

N/A: Data not available, * some data modified as a mean average from origin sources a: Adegbe et al. (21), b: Leone et al. (1), c: Ghazali and Mohammed (37), d: Ogunsina et al. (24), e: Barakat and Ghazal (5), f: Lalas and Tsaknis (32).

REFERENCES

1. Leone A, Spada A, Battezzati A, Schiraldi A, Aristil J, Bertoli S. Moringa oleifera seeds and oil: characteristics and uses for human health. International Journal of Molecular Sciences. 2016 Dec;17(12):2141.

2. Gopalakrishnan L, Doriya K, Kumar DS. Moringa oleifera: A review on nutritive importance and its medicinal application. Food science and human wellness. 2016 Jun 1;5(2):49-56.

3. Mathur A. Renewable energy sources from Moringa Oleifera seed oil: a rich source of oil for bio diesel. International Journal of Computer Applications. 2014;975:8887.

4. Maizuwo AI, Hassan AS, Momoh H, Muhammad JA. Phytochemical constituents, biological activities, therapeutic potentials and nutritional values of Moringa oleifera (Zogale): A review. Drug Des. Med. Chem. 2017 Oct 28;3:60-6.

5. Barakat H, Ghazal GA. Physicochemical properties of Moringa oleifera seeds and their edible oil cultivated at different regions in Egypt. Food and Nutrition Sciences. 2016;7(06):472.

6. Orhevba BA, Sunmonu MO, and Iwunze HI. Extraction and Characterization of Moringa oleifera Seed Oil. Res Rev J Food Dairy Technol. 2013;1(1):22–7.

7. Nour AH, Elhussein SA, Osman NA. Characterization and chemical composition of the fixed oil of fourteen basil (Ocimum basilicum L.) accessions grown in Sudan. International journal of chemical technology. 2009;1(2):52-8.

8. Ramaiya SD, Bujang JS, Zakaria MH. Physicochemical, fatty acid and antioxidant properties of passion fruit (Passiflora species) seed oil. Pakistan Journal of Nutrition. 2019;18(5):421-9.

9. Jessinta S, Azhari HN, Saiful NT, Abdurahman HN. Impact of geographic variation on physicochemical properties of neem (Azadirachta indica) seed oil. Int J Pharm Sci Res. 2014 Oct 1;5(10):4406-13.

10. Ustun-Argon Z, İlhan N, Gökyer A, Büyükhelvacıgil-Öztürk S, Koparal B. Phytochemical Evaluation of Morus alba Seeds and Cold Pressed Oil. JOTCSA. 2019;6(1):41–50.

11. Yabalak E. Radical Scavenging Activity and Chemical Composition of Methanolic Extract from Arum dioscoridis SM. var. dioscoridis and Determination of Its Mineral and Trace Elements. JOTCSA. 2018;5(1):205–18.

12. Tegin I, Yabalak E, SADIK B, Fidan M. Evaluation of chemical content and radical scavenging activity of Allium Vineale L. extract and its elemental analysis. Rev Roum De Chim. 2019 Aug 1;64(8):673-9.

13. Ouilly JT, Bazongo P, Bougma A, Kaboré N, Lykke AM, Ouédraogo A, Bassolé IH. Chemical composition, physicochemical characteristics, and nutritional value of Lannea kerstingii seeds and seed oil. Journal of analytical methods in chemistry. 2017 Jan 31;2017.

14. Chatepa LE, Uluko H, Masamba K. Comparison of oil quality extracted from selected conventional and non-conventional sources of vegetable oil from

Malawi. African Journal of Biotechnology. 2019 Feb 20;18(8):171-80.

15. Ayadi MA, Grati-Kamoun N, Attia H. Physico-chemical change and heat stability of extra virgin olive oils flavoured by selected Tunisian aromatic plants. Food Chem Toxicol. 2009;47(10):2613–9.

16. Aleksic V, Knezevic P. Antimicrobial and antioxidative activity of extracts and essential oils of Myrtus communis L. Microbiological Research. 2014 Apr 1;169(4):240-54.

17. Kaur H, Singh PG, Yusup S, Wai CK. Physicochemical properties of crude rubber seed oil for biogasoline production. Procedia engineering. 2016 Jan 1;148:426-31.

18. Radha KV, Manikandan G. Novel production of biofuels from neem oil. InWorld Renewable Energy Congress-Sweden; 8-13 May; 2011; Linköping; Sweden 2011 Nov 3 (No. 057, pp. 471-478). Linköping University Electronic Press.

19. Fernandes RV, Borges SV, Botrel DA, Silva EK, Costa JM, Queiroz F. Microencapsulation of rosemary essential oil: characterization of particles. Drying Technology. 2013 Aug 18;31(11):1245-54.

20. Ibeto CN, Okoye CO, Ofoefule AU. Comparative study of the physicochemical characterization of some oils as potential feedstock for biodiesel production. ISRN Renewable Energy. 2012;2012.

21. Adegbe AA, Larayetan RA, Omojuwa TJ. Proximate analysis, physicochemical properties and chemical constituents' characterization of Moringa oleifera (Moringaceae) seed oil using GC-MS analysis. American Journal of Chemistry. 2016;6(2):23-8.

22. Talkit KM, Mahajan DT, Masand VH. Study on physicochemical properties of vegetable oils and their blends use as possible ecological lubricant. Journal of Chemical and Pharmaceutical Research. 2012;4(12):5139-44.

23. Warra AA, Wawata IG, Gunu SY, Aujara KM. Extraction and physicochemical analysis of some selected Northern Nigerian industrial oils. Archives of Applied Science Research. 2011;3(4):536-41.

24. Ogunsina BS, Indira TN, Bhatnagar AS, Radha C, Debnath S, Krishna AG. Quality characteristics and stability of Moringa oleifera seed oil of Indian origin. Journal of Food Science and Technology. 2014 Mar 1;51(3):503-10.

25. Pereira FS, Galvão CC, de Lima VF, da Rocha MF, Schuler AR, da Silva VL, de Lima Filho NM. The versatility of the Moringa oleifera oil in sustainable applications. OCL. 2016 Nov 1;23(6):A601.

26. Mohammed MI, Hamza ZU. Physicochemical properties of oil extracts from Sesamum Indicum L. seeds grown in Jigawa State–Nigeria. Journal of Applied Sciences and Environmental Management. 2008;12(2).

27. Abiodun OA, Adegbite JA, Omolola AO. Chemical and physicochemical properties of Moringa flours and oil. Global Journal of Science Frontier Research Biological Sciences. 2012;12(5):1-7.

28. Adejumo BA, Alakowe AT, Obi DE. Effect of heat treatment on the characteristics and oil yield of Moringa oleifera seeds. Int. J. Eng. Sci. 2013;2(1):232-9.

29. Adejumo BA, Inaede SG, Adamu TS. Effect of moisture content on the yield and characteristics of oil from Moringa oleifera seeds. Academic Research International. 2013 Jul 1;4(4):160.

30. Anwar F, Ashraf M, Bhanger MI. Interprovenance variation in the composition of Moringa oleifera oilseeds from Pakistan. Journal of the American Oil Chemists' Society. 2005 Jan;82(1):45-51.

31. Tamboli Y, Selokar GR, Paul A, Zala J. Feasibility testing of VCR engine using various blend of Neem oil. International journal of innovations in engineering and technology. 2013 Jun;2:170-82.

32. Lalas S, Tsaknis J. Characterization of Moringa oleifera seed oil variety" Periyakulam 1". Journal of food composition and analysis. 2002 Feb 1;15(1):65-78.

33. NIST [Internet]. NIST: National Institute of Standards and Technology. Available from: https://webbook.nist.gov/chemistry/

34. Chemspider [Internet]. ChemSpider | Search and share chemistry. Available from: https://www.chemspider.com/Search.aspx

35. Janaki S. Characterization of cold press Moringa oil. International Journal of Science and Research. 2015;4:386-9.

36. Arafat MG. Physico-chemical properties of oil produced from Moringa oleifera, Jatropha curcas and Carthamus tinctorius L seeds. International Journal of Advanced Research. 2013;1(4):181-7.

37. Ghazali HM, Mohammed AS. Moringa (Moringa oleifera) seed oil: composition, nutritional aspects, and health attributes. In: Nuts and seeds in health and disease prevention 2011 Jan 1 (pp. 787-793). Academic Press.